**Robert McIntire**
**Pierre Donnell**
**Editors**

# Integrated Circuits, Photodiodes and Organic Field Effect Transistors

NOVA

# INTEGRATED CIRCUITS, PHOTODIODES AND ORGANIC FIELD EFFECT TRANSISTORS

No part of this digital document may be reproduced, stored in a retrieval system or transmitted in any form or by any means. The publisher has taken reasonable care in the preparation of this digital document, but makes no expressed or implied warranty of any kind and assumes no responsibility for any errors or omissions. No liability is assumed for incidental or consequential damages in connection with or arising out of information contained herein. This digital document is sold with the clear understanding that the publisher is not engaged in rendering legal, medical or any other professional services.

# INTEGRATED CIRCUITS, PHOTODIODES AND ORGANIC FIELD EFFECT TRANSISTORS

ROBERT MCINTIRE
AND
PIERRE DONNELL
EDITORS

**Nova Science Publishers, Inc.**
*New York*

Copyright © 2009 by Nova Science Publishers, Inc.

**All rights reserved.** No part of this book may be reproduced, stored in a retrieval system or transmitted in any form or by any means: electronic, electrostatic, magnetic, tape, mechanical photocopying, recording or otherwise without the written permission of the Publisher.

For permission to use material from this book please contact us:
Telephone 631-231-7269; Fax 631-231-8175
Web Site: http://www.novapublishers.com

**NOTICE TO THE READER**
The Publisher has taken reasonable care in the preparation of this book, but makes no expressed or implied warranty of any kind and assumes no responsibility for any errors or omissions. No liability is assumed for incidental or consequential damages in connection with or arising out of information contained in this book. The Publisher shall not be liable for any special, consequential, or exemplary damages resulting, in whole or in part, from the readers' use of, or reliance upon, this material. Any parts of this book based on government reports are so indicated and copyright is claimed for those parts to the extent applicable to compilations of such works.

Independent verification should be sought for any data, advice or recommendations contained in this book. In addition, no responsibility is assumed by the publisher for any injury and/or damage to persons or property arising from any methods, products, instructions, ideas or otherwise contained in this publication.

This publication is designed to provide accurate and authoritative information with regard to the subject matter covered herein. It is sold with the clear understanding that the Publisher is not engaged in rendering legal or any other professional services. If legal or any other expert assistance is required, the services of a competent person should be sought. FROM A DECLARATION OF PARTICIPANTS JOINTLY ADOPTED BY A COMMITTEE OF THE AMERICAN BAR ASSOCIATION AND A COMMITTEE OF PUBLISHERS.

**LIBRARY OF CONGRESS CATALOGING-IN-PUBLICATION DATA**

Integrated circuits, photodiodes, and organic field effect transistors / editors, Robert McIntire and Pierre Donnell.
p. cm.
Includes index.
ISBN 978-1-61761-868-0 (Ebook)
1. Integrated circuits. 2. Diodes. 3. Organic field-effect transistors. I. McIntire, Robert. II. Donnell, Pierre.
TK7874.I47142 2009
621.3815--dc22
2009004983

*Published by Nova Science Publishers, Inc. ✢ New York*

# CONTENTS

**Preface** **vii**

**Research and Review Studies** **1**

**Chapter 1** Metamaterials Technology: Application to Radiofrequency and Microwave Circuits **3**
*Ferran Martín and Jordi Bonache*

**Chapter 2** Reliability Assessment of Integrated Circuits and its Misconception **45**
*Cher Ming Tan*

**Chapter 3** Design of a Multichannel Integrated Biosensor Chip and Microelectronic System for Extracellular Neural Recording **69**
*Xin Zhang, Yingxin Li, Yulong Zhang, Zuhui Chen, Shi Liu, Richard D. Nelson and John C. LaRue*

**Chapter 4** Scene Analysis of Unstable Video Flows – Using Multiple Retina Channels and Attentional Methods **95**
*Anna Lázár, Karl Pauwels, Marc Van Hulle and Tamás Roska*

**Chapter 5** Photocurrent Study of the Transport Mechanism in Molecular Self-Assembling Field Effect Transistors **115**
*Andrei V. Pakoulev, Dmitry Zaslavsky and Vladimir Burtman*

**Chapter 6** Electron Spectroscopy and near Infrared Photocurrent Measurement of Working Organic Thin Film FETs **161**
*Toshihiro Shimada, Manabu Ohtomo and Tetsuya Hasegawa*

**Chapter 7** Solution-processed Organic Thin-Film Transistors **185**
*Jeong-In Han, Sung Kyu Park and Yong-Hoon Kim*

**Chapter 8** Organic Luminescence Device Degradation Analysis and Lifetime Improvement **209**
*Ke Lin, Ramadas Senthil Kumar, Lai Szu Cheng and Chua Soo Jin*

**Chapter 9** Photodiodes: A Powerful Tool in HPLC for Peak Detection and Identification **227**
*Victoria F. Samanidou, Ioannis N. Papadoyannis and Eftichia G. Karageorgou*

**Chapter 10** Photodiodes: Characteristics and Applications in Textile Industry and Biomedicine **293**
*V. Carvalho, G. Minas, F. Soares, M.R. Vasconcelos and M. Belsley*

**Chapter 11** Cardiac Optical Mapping: Biomedical Research Application of Photodiodes **343**
*Herman D. Himel IV, Joseph Savarese, Vikram Lakireddy and Nabil El-Sherif*

**Short Communications** **367**

**Short Communication A**
Basal Ganglia Circuit and Bladder Function: Clinical Implication to Parkinson's Disease **369**
*Ryuji Sakakibara*

**Short Communication B**
Charge Injection and Surface Modification Route for Pentacene - Based Ambipolar Field-Effect Transistors **383**
*Chih-Wei Chu*

**Short Communication C**
The Coupling of the MRS Photodiode with Coated Extruded Scintillator using Y7 and Y11 WLS Fibers **395**
*D. Beznosko, A. Dyshkant, C.K. Jung, C. McGrew, A. Pla-Dalmau and V. Rykalin*

**Short Communication D**
Avalanche Photodiode as an Electron Detector **405**
*Keiichi Ogasawara*

**Index** **421**

# PREFACE

This book begins with metamaterials technology, a novel approach for the design of radiofrequency and microwave components and circuits. Since reliability is a key success factor to engineering products today, the different misconceptions in the common reliability practices of integrated circuits manufacturers are presented.

A bio-inspired approach designed to solve some tasks raised in the "Bionic Eyeglass Project" is described, which aims to help the everyday life of visually impaired people.This book also discusses the intrinsic charge transport in organic field-effect transistors based on self-assembled monolayers and on the nature of transport in organic systems. A combined view of spectroscopic studies on electronic states in working organic thin film is presented based on experimental results. Solution-processed organic thin-film transistors are also introduced.

The use of photodiode array detectors as a powerful tool in HLPC is examined with an emphasis in peak identification and confirmatory results. The mechanisms of avalanche photodiodes as a particle detector and its latest results are reviewed. The main characteristics and properties of photodiodes and their applications in textile industry and biomedicine are also discussed. Finally, the specific application of photodiodes in cardiac optical mapping is presented.

Recently, metamaterials technology has emerged as a novel approach for the design of radiofrequency and microwave components and circuits. Metamaterials are artificial materials, made of small size inclusions (or “atoms”), whose electromagnetic properties can be tailored to some extent, and rather than depending on the composition, these properties depend on the arrangement of the constitutive elements. Thus, for instance, it is possible to synthesize artificial media exhibiting a negative effective magnetic permeability and dielectric permittivity with non-magnetic metallic particles etched on a dielectric slab. Media with such properties (negative permeability and permittivity) are not present among natural materials. These controllable properties can be achieved by designing the structures with electrically small inclusions, so that effective media properties are obtained. Metamaterials are of interest in many areas. For instance, it has been recently demonstrated the possibility of implementing invisible cloaks for microwave radiation. However, one of the main areas where metamaterials are of major interest is in RF/microwave engineering. The small size of the unit cells and the controllable properties, are very interesting for the design of planar components with small dimensions and high performance. Also, it is possible to design devices based on new functionalities, multiband components and circuits with enhanced operative bandwidths. These metamaterial based design techniques can be applied in a wide range of frequencies, from RF up to millimetre wave circuits. Several prototype devices (filters, diplexers, power dividers, couplers, and reconfigurable components) in planar technology, illustrative of the possibilities of the approach, will be presented in Chapter 1. This will include realizations in PCB and also in advance microelectronics technologies, such as RF-MEMS and MCM-D technologies.

Reliability is a key success factor to Engineering products today, and the requirement for integrated circuit reliability is increasing due to increasing complexity of electronic products, market globalization and manufacturing outsourcing. This chapter illustrates the important of integrated circuit reliability and the rationale behind its “ridicules” requirement of more than 50 years.

Reliability test is not new to the integrated circuit manufacturers. However, there are several seemingly intuitive concepts in the reliability tests and test data analyses that are being practice in the manufacturers today are incorrect and can lead to over-estimation of product reliability grossly. This chapter shows the different misconceptions in the common reliability practices of integrated circuits manufacturers with examples.

The purpose of Chapter 2 is to bring awareness of these misconceptions. All these misconceptions can be resolved with the proper use of reliability statistics which is beyond the scope of this chapter.

As presented in Chapter 3, a multi-channel mixed-signal full-customized CMOS integrated biopotential sensor chip and microcontroller based electronic system have been developed for *in vitro* extracellular recording of neural signals. The multi-site planar microelectrode array sensors for simultaneous neural signal recording have been designed and prototyped with on-chip fully integrated analog signal processing circuitry and control system. The biosensor system is built with hierarchical modules that incorporate microelectrode electrophysiological sensors, analog signal buffers configured with two-stage amplifier, gain providing amplifiers based on operational transconductance amplifier (OTA) with capacitive feedback and digital logic and interface units including clock generation and time division multiplexing control circuitry. The prototype IC was fabricated by MOSIS using AMI C5 0.5 μm, double poly, triple metal layer CMOS technology. The electroless gold plating process is used to replace the aluminum material obtained from the standard CMOS process with biocompatible metal gold in the planar microelectrode array sensors to prevent cell poisoning and undesirable electrochemical corrosion. The post-CMOS processing and packaging techniques applied to the biosensor chip promotes biocompatibility and stability in the aqueous cell culture environment. A microcontroller based electronic system interfacing the biosensor IC with a client PC for the post processing of the action potential signals sensed by the biopotential sensor chip was also developed. The biosensor has been tested electrically in the presence of electrolyte environment and is shown to provide a satisfactory signal-to-noise ratio for neural signals with amplitudes in the range of 600μV-2mV and frequencies in the range of 100 Hz – 10 kHz. Biological example *in vitro* recordings conducted with neurons from *Aplysia californica* are shown in this research work, which proves the full functionality in neural recording of the biosensor chip incorporated with the interfacing electronic system based on 32-bit Motorola ColdFire MCF5307 RISC processor. On-chip amplification and time division multiplexing techniques of the multi-channel biosensor chip allow the large-scale simultaneous recording of biological activities of neurons.

Chapter 4 describes a bio-inspired approach designed to solve some tasks raised in the 'Bionic Eyeglass Project' [1], which aims to help the everyday life of blind or visually impaired people. The purpose of this approach is to provide a specific kind of information or to determine the region of interest ("ROI") in a low-resolution and unstable video flow recorded with a mobile phone by the visually impaired person. In the present paper the authors introduce a new stabilization method and three different tasks are resolved: firstly, locating LED (light-emitting diode) indicators, secondly, locating traffic signs, and thirdly, deciding whether there is any switched-on lamp in a room. The test database has been made out of real-life scenes. The authors provide detailed evaluation results referring to the execution of those tasks.

Our descriptive context refers to the recently modeled mammalian retina channel decomposition [2]. Using it the authors can avoid - at least partially - the classical difficulty that image processing algorithms nowadays face, namely that the intensity or color values of the same object largely depend on the actual lighting conditions. A further difficulty referring to the lamp-detection is that the solution has to be completely independent of the input's actual brightness. The method the authors introduce relies only on a single retina channel and achieves a very high accuracy: the ratio of the correct answers is around 99%. The other two tasks are to carry out an approximately real-time ROI-detection algorithm based solely on image information from an unstable low-resolution video-flow containing complex real-life scenes with unconstrained lighting conditions. The accuracy of the introduced methods is around 80%.

The authors also make use of a stabilization algorithm designed especially for this project. In order to yield the desired information, they process channel-data as well as saliency maps. The presented method can be useful in a variety of other application areas.

Chapter 5 focuses on the intrinsic charge transport in organic field-effect transistors (OFETs) based on self-assembled monolayers (SAMs) and on the nature of transport in organic systems, in which surface and bulk properties are undistinguishable due to scale of consistent materials. Recently developed SAM-OFETs are characterized by photovoltaic measurements. The dynamics of charge transport are determined and used to clarify a transport mechanism. Taken together, these SAM devices provide a unique tool to study the fundamentals of polaronic transport on organic surfaces and to discuss the SAM OFET performance. An outline is presented of the outstanding problems that are now becoming experimentally reachable owing to the development of SAM-OFETs. Vapor phase molecular self-assembly of 1,4,5,8-Naphthalene-tetracarboxylic diphenylimide (NTCDI) having a rich $\pi$-stacking charge delivery system is used to enhance the performance of molecular field-effect devices. Charge mobility in SAM-OFET could achieve values of more than 30 $cm^2 V^{-1} s^{-1}$. The dynamics of charge transport in NTCDI-derived SAM-OFETs were probed using time-resolved measurements in an NTCDI-derived photovoltaic cell device. Time-resolved photovoltaic studies allow us to separate the charge annihilation kinetics in the conductive NTCDI channel from the overall charge kinetic in a SAM-OFET device. It has been demonstrated that tuning of the type of conductivity in NTCDI SAM-OFET devices is possible by changing Si substrate doping. In addition, the possibility of measuring transport in highly ordered SAM structures shines light on the polaron charge transfer in organic materials. Our study proposes that a cation-radical exchange (redox) mechanism is the major transport mechanism in SAM nanodevices. The role and contribution of the transport through delocalized states of redox active surface molecular aggregates of NTCDI are exposed and investigated in this chapter.

Chapter 6 is intended to provide a combined view of spectroscopic studies on electronic states in working organic thin film FETs based on our experiments. Three kinds of spectroscopic techniques are presented: Ultraviolet Photoelectron Spectroscopy (UPS), Electron Energy Loss Spectroscopy(EELS), and near infrared photocurrent spectroscopy (NIRPCS). Information on energy levels, effective mass, location of field induced carriers and gap states related with traps and off-current of the devices can be obtained from those spectroscopic techniques.

In Chapter 7, solution-processed organic thin-film transistors (OTFTs) using poly (3-hexylthiohpene) (P3HT) and 6,13-bis(triisopropylsilylethynyl) (TIPS) pentacene are introduced. By properly selecting the organic solvent for semiconductor, adjusting the surface energy of gate insulator and introducing a novel source/drain electrode structure, high performance OTFTs can be realized. This chapter focuses on effect of solvent on the crystallinity, morphology and electrical performances of OTFTs based on P3HT and TIPS pentacene.

Organic light emitting device degradation mechanisms have been elaborated. In Chapter 8, a novel technique to inhibit the growth of dark spots and improve device lifetime have been proposed. The technique involved the development of organic film such as Parylene, Teflon and other suitable high barrier and dielectric organic polymer materials in the device structure which proved to improve device lifetime by 100 folds. A new analytical tool, low frequency fluctuation, has been setup for organic device lifetime characterization. Correlation between the process of device degradation and the low frequency fluctuation was successfully established.

Photodiodes are semiconductor devices with a p–n or p–i–n structure for the detection of light. When used as an array (a number of diodes placed side by side), they serve as light sensors characterized by excellent linearity with respect to incident light, low noise, wide spectral response and mechanical ruggedness. This advanced type of detection is the most sophisticated UV-Vis detector widely applied in HPLC. In contrast to a conventional single wavelength detector, photodiode array (PDA) detectors are used for monitoring spectra of analytes passing through a sample flow cell over the entire wavelength range. Continous monitoring of the absorbance spectra of eluted components provides a great deal of information for an analysis. One of the most significant advantages of the PDA detector to the HPLC analyst is that it permits the recognition of unknown constituents in a complex matrix. Peak identification is achieved using spectral information and detection is not only based on retention time. Spectral data stored in a computer, can serve as a bank for identifying unknown peaks. PDA detectors can be used both for routine applications and applications such as method development and peak characterization.

Additionally a PDA detector can provide information using the acquisition of spectra to determine peak purity. The latter is of paramount importance in pharmaceutical industry, where it is designated to detect the presence of co-eluting impurities.

Applications of PDA detection can be found in all analytical fields, especially in cases where confirmatory analytical methods are required. In food quality control samples, residual analytes in food of animal origin can be detected so that non-compliant samples can be traced. In clinical analysis, it can be used in pharmacokinetics, metabolism and bioavailability studies. Moreover, drugs can be monitored so that therapeutic levels can be estimated and effective drug doses can be personalized in patients.

In Chapter 9, the use of PDA detectors as a powerful tool in HPLC will be discussed with emphasis in peak identification and confirmatory analysis. Examples of applications in several analytical fields will be provided.

Chapter 10 presents the main characteristics and properties of photodiodes, discussing also their applications in the Textile Industry and Biomedicine.

In the Textile Industry photodiodes can be used to characterize both yarn diameter and hairiness using a coherent optical signal processing technique based on Fourier analysis. The characterization of the degree of hairiness using a high-pass spatial Fourier filter introduces several advantages in the hairiness measurement compared to other conventional approaches. These advantages include a signal reference for 0 % yarn hairiness, the elimination of contributions from the yarn contours, a measurement technique which is largely independent of the specific yarn diameter, yarn shape or orientation in the plane perpendicular to the optical axis. On the other hand, a reliable measurement of yarn diameter can be made using the same optical set-up but employing a low-pass spatial filter to eliminate yarn hairiness contribution, increasing the final measurement precision. In both measurements, a single projection direction is sufficient for a correct characterization, as both hairiness and yarn irregularities tend to be uniformly distributed over a full rotation of the yarn. These characteristics are fundamental for a reliable and precise characterization of yarn, introducing a superior level of yarn parameterization in Textile Industry.

In Biomedicine photodiodes can be used, as the detection element, in biochemical analysis of body fluid samples based on spectrophotometry (interaction of electromagnetic radiation with biochemical compounds). They can be used to read the light intensity that is absorbed, emitted or reflected by a sample and therefore determine the concentration, activity, amount and structure of a compound. They can also be used in CMOS (Complementary Mosfet Oxide Semiconductor) imagers for X-ray detection or for being integrated in endoscopic capsules. They benefit from their wide availability, reduced component and costs and, more importantly, the capacity to accommodate multi-functional circuitry on-chip, all functions available in CMOS processes. All these applications take advantage of the fact that absorption of light in silicon and other semiconductor materials is wavelength dependent, which causes the penetration depth of light to be wavelength dependent. Therefore, selecting both the suitable junction depth and the oxide layers on top, photodiodes can be programmed to have their quantum efficiency increased at a particular wavelength.

As discussed in Chapter 11, with the emergence of $V_m$-sensitive dyes in the 70's, it became possible to interrogate cardiac tissue optically, and soon afterward optical methods were developed to interrogate multiple spots simultaneously in a small (~$cm^2$) region of tissue. Since then the field of cardiac optical mapping (COM) has greatly expanded in scope, from relatively simple early recordings using one or relatively few spots to highly complex optical systems. These include high spatiotemporal resolutions systems, panoramic systems, and systems which are capable of interrogating electrophysiological activity beneath the surface. In addition, several labs have used photodiode-based optical mapping systems to map $V_m$ and $Ca_i$ simultaneously, on both the whole heart and in monolayer cell cultures of cardiac myocytes.

Bladder dysfunction (urinary urgency / frequency) is a common non-motor disorder in Parkinson's disease (PD), which significantly affects quality of life in the patients. According to the animal studies and the clinical imaging studies, basal ganglia circuit influences not only motor but also bladder function. Bladder (detrusor) overactivity is the major cause of bladder dysfunction, which considered an exaggerated micturition reflex in PD. The net effect of the basal ganglia on micturition is thought to be inhibitory. Functional neuroimaging during bladder filling resulted in activation in the globus pallidus of normal volunteers and in the putamen in patients with PD. In contrast, dopamine transporter imaging was decreased in PD patients with urinary dysfunction than in those without it. Bladder overactivity can be reproduced in experimental parkinsonism. Electrical stimulation of the substantia nigra pars compacta (SNc) inhibited the micturition reflex, and striatal dopamine levels *in situ* significantly increased in the urinary storage phase. The micturition reflex is under the influences of dopamine (both inhibitory in D1 and facilitatory in D2) and GABA (inhibitory). Both the SNc neuronal firing and the released striatal dopamine seem to activate the dopamine D1-GABAergic *direct pathway*, which not only inhibits the basal ganglia output nuclei, but also may inhibit the micturition reflex via GABAergic collateral to the micturition circuit. Intracerebroventricularly administered dopamine inhibits the micturition reflex, and high frequency stimulation in the subthalamic nucleus results in bladder inhibition. In patients with PD, disruption of this pathway may lead to bladder overactivity and resultant urinary urgency/frequency. Manifestation of the disrupted basal ganglia circuit on bladder function in patients with Parkinson's disease and its clinical management are reviewed briefly in the first Short Communication.

The complexity of the device fabrication process for the complementary metal-oxide-semiconductor (CMOS) technology could greatly be reduced by the utilization of ambipolar thin film transistors. Wide variety of techniques was employed for the realization of such ambipolar TFTs. One such method which is simple and robust is discussed herein. The contribution to the occurrence of ambipolar conduction of a pentacene-based field-effect transistor can be realized by dual interface engineering, which occurs at the dielectric/semiconductor and electrode/semiconductor interface. The former utilized a hydroxyl-free interfacial modified layer, and the latter was made feasible by the use of appropriate metal source/drain electrodes and ultra-thin nano-scale chemical compound insertion layer. For a hydroxyl-free interfacial modified layer, polymethylmethacrylate (PMMA) and Polyvinyl Alcohol (PVA) are appropriate candidates, and one can use alkali halogen materials (e.g. LiF, CsF) or carbonate (e.g. $Cs_2CO_3$) or metal oxide (e.g. MgO) or ultra-thin low work function metal (e.g. Ca) or polymer insulator (e.g. PMMA) etc for the enhancement of the carrier injection. The field-effect hole and electron mobility of around 0.02 $cm^2$/V-s and 0.002 $cm^2$/V-s, respectively, were extracted from the transfer characteristics of pentacene organic field-effect transistors (OFETs) utilizing PMMA as the trap-reduction interfacial modified layer and Al as the source and drain (S/D) electrodes. In addition, the mobility values for hole and electron are estimated as 0.01 and 0.009 $cm^2$/V-s, which were measured from pentacene organic field-effect transistors (OFETs) utilizing PMMA as the trap-reduction interfacial modified layer and LiF as the ultra-thin nano-scale chemical compound. One of the applications of the ambipolar transport is the organic light-emitting transistors, and light emitting transistors combine the light emission properties of an organic light-emitting diode and the switching properties of an organic field-effect transistor. Hence, the organic light-emitting transistors can further offer a new opportunity to the development of organic optoelectronic integrated circuit. Keeping in view of such window of applications, the second Short Communication describes the fabrication routes and the demonstration of the ambipolar TFTs and their complementary circuits.

In the third Short communication, extruded scintillator with co-extruded hole and reflective coating will be used both in MINERvA and T2K experiments. The authors have studied WLS (wavelength shifting) fibers (Y11 and Y7) for different shapes of the extruded scintillator readout using MRS (Metal/Resistor/Semiconductor) photodiode. The Y7 fiber was considered because of its lower then Y11 cost. The purpose was to find out which fiber performs better in above configurations. First, the responses for both types of fibers, with and without optical grease, were measured by PMT (Photomultiplier Tube). The PE (photoelectron) yield from cosmic rays for different scintillator shapes and both fiber types, as seen by MRS photodiode, are reported. The attenuation lengths of Y11 and Y7 were measured using MRS Photodiode. Y7 fiber shows somewhat better performance at short distances from the photo detector, while Y11 performs better at larger lengths.

Compared to normal photodiodes, an avalanche photodiode (APD) has internal gain. With a large reverse bias voltage on diodes, the electric field in the active region can exceed a critical value. There, signal carriers are accelerated to a certain velocity and create other electron-hole pairs in the active region. Then the avalanche-like multiplication of the signals can occur incrementally. APDs offer fascinating properties in terms of the detection of minute signals and fast response. The high electric field makes signal carriers fast when passing through the active region. Although APDs are widely used for photo-electronic devices, they are also applicable for ionizing particles. Because of these properties, APD makes it possible to detect extremely low energy particles even under the environment of high temperature. Thanks to technological improvements of the semiconductor process in recent days, excellent APDs for electrons are available. In the fourth Short Communication, the mechanism of APDs as a particle detector and its latest results are reviewed.

# RESEARCH AND REVIEW STUDIES

In: Integrated Circuits, Photodiodes…
Editors: R. McIntire and P. Donnell, pp. 3-44

ISBN: 978-1-60692-660-4

© 2009 Nova Science Publishers, Inc.

*Chapter 1*

# METAMATERIALS TECHNOLOGY: APPLICATION TO RADIOFREQUENCY AND MICROWAVE CIRCUITS

***Ferran Martín*[*] *and Jordi Bonache***
GEMMA/CIMITEC, Departament d'Enginyeria Electrònica
Universitat Autònoma de Barcelona, 08193 BELLATERRA (Barcelona), Spain

## ABSTRACT

Recently, metamaterials technology has emerged as a novel approach for the design of radiofrequency and microwave components and circuits. Metamaterials are artificial materials, made of small size inclusions (or "atoms"), whose electromagnetic properties can be tailored to some extent, and rather than depending on the composition, these properties depend on the arrangement of the constitutive elements. Thus, for instance, it is possible to synthesize artificial media exhibiting a negative effective magnetic permeability and dielectric permittivity with non-magnetic metallic particles etched on a dielectric slab. Media with such properties (negative permeability and permittivity) are not present among natural materials. These controllable properties can be achieved by designing the structures with electrically small inclusions, so that effective media properties are obtained. Metamaterials are of interest in many areas. For instance, it has been recently demonstrated the possibility of implementing invisible cloaks for microwave radiation. However, one of the main areas where metamaterials are of major interest is in RF/microwave engineering. The small size of the unit cells and the controllable properties, are very interesting for the design of planar components with small dimensions and high performance. Also, it is possible to design devices based on new functionalities, multiband components and circuits with enhanced operative bandwidths. These metamaterial based design techniques can be applied in a wide range of frequencies, from RF up to millimetre wave circuits. Several prototype devices (filters, diplexers, power dividers, couplers, and reconfigurable components) in planar technology, illustrative of the possibilities of the approach, will be presented. This will include realizations in PCB and also in advance microelectronics technologies, such as RF-MEMS and MCM-D technologies.

---

[*] E-mail address: Ferran.Martin@uab.es

# 1. INTRODUCTION TO METAMATERIALS

Metamaterials are artificial structures made of a periodic (or quasi-periodic) arrangement of electrically small inclusions (or "atoms"), whose electromagnetic (or optical) properties can be controlled to some extent. The dimensions of the inclusions (usually consisting on metals, dielectrics and or metallic patterns etched on a dielectric slab) are small as compared to signal wavelength at the frequencies of interest. This means that the radiation interacting with the artificial media "sees" it as a continuous medium, and effective media properties arise. Indeed, the achievable properties of metamaterials are dependent on the shape of the inclusions, rather than on its composition. To better understand this, let us consider the artificial medium proposed by Smith and co-workers in 2000 (see Figure 1) [1]. It consists on a combination of metallic posts and split ring resonators etched on a dielectric slab (we will consider these resonators in more detail later). If this structure is illuminated with microwave radiation polarized with the electric field parallel to the posts and the magnetic filed axial to the rings, there exists a certain region of the electromagnetic spectrum, above the resonance frequency of the rings, where the effective magnetic permeability, $\mu_{eff}$, and dielectric permittivity, $\varepsilon_{eff}$, are both negative. That is, certain magnetic activity is achieved with the use of non-magnetic resonant particles, and, more surprisingly, the constitutive parameters of the medium, $\varepsilon_{eff}$ and $\mu_{eff}$, are both negative, something not present among any natural know material. The artificial medium of Smith is considered to be the first bulk metamaterial exhibiting backward wave propagation, that is wave propagation opposite to the direction of the energy flow, or propagation with antiparallel phase and group velocities. This anti-parallelism between the phase and group velocities is consequence of the simultaneous negative sign of the effective permeability and permittivity. As already anticipated by Veselago 40 years ago [2], substances with $\varepsilon_{eff} < 0$ and $\mu_{eff} < 0$ are transparent media (such as those with positive values of permeability and permittivity), but they exhibit backward wave propagation. Such media are also called left handed media, negative refractive index media (a property that arises from the negative sign of the constitutive parameters), or double negative media. The term left handed media comes from the fact that in structures with negative constitutive parameters, the propagating vector, **k**, the magnetic field vector **H** and the electric field vector **E**, form a left handed triplet, as opposite to the right handed triplet that results in conventional dielectrics with positive parameters (see Figure 2). This directly comes from Maxwell's first order differential equations:

$$\nabla \times E = -j\omega\mu H \tag{1}$$

$$\nabla \times H = j\omega\varepsilon E \tag{2}$$

For plane waves, the above equations reduce to:

$$k \times E = \omega\mu H \tag{3}$$

$$k \times H = -\omega\varepsilon E \tag{4}$$

and it is apparent that depending on the sign of $\varepsilon_{eff}$ and $\mu_{eff,}$ a left handed or a right handed triplet for **k**, **H** and **E** results. Since the Pointing vector **S**, and hence the group velocity, form a right handed triad with **H** and **E,** it follows the abovementioned different sign of the phase and group velocities in left handed media.

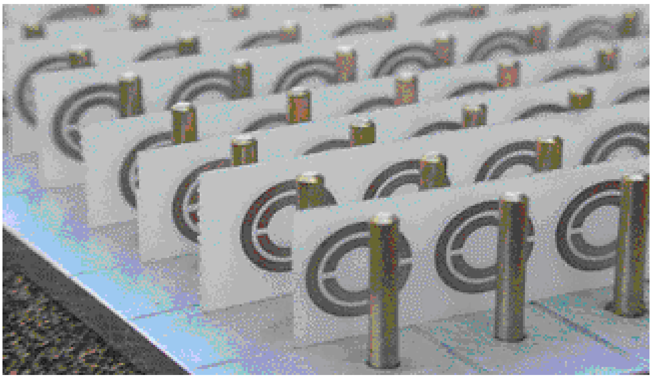

Figure 1. First artificial left handed medium proposed by Smith *et al*. Photo courtesy by D.R. Smith.

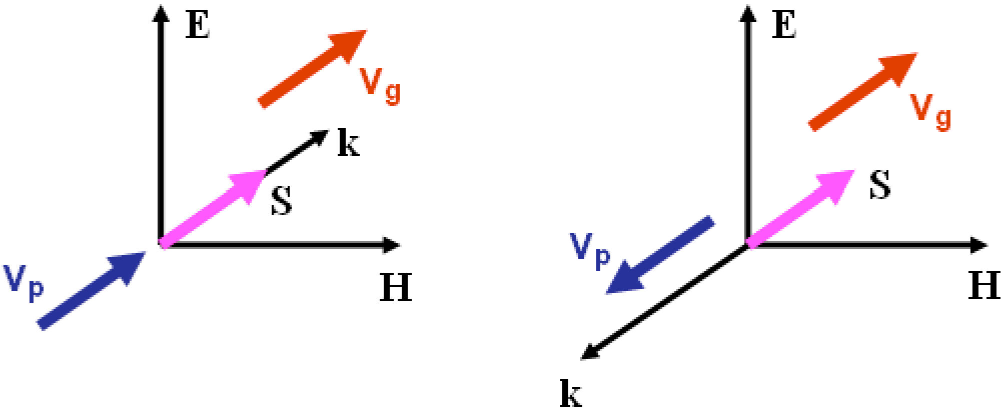

Figure 2. Illustration of the systems of vectors E, H, k and S for a plane transverse electromagnetic (TEM) wave in an ordinary (left) and left handed (right) medium.

Although the synthesis of the first left handed metamaterial (Figure 1) represented the beginning of the Metamaterials Science and Technology, such structure is highly anisotropic, and exhibits these “exotic” properties in a very narrow band. The present challenges in metamaterials research are the development of isotropic three dimensional metamaterials, operating in wide bands, and including the optical range of the electromagnetic spectrum. We recommend those readers interested on metamaterials several recent books co-authored by researchers very active in the field [3-8]. In such books, not only the application of metamaterials to RF and microwave circuit design are considered, but also many other potential applications of metamaterials, as well as the recent advances in the field. We would like to explicitly comment the high impact that the seminal work by Schurig *et al*. [9] on invisibility has caused on the Scientific Community, with an increasing number of Groups worldwide working on this stimulating topic.

## 2. METAMATERIALS IN PLANAR TECHNOLOGY: METAMATERIAL TRANSMISSION LINES

The structure of Figure 1 is a volumetric structure, but it is a one-dimensional metamaterial. Namely it exhibits left handed wave propagation for a specific direction of the propagating vector (or polarization of the magnetic and electric fields). One dimensional metamaterials in planar technology, or one-dimensional planar metamaterials, are of interest in radiofrequency (RF) and microwave engineering since the controllability of the electromagnetic properties of such structures opens the door to many circuits and devices with superior performance or based on novel functionalities. Also, due to the small size of the metamaterial inclusions, the potentiality on miniaturization is evident. Such one-dimensional planar metamaterials are referred to as metamaterial transmission lines, or "metalines" from now on, and they have found many applications that will be highlighted along this chapter. Before introducing the techniques for the synthesis of such lines, let as discuss briefly the meaning of the term metaline. Obviously, metalines are artificial lines, not artificial media. In these lines, the relevant aspect is neither the homogeneity nor the periodicity, but the controllability of the electromagnetic properties. These are the phase constant and the characteristic impedance, rather than the effective permeability and permittivity (in spite that these latter parameters can be defined and are related to the former). This is an important aspect to highlight because metamaterials are usually comprised of a high number of unit cells. Metalines can be also comprised of a high number of unit cells, but this condition is not actually necessary. Indeed, metalines can be implemented by means of a single unit cell.

### 2.1. The Dual Transmission Line Concept

There are two main approaches to the synthesis of metamaterial transmission lines: (i) the dual line concept and [10-12] (ii) the resonant type approach [13,14]. The former approach is based on the circuit dual of the transmission line model of a conventional line. This model consists on a cascade of series capacitances alternating with shunt connected inductances, as Figure 3 illustrates (the model of a conventional line is also included in Figure 3). Both transmission line models support propagating waves in a limited region of the electromagnetic spectrum, which is given by that frequency range that gives real solution to the phase constant, $\beta$, given by:

$$\cos \beta l = 1 + \frac{Z_s(\omega)}{Z_p(\omega)} \tag{5}$$

where $l$ is the unit cell length and $Z_s$ and $Z_p$ are the series and shunt impedances of the unit cell of the T-circuit model of the transmission lines. The characteristic impedance is given by:

$$Z_B = \sqrt{Z_s(\omega)[Z_s(\omega)+2Z_p(\omega)]} \tag{6}$$

For the dual transmission line model, the dispersion relation and characteristic impedance are:

$$\cos\beta_L l = 1-\frac{1}{2LC\omega^2} \tag{7}$$

$$Z_{BL} = \sqrt{\frac{L}{C}\left(1-\frac{\omega_{cL}^2}{\omega^2}\right)} \tag{8}$$

whereas for the model of a conventional line:

$$\cos\beta_R l = 1-\frac{LC}{2}\omega^2 \tag{9}$$

$$Z_{BR} = \sqrt{\frac{L}{C}\left(1-\frac{\omega^2}{\omega_{cR}^2}\right)} \tag{10}$$

where $\omega_{cR}=2/(LC)^{1/2}$ and $\omega_{cL}=1/2(LC)^{1/2}$ are angular cut-off frequencies and the sub-indices *L* and *R* are used to distinguish between the left handed –backward wave– and right handed –forward wave– structures. Such dispersion diagrams as well as the characteristic impedances are depicted in Figure 4. It is worth mentioning that frequency dispersion is present in both structures. Even though the circuit of Figure 3(b) models an ideal lossless forward transmission line, where dispersion is absent, actually this circuit is only valid for frequencies satisfying $\omega << \omega_{cR}$, i.e., in the long wavelength limit (corresponding to those frequencies where wavelength for guided waves satisfies, $\lambda_g >> l$, i.e. homogeneity conditions). To correctly model an ideal lossless transmission line at higher frequencies, we simply need to reduce the period of the structure, and accordingly the per-section inductance and capacitance of the line, *L* and *C*, with the result of a higher cut-off frequency. Thus, the lumped element T-circuit model can properly describe ideal transmission lines without dispersion. To this end we simply need to select the period such that the long wavelength limit approximation holds. Under this approximation, expressions (9) and (10) become:

$$\beta_R = \omega\sqrt{L'C'} \tag{11}$$

and

$$Z_{BR} = \sqrt{\frac{L'}{C'}} \equiv Z_{lw} \tag{12}$$

where *L'* and *C'* are the per-unit length inductance and capacitance of the transmission line (in expression 12, *L'* and *C'* can be replaced by *L* and *C* with no effect). From (11), the phase and group velocities of the forward transmission line are found to be:

$$v_{pR} = \frac{\omega}{\beta_R} = \frac{1}{\sqrt{L'C'}} = \frac{l}{\sqrt{LC}} \tag{13}$$

$$v_{gR} = \left(\frac{\partial \beta_R}{\partial \omega}\right)^{-1} = v_{pR} \tag{14}$$

and they are both positive and constant.

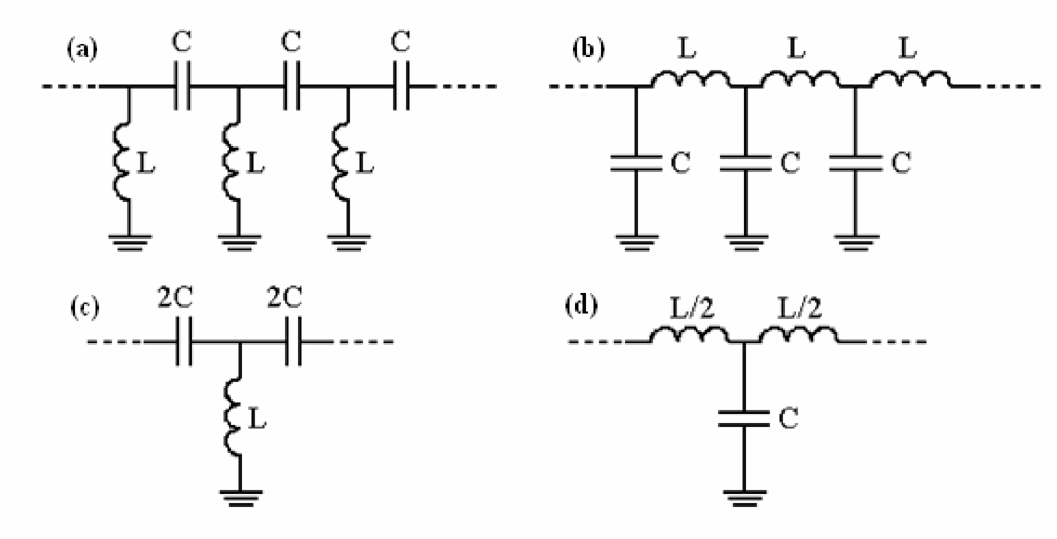

Figure 3. Equivalent circuit model of a backward (a) and forward (b) transmission lines. The T-circuit models of the basic cell structures are also indicated in (c) and (d).

For the left handed transmission line, dispersion is even present in the long wavelength limit (where homogeneity is satisfied), which in this case is obtained for frequencies satisfying $\omega >> \omega_{cL}$. Under this approximation the following results are obtained:

$$\beta_L l = -\frac{1}{\omega\sqrt{LC}} \tag{15}$$

$$Z_{BL} = \sqrt{\frac{L}{C}} \equiv Z_{lw} \tag{16}$$

$$v_{pL} = \frac{\omega}{\beta_L} = -\omega^2 l\sqrt{LC} < 0 \tag{17}$$

$$v_{gL} = \left(\frac{\partial \beta_L}{\partial \omega}\right)^{-1} = +\omega^2 l\sqrt{LC} > 0 \tag{18}$$

and the phase and group velocities have opposite signs.

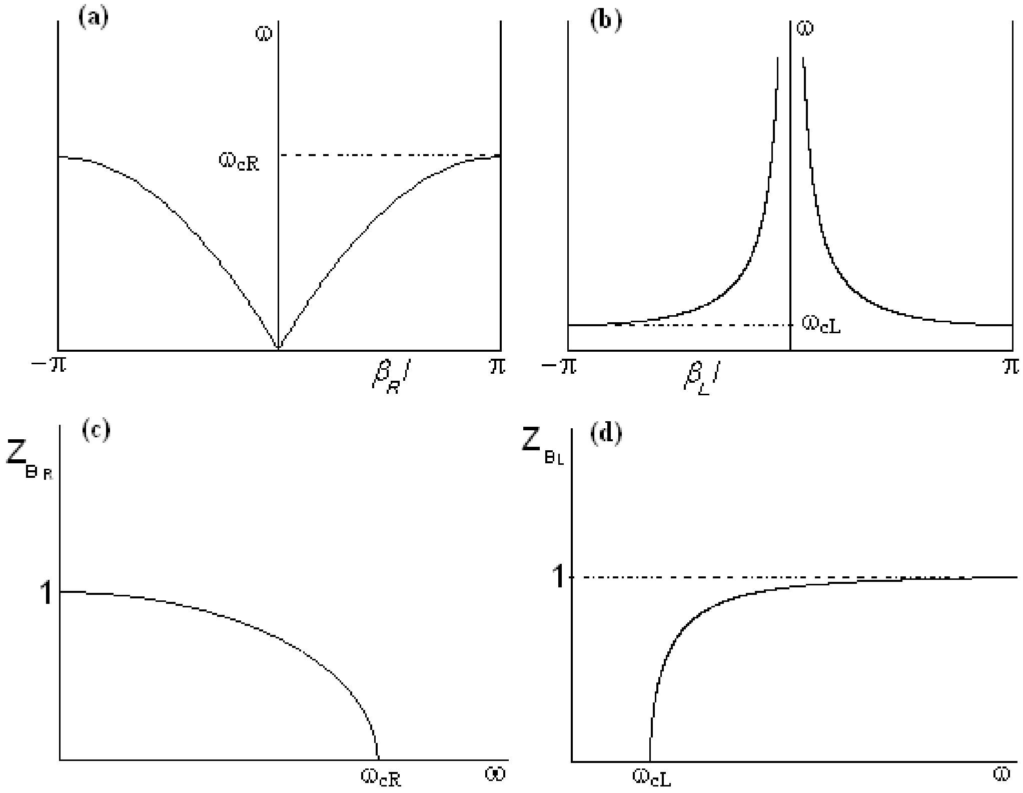

Figure 4. Typical dispersion diagram of a forward (a) and backward (b) transmission line model. The dependence of the normalized ($Z_B/Z_{lw}$) characteristic impedance with frequency is shown in (c) and (d) for the forward and backward lines, respectively.

In the backward and forward transmission lines depicted in Figure 3, it is possible to identify effective constitutive parameters. To this end, we should take into account that transverse electromagnetic (TEM) wave propagation in planar transmission media and plane wave propagation in isotropic and homogeneous dielectrics are described by identical equations (telegraphist's equation) provided the following mapping holds:

$$Z_s'(\omega) = j\omega\mu_{eff} \tag{19}$$

$$Y_p'(\omega) = j\omega\varepsilon_{eff} \tag{20}$$

where $Z'_s$ and $Y'_p$ are the series impedance and shunt admittance per unit length. Thus, for the forward line the effective permittivity and permeability are constant and they are given by:

$$\varepsilon_{eff} = C/l \tag{21}$$

$$\mu_{eff} = L/l \tag{22}$$

whereas for the backward transmission line, the constitutive parameters are:

$$\varepsilon_{eff} = -\frac{1}{\omega^2 Ll} \tag{23}$$

$$\mu_{eff} = -\frac{1}{\omega^2 Cl} \tag{24}$$

and they are both negative, a sufficient condition to obtain left handed wave propagation.

### 2.2. CL-Loaded Lines: The Composite Right/Left Handed Transmission Line Concept

The implementation of dual lines in planar technology can be done in microstrip or coplanar waveguide (CPW) structures, as Figure 5 illustrates. The host line may play a role so that an accurate model of the structures of Figure 5 must account for the line parameters. Thus, the T-circuit model of the unit cell of these transmission lines is that depicted in Figure 6. At low frequencies, the loading elements ($C_L$ and $L_L$) are dominant and wave propagation is backward. However, at high frequencies, line parameters ($L_R$ and $C_R$) are dominant and forward wave transmission arises. The dispersion relation and the characteristic impedance of these composite right/left handed (CRLH) [15] metalines lines are (from 5 and 6):

$$\cos\beta l = 1 - \frac{\omega^2}{2\omega_R^2}\left(1-\frac{\omega_s^2}{\omega^2}\right)\left(1-\frac{\omega_p^2}{\omega^2}\right) \tag{25}$$

$$Z_B = \sqrt{\frac{L_R}{C_R}\frac{\left(1-\frac{\omega_s^2}{\omega^2}\right)}{\left(1-\frac{\omega_p^2}{\omega^2}\right)} - \frac{L_R^2\omega^2}{4}\left(1-\frac{\omega_s^2}{\omega^2}\right)^2} \tag{26}$$

where the following variables

$$\omega_R = \frac{1}{\sqrt{L_R C_R}} \tag{27}$$

$$\omega_L = \frac{1}{\sqrt{L_L C_L}} \tag{28}$$

and the series and shunt resonance frequencies

$$\omega_s = \frac{1}{\sqrt{L_R C_L}} \tag{29}$$

$$\omega_p = \frac{1}{\sqrt{L_L C_R}} \tag{30}$$

have been introduced to simplify the mathematical formulas. Expressions (25) and (26) are depicted in Figure 7. The left handed and right handed band can be easily identified. The gap in between such transmission bands is delimited by the following frequencies:

$$\omega_{G1} = \min(\omega_s, \omega_p) \tag{31}$$

$$\omega_{G2} = \max(\omega_s, \omega_p) \tag{32}$$

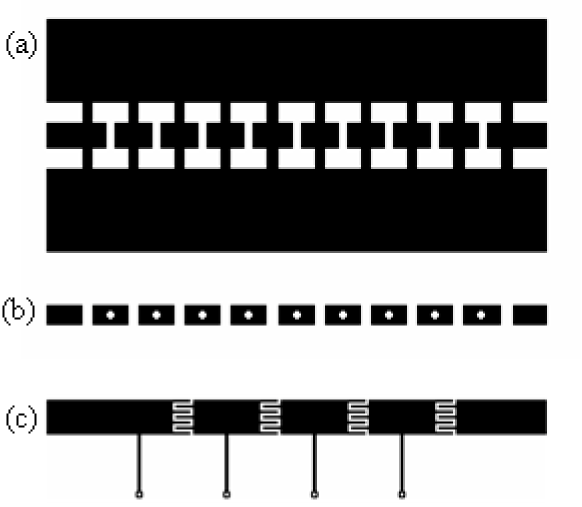

Figure 5. Typical topologies (top view) of CL-loaded metamaterial transmission lines. (a) CPW structure loaded with shunt strips and series gaps; (b) microstrip structure loaded with vias and series gaps; (c) microstrip structure loaded with grounded stubs and interdigital capacitors. In the microstrip structures (b and c), the ground plane is not shown.

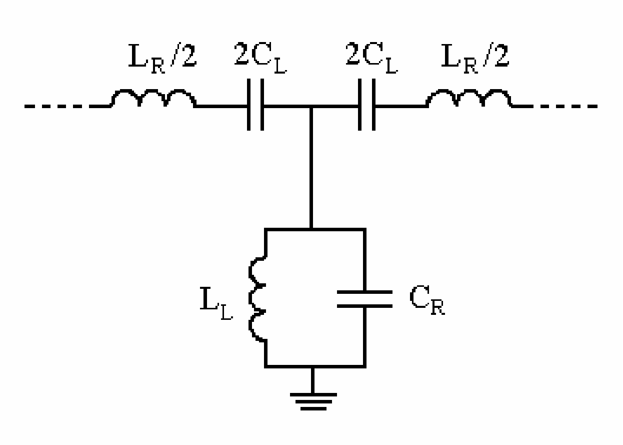

Figure 6. Equivalent circuit model (basic cell) of the CRLH transmission line.

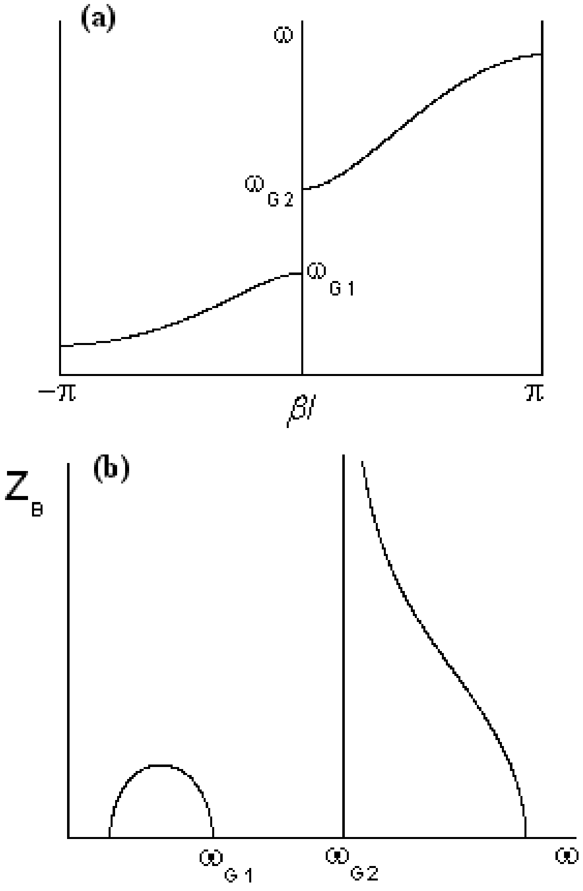

Figure 7. Typical dispersion diagram (a) and variation of Bloch impedance with frequency (b) in a CRLH transmission line model. In this example, $\omega_s<\omega_p$.

In the long wavelength limit, expression (25) rewrites as:

$$\beta = \frac{s(\omega)}{l}\sqrt{\frac{\omega^2}{\omega_R^2}\left(1-\frac{\omega_s^2}{\omega^2}\right)\left(1-\frac{\omega_p^2}{\omega^2}\right)} \tag{33}$$

where $s(\omega)$ is the following sign function:

$$s(\omega) = \begin{cases} -1 & \text{if} \quad \omega < \min(\omega_s, \omega_p) \\ +1 & \text{if} \quad \omega > \max(\omega_s, \omega_p) \end{cases} \tag{34}$$

From the phase constant (equation 33), the phase and group velocities can be easily inferred, these velocities being of opposite sign in the left handed band and both being positive in the right handed band.

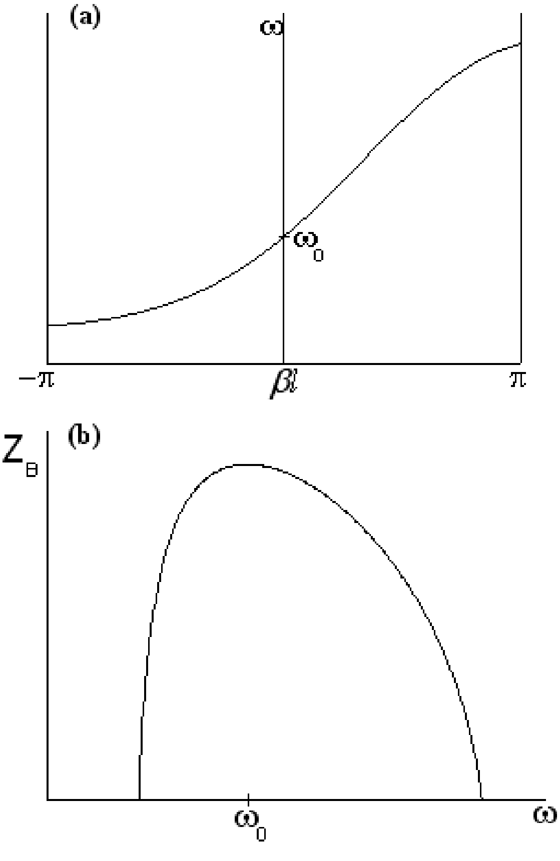

Figure 8. Typical dispersion diagram (a) and variation of Bloch impedance with frequency (b) in a balanced CRLH transmission line.

With regard to the constitutive parameters for the CRLH transmission line, they can be inferred as previously indicated, i.e.:

$$\varepsilon_{eff} = \frac{C_R}{l} - \frac{1}{\omega^2 L_L l} \tag{35}$$

$$\mu_{eff} = \frac{L_R}{l} - \frac{1}{\omega^2 C_L l} \tag{36}$$

and they can be positive or negative, depending on the frequency range.

One particular case of interest is the balanced case, where the series and shunt resonance coincide and the gap collapses. In this case there is a continuous transition between the left handed and the right handed bands, and the group velocity is finite at the so called transition frequency$\omega_o$=$\omega_s$=$\omega_p$. It is worth mentioning that the characteristic impedance varies very smoothly in the vicinity of the transition frequency, where it takes the maximum value given by:

$$Z_B = \sqrt{\frac{L_R}{C_R}} = \sqrt{\frac{L_L}{C_L}} \tag{37}$$

The typical dispersion diagram and characteristic impedance of a balanced CRLH line are depicted in Figure 8.

## 2.3. Resonant Type Metamaterial Transmission Lines

Resonant type metamaterial transmission lines are artificial lines consisting on a host line loaded with split ring resonators, SRRs (formerly proposed by Pendry [16]), or with complementary split ring resonators, CSRRs (first introduced by Falcone [17]). Many other resonator topologies, based on the SRR or CSRR, have been also considered for the implementation of metamaterial transmission lines [6]. The first left handed line implemented by means of SRRs [13] is depicted in Figure 9. It is a CPW with SRRs etched in the back substrate side and shunt connected strips. The SRRs provide a negative effective permeability in a narrow band above their resonance frequency, whereas the strips act as shunt connected inductances, thus providing a negative value of the effective permittivity up to a cut-off frequency. Alternatively left handed transmission lines can be implemented by loading a microstrip line with CSRRs (etched in the ground plane) and series capacitive gaps [14]. The first reported structure is depicted in Figure 10. In this case, the CSRR are responsible for the negative effective permittivity in the vicinity of the resonance frequency, and the series gaps introduce the required negative permeability.

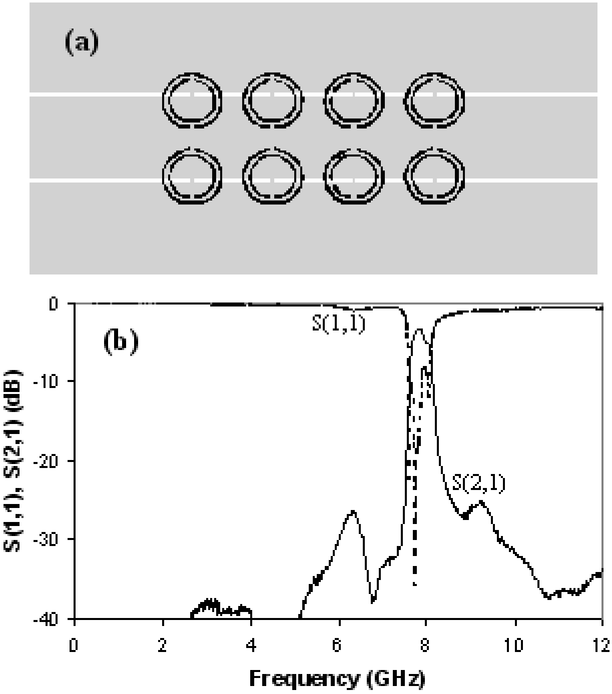

Copyright 2003, American Institute of Physics.

Figure 9. First left handed line implemented by loading a CPW with shunt strips and SRRs (a) and measured frequency response (b). Reprinted with permission from [13].

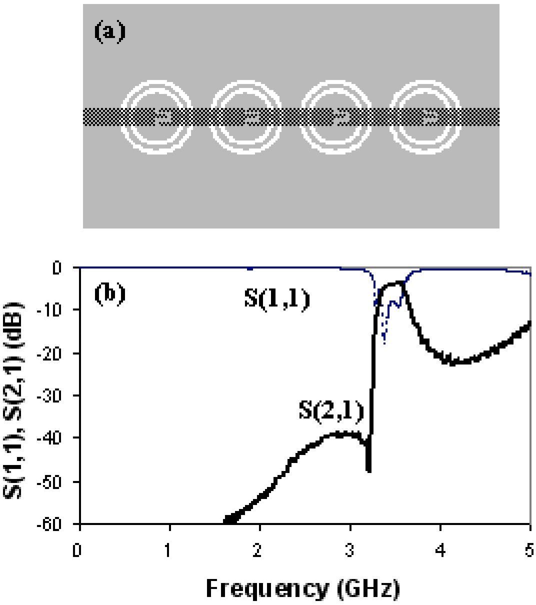

Figure 10. First left handed line implemented by loading a microstrip line with series gaps and CSRRs (a) and measured frequency response (b).

As it has been previously mentioned, an array of SRRs provides a negative effective permeability if the incident radiation is polarized with the magnetic field in the axial direction. In the vicinity of resonance, currents are induced in the rings that are closed through the distributed (edge) capacitance between the concentric rings. Thus, the SRRs can be modelled by means of a closed resonant tank (see Figure 11) that can be magnetically excited (indeed, the SRR can be also excited by means of a time varying electric field applied in the plane of the particle, but this mode of excitation does not apply in the structure of Figure 9). SRRs are electrically small particles because these resonators can be considered as composed of a pair of highly coupled (through the edge capacitance) rings. Indeed, the particle exhibits multiple resonances, but the first resonance can be made small by decreasing the distance between the concentric rings. This enhances the coupling and hence decreases the first resonance frequency. In practice, the electrical size of the particle is limited by the minimum distance between concentric rings that can be achieved by means of the technology in use. The first resonance is the resonance of interest because it is at this resonance that the particle is electrically small. On the other hand, above the resonance frequency, the magnetic field generated by the induced currents in the particles is opposite to the external magnetic field. For this reason, the effective magnetic permeability is negative in a certain band above resonance. An exhaustive analysis of SRRs can be found in [18-20].

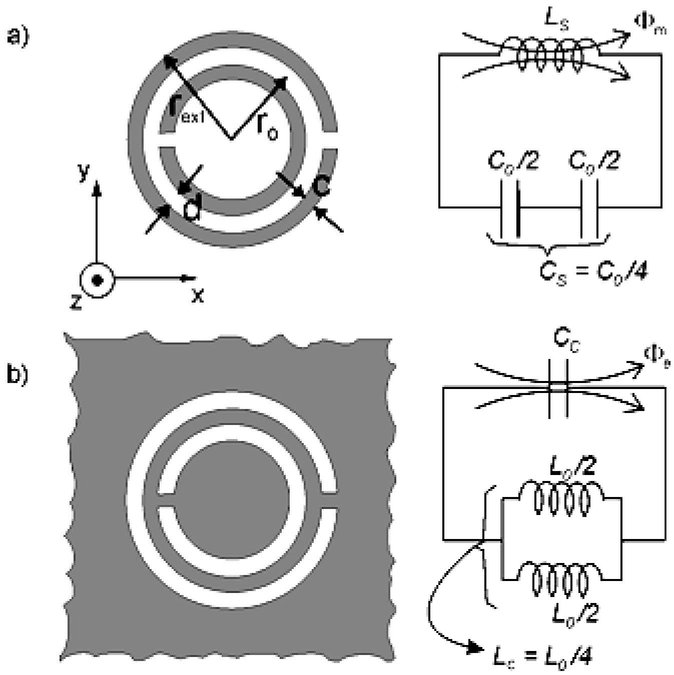

Figure 11. Topology and equivalent circuit model of the SRR (a) and CSRR (b).

Concerning CSRRs, this particle is a useful building block for the synthesis of negative permittivity media. The CSRR is the dual counterpart of the SRR, and this particle can be excited by means of an axial electric field, rather than magnetic field. This particle can be also modelled by means of a resonant tank, such as Figure 11 illustrates, and the resonance frequency of SRRs and CSRRs of identical dimensions are roughly the same. These resonance frequencies are identical if the particles are perfect duals [19]. In practice, however, this is not possible due to the finite width and conductivity of the metal layer (for this reason these particles have been called complementary split ring resonators, rather than dual split ring resonators).

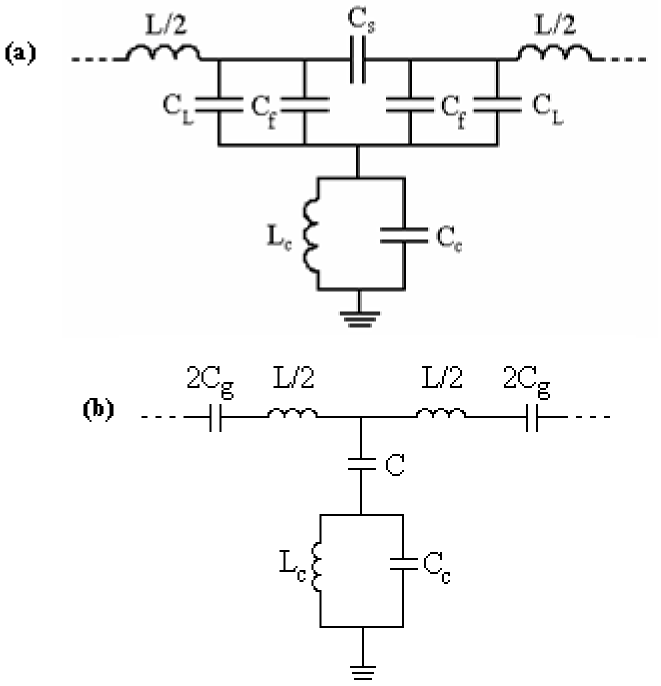

Figure 12. Lumped element equivalent circuit model (unit cell) for the left handed lines loaded with CSRRs. The circuit (a) can be transformed to circuit (b) as explained in the text.

Let us now analyze in certain detail the CSRR-based metalines since most of the results presented later are based on such lines (an exhaustive analysis of SRR-based metalines can be found in [6]). The equivalent circuit model (unit cell) of a microstrip line loaded with series gaps and CSRRs is depicted in Figure 12(a) [21]. In this circuit model, $C_s$ is the series capacitance of the gap or interdigital capacitor, $C_f$ is the fringing capacitance, $C_L$ is the line capacitance, $L$ is the line inductance, and the CSRR is described by the resonant tank $L_c$-$C_c$. This circuit can be transformed to the circuit shown in Figure 12(b), where the following transformations apply:

$$C_g = 2C_s + C_{par} \tag{38}$$

$$C = \frac{C_{par}(2C_s + C_{par})}{C_s} \tag{39}$$

with $C_{par}$=$C_L$+$C_f$. Notice that the circuit depicted in Figure 12(b) is the formerly proposed circuit of CSRR-loaded lines [19]. Such circuit is correct, but the interpretation of some of the parameters was inaccurate. Thus, $C_g$ actually accounts for the series capacitance plus the capacitance of the line and the fringing capacitance, and $C$, the coupling capacitance, depends also on the series capacitance. Indeed, this capacitance can be very large if the gap is wide, as has been verified [22]. Notice that in the limit where $C_s$ is large (as compared to $C_{par}$), $C_g$ and $C$ have the interpretation given in [19], but these conditions are not easily achievable in practice.

The model of Figure 12(b) is very similar to the model of Figure 6. CSRR-loaded lines do also exhibit CRLH behaviour and, as occurs in SRR loaded lines, these lines exhibit a transmission zero to the left of the left handed band [23]. The dispersion relation and the characteristic impedance of these CSRR-based CRLH lines are (from 5 and 6):

$$\cos\beta l = 1 + \frac{\frac{C}{2C_g}\left(1-\frac{\omega^2}{\omega_s^2}\right)\left(1-\frac{\omega^2}{\omega_p^2}\right)}{\left(1-\frac{\omega^2}{\omega_p^2}-CL_c\omega^2\right)} \tag{40}$$

$$Z_B = \sqrt{\frac{L}{C_c}\frac{\left(1-\frac{\omega_s^2}{\omega^2}\right)}{\left(1-\frac{\omega_p^2}{\omega^2}\right)} - \frac{L^2\omega^2}{4}\left(1-\frac{\omega_s^2}{\omega^2}\right)^2 + \frac{L}{C}\left(1-\frac{\omega_s^2}{\omega^2}\right)} \tag{41}$$

where $\omega_s$ and $\omega_p$ are the series and shunt resonance, respectively. By forcing the balance condition, that is, $\omega_s$=$\omega_p$=$\omega_o$, the gap between the left handed and the right handed region disappears, and the characteristic impedance exhibits continuity in the vicinity of the transition frequency $\omega_o$ (notice however that the maximum value of the characteristic impedance is slightly shifted to the right of $\omega_o$). By balancing the line, the structure may exhibit a very broadband [23]. This, combined with the presence of a transmission zero, has been used for the design of ultra wide band filters [24,25]. Figure 13(a) depicts the layout of a unit cell CSRR-loaded CRLH microstrip line that has been designed to be balanced. The measured and simulated dispersion, shown in Figure 13(b), reveals that the structure is roughly balanced (perfect balance is difficult to achieve in practice). The transmission coefficient is depicted in Figure 13(c). As expected, a broad band that includes the left handed and the right handed region, and a sharp cut-off at the lower band edge are obtained. Other unbalanced CSRR-loaded CRLH lines have been reported in the recent literature, and it has been shown that the model of Figure 10 describes accurately the frequency response up to the second band [26].

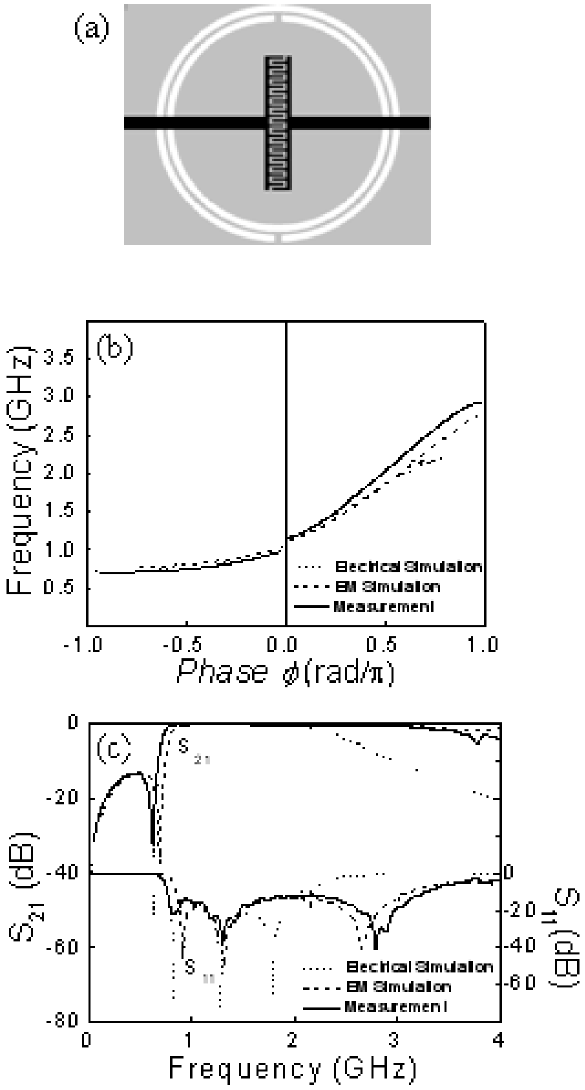

Reprinted with permission from [23]. Copyright 2007, IEEE.

Figure 13. Balanced CRLH cell based on a microstrip line loaded with CSRRs (a), dispersion diagram (b) and frequency response (c). The structure has been implemented in *Rogers RO3010* substrate with dielectric constant $\varepsilon_r$=10.2 and thickness $h$=1.27mm. Dimensions are: line width $W_m$=0.8mm, internal radius $r$=6.3mm, ring width $c$=0.4mm and ring separation $d$=0.2mm; the interdigital capacitor, formed by 28 fingers separated 0.16mm, has been used to achieve the required capacitance value.

To end this section we would like to mention that SRR-loaded and CSRR-loaded metamaterial transmission lines exhibit a very similar behaviour. It has been found that the effect of varying the strip width in SRR-loaded CPWs is the same as varying the gap width in CSRR-loaded microstrip lines. This is not actually surprising since these lines are roughly dual, and their equivalent circuits are formally circuit duals. This aspect is discussed in [27].

# 3. APPLICATIONS OF METAMATERIAL TRANSMISSION LINES

In this section, several applications of metamaterial transmission lines are pointed out. This includes the design of compact and reconfigurable filters, and other metamaterial-based microwave components that exhibit certain advantages as compared to conventional implementations, thanks to the controllability of the electrical characteristics of metalines. We will focus on the resonant type approach of metalines, and more specifically in CSRR-based lines. Implementations in low loss microwave substrates (PCB substrates) as well as in advanced microelectronic technologies (MCM-D and RF-MEMS) will be presented.

## 3.1. Metamaterial Filters

As long as metamaterial transmission lines are frequency selective structures by nature, their application to filters is straightforward. The main benefit of metamaterial-based filters is their size, which can be made very small on account of the small size of CSRRs (or SRRs). The possibility of synthesizing filters exhibiting wide and ultra wide pass bands, as well as spurious suppression are additional capabilities of metamaterial-based filters.

### 3.1.1. Stop Band Filters: Application to Spurious Suppression in Conventional Filters

Let us start by considering the synthesis of stop band filters based on CSRRs. This can be achieved by etching CSRRs in the ground plane of a microstrip line, where the electric field is axial to the rings, or either in the ground plane or in the central strip of a CPW structure. At the resonance frequency, the rings are excited, and the injected power is returned back to the source. Actually, inspection of the circuit model of Figure 12 indicates that there is a transmission zero at that frequency that nulls the shunt impedance.

If the series gap is absent the structure behaves as a stop band filter centred at the transmission zero frequency. In order to enhance the bandwidth, we can etch different CSRRs tuned at different, but close, frequencies within the desired gap. This technique has been demonstrated to provide wide stop bands [28,29], and it has been used for the elimination of spurious bands in conventional filters, as Figure 14 illustrates. The idea is as simple as etching slightly different tuned CSRRs covering the spurious band to be eliminated. Other conventional filters with spurious suppression by using metamaterial resonators have also been reported [30,31].

It is also possible to design stop band or notch filters with tuning capability. To this end, we need a tuning element such as a variable capacitance. This variable capacitance can be implemented by means of varactor diodes. Thus, by introducing a varactor diode in either the SRR or the CSRR topology, we can obtain tunable notch or stop band filters (see references [32-34] for further details). Another possibility is to combine CSRRs with RF-MEMS (micro-electro-mechanical-systems) in a CPW structure [35]. This technique is illustrated in Figure 15, where a tunable stop band filter at Q-band with 20% tuning range is depicted. This structure has been fabricated at IMEC's Facilities, and it consists on a periodic array of CSRRs etched in the central strip of a 50 Ω CPW transmission line, with MEMS bridges on top of the CSRRs. The MEMS devices implemented in the CSRRs uses an electrically floating bridge anchored directly on the substrate in holes of the CPW ground planes. The position of the bridge is controlled through an actuation voltage and it modifies the electrical characteristics (resonance frequency) of the CSRRs, with the result of certain tuning (see Figure 15 and [35] for further details).

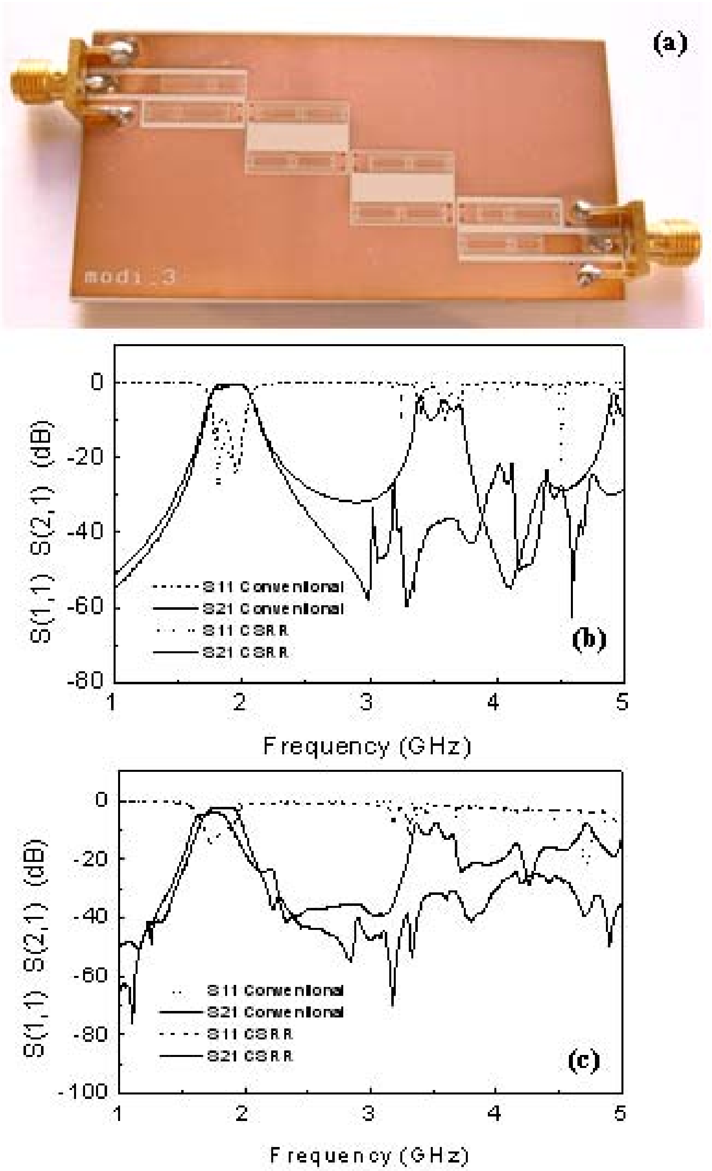

Reprinted with permission from [28]. Copyright 2005, IEEE.

Figure 14. (a) CSRR coupled line band pass filter in CPW technology; (b) simulated frequency response compared to that obtained in the device without rings, and (c) measured frequency responses. The device has been fabricated on the *Rogers RO3010* substrate (thickness $h$=1.27mm, dielectric constant $\varepsilon_r$=10.2).

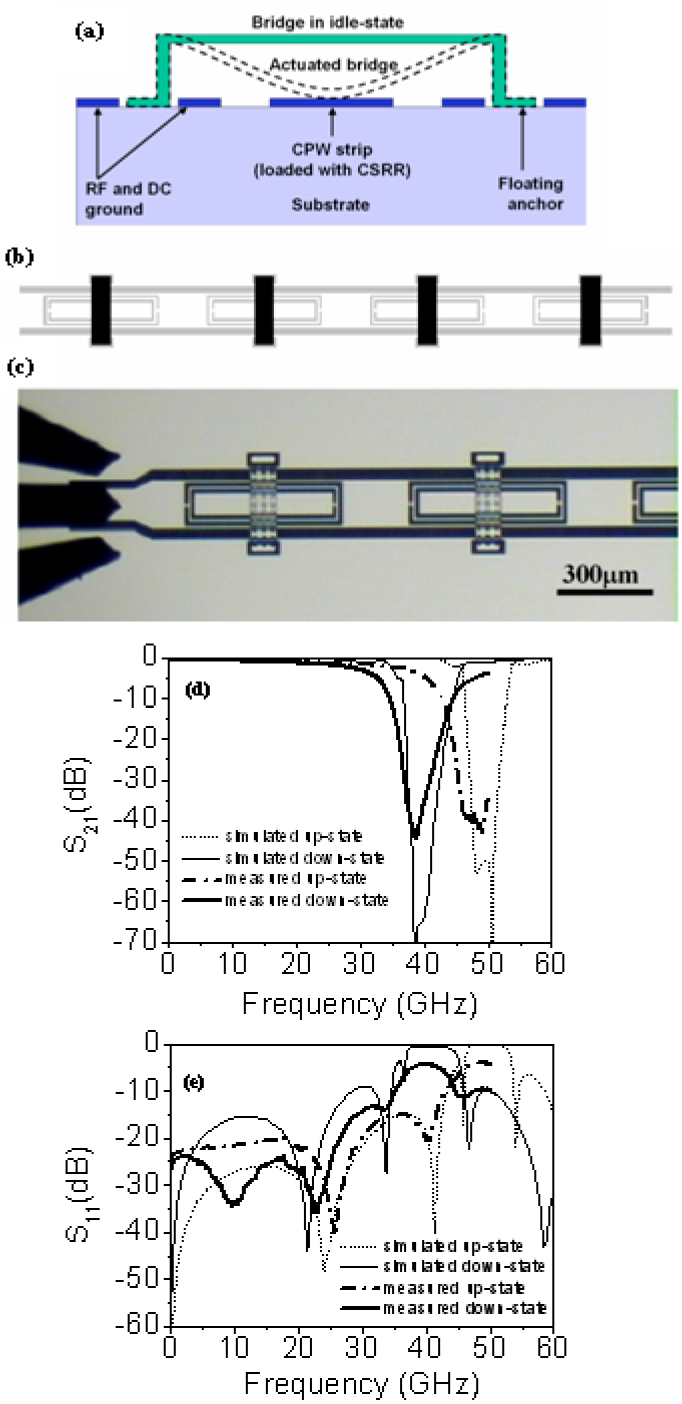

Reprinted with permission from [35]. Copyright 2007, IET.

Figure 15. (a) Cross section of the microstirp lines loaded with CSRRs and RF-MEMS bridges, (b) designed tunable stop-band filter, (c) microphotograph of the fabricated filter, (d) measured and simulated insertion losses and (e) measured and simulated return losses. The simulations have been done by considering plate heights of 0.5μm and 2μm for the down and up-state, respectively.

### 3.1.2. Narrow Band Pass Filters and Diplexers

Narrow band pass filters and diplexers can be implemented by means of the alternate right/left handed (ARLH) concept. It consists on cascading left handed and right handed cells alternating. Notice that this concept is different than the CRLH concept introduced before. We have previously discussed how to implement left handed (actually CRLH) artificial lines with CSRRs. To implement right handed lines by means of CSRRs, we have to replace the series gaps with shunt connected inductors (grounded stubs). A typical layout and dispersion diagram of these right handed lines based on CSRR is depicted in Figure 16. As can be seen two right handed bands do appear, although the interest is the operation in the first band, where the structure is electrically small[1]. One key aspect of the right handed cells is the fact that they exhibit a transmission zero above the first right handed band. Thus, by combining left handed and right handed cells, designed to exhibit the pass band of interest at the same frequency, we can obtain high frequency selectivity thanks to the presence of a transmission zero below and above the filter band. This idea has been implemented for the design of narrow band pass filters based on CSRRs [36] and also for the design of diplexers [37]. The designed diplexer is depicted in Figure 17, where the receiver (Rx) and transmitter (Tx) filters are cascaded at the output ports of a Y-junction. The main relevant parameters representative

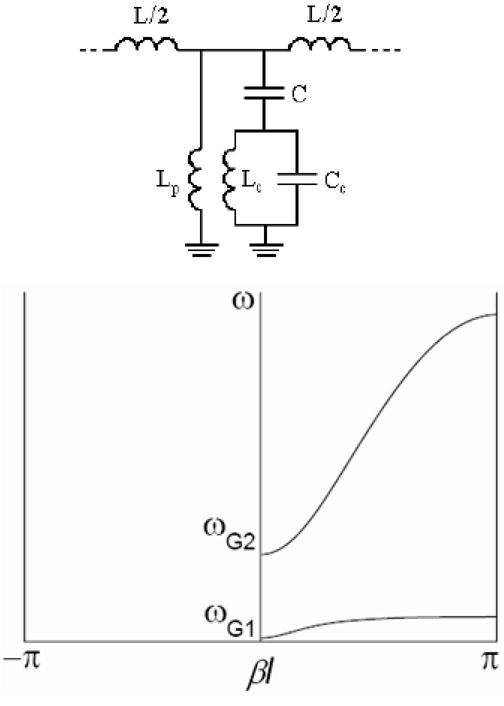

Figure 16. T-circuit of a right handed cell implemented by means of CSRRs (a) and typical dispersion diagram (b).

---

[1] Notice that in the left handed cells, the interest is also in the first (left handed) band, not in the right handed band, present at higher frequency, but where the structures is not electrically small.

of diplexer performance are in-band looses for the Tx and Rx channels (which should be as small as possible) and Rx/Tx isolation (which should be high to avoid interfering signals between the Rx and Tx channels). The device of Figure 17(a) has been designed to be operative in the 2.4GHz-3.0GHz frequency band. The Tx and Rx filters implemented by means of CSRR-based ARLH microstrip lines[2] have been designed to provide pass bands centered at 2.4GHz and 3.0GHz, respectively, with absolute bandwidths of 0.25GHz (namely 10.3% and 8% fractional bandwidths for transmission and reception). Figure 17(b) depicts the measured transmission coefficient for the Tx and Rx filters (i.e., $S_{21}$ and $S_{31}$, respectively), as well as the measured Rx/Tx isolation ($S_{32}$). In-band losses lower than 2dB are measured for either filter, while return losses (also represented in Figure 17b) are better than 10dB. The frequency response of the filters is quite symmetric and the measured isolation between ports 2 and 3 is in the vicinity of 40dB. Remarkable are also the dimensions of the diplexer (see the region indicated in Figure 17a), which are as small as 29.8mm×16.3mm (namely $0.63\lambda \times 0.34\lambda$, $\lambda$ being signal wavelength at the Tx frequency) thanks to the compact resonators employed.

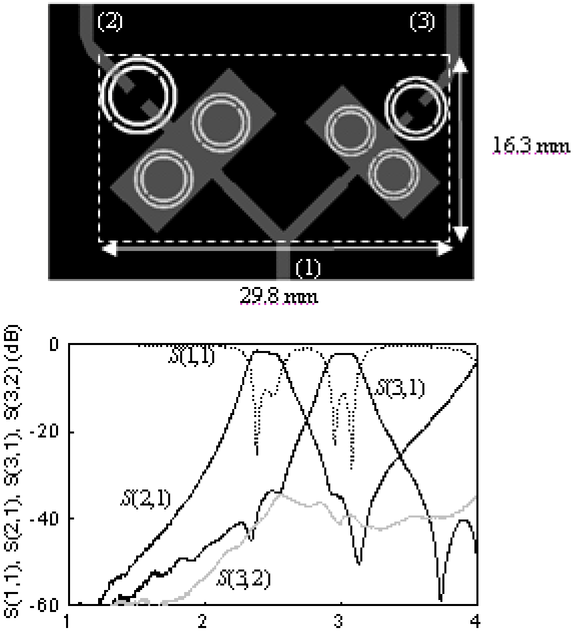

Copyright 2005, IET.

Figure 17. Topology of the fabricated diplexer. The upper metal level is depicted in grey, whereas the lower metal is drawn in black. Gap spacing is 1.33mm and 1.67mm for the Rx and Tx filters respectively, whereas shunt strip dimensions are 4.54mm×11.9mm and 5.70mm×14.48mm. External CSRR radius are 2.18mm, 2.73mm, 2.56mm and 3.27mm for the Rx (1st stage), Rx (2nd stage), Tx (1st stage), and Tx (2nd stage), respectively. The measured insertion and return losses of the Rx and Tx filters and Rx/Tx isolation are also indicated. Reprinted with permission from [37].

---

[2] Notice that in the right handed sections of the Rx and Tx filters, two CSRRs are used. The reason is the moderate bandwidth (rather than narrow) of either filter. To achieve such bandwidths, it is necessary to implement unit cells also with moderate 3dB bandwidths. For the forward sections, this is more easily achieved by using two CSRRs, rather than only one.

### 3.1.3. Wide and Ultra Wide Band (UWB) Pass Filters

For the design of wide and ultrawide band pass filters we can make use of balanced CSRR-based CRLH lines, as that depicted in Figure 13. Actually, these structures can be considered as high pass filters, since we do not have control on the position of the upper band edge. To limit the bandwidth, we can add electrically small resonators to the structure tuned at the desired upper limit of the pass band. Following this idea, we have designed several prototype devices [38]. One of them is depicted in Figure 18. This is an UWB pass filter designed to cover the standard band (3.1GHz-10.6GHz) defined by the Federal Communication Commission (FCC) for UWB communications. However, in the design of the filter of Figure 18, we have also included additional elements in order to introduce an attenuation pole at 5.5GHz, which may be of interest for the elimination of interfering signals (attenuation poles have also been introduced in other UWB pass filters implemented by means of different approaches [39,40]). Such elements responsible for the attenuation pole are the two rectangular shaped spiral resonators, whereas the two pairs of SRRs at the extremes have been added to limit the upper stop band.

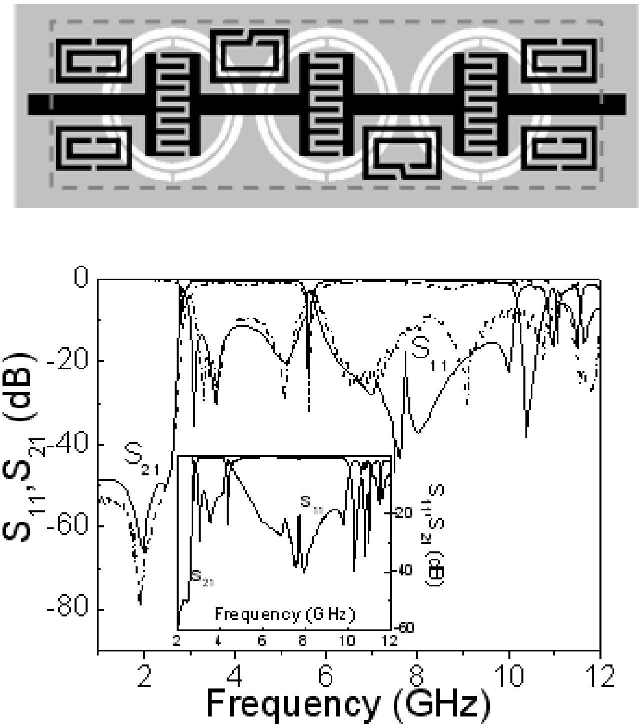

Reprinted with permission from [38]. Copyright 2007, John Wiley.

Figure 18. (a) Layout of the fabricated UWB band pass filter. Dimensions of the SRRs are $c$=0.14mm, $d$=0.165mm $l_{ext}$=2.1mm and $h_{ext}$=1.2 mm ($l_{ext}$ and $h_{ext}$ are the length and width of the SRRs). SRs provide a transmission zero at 5.5 GHz ($c$=0.14mm, $d$=0.166mm $l_{ext}$=2.03mm and $h_{ext}$=1.46 mm). The area of the device (dashed rectangle) is $A$=1.57cm × 0.42cm = 0.66cm$^2$. CSRRs are etched on the ground plane (in grey). (b) Simulated (solid line) and measured (dashed line) insertion and return losses for the designed filters. The small graph shows the simulated response of the filter with the notch at 4.5GHz.

Alternatively, for the implementation of wide band filters, we have considered the hybrid cell [41], consisting on a combination of CSRRs series gaps and shunt stub, as Figure 19 illustrates. Such unit cell exhibits a transmission zero above the pass band of interest, and it can be designed to be balanced. It has been applied to the design of periodic structures based on them. The top result achieved by the authors has been the design of a wide band filter covering at least the band 4GHz-6GHz, exhibiting 80dB rejection in the vicinity of 2GHz, and smaller dimensions than 1cm$^2$ [24]. The device and its performance are depicted in Figure 19.

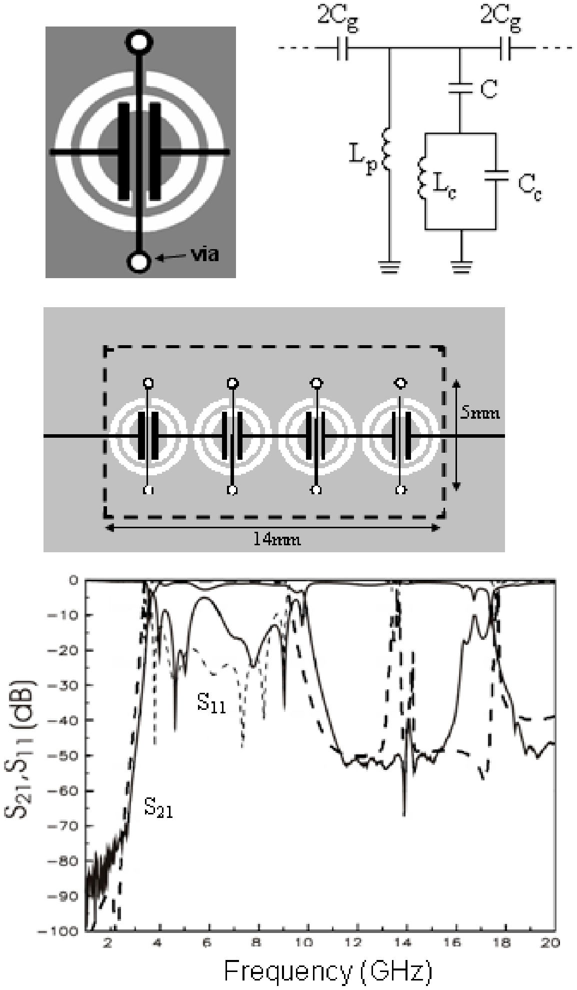

Reprinted with permission from [24]. Copyright 2007, IEEE.

Figure 19. (a) Topology of the hybrid cell and equivalent T-circuit model (where the series inductance has been neglected); (b) layout of the fabricated filter, formed by cascading four balanced hybrid cells; (c) Simulated (dashed line) and measured (solid line) frequency response. The metallic parts are depicted in black in the top layer, and in grey in the bottom layer. The rings are etched on the bottom layer. The dashed rectangle has an area of 1cm$^2$. Dimensions are: line width $W$=0.126mm, external radius of the outer rings $r$=1.68mm, rings width $c$=0.32mm and rings separation $d$=0.19mm; inductor width is 0.10mm and the distance between the metals forming the gap is 0.4mm.

### 3.1.4. Metamaterial Based Filters Subjected to Standard Responses: A Design Methodology

Based on the hybrid cell as building block for the implementation of planar filters, a design methodology has been developed. Following this methodology, standard frequency responses, such as Butterworth, Chebyshev, etc., can be implemented. An exhaustive analysis of this design methodology can be found in [42], but we briefly reproduce it here. This design methodology is based on the generalized network of a band pass filter [43], consisting on a cascade of admittance inverters alternating with shunt connected resonators (see Figure 20)[3]. The design consists on determining the circuit parameters of the equivalent circuit model for either filter cell from given specifications (central frequency, fractional bandwidth and filter order), as well as the determination of the layout of the structure. In the structure of Figure 19(a), the resonators and the impedance inverters are intermixed. Thus, at the central filter frequency, $f_o$, neither the CSRRs are at resonance, nor the admittance of the shunt branch nulls. Nevertheless, at $f_o$ the phase shift and transmission coefficient between the input and output ports of the basic cell should be $\phi=90^o$ and $|S_{21}|=1$, respectively. This means that at $f_o$ the image impedance, $Z_B$, should coincide with the reference impedance of the ports, which is usually set to $Z_o=50\Omega$. If we now consider that the circuit of Figure 19(a) can be described by means of its T-circuit model, with series impedance $Z_s$ and shunt impedance $Z_p$, and we take into account that the phase shift and image impedance for this circuit are given by expressions 5 (with $\phi=\beta l$) and 6, respectively, the previous conditions lead us to $Z_s=-jZ_o$ and $Z_p=jZ_o$. Actually, the dual solution ($Z_s=jZ_o$ and $Z_p=-jZ_o$) satisfies also the previous conditions on phase shift and impedance matching, but this solution is not compatible with the circuit of Figure 19(a) since the series impedance of this circuit is capacitive. Consequently, at the central filter frequency, the series reactance is negative (capacitive) while the shunt reactance (corresponding to the parallel combination of $L_p$ and the impedance of the CSRRs coupled to the line) is positive and, hence, inductive. According to the signs of these reactances, the filter structure composed of the elemental cells depicted in Figure 19 supports backward waves and behaves as a left handed transmission line. To determine the element values for the circuit of Figure 19(a), the series and shunt impedances have to be set to $Z_s=-jZ_o$ and $Z_p=jZ_o$, respectively, at $f_o$. This does not univocally determine the element values for the shunt impedance. These values are also determined by the 3dB bandwidth of the resonators,

$$\Delta = \frac{\omega_2 - \omega_1}{\omega_o} \tag{42}$$

(where $\omega_o$, $\omega_1$ and $\omega_2$ are the central –angular– frequency and 3dB frequencies, respectively), and by the transmission zero, which occurs at that frequency where the shunt impedance reduces to zero, namely:

$$f_Z = \frac{1}{2\pi\sqrt{L_c(C_c + C)}} \tag{43}$$

---

[3] A cascade of impedance inverters and series resonators do also provide a band pass response.

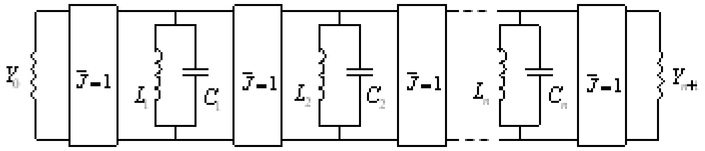

Figure 20. Generalized network of a band pass filter consisting on a cascade of shunt resonators and admittance inverters alternating.

For a *LC* parallel resonant tank, with inductance and capacitance $L_{eq}$ and $C_{eq}$, respectively, we have:

$$\Delta = \frac{2}{Z_o}\sqrt{\frac{L_{eq}}{C_{eq}}} \tag{44}$$

If we consider the filter structure of Figure 20, where the *L* and *C* values come from the low pass filter prototype by frequency and element transformation according to [43]:

$$C_{eq} = \left[\frac{1}{FWB \cdot \omega_o \cdot Z_o}\right] g_i \tag{45}$$

$$L_{eq} = \frac{1}{\omega_o{}^2 C_{eq}} \tag{46}$$

and (45) and (46) are introduced in (44), the following expression for resonator bandwidths results:

$$\Delta_i = \frac{2FBW}{g_i} \tag{47}$$

where $g_i$'s are the element values of the low pass filter prototype (which depend on the specific filter approximation and can be inferred from published tables) and $\Delta_i$ is the 3dB bandwidth of the resonators. According to expression (47), $\Delta_i$ is proportional to the fractional bandwidth, *FBW*, and hence it is determined from the required bandwidth of the filter. Obviously, $\Delta_i$ is also dependent on $g_i$ and it is therefore determined by the type of response and order. Once $\Delta_i$ are known, we can force the frequencies $\omega_1$ and $\omega_2$ to be equidistant from the central filter frequency. At these frequencies, under the assumption that $Z_s(\omega)$ does not substantially vary along the pass band, the shunt impedance of the unit cell becomes $Z_p$=j$Z_o$/2 and infinity, respectively, while, as has been previously indicated, $Z_p$=j$Z_o$ at $\omega_o$. These conditions can be expressed as:

$$\frac{L_pL_c\omega_1^3(C+C_c)-L_p\omega_1}{L_c\omega_1^2(C+C_c)-C\omega_1^2L_p(L_cC_c\omega_1^2-1)-1}=\frac{Z_o}{2} \tag{48}$$

$$L_c\omega_2^2(C+C_c)-C\omega_2^2L_p(L_cC_c\omega_2^2-1)-1=0 \tag{49}$$

$$\frac{L_pL_c\omega_o^3(C+C_c)-L_p\omega_o}{L_c\omega_o^2(C+C_c)-C\omega_o^2L_p(L_cC_c\omega_o^2-1)-1}=Z_o \tag{50}$$

The previous approximation (which is valid for narrow and moderate bandwidths) leads us to simple analytical expressions (equations (48) and (49)). If this approximation is not applied, then the conditions arising from the 3dB frequencies are not mathematically simple. Solution of equations (48)-(50) and (43) leads us to the parameters of the shunt reactance, while the series capacitance is given by:

$$C_g=\frac{1}{2Z_o\omega_o} \tag{51}$$

The criterion to set the transmission zero frequency, $f_Z$, obeys to a compromise between the need to obtain a sharp transition in the upper band edge, and the convenience to far the spurious responses as much as possible, and thus optimize the out-of-band performance of the filter.

Let us now consider two illustrative examples of this approach. The first one [42] consists on a band pass filter based on a periodic repetition of the basic cell. The specifications are as follows: order 3, central frequency $f_o$=1GHz and fractional bandwidth *FBW*=10%. Obviously, due to periodicity, all resonators must have the same Δ, and accordingly the same *g*. To obtain the value of *g*, an order-3 low pass filter prototype with identical element values has been considered, and it has been forced to exhibit the 3dB cutoff at the normalized $\omega$=1rad/s angular frequency. From this, it is obtained *g*=1.521; hence the 3dB bandwidth of the resonators, Δ, is perfectly determined. From the previously explained procedure, the element values of the equivalent circuit model have been obtained. They are identical for the three filter cells and are depicted in table 4.1. The filter layout and the frequency response are depicted in Figure 21 (the parameters of the *Rogers RO3010* substrate have been used – thickness *h*=1.27mm, dielectric constant $\varepsilon_r$ =10.2).

**Table 1. Element Values Of The Equivalent Circuit Model For The Filter Of Figure 21.**

| $C_g$ (pF) | $L_p$ (nH) | C(pF) | $C_c$ (pF) | $L_c$ (nH) |
|---|---|---|---|---|
| 1.59 | 1.33 | 12.33 | 21.7 | 0.23 |

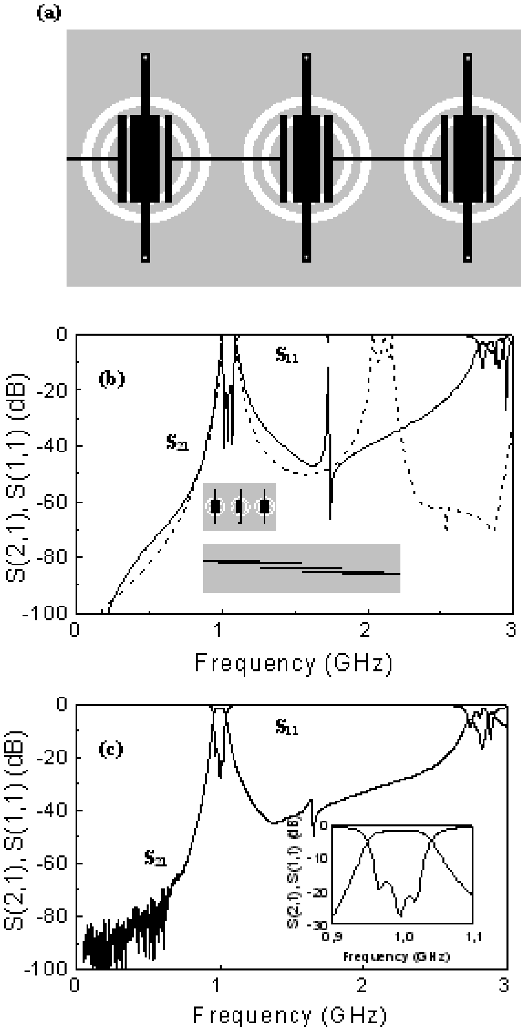

Copyright 2006, IEEE.

Figure 21. Layout of the fabricated periodic filter (a), simulated (b) and measured (c) insertion and return losses. Total device length excluding access lines is 4.56 cm. In (b), the simulated insertion losses for a conventional order-3 coupled line filter with similar performance are depicted (dashed line). Reprinted with permission from [42].

The second filter is an order-2 band pass filter at K-band implemented in IMEC's high-resistivity silicon (HRSi) MCM-D technology [44], consisting of alternating layers of BCB (benzo-cyclobutene, dielectric constant $\varepsilon_r$=2.65) and Cu metallizations, deposited on a HRSi carrier substrate (ρ > 9KΩcm). The technology has 3 metal layers: metal-1 (M1, 1μm thick Al), metal-2 (M2, 5μm thick Cu) and metal-3 (M3, 5μm thick Cu/Ni/Au). The lower BCB layer is 4.3μm thick and the top BCB layer is 8μm thick. Low-loss dielectrics and copper metallizations are used, and therefore, high quality integrated passives can be realized, such as low loss transmission lines and high-*Q* inductors [45]. High-density thin-film microstrip lines can also be integrated using the BCB as substrate material. In the designed filter, the ground plane (where CSRRs are etched) is metal-1, whereas in metal-2 it has been defined the filter layout (excluding CSRRs). The central filter frequency is $f_o$=19GHz and the fractional bandwidth is *FWB*=18%. The filter, depicted in Figure 22, is as small as 918µm×450µm, i.e., $0.094\lambda_g \times 0.045\lambda_g$, where $\lambda_g$ is the guided wavelength at $f_o$. The frequency response of the filter is also depicted in Figure 22.

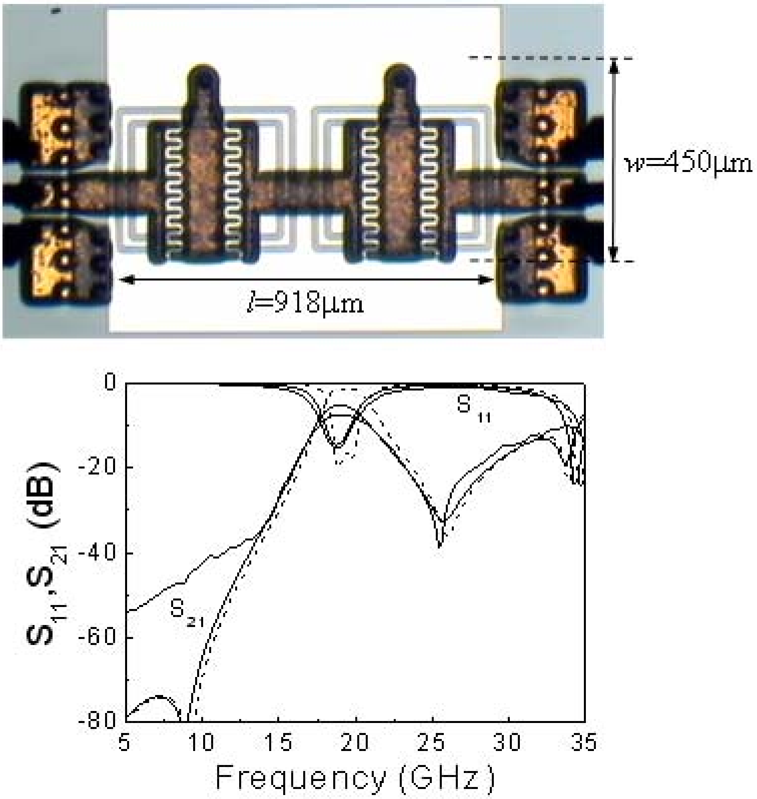

Reprinted with permission from [44]. Copyright 2007, IET.

Figure 22. (a) Photograph of the fabricated K-band filter. The slot width and the separation between slots in the CSRR is 15µm in both cases (total size of the CSRRs is 422µm × 314µm). The interdigital capacitors are formed by 8 face-to-face fingers separated 10µm. The width of these capacitors is 314µm. The inductors, with a length of 132µm, are grounded by means of vias with a diameter of 27µm. (b) Insertion and return losses of the fabricated filter. Measured results (bold solid line), simulation with perfect rings (thin dashed line) and simulation with lossy rings (thin solid line).

To conclude this sub-section devoted to metamaterial based filters, we would like to highlight that the presented filters are small thanks to the small electrical size of the resonators employed. It has been also demonstrated that metamaterial based filters can exhibit broad transmission bands, including the possibility of fabricating filters with UWB bands, and, also, it is possible the design of filters with improved out-of-band performance through spurious suppression. Other metamaterial based filters can also be found in the recent literature [46-49].

### 3.2. Enhanced Bandwidth Components

Thanks to the controllability of the dispersion diagram of metamaterial transmission lines, such lines can be applied to the design of microwave components with wider operative bands, as compared to conventional (distributed) implementations. The principle for bandwidth enhancement is simple: the operative bandwidth of microwave components is given by that frequency interval where the required characteristics are satisfied within certain limits. In distributed circuits, bandwidth is limited by the phase shift experienced by transmission lines and stubs when frequency is varied from the nominal operating value. In a conventional transmission line of length $l$, the phase of the line at a certain angular frequency $\omega_o$ is given by:

$$\phi_o = \beta l = \frac{l}{v_p}\omega_o \tag{52}$$

where $v_p$ is the phase velocity of the line. According to the previous comment, bandwidth is intimately related to the derivative of $\phi$ with frequency, also known as group delay. From this, it follows that the shorter the line is, the broader the bandwidth becomes. In other words, bandwidth is inversely proportional to the required phase of the line, which is dictated by the design. This means that the operative bandwidth is not an easily controllable parameter in conventional distributed circuits. The reason is the limited number of degrees of freedom of conventional transmission lines. However, in metamaterial transmission lines, the loading elements provide additional parameters and certain control of the phase response is expected. Namely, one expects that the required phase does not dictate bandwidth. However, bandwidth enhancement is not always possible, since, as it has been demonstrated [50], for transmission lines with phase shift below a certain limit, it is not possible to enhance bandwidth (the detailed discussion is reported in [50], but it is out of the scope of this chapter). Nevertheless, many devices are based on phase differences, and, in this case, the key idea is to design the devices by replacing the conventional lines with artificial lines, so that the dispersion of these lines exhibit parallel slopes in the vicinity of the design frequency (see Figure 23). Obviously, the characteristic impedance, frequency dependent, must be set to the required value.

Several enhanced bandwidth components based on the resonant type approach have been recently proposed [51-53]. We will select one of them to illustrate the possibilities of the approach. It is a rat-race hybrid coupler [51]. A typical layout of the conventional implementation is depicted in Figure 24(a). It is essentially a 4-port device consisting on a $1.5\lambda$ ring structure (where $\lambda$ is the guided wavelength at the design frequency, $f_o$) with the ports equally spaced in the upper half of the ring. Since the $270^o$ ($0.75\lambda$) line section is formally equivalent to a $-90^o$ LH line, the conventional $0.75\lambda$ line can be substituted by a LH artificial line designed to provide the required characteristic impedance ($70.7\Omega$) and phase ($-90^o$) at the operating frequency. This was done previously by Okabe *et al.* [54] by using the dual transmission line approach, where the host line was loaded with lumped inductors and capacitors in shunt and series connection, respectively. In the reported example, not only the $270^o$ line is replaced with an artificial $-90^o$ LH line, but also the three $90^o$ transmission lines

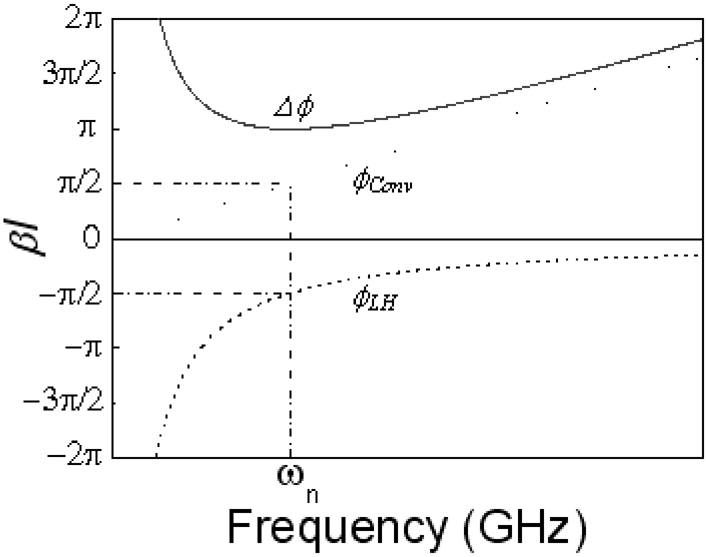

Figure 23. Illustration of bandwidth enhancement by using a conventional and a left handed transmission line. At the design frequency, $\omega_n$, the phase difference, $\Delta\phi$, between the two lines is π, and this difference is roughly preserved in a wide band.

are implemented as artificial right handed lines based on CSRRs (using the topology shown in Figure16). This allows us to achieve a further controllability on the frequency dependence of phase in the lines, with the result of an excellent performance in terms of phase-balance. Moreover, the design is fully compatible with planar technology since no lumped elements are used. The topology of the designed rat-race is depicted in Figure 24(b), and the photograph of the fabricated prototype is depicted in Figure 24(c), where it is compared to the conventional implementation. The artificial lines have been all designed to exhibit a characteristic impedance of $Z_o$=70.71Ω at the design frequency (1.6GHz). The device has been fabricated on the *Rogers RO3010* substrate with dielectric constant $\varepsilon_r$=10.2 and thickness $h$=635μm. The active area (excluding access lines) of the new hybrid coupler based on LH and RH artificial lines is 3.62cm$^2$, whereas the conventional one occupies an area of 10.33cm$^2$, i.e., the meta-coupler is roughly 3 times smaller. The simulated and measured impedance matching, coupling and isolation for both couplers are depicted in Figure 25. In Figure 26, it is depicted the phase-balance for the Σ and Δ ports, namely $\phi(S_{42})$-$\phi(S_{32})$ and $\phi(S_{41})$-$\phi(S_{31})$, respectively. The CSRR-based coupler exhibits good isolation, coupling and matching. These magnitudes are comparable to those of the conventional device. Specifically, the measured power splitting between ports 3 and 4, considering the port 1 as the input port, exhibits similar characteristics in terms of flatness. Measured isolation and matching are comparable in both devices at the operating frequency ($f_o$=1.6GHz). However, phase balance in the CSRR-based rat-race is clearly superior than that obtained in the conventional hybrid, specially for the Δ input (see Figure 26). Namely, the phase balance variation with frequency is smaller in the new CSRR-based hybrid and hence the operating phase bandwidth is enhanced. This has been achieved thanks to an accurate control of the phase response of the individual artificial lines forming the proposed coupler. The combination of dimensions and performance for the metamaterial-based rat-race hybrid is satisfactory.

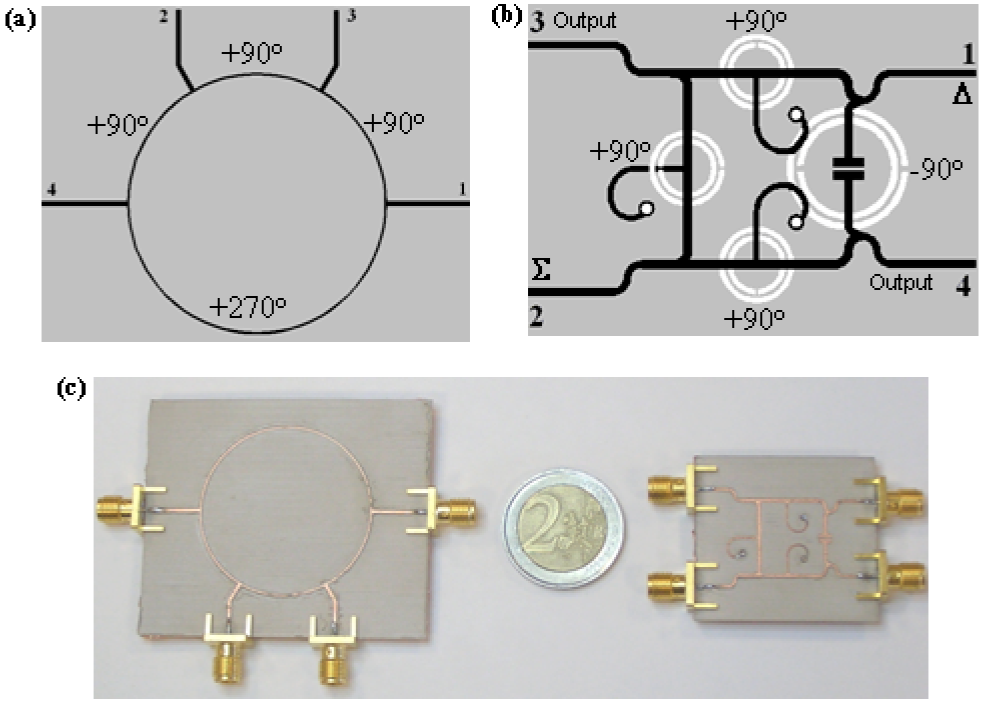

Figure 24. Topology of the conventional rat-race hybrid coupler (a) metamaterial-based coupler (b) and photograph with the comparison of both devices. The device has been fabricated on the *Rogers RO3010* substrate with dielectric constant $\varepsilon_r$=10.2 and thickness $h$=635μm. The active area (excluding access lines) of the CSRR-based hybrid coupler is 3.62cm$^2$, whereas the conventional one occupies an area of 10.33cm$^2$.

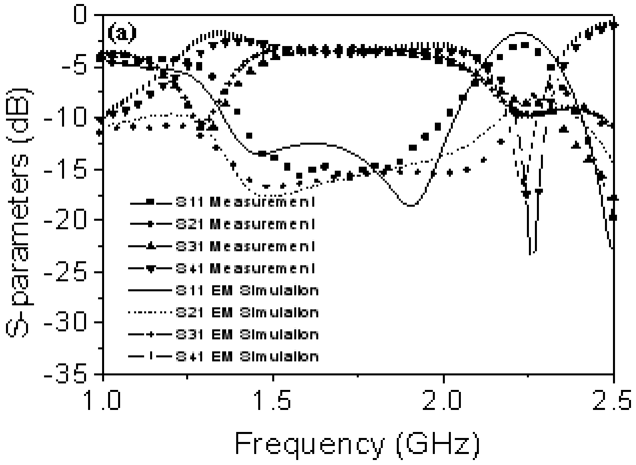

Figure 25. Continued on next page.

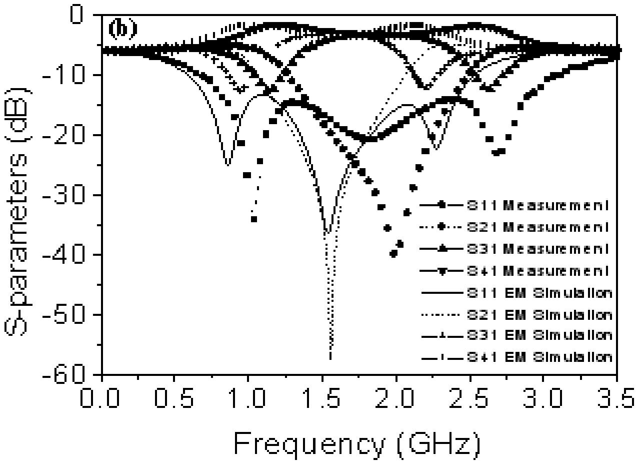

Reprinted with permission from [51]. Copyright 2008, John Wiley.

Figure 25. Impedance matching ($S_{11}$), coupling ($S_{31}$, $S_{41}$) and isolation ($S_{21}$) for the CSRR-based hybrid coupler (a) and conventional coupler (b). The slight discrepancies between simulation and measurement in the conventional coupler are attributed to fabrication related tolerances.

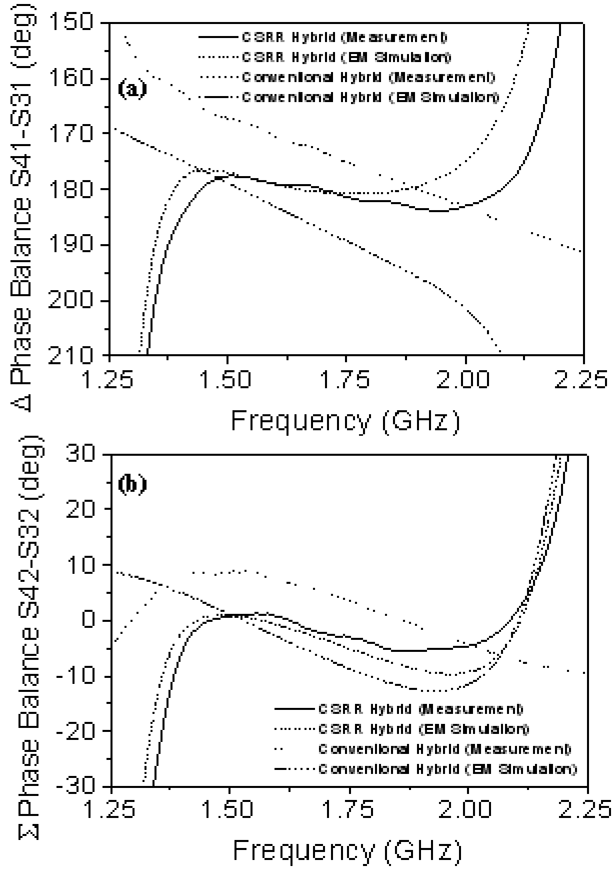

Reprinted with permission from [51]. Copyright 2008, John Wiley.

Figure 26. Phase balance for the Δ (a) and Σ (b) ports of the fabricated rat-race hybrids.

Some other works have shown the possibilities of bandwidth enhancement by using CL-loaded lines (see for instance the design of broadband series power dividers [55], phase shifters [56,57] and Wilkinson baluns [58]).

### 3.3. Multiband Components

The design of multiband metamaterial based components relies on the controllability of the dispersion diagram of metamaterial transmission lines. Multiband components are components exhibiting certain functionality at least at two arbitrary frequencies. Although recent works reveal that the design of up to quad-band components is potentially possible [59], most of the works in the recent literature have been focussed on the design of dual-band components. Conventional microwave components typically exhibit a periodic response and hence they exhibit the required functionality at the design frequency and its odd harmonics. However, such components cannot be considered multi-band components since the operating frequencies cannot be set to those values corresponding to system requirements (namely, arbitrariness is missing). To achieve dual-band operation, it is necessary to satisfy the phase and impedance requirements (for the transmission lines and stubs of the circuit) at the two design frequencies, $f_1$ and $f_2$. Let us consider that the required phases are $\phi_1$ and $\phi_2$ at the design frequencies. As can be seen in Figure 27, in general, such phases cannot simultaneously be satisfied. However, by using artificial lines, we can tailor the dispersion diagram to set the phases to the required values at the two operating frequencies (such as Figure 27 illustrates). One important aspect is that, contrary to conventional lines, metamaterial transmission lines exhibit frequency dependent characteristic impedance. Thus,

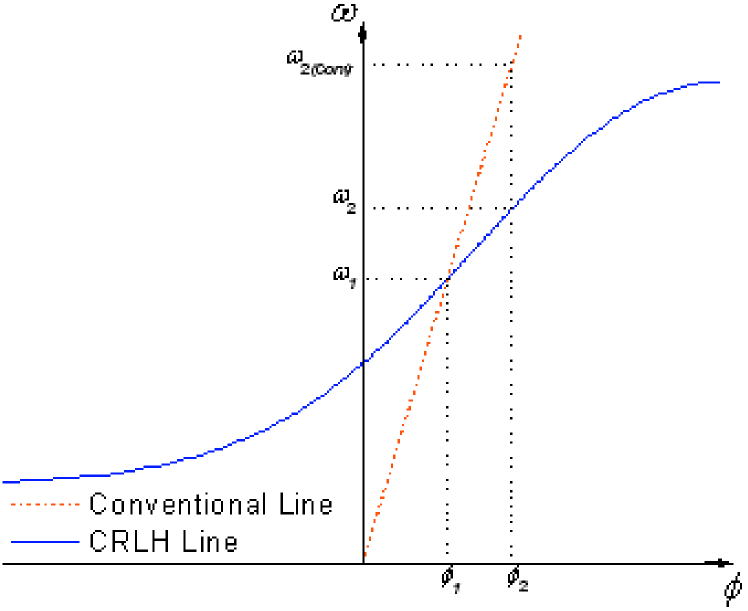

Figure 27. Illustration of the mono-band operation of conventional lines, as compared to the possibility of designing dual band metamaterial transmission lines, with the required phase at arbitrary frequencies.

such artificial lines must be designed to satisfy also the impedance requirements at the design frequencies.

For the implementation of dual-band metamaterial transmission lines, one approach is to cascade multiple effectively homogeneous unit cells. For instance, a balanced line in the vicinity of the transition frequency exhibits roughly constant (i.e., frequency independent) characteristic impedance. Thus, by setting this impedance to the required value and adjusting the slope of the dispersion diagram so that the phases of the unit cells are $\phi_1$/N and $\phi_2$/N at the design frequencies, dual-band operation can be achieved. Practical dual band components have been indeed implemented by cascading conventional lines (with positive phase shift) and backward lines implemented by means of lumped elements. As long as the phase shift per unit cell in the backward lines is small, the phase can be approximated by:

$$\phi_C = \phi_R - \frac{N}{\omega\sqrt{L_L C_L}} \tag{53}$$

where the sub-index $C$ denotes the phase of the composite structure and $N$ is the number of unit cells of the backward wave line. Following this strategy, several dual band components have been implemented (see for instance [49,60-62]).

Another approach consists on implementing such dual-band artificial lines by means of a single unit cell, designed to satisfy the impedance and phase requirements at the operating frequencies. In general this approach cannot be applied, but it is useful, for instance, for the design of dual-band 90° transmission lines (of application in many circuits as impedance or admittance inverters). The key idea behind this approach is to design the line so that the lower frequency lies within the left handed band, and the upper frequency within the right handed band. According to this, we must force the electrical length and characteristic impedance to $\phi=\phi_1=-90^{\circ}$ and $Z_B=Z_1$, at the lower frequency, and $\phi=\phi_2=+90^{\circ}$ and $Z_B=Z_2$ at the upper frequency (notice that in principle we consider that the characteristic impedance can be different at each frequency). Let us consider the implementation of these dual-band impedance inverters by means of CSRR-loaded CRLH transmission lines. The lumped element model of the unit cell is described by means of 5 independent parameters, whereas the phase and impedance pairs represent 4 conditions. Thus, these parameters cannot be univocally determined unless an additional condition is imposed. If we force the structure to be balanced, that is, to exhibit a continuous transition between the left handed and right handed bands, the series and shunt resonance must be identical, as discussed before. Under these conditions the electrical parameters of the circuit model can be isolated. The following results are obtained:

$$L = \frac{2(Z_1\omega_1 + Z_2\omega_2)}{\omega_2^2 - \omega_1^2} \tag{54}$$

$$C_g = \frac{\omega_2^2 - \omega_1^2}{2\omega_1\omega_2(Z_1\omega_2 + Z_2\omega_1)} \tag{55}$$

$$C = \frac{Z_1\omega_2 + Z_2\omega_1}{(Z_2^2 - Z_1^2)\omega_1\omega_2} \tag{56}$$

$$C_c = \frac{Z_1\omega_2 + Z_2\omega_1}{(\omega_2^2 - \omega_1^2)Z_1 Z_2} \tag{57}$$

$$L_c = \frac{(Z_1\omega_1 + Z_2\omega_2)(\omega_2^2 - \omega_1^2)Z_1 Z_2}{\omega_1\omega_2(Z_1\omega_2 + Z_2\omega_1)^2} \tag{58}$$

with $\omega_1=2\pi f_1$ and $\omega_2=2\pi f_2$. Inspection of equations (54)-(58) reveals that $L$, $C_g$, $C_c$ and $L_c$ are always positive. However, $C$ may be negative ($Z_1>Z_2$) or, even, $C=\infty$ for a dual-band impedance inverter with identical impedances ($Z_1=Z_2$). If $Z_1>Z_2$ ($C<0$), the inverter cannot be synthesized by means of a balanced cell described by the model of Figure 12. If $Z_1=Z_2$, as most applications require, the inverter can be synthesized by balancing the line, but substituting the capacitance $C$ with an electrical short. In practice, this is not possible by using the cell topology shown in Figure 13(a), although this is possible through the CL-loaded approach. Hence, in order to implement dual-band quarter wavelength impedance inverters with identical impedances (at the frequencies of interest) by means of CRLH CSRR-based cells, such cells must be designed without the restriction of being balanced. Nevertheless, the circuit parameters of the series branch, $L$ and $C_g$ are still univocally determined under the un-balance condition (namely, expressions 54 and 55 hold). The reason is simple: since the $\pm 90^o$ phases lead to $Z_s=-Z_p$ at both $\omega_1$ and $\omega_2$ (see expression 5), it follows from (6) that $Z_1=+jZ_s(\omega_1)$ and $Z_2=-jZ_s(\omega_2)$, and expressions (54) and (55) result. The conditions involving the shunt branch are simply $Z_1=-jZ_p(\omega_1)$ and $Z_2=+jZ_p(\omega_2)$. Thus, $C$, $L_c$ and $C_c$ are not univocally determined unless the structure is balanced. In general, it is convenient to design the dual-band impedance inverters by means of un-balanced unit cells. This provides more flexibility to the electrical parameters and it easies the implementation of the structure through the layout of Figure 13(a). Furthermore, as has been mentioned, if $Z_1=Z_2$ (as usual), the structure must necessarily be un-balanced.

Based on these CSRR-based CRLH transmission line impedance inverters, dual band components have been designed [63,64]. Let us illustrate this by means of an example consisting on a dual band Y-juntion power divider operating at the mobile GSM bands ($f_1$=0.9GGHz and $f_2$=1.8GGHz). The frequency ratio is 2, this being a good choice to demonstrate the possibilities of the approach. The dual band power divider has been implemented by using CSRRs and complementary spiral resonators (CSRs) [64]. As compared to CSRRs, the electrical size of CSRs is roughly one half [65]. This allows further size reduction. Both dual band devices are depicted in Figure 28, where it is also depicted the corresponding power splitting and matching. Dual band operation is confirmed.

Dual band devices based on the CL-loaded approach have been also reported in various works [49,60-62,66,67].

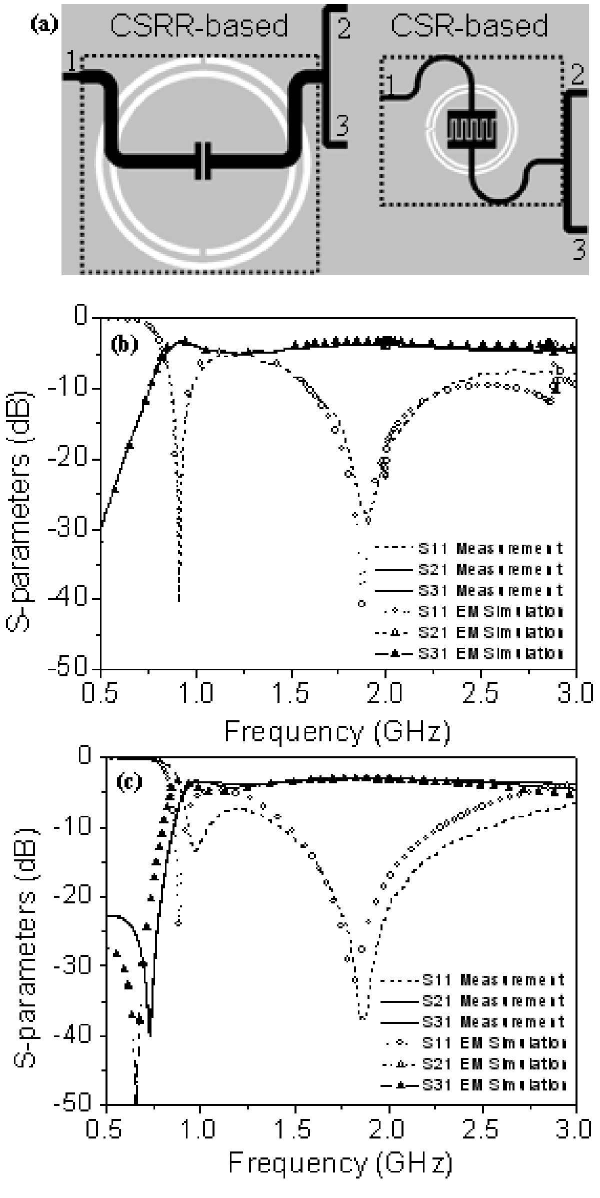

Reprinted with permission from [64]. Copyright 2008, IEEE.

Figure 28. Topology of the dual-band CSR- and CSRR-based Y-junction power dividers drawn to scale (a), frequency response of the CSRR-based device (b) and frequency response of the CSR based device (c). For the CSRR-based power divider dimensions are: external radius *r*=7.90mm, ring width *c*=0.50mm and separation between rings *d*=0.57mm. The width of the host line is *W*=1.00mm and gap dimensions are: separation *s*=0.27mm and width $W_g$=2.77mm. For the CSR power divider, dimensions are: external radius of the CSR *r*=3.35mm, spiral width *c*=0.21mm and separation *d*=0.24mm. The width of the host line is *W*=0.37mm and gap is an interdigital capacitor formed by 5 fingers separated a distance of 0.17mm. The *Rogers RO3010* substrate with thickness *h*=0.635mm and dielectric constant $\varepsilon_r$=10.2 has been used. The rectangles in dotted lines, corresponding to the active regions of the devices are 17.7mm×15.8mm and 13.5mm×11.1mm for the CSRR- and CSR-based dividers, respectively.

## 4. CONCLUSION

In conclusion, Metamaterial's Technology is a promising technology for the design of novel RF and microwave components that represent an alternative to the state-of-the-art. The small electrical size of the constitutive building blocks of metamaterials has been demonstrated to be applicable to the design of compact components, while dispersion engineering allows for further degrees of freedom that can be useful for the design of devices with superior performance, such as enhanced bandwidth components, or multiband components. Examples of applications based on the resonant type approach of metamaterials, that is, by using split ring resonators (SRRs), complementary split ring resonators (CSRRs), or alternative topologies, have been presented. Metamaterials are compatible with advanced planar technologies, including low loss microwave substrates, and microelectronic technologies such as MCM-D and RF-MEMS.

## REFERENCES

[1] D.R. Smith, W.J. Padilla, D.C. Vier, S.C. Nemat-Nasser and S. Schultz, "Composite medium with simultaneously negative permeability and permittivity", *Phys. Rev. Lett.*, vol. 84, pp. 4184-4187, May 2000.

[2] V.G. Veselago, "The electrodynamics of substances with simultaneously negative values of ε and μ", *Sov. Phys. Usp.* Vol. 10, pp. 509-514, January 1968.

[3] G.V. Eleftheriades and K.G. Balmain Editors, *Negative-Refraction Metamaterials: Fundamental Principles and Applications*, John Wiley & Sons Inc., New York, 2005.

[4] N. Engheta and R.W. Ziolkowski Editors, *Metamaterials: Physics and Engineering Explorations*, John Wiley & Sons Inc., New York, 2006.

[5] C. Caloz and T. Itoh, *Electromagnetic Metamaterials: Transmission Line Theory and Microwave Applications*, John Wiley & Sons, Inc., New York, 2006.

[6] R. Marqués, F. Martín and M. Sorolla, *Metamaterials with Negative Parameters: Theory, Design and Microwave Applications*, John Wiley & Sons Inc., New York, 2007.

[7] K. Sarychev and V.M. Shalaev, *Electrodynamics of Metamaterials*, World Scientific Publishing Co., Singapore, 2007.

[8] P. Markos and C.M. Sokoulis, *Wave Propagation: From Electrons to Photonic Crystals and Left-Handed Materials*, Princeton University Press, 2008.

[9] D. Schurig, J. J. Mock, B. J. Justice, S. A. Cummer, J. B. Pendry, A. F. Starr, D. R. Smith, "Metamaterial Electromagnetic Cloak at Microwave Frequencies", *Science,* vol. 314, pp. 977-980, Nov. 2006.

[10] K. Iyer and G. V. Eleftheriades. "Negative refractive index metamaterials supporting 2-D waves," in *IEEE-MTT Int'l Microwave Symp.,* vol. 2, Seattle, WA, pp. 412– 415, June 2002.

[11] Oliner. "A periodic-structure negative-refractive-index medium without resonant elements," in *URSI Digest, IEEE-AP-S USNC/URSI National Radio Science Meeting,* San Antonio, TX, pp. 41, June 2002.

[12] Caloz and T. Itoh. "Application of the transmission line theory of left-handed (LH) materials to the realization of a microstrip LH transmission line," *in Proc.IEEE-AP-S*

*USNC/URSI National Radio Science Meeting,* vol. 2, San Antonio, TX, pp. 412–415, June 2002.

[13] F. Martín, F. Falcone, J. Bonache, R. Marqués and M. Sorolla, “Split ring resonator based left handed coplanar waveguide”, *Appl. Phys. Lett.*, vol. 83, pp. 4652-4654, December 2003.

[14] F. Falcone, T. Lopetegi, M.A.G. Laso, J.D. Baena, J. Bonache, R. Marqués, F. Martín, M. Sorolla, “Babinet principle applied to the design of metasurfaces and metamaterials”, *Phys. Rev. Lett.*, vol. 93, pp. 197401-4, November 2004.

[15] Caloz and T. Itoh, “Novel microwave devices and structures based on the transmission line approach of metamaterials”, in *IEEE-MTT Int’l Microwave Symp*, vol. 1 Philadelphia, PA, pp. 195-198, June 2003.

[16] J.B. Pendry, A.J. Holden, D.J. Robbins and W.J. Stewart, “Magnetism from conductors and enhanced nonlinear phenomena”, *IEEE Transactions Microwave Theory Tech.,* vol. 47, pp. 2075-2084, November 1999.

[17] F. Falcone, T. Lopetegi, J.D. Baena, R. Marqués, F. Martín and M. Sorolla, “Effective negative-ε stop-band microstrip lines based on complementary split ring resonators”, *IEEE Microwave and Wireless Components Letters*, vol. 14, pp. 280-282, June 2004.

[18] R. Marqués, F. Medina and R. Rafii-El-Idrissi, “Role of bianisotropy in negative permeability and left handed metamaterials”, *Phys. Rev. B*, vol. 65, 144440, April 2002.

[19] J.D. Baena, J. Bonache, F. Martín, R. Marqués, F. Falcone, T. Lopetegi, M.A.G. Laso, J. García, I Gil and M. Sorolla, “Equivalent circuit models for split ring resonators and complementary split rings resonators coupled to planar transmission lines”, *IEEE Transactions on Microwave Theory and Techniques*, vol. 53, pp. 1451-1461, April 2005.

[20] J. García-García, F. Martín, J.D. Baena, R.Marques, L. Jelinek “On the resonances and polarizabilities of split rings resonators”, *J. Applied Physics*, vol. 98, pp. 033103-1-9, September 2005.

[21] J. Bonache, M. Gil, O. García-Abad and F. Martín, “Parametric analysis of microstrip lines loaded with complementary split ring resonators”, *Microwave and Optical Technology Letter*s, vol. 50, pp. 2093-2096, August 2008.

[22] J. Bonache, M. Gil, I. Gil, J. Garcia-García and F. Martín, “On the electrical characteristics of complementary metamaterial resonators”, *IEEE Microwave and Wireless Components Letters*, vol. 16, pp. 543.545, October 2006.

[23] M. Gil, J. Bonache, J. Selga, J. García-García and F. Martín, “Broadband resonant type metamaterial transmission lines”, *IEEE Microwave and Wireless Components Letters*, vol. 17, pp. 97-99, February 2007.

[24] M. Gil, J. Bonache, J. García-García and F. Martín, “Composite Right/Left Handed (CRLH) Metamaterial Transmission Lines Based on Complementary Split Rings Resonators (CSRRs) and Their Applications to Very Wide Band and Compact Filter Design”, *IEEE Transactions on Microwave Theory and Techniques*, vol. 55, pp. 1296-1304, June 2007.

[25] Li, K.-Y Liu, F. Li, “Design of microstrip highpass filters with complementary split ring resonators”, *Electronics Letters*, vol. 43, pp. 35-36, January 2007.

[26] Gil, J. Bonache, M. Gil, J. García-García, F. Martín, “Left handed and right handed transmission properties of microstrip lines loaded with complementary split rings resonators”, *Microwave and Optical Technology Letters*, vol. 48, pp. 2508-2511, December 2006.

[27] Aznar, M. Gil, J. Bonache and F. Martín, "Revising the Equivalent Circuit Models of Resonant-Type Metamaterial Transmission Lines", 2008 IEEE MTT-S Int. Microwave Symposium Digest, Atlanta (USA), June 2008, pp. 323-326.

[28] J. García-García, F. Martín, E. Amat, F. Falcone, J. Bonache, I. Gil, T. Lopetegi, Miguel A.G. Laso, A. Marcotegui, M. Sorolla,and Ricardo Marqués, "Microwave Filters with Improved Stop Band based on Sub-wavelength Resonators", *IEEE Transactions on Microwave Theory and Techniques*, vol. 53, pp. 1997-2006, June 2005.

[29] J. García-García, J. Bonache, I. Gil, F. Martín, R. Marqués, F. Falcone, T. Lopetegi, M.A.G. Laso, M- Sorolla, "Comparison of electromagnetic bandgap and split rings resonator microstrip lines as stop band structures", *Microwave and Optical Technology Letters*, vol. 44, pp. 376-379, February 2005.

[30] J. García-García, F. Martín, F. Falcone, J. Bonache, I. Gil, T. Lopetegi, M.A.G. Laso, M. Sorolla, R. Marqués, "Spurious passband suppression in microstrip coupled line band pass filters by means of splir ring resonators", *IEEE Microwave and Wireless Components Letters*, vol. 14, pp- 416-418, September 2004.

[31] J. García-García, J. Bonache, F. Falcone, J.D. Baena, F. Martín , I. Gil, T. Lopetegi, M.A.G. Laso, A. Marcotegui, R. Marqués and M. Sorolla, "New stepped-impedance low pass filters with spurious passband suppression", *Electronics Letters*, vo.l. 40, pp. 881-883, July 2004.

[32] Gil, J. García-García, J. Bonache, F. Martín, M. Sorolla, R. Marqués, "Varactor-loaded split rings resonators for tuneable noth filters at microwave frequencies", *Electronics Letters*, vol. 40, pp. 1347-1348, October 2004.

[33] Gil, J. Bonache, J. García-García, F. Martín "Tunable Metamaterial Transmission Lines Based on Varactor Loaded Split Rings Resonators", *IEEE Transactions on Microwave Theory and Techniques*, vol. 54, pp. 2665-2674, June 2006.

[34] Vélez, J. Bonache and F. Martín, "Varactor-Loaded Complementary Split Ring Resonators (VLCSRR) and their Application to Tunable Metamaterial Transmission Lines", *IEEE Microwave and Wireless Components Letters*, vol. 18, pp. 28-30, January 2008.

[35] Gil, X. Rottenberg, W. De Raedt and F. Martín, "Tunable stop-band filter at Q-band based on RF-MEMS metamaterials", *Electronics Letters*, vol. 43, p. 1153, October 2007.

[36] J. Bonache, F. Falcone, J.D. Baena, T. Lopetegi, J. García-García, M.A.G. Laso, I. Gil, A. Marcotegui, R. Marqués, F. Martín and M. Sorolla, "Application of complementary split rings resonators to the design of compact narrow band pass structure in microstrip technology" *Microwave and Optical Technology Letters*, vol. 46, pp. 508-512, September 2005.

[37] J. Bonache, I. Gil, J. García-García and F. Martín, "Complementary split rings resonator for microstrip diplexer design", *Electronics Letters*, vol. 41, pp. 810-811, July 2005.

[38] M. Gil, J. Bonache and F. Martín, "Metamaterial Filters with Attenuation Poles in the Pass Band for Ultra Wide Band (UWB) Applications", *Microwave and Optical Technology Letters*, vol. 49, pp. 2909-2913, December 2007.

[39] W. Menzel and P. Feil, Ultra-wide band (UWB) filter with WLAN notch, *Proc. of the 36th European Microwave Conference*, Manchester (UK), September 2006, pp. 595–598.

[40] K. Li, D. Kurita, and T. Matsui, UWB band pass filters with multi notched bands, *Proc. of the 36th European Microwave Conference*, Manchester (UK), September 2006, pp. 591–594.

[41] J. Bonache, M. Gil, I. Gil, J. García-García and F. Martín, “Limitations and Solutions of Resonant-Type Metamaterial Transmission Lines for Filter Applications: the Hybrid Approach”, *2006 IEEE MTT-S International Microwave Symposium Digest*, pp. 939-942, San Francisco (CA), USA, June 2006.

[42] J. Bonache, I. Gil, J. García-García, F. Martín, “Novel Microstrip Band Pass Filters Based on Complementary Split Rings Resonators”, *IEEE Transactions on Microwave Theory and Techniques,* vol. 54, pp. 265-271, January 2006.

[43] J-S. Hong and M.J. Lancaster, *Microstrip filters for RF/microwave applications*, John Wiley & Sons, New York (USA), 2001.

[44] J. Bonache, G. Posada, G. Garchon, W. De Raedt and F. Martín, “Compact (<0.5mm$^2$) K-band metamaterial band pass filter in MCM-D technology”, *Electronics Letters*, Vol. 43, No 5, pp. 45-46, March 2007.

[45] Carchon, X. Sun, G. Posada, D. Linten, and E. Beyne, “Thin-Film as Enabling Technology for RF-SoC and RF-SiP” presented at *ISSCC*, San Francisco, CA, pp. 21.5, Feb. 6-10, 2005.

[46] H.V. Nguyen and C. Caloz, “Broadband highly selective bandpass filter based on a tapered coupled-resonator (TCR) CRLH structure”, *Proc. European Microwave Association*, vol. 2, pp. 44-51, March 2006.

[47] P. Mondal, M.K. Mandal, A. Chaktabarty, S. Sanyal. “Compact Bandpass Filters with Wide Controllable Fractional Bandwidth”. *IEEE Microwave and Wireless Components Letters*, vol. 16, pp. 540-542, Oct. 2006.

[48] J. García-García, I. B. Vendik, B. Sans, D. Kholodnyak, P. Kapitanova, J. Bonache and F. Martín, “Miniaturization and Optimization of Planar Microwave Filters Based on Metamaterials”, *2007 European Microwave Conferenc*e, Munich (Germany), 9-12 Octobre 2007, pp. 500-503.

[49] C-H. Tseng and T. Itoh, “Dual-Band Bandpass and Bandstop Filters Using Composite Right/Left-Handed Metamaterial Transmission Lines”, 2006 IEEE MTT-S Int’l Microwave Symposium Digest, pp. 931-934, San Francisco, CA, June 2006.

[50] Sisó, M. Gil, J. Bonache and F. Martín, “On the dispersion characteristics of metamaterial transmission lines”, *J. Appl. Phys*., vol. 102, paper 074911, 2007.

[51] Sisó, J. Bonache, M. Gil and F. Martín, “Application of resonant-type metamaterial transmission lines to the design of enhanced bandwidth components with compact dimensions”, *Microwave and Optical Technology Letters*, vol. 50, pp. 127-134, January 2008.

[52] G. Sisó, M. Gil, J. Bonache and F. Martín, “Application of metamaterial transmission lines to the design of quadrature phase shifters”, *Electronics Letters*, vol. 43, pp. 1098-1100, September 2007.

[53] G. Sisó, M. Gil, J. Bonache and F. Martín, “Dispersion engineering with resonant type metamaterial transmission lines”, *Laser and Photonics Reviews*, Vol. 3 (Issue 1-2), pp. 12-29, March 2009**.**

[54] Okabe, C. Caloz and T. Itoh, “A compact enhanced bandwidth hybrid ring using an artificial lumped element left handed transmission line section”, *IEEE Trans. Microwave Theory and Techniques*, vol. 52, pp. 798-804, March 2004.

[55] M.A. Antoniades and G.V. Eleftheriades, “A broadband series power divider using zero-degree metamaterial phase shifting lines”, IEEE *Microwave and Wireless Components Letters*, vol. 15, pp. 808-810, November 2005.

[56] D. Kholodnyak, E. Serebryakova, I Vendik, O. Vendik, “Broadband digital phase shifter based on switchable right- and left-handed transmission line sections”, *IEEE Microwave Wireless Comp. Lett*., vol. 16, pp. 258-260, May 2006.

[57] O.G. Vendik, I.B. Vendik, D.V. Kholodnyak, S.P. Zubko, and E.V. Serebryakova, “Electronically Controlled Phase Shifters Based on Right/Left-Handed Transmission Lines”, *2005 European Microwave Conference*, vol. 2, Paris (France), October 2005.

[58] M.A. Antoniades and G.V. Eleftheriades, "A broadband Wilkinson balun using microstrip metamaterial lines", *IEEE Antennas and Wireless Propagation Lett*., vol. 4, pp. 209–212, November 2005.

[59] G.V. Eleftheriades, “A generalized negative-refractive-index transmission-line (NRL-TL) metamaterial for dual-band and quad-band applications”, *IEEE Microwave Wireless Comp. Lett*., vol. 17, pp. 415-417, June 2007.

[60] I-H. Lin, M. DeVincentis, C. Caloz, and T. Itoh, “Arbitrary Dual-Band Components Using Composite Right/Left-Handed Transmission Lines”, *IEEE Transactions on Microwave Theory and Techniques*, Vol. 52, pp. 1142-1149, April 2004.

[61] I.-H. Lin, K.M.K.H. Leong, C. Caloz and T. Itoh, “Dual-band sub-harmonic quadrature mixer using composite right/left-handed transmission lines”, *IEE Proc. Microw. Antennas Propag*., vol. 153, pp. 365-375, August 2006.

[62] S.H. Ji, C.S. Cho, J.W. Lee, and J. Kim, “Concurrent Dual-Band Class-E Power Amplifier Using Composite Right/Left-Handed Transmission Lines”, *IEEE Transactions on Microwave Theory and Techniques*, vol. 55, pp. 1341-1347, June 2007.

[63] Bonache, G. Sisó, M. Gil, A. Iniesta, J. García-Rincón and F. Martín, “Application of composite right/left handed (CRLH) transmission lines based on complementary split ring resonators (CSRRs) to the design of dual band microwave components”, *IEEE Microwave and Wireless Components Letters*, vol. 18, pp. 524-526, August 2008.

[64] G. Sisó, J. Bonache and F. Martín, “Dual-Band Y-Junction Power Dividers Implemented Through Artificial Lines Based on Complementary Resonators”, *IEEE MTT-S International Microwave Symposium*, Atlanta (USA), June 2008, Atlanta (USA), June 2008, pp. 663-666.

[65] D. Baena, R. Marqués, F. Medina and J. Martel, “Artificial magnetic metamaterial design by using spiral resonators,” *Phys. Rev. B*, vol. 69, paper 014402, 2004.

[66] V. Piatnitsa, D. Kholodnyak, P. Kapitanova, I. Fischuk, T. Tick, J. Jantti, H. Jantunen, and I. Vendik, “Right/Left-Handed Transmission Line LTCC Directional Couplers”, *Proceedings of the 37th European Microwave Conference*, pp. 636-639, Munich (Germany), October 2007.

[67] X.Q. Lin, R.P. Liu, X.M. Yang, J.X. Chen, X.X. Yin, Q. Cheng, and T. J. Cui, “Arbitrarily Dual-Band Components Using Simplified Structures of Conventional CRLH TLs”, *IEEE Transactions on Microwave Theory and Techniques*, vol. 54, pp. 2902-2909, July 2006.

In: Integrated Circuits, Photodiodes…
Editors: R. McIntire and P. Donnell, pp. 45-67

ISBN: 978-1-60692-660-4
© 2009 Nova Science Publishers, Inc.

*Chapter 2*

# RELIABILITY ASSESSMENT OF INTEGRATED CIRCUITS AND ITS MISCONCEPTION

***Cher Ming Tan***[*]
School of EEE, Nanyang Technological University, Singapore

## ABSTRACT

Reliability is a key success factor to Engineering products today, and the requirement for integrated circuit reliability is increasing due to increasing complexity of electronic products, market globalization and manufacturing outsourcing. This chapter illustrates the important of integrated circuit reliability and the rationale behind its “ridicules” requirement of more than 50 years.

Reliability test is not new to the integrated circuit manufacturers. However, there are several seemingly intuitive concepts in the reliability tests and test data analyses that are being practice in the manufacturers today are incorrect and can lead to over-estimation of product reliability grossly. This chapter shows the different misconceptions in the common reliability practices of integrated circuits manufacturers with examples.

The purpose of this chapter is to bring awareness of these misconceptions. All these misconceptions can be resolved with the proper use of reliability statistics which is beyond the scope of this chapter.

## I. THE IMPORTANCE OF INTEGRATED CIRCUIT RELIABILITY

Reliability is the probability that a product is operational for specified functions under stated operating conditions after some operation time. On the other hand, quality is the percentage of the production lot that conforms to the product specifications. There is no time factor in the quality engineering, and hence ensuring quality does not necessary ensure product reliability. A product can be within its specification at the start, but how long this product can remain within specification is a question for reliability.

Looking at the difference between quality and reliability, it is clear that while quality assurance activities such as 6 sigma are beneficial to the manufacturers because it reduces

---

[*] E-mail address: ecmtan@ntu.edu.sg

yield loss, it may not produce benefit to the customers. Of course, poor quality will result in poor reliability and it may cause many early failures of the product, good quality may not result in good reliability because the methodology to improve reliability is vastly different from the quality methodology. On the other hand, customers are experiencing the reliability of the products, and thus customer satisfaction should be derived from product reliability, including early failures.

Electronic products are common in our daily life, and most people cannot live without an electronic product today. Examples of electronic products are electronic watch, radio, and handphone, to name a few. Our reliance on electronic products is increasingly significant.

The more we rely on electronic products, the greater inconvenience or loss will be if the products are not reliable. Also, the higher the price of the product, the higher the expected reliability of the product will be. In fact, product reliability is increasingly important because of market globalization and manufacturing outsourcing.

Through globalization, customers can purchase products easily from anywhere in the world, and any products that are not reliable will not be able to remain in the market for long, especially for products with high pricing. The internet technology enables customers' complaining to be "heard" from all part of the world, and customers can compare the product performance, price and reliability through the internet before they purchase.

With outsourcing, manufacturers are able to reduce the cost of production, and the price of the product can be reduced in order to capture a larger market. Therefore, price competition will be a brutal game which can result in loss-loss situation, and value competition should be employed in order to survive this global competition. Customers today make their purchasing decision based on which product offer the best value defined as[1]

$$\text{Product Value} = (\text{Customer Perceived Value})/\text{Price}$$

The customer perceived value is related to the performance and reliability of the product. In other word, achieving high product reliability at reasonable cost is the key success factor in today electronic industry.

In fact, in contrast to the common understanding, one of the key advantages of implementing reliability throughout the organization and at every phase of the product is that the product value increases due to an improved customer perception of the value of the product and the lower cost of production. This lower cost derives from the fact that products that are reliable generally have the following characteristics[1]:

a. Higher first pass yield in test
b. Less material scrap
c. Less product rework
d. Fewer field failures
e. Reduced warranty costs
f. Lower risk of recall
g. Better designs that are easier to manufacture.

Reliabilities of electronic products depend mainly on their components. Thus components' reliabilities are the determining factors for product reliability. With the increasing complexity of the products due to added functionality, the requirement for components' reliabilities will be more stringent. This is illustrated in the following example.

Assume a product consists of three components as shown in Figure 1, and each component must be operational in order for the product to function. Such a system is called series connected system in reliability engineering. The reliability of the product is then the probability that all the components are functioning. Mathematically, it is expressed as

$$R_p = R_1 \times R_2 \times R_3 \tag{1}$$

where $R_p$ is the product reliability, and $R_i$ is the respective component reliability with the subscript representing the component number.

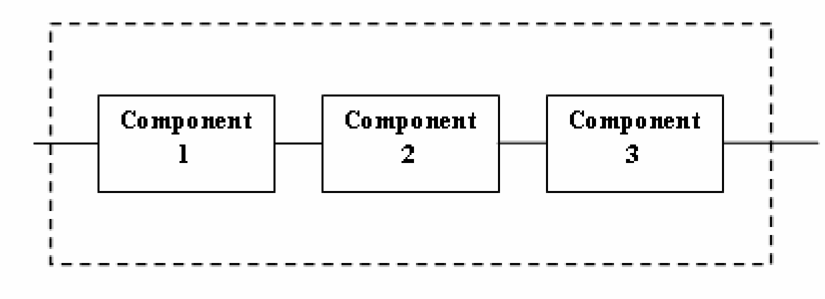

Figure 1. Series connected System with 3 components.

If $R_1 = R_2 = R_3 = R$, $R_p = R^3$. Thus, if $R$=0.90 after one year of operation, $R_p$=0.729 after one year, and it is low for a product because it represents that 37% of the product will fail in the first year. If $R$=0.95, then $R_p$=0.86.

With the increasing complexity of a product, the number of component will also be increased. Again assume all the $R_i = R$, we can plot the value of $R_p$ versus the number of component ($n$) as in Figure 2. One can see that with the same value of $R$, $R_p$ decreases significantly with $n$, especially when the value of $R$ is smaller.

Assuming a product reliability requirement $R_p$=0.95, $R$ should be greater than 0.95 if $n$ is 1. When $n$ increases to 6, minimum $R$ should be 0.99. Thus one can see clearly that the reliability requirement for the components will have to be increased in order to keep the same product reliability when $n$ is increasing due to the increased complexity of a product. Figure 3 shows the minimum component reliability requirement $R$ with respect to $n$ in order to have $R_p$=0.95.

While the increase in the required reliability for the components seem minimal beyond $n = 10$ in Figure 3, this is deceiving as can be seen from the corresponding increase in the required mean time to failure (MTTF) for the component in Figure 3. The MTTF is computed assuming the time to failure distribution is exponential distribution for illustration purpose.

From Figure 3, we can also understand the lifetime requirement for IC to be 10 years or even 100 years though the IC and the product never need to be operated for so long the period.

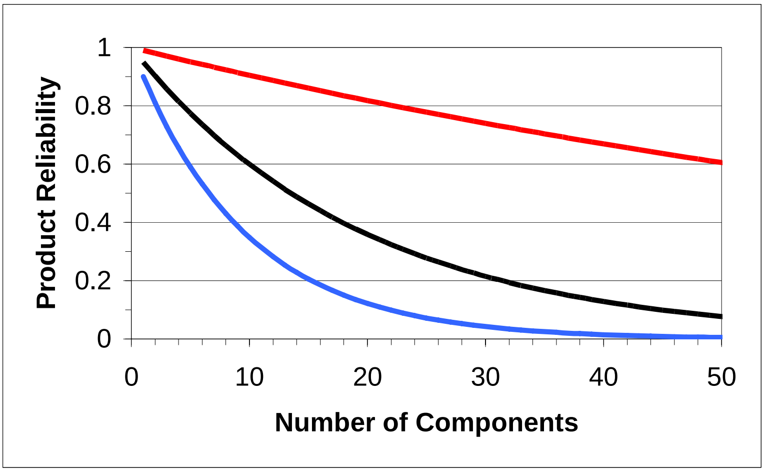

Figure 2. Product reliability with increasing complexity. Here The reliability of all the components are assumed to be the same. For the upper red curve, the component reliability is 0.99. For the middle black curve, the component reliability is 0.95. The bottom blue curve is for component reliability of 0.90.

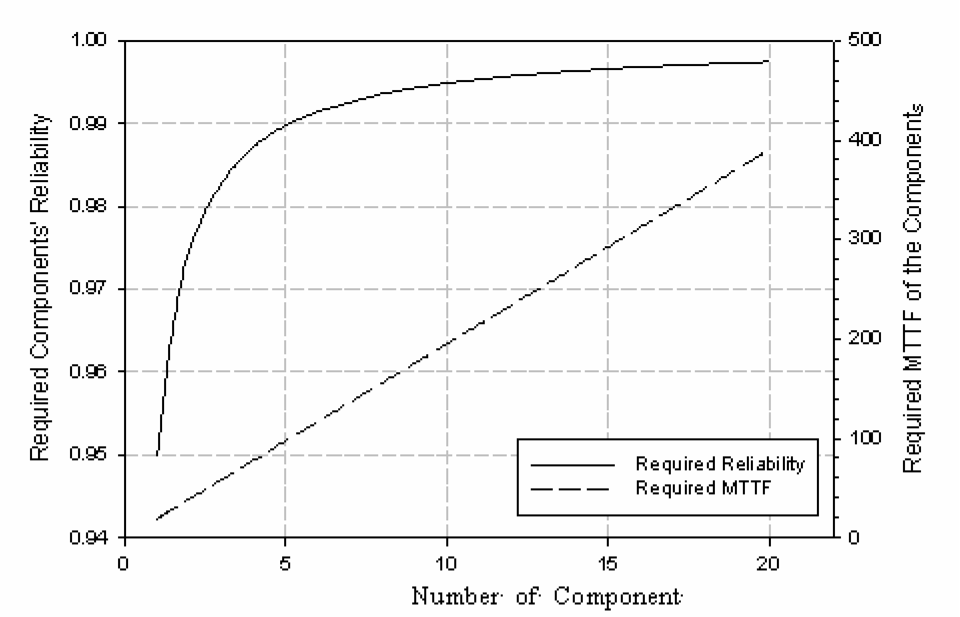

Figure 3. Required Components' Reliability and Mean Time to Failure (MTTF) in year as a function of the number of components to achieve product reliability of 0.95.

# II. COMMON RELIABILITY PRACTICES IN INTEGRATED CIRCUIT INDUSTRY

Understanding the stringent requirement for IC reliability, accelerated stress tests are conducted in almost all the IC manufacturers, including the wafer fabrication and IC assembly/packaging manufacturers.

The purpose of the accelerated stress tests is to obtain information on the failure time of various failure mechanisms in a reasonable short time. With the understand of the importance of reliability as mentioned earlier, the purpose of the accelerated tests will translate into the following requirements for the tests as spelled out in the Blueprint for Product Reliability (RBPR-4 and RBPR-5) [2]:

a) The failure mechanisms uncovered at higher stress must be the same failure mechanisms as at the normal operating levels.
b) The stress used will accelerate the action of the failure mechanisms that are dominant at the normal operating condition.
c) There is a good way to translate the lifetime data under high stress to useful data at the normal operating condition. In other word, the same statistical model of failure will be true for use at the normal and accelerated conditions
d) Test units must be identical to the final product
e) The stress levels do not exceed the maximum component design.

Let us now look at the common process and product reliability tests in IC industry.

## 1. Process Reliability Test in Wafer Fabrication Manufacturers

In the wafer fabrication manufacturers, the common process reliability tests conducted are the following, and the detail of each test can be found in the standards quoted besides the list of tests.

Take Electromigration test as an example from the tests listed in Table 1, the test is usually conducted at 2 different temperatures and 2 different current densities as shown in the test matrix in Table 2. Median time to failure $t_{50}$ is computed from each test condition, and the values of activation energy $E_a$ and current exponent $n$ in the Black’s equation shown in Eqn (2) are determined according to JESD63. The test is done with at least 50% of the samples failed or at least 12 samples have failed if the sample size is below 24, according to ASTM F1260-96.

$$t_{50} = AJ^{-n}e^{-E_a/(k_B T)} \tag{2}$$

With reference to Eqn (2), using the ratio of $t_{50,1}$ and $t_{50,2}$, the value of $n$ can be determined. Using the ratio of $t_{50,1}$ and $t_{50,3}$, the value of $E_a$ can be determined. Care must be taken to include the Joule heating due to the current density in such a way that actual interconnect temperature should be estimated from its Temperature Coefficient of Resisvity (TCR) and used in the calculation. Detail of the test can be found in [3].

**Table 1. Common Process Reliability Tests in Wafer Fabrication Plants**

| S/No. | Test | Reference Procedures |
|---|---|---|
| **Interconnect Reliability** | | |
| 1. | Electromigration | ASTM F1260-96, JESD 33-A, JESD37, JESD61, JESD63, JESD87 |
| 2. | Stress migration | JEP139, JESD37, JESD87 |
| 3. | Thermal Cycling | JESD22 |
| 4. | Inter/Intra-metal dielectric integrity | JEDEC JP001.01 |
| **Oxide Reliability** | | |
| 5 | Gate oxide integrity test | JESD35 |
| 6 | Time Dependent Dielectric Breakdown | JESD92 |
| 7. | Plasma process-induced damage | JEDEC JP001.01 |
| 8 | Ionic contamination (BTS and TVS) | JEDEC JP001.01 |
| **Dielectric/Si interface reliability** | | |
| 9. | Hot Carrier Injection | JESD60, JESD28 |
| 10. | Negative bias temperature instability | JESD90 |
| **Junction reliability** | | |
| 11. | Latch up | JESD78 |
| 12. | ESD | JESD22 |

*JESD standard can be found in www.jedec.org.

**Table 2. Test Matrix for Electromigration**

| | **Current Density $J_1$** | **Current Density $J_2$** |
|---|---|---|
| Temperature $T_1$ | $t_{50,1}$ | $t_{50,2}$ |
| Temperature $T_2$ | $t_{50,3}$ | |

Once the values of $E_a$ and $n$ are determined, the $t_{50}$ at any other current density and temperature can be computed from Eqn (2). In this way, lifetime of an interconnect under normal operating condition can be determined.

## 2. Product Reliability Tests in IC Assembly and Packaging Manufacturers

In the IC assembly and packaging manufacturers, the common reliability tests conducted are the following, and the detail of each test can be found in the standards quoted besides the list of tests.

Take the THB life test as an example. The sample size is generally 77, and the test is conducted at 85%RH, 85°C with the input/output pins reverse biased. At different interval of test time, the devices under test will be taken out for electrical test to examine if they are still functional, and the number of failure is recorded at different monitoring interval.

**Table 3. Common Product Reliability Tests in IC Assembly and Packaging Plants**

| S/No. | Test | Reference Procedures |
|---|---|---|
| **Hermetic Test** | | |
| 1. | Temperature-humidity-bias (THB) life test | JESD22 |
| 2. | Unbiased autoclave | JESD22 |
| 3. | Moisture soak | JESD22 |
| **Storage Test** | | |
| 4. | High temperature storage life test | JESD22 |
| **Operating Life Test** | | |
| 5. | Power and temperature cycling | JESD22 |
| 6. | Temperature cycling | JESD22 |

*JESD standard can be found in www.jedec.org.

Generally, there is no further analysis to the test data. The goal is to ensure zero failure upto 1000 hours.

### 3. Highly Accelerated Stress Test (HAST)

As technology advances, the reliability of integrated circuits is also increasing, and the time to failure for IC is longer with very few or even no failure generally observed during reliability test. With the increasing demand on reliability for ICs, HAST is now commonly used to assess the reliability of ICs. As the name implied, HAST applies extreme high stress to surface out the weakness of the component, and re-design or process change will be initiated until the failures observed in the HAST is no longer exist. Components that pass HAST is deemed as having adequate reliability to meet the reliability requirement.

The main impetus of HAST is for product reliability improvement. It does not allow one to compute a reliability number. It uncovers defects and lead to product improvements. A shortcoming for HAST is that it has not been totally quantified by equations and theories. For detail on HAST, readers may refer to [1, 4] and the references therein.

## III. MISCONCEPTIONS IN COMMON RELIABILITY ASSESSMENT OF INTEGRATED CIRCUITS

While almost all the IC manufacturers are performing reliability assessment of their ICs, a few common practices are however, could produce incredible reliability data. This is due to the misconception in some aspects of reliability data analysis which will be discussed as follows.

## 1. Zero Failure Represents Good Reliability

It is intuitive to think that for two set of samples undergo same reliability test, the set with zero failure indicates better reliability than the other set with some failures. However, this may not be true all the time. Let us look at the following example.

Assume we have two set of samples with their actual failure times as shown in Table 4 under a given reliability test condition, and the time to failure follows Weibull distribution. For the discussion on the different failure distributions, readers may refer to [5].

If the reliability test is run for 480 hours, we will have 2 failures from sample set #1, and no failure from sample set #2. However, if we plot the reliability vs. time for the two set of samples using their actual failure times, we have Figure 4. One can easily see that the reliability of sample set #1 is actually more reliable than that of sample set #2..

In fact, with zero failure from a reliability test, there is no way to predict its lifetime and reliability. One cannot predict the % of failure during the life cycle of the product. It may or may not meet the customer specification, and there is simply no way to be sure about it. **It takes faith to ship product with zero reliability failure to customers.**

**Table 4. Actual Failure Times of Units in the two set of samples**

| S/No. | Time to Failure (hours) | |
|---|---|---|
| | Sample set #1 | Sample set #2 |
| 1 | 109.7 | 6042.8 |
| 2 | 168.83 | 7221.44 |
| 3 | 903.93 | 7953.01 |
| 4 | 1240.95 | 8351.6 |
| 5 | 1450.37 | 8791.62 |
| 6 | 1704.86 | 8931.55 |
| 7 | 2150.06 | 9239.77 |
| 8 | 2151.46 | 9322.41 |
| 9 | 2620.3 | 9605.9 |
| 10 | 2706.32 | 10144.46 |
| 11 | 3115.17 | 10248.35 |
| 12 | 3413.42 | 11567.18 |
| 13 | 3777.57 | 12192.96 |
| 14 | 4380.26 | 12196.66 |
| 15 | 5009.82 | 12599.67 |
| 16 | 5780.62 | 12936.78 |
| 17 | 5892.4 | 13198.02 |
| 18 | 5900.49 | 13224.26 |
| 19 | 6285.2 | 14536.72 |
| 20 | 6331.67 | 14876.02 |

For two set of samples with zero failure after a reliability test, it is not correct to say that the two sets are having equivalent reliability. An example is shown in Figure 5 where no failure is observed if the reliability test is terminated at 1200 hours. However, the reliability of sample #2 is significantly poorer than that of sample #1, and more than 60% of the product will fail for sample #2 after 12000 hours of operation. Unfortunately, the above-mentioned zero failure comparison is a common way in industry to compare new design/process recipe with the present one, or to compare materials from different suppliers.

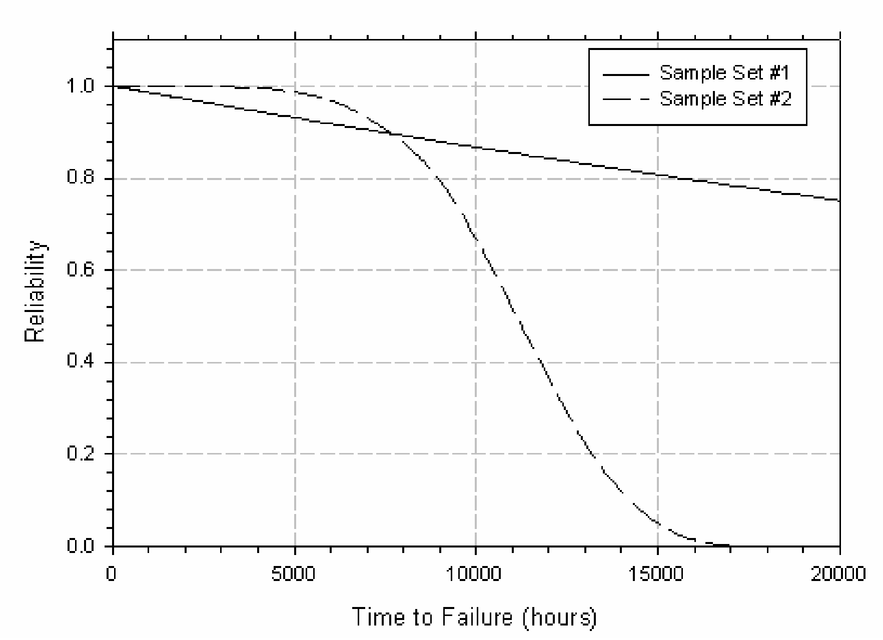

Figure 4. Reliability vs. Time for the two sets of samples with failiure times shown in Table 4.

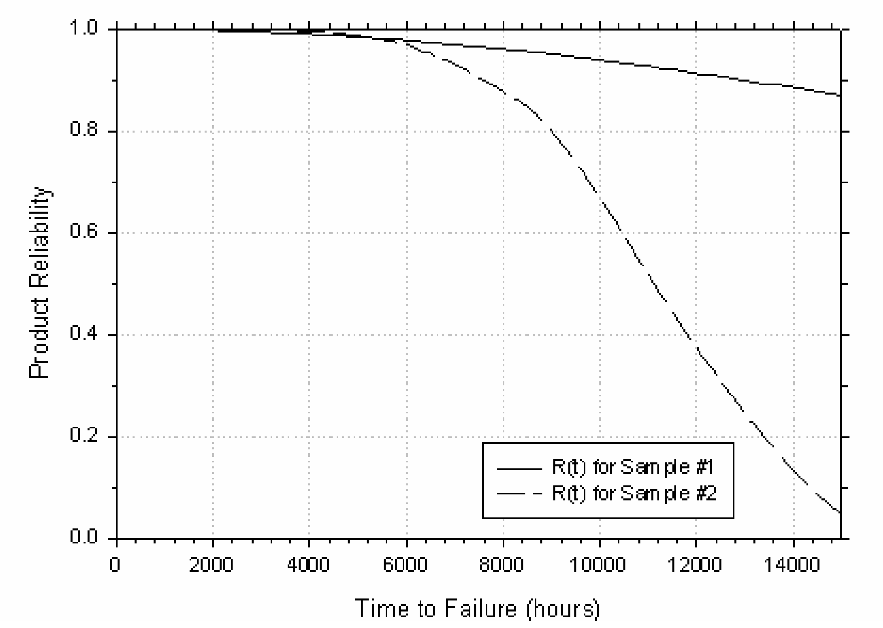

Figure 5. Reliability Curves for two sets of samples with zero failure up to 1200 hours.

## 2. Higher MTTF Represents Better Reliability

Assume we have three different lot of products, and eight samples are chosen from these lots to perform reliability test. Their times to failure follow Weibull distribution, and their failure times after the reliability test are shown in Table 5.

**Table 5. Failure time of Samples from three Different Lots**

| | Test Lot 1 | Test Lot 2 | Test Lot 3 |
|---|---|---|---|
| Failure #1 | 8664.8 | 3.1 | 59857.5 |
| Failure #2 | 22439.4 | 74.1 | 75933.3 |
| Failure #3 | 38713.4 | 456.6 | 87025.1 |
| Failure #4 | 57981.8 | 1755.2 | 96272.5 |
| Failure #5 | 82098.1 | 5595.1 | 105017.6 |
| Failure #6 | 113631.4 | 16533.2 | 113907.9 |
| Failure #7 | 160445.0 | 52213.7 | 124168.3 |
| Failure #8 | 248891.5 | 225630.0 | 138573.9 |

From their failure times and using the MTTF formula for the Weibull distribution, all the three lots have the same high MTTF of 100,000 hours. Intuitively, one might conclude that the three lots have the same reliability, and with their high MTTF, their reliabilities are good.

If we plot the reliability vs. time for the three different lots based on the test failure data, we have Figure 6 below. One can see that their reliability are vastly different despite their same and high MTTF. One of them will have a lot of early failure of which **40%** will fail in the first 3000 hours, i.e. 125 days. MTTF alone is not a good reliability index to a product.

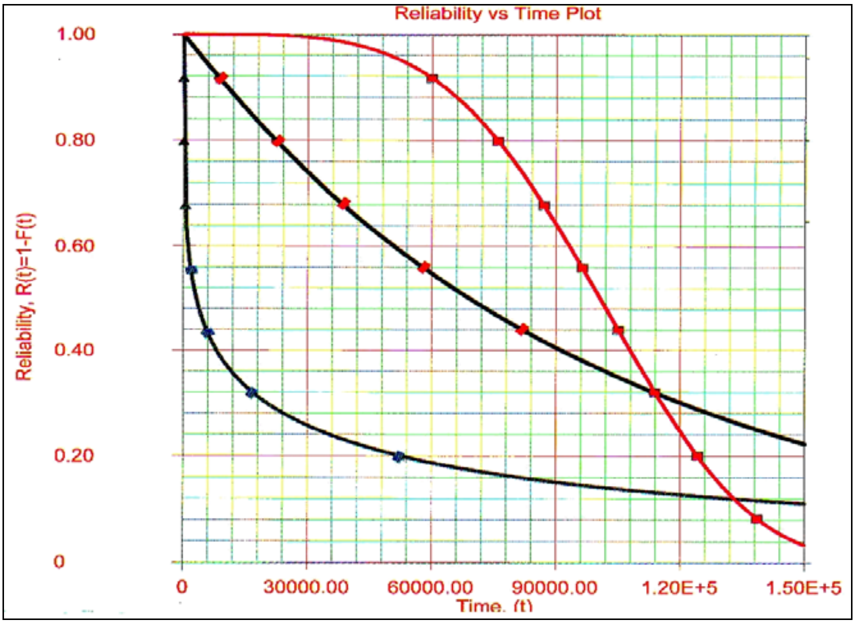

Figure 6. Reliability Curve for the three different lots.

## 3. MTTF Is the Mean Failure Time

There is a common misunderstanding in electronic industry that $t_{50} = MTTF$ . This is because MTTF is the mean time to failure, and time for 50% failure is median failure time which is sometimes taken as mean failure time. To estimate the mean failure time, it is quite common to sum all the failure times in a sample set and divide by the number of failure. But this gives the average failure time.

Statistically, MTTF is the expected time to failure, and $t_{50}$ is the median time to failure. They are not the same, and they are also not equal to the average failure time. MTTF=$t_{50}$=average failure time is true only for the familiar normal distribution or any statistical distribution that is symmetrical with respect to its mean value. However, in reliability engineering, normal distribution is just a kind of failure distribution, and most failure time distributions do not follow normal distribution.

The common failure time distributions in reliability are the Weibull and Lognormal distribution for electronic components. For the Weibull distribution, the expression for MTTF and $t_{50}$ are given in the following equations which will give very different values. Here, $\eta$ and $\beta$ are the scale and shape parameters of a Weibull distribution, and $\Gamma(.)$ is the gamma function[5].

$$MTTF = \eta\Gamma\left(1+\frac{1}{\beta}\right) \tag{3}$$

$$t_{50} = \eta\left[\ln(2)\right]^{1/\beta} \tag{4}$$

Neither Eqn (3) nor (4) resembles the average time to failure.

## 4. Exponential Distribution Is Sufficient to Analyze the Test Data

Most of the closed form formulas in reliability engineering are derived based on the exponential distribution, a type of failure time statistical distribution. This distribution is very widely used in industry due to its simplicity in applications, and it is the underlying distribution for Mil-HDBK-217.

One must realize that if a product failure time follows exponential distribution, the product's reliability for "used" one is as good as "new" one. In other word, the reliability of the product after being used for some times has the same reliability as that of a brand new product [6]. Obviously, there is no such engineering product. However, if the early failures of a production lot is effectively screened away, and the wear out time for the component is well beyond the life cycle of the component, one may use the exponential distribution to model the failure time of the component approximately.

In the analysis of reliability test data, statistical distribution of the time to failure is crucial. Without the knowledge of the statistical distribution, there is no way to extrapolate the test data to the normal operating condition, and thus defeat the very purpose of an accelerated test as mentioned earlier. On the other hand, one cannot choose any distribution to represent its failure time because a wrong choice may lead to grossly over-estimation of product reliability as shown in the following example.

Assume we have a product with the failure times shown in Table 6, and the failure time follows the Weibull distribution. If we wrongfully use different statistical distribution to analyze the failure time data, the estimated $t_{50}$ will be as shown in Table 7. One can see the grossly over-estimation of the product reliability if exponential or normal distribution is assumed.

**Table 6. Failure time (in hours) of a component after reliability test**

| | | | | | | |
|---|---|---|---|---|---|---|
| 0 | 0 | 0.82 | 1.06 | 2.53 | 53.86 | 86.04 |
| 122.4 | 464.14 | 2018.63 | 2885.21 | 6454.48 | 16870.22 | 17067 |
| 22209 | 24849 | 63029.8 | 648734.4 | 1607971 | 7000252 | |

**Table 7. Estimated $t_{50}$ (in hours) from the failure time data of Table 6**

| Distribution | $t_{50}$ |
|---|---|
| Weibull | 1293.18 |
| Exponential | $6.07 \times 10^5$ |
| Lognormal | 492.29 |
| Normal | $4.71 \times 10^5$ |

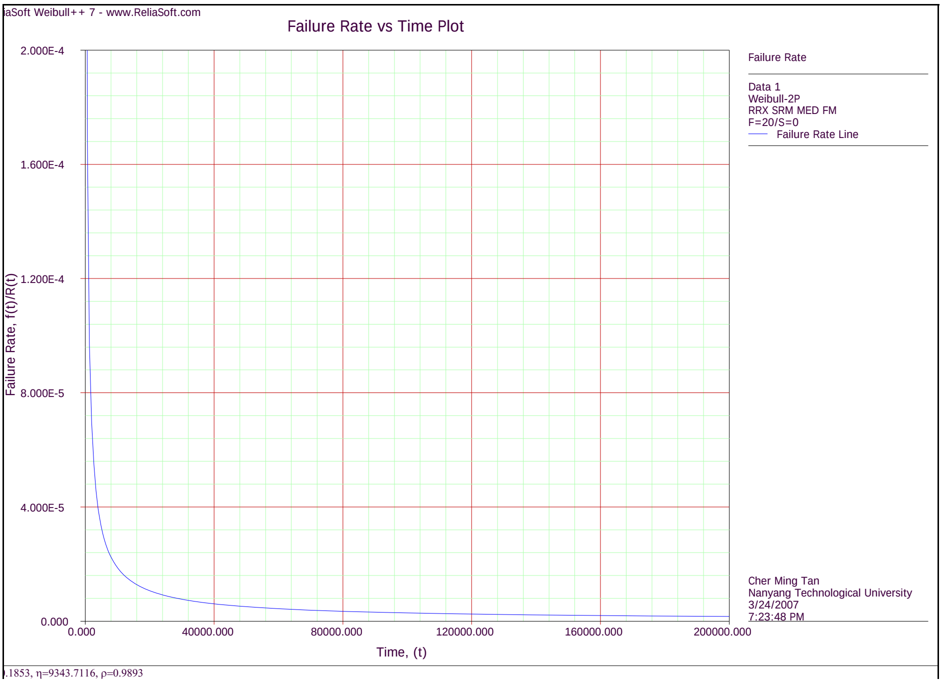

Figure 7. Failure Rate vs. Time for actual data set which follows Weibull distribution.

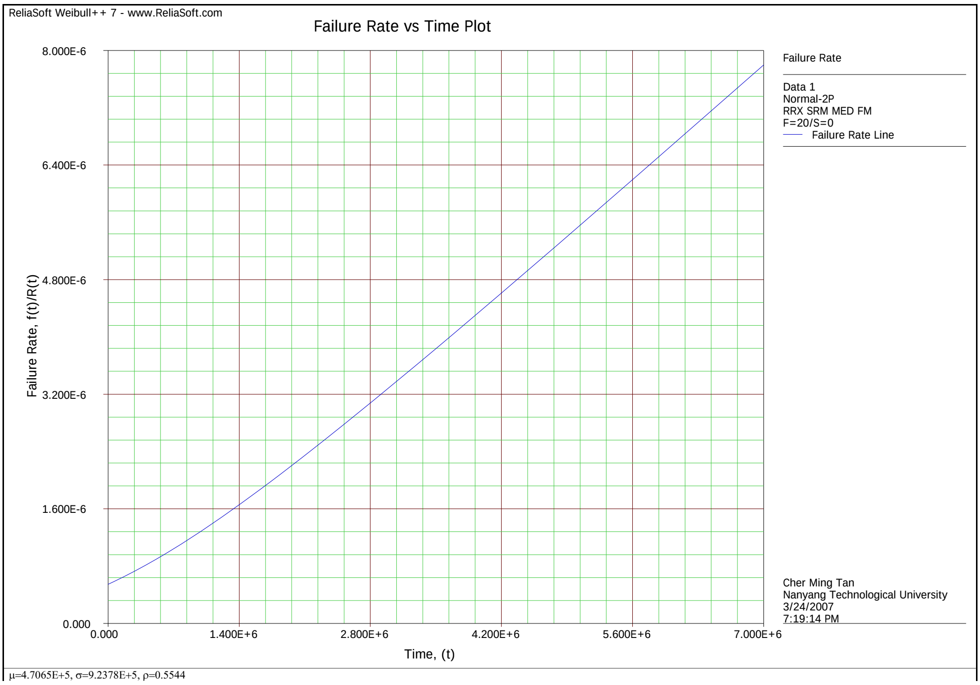

Figure 8. Failure rate vs. time curve by assuming Normal Dsitribution.

Also, with the wrong distribution assumed, the failure rate curve will be different. The actual data which follows Weibull distribution is having high early failure as shown in Figure 7, and hence its reliability can be improved through burn-in. However, if normal distribution is assumed, we will think that the product is undergoing wear out as shown in Figure 8, and hence burn-in will be avoided.

## 5. The Higher the Stress, the More Effective Is the Reliability Test

In the pursuit of shortening the reliability test time, it is common to increase the stress condition. However, at least two problems arise when the stress is increased without a careful evaluation as follows.

### A. Masked Failure Mechanism

Meeker and Escobar [7] show the situation of masked failure mechanism (or mode) when the applied stress is too high and the test time is too short. Figure 9 is reproduced from [7] for ease of discussion.

As can be seen in Fig 9, if the test temperature is set at 120$^{o}$C and the test time is stopped at 200 hours, only failure mode 1 will be observed, and no failure is due to failure mode 2. However, at the normal operating condition, units that failed early are mainly due to failure mode 2, and hence the reliability test conducted at high stress is not useful at all in predicting the reliability of the product at the normal operating condition.

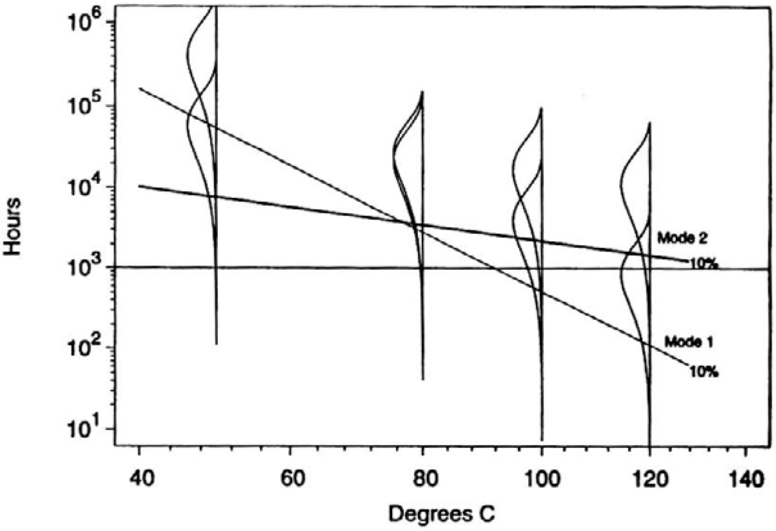

Figure 9. Failure Mode 2 with lower activation energy was masked at high temperature, but unmasked at low temperature [7].

## B. Variation of Failure Mechanism

Kraft et. al. [8] studied the electromigration damage map of Al interconnect as reproduced in Figure 10, and they found that at high stress  current condition, most of the failure will be wedge like void as reproduced in Figure 11. However, under the normal operating condition where the current density is lower, most of the failure will be a slit-like void as reproduced in Figure 12. Their results are verified with experiments.

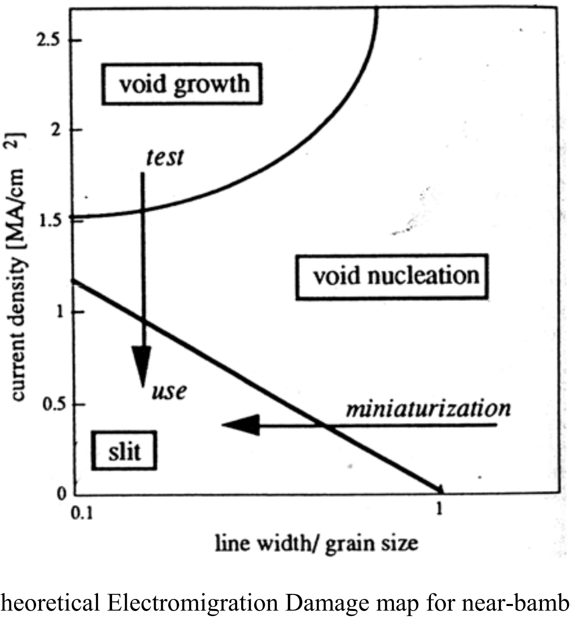

Figure 10. Theoretical Electromigration Damage map for near-bamboo lines [8].

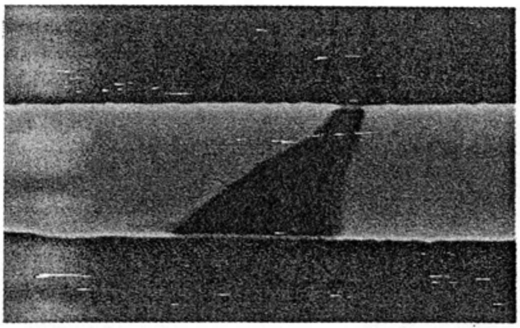

Figure 11. SEM Micrograph of an extended wedge-shape void in a pure Al line [8].

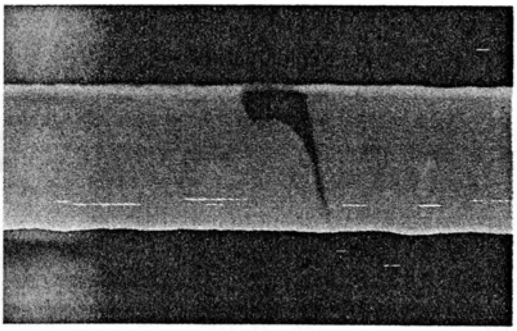

Figure 12. SEM Micrograph of a slit-like void in an AlSiCu line [8].

Roy et. al. [9] studied the failure physics of electromigration in ULSI interconnections, and they found that the failure locations are different at the accelerated stress condition and at the normal operating condition. The dominant driving force for failure is also different at the different test conditions.

Since the invariance of failure mechanism at the stress condition and at the normal operating condition are essential for lifetime extrapolation [10], the change in the failure mechanism by employing too high the stress will render the accelerated life test non-effective, wasting the resources and may even lead to over-estimation of product reliability.

## 6. All Test Data Are Valid

In the analysis of reliability test failure times, it is customary assumed that all the failure times are valid data. In reality, due to the high stress condition used, it is very likely that other failure mechanisms may evolve, and hence the "failure" times associated with the other failure mechanisms exists. These "failure" times are not the true failure times for the failure mechanism of interest designed for the given reliability test, and should therefore be treated as outlier points. Here we need to note that all accelerated life tests are designed with their associated respective failure mechanism of interest. For example, THB (Temperature-humidity-bias) test is designed for the galvanic corrosion. Electromigration test is designed for the electromigration of interconnection.

Let us consider the following example where the actual time to failure distribution follows the Weibull distribution with $t_{50}$=1333.69 hours and $MTTF$ =3137.77 hours. Table 8 shows the failure times and Suspension times as denoted as F and S respectively. Suspension time (also called censored time) is the time where unit cannot be tested further since other failure mechanism has occurred that render the unit not operative.

If we consider all the "failure time" as valid failure time, and using the Weibull distribution, we will find that $t_{50}$=727.10 hours, and $MTTF$ =1944.13 hours. This is a significant difference with the actual values, and the difference will be even larger after extrapolation because an acceleration factor will be multipled to the $t_{50}$ and $MTTF$ obtained from the accelerated test conditon, thus grossly under-estimate the product reliability.

**Table 8. Reliability Failure Time of 27 Devices Under Test**

| Status | TTF (hrs) | Status | TTF (hrs) | Status | TTF (hrs) |
|---|---|---|---|---|---|
| S | 12.00 | F | 254.00 | F | 3492.20 |
| F | 15.90 | F | 277.95 | S | 3546.00 |
| S | 30.00 | F | 401.20 | F | 3630.81 |
| F | 37.47 | F | 439.28 | F | 3956.43 |
| S | 48.00 | S | 450.00 | F | 4021.37 |
| F | 70.18 | F | 521.71 | F | 4853.51 |
| F | 123.56 | F | 1065.83 | F | 4969.72 |
| S | 234.00 | S | 1200.00 | F | 9115.77 |
| F | 247.26 | F | 1806.12 | F | 9248.72 |

## 7. Only One Failure Mechanism Exist in the Failed Units

It is customary to assume that only one failure mechanism exist with the failure data. Again, with the high applied stress, the existence of more than one failure mechanism in the data is quite common. Failure to account for multiple failure mechanisms in the test data will make the extrapolation invalid, and the conclusion made regarding the product reliability will not be credible.

Table 9 shows the time to failure of 24 units subjected to electromigration test [11]. Since electromigration failure is known to follow the Lognormal distribution, and if one analyzes the data by assuming one failure mechanism (since all their failure modes are the same) and employs Lognormal distribution, we have the probability plot as shown in Figure 13. From the plot, we can find the $t_{50}$=136.17 hours at the stress condition.

**Table 9. Time to Failure Data in Electromigration Test**

| | | | | | |
|---|---|---|---|---|---|
| 9.04 | 23.06 | 28.55 | 94.18 | 105.05 | 112.01 |
| 118.24 | 118.37 | 120.97 | 126.21 | 130.23 | 145.35 |
| 148.74 | 150.08 | 175.45 | 179.66 | 213.33 | 247.21 |
| 263.12 | 274.24 | 331.73 | 345.25 | 425.63 | 474.34 |

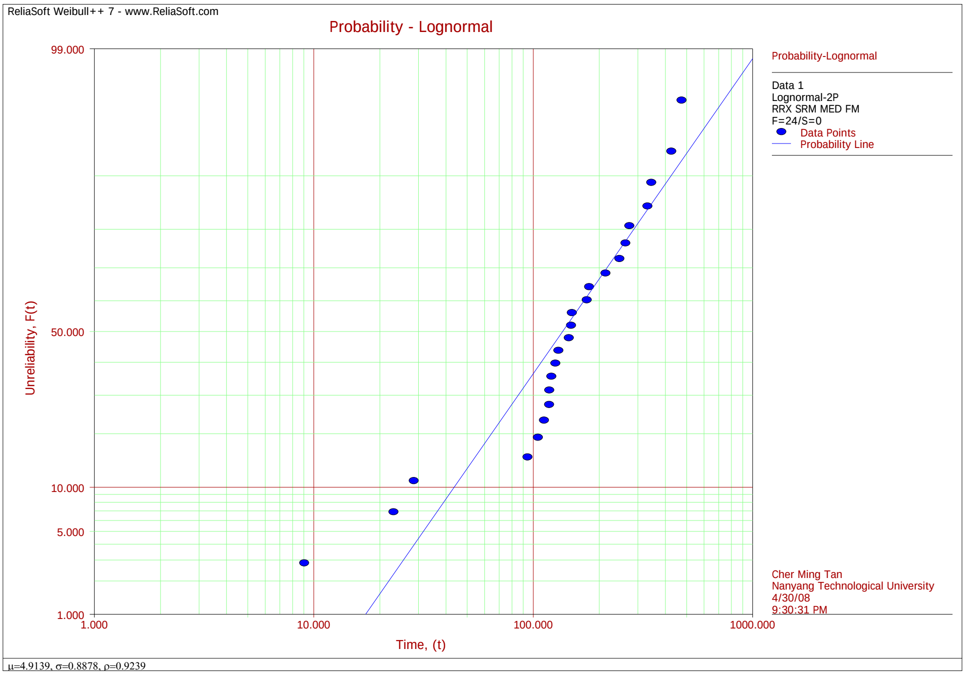

Figure 13. Lognormal Plot of the Time to Failure Data shown in Table 9.

By using the method of mixture distribution, one can indeed find that there are two failure mechanisms exist in the data, and the failure units that belong to each of the failure mechanisms can be determined as shown in Table 10 [12]. The nature of the failure mechanisms are confirmed with detail failure analysis as shown in Figures 14 and 15 for the Line and Via EM.

**Table 10. Mixture Distribution Analysis of the Test Data shown in Table 9**

| Failure No. | TTF | Missing data matrix | | FIB analysis | Failure No. | TTF | Missing data matrix | | FIB analysis |
|---|---|---|---|---|---|---|---|---|---|
| | | Probability due to component #1 | Probability due to component #2 | | | | Probability due to component #1 | Probability due to component #2 | |
| 1 | 9.04 | 1 | 4.23E-08 | - | 13 | 148.74 | 2.31E-05 | 0.99998 | - |
| 2 | 23.06 | 0.99934 | 0.000664 | Line EM | 14 | 150.08 | 2.13E-05 | 0.99998 | - |
| 3 | 28.55 | 0.99436 | 0.00564 | Line EM | 15 | 175.45 | 5.09E-06 | 0.99999 | - |
| 4 | 94.18 | 0.0016327 | 0.99837 | - | 16 | 179.66 | 4.10E-06 | 1 | - |
| 5 | 105.05 | 0.00058541 | 0.99941 | - | 17 | 213.33 | 8.62E-07 | 1 | - |

**Table 10. Continued**

| Failure No. | TTF | Missing data matrix | | FIB analysis | Failure No. | TTF | Missing data matrix | | FIB analysis |
|---|---|---|---|---|---|---|---|---|---|
| | | Probability due to component #1 | Probability due to component #2 | | | | Probability due to component #1 | Probability due to component #2 | |
| 6 | 112.01 | 0.00032125 | 0.99968 | - | 18 | 247.21 | 2.29E-07 | 1 | - |
| 7 | 118.24 | 0.00019389 | 0.99981 | - | 19 | 263.12 | 1.31E-07 | 1 | - |
| 8 | 118.37 | 0.00019192 | 0.99981 | - | 20 | 274.24 | 9.04E-08 | 1 | VIA EM |
| 9 | 120.97 | 0.00015677 | 0.99984 | - | 21 | 331.73 | 1.67E-08 | 1 | - |
| 10 | 126.21 | 0.0001057 | 0.99989 | VIA EM | 22 | 345.25 | 1.17E-08 | 1 | - |
| 11 | 130.23 | 7.90E-05 | 0.99992 | - | 23 | 425.63 | 1.88E-09 | 1 | - |
| 12 | 145.35 | 2.86E-05 | 0.99997 | - | 24 | 474.34 | 7.33E-10 | 1 | - |

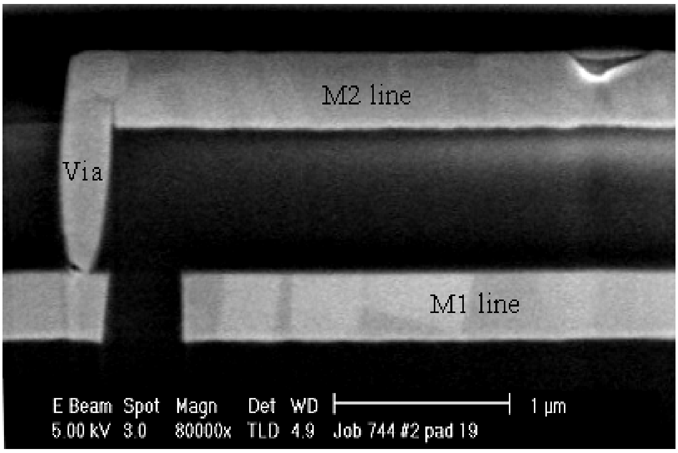

Figure 14. SEM Micrograph of the Test Structure after FIB Cut showing that failure component #1 is the Line Electromigration.

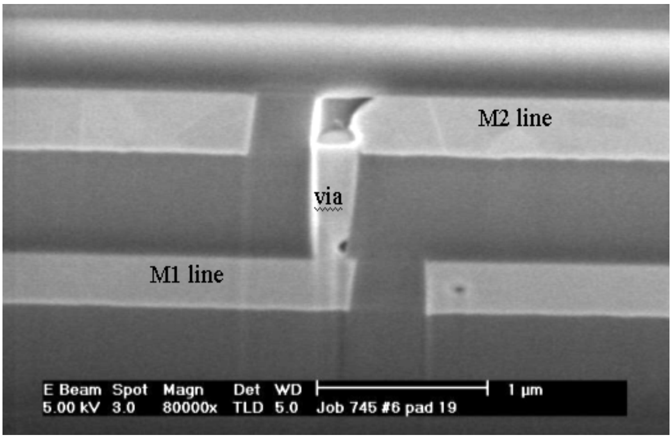

Figure 15. SEM Micrograph of the Test Structure after FIB Cut showing that failure component #1 is the Line Electromigration.

With the separation of the two failure mechanisms, $t_{50}$=18.17 hours for line electromigration, and $t_{50}$=181.27 hours for the Via electromigration under the stress condition, and the probability density function (pdf) of the test data can thus be given as

$$pdf = 0.12 \times \Phi(\frac{\ln t - 2.9}{0.5}) + 0.88 \times \Phi(\frac{\ln t - 5.2}{0.48}) \tag{5}$$

From the $t_{50}$'s of the two failure mechanisms, it is obvious that via electromigration is more reliable as compare to its line electromigration for these samples. However, upon extrapolation to the normal operating condition using the Black's equation and their respective activation energies and pdf, the probability of failure due to the two failure mechanisms is shown in Figure 16. The early failure in the field is the via electromigration instead of the line electromigration. In other words, attempt to improve the line electromigration due to its short $t_{50}$ at the accelerated stress condition will be in vain in this present case. Hence, the important of accurately obtaining the various failure mechanisms in a test data and their respective pdf is crucial in ensuring product reliability at the field operating condition.

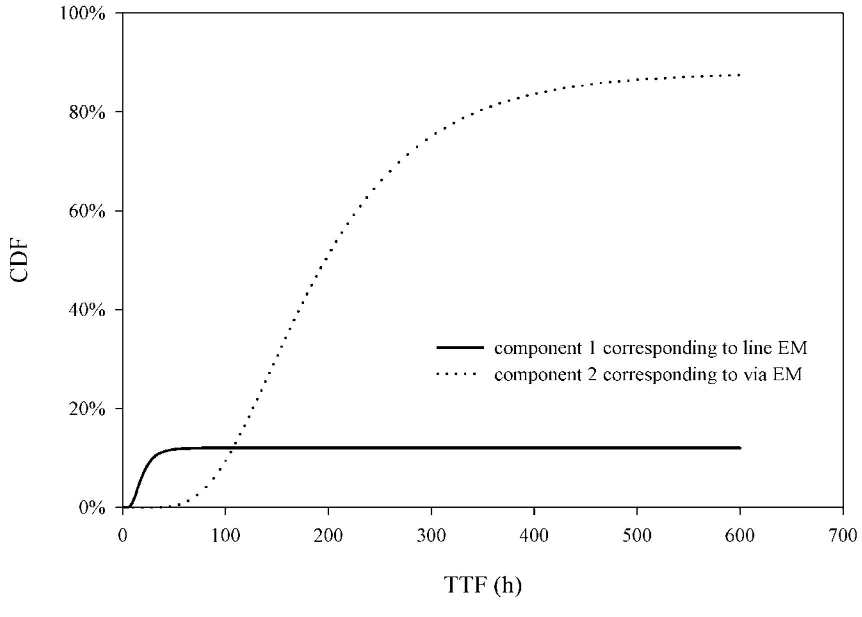

Figure 16. Probability of Failure (CDF) vs. Time to Failure (TTF) for the test data shown in Table 9. Here CDF is the cumulative density function.

## 8. Probability Plot Is Sufficient for Test Data Analysis

Probability plot is a useful tool to determine the parameters of a failure time distribution. However, the accuracy of the parameters' values determined from the plot depends on the sample size. Figure 17 shows the % error in the estimation of MTTF using the probability plot for the Lognormal and Weibull distributions respectively. One can see that unless the sample size is very large (to the point of impractical), the accuracy from the plot is indeed very poor.

Furthermore, there are several circumstances that render the data plot not lying on a straight line even if the right probability graph paper is used, increasing the error of estimation. The reasons for not getting a straight line in the plot are:

a. The presence of failure free life [5]
b. The presence of outlier points
c. The presence of multiple failure mechanisms, including freak distribution which renders the plot as S-shape curve [13].

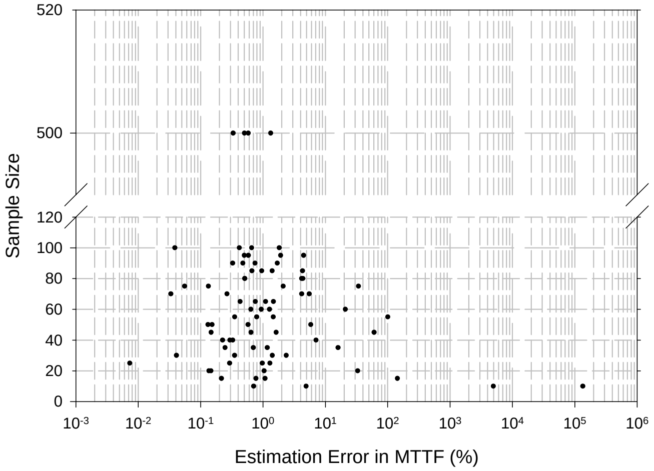

(a) Lognormal Distribution

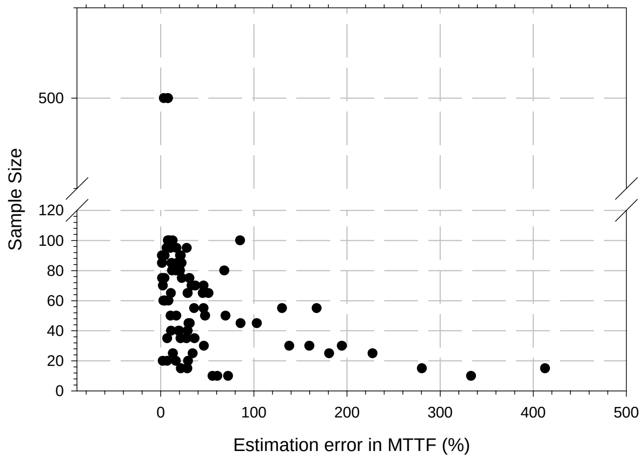

(b) Weibull Distribution

Figure 17. Effect of Sample Size on the estimation Error of MTTF using Probability Plot. The dot in the graph represents the possible error in MTTF estimation from a set of sample for a given sample size.

## 9. Small Sample Size Is Sufficient

It is generally difficult to have a large sample size for reliability test because all the test units after the test cannot be used or shipped. On the other hand, for small sample size, the estimation of the failure distribution parameters will be inaccurate and thus the estimated reliability.

Meeker and Escobar [7] studied the effect of sample size on the estimation of time for a given % of failure. Figure 18 reproduces their work which shows the probability plot of a number of sample set from a given Weibull distribution, for different sample size. These sample set simulate the possible sample that one might have for actual reliability test.

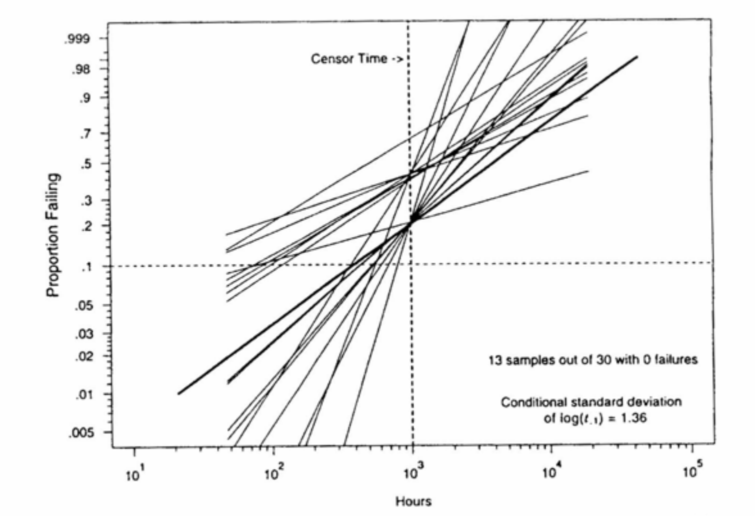

(a) ML cdf estimates from 30 simulated samples of size n=5

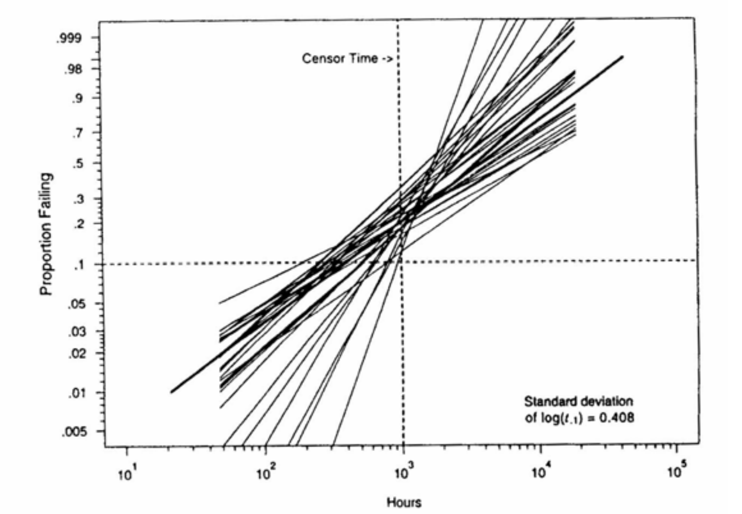

(b) ML cdf estimates from 30 simulated samples of size n=50

Figure 18. Continued on next page.

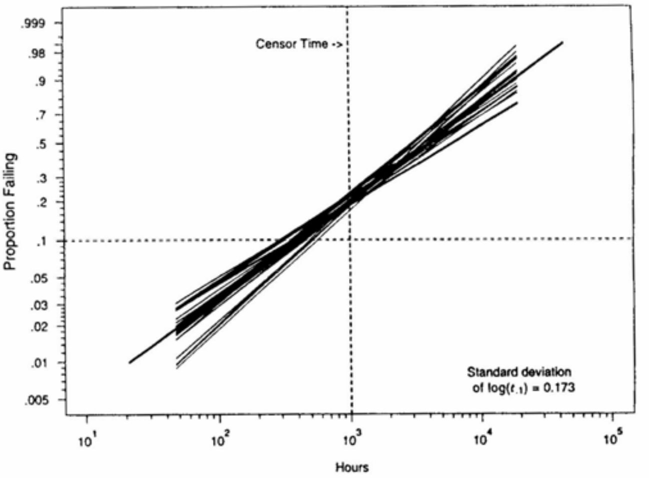

(c) ML cdf estimates from 30 simulated samples of size n=500

The Figure is reproduced from Ref [7].

Figure 18. The effect of sample size on the variation in the estimation of $t_{.1}$. The solid line represents the actual population. The standard deviation of log($t_{.1}$) in the figure represents the possible variation of the estimation. $t_{.1}$ is the time for 10% failure, and ML means Maximum Likelihood.

From Figure 18, one can see that if the sample size is small, the variation in the estimation of $t_{.1}$ will be very large. Also, with small sample size, we might not even observe any failure, making the estimation of $t_{.1}$ impossible. Since we do not know which sample set we will actually have, the estimated $t_{.1}$ obtained from the test can be either the lowest one or the largest one, but both of them can be far from the actual population value when the sample size is small. In other word, the reliability estimation will be very inaccurate if small sample size is used.

## 10. The Important of Confidence Interval

Since the estimation of reliability is based on a small sample set, and as can be seen in the above, the variation of the estimation can be large, it is important to present the confidence interval associated with the estimated reliability. For example, if the estimated $t_{50}$ from a reliability test is 100 hours, one is not sure if this value is close to or far away from the corresponding value in the population (i.e. the batch of the products where the sample is drawn). If 95% confidence level is chosen, and the confidence interval of the $t_{50}$ is [1, 10000 hours], the estimation is basically useless because such a conclusion can be made even without conducting the test. Hence, with the establishment of the confidence interval, one can examine if the estimated reliability is a reasonable estimation to the population reliability.

## IV. CONCLUSION

While the important of reliability for IC is unquestionable, and many companies are performing reliability tests on their products, there are many seemingly intuitive but misconceptions exist in carrying out the analysis of the reliability test data. Unless these misconceptions are taken care of, the estimated reliability of the ICs can be grossly over-estimated or under-estimated. Fortunately, statistical methods exist that prevent these misconceptions during the reliability test and its data analysis, and one can indeed provide a credible estimation if reliability tests are properly planned and analyzed.

## REFERENCES

[1] M. A. Levin and T. T. Kalal, "Improving Product Reliability, Strategies and Implementation," in *Wiley Series in Quality and Reliability Engineering*, P. D. T. O'Connor, Ed.: John Wiley & Sons Ltd., 2003.

[2] "RAC Blueprint for Product Reliability," in http://src.alionscience.com/DATA/JOURNAL/blueprints_ab.html: Reliability Analysis Center.

[3] C. M. Tan and A. Roy, "Electromigration in ULSI interconnects," *Mater. Sci. Eng., Rev.,* vol. 342, pp. 1-75, 2007.

[4] H. W. McLean, *HALT, HASS, and HASA explained: accelerated reliability techniques*: ASQ, 2000.

[5] P. D. O'Conor, *Practical Reliability Engineering*: John Wiley & Sons Ltd, 2002.

[6] C. E. Ebeling, *An Introduction to Reliability and Maintainability Engineering*: McGraw-Hill 1997.

[7] W. Q. Meeker and L. A. Escobar, *Statistical Methods for Reliability Data*: John Wiley & Sons Ltd, 1998.

[8] O. Kraft, U. E. Mockl, and E. Arzt, "Shape changes of voids in bamboo lines: A new electromigration failure mechanism," *Quality and Reliability Engineering International,* vol. 11, pp. 279-283, 1995.

[9] A. Roy, C. M. Tan, R. Kumarb, and X. T. Chenb, "Effect of test condition and stress free temperature on the electromigration failure of Cu dual damascene submicron interconnect line-via test structures," *Microelectron. Reliab.,* vol. 45, pp. 1443-1448, 2005.

[10] E. A. Elsayed, *Reliability Engineering*: Addison Wesley Longman, Inc., 1996.

[11] A. V. Vairagar, S. Mhaisalkar, and A. Krishnamoorthy, "Electromigration behavior of dual damascence Cu interconnect structures - structure, width and length dependences," *Microelectronics Reliability,* vol. 44, pp. 747-754, 2004.

[12] C. M. Tan, V. A. Anand, G. Zhang, A. rishnamoorthy, and S. Mhaisalkar, "New Analysis Technique for Time to Failure Data in Copper Electromigration," in *JEDEX Conference* San Jose, 2005.

[13] J. Yuan and S.W. Shih, "Mixed hazard models and their applications," *Reliability Engineering and System Safety,* vol. 33, pp. 115-129, 1991.

In: Integrated Circuits, Photodiodes…
Editors: R. McIntire and P. Donnell, pp. 69-93
ISBN: 978-1-60692-660-4
© 2009 Nova Science Publishers, Inc.

*Chapter 3*

# DESIGN OF A MULTICHANNEL INTEGRATED BIOSENSOR CHIP AND MICROELECTRONIC SYSTEM FOR EXTRACELLULAR NEURAL RECORDING

***Xin Zhang*[*,a,e]*, Yingxin Li*[b]*, Yulong Zhang*[c]*, Zuhui Chen*[c]*, Shi Liu*[d]*,***
***Richard D. Nelson*[e] *and John C. LaRue*[f]**
[a] Z&L Creative Corporation, Lewes, DE, USA
[b] Department of Physiology, Temple University School of Medicine,
Philadelphia, PA, USA
[c] Pen-Tung Sah MEMS Research Center, Xiamen University,
Xiamen, 361005, P.R.China
[d] Beijing CRX Science & Technology LLC, Beijing, 100101, P.R. China
[e] Department of Electrical Engineering and Computer Science, University of California,
Irvine, Irvine, CA, USA
[f] Department of Mechanical and Aerospace Engineering, University of California, Irvine,
Irvine, CA, USA

## ABSTRACT

A multi-channel mixed-signal full-customized CMOS integrated biopotential sensor chip and microcontroller based electronic system have been developed for *in vitro* extracellular recording of neural signals. The multi-site planar microelectrode array sensors for simultaneous neural signal recording have been designed and prototyped with on-chip fully integrated analog signal processing circuitry and control system. The biosensor system is built with hierarchical modules that incorporate microelectrode electrophysiological sensors, analog signal buffers configured with two-stage amplifier, gain providing amplifiers based on operational transconductance amplifier (OTA) with capacitive feedback and digital logic and interface units including clock generation and time division multiplexing control circuitry. The prototype IC was fabricated by MOSIS using AMI C5 0.5 μm, double poly, triple metal

---

[*] E-mail address: xinz@zlcreative.com, xinz@uci.edu. phone: +1-800-516-0723. fax: +1-888-851-8391. Primary contact: Xin Zhang, University of California, Irvine, 4100 CALIT2 Bldg. 3rd floor, Irvine, CA 92697-2800, U.S.A.

layer CMOS technology. The electroless gold plating process is used to replace the aluminum material obtained from the standard CMOS process with biocompatible metal gold in the planar microelectrode array sensors to prevent cell poisoning and undesirable electrochemical corrosion. The post-CMOS processing and packaging techniques applied to the biosensor chip promotes biocompatibility and stability in the aqueous cell culture environment. A microcontroller based electronic system interfacing the biosensor IC with a client PC for the post processing of the action potential signals sensed by the biopotential sensor chip was also developed. The biosensor has been tested electrically in the presence of electrolyte environment and is shown to provide a satisfactory signal-to-noise ratio for neural signals with amplitudes in the range of 600μV-2mV and frequencies in the range of 100 Hz – 10 kHz. Biological example *in vitro* recordings conducted with neurons from *Aplysia californica* are shown in this research work, which proves the full functionality in neural recording of the biosensor chip incorporated with the interfacing electronic system based on 32-bit Motorola ColdFire MCF5307 RISC processor. On-chip amplification and time division multiplexing techniques of the multi-channel biosensor chip allow the large-scale simultaneous recording of biological activities of neurons.

**Keywords**: Biopotential Sensor, Extracellular Recording, Mixed-signal CMOS Circuits, Analog Integrated Circuits, Microelectrode Arrays, Microcontroller.

## 1. INTRODUCTION

Neurons, also called nerve cells, are special cells that comprise the nervous systems of all living things. Nerve tissues are organized with many associated neurons, which are the primary component of the brain and spinal cord. Neurons communicate with each other through neural signals in form of electrical pulses, which are called action potentials. Action potentials, traveling along the membrane of the neurons in form of waves of electrical discharge, are the essential feature of living life. Since action potentials carry the action information within and between tissues, how to sense these signals, record them and interpret them in an electronics system is of great importance to neuroscientists. (Augustine et al., 2004) In the past years there have been striking advances in the development of neural recording techniques for both *in vitro* and *in vivo* neural measurements. Development of micro devices with the function of chronicle and non-invasive monitoring of neural activities holds the promise of new insights into neurological processes. (Patterson et al., 2004)

For many years in neurosciences, micromachined extracellular microelectrode arrays (MEA) have been widely applied to study the neural activity of electrically excitable cells (Pancrazio et al., 1998). The dimension of the electrodes is implemented with similar size as neurons (Kawano et al., 2003). The use of the microelectrode for the non-invasive extracellular recording the electrical activity of neurons has contributed greatly to the understanding of the nervous system. Simultaneous *in-vitro* recording from populations of neurons has been increasingly acknowledged as essential to better understanding of functional relationships between cells in brain and other neuronal networks (Csicsvari et al., 2000). One of the difficulties encountered in these devices is the small magnitude of the neural signal (Blum et al., 2003). The processing circuitry, which can access addressed electrode site, amplifies the neural signals and performs analog-digital conversion for transmission of the neural signals (Litke and Meister, 1991; Oka et al., 1999), is a common technique to precondition and postprocess the neural signal sensed by MEA. With the development of technology in complementary metal-oxide-semiconductor (CMOS) fabrication, microelectrode arrays incorporated with CMOS based application specific integrated circuit (ASIC) techniques has become an obvious approach for non-invasive, long-term and multi-channel extracellular neural signal recording (Ji et al., 1992; Akin and Najafi, 1998; Wrobel et al., 2007; Najafi and Wise, 1986; Dabrowski et al., 2003). Introducing ASIC into the microelectrode array substrate provides an efficient technique for on-chip preliminary signal conditioning and processing, which reduce the complexity of off-package electronics (Blum et al., 2003). Microelectrode arrays combined with ASIC establishes the possibility of creating the biosensor system on chip (SoC) with large site number of simultaneous measurements without introducing significant noise from the signal conditioning and processing circuitry. Integration and packaging of these multi-channel arrays with analog and digital signal processing and control functions into a lightweight, low power dissipation and low noise ASIC is highly desirable for neurophysiological applications (Nicolelis, 2001).

In this research work, a full-customized biopotential chip for sensing the propagation of action potentials in nerve cells is designed, fabricated and tested. This neural probe chip is designed around typical neural signal constraints such as large low-frequency offset voltages, small signal amplitudes, and low signal to noise ratios (Won et al., 2002). In this design, a multi-channel electrode sensor array with 150μm site spacing was realized. A diagrammatic representation of the biopotential sensor chip experiment with a single nerve cell for sensing propagation of action potentials is illustrated in Figure 1. This biosensor IC functions as an interface between neurons and the external data acquisition and processing system. It is designed to measure contact-neuron interface voltages, which will enable modeling of the interface, and furthermore, the calculation of internal cell potentials. Presented in this research work, a microcontroller based testing workbench with firmware to interface the biosensor chip with a client PC running Matlab/Simulink platform was also developed for post-IC signal processing and control.

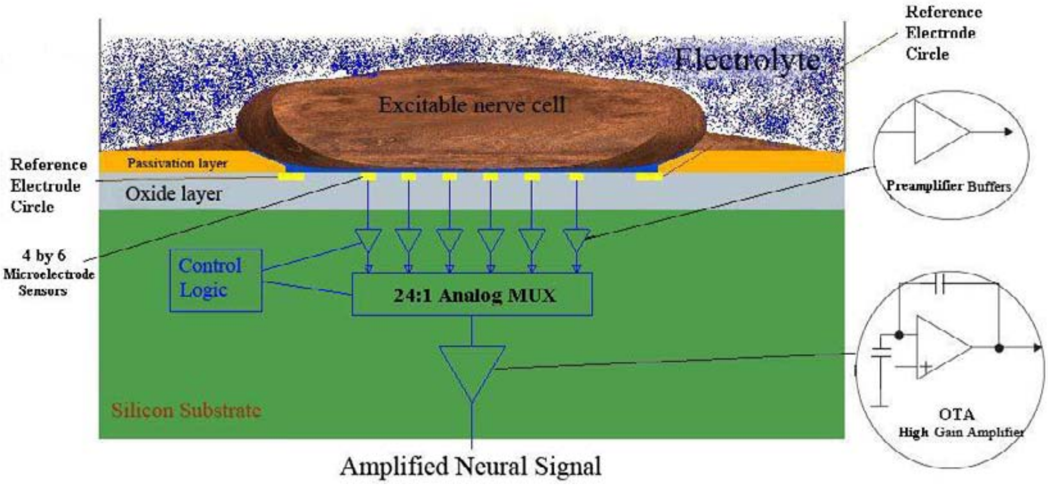

Figure 1. Diagrammatic representation of the cross-section view of the biosensor chip experimental with single nerve cell.

## 2. SYSTEM OVERVIEW

Figure 2 depicts the biosensor chip architecture and the functional blocks of the biosensor system setup. The integrated sensor array consists of four major blocks: 24 (4 × 6) microelectrode array sensor pixels, 24 parallel analog signal processing channels repeated with each electrode sensor contact, high gain amplifier and the control/interface circuits including the 24-to-1 analog multiplexer. The 4 by 6 microelectrode array sensor pixels with a dimension of 60µm × 60µm were spaced at a distance of 150µm (center-to-center) from each other. They sense the changes of internal cell action potentials using capacitive coupling through the cell membrane of single neuron or monolayer nerve cell slices. The electrode separation was chosen to allow for monitoring of cultured cell network properties if desired while limiting crosstalk due to neighboring cells. Studies have demonstrated that the inter-electrode crosstalk can be significantly limited at a minimum of 80-100µm separation between electrodes (Breckenridge et al., 1995), which was proved consistently with finite element analysis modeling performed in the same research group (Lind et al., 1991). The 24 addressable analog signal processing channels are connected to the microelectrode array sensors. Each analog channel consists of a two-stage amplifier buffer with a midband gain of 20dB via resistive feedback, which buffer the neural signals taken directly from each sensor contact into the high gain amplifier. The high gain amplifier is the gain providing stage and is shared among the 24 channels via time multiplexing. The design of preamplifier buffers minimizes the systematic DC offset voltage and provides high input impedance in the first stage in order not to overload the high-impedance recording microelectrode. The preamplifier buffer features a voltage follower with a midband gain around 10V/V formed from the two-stage amplifier with resistive feedback. After being buffered, the 24 neural signals are time multiplexed by a 24-to-1 analog multiplexer to reduce the number of output leads. The analog multiplexer is controlled by 5-bit digital sequence, which periodically selects one of the 24 channels causing the signal from its sensor pixel to be placed on an output wire of the biopotential sensor chip. The output of the biosensor chip is serial of neural signals sensed by the 4 by 6 sensor pixels, with the neural signal from only one microelectrode sensor pixel

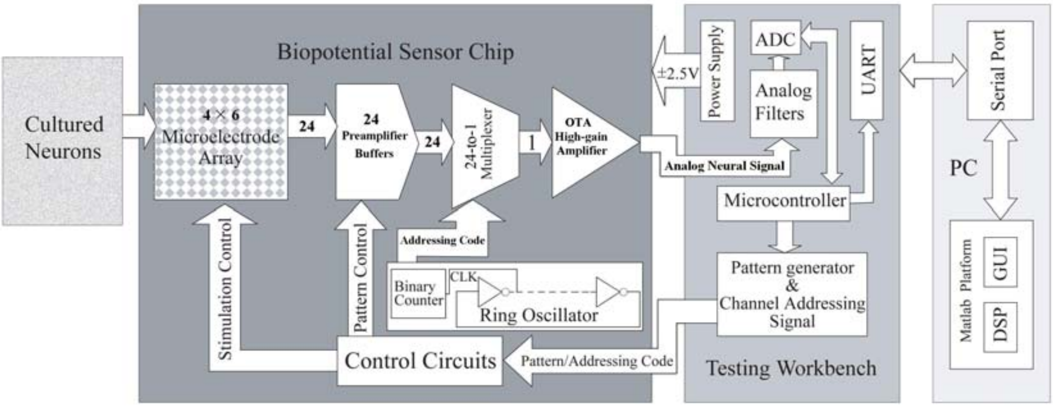

Figure 2. IC Architecture of biopotential sensor chip with complete testing system.

appearing on the output wire at a time. An additional output transconductance amplifier (OTA) with capacitive feedback interfaces the output of the preamplifier buffer to an external pad. This stage applies high closed-loop gain (30-40dB) to the buffered neural signal before driving it out onto the output lead of the biosensor chip. The amplified neural signals will be conditioned, digitized and transmitted to a client PC by the microcontroller based testing workbench that interfaces the biopotential sensor chip with PC. The noise level in the signal conditioning and processing channels varied from 50 to 60 μVpp, while the minimum amplitude of the biopotential signals recorded was 0.6mVpp, which corresponds to a >20dB SNR for the analog signal processing front end.

## 3. SYSTEM ARCHITECTURE AND DESIGN

### 3.1. Neural Signal Input

Figure 3 gives the block diagram of a single analog channel on the biosensor chip. There are four major units in each analog signal channel: signal input, preamplifier buffer, high gain amplifiers and biasing circuitry. When converting the single channel readout circuit to multi-channel systems, we will add analog multiplexing block and some digital control blocks into the system. The 4 by 6 planar microelectrode array sensors are capable of obtaining the action potentials through capacitive coupling with cell membranes, which enables *in vitro* neural signal monitoring. With the dual signal-sensing function based on the time division multiplexing input, the input of the analog signal processing channels can be either from the 4 by 6 on-chip planar microelectrode array sensing sites or from the external pads of the biosensor chip. This design method makes the connection of the biosensor chip to external microelectrodes possible. In the meantime, this approach increases the electrical testability of the biosensor chip. The traditional electrical testing process requires the direct contact of planar microelectrode array sensors with the micromanipulators to apply the emulated electrical signals to the biosensor chip. The microelectrode array sensors are very fragile and can be easily damaged through the direct contact with micromanipulator during the electrical

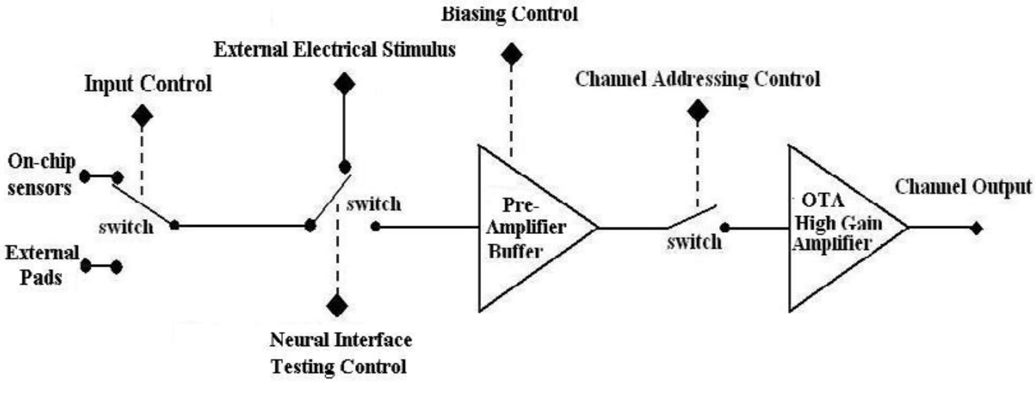

Figure 3. Block Diagram of a Single Channel on Biosensor Chip.

testing since the planar microelectrode array sensors are the only part in the biosensor chip that is not shield by the top cover glass. With the dual signal-sensing design, we can setup the chip pad as the input source of electrical signals without the direct contact of micromanipulator (served as electrical stimulator) with the microelectrode array sensing sites, which greatly improves the lifetime of the biosensor chip.

## 3.2. Preamplifier Buffers

The preamplifier buffers are mainly responsible for the circuit noise performance. Since the microelectrode sensor pixels acquire the action potential signal from the cell membrane via capacitive coupling, the parasitic capacitance presented to the microelectrode array sensing sites is important. Furthermore, the signals to be detected are typically of order 100 μV – 5mV peak to peak (Eversmann et al., 2003). Therefore, on-chip buffering to produce high drive capability and low output impedance is very important. Good noise performance, high drive capability, low output impedance, low power dissipation and small area consumption are major concerns when designing a voltage buffer, and tradeoffs among these parameters have to be made (Bai and Wise, 2001). The preamplifier buffers can also minimize the possible cross talk of neural signals and charge injection associated with MOS transistor switching, since the not-addressed signal processing channels are isolated from the microelectrode sensors and neurons by the buffers. Charge injection could significantly disturb adjacent sensed signals as charge is injected back into the neuron under test (Mojarradi et al., 2003). 24-to-1 time division multiplexing is used to covert the single analog signal channel into multiple channel arrays. In the meantime, since multiplexing is used on-chip, the preamplifier buffers must be able to drive the subsequent amplifier at high-speed.

When a channel is addressed, the bias current will be applied to the preamplifier buffer circuit. The buffered neural signal will be directed out of the preamplifier into the next stage. The preamplifier buffer presents low impedance to the output wire when the corresponding channel is addressed. On the other hand, when a channel is not addressed, the bias current for the corresponding channel will be turned off. The microelectrode sensing site will also be isolated from the preamplifier buffer, which reduces the inter-channel cross talk. The buffer presents high impedance to the output wire when the channel is not addressed. The shutdown of not-addressed preamplifier buffers will reduce the power consumption of the biosensor chip. Unfortunately, in order to achieve the desired power dissipation, other performance parameters, typically indicated by the multiplexing speed are usually compromised due to the delay in settling of the circuit, which is related to the switching on and off the bias current of the preamplifier buffer. The tradeoff between the power consumption and multiplexing speed can be justified since high speed multiplexing is not necessary for most of the action potential measurement systems.

The schematic diagram of the preamplifier buffer is shown in Figure 4. It is composed of a two-stage amplifier configured with the closed-loop gain of 20dB via resistive feedback and some state controls. The two-stage CMOS amplifiers are extensively used in the various analog and mixed-signal circuits and systems due to its simple structure and robustness. (Mahattanakul, 2005) When designing a two-stage amplifier, numerous electrical characteristics, e.g., power dissipation, stability, overshoot, common-mode (CM) input swing,

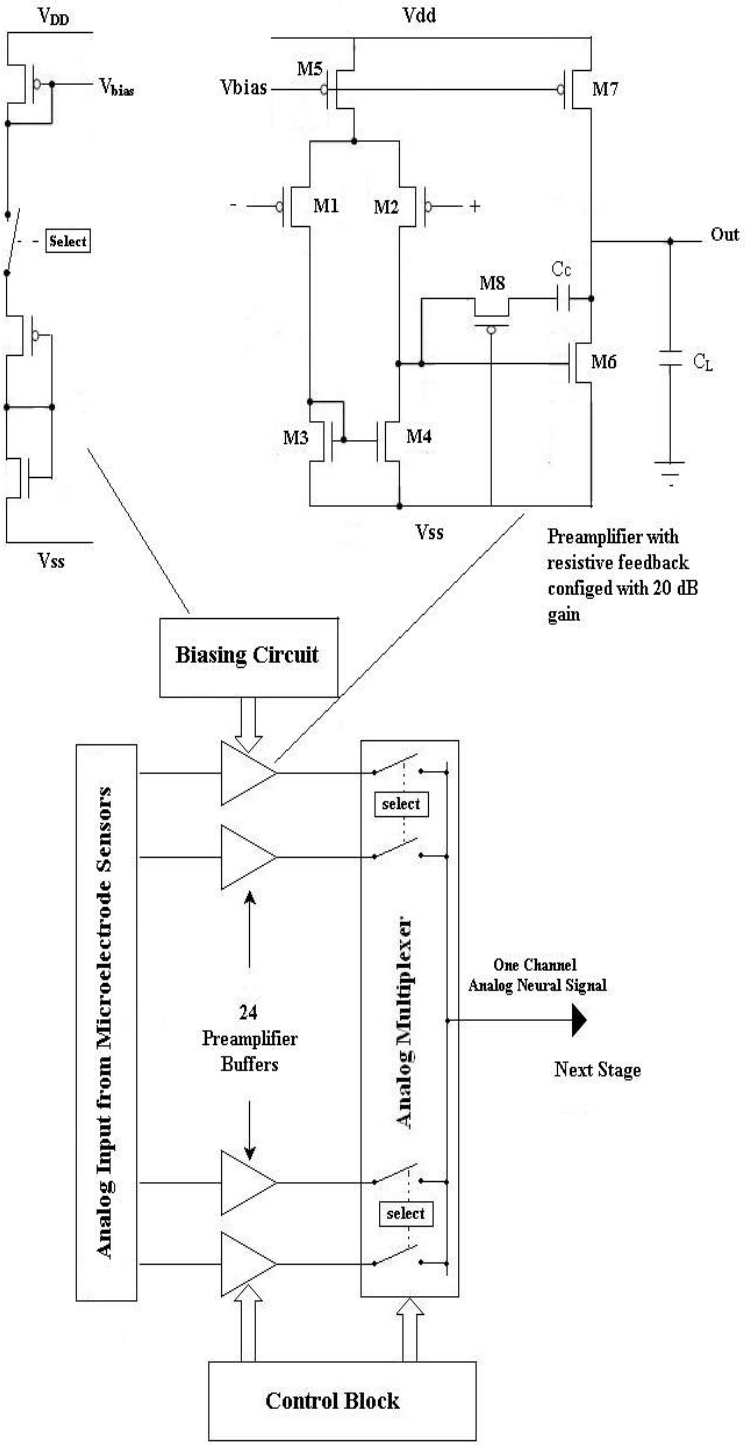

Figure 4. Schematic of preamplifier buffers with analog multiplexer.

output swing, open-loop gain, systematic input-referred offset voltage, gain-bandwidth, slew rate, input-referred noise voltage, should all be taken into consideration by the designer. Furthermore, closed-loop stability of the designed amplifier is of the most importance among all of the specifications. A minimum of 60 degree of phase margin is typically required under the worst-case analysis (unity gain configuration). A trade-off between the desired stability margin and other performance parameters should be justified by the designer with respect to the application field of the amplifier. Miller compensation technique was employed in this design, which connects a compensation capacitor Cc serial with a zero generating resistor across the high-gain stage (second stage). In this work, the design of the CMOS two-stage preamplifier starts from Miller compensation step by determining of the Miller capacitance Cc.

## 3.3. Analysis and Design of the Two-Stage Amplifier Based Preamplifier Buffer

### 3.3.1. Device Model

We neglect the 2nd order effect (body effect, channel length modulation, velocity saturation) during the analysis for simplicity. Typically, the MOS transistors are desired to work in saturation region, which is described by the following equations:

$$I_D = \frac{1}{2}\mu_{n,p}C_{ox}(\frac{W}{L})V_{ov}^2 \tag{1}$$

$$g_m = \sqrt{2\mu_{n,p}C_{ox}(\frac{W}{L})I_D} \tag{2}$$

$$g_m = \frac{2I_D}{V_{ov}} \tag{3}$$

where $V_{ov} = V_{GS} - V_{tn}$ for NMOS and $V_{ov} = V_{SG} - |V_{tp}|$ for PMOS.

### 3.3.2. Frequency Response and Pole/Zero Locations

The low frequency small signal gain of the two-stage amplifier shown in Figure 4 can be expressed as:

$$A_o = A_1 \times A_2 \tag{4}$$

where $A_1$ is the low frequency small signal gain of the first stage, and $A_2$ is the low frequency small signal gain of the second stage. $A_1$ and $A_2$ can be expressed as:

$$A_1 = g_{m1,2}(r_{o2} // r_{o4}) \tag{5}$$

$$A_2 = g_{m6}(r_{o6} // r_{o7}) \tag{6}$$

The frequency response of the amplifier can be expressed as

$$A(s) = A_o \frac{(1 + s/\omega_z)}{(1 + s/\omega_{p1})...(1 + s/\omega_{p4})} \tag{7}$$

The poles and zeros of the frequency response of the amplifier shown in Figure 4 can be found at (Allen, 2002):

$$\omega_{p1} \approx -\frac{1}{(r_{o4} // r_{o2})A_{v2}C_c} = -\frac{g_{m1}}{A_o C_c} \quad \text{(Dominant pole)} \tag{8}$$

$$\omega_{p2} = -\frac{g_{m6}}{C_L} \qquad \text{(Output pole)} \tag{9}$$

$$\omega_{p3} = -\frac{g_{m3}}{C_{gs3} + C_{gs4}} = -\frac{g_{m3}}{2C_{gs3}} \quad \text{(Mirror pole)} \tag{10}$$

$$\omega_{p4} = -\frac{1}{R_z C_I} \quad (\mathrm{R_z} \text{ pole}) \tag{11}$$

$$\omega_z \approx \frac{1}{C_c(g_{m6}^{-1} - R_z)} \tag{12}$$

The relationship between poles can be found as: $|\omega_{p1}| << |\omega_{p2}| < |\omega_{p4}| < |\omega_{p3}|$. If $R_z \geq g_{m9}^{-1}$, we will have the zero also in the left half plane, which makes the system a desirable minimum phase system. Also, we could have the zero cancel out the 1st non-dominant pole $\omega_{p2}$ in the design, which makes

$$\frac{1}{C_c(g_{m6}^{-1} - R_z)} = \frac{-g_{m6}}{C_L} \tag{13}$$

which is,

$$R_z \approx \frac{C_L + C_c}{g_{m6} C_c} \tag{14}$$

We also note that the gain-bandwidth can be expressed as:

$$\omega_u = A_o \omega_{p1} = \frac{g_{m1}}{C_c} \tag{15}$$

### 3.3.3. Output Swing

According to the Figure 4, it’s obvious that output swing can be expressed as:

$$\text{Output Swing} = V_{DD} - V_{ov6} - V_{ov7}$$

### 3.3.4. Common-Mode Input Range

If $V_{HR}^{CM}$ represents the amplifier head room voltage of the common-mode input range, which indicates $V_{HR}^{CM+} = V_{DD} - V_{CM(\max)}$ and $V_{HR}^{CM-} = V_{CM(\min)} - V_{ss}$ according to Figure 4, it can be derived that, to make the M$_1$ work in saturation region,

$$V_{HR}^{CM+} = V_{GS3} - V_t \tag{16}$$

and to make the M$_5$ work in saturation region, we should have

$$V_{HR}^{CM-} = V_{ov5} + V_{ov1,2} + V_t \tag{17}$$

### 3.3.5. Internal Slew Rate

The internal slew rate is the slew rate associated with the compensation capacitor Cc, which can be expressed as

$$SR_{\text{int}} = \frac{I_{D5}}{C_c} \tag{18}$$

### 3.3.6. External Slew Rate

The external slew rate is associated with the load capacitor C$_L$ (reference), it can be found as

$$SR_{ext} = \frac{I_{D7} - I_{D5}}{C_L} \tag{19}$$

Associating (18) with (19), we have

$$I_{D7} = SR_{ext}(C_c + C_L) \tag{20}$$

Combining (3), (15), (18), with the current equations $I_{D5} = 2I_{D1} = 2I_{D2}$, we have

$$V_{ov1,2} = \frac{SR_{ext}}{\omega_u} \tag{21}$$

### 3.3.7. Systematic Input-Referred Offset Voltage Minimization

The preamplifier buffers were designed to minimize the systematic offset, which is caused by current imbalance in the 2nd stage, i.e., between the drain current of $M_6$ ($I_{D6}$) and that of $M_7$ ($I_{D7}$), when there is no input voltage (Gray, 2001). With perfect matching and zero input voltages, $I_{D3} = I_{D4} = I_{D5}/2$ and thus $V_{GS3} = V_{DS3} = V_{DS4} = V_{GS6}$. Therefore, $V_{ov3} = V_{ov4} = V_{ov6}$ is required, where $V_{ov} = V_{GS}-V_t$. Ignoring the channel-length modulation effect and according to the square-law behavior of MOS transistor in saturation region:

$$I_D = \frac{1}{2}\mu_{n,p}C_{ox}\frac{W}{L}V_{ov}^2,$$

the following relationship between $I_D$ and W/L ratio is obtained:

$$\frac{I_{D6}}{I_{D3}} = \frac{I_{D6}}{\frac{1}{2}I_{D5}} = \frac{\left(W/L\right)_6}{\left(W/L\right)_3} \tag{22}$$

Now considering $M_5$ and $M_7$, which have equal gate-source voltages, we have $\frac{I_{D5}}{I_{D7}} = \frac{\left(W/L\right)_5}{\left(W/L\right)_7}$. To achieve the minimum systematic offset, we should have balanced drain current of $M_7$ and $M_6$, which is $I_{D7} = I_{D6}$. As a result, the current imbalance in the 2nd stage can be minimized by the following aspect ratio condition:

$$\frac{\left(W/L\right)_6}{2\left(W/L\right)_{3,4}} = \frac{\left(W/L\right)_7}{\left(W/L\right)_5} \tag{23}$$

which was considered in the preamplifier buffer design to minimize the DC offset voltage.

### 3.3.8. Input-Referred Thermal Noise

The input-referred thermal noise of the two-stage amplifier in Figure 4 can be shown to be

$$\overline{V_{n,in,th}^2} = 2 \times 4kT\gamma \frac{1}{g_{m1,2}} \left[ 1 + \frac{g_{m3,4}}{g_{m1,2}} \right] \tag{24}$$

From (3), (12), and (16), we have

$$g_{m3} = \frac{SRCc}{V_{ov3}} \tag{25}$$

substitute $g_{m1,2}$ and $g_{m3,4}$ in (24) with (15) and (25) , we obtain

$$\overline{V_{n,in,th}^2} = 2 \times 4kT\gamma \frac{1}{\omega_u C_c} \left[ 1 + \frac{SR}{\omega_u V_{ov3}} \right] \tag{26}$$

### 3.3.9. Preamplifier Buffer Design

The design starts from the phase margin analysis, since the most important issue in preamplifier design is to achieve good stability margin. From the expected unity gain-bandwidth $\omega_u$, to make the amplifier achieve $60^o$ phase margin, we should have the 2nd pole (1st non-dominant pole) further away from the gain crossover frequency, this gives us the following equation to evaluate the location of 2nd pole:

$$90^o + \tan^{-1} \frac{\omega_u}{\omega_{p2}} = 180^o - 60^o - M \tag{27}$$

where M is the phase margin over $60^o$. Typically, we would like to have at least $60^o$ phase margin. In this design, we choose $10^o$ margin, which leads to $M=10^o$. Thus, we can obtain the 2nd pole $\omega_{p2}$. Combine (9) and (27) we have obtain the proper value of $g_{m6}$ and from (2) we can calculate the $(W/L)_6$. Also, note that the $V_{ov6}$ can be obtained from the expected output swing. Thus, $I_{D6}$ is obvious to calculate.

The following calculation focus on obtaining the value of compensation capacitor Cc from the specified input referred noise. With (26) we can obtain the value of Cc. In this estimation, we assume $\gamma=2.5$ for short channel device. From the specified Slew Rate (SR), we can estimate the $I_{D6}$, $I_{D7}$ and also $I_{D5}$ with (18) and (20). From the relationship $I_{D1} = I_{D2} = \frac{I_{D5}}{2}$ and (15), we can calculate the value of $I_{D1}$ and $g_{m1}$, combining (2) $(W/L)_{1,2}$ can be obtained.

### 3.4. Channels Addressing and Sequencing

The biopotential sensor chip has a built-in 5-bit address decoder to address the 24 analog signal channels associated with the 24 microelectrode pixels in the sensor array, which implements the function of a 24-to-1 analog multiplexer. When an analog signal channel is addressed, its associated preamplifier buffer bias current is turned on activating the preamplifier. Also, the output of the corresponding preamplifier buffer is connected to the input of the OTA based high-gain amplifier. The on-chip 24-to-1 analog multiplexer serves as site-selection circuits, which can be used to select site of the 4 by 6 sensor arrays. A five-bit binary counter is built on-chip to drive the input of the 5-bit address decoder to implement the spatial sequencing of the 24 sensing sites. The 5-bit binary counter starts with 00000 after reset, which is associated with the first analog signal channel. As the counter sequences through the consecutive binary numbers from 00000 till 11000 (no state defined for binary number from 11001 to 11111), the analog signal channels will be addressed in sequence and the corresponding neural signal will be buffered, amplified and lead onto the output pad of the biosensor chip. The multiplexing rate for the readout system is governed by the clock rate of the binary counter, which may vary for different application purposes. For example, the required multiplexing rate for the retinal readout system is up to 5 MHz (Mathieson et al., 2004). The clock of the binary counter can be provided either by a built-in ring oscillator or an external clock from the testing system.

### 3.5. Biasing Circuitry

The amplifier stability margin (phase margin) is determined by the location of dominant pole, where the dominate pole is a function of the input stage transconductance $g_{m1,2}$ controlled by the bias currents. The biasing circuitry of the preamplifier buffers and gain providing amplifiers are illustrated in Figure 5 (a) and (b). The biasing circuit for the two-stage preamplifier buffers adopts the basic current source and current mirror structure to produce biasing current and copy it into the input stage and gain-stage of the two-stage preamplifier with no dependence on process and temperature (neglecting the channel-length modulation). Considering the limited layout space on the total die area of $1.5 \times 1.5$ mm$^2$, the diode connected NMOS and PMOS serving as the biasing resistor replace the passive element. Each of the 24 preamplifier buffers is addressable. These buffers receive no bias current unless they are addressed. Addressing turns on the buffer by switching the bias current into the addressed preamplifier and also, switches the preamplifier output onto the output wire that feeds the gain-stage amplifier. This design architecture is a trade-off between speed and power dissipation. We only switch on the biasing circuitry for the preamplifier buffer corresponding to the addressed analog channel. For those analog channels that are not addressed, we shut off their biasing current to reduce the total power consumption. However, switching the amplifier on and off will increase the settling time of the analog signal processing channels and thus reduce the frame rate of the microelectrode array controlled by the running frequency of the on-chip ring oscillator.

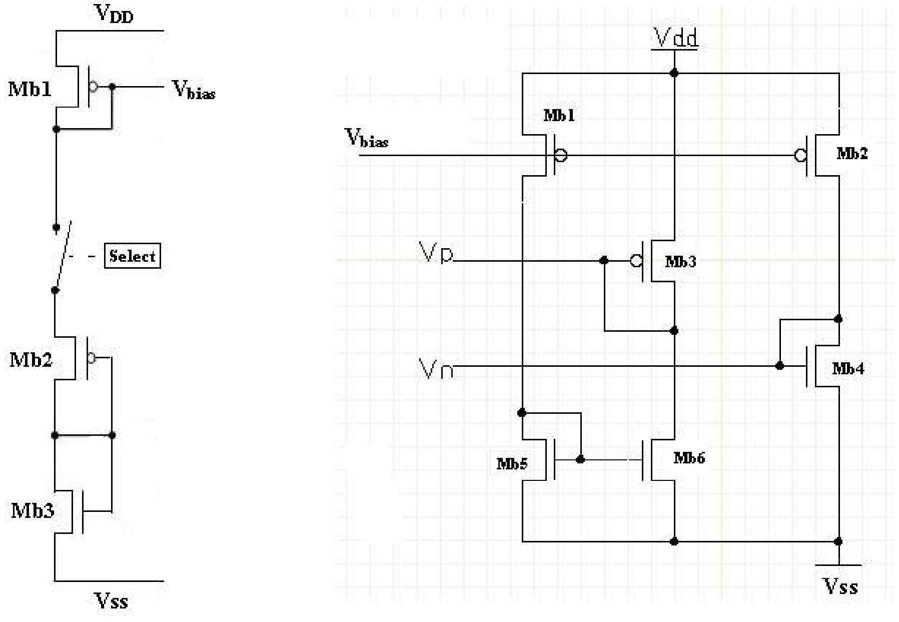

**(a)**
**Biasing Circuit for preamplifier buffers**

**(b)**
**Biasing Circuit for OTA based high-gain amplifier**

Figure 5. Schematics of Biasing Circuitry for the preamplifier and high-gain amplifier.

### 3.6. High-gain Amplifier

The gain-stage amplifier will apply the higher gain to the buffered signal to bring it from the level of hundreds of micro-volts to a couple of volts. The main constraints in the design of bio-amplifiers (preamplifier and gain stage amplifier) are the requirement of low input referred noise, low power consumption, and a small area on chip. In the meantime, the bio-amplifiers should have the capability of removing the DC offsets from the input. The structure of the two-stage amplifier is simple and easy to implement, however, the compensation capacitor will consume much chip area in layout. In the meantime, the two-stage preamplifier structure will be unable to eliminate the DC offset with the resistive feedback configuration. We consider the operational transconductance amplifier (OTA) for the gain stage amplifier in this biosensor chip since the compensation capacitor for the OTA is the load capacitor which can be the input capacitance of the next stage or off chip and thus the on chip compensation capacitor is not necessary for the OTA based high-gain amplifier stage. The gain stage amplifier implemented in this design comprises an operational transconductance amplifier (OTA) coupled in capacitive feedback configuration, shown in Fig 6. This OTA structure is very simple and popular, adopted by many researchers in designing the low-noise CMOS bio-amplifier. (Harrison and Charles, 2003; Wu et al., 2005) The closed-loop midband gain of the capacitive feedback OTA amplifier is determined by the value of $C_1$ and $C_2$ (feedback gain = $C_1/C_2$). Cascode topology is chosen at the output stage to boost the open loop gain of the OTA with the trade-off with the output swing. Since both of the two input nodes of the OTA amplifier are floating, switched capacitor circuitry will be necessary for the proper operation of the OTA with the capacitive coupling. However, the switched capacitor circuitry will introduce the clock-controlled operation, which will make the design complicated with the challenges of high precision clock generation, channel charge injection and clock feed-through. To avoid the switched capacitor operation, we need to provide DC biasing path for both of the input nodes in the OTA amplifier. Since the serpentine polysilicon resistor with large value takes huge die area in the layout, the diode connected pMOS transistors serve as large resistors for the DC biasing purpose.

Compensating the OTA is simply a matter of choosing the minimum load capacitance. (Baker et al. 1998) The phase margin of the OTA will improve with the increasing of load capacitance. Unlike the two-stage amplifier, the on-chip compensation capacitor for OTA is unnecessary, thus, it saves significant chip area in the OTA layout compared with the two-stage amplifier. However, the structure of the OTA is more complicated compared with the two-stage amplifier, especially for the biasing circuit. For the layout of large transistors (high W/L ratios), such as $M_2$, $M_7$, $M_8$ and $M_{12}$ in Figure 6, we split them into two transistors equivalent to one large transistor to reduce the parasitic capacitance. The values of feedback capacitors $C_1$ and $C_2$ are chosen to give the appropriate closed-loop gain. $C_1$ and $C_2$ are implemented on chip and the load capacitor $C_L$ will be the off-chip capacitance, including the load of the measurement stage too. The proposed value of $C_1$ is 10pF and $C_2$ is 0.2pF to achieve the closed-loop gain around 30 – 40 dB. The on-chip capacitors are implemented with two overlapped layers of poly-silicon materials (poly1 and poly2). The AMI 0.5um design rules require the poly2 stays inside the area of poly1.

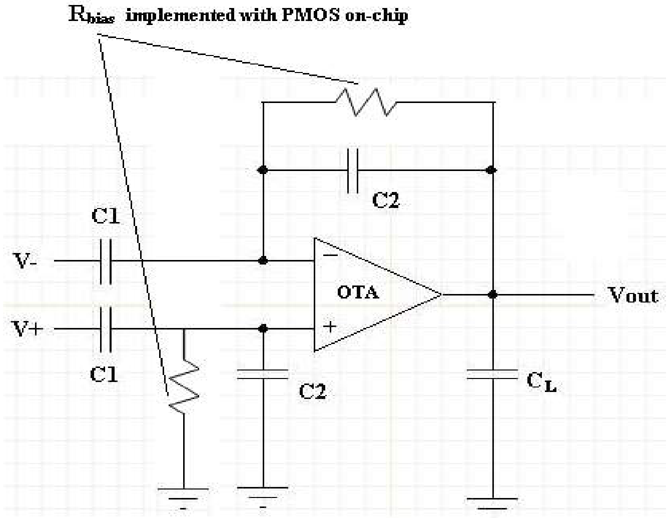

(a) OTA with Capacitive Feedback

Figure 6. Continued on next page.

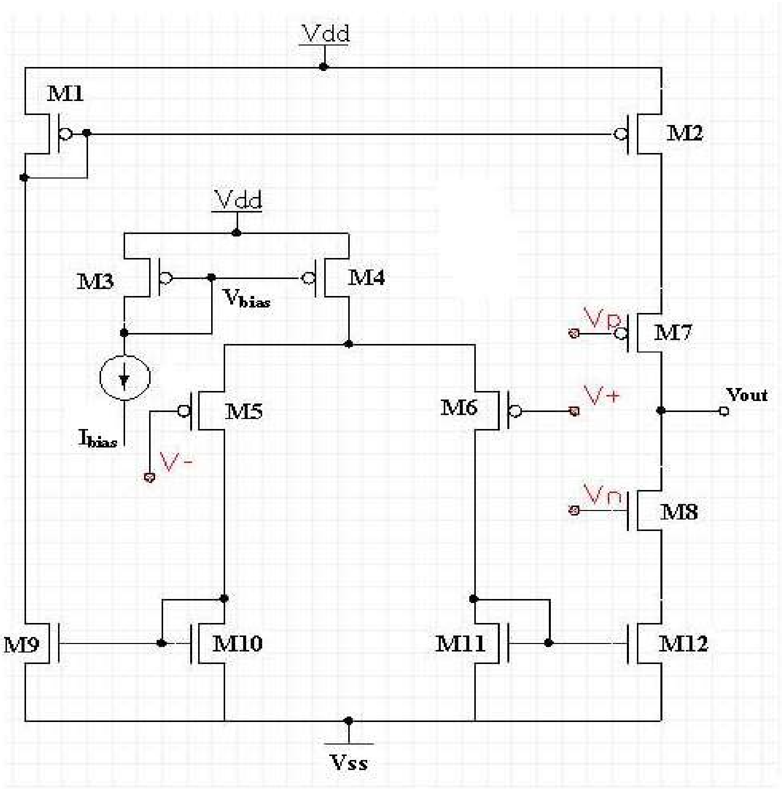

**(b) Schematics of OTA**

Figure 6. Schematic of OTA based high-gain amplifier.

Though careful design applies to eliminate DC offset voltage of the preamplifier buffer, it may still exist in the preamplifier buffers due to the mismatches in the supposedly identical pairs of devices. The OTA based high-gain amplifier will be helpful to reduce the DC offsets due to the AC coupling principle of the OTA with capacitive feedback topology.

## 4. BIOSENSOR FABRICATION AND PACKAGE

The layout of the biosensor device was implemented using Magic Ver 7.1 (U.C. Berkeley, Berkeley, CA). Magic provides a mask oriented description of the high-level description (HLD) circuit. Its hierarchical layout editor allows for the inclusion of library cells, which extends the complexity of the design capabilities (Davis, 2005). To minimize the circuitry layout area, hand layout was chosen for all circuit building blocks and wire routing. The total layout of the biosensor chip consumes an area of 2.25 mm$^2$. We fabricated the biosensor chip in the AMI C5 0.5 μm double-poly three-metal CMOS process via the MOS Implementation Service (MOSIS) foundry service. The fabricated chip is powered by 5V and packaged with the ceramic 40 pin dual-inline package (DIP) by MOSIS. Figure 7 is the micrograph of the packaged 40 pin DIP biosensor chip mounted onto a 35-mm petri dish with a centered round hole through the bottom. The square at the center of the biosensor IC chip in Figure 7 is the area of the bare die containing the sensing array and signal processing channels, which are not visible at this magnification. Figure 8 illustrates the microphotograph of the biosensor chip and its functional blocks including the sensing area of the fabricated 4 by 6 microelectrode array sensors, reference electrodes and analog signal processing channels with built-in digital logic control/interface.

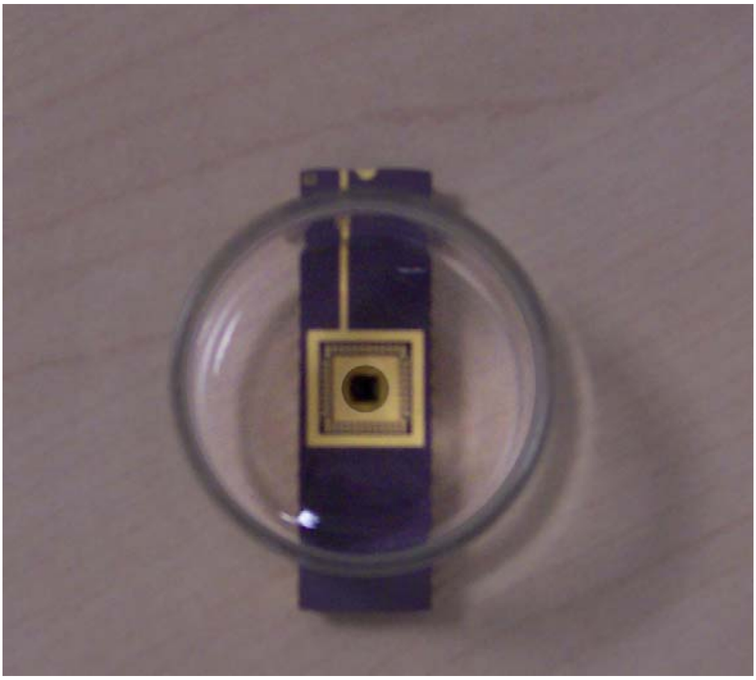

Figure 7. Micrograph of the packaged 40 pin DIP chip mounted with 35-mm petri dish.

The layout of the planar metal sensor pixels are implemented with three layers of metals: metal 1, metal 2 and metal 3 with the top cover glass open, which is similar to the pads of the IC chip. This will leave the metal open to external world and not covered by the glass after the IC fabrication. We shrink down the size of the individual planar metal sensor pixel compared with the pad of the IC chip to make the 6 by 4 sensor pixels array fit into the $1.5 \times 1.5 \text{ mm}^2$ die size.

The 24 planar electrodes of the biosensor chip are fabricated using the standard CMOS fabrication process. Compared with MEMS techniques, this fabrication technique for the sensor contacts is simple and easy to realize. However, the microelectrode array sensing site material as received from the standard CMOS process is aluminum, which is deficient both in biocompatibility and corrosion resistance (Zhu and Zhu, 2006; Reeves et al., 2004; Kovacs, 1998). To avoid cell poisoning and undesirable electrochemical corrosion, electroless-plated gold, which is biocompatible (Geddes, 1972), is used to cover the open aluminum electrodes of the biosensor chip. Gold is widely used as the microelectrode material in biological experiments because it is a relatively inert metal and does not react with the biological tissue (Mathieson et al., 2004). The electroless gold plating process is preferred for this purpose because neither a photolithographic process nor an electrical connection to the plated surface is required. These processes will reduce sensitivity and increase noise during the measurement (Reeves et al., 2004). Bond wires and pads are encapsulated using a water-resistant biocompatible epoxy resin to prevent shorting when the biopotential sensor array is immersed in the aqueous medium. Polydimethylsiloxane (PDMS) is used to form a well to isolate the bond wires from the aqueous culture medium. A 35-mm petri dish with a centered round hole through the bottom is mounted on the surface of the biosensor IC with PDMS, forming the larger bath to hold the aqueous culture medium and isolate the packaging material from the living cells. The post-CMOS processing and packaging techniques applied to the biosensor chip promotes biocompatibility and stability in the aqueous cell culture environment (Heer et al., 2006).

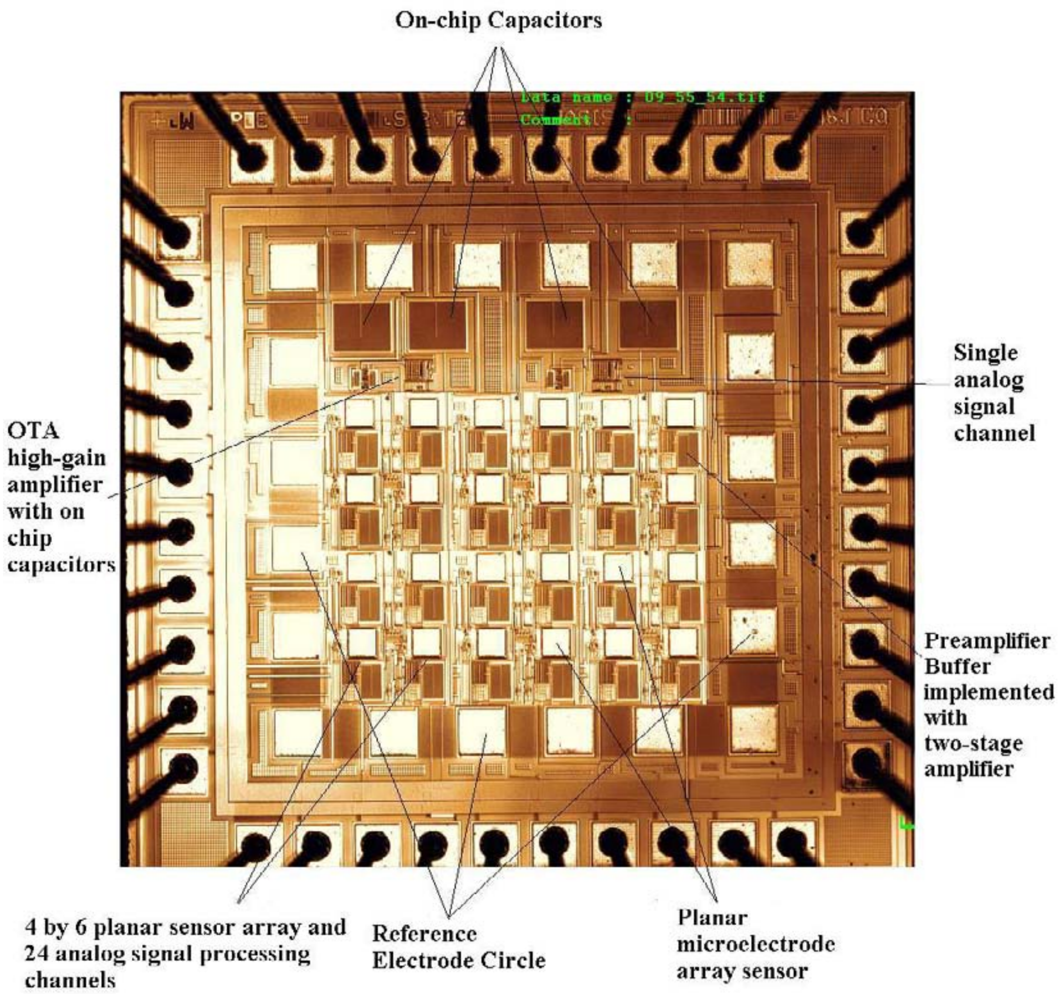
On-chip Capacitors
Data name : 09_55_54.tif
Comment :
Single analog signal channel
OTA high-gain amplifier with on chip capacitors
Preamplifier Buffer implemented with two-stage amplifier
4 by 6 planar sensor array and 24 analog signal processing channels
Reference Electrode Circle
Planar microelectrode array sensor

Figure 8. Microphotograph of the multichannel neural recording sensor chip.

# 5. TESTING SYSTEM ELECTRONIC DESIGN

A testing workbench that interfaces the biopotential sensor chip with a client PC running Matlab/Simulink (MathWorks, Natick, MA) platform was implemented using the Motorola ColdFire MCF5307 (Motorola, Austin, TX) microcontroller, which is a 32-bit RISC processor running at 45MHz and clock-double internally. The primary features of the MCF5307 integrated processor include: 8 Kbyte unified cache, 4 Kbyte SRAM, four fully programmable DMA channels, DRAM controller supporting up to 256 Mbyte of DRAM, full duplex DUART, dual 16-bit general-purpose multimode timers and fully $I^2C$ bus compatible Motorola bus (M-Bus) module. The firmware program was developed using the ColdFire Family assembly language. The testing workbench realizes four major functions: (1) Control signal/Pattern generation, (2) Analog and digital filter (3) A/D conversion of analog biopotential signals, and (4) Serial communication with PC system.

## 5.1. Control Signals/Sequence Generation

The mode control signal and pattern sequence of the biosensor chip are generated with the parallel I/O port of the MCF5307. The MCF5307 has one 16-bit parallel port (PP) for general I/O purpose. All the pins have dual functions. They can be configured as I/O or the alternate function via the Pin Assignment Register (PAR). In this design PP[7:0] are configured as output and PP[15:8] as input. PP[15:8] is used for input of the 8-bit data on the A/D converter ADC0820 data bus; control signals for ADC0820 ($\overline{RD}$ and $\overline{WR}$), bio-IC addressing sequence control signals are generated by PP[7:0]. To interface the biosensor chip with the MCF5307 microcontroller, a voltage level shifter is necessary to translate the 0-5V digital logic signals from the MCF5307 into the logic signals of the biosensor chip (powered by ±2.5V).

## 5.2. Analog and Digital Filters

The choice of building analog and digital filters are driven by eliminating the undesired components from the measured neural signals. We choose a continuous-time RC band-pass filter as it offers an easy way to build the modular multi-channel system (Dabrowski et al., 2004). The band-pass filter in this design is comprised of a high-pass filter cascaded with a low-pass filter. The first step of the two-stage band-pass filter is a 2nd order Butterworth low-pass filter and the subsequent stage is implemented with a 3rd order Chebyshev high-pass filter. The low-pass filter limits the crosstalk from the off-chip noise sources and provides anti-aliasing (Heer et al., 2004) and the high-pass filter rejects the electrode low frequency offset voltage (Won et al., 2002). The corner frequencies of the band-pass filter are 100 Hz and 10 KHz, which is the typical frequency range of action potentials (Heer et al., 2004; Bai and Wise, 2001; DeBusschere and Kovacs, 2001). Digital filters are implemented using Matlab's powerful signal processing toolbox. A 6th order low pass elliptic filter is used to smooth the digitized neural signals to eliminate the noise introduced by the measurement and data acquisition system.

### 5.3. A/D Conversion of Neural Signals

Since the MCF5307 does not have a built-in analog-to-digital (A/D) converter, the National Semiconductor (Santa Clara, CA) 8-bit medium speed off-chip A/D converter ADC0820 was used in this design. Using a half-flash conversion technique, the 8-bit ADC0820 CMOS A/D offers a 1.5 μs conversion time and dissipates only 75 mW of power. The input to the ADC0820 is tracked and held by the input sampling circuitry eliminating the need for an external sample-and-hold for signals changing in less than 100mV/μs. For ease of interface to microprocessors, the ADC0820 has been designed to appear as a memory location or I/O port without the need for external interfacing logic (National Semiconductor, 2001). ADC0820 has two working modes: RD mode and WR-RD mode. RD mode was considered in this design by pulling the pin of Mode down to ground. Tri-state buffers are necessary interfacing between the parallel port of MCF5307 and ADC0820. Octal tri-state buffer MC74LC244DW (Motorola, Austin, TX) was used here as the buffers between ADC and parallel port. For each neural recording channel, the sampling rate of this testing system is 40 kHz, which is high enough for a faithful reproduction of the measured analog action potentials. By polling the data-ready bit on ADC0820, the ready-to-transmit data on the data bus of ADC0820 can be accessed from the parallel port (PP) of MCF5307.

### 5.4. Serial Communication

Asynchronous serial communication with RS-232C was used to transmit data from the MCF5307 microcontroller system to a client PC. The MCF5307 contains two universal asynchronous/synchronous receiver/transmitters (UARTs), which act independently. Each UART is clocked by the system clock, eliminating the need for an external crystal. The UART module interfaces directly to the CPU. The asynchronous serial communication runs at 19200 bps baud rate with the frame format of non-parity, 8-bit data and 1-bit stop. MC145407DW (Motorola, Austin, TX) was used to interface the RS-232 voltage level with the TTL/CMOS compatible logic levels of MCF5307.

## 6. ELECTRICAL TESTS

The operation of the biosensor chip and testing workbench was demonstrated by the electrical testing experiment. The electrical test was performed with the petri dish filled with 0.5M NaCl solution. The biopotential signal was then emulated using the D/A function of PCI-DAS1002 (Measurement Computing, Norton, MA) in the platform of Matlab Simulink Real Time Workshop (Math Works, 1997). Hodgkin-Huxley neuron model was used as the mathematical model of biological neurons to generate the numerical data of the biopotential signal (Hodgkin and Huxley, 1952). Band-limited white noise was added to the biopotential data generated by Hodgkin-Huxley neuron model. Figure 9 depicts the electrical testing results of the emulated neural signal. The electrical testing results illustrated in Figure 9 demonstrate the full system functionality.

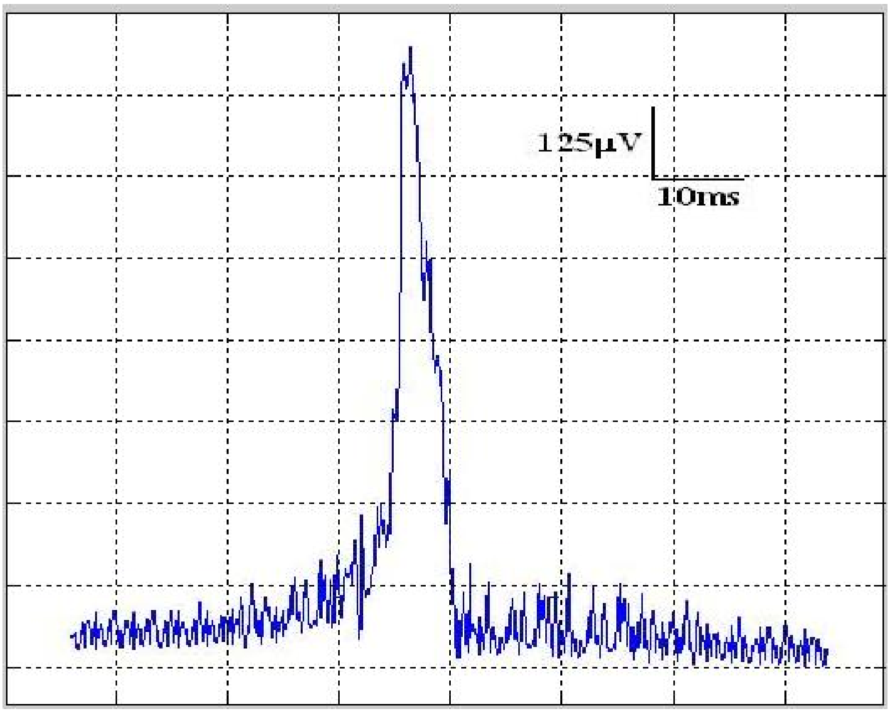

Figure 9. Measured biopotential output voltage when an emulated action potential signal applied for electrical testing of the biosensor chip.

We can use the biosensor chip to test the electrode-neuron interface, which permits modeling of the interface and calculation of the internal cell potentials based on the array contact voltage measurements external to the nerve cell. We can obtain the electrode-neuron interface model parameters by injecting a test current pulse (8nA, 100 ms duration) into the sensing site of the addressed channel. A NMOS switch shields the preamplifier circuit from the test current coupling effect when the test current applies to the sensor. The 8nA current pulse is considered as a moderate to high amount of current in the realm of cellular neurophysiology (DiCecco et al., 2005). This current pulse charges the electrode-cell membrane interface capacitance. The system monitors the evoked contact voltage. A passive RC circuit model for this type of electrode-cell (electrolyte) interface has been proposed by Kovacs (Kovacs, 1994). The RC model for the interface impedance can be determined from the voltage changing rate and its steady state value. More detail reports will be published in forthcoming papers with the more biosensor testing related focus.

## 7. BIOLOGICAL TESTS

The extracellular neural recordings were conducted with neurons from *Aplysia californica*, an invertebrate of the phylum mollusca and the class gastropoda (DiCecco and Sun, 2005). The invertebrate central nervous system is ideally suited for the biological testing of the biosensor chip, as the comparative size of the individual neuron is large enough, on the order of 200 to 400 μm (DiCecco and Sun, 2005), for the extracellular neural recording of the action potential with the multi-channel biosensor chip described above. The experimental neurons were prepared by the dissection of *Aplysia californica* with the circulation of filtered seawater. The neurons extracted from *Aplysia californica* were cultured for two days before the biological measurement. During the *in vitro* recordings, the neural reference electrode contacts were tied to the ground rail in order to ground the subject on the reference and prevent offset saturation (Won et al., 2002). A 600 ms square voltage pulse with 500 mV peak to peak as the stimulus was applied to the neurons in the culture chamber through the external stimulating electrodes. The resulting biopotential signals measured on a selected microelectrode sensor channel are shown in Figure 10.

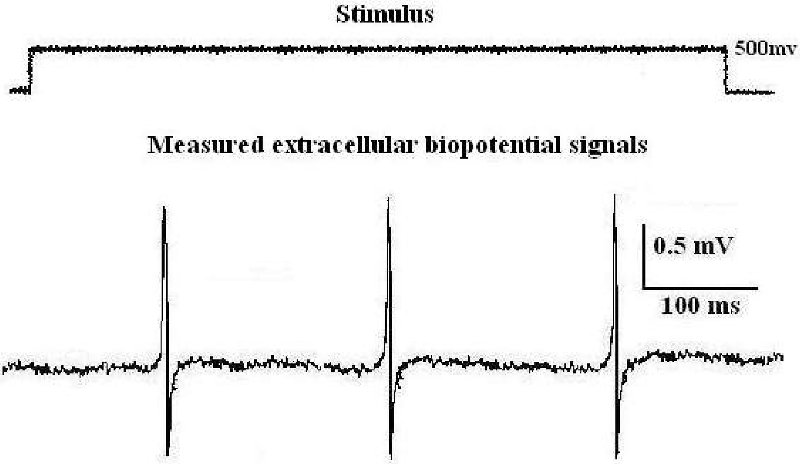

Figure 10. Measured action potential signals from *Aplysia californica* with the biosensor system.

## 8. CONCLUSION

In this research work we presented the circuit design, layout, packaging and testing for a full-customized multi-channel biopotential sensor chip based on AMI C5 0.5 μm two poly layers and three metal layers CMOS process. This biosensor allows the measurement of propagation of action potential in a nerve cell. This biosensor system is structured in a hierarchy design where a repeatable module comprises of the planar microelectrode sensor, preamplifier buffer and the channel addressing control unit. This system offers performance that is competitive to commercial systems. Integrated with the firmware based on the ColdFire MCF5307 microprocessor system, the biosensor provides a satisfactory signal-to-noise ratio for neural signals with amplitudes of order 50μV to 2 mV peak-to-peak and the frequency spectrum in the range of 100Hz – 10kHz. We demonstrated the full functionality of all components of this biopotential measurement system. Biological tests show that this biosensor chip is capable of highly precise measurement of action potential signals from excitable cells using *Aplysia californica*.

## Acknowledgement

The authors wish to acknowledge the many helpful contributions from the Biomedical Engineering Division at CRX Science and Technology LLC for their assistance with the biological experiment setup and neural recording measurement. Dr. Yi Zhang at the Engineering Division, CRX Science and Technology is also acknowledged for his helpful guidance in the layout of the biosensor chip. Thanks also to Yanhui Hu at the Department of Physics, Xiamen University for her efforts in schematics and diagrams drawing. This work was sponsored by Sigma Investment Group, CRX Science and Technology LLC.

## REFERENCES

Akin, T., and Najafi, K., 1998. A wireless implantable multichannel digital recording system for a micromachined sieve electrode. *IEEE J. Solid State Circuits*, **33**, 109-118.

Allen, P. E. and Holberg, D. R., 2002. *CMOS Analog circuit design*, 2nd Edition, Oxford University Press, New York.

Augusting, J. G., Fitzpatrick, D., and Purves, D., 2004. *Neuroscience*, 3rd Edition, Sinauer Associates, Inc, Massachusetts.

Bai, Q., and Wise, K.D., 2001. Single-unit neural recording with active microelectrode array. *IEEE Trans. Biomed. Eng.* **48** (8), 911-919.

Baker, R.J., Li, H.W., and Boyce, D. E., 1998. CMOS: Circuit Design, Layout, and Simulation. John Wiley & Sons, Inc., New York.

Blum, R. A., Ross, J. D., and Simon, C. M., 2003. A custom multielectrode array with integrated low-noise preamplifiers. *Proceedings of the 25th Annual International Conference of the IEEE EMBS*, Cancun, Mexico, 2003, 3396-3399.

Breckenridge, L.J., Wilson, R.J.A., Connolly, P., Curtis, A.S.G., Dow, J.A.T., Blackshaw, S.E. and Wilkinson, C.D.W., 1995. Advantages of using microfabricated extracellular electrodes for in vitro neuronal recording, *Journal of Neuroscience Research*, **42**, 266-276

Csicsvari, J., Hirase, H., Mamiya, A., Buzsaki, G., 2000. Ensemble patterns of hippocampal CA3-CA1 neurons during sharp wave-associated population events, *Neuron* **28**, 585-594.

Dabrowski, W., Grybos, P., Hottowy, P., Skoczen, A., Swientek, K., Bezayiff, N., Grillo, A. A., Kachiguine, S., Litke, A. M., and Sher, A., 2003. Development of integrated circuits for readout of microelectrode arrays to image neuronal activity in live retinal tissue. *IEEE Nuclear science symposium conference,* **19-25**(2), 2003, 956-960.

Dabrowski, W., Grybos, P., Litke, A. M., 2004. A low noise multichannel integrated circuit for recording neuronal signals using microelectrode arrays, *Biosensors and Bioelectronics* **19**, 749-761.

Davis, J. A., 2005. Introduction to integrated circuit design, layout and simulation, University of Rhode Island Copy Center, Rhode Island.

DeBusschere, B. D., and Kovacs, G. T. A., 2001. Portable cell-based biosensor system using integrated CMOS cell-cartridges. *Biosensors and Bioelectronics* **16**(7-8), 543-556.

DiCecco, J., Wu, J., and Sun, Y., 2005. A fully digital implementation of voltage current, and dynamic clamping methodologies. *Proceedings of 31st annual northeast bioengineering conference*, Hoboken, NJ, USA, April2-3, 2005, 37-38.

DiCecco, J., and Sun, Y., 2005. *Californica* Dreaming: Neurotransmitter 'Doze' Response and Neruonal Signal Analysis of *Aplysia californica*. Proceedings of IEEE 31st Annual Northeast Bioengineering Conference, Hoboken, NJ, April 2-3, 2005, 46-47.

Eversmann, B., Jenkner, M., Hofmann, F., Paulus, C., Brederlow, R., Holzapfl, B., Fromherz, P., Merz, M., Brenner, M., Schreiter, M., Gabl, R., Plehnert, K., Steinhauser, M., Eckstein, G., Schmitt-Landsiedel, D., and Thewes, R., 2003. A 128×128 CMOS biosensor array for extracellular recording of neural activity. *IEEE J. Solid State Circuits*, **38**(12), 2306-2317.

Geddes, L A., 1972. Electrodes and the Measurement of Bioelectric Events. Wiley-Interscience, New York.

Gray, R. P., Hurst, J. P., Lewis H. S., and Meyer, G. R., 2001. *Analysis and Design of Analog Integrated Circuits, 4th* Edition, John Wiley & Sons, Inc., New York.

Harrison, R. R. and Charles, C., 2003. A Low-power low-noise CMOS amplifier for neural recording applications, *IEEE J. Solid State Circuits*, **38**(6), 958-965.

Heer, F., Franks, W., Blau, A., Taschini, S., Ziegler, C., Hierlemann, A., and Baltes, H., 2004. CMOS microelectrode array for the monitoring of electrogenic cells, *Biosensors and Bioelectronics,* **20**, 358-366.

Heer, F., Hafizovic, S., Ugniwenko, T., Frey, U., Franks, W., Perriard, E., Perriard, J.-C., Blau, A., Ziegler, C., and Hierlemann, A., 2006. Single-chip microelectronic system to interface with living cells, *Biosensors and Bioelectronics*, **22**, 2546-2553.

Hodgkin, A.L. and Huxley, A.F., 1952. A quantitative description of membrane current and its application to conduction and excitation in nerve, *J. Physiol. (London)* **117** 500-544.

Ji, J., and Wise, K. D., 1992. An implantable CMOS circuit interface for multiplexed microelectrode recording arrays. *IEEE J. Solid State Circuits*, **27**, 433-443.

Kawano, T., Kato, Y., Tani, R., Ishino, H., Takao, H., Sawada, K., and Ishida, M., 2003. Neuron size Si probe array fabricated integrated circuits for multichannel electrode. *Proceedings of the 12th international conference on solid state sensors, actuators and Microsystems*, Boston, MA, USA, June 8-12, 2003, 1679-1682.

Kovacs, G. T. A., 1994. Introduction to the theory, design, and modeling of thin-film microelectrodes for neural interfaces, in *Enabling Technologies for Cultured Neural Networks*, D. A. Stenger and T. M. Mckenna, Eds. San Diego, CA: Academic, 121-166.

Kovacs, G. T. A., 1998. *Micromachined Transducers Sourcebook.* WCB McGraw-Hill, Boston.

Lind, R., Connolly, P. and Wilkinson, C.D.W., 1991. Finite-element analysis applied to extracellular microelectrode design, *Sensors and Actuators*, **B(3),** 23-30

Litke, A. M., and Meister, M., 1991. The retinal readout array. *Nucl. Instrum. Methods* **A310**, 389-394.

Mahattanakul, J. and Chutichatuporn, J., 2005. Design procedure for two-stage CMOS opamp with flexible noise-power balancing scheme, *IEEE Transactions on circuits and systems*, **52**(8), 1508-1514.

Mathieson, K., Kachiguine, S., Adams, C., Cunningham, W., Gunning, D., O'Shea, V., Smith, K. M., Chichilnisky, E. J., Litke, A. M., Sher, A., and Rahman, M., 2004. Large-area microelectrode arrays for recording of neural signals, *IEEE Transactions on nuclear science*, **51**(5), 2027-2031.

Math Works Inc., 1997. *MATLAB target language compiler reference guide*, Ver. 1, Mathworks, Inc., Natick, Massachusetts.

Math Works Inc., 1997. *Real-time workshop user's guide*, Ver. 2, Mathworks, Inc., Natick, Massachusetts.

Mojarradi, M. Binkley, D., Blalock, B., Andersen, R., Ulshoefer, N., Johnson, T., and Del Castillo, L, 2003. A miniaturized neuroprosthesis suitable for implantation into the brain. *IEEE Transaction on Neural Systems and Rehabilitation Engineering*, **11**(1), 38-42.

Najafi, K., and Wise, K. D., 1986. An implantable multielectrode array with on-chip signal processing. *IEEE J. Solid State Circuits*, **21-6**, 1035-1044.

National Semiconductor Corporation, 2001. ADC0820 8-bit high speed uP compatible A/D converter with track/hold function, National Semiconductor Corp.

Nicolelis, M. A. L., 2001. Actions from Thoughts. *Nature* **409**, 403-407.

Oka, H., Shimono, K., Ogawa, R., Sugihara, H., and Takateni, M., 1999. A new planar multielectrode array for extracellular recording application to hippocamal acute slice. *J. Neurosci. Methods*, **93**, 61-67.

Pancrazio, J. J., Bey, P. P. Jr., Loloee, A., Manne, S., Chao, H., Howard, L. L., Gosney, W. M., Borkholder, D. A., Kovacs, G. T. A., Manos, P., Cuttino, D. S., David A. and Stenger, D. A., 1998. Description and demonstration of a CMOS amplifier-based-system with measurement and stimulation capability for bioelectrical signal transduction. *Biosensor and Bioelectronics,* **13**, 971-979.

Patterson, R. W., Song, Y. K., Bull, W. C., Ozden, I., Deangellis, P. A., Lay, C., McKay, L. J., Nurmikko, V. A., Donoghue, D. J., and Connors, W. B., 2004. A microelectrode/microelectronic hybrid device for brain implantable neuroprosthesis applications. *IEEE Transactions on Biomedical Engineering*, **51**(10), 1845-1852.

Reeves, N., Liu, Y., Nelson, N. M., Malhotra, S., Loganathan, M., Lausenstein, J.-M., Chaiyupatumpa, J., Smela, E., and Abshire, P. A., 2004. Integrated MEMS structures and CMOS circuits for bioelectronic interface with single cells, *Proceedings of the 2004 International Symposium of Circuits and Systems*, **3**(3), (2004), 673-676.

Won, D., Obeid, I., Morizio, J. C., Nicolelis, M. A. L., and Wolf, P.D., 2002. A Multichannel CMOS Analog Front End for Neural Recordings, *Proceedings of the Second Joint EMBS/BMES Conference*, **3**, 2002, 2070-2071.

Wrobel, G., Zhang, Y., Krause, H. J., Wolters, N., Sommerhage, F., Offenhäusser, A. and Ingebrandt, S., 2007. Influence of the first amplifier stage in MEA systems on extracellular signal shapes. *Biosensors and Bioelectronics*, **22**, 1092-1096.

Wu, J., Feng, W.F., and Tang, W. C., 2005. A multi-channel low-power circuit for implantable auditory neural recording microsystems, *Proc. 12th Int. Conf. BioMed. Engin*, December, 2005, paper #4B1-05.

Zhu, T., and Zhu, D., 2006. Research of CMOS Integrated Biosensor for Extracellular Bioelectrical Signal Recording, *Chinese Journal of Sensors and Actuators*, **19-4**, 941-946.

In: Integrated Circuits, Photodiodes… ISBN: 978-1-60692-660-4
Editors: R. McIntire and P. Donnell, pp. 95-113 © 2009 Nova Science Publishers, Inc.

*Chapter 4*

# SCENE ANALYSIS OF UNSTABLE VIDEO FLOWS – USING MULTIPLE RETINA CHANNELS AND ATTENTIONAL METHODS

***Anna Lázár*[1]*, *Karl Pauwels*[2], *Marc Van Hulle*[2] *and Tamás Roska*[1,3]**
[1]Pázmány Péter Catholic University, Faculty of Information Technology,
Prater utca 50/a, 1083 Budapest, Hungary
[2]Laboratorium voor Neuro- en Psychofysiologie, K.U.Leuven, Belgium
[3]MTA SZTAKI, Computer and Automation Research Institute,
Hungarian Academy of Sciences,
Kende u. 13-17, 1111 Budapest, Hungary

## ABSTRACT

The present work describes a bio-inspired approach designed to solve some tasks raised in the 'Bionic Eyeglass Project' [1], which aims to help the everyday life of blind or visually impaired people. The purpose of this approach is to provide a specific kind of information or to determine the region of interest ("ROI") in a low-resolution and unstable video flow recorded with a mobile phone by the visually impaired person. In the present paper we introduce a new stabilization method and three different tasks are resolved: firstly, locating LED (light-emitting diode) indicators, secondly, locating traffic signs, and thirdly, deciding whether there is any switched-on lamp in a room. The test database has been made out of real-life scenes. We provide detailed evaluation results referring to the execution of those tasks.

Our descriptive context refers to the recently modeled mammalian retina channel decomposition [2]. Using it we can avoid - at least partially - the classical difficulty that image processing algorithms nowadays face, namely that the intensity or color values of the same object largely depend on the actual lighting conditions. A further difficulty referring to the lamp-detection is that the solution has to be completely independent of the input's actual brightness. The method we introduce relies only on a single retina channel and achieves a very high accuracy: the ratio of the correct answers is around 99%. The other two tasks are to carry out an approximately real-time ROI-detection algorithm based solely on image information

---

[*] E-mail address: anna.lazar@gmail.com.

from an unstable low-resolution video-flow containing complex real-life scenes with unconstrained lighting conditions. The accuracy of the introduced methods is around 80%.
We also make use of a stabilization algorithm designed especially for this project. In order to yield the desired information, we process channel-data as well as saliency maps. The presented method can be useful in a variety of other application areas.

**Keywords:** Video flow stabilization, retina channel, CNN, Cellular Wave Computing, region of interest, saliency map

## 1. INTRODUCTION

Although an encouraging progress has been already achieved concerning retinal prostheses, the everyday usage of the related techniques still seems to be remote. Until then, and in many other situations, different methods should help the everyday life of the blind or visually impaired people. This paper describes a bio-inspired method aiming to locate those regions in the visual scene that, with a high probability, contain important information for visually impaired people – that is: to define the Region of Interest (ROI) in an unstable, low resolution video input. For this purpose, we also use the mammalian retina channel decomposition. After locating the regions that include the required information, according to the actual task, different pattern-detection or object recognition algorithms can be used. Similar situations arise at some other blind navigation tasks, in robotics, and other applications.

In this stage of the project, the input comes from a mobile phone's video camera in 176 x 144 pixel resolution, but the phone is now being extended by a Cellular Visual Microprocessor[*]. The diversity of interesting tasks as well as the construction of the required database has been compiled with the help of members of the 'Hungarian National Association of Blind and Visually Impaired People' [1]. In this paper we present efficient new algorithms for:

- Finding light sources (lamps) – this task (although it seems to be a trivial 'problem' for a person with normal vision), could prevent annoyance for visually impaired people, for example, by preventing the lamps to remain switched-on for weeks after a guest.
  Here, the most important criterion is that the solution has to be independent from the input's actual brightness, that is, the accuracy should be the same in the case of a sun-drenched and a dark room.
- Locating LED indicators (in real-life indoor and outdoor scenes)
- Finding traffic signs in real-life street scenes.

The main purpose of these two latter tasks are to realize a fast method that locates the areas which contain the traffic signs / LED indicators with high probability, on complex real-life outdoor scenes. Subsequently, a classifier algorithm has to analyze only the located ROIs instead of the whole input, which can fasten up the whole process significantly. The main difficulties derive from the instability of the by-default bad-resolution input, the unconstrained lighting conditions, and from the *variety* of the possible inputs.

---

[*] This visual microprocessor is the Q-Eye in the Eye-RIS system: www.anafocus.com

The algorithms' main functional components are: video stabilization, retina channel decomposition, (or "low-level feature extraction"), and saliency map generation.

A summarizing flow chart can be seen on figure 1.

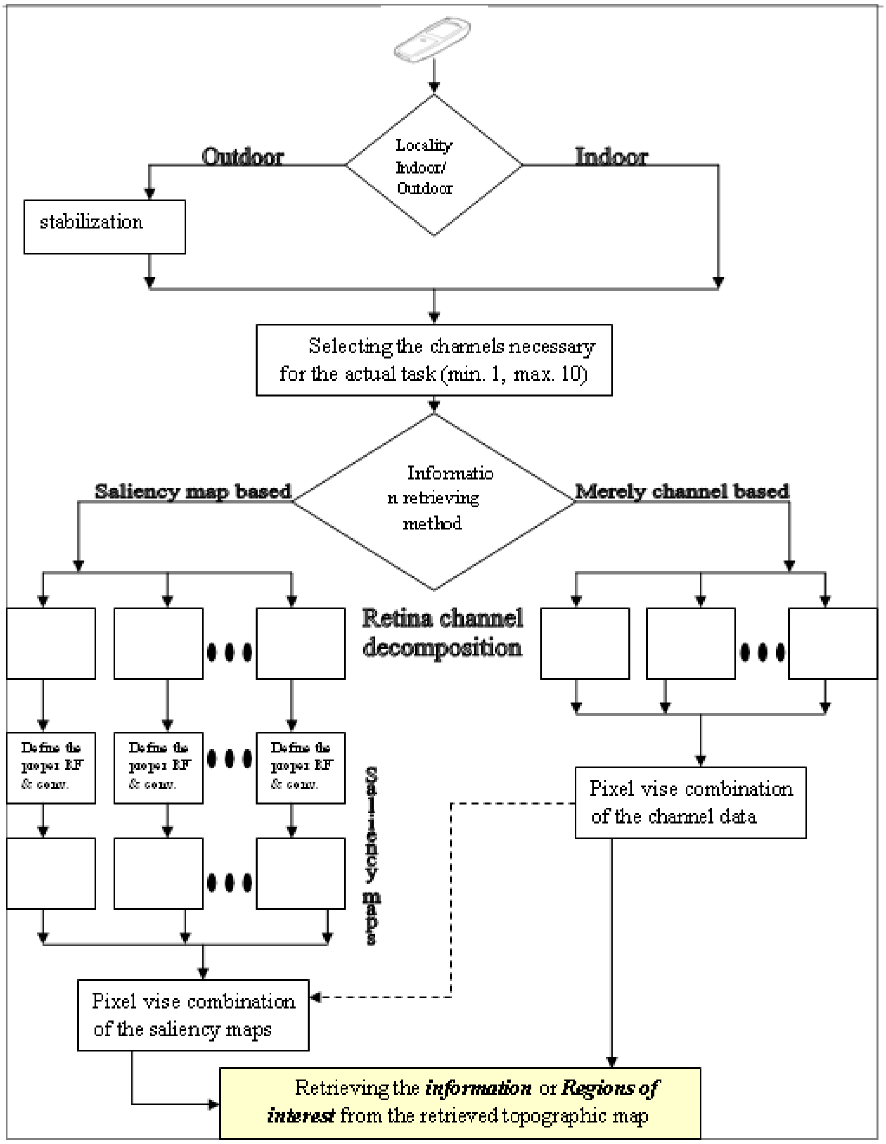
Locality Indoor/ Outdoor
Outdoor
Indoor
stabilization
Selecting the channels necessary for the actual task (min. 1, max. 10)
Information retrieving method
Saliency map based
Merely channel based
Retina channel decomposition
Define the proper RF & conv.
Define the proper RF & conv.
Define the proper RF & conv.
Saliency maps
Pixel vise combination of the channel data
Pixel vise combination of the saliency maps
Retrieving the *information* or *Regions of interest* from the retrieved topographic map

Figure 1. The flow chart of the proposed method. The input is a strongly unstable, low resolution video flow coming from a mobile phone's camera held by a visually impaired person. The output can be: Regions of interest (e.g. locations of LED indicators, traffic signs), or Specific information (e.g. is there any switched-on lamp).The dashed line shows an optional information combination step (raised in the task of locating traffic signs, where retina channel data and saliency map data had been combined, see section 2.3.1)

## 2. THE PROPOSED METHOD

Figure 1 summarizes the algorithm. The input of the *whole* process is an image flow taken by a mobile phone extended with a Cellular Visual Microprocessor, and the output consists of audio information for the person using the equipment. The present paper does not deal with the methodology of transformation of the demanded information into audio format, but with the problem of *locating* the demanded information within a video flow.

These steps are described in detail in the following sections.

### 2.1. Stabilizing the Input Frame

Image flows provided by a camera held by a blind walking person are usually extremely noisy and unstable, often accompanied by fast, unexpected camera motions. The recording equipment (camera) can be

- rotated
- shifted in the vertical and horizontal direction, and
- transported in the direction of motion.

Additionally, often the picture's main objects shift significantly from one frame to another, e.g. during turning around.

The goal of the image stabilization step is to keep the steady objects (e.g. buildings) in the same pixel positions, while the moving objects (for example the pedestrians) can change position.

It is useful to define the transformation-parameters between *adjacent* frames, instead of estimating the difference between the reference frame and the actual frame. In this manner, it is possible to trace bigger deformations throughout longer frame-series. Then, the calculated transformation 'inherits' from frame to frame, as follows:

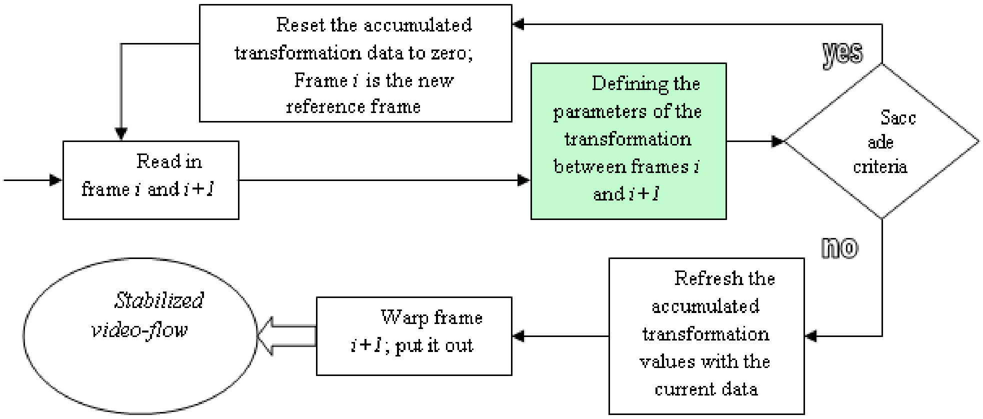
Reset the accumulated transformation data to zero; Frame i is the new reference frame
yes
Defining the parameters of the transformation between frames i and i+1
Sacc ade criteria
Read in frame i and i+1
no
Refresh the accumulated transformation values with the current data
Stabilized video-flow
Warp frame i+1; put it out

Figure 2. The flow chart diagram of the stabilization. The input (left hand side, top of the picture) is an unstable video-flow coming from a mobile phone's camera. The output of this algorithm is the stabilized video flow (left hand side, bottom of the picture; Details in section 2.2). The goal is to keep the steady objects (e.g. buildings) in the same pixel positions, while the moving objects (e.g. pedestrians) can change position.

If the actual reference frame is the $i^{th}$ one, then the $\boldsymbol{P}_{i+k,i}$ vector contains the transformation parameters between the actual frame $i+k$ and the reference frame $i$. In the next step, the vector $\mathbf{P}_{i+k+1,\ i+k}$ is calculated, which contains the transformation values between the actual adjacent frames: $i+k+1$ and $i+k$. Then $\boldsymbol{P}_{i+k+1,\,i} = \boldsymbol{P}_{i+k,\,i} \oplus \boldsymbol{P}_{i+k+1,\,i+k}$ will be updated, and will comprise of the differences accumulated throughout the $k+1$ frames that have been captured since the last reference-frame updating.

Figure 2 depicts the flow chart of the stabilization. (See also [3, 4]) The key element in it, is how the transformation parameters are defined (we highlighted this step with a bit darker shade on the diagram).

We have estimated the transformation parameters between frames $i$ and $i+1$ as follows:

Let $f$ denote the *image intensity function*, which is the intensity value at $x$-$y$ coordinate position at time $t$. [5] ( $f = f(x, y, t)$) Thus:

$$-\frac{\partial f}{\partial t} = \frac{\partial f}{\partial x}u + \frac{\partial f}{\partial y}v \tag{1}$$

where $\partial f/\partial x$ and $\partial f/\partial y$ are the spatial gradients in $x$ and $y$ directions, and $\partial f/\partial t$ is the time gradient. Since these quantities are measurable, using equation (1), $u$ and $v$ can be defined, which are the velocities in $x$ and $y$ directions, respectively. (The unit can be pixel/frame.) Since the frames are not only translated, $u$ and $v$ differ for every single pixel position. To estimate these, we have used an affine transformation model, which can handle translation, scaling, rotation and shear: [3]

$\begin{bmatrix} \mathrm{u} \\ \mathrm{v} \end{bmatrix} = \begin{bmatrix} \mathrm{a}_0 \\ \mathrm{b}_0 \end{bmatrix} + \begin{bmatrix} \mathrm{a}_1 & \mathrm{a}_2 \\ \mathrm{b}_1 & \mathrm{b}_2 \end{bmatrix} \begin{bmatrix} \mathrm{x} \\ \mathrm{y} \end{bmatrix}$, where $\begin{bmatrix} a_0 \\ b_0 \end{bmatrix}$ defines the translation in $x$ and $y$ directions, and $\begin{bmatrix} \mathrm{a}_1 & \mathrm{a}_2 \\ \mathrm{b}_1 & \mathrm{b}_2 \end{bmatrix}$ describes the scaling, rotation and shear.

Finally, for every frame, the following matrix-equation has to be solved, where the vector $\boldsymbol{P}$ contains the six parameters: $a_0$, $a_1$, $a_2$, $b_0$, $b_1$, $b_2$, which describes the transformation.

$$P = A^{+} \cdot (-I_t)$$

$\boldsymbol{A}$ and $\boldsymbol{I_t}$ contain the intensity gradients and the general coordinates, the sign ‘+’ denotes pseudo inverse. For the detailed definitions and derivations, see the Appendix.

## 2.2. Retinal Output Channels

This section describes the background and the usage of the retinal output channels. We use:

- Seven “spatio-temporal” channels (which are the ‘Transient’, Local Edge Detector, ‘Bistratified’, ‘Alpha’, ‘Beta’, ‘Delta’ and the ‘Polar’ channels) [6,2].
- Three color channels (which are the Intensity and the two color opposition channels): (“R” is the red value in the RGB system, “G” is the green, and “B” is the blue) [7]:
    - Red-Green opponent = R-G
    - Blue-Yellow opponent = B – (R + G) / 2
    - Intensity = 0.18*R + 0.81*G + 0.01*B

Systems designed to retrieve information of visual input often use some kind of “low level visual feature-extraction” before further processing. The main reason for this is that, otherwise, the appearance of the different objects bewilderingly depends on the illumination, perspective, scaling and other actual circumstances. That is, the same object can have completely different intensity- or color values according to some accidental conditions.

The mammalian nervous system also applies this ‘trick’: it dissolves the visual information simultaneously in approximately a dozen different specialized channels, each coding different low level features [8]. Their exact function is defined by certain ganglion-cell types [6]. These spatio-temporal channels arise in the retina and persist up to the high brain areas, while performing several processing steps.

Our model includes all the ten, biologically measured [6] and artificially modeled [2] channels. This means that we take into account three time-independent (one intensity and two color opposition channels) as well as seven “spatio-temporal” channels. Although some basics are known, the method specifying how the colors are being processed is mainly undiscovered. From the viewpoint of the realization, we have applied what is known by the present: the Intensity channel is calculated as: 0.18*R + 0.81*G + 0.01*B [7], the red-green opponent channel is the difference between the red-value and the green-value, while the blue-yellow is calculated like “blue – (red + green) / 2”, as described above.

The seven parallel pathways have the same design; they only differ in the parameters that determine their distinct spatio-temporal characteristics [6, 2, 11]. For these channels, a neuromorphic model has been created, based on Cellular Neural/Nonlinear Network (CNN) architecture [9, 10]. In this, the basic processing principles of the retina have been kept, but in a simplified form. We mention that choosing a CNN simulator has been plausible because of the striking similarity between the CNN structure and the living retina layers.

The exact retina channel model we have taken as a basis is detailed in [2].

Figure 3 shows a snapshot of the ten retina channels for a natural scene. Interesting to notice, that only half of the channels’ function is known, in the sense that the aim of the process of the remaining five channels could not be formulated explicitly, at least up to present. Thus: the Transient channel filters out everything that is in motion and eliminates all the steady parts [11], the Intensity channel codes the intensity, as its’ name presumes, the Blue-Yellow and the Red-Green are color opposition channels, and finally the ‘LED’ is for ‘Local Edge Detector’, whose role is to emphasize the edges. The function of the Bistratified, Polar, Alpha, Beta and Delta are unknown, they are primary named after the ganglion cells that code them.

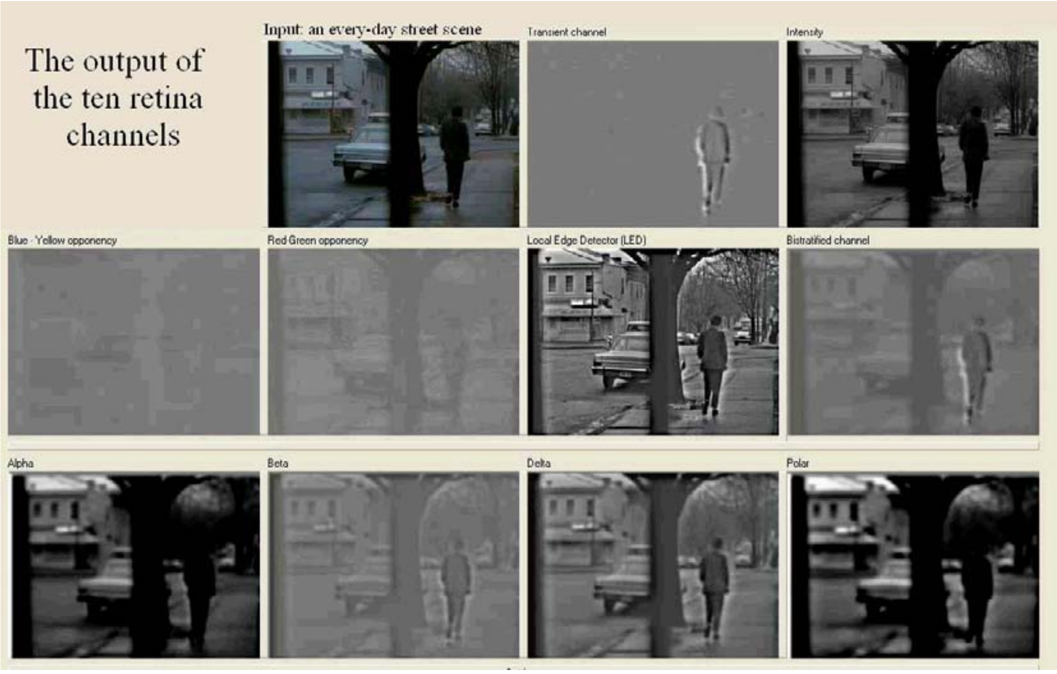

Figure. 3. An example for the ten retina channels. The input image (first picture) is processed by ten different pathways resulting in ten ganglion-cell types which form the ten retina channels [6]. The second picture in the first row (next to the input image) is the output of the “transient” channel which filters out the mobile parts of the visual scene and removes all the steady sections: at this moment the walking girl triggers the only response. Normally this is one of the ‘strongest’ channels. The last image in the first row depicts the output of the “intensity” channel. In the second row we can see the blue-yellow- and the red-green contrast channels (these are the color opposition channels), the LED (local edge detector) and the “bistratified” channels. The functions of the channels depicted in the third row (alpha-, beta-, delta- and polar) are unknown at present (in the sense that we can not ‘phrase’ their function), as well as the bistratified channel’s task. Note that many of these channels can not be represented by still images or still inputs.

## 2.3. Receptive Fields and Saliency Maps for the Depiction of Regions of Interest

Saliency maps are two-dimensional, scalar maps of the physical world, whose activity topographically represent visual conspicuity. In most attentional models, every channel creates its’ own saliency map, which is feature-dependent (the feature refers to what the given channel codes). Those saliency maps are afterwards usually unified into a final “master” map, which is thus feature-independent [12]. This process can be used effectively in different real applications as well.

In nature, saliency is “calculated” via receptive fields (RF), in which neurons are organized into concentric circles: a central and a peripheral part, which respond antagonistically. If the central part of an ON-center - OFF surrounding RF is stimulated with light, the RF’s response will increase, while if the light falls onto the surrounding part, then the response will decrease. If both parts are exposed to light, then there will be no change in the ganglion cells' response [7].

Practically, from an engineering viewpoint, a saliency map is a retina channel output (or the result of the 'low level visual feature extraction') convolved with a receptive field. RFs can be represented in matrix form.

As an example of the used receptive fields, we show how we have determined the optimal RF in the task of finding traffic signs. The outcome is depicted on figure 4.

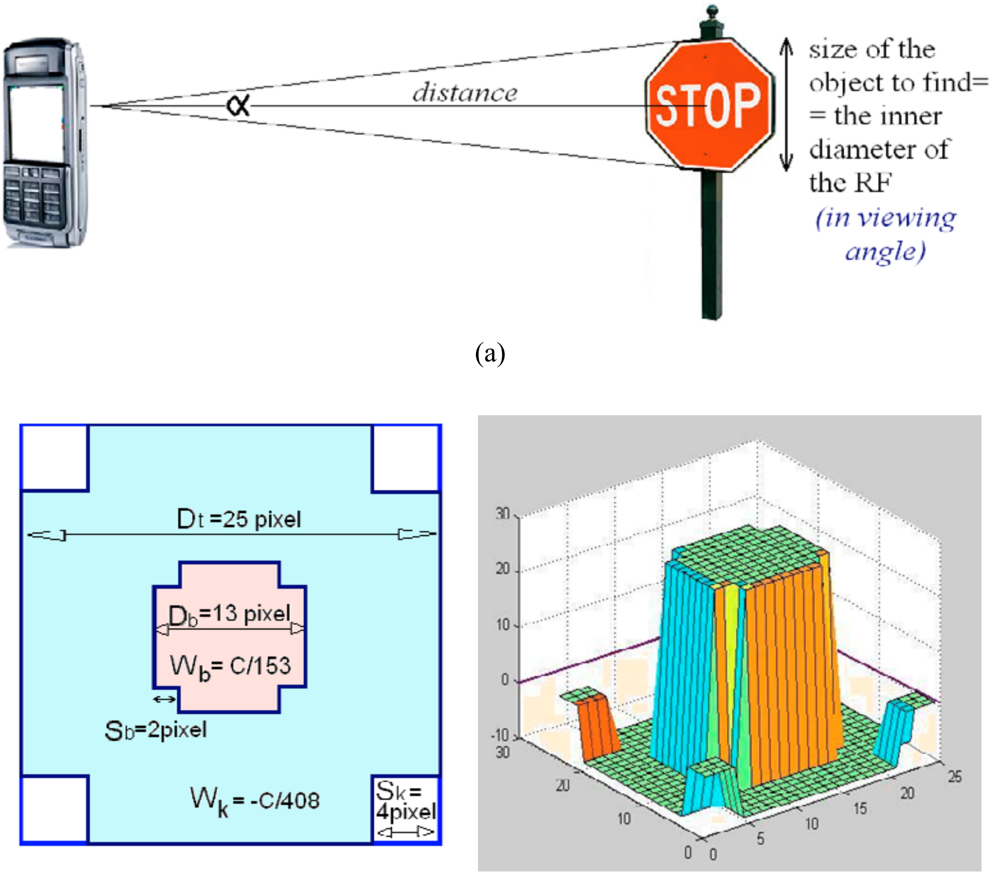

(a)

(b) (c)

Figure 4. Receptive field adjusted for the task of finding traffic signs. Figure *a)*: the inner diameter of the receptive field and the size of the searched object should be the same in viewing angle. This criterion helps to determine the size of the RF. *b)* and *c)*: the resultant; On *c)* the height and the depth are proportional to the weights, which have – due to the antagonistical behaviour of the RF's inner and outer part – opposite sign. The zero level is emphasized with purple line.

- The *size* of the receptive field is determined as follows:
    - from one hand, the viewing-angle of the mobile phone is ~45°, which occupies 176 pixels. This means, that roughly 3.9 pixels cover 1°.

  - from the other hand, on the video flow, the size of an object depends on its distance. Namely, its’ size in viewing angle is $\mathrm{tg}\,{}^{\alpha}\!/_{2} = \frac{\mathrm{radius\_of\_the\_object}}{\mathrm{dis}\tan\mathrm{ce}}$ (figure 4 a). So, if we want to set the sensing-distance of a 45 cm diameter (0.225 m radius) traffic sign for ~7-8 m, then it covers a bit more than 3.3°. Thus, the optimal inner diameter of the receptive field is 13 pixels. (figure ***4 (a)*** and (***b)*** )
  - The outer size of the RF has been adjusted according to ‘real’ RFs, in which the inner part covers around the half of the whole RF in viewing angle.

- The *values* of the matrix have to satisfy the criteria of

  - giving maximal response if antagonistic stimuli hit the RF’s inner and outer area
  - giving no answer if the input image-region contains equal values – that is, in case of uniform lighting.

  The maximal value is arbitrary, since it is only a constant multiplier (“C” on figure ***4 (b)***).

### 2.3.1. Locating Traffic Signs

The main purpose of the present algorithm is to realize a fast method locating the areas which contain traffic signs with high probability, on complex real-life outdoor scenes. The main difficulties derive from the instability of the input – which has by default bad resolution – and from the fact that the lighting circumstances can vary on a wide range.

Traffic signs – due to their color and shape design - can effectively be detected by circle-shaped receptive fields on color opposition channels. For solving this task, we have used the RF determined in the previous section (figure 4 b) on the Blue-Yellow color opposition channel. According to the experiments, rooftops and building walls often effectuate salient areas with the blue sky, something that can lead to false results. In order to avoid these errors, we have applied the Delta channel’s data as well: since it gives a vivid response on light sources, only those regions have been taken into account, where this channel has given a smaller response than a given threshold.

Figure 5 shows some typical frames from the test database. The distortions of the input frames are due to the stabilization method. Important to note, that this method does not exploit any additional information or knowledge (for example, that traffic signs are primarily expected in a given height), thus with the guidance of the equipment the results can be further improved. According to the test results, the main error sources have been: from one hand, *shadow*, which leads to false negative results because of the loss of color information (figure 5 c), and from other hand, objects with ‘appropriate’ size and vivid colors, which lead to false positive results (figure 5 d). Important to note, that – because of the lack of a commonly accepted test database for these problems - the evaluated information significantly depends on the test database. Tables 1 and 2 show our test results.

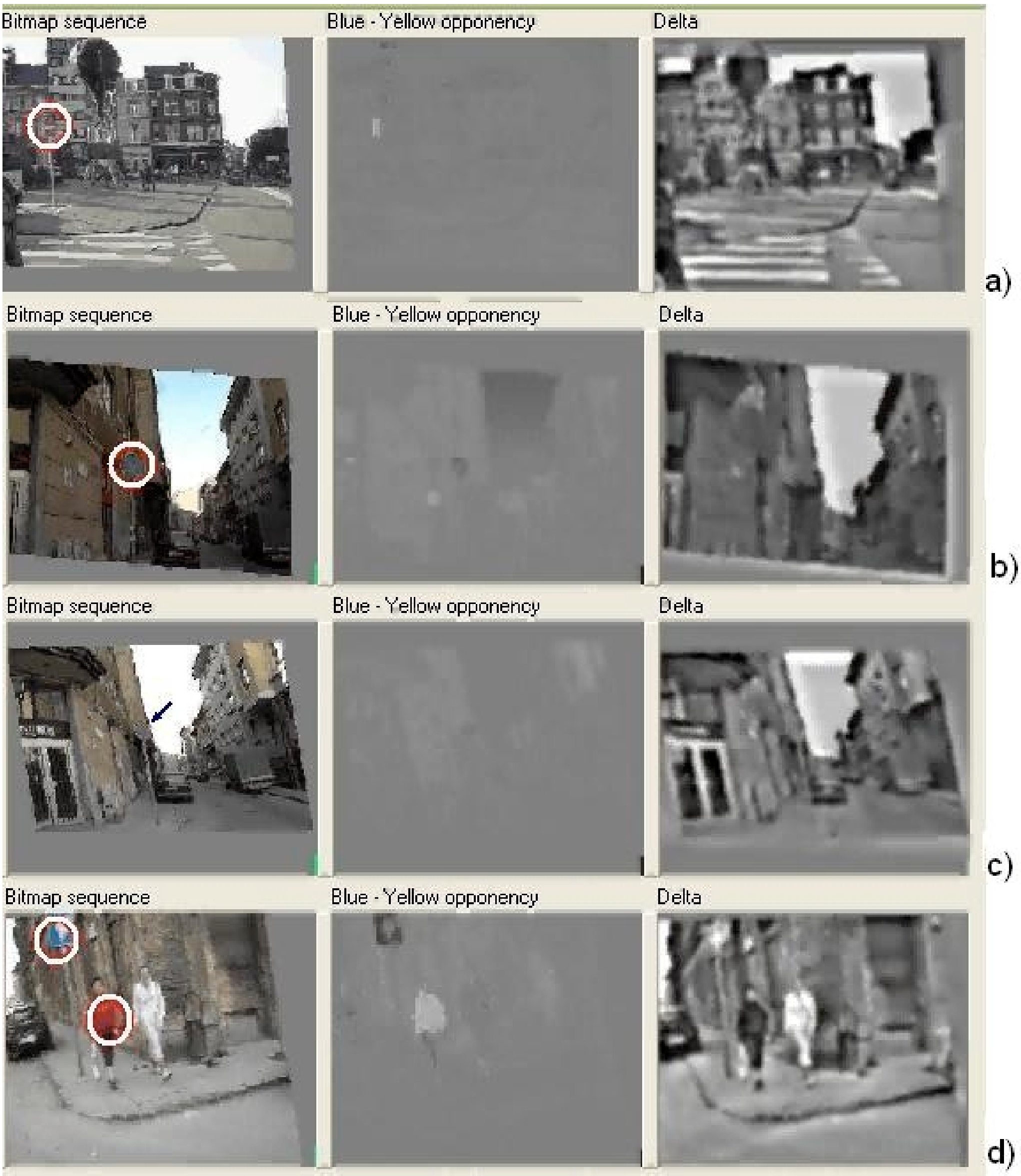

Figure 5. Some typical frames from the test database we have used to evaluate the task aiming to locate traffic signs. In all the four rows, the left-most image is a frame from the input video flow with the areas identified as traffic signs (white circles). The other two images in each row are the corresponding outputs of the used channels: the middle ones are the Blue-Yellow color opposition channels' output and the right ones are the response of the Delta channel. a) and b) are examples for correct results. c) The prime cause of the false negative answers (when the sign is not located) was due to the loss of the color information, which happened when the sign was in shadow. On figure c) the blue arrow points to a traffic sign being in shadow. (These signs are difficult to see even with "pure eyes") From closer they can be identified: b) is the same as c) from a few meters nearer). d) depicts the typical reason for false positive results: vivid colors with the 'appropriate size'. The input frames are distorted because of the stabilization. Table 1 and 2 indicate the test results.

**Table 1. The results for the task: "Locating traffic signs". "Correct" answer means that EITHER the input frame has no traffic signs on it *and* there are no located areas on the output either, OR, there is at least one sign on the input *and* there are located areas on the output as well. The test video set included 916 real-life frames from different locations and with different lighting conditions**

| (frame percentage) | Correct answer | False answer |
|---|---|---|
| There *is* traffic sign on the input video frame (total 502 frames) | **73.7%**<br>(370 frames out of 502 frames) | **26.3%**<br>(132 frames out of 502 frames) |
| There is *no* traffic sign on the input video frame (total 414 frames) | **95.4%**<br>(395 frames out of 414 frames) | **4.6%**<br>(19 frames out of 414 frames) |
| Total (916 frames) | **83.5%**<br>(765 frames out of 916 frames) | **16.5%**<br>(151 frames out of 916 frames) |

Since Table 1 does not indicate the *accuracy* of the located areas ("ROIs"), we provide another table (Table 2) showing these results.

**Table 2. The accuracy of the identified locations. Only those frames are included, where there was at least one located area. A ROI is "correct" if there is a traffic sign at that very location, and "incorrect" otherwise. Thus, an answer belonging to one single frame can contain both correct and incorrect locations (see for example figure 5 d)**

| | Correctly identified locations | Incorrectly identified locations |
|---|---|---|
| Altogether 490 located areas | **73.7%**<br>(361 ROIs out of 490) | **26.3%**<br>(129ROIs out of 490) |

### 2.3.3. Finding Light Sources

A trivial matter for people with normal vision but often a hard task for the blind ones, is to detect whether the lamps are switched on or switched off - for example after guests. According to our consultant from the "Hungarian National Association of Blind and Visually Impaired People" – with whom the tasks has been defined together – an algorithm solving this task could prevent much annoyance.

Here, the most important criterion is that the solution has to be independent of the input's actual brightness, that is, its' reliability should be the same in the case of a sun-drenched room and a dark cell.

The solution for this subtask differs from the former one in the sense that here we rely merely on retina channel information – instead of saliency maps. One channel proved to be enough for this task, namely the "Polar" channel, which seems to respond on light sources [2, 6] (figure 6). It gives strong reaction on primary light sources, both for natural (sun) and artificial ones (lamps) – and, to reflecting surfaces as well (mirrors, glass-tables, etc.) which cause a small error rate. Still, the accuracy this channel enables is very high: the ratio of the correct answers reaches 98-99% (see Table 3).

Since this channel responds on natural light sources as well (Figure 6 c), the user is supposed to know where the window is, but this is not a real restriction in every-day practice. Otherwise, precise knowledge about the location of the lamp(s) is not a demand, since the visual environment can be scanned.

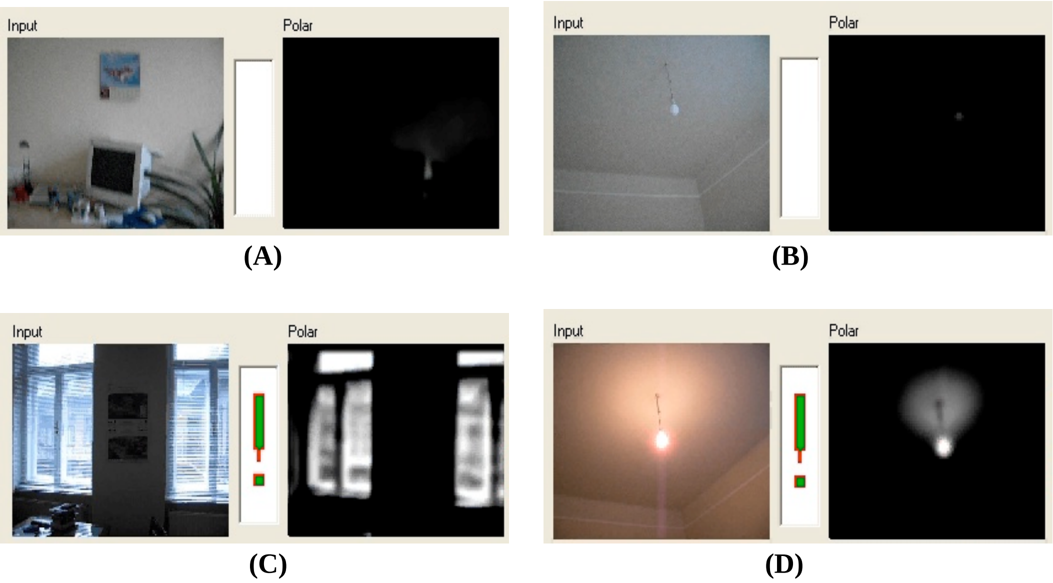

**(A)** **(B)**

**(C)** **(D)**

Figure 6. The “Polar” channel responds on light sources, both for natural ***(c)*** and for artificial ones ***(d)***. The pictures are taken from the test video set. All the four figures show the input on the left, and the corresponding output of the Polar channel, on the right. ***(a)*** and ***(b)***: a part of a bright room in day light; the Polar channel is basically silent. ***(d)*** had been recorded a few seconds after ***(b)***: the lamp is switched on, the Polar channel is excited. (The exclamation mark between the two channels indicates that the answer is: “there is light source on the input”.) The Polar channel enables very high reliability for this task (see table).

**Table 3. The test results of the algorithm aiming to detect primary light sources, independently from the brightness of the input, or in other words, from the intensity values. The process is based on one of the mammalian retina channels (namely the “Polar” channel [2]), which reacts on light sources. The small error is due to reflecting surfaces (a glass table in our case). These values are based on the evaluation of test videos made on shiny rooms, including 1563 frames together**

| | **Correct answer** | **False answer** |
|---|---|---|
| There *is* light source on the input video frame | 98.8% | 1.2% |
| There is *no* light source on the input video frame | 99.38% | 0.62% |

According to the experiments, the Polar channel saturates (gives maximal response) on those areas where primary light sources are present, and give no answer elsewhere (Figure 6). It follows that the accuracy of the algorithm is completely independent of the quality of the input video-flow, and also, it does not depend on the *brightness* either. The results depicted in table 3 are based on test videos made in sunshiny rooms.

### 2.3.4. Locating LED Indicators

In many public buildings, offices and transport vehicles basic information is transmitted by LED indicators. The aim of this method again is to carry out a fast solution that localizes the areas that contain the indicators in question with high probability, on various indoor and outdoor real-life scenes. The main difficulty – except the bad resolution and the instability – originates from the *variety* of the possible inputs.

**Table 4. The results for the task: "finding LED indicators". The values are based on the evaluation of 1207 frames. First row first column is the correct positive (96,6%), second row first column is the correct negative result (41%). The test database included complex real-life scenes with different lighting conditions, colored and reflecting areas and colored lamps. As it turned out, the algorithm in *not* sensitive to the quality of the input (resolution), to the lighting conditions and colors, either to the reflecting areas, but it *is* sensitive to colored lamps – which the few frames (total 256) that did not contain LED happened to teemed in. The bad results are due to these lamps (Figure 8 b). In the third row ("Total"), all the frames are counted, that is, "correct answer" indicates the percentage of the frames where either the input included LED indicator (one or more) and the output was at least one located area, or the input did not include LED indicator and the output had no located areas. Accordingly, the line "False" indicates the rest. The percentage means *frame* percentage**

| | Correct answer | False answer |
|---|---|---|
| There *is* LED indicator on the input video frame (total 951 frames) | **96.6%**<br>(919 frames out of 951 frames) | **3.4%**<br>(32 frames out of 951 frames) |
| There is *no* LED indicator on the input video frame (total 256 frames) | **41%**<br>(105 frames out of 256 frames) | **59%**<br>(151 frames out of 256 frames) |
| Total (1207 frames) | **84.83%**<br>(1024 frames out of 1207 frames) | **15.17%**<br>(183 frames out of 1207 frames) |

The test video set we have used includes multifarious scenes including different public and private places. Some of these can be seen on Figure 7 and 9. On Figure 7 we have also visualized those three channels that we have used for solving this task. These are the two color-opposition channels (blue-yellow and red-green) and the Delta channel. The function of the Delta channel has not yet been precisely formulated up to present (see above), but according to the observations, it gives significant response for small or fragile light sources as well (similarly to strong light sources).

From here, the selection algorithm is the following: if on a given location at least one of the two color opposition channels gave bigger response than a certain threshold, then a “fitness – value” would be calculated, being directly proportional to the three channel-data at the given point. Afterwards these values would be arranged into descending order, and the first few locations would be the *solution* for the given frame, that is *regions* that the algorithm defines as presumptive LED locations.

Table 4 shows the results we have measured on this task. The results are based on the evaluation of 1207 frames. We have tested our method on real-life scenes, taken from different areas with various lighting conditions, reflecting areas, light sources, colors, etc. As it turned out, the algorithm is *not* sensitive to the quality of the input (e.g. resolution), to the lighting conditions or colors, either to the reflecting areas, but it *is* sensitive to colored lamps – which is not surprising since LEDs basically *are* small colored lamps, until no further object or pattern recognition algorithm is used.

Since the input frame may contain more than one LED indicator, and also, the output can be more than one located region (see Figure 7 and 8), the evaluation of this task – similarly to the task of finding traffic signs – is not as straightforward as in the previous task, where the answer was binary (“there *IS* light source on the input”/“there is *NO* light source on the input”). Thus we give another table as well, which indicates the correctness of the locations which the algorithm has given as solutions. In contrast with table 4, table 5 depicts *ROI percentage* instead of frame percentage, that is, the ratio of the correct and false located areas. Only those frames are included, where there was at least one located area.

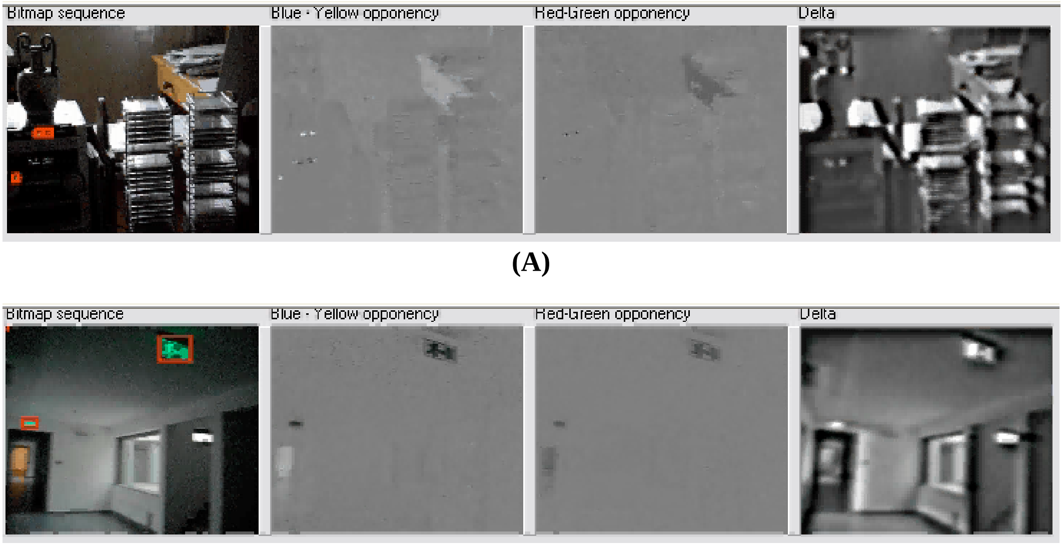

**(A)**

**(B)**

Figure 7. Two frames of the test database for the task “finding LED indicators”. The left-most pictures in both lines show the input with the identified locations on them. The other three pictures belong to those channels, whose data has been used in the execution of the task. These are the red-green and blue-yellow color opposition channels and the Delta channel. *(a)* LEDs belonging to a hi-fi set in a room. The various reflecting surfaces do not confuse the algorithm. *(b)* corridors in the university.

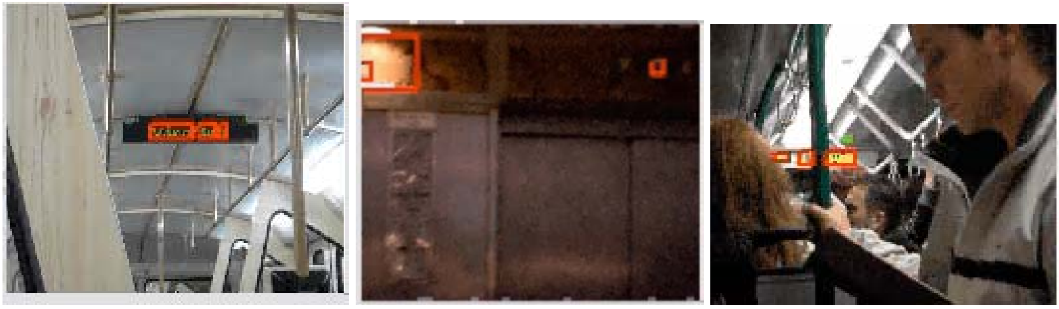

**(A)** **(B)** **(C)**

Figure 8. Some frames from the videos that we have used for testing the algorithm that finds LED indicators. *a)* rack-railway from the inside (these indicators show the name of the next stop and the actual time) *b)* a colored decorating lamp (left) and a LED indicator (right) showing the floor-number on a lift-panel in a department store. *c)* tram interior.

**Table 5. The accuracy of the identified locations. Only those frames are included, where there was at least one located area. A ROI is "correct" if there were a LED indicator at that very location, and "incorrect" otherwise. Thus, an answer belonging to one single frame can contain both correct and incorrect locations (see for example Figure 8 b, where the marking of the colored lamp is incorrect (left hand side, top of the picture), while the sign on the elevator panel is correct – right hand side, top of the picture)**

| | **Correctly identified locations** | **Incorrectly identified locations** |
|---|---|---|
| Altogether 2075 located areas | **81.36%**<br>(1688 ROIs out of 2075) | **18.64%**<br>(387 ROIs out of 2075) |

## 4. FUTURE TASKS

- During walking, a camera held in a hand, makes a quasi-periodic motion. Most of the people have their own way of "swinging" the phone, thus the transformation-parameters (vertical/horizontal shifts, the angle of the rotation, etc.) characterizes the certain users. These quasi-periodic parameter values could be learned during a certain amount of frames (and could even be adjusted during the entire usage), thus they become predictable for a given user. In this manner, by taking the predicted transformation values into account, the quality of the stabilization can be improved.
- The model described in this paper is *attentional* in the sense that it locates regions on the input where something important appears. Naturally arises the possibility of applying a more elaborated pattern or object recognition algorithm onto the selected area.
- Many possibilities lie in the retina channel decomposition. Thus, the further investigation of the individual channels can lead to a promising basis for different scene analyzer and object recognition algorithms. For example, some time-dependent channel (primarily the Transient, Beta and the Bistratified channels) seem to play an

important role in separating the different objects from each other – although, this area needs further investigations.

- In a more elaborated version, the threshold values can be adjusted by a learning algorithm, and also could be adaptive according to the different scenes and tasks.

## Acknowledgements

This work has been supported by the National R&D Agency of Hungary (HKTH) via the RET initiative, by the National Research Found (OTKA) and the Faculty of Information Technology of the Pazmany University..

### Reviewed by

Dr. György Cserey, Pázmány Péter Catholic University, Faculty of Information Technology, Prater utca 50/a, 1083 Budapest, Hungary

## APPENDIX

## The Normal Flow Algorithm

To estimate the instantaneous velocity field we model the motion image by a continuous variation of image intensity as a function of position and time. The intensity value on position (*x, y*) at time *t* is described by the *f(x, y, t)* intensity function.

If we expand this function in a Taylor series we get:

$$f(x+dx, y+dy, t+dt) = f(x,y,t) + \frac{\partial f}{\partial x}dx + \frac{\partial f}{\partial y}dy + \frac{\partial f}{\partial t}dt + HT \qquad \text{(A1)}$$

where ‘HT’ is for higher-order terms, which are usually ignored.

The crucial observation that is exploited, is that if the image at some time *t+dt* is a result of the original image at time *t* being moved translationally by *dx* and *dy*, then

$$f(x+dx, y+dy, t+dt) = f(x,y,t) \qquad \text{(A2)}$$

Thus, from equations (A1) and (A2) we get:

$$0 = \frac{\partial f}{\partial x}dx + \frac{\partial f}{\partial y}dy + \frac{\partial f}{\partial t}dt, \quad \text{or, in other form:} \quad -\frac{\partial f}{\partial t} = \frac{\partial f}{\partial x}\frac{dx}{dt} + \frac{\partial f}{\partial y}\frac{dy}{dt} \qquad \text{(A3)}$$

$\frac{\partial f}{\partial t}$, $\frac{\partial f}{\partial x}$, and $\frac{\partial f}{\partial y}$ are measurable quantities, while $\frac{dx}{dt}$ and $\frac{dy}{dt}$ are the quested values, namely the velocity in *x* and *y* directions.

Using the $\frac{dx}{dt} = u$ and $\frac{dy}{dt} = v$ notation, we get $-\frac{\partial f}{\partial t} = \frac{\partial f}{\partial x}u + \frac{\partial f}{\partial y}v$, (A4)

or, equivantly, $-\frac{\partial f}{\partial t} = \nabla f \cdot u$,

where $\nabla f$ is the spatial gradient of the image and $\boldsymbol{u}=(u,v)$ is the velocity vector.

## The Calculation Steps

- *Measured values*: $I_x(=\frac{\partial f}{\partial x})$, $I_y(=\frac{\partial f}{\partial y})$, and $I_t(=\frac{\partial f}{\partial t})$, the intensity gradients

- *Calculated values (the estimations)*: $u(=\frac{dx}{dt})$ and $v(=\frac{dy}{dt})$

With these notations (A4) will be, for every pixel: $I_x u + I_y v + I_t = 0$ (A5)

## The Measured Values

The $I_x$, $I_y$ *spatial gradients* can be determined with a convolution, where the kernel is the [-1 8 0 -8 1] / 12 vector, which is a commonly used estimation in the literature [13]. (This kernel is applyed on the Gauss-filtered image, that is, we use the $\begin{bmatrix} \frac{1}{16} & \frac{2}{16} & \frac{1}{16} \\ \frac{2}{16} & \frac{4}{16} & \frac{2}{16} \\ \frac{1}{16} & \frac{2}{16} & \frac{1}{16} \end{bmatrix}$ as “A” template, accoring to the CNN terminology.)

The $I_t$ *time gradient* is simply the difference between the two Gauss-filtered images.

(As it follows from the above process, these values are defined for each and every pixels, so $I_x$ is not a scalar, but a matrix, and $I_y$, $I_t$ similar.)

## Defining the Quested Paramteres

For *mapping function*, we choose a linear affine transformation, which can handle shifts in *x* and *y* directions, scaling, rotation and shear, as next:

$$u = a_0 + a_1 x + a_2 y \qquad \text{(A6)}$$

$$v = b_0 + b_1 x + b_2 y$$

where $a_0$, $a_1$, $a_2$, $b_0$, $b_1$ and $b_2$ are the parameters of the transformation, which we want to determine. In the matrix-form of (A6), the meaning of these parameters can be followed better:

$$\begin{bmatrix} u \\ v \end{bmatrix} = \begin{bmatrix} a_0 \\ b_0 \end{bmatrix} + \begin{bmatrix} a_1 & a_2 \\ b_1 & b_b \end{bmatrix} \begin{bmatrix} x \\ y \end{bmatrix} \tag{A7}$$

In this equation $\begin{bmatrix} a_0 \\ b_0 \end{bmatrix}$ defines the translation in $x$ and $y$ directions, while $\begin{bmatrix} a_1 & a_2 \\ b_1 & b_b \end{bmatrix}$ describes the scaling, rotation and shear.

Thus, from (A5) and (A6), for every pixel we get:

$$(a_0 + a_1 x + a_2 y) I_x + (b_0 + b_1 x + b_2 y) I_y + I_t = 0 \tag{A8}$$

which will be

$$\begin{bmatrix} I_x^{(1)} & I_x x^{(1)} & I_x y^{(1)} & I_y^{(1)} & I_y x^{(1)} & I_y y^{(1)} \\ I_x^{(2)} & I_x x^{(2)} & I_x y^{(2)} & I_y^{(2)} & I_y x^{(2)} & I_y y^{(2)} \\ & & . & . & . & \\ I_x^{(k)} & I_x x^{(k)} & I_x y^{(k)} & I_y^{(k)} & I_y x^{(k)} & I_y y^{(k)} \end{bmatrix} \begin{bmatrix} a_0 \\ a_1 \\ a_2 \\ b_0 \\ b_1 \\ b_2 \end{bmatrix} = - \begin{bmatrix} I_t^{(1)} \\ I_t^{(2)} \\ \dots \\ I_t^{(k)} \end{bmatrix} \tag{A9}$$

where $k$ (the number of rows) is the number of the pixels.

With the notations:

$$A = \begin{bmatrix} I_x^{(1)} & I_x x^{(1)} & I_x y^{(1)} & I_y^{(1)} & I_y x^{(1)} & I_y y^{(1)} \\ I_x^{(2)} & I_x x^{(2)} & I_x y^{(2)} & I_y^{(2)} & I_y x^{(2)} & I_y y^{(2)} \\ & & . & . & . & \\ I_x^{(k)} & I_x x^{(k)} & I_x y^{(k)} & I_y^{(k)} & I_y x^{(k)} & I_y y^{(k)} \end{bmatrix},$$

and

$$P = \begin{bmatrix} a_0 \\ a_1 \\ a_2 \\ b_0 \\ b_1 \\ b_2 \end{bmatrix}, \text{ we get}$$

$$A \cdot P = -I_t \quad \text{, from where } P = A^+ \cdot (-I_t) \qquad \text{(A10)}$$

where '+' denotes pseudo-inverse, and the *P* vector contains the transformation-parameters, which we were looking for.

## REFERENCES

[1] Roska, T., Karacs, K., Wagner, R., Lazar, A., Balya, D., and Szuhaj, M.: Bionic Eyeglass: an audio guide for visually impared. *Proceedings of the 1st Biomedical Circuits and Systems Conference*, London, pp. 190-193 (2006)

[2] Balya, D., Roska, B., Roska. T.and Werblin, F. S.: A CNN framework for Modeling Parallel Processing in a Mammalian Retina. *Int. J. on Circ. Theory and Appl*. **30**, 363-393 (2002).

[3] Zitova, B ., and Flusser, J.: Image registration: a survey. *Image and Vision Comp*. **21**, 977-1000 (2003).

[4] Otte, M., and Nagel, H. H.:. Optical flow estimation: Advances and comparisons, *Computer Vision*, ECCV-94, 800, 51-60, (1994).

[5] Horn, B., and Schunck B.: Determining optical flow. *Artificial Intelligence*, **17**, 185-204, (1981).

[6] Roska B., and Werblin, F. S.: Vertical interactions across ten parallel, stacked representations in the mammalian retina, *Nature*, **410**, 583-587 (2001).

[7] Kandel, E. R., Schwartz, J. H. and Thomas, M. J.: *Principles of Neural Science*, McGraw-Hill / Appleton&Lange, 3rd edition, New York (1996).

[8] Masland, R. H.: The fundamental plan of the retina, *Nat. Neuroscience*, **4**, 877-886 (2001).

[9] Chua, L. O., and Roska, T.: *Cellular Neural Networks and Visual Computing*, Cambridge University Press, Cambridge (2002).

[10] Werblin, F. S., Roska, T., and Chua, L. O.: The analogic cellular neural network as a bionic eye, *Int. J. of Circuit Theory and Applications*, **23**, 541-569 (1995).

[11] Lazar, A. K., Wagner, R., Balya, D., and Roska, T.: Functional representations of retina channels via the RefineC retina simulator, *Paper presented at the 8th IEEE International Biannual Workshop on Cellular Neural Networks and their Applications*, Budapest (2004)

[12] Itti, L., and Koch, Ch: Computational modelling of visual attention. *Nat. Neuroscience*. **2,** 1-10 (2001).

[13] Barron, J.L., Fleet, D.J., and Beauchemin, S.: Performance of optical flow techniques. *International Journal of Computer Vision*, **12**(1) 43-77 (1994).

In: Integrated Circuits, Photodiodes…
Editors: R. McIntire and P. Donnell, pp. 115-159
ISBN: 978-1-60692-660-4
© 2009 Nova Science Publishers, Inc.

*Chapter 5*

# PHOTOCURRENT STUDY OF THE TRANSPORT MECHANISM IN MOLECULAR SELF-ASSEMBLING FIELD EFFECT TRANSISTORS

***Andrei V. Pakoulev*[a]*, Dmitry Zaslavsky*[b] *and Vladimir Burtman*[c*]**
[a]Department of Chemistry, University of Wisconsin-Madison, 1101 University Ave., Madison, WI 53706-1322, USA
[b]School of Chemical Sciences, University of Illinois at Urbana-Champaign, 106 Noyes Lab, 505 S. Mathews, Urbana, IL 61801, USA
[c]University of Utah, Department of Geology and Geophysics, 115 So. 1460 E. Rm 383, Salt Lake City, Utah 84112-0830, USA

## ABSTRACT

This chapter focuses on the intrinsic charge transport in organic field-effect transistors (OFETs) based on self-assembled monolayers (SAMs) and on the nature of transport in organic systems, in which surface and bulk properties are undistinguishable due to scale of consistent materials. Recently developed SAM-OFETs are characterized by photovoltaic measurements. The dynamics of charge transport are determined and used to clarify a transport mechanism. Taken together, these SAM devices provide a unique tool to study the fundamentals of polaronic transport on organic surfaces and to discuss the SAM OFET performance. An outline is presented of the outstanding problems that are now becoming experimentally reachable owing to the development of SAM-OFETs. Vapor phase molecular self-assembly of 1,4,5,8-Naphthalene-tetracarboxylic diphenylimide (NTCDI) having a rich $\pi$-stacking charge delivery system is used to enhance the performance of molecular field-effect devices. Charge mobility in SAM-OFET could achieve values of more than 30 $cm^2 V^{-1} s^{-1}$. The dynamics of charge transport in NTCDI-derived SAM-OFETs were probed using time-resolved measurements in an NTCDI-derived photovoltaic cell device. Time-resolved photovoltaic studies allow us to separate the charge annihilation kinetics in the conductive NTCDI channel from the overall charge kinetic in a SAM-OFET device. It has been demonstrated that tuning of the type of conductivity in NTCDI SAM-OFET devices is possible by changing Si substrate doping. In addition, the possibility of measuring transport in

---

[*] E-mail address: vlad.burtman@utah.edu

highly ordered SAM structures shines light on the polaron charge transfer in organic materials. Our study proposes that a cation-radical exchange (redox) mechanism is the major transport mechanism in SAM nanodevices. The role and contribution of the transport through delocalized states of redox active surface molecular aggregates of NTCDI are exposed and investigated in this chapter.

# INTRODUCTION

## 1. OFETs: Achievements vs. Problems

The invention of an organic donor-acceptor structural analog of a silicon p-n junction in 1974 [1] marked the beginning of the intensive research in the field of molecular electronic devices. As a part of the semiconductor research area, this field has traditionally been closely related to applications, and is unique in the synergy between device development and fundamental science. The emergence of new approaches for molecular engineering is a vital requirement for progress in molecular electronics and should eventually lead to molecular devices with pre-designed properties that may compete with silicon technologies, especially due to the small size involved. In the last 10 years a number of different experimental strategies have been used to fabricate organic field effect transistors (OFETs) and to study electron transport in these devices. Despite the very impressive results in device fabrication and initial insight into device transport, the new field also brought many open questions [2, 3]. One of the most complete analyses of this field could be found in a review by Frisbie et al. [4]. In the current chapter we will focus on kinetic studies in OFET structures with a pre-defined epitaxial order and on the development of adequate analytical tools to analyze charge transport in these structures.

A lack of basic understanding of structure-property relationships in OFET materials (and in organic solids in general) results in a knowledge gap that impedes rational efforts to design organic semiconductors with further enhancements in electrical performance [4]. One of the major obstacles for achieving efficient OFET is the low charge mobility in most organic materials. This is an acute problem, since carrier mobilities in disordered organic semiconductor films are several orders of magnitude smaller than in inorganic semiconductors. In contrast, carrier mobility in organics could be dramatically enhanced in ordered structures, such as spontaneously ordered regio-regular polythiophene [RR-P3HT] films. However, the inherent problem of such ordered systems is the interchain coupling. The charge-transfer probability between charged polarons and bipolarons belonging to neighboring chains [5], along with high electron-phonon coupling and the Peierls transition, leads to charge trapping [6]. The strong coupling could result in low mobility and even induce pseudo-gaps [7]. In addition, disordered thin films of small organic-molecule-based electronic devices have considerable charge quenching due to carrier trapping at defects, and charge recombination at grain boundaries and interfaces that result in low electron mobility. The scope of questions about SAM-OFET systems provides a host of other unanswered issues, inherent in traditional OFET technology, including the following: What is the role of order-disorder interplay in search for good mobilities? In particular, how is crystalline or partially crystalline ordering involved in the transport mechanism in organic solids? What is an impact of the thin film technology on device properties [4]? What are the structural and electronic factors that facilitate or impede transport in organic semiconductor films? Are there particular molecular structures and crystal packing motifs that are especially favorable for transport? What is the role of film quality, defects and grain boundaries? *Most of these unanswered questions are a direct consequence of the lack of basic knowledge in transport mechanisms in organic semiconductors.*

The other challenge in OFET fabrication is preparation of an efficient n-type conductive channel. OFETs based on *n-channel* (also commonly referred to as “n-type”) semiconductors conduct electrons and achieve their high conductivity “*on*” state with positive gate voltages, whereas most OFETs (e.g., pentacene OFETs) are *p-channel* devices (i.e., they conduct holes) and turn on with negative gate voltages. The motivation for seeking good n-channel OFETs is that they enable complementary circuit design. Electrical engineers are proficient at developing low-power complementary circuits that utilize both positive and negative gate voltages to turn transistors *on* and *off*. Consequently, the development of good *n-channel* OFETs with performance comparable to that of pentacene OFETs is a major goal for organic electronics. Relatively fewer n-type materials have also been reported, including $C_{60}$ and its derivatives [8, 9], oliothiophene and its derivatives [10], copper hexadecafluorophthalocyanine [10], naphthalene diimides, and perylene diimides [11, 12, 13, 14]. However, some organic n-channel semiconductor materials cannot operate in air due to electron trapping by oxygen and carrier injection issues [15]. The approaches to achieve n-channel materials with air stability and high mobility have been reported by the incorporation with strong electron-withdrawing groups, such as -CN and –F [16, 17, 18]. Currently, the highest mobility of n-type organic semiconductor is obtained from a thiazole oligomer derivative (1.83 $cm^2\ V^{-1}\ s^{-1}$) measured in a vacuum environment [19] or from a perylene diimide derivative with a mobility of 0.64 $cm^2\ V^{-1}\ s^{-1}$ measured in air.

## 2. Analytical Tools to Study OFET Device Operation

Lack of structure-property understanding is partly due to a shortage of adequate analytical tools to study OFET device operation. For example, at the current stage of development, mobility is still the most important characteristic in OFETs. Does an OFET device have a special structure, special organic-metal interface or a peculiar charge transport mechanism? Is it just a mobility in organics, or should the whole OFET device structure be optimized? The situation is complicated by the strong dependence of the current through the molecular junction on the nature of the chemical bond to the electrodes [20]. Chemically bounded to the semiconductor, molecules are likely to affect the energy and density of surface states and, therefore, the semiconductor band bending [21]. Furthermore, the presence of a dipolar layer at the semiconductor/metal interface can affect the barrier for electron transport inside the semiconductor [22, 23]. It is clear that OFET experimental results should be analyzed in terms of multiple mechanisms, and it is crucial to establish whether this is justified or if, in doing so, new mechanisms are ignored. It would be also very helpful to study independently charge injection *into-* and charge transport *in* the organic channel. However, the methods for observation and evaluation of such kinetics in organic devices at the component level have yet to be developed.

Current state of the art employs varieties of Kelvin probe-derived techniques that are widely used to determine electron work function and bend banding in organic-inorganic heterostructures. UV photoemission and inverse photoemission spectroscopies (UPS, IPES) are used to determine the position of the highest occupied and lowest unoccupied molecular orbitals (HOMO and LUMO, respectively). X-ray photoelectron spectroscopy (XPS) measurements served to estimate band bending. Comparison of these techniques with measured I-V characteristics enables one to determine mechanism(s), which control charge transfer in molecular diodes. These methods are static, since probing interfaces in time-scale compared to interface charge transfer is very challenging. Fast spectroscopy was applied to clarify dynamic of charge transfer in organic polymers, polymer-fullerenes and hybrid single-wall-carbon-nanotube strucrures and even in hybrid structures like dye-sensitized photovoltaic cells. Nevertheless, direct observation of complete dynamic of charge transfer in the interface is still far from the scope of these methods. *A relatively simple and sensitive photocurrent method to probe transport mechanisms in organic ordered system in time resolved regime is introduced in this chapter.*

## 3. Self-assembly and SAM OFET Devices

The way to achieve epitaxial control in organic devices is not trivial too. The transport mechanism in low-dimensional organic structures is intimately related to the *ordering and dimensionality* of the underlying electronic system, which may transform with the *molecular packing* [24]. Therefore, a systematic research in organic semiconducting materials and structures with controlled order is a pre-requirement for efficient OFET fabrication. This fine structural tuning is a very challenging goal since tunable organic epitaxial structures have not been studied at all, in contrast to inorganic semiconductors. We have developed such approach [25]. We explored ordered *self assembled monolayer (SAM) structures* of small molecules with the potential of high charge mobilities and low intermolecular interaction.

SAMs [26, 27] are ordered assemblies of functional molecules, which are formed spontaneously on an appropriate surface and are typically used to modify surface properties of materials. The tendency of certain types of molecules to spontaneously form assemblies arises from their characteristic, amphiphilic chemical structure. Self-assembling molecules are typically composed of two groups: a head group which has high affinity for an appropriate surface and a tail group with a high affinity for similar tail groups of other, neighbouring molecules. When such molecules are brought in contact with the appropriate surface, the head groups of the molecules will physisorb or form a chemical bond to the surface (chemisorption). As the density of a SAM increases, the tail groups of the molecules on the surface will come closer and start to interact, typically giving rise to the order within the self-assembled monolayer. Often the molecules also contain a functional end group which allows further physical or chemical functionalization. Both the self-assembling and self-ordering properties of SAMs, combined with the presence of this functional end group and with the SAMs stability (due to the surface bond) are the keys to a wide range of possibilities and applications such as surface engineering and surface modification for controlling adhesion, corrosion, lubrication, (bio)chemical sensing and mimicking, etc. By choosing precursors with suitable physicochemical properties, it is possible to exert a fine control on the formation processes in order to obtain complex architectures. Clearly, when it comes to designing a synthesis strategy for a material the most important tool is the knowledge of the chemistry of the building units. SAM is a process that is easily influenced by external parameters. This can make synthesis more problematic due to the many free parameters that require control. On the other hand, this has the exciting advantage that a large variety of shapes and functions on many length scales can be obtained [1].

## 4. NTCDI Thick Film and SAM OFETs

NTCDI-derived compounds were already tried in organic devices, including thin and thick film OFETs [29, 30, 31, 32]. The highest mobilities of solution-processed n-type semiconductors were achieved from quaterthiophene [33] (0.2 $cm^2 V^{-1} s^{-1}$) measured in a vacuum and from naphthalene diimide (NTCDI) with a long-chain fluorinated alkyl group (0.01 $cm^2 V^{-1} s^{-1}$) solution-processed in air by Katz et al. The highest n-channel mobilities of these devices, which were based on NTCDI derivatives were calculated to be about $1.2 \times 10^{-3}$ $cm^2 V^{-1} s^{-1}$ [34]. Direct fabrication of ordered organic structures as SAM and there incorporation in molecular device is still a challenging task, and only few reports are available. Several known and new SAM deposition and characterization techniques were explored and optimized to obtain the required, qualitative SAMs for use in organic thin-film transistors for a first time in ref. [35]. Various SAMs were then applied to different interfaces in SAM-OFETs, which allowed a better control of the morphology and properties of the organic semiconducting material. This resulted in a significant improvement of the electrical performance of the organic transistors and even enabled a new way to pattern the organic semiconductor. Alternatively, using a technique called ‘molecular layer epitaxy’ [36, 37], multilayer structures with 2D π-stacking and semiconducting properties have been obtained. This structures have been applied in organic light emission dioded (SAM-OLEDs), and in SAM-OFETs fabrication [38, 39]. A room-temperature electron mobility as high as 90 $cm^2 V^{-1}s^{-1}$ was reported using MLE [40]. The MLE technology is a vapor-phase oriented technique that allows the buildup of organic heterostructures via epitaxial growth of subsequent layers by interlayer covalent bonding. Vapor-phase self-assembly protocol for device fabrication introduced below is a modification of MLE approach used for new generation of SAM-OFETs. The same approach was used for a fabrication of SAM photovoltaic devises (SAM-PVC) to study photophysics of charge transfer phenomena in NTCDI channel and to model charge transport in NTCDI SAM-OFETs.

## 5. Transport in NTCDI SAM OFETs

This chapter is focused on self-assembled monolayres of small organic molecules with extended π-electron system, NTCDI, containing two benzene rings, four carboxyl groups and two anhydrides. These two anhydrides are used to connect NTCDI molecules to substrate by chemical imide bonds (out-of-plane bonding), while two adjacent NTCDI molecules held together in a solid monolyares by van der Waals forces (in-plane bonding). Weak van der Waals bonding in in-plane direction and weak intermolecular overlap of electronic orbitals lead to the narrow electronic bands (a typical bandwidth W~0.1 eV is two orders of magnitude smaller than that in silicon) and the low mobility of charge carriers ($\mu$ ~1–10 $cm^2 V^{-1} s^{-1}$at room temperature). Anisotropy of the transfer integrals between adjacent molecules reflects the low symmetry of the molecular packing. It is believed that the most adequate description of charge transport in these organic semiconductors is based on the concept of polarons, molecular states with a correlation between the electronic and lattice degrees of freedom at the scale of the order of the lattice constant [41, 42, 43, 44].

After several decades of intensive research, our basic understanding of charge transport in small-molecule organic semiconductors remains limited [45]. The complexity of transport phenomena in these systems is caused by the polaronic nature of charge carriers and the strong interaction of the polarons with defects. OFETs are aimed to be used at room temperature. Therefore, the high-temperature polaronic transport should be developed. At room temperature, which is typically comparable to or even higher than the characteristic phonon energies, lattice vibrations might become sufficiently strong to destroy the translational symmetry of the lattice. In this regime the fluctuation amplitude of the transfer integral becomes of the same order of magnitude as its average value [46]. The band description breaks down, and a crossover from the transport in delocalized states to the incoherent hopping between localized states is predicted with temperature increase [47, 48, 49, 50, 51, 52, 53]. While time-of-flight experiments demonstrated that a possibility of the intrinsic (not limited by static disorder) charge transport can be realized in the bulk of these crystals [54], the mechanism of the charge transport on the *surface* of organic semiconductors is less studied [55, 56, 57]. It is clear that in SAM-OFET devices field-induced charges should propagate along the interface between an SAM and a gate dielectric, which are true surface conditions. The differences in transport mechanism for surface and bulk media include: (i) *the density of carriers*, which in field-effect experiments can exceed that in bulk measurements by many orders of magnitude, approaching the regime when the intercharge distance becomes comparable with the size of polarons [58] (ii) motion of charge carriers in the field-induced conduction channel may be affected by the *polarization of the gate dielectric* [59], and (iii) *molecular packing* on the surface can also be different from that in the bulk. *This chapter will expand the study of correlation between dynamic characteristics (time-of-flight measurements) and charge mobility in bulk crystals to the case of SAM system.*

Exploration of the polaronic transport on organic surfaces is crucial for a better understanding of fundamental processes that determine operation and ultimate performance of organic electronic devices. Fundamental research has been hampered by the lack of a proper tool for exploring the polaronic transport on surfaces of organic semiconductors. The most common organic electronic device whose operation relies on surface transport is the organic thin-film transistor. Over the past two decades a large effort in the development of OFETs has resulted in improvement of the characteristics of these devices [60], so that currently the best organic OFETs outperform the widely used amorphous silicon transistors. However, even in the best OFETs, charge transport is still dominated by the presence of structural defects and chemical impurities.

## 6. The Scope of This Chapter

In this chapter we present a brief overview of the experimental results obtained with NTCDI SAM-OFETs over the last eight years. Because we focus on the physics of electronic processes in these devices, many surface chemistry oriented issues will not be discussed here; we refer the reader to a bible of self-assembling by A. Ulman for details on SAM fabrication and characterization. This much-cited, definitive text has become the standard resource on the SAM topic worldwide. In the *Materials and Methods* section we briefly describe the SAM growth, OFET and organic photovoltaic cells (PVC) fabrication techniques and measurement techniques. The *Results* section focuses on the observation of intrinsic polaronic transport in SAM devices. Electronic mechanisms of charge transport are discussed in the *Discussion* section. The *Conclusion* section outlines several basic issues that are now starting to be experimentally reachable due to the development of SAM-OFETs and for which theoretical work is still to be done.

## MATERIALS AND METHODS

Several variations of SAM devices were studied for the same 1,4,5,8-Naphthalene-tetracarboxylic diphenylimide (NTCDI) SAM system to evaluate a transport mechanism in SAM-OFETs. These SAM devices are: (i) SAM-OFETs and (ii) hybrid self-assembled photovoltaic cells (SAM-PVC). SAM-PVC devices were fabricated on p-and n-Si substrate.

### 1. Preparation of Organic Films

### Step-A

*SAM on $SiO_2$ and glass for SAM-OFET conductive channels and SAM-PVCs* (Figure 1A). Thick, impermeable to light wafers of n-type (500 Ω·cm, Virginia Semiconductors) Si(100) having 20 Å of $SiO_2$ coating and glass slides were cleaned and functionalized with amino groups (*step a*), Figure 1A as described in ref. [61]. In experiment, which was aimed to invert

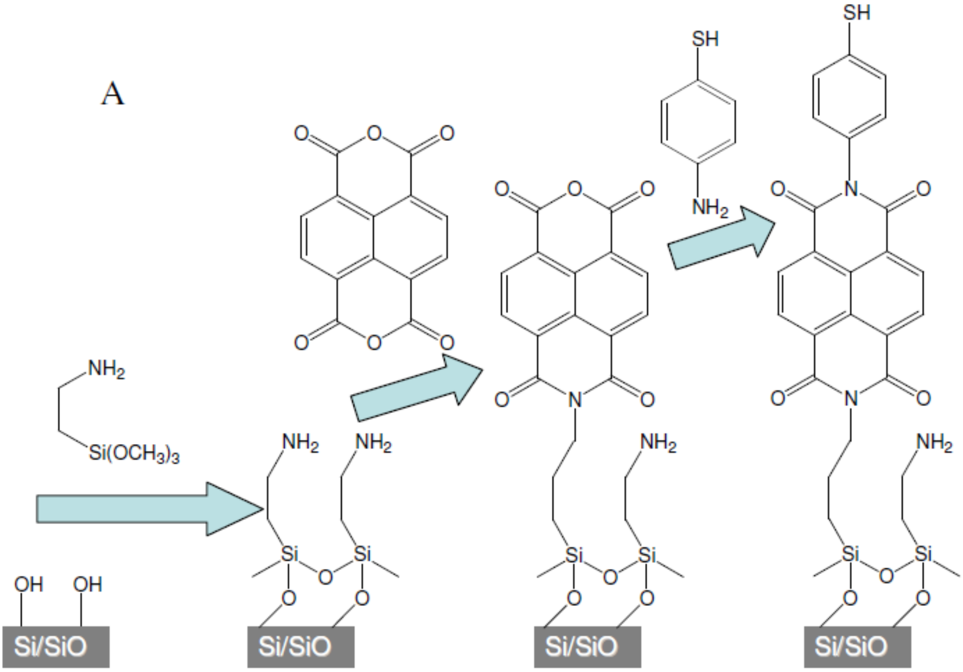

Figure 1. Continued on next page.

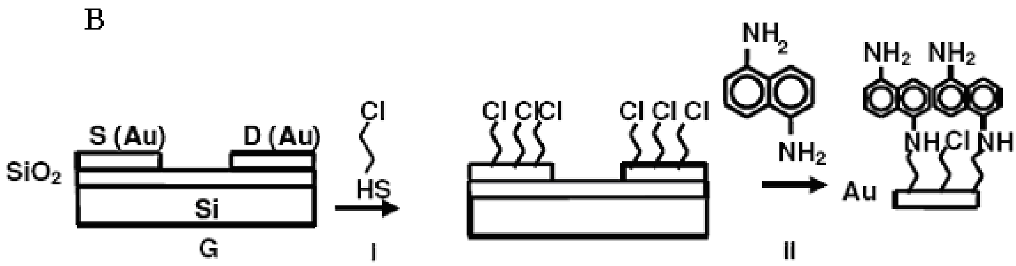

Figure 1. Fabrication of SAM devices. (A) The three-step assembly of monomolecular films of NTCDI on oxides Si and $Si_3N_4$ substrates (conductive channel at SAM-OFET and at SAM-PVC). (B) The two-step assembly of amino-coated template layer on Au electrodes used only for SAM-OFET source and drain. SAM of NTCDI was continued from stage b at panel A, following assembly of aminated template layer on Au.

the conductivity type of NTCDI channel, a p-type Si(100) having 20 Å of $SiO_2$ (100 Ω·cm, Virginia Semiconductors) was used in addition to the n-type silicon wafers. NTCDA (1,4,5,8-naphthalene tetracarboxylic anhydride) evaporated at 110°C and reacted with the $NH_2$-functionalized surface for 45 min in a Bell Jarr chamber at $10^{-5}$ Torr (*step b*).

The product of assembly lacks the amino group preventing formation of the second layer. The substrate was kept on a heated sample holder (180°C) preventing physadsorption of the precursor. Vacuum deposition modified over 60% of the surface amino groups [$^{6}$2]. A layer of 4-aminophenylthiol was added within 20 min (step c). This reaction tops the surface with SH-groups reactive toward metals [63]. The chip was gently rinsed with 2-propanol and heated at 80°C for 1 h. A silver contact was placed on top of the films by placing a drop of colloidal silver in acetonitrile and allowing the solvent to evaporate; the area or the contact between the silver and the coated silicone was ~3 mm$^2$.

## Step-B

*SAM on Au electrodes for SAM-OFET source and drain (Figure 1B).* First, a 3 mM solution of 3-chloro-1-propanethiol (Cl-Pr-SH) in ethanol was spin-coated on the OFET substrate to form AuS bonds (*i* in Figure 1B). The substrates were held under Ar flow for 20 min after spin-coating and after that the substrates were rinsed with isopropyl alcohol and heated at 100°C for 1 h. Next, a 5 mM solution of 1,5-Diaminonaphtalene (DAN) in ethanol was spin coated on the surface followed by annealing at 100 °C for 1 h to form imine bonds with template layer (*ii* in Figure 1B). The excess DAN was removed by an ethanol rinse and annealed at 100°C for 1 h. A self-assembly route described above for oxidize surface and depicted at Figure 1A was completed SAM-OFET device fabrication. Different self-assembly of template layers on OFET conductive channel, following *step a* in Figure 1A, and electrodes, following *step ii* in Figure 1B insure formation of unified NTCDI layer across SAM-OFET surface and device integrity.

In addition, few samples were prepared for SAM-PVC devices. Thick (~300 nm) films of NTCDA and $C_6$-NTCDI were prepared by physadsorption of NTCDA on the cold functionalized surface of silicon. Sparse NTCDI films were obtained from thick films of

NTCDA by heat desorption of the excess of NTCDA followed by *step c*. Step B was not employed in SAM-PVC devices.

## 2. Characterization of the NTCDI Monolayer

A step-by-step buildup of the layers was characterized by contact angle (CA) changes, IR spectroscopy, XPS, and UV-vis spectroscopy. The results agree well with previous characterization of NTCDI SAM monolayers and are briefly summarized below. After step a, CA changed from 17° to 45°, and the appearance of the 3200 $cm^{-1}$ alkylamine IR peak was observed. The N (1s) XPS core level spectra showed a predominantly 398.8 eV (85%) peak on the amine surface because of the nonprotonated $NH_2$-group [64]. The minor N1(s) component at 400.6 eV is attributed to protonated $NH_3^+$ (15%). The UV-vis spectrum of the film grown on the glass slide did not reveal any peaks. After step b, the CA changed from 45° to 92° and the 1655 $cm^{-1}$ IR peak of the imide bond formation was detected. In accord with previous studies [65], formation of imides on the surface results in disappearance of the majority of the original peaks at 400.6 eV (29%) and 399.8 eV and formation of a new single broad N(1s) peak at 399.6 eV (67%) because of formation of imido groups with a possible presence of amido groups [66] When step b was performed on a glass slide, two peaks appeared in the UV spectrum: 360 and 390 nm; OD ~ 0.004 and 0.006, respectively (Figure 3). We also observed an appearance of a new broad peak in the greenish-orange region (OD = 0.001) that characterized a formation of an in-plane ordered organic heterostructure in SAM structure. After step c, the CA changed from 92° to 60° and a new peak (236 eV) associated with HS groups was observed in the XPS spectrum. No significant changes were found in the UV-vis and the IR spectra after step c. Variable angle spectroscopic ellipsometery (VASE, Woollam Co.) was used to verify the monolayer growth as it was reported for NTCDI SAM structure. The variable angle spectroscopic ellipsometer measured spectra with 5-nm intervals in the range 300-1700 nm. The structural model for fitting ex-situ ellipsometry data uses the data of three different incident angles: 65°, 70°, and 75°. Measured and fitted ellipsometric data for a structure containing Si/$SiO_2$, siloxane matrix, NTCDI-benzene thiol exhibit molecular c-axis interplanar spacing are 20 Å for $SiO_2$ native oxide, 3.5 Å for the siloxane matrix, 7.0 Å for NTCDI, and 6.9 Å for the benzene thiol layer.

## 3. SAM-OFET Electrode Configuration

Substrates for OFETs and tunneling devices were fabricated using reactive ion etch-grown silicon nitride (100 nm) as the insulating layer on highly doped n-type silicon, which also functioned as the gate electrode. Gold source and drain interdigitated contacts were photolithographically defined on the silicon nitride to give total channel width $W_1$=6000 μm (width is 400 μm for 15 meander elements) and channel lengths $L_1$=20 μm. Figure 1A shows a top view of the interdigitated finger array. The substrates were cleaned by immersing for 1 h into a solution containing $H_2O/H_2O_2/NH_3$ (5:1:1) while sonicating. After that, they were washed with deionized water (17.8MΩcm) and acetone, subsequently, and heated in an oven for 30 min at 100 °C. Following fabrication step A and step B, which are describe above, indium contacts were attached to drain and source Au pads (Fig 2). Silver paste was used to connect to bottom gate electrode.

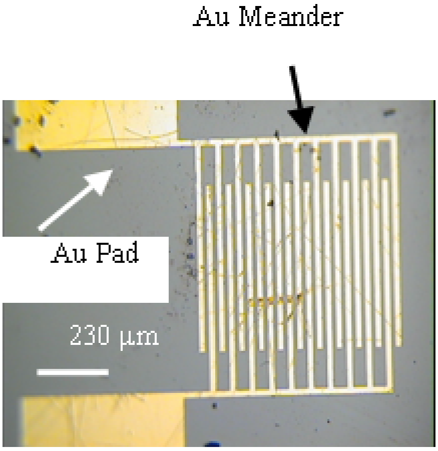

Figure 2. FET electrode configuration. Optical image of electrode meander before deposition.

## 4. Determination of the Absorption and External Quantum Efficiencies in Closed-Circuit SAM-PVCs

The spectra of dense and sparse monolayers of NTCDI grown on glass slides were recorded in a Shimadzu spectrophotometer. Comparison of the films grown on Si and glass is justified by the surface titration, which shows that the density of amino groups on glass and $SiO_2$ coating of Si(100) is approximately the same [62] (2-3 per 100 $Å^2$). The EQE was calculated as a ratio of the number of electrons passed through a 500 Ω resistor to the number of photons in the light flow. The output of a Xenon lamp/monochromator assembly (8-nm bandwidth) standardized to the Oriel calibrated light source was used to illuminate the photoelement. The EQE was also measured at 532 nm by referring to nonsaturating output of CW YAG laser calibrated with a photocalorimeter.

## 5. Time-Resolved Photovoltaic Measurements in Closed-Circuit SAM-PVCs

These were performed with a picosecond laser system consisting of a Ti: Sapphire femtosecond laser, stretcher/compressor/amplifier of picosecond laser pulse ("Titan", Quantronix), and optical parametric amplifier of superflourescense ("TOPAS", Qunantronix/ Light Conversion). The output pulse parameters were: wavelength 532 nm, energy 10 μJ, pulse duration 1 ps, and repetition rate 1 kHz. To avoid saturation effects, the pulse energy was attenuated to a 0.1 μJ level with a beam diameter of 1 mm. The photovoltage transients were recorded by Tektronix TDS 3025 digital oscilloscope bypassed with a 7.6 kΩ resistor (Fig 3).

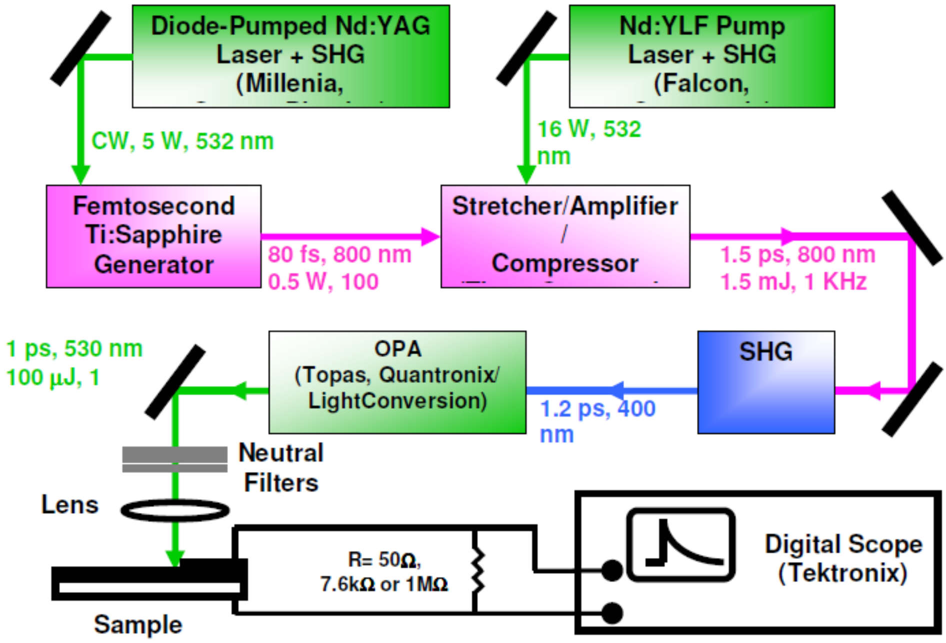

Figure 3. Experimental setup for a time-resolved photovoltage measurement in closed-circuit SAM-PVCs.

## 6. Capacitance Coupling (Open-Circiut) Measurements in SAM-PVC

To learn the charge separation we studied the formation and decay of the surface photovoltage by an auxiliary transparent electrode, which serves as a capacitive probe that picks the transient surface photovoltage. This method has been used in electronics and biophysics but is novel for the surface redox chemistry. The probe both provides the direction of the charge transfer and resolves its dynamics. Its application is independent of the optical properties of the semiconductor. Laser initiation of the reaction permits quantitative measurements of the reactions with the rate constants ~$10^8$-$10^3$ $s^{-1}$. The back electron transfer is poly-disperse with the components ranging from ~10 microseconds and up. Measurement scheme was the same as at Figure 3, but instead of upper electrode a semi-transparent indium tin oxide electrode was used to achieve a capacitor coupling. More details for this measurement setup and principles of capacitive probe operation are shown at Discussion *section 2.2,* Figure 11 and Figure 12.

# RESULTS

## 1. NTCDI SAM OFET Devices

In order to have high mobility and low charge trapping in organic semiconductors, we have focused on the class of organic materials with *herring-bone* crystallographic packing. Herring-bone packing could prevent interchain quenching and, at the same time, to have high electron and hole mobilities. The aromatic polycyclic structures, which are based on small molecules, and have a natural herring-bone pattern packing in the crystals [67] are promising candidates to that end. For example, one of them with the highest mobility in crystalline form ($\mu = 3 \cdot 10^{-3}$ cm$^{2}$ V$^{-1}$ s$^{-1}$), naphthalene tetracarboxylic dianhydride (NTCDA) has such herring-bone pattern (Fig 4) [68]. Moreover, it was shown that NTCDA conductance in crystalline could be enhanced by two orders of magnitude by increasing charge concentration through doping [69]. Our research showed that SAM of NTCDI molecules results in ordered structures, which have even higher electron mobility.

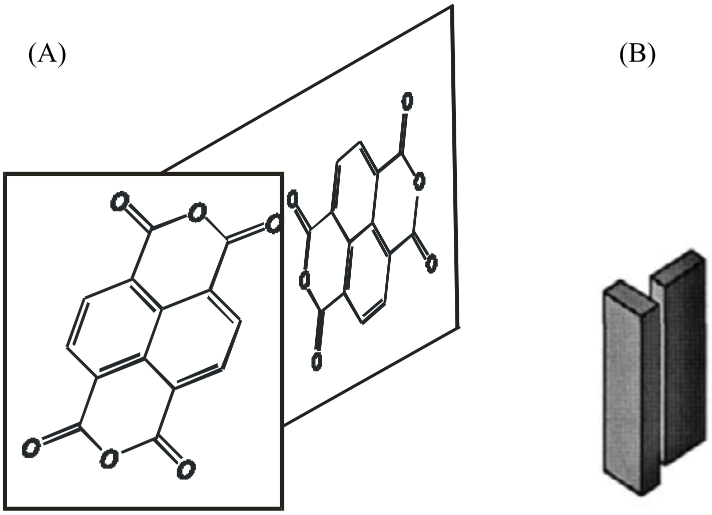

Figure 4. A) Natural herring-bone pattern packing of NTCDA molecules. B) Scheme of orthogonal NTCDI intermolecular plane configuration.

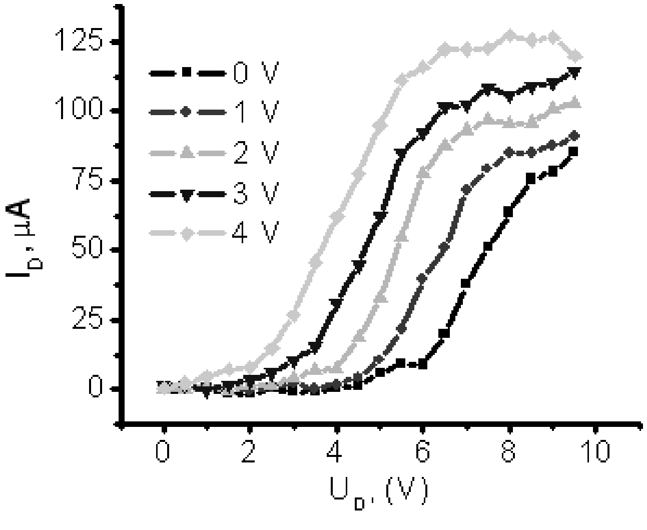

Figure 5. Resulting $I_D$-$U_D$ curves at different gate biases.

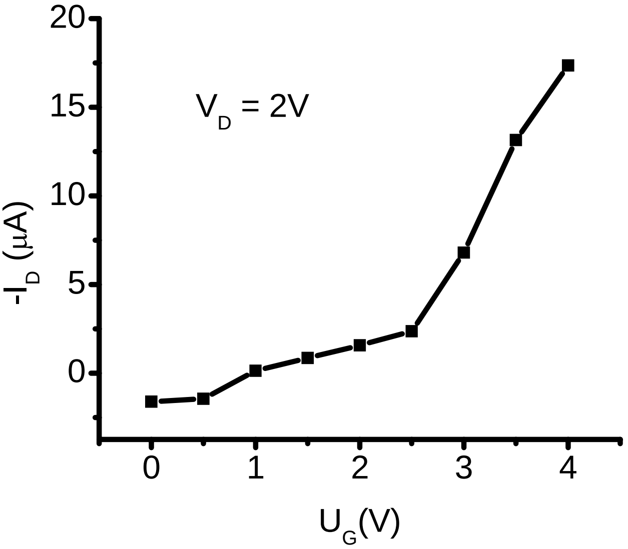

Figure 6. Transconductance measurements of SAM-OFET device showing n-type behavior at $V_D$ = 2V.

Figure 5 shows the I-V curves of a SAM-OFET device. The device exhibits saturation regime at high enough drain voltages. $V_D$ of 0.5 V was required in order to obtain the drain current. The nature of this barrier will be clarified at discussion section following photocurrent studies in NTCDI hetero-structures. Detailed discussion of the ways to decrease metal-organic injection barrier in SAM-OFET is beyond the scope of our contribution. Our preliminary experiments indicate that doping of template layer by molecules carrying positive and negative charge could essentially affect this barrier. In particular, using of 0.01μM solution of tri-phenyl amines decreases this barrier to 0.1V without effecting essentially mobility in SAM-OFET device.

The mobility of this n-type device was calculated at the saturation region using the nex equation:

$$\mu_e = \frac{\Delta I_D}{\Delta V_G}\frac{L}{W}\frac{1}{V_D}\frac{1}{C_{OX}} \tag{1}$$

where $C_{OX} = \dfrac{t_{OX}}{\varepsilon_S + \varepsilon_0}$ is capacity of $SiO_2$ layer, $t_{OX}$ is thickness of $SiO_2$ layer, $\varepsilon_S$ he static permittivity of the material and $\varepsilon_0$ is dielectric constant, $L$ and $W$ are length and width of conductive NTCDI channel, $V_D$ is drain bias, under which mobility is calculated, $\Delta I_D$ and $\Delta V_G$ are drain current and gate bias range in which mobility is calculated. Here $C_{OX} = \dfrac{2 \cdot 10^{-6}}{4 \cdot 8.86 \cdot 10^{-14}}\left(\dfrac{cm}{F/cm}\right)$, $L$ and $W$ are 20 μm and 6000 μm, $V_D$ is 2V

(Figure6) and ratio $\frac{\Delta I_D}{\Delta V_G} = \frac{6 \cdot 10^{-3}}{2}\left(\frac{A}{V}\right)$. n-type mobility ($\mu_e$) of 31.5 $cm^2$ $V^{-1}$ $s^{-1}$ is obtained by applying eq. 1 to the data in figure 4 and a high on/off ratio of up to $10^9$ is obtained. We note that such a high mobility was achieved only in 10% of fabricated devices. Totally 20 SAM-OFET devices were tested. 20% of tested devices were shortened and about 35% of devices were damaged during measurements. Roughly 35% of devices have a lower mobilities or exhibit properties of gated tunneling diodes. These tunneling diodes demonstrated typical Flowler-Nordhaim tunneling features [70]. Here we will discuss transport properties only of the best devices. The device reproducibility aspect will not be discussed in this chapter. This is a rather high mobility, considering the thickness of the organic semiconducting layer. The transconductance of device is shown in Figure 6 and demonstrates the turn on voltage of the device in an n-type mode on the same device. In this device a $V_D$ = 2V drain voltage was required to overcome the blocking contacts, consequently the channel currents were measured at much lower drain voltages. Mobility in p-channel was $10^2$ lower compared to n-channel. Thus, the possibility to have high mobility in SAM-OFET molecular systems is demonstrated. These studies, along with photophysics transport studies of SAM structures, demonstrate that molecules with natural herring-bone pattern packing might be favorable for OFET applications. This peculate will be discussed in detail in Discussion section.

## 2. NTCDI SAM PVC Devices

To achieve hybrid SAM-PVC we self-assemble the NTCDA molecules, which are the same molecules used in conductive channel of SAM-OFET, on n-type silicon substrate. The self-assembly strategy followed *step-A* synthetic protocol (Figure 1A). Two kind of measurement set up were used to evaluate transport in NTCDI-based SAM-PVC. The first measurements scheme relies on closed and second on open electrical circuit measurements. In first set up the Ag upper electrode was used to collect *photocurrects (section 2.1,* Discussion*).* Semi-transparent ITO electrode was used to probe electric field created by photogenerated charges in second set-up *(section 2.2,* Discussion*).* Combination of these measurements should (*i*) provide a kinetic of charge transfer in 2D NTCDI molecular system and (*ii*) prove that this charge dynamic solely attributed to transport properties of 2D NTCDI molecular system, and not to capacitor discharge and interface charge transfer at SAM-PVC. The last section (*(section 2.3)* of SAM-PVC sub-chapter demonstrates possibility to change the type of conductivity in 2D NTCDI molecular system by changing of substrate type from traditional n-type Si to p-type Si substrate.

### 2.1. Measurements of In-Plane Currents in SAM-PVC: Closed-Circuit Electrical Measurements

We topped the film with a small-area silver electrode and found that the resulting Ag/NTCDI monolayer/Si sandwich (Figure 7) was sensitive to light.

In the dark, the current-voltage (I-V) curve goes through the origin (Figure 8) and straightens at the slopes that correspond to ~30 and ~10 kΩ, respectively, as the positive or negative voltage increases.

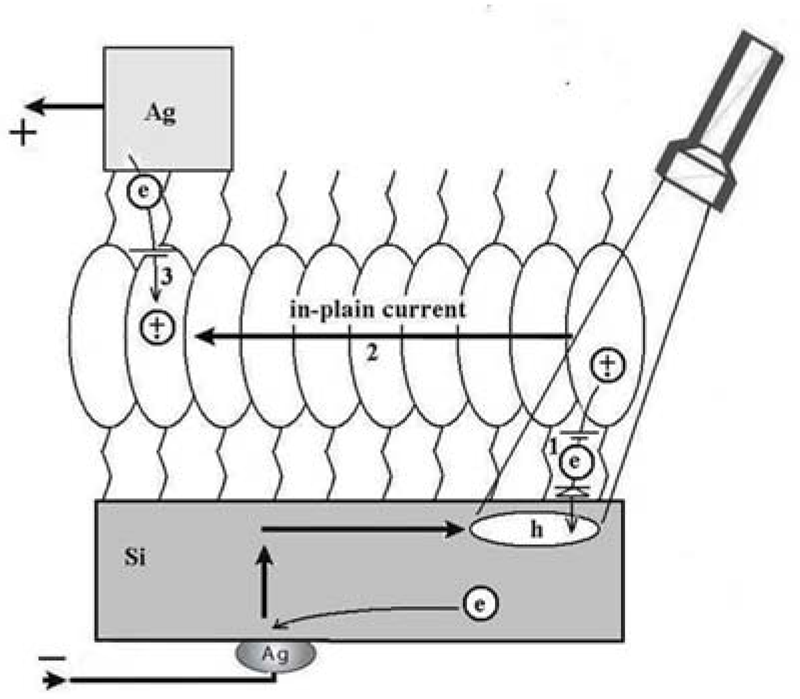

Figure 7. Operation of the SAM-PVC. Incident light creates holes (h) in the valence band of silicon. Upon ejection of electrons (reaction 1) from the immobilized molecules into the holes, cation radicals are formed. Cation radicals rapidly exchange with the neutral molecules (2); the positive charge travels through the film, resulting in the in-plain current. Rereduction of cation radicals by silver (3) completes the photovoltaic element. Reactions 1-3 generate electromotive force. The diode (1) reflects rapid photoejection of electrons from the film and slow back-reaction. The external electric connections used in the voltammetric experiments (Figure 2) include a power source, an ammeter, and a voltmeter.

Illumination with continuous monochromatic light changes this characteristic dramatically. Now, the I-V curve also goes through the bottom right quadrant where the current through the element opposes the external bias. This plainly manifests that light generates electromotive force, which induces a negative charge on silicon (photocathode) and a positive charge on silver (photoanode). The maximal photovoltage at the saturating light power was as high as 280 mV. In the absence of the film or only with the amino layer present, the maximal photovoltage was below 0.1 mV and could not be characterized accurately. The mutual arrangement of the cell and the incident light, the external quantum efficiency (EQE) of 0.4-0.7 (Figure 9), which cannot be accounted for by the absorption efficiency of the film, the dissimilarity of the EQE, and the absorption efficiency of the film and resemblance of EQE to the spectrum of silicon [71] suggest that the light is productively absorbed by the semiconductor (Figure 7).

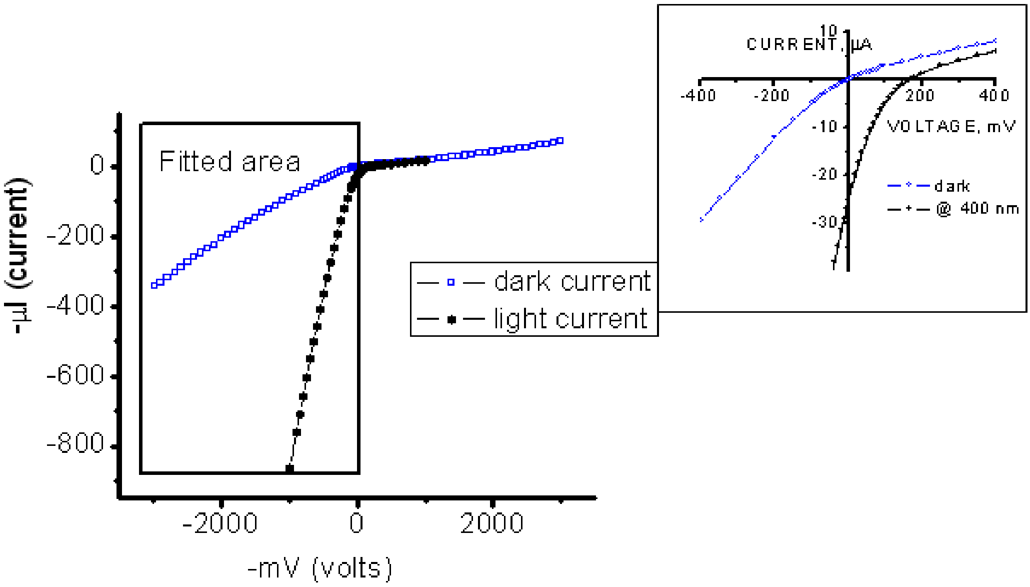

Figure 8. Electrooptical properties of the Si/NTCDI/Ag heterostructure. All experiments have been carried out at room temperature. Constant monochromatic 400-nm light illuminated an ~10-mm spot centered ~5 mm away from the silver electrode. When the Ag electrode is highly electronegative, the element behaves as a photoamplifier and light noticeably increases the asymmetry of the I-V curve. Marked "Fitted area" will be used in discussion section to model transport mechanism in SAM NTCDI channel.

This contrasts with light harvesting in the dye-sensitized photovoltaic cells [72, 73] or the hybrid nanorod-polymer cells [74] which require special junctions with enormous contact areas between the materials to enhance their absorption efficiency. The geometry of the cell also suggests that light harvesting incorporates a longitudinal spatial energy transfer. In contrast to natural photosynthesis [75] the conserved energy does not migrate in the form of excitons. The absence of long range light harvesting, when the uncoated side of the chip was illuminated, establishes importance of the film and rules out energy transfer within the silicon bulk.

The process starts with a redox reaction separating charges between silicon and film (reaction 1, Figure 8). Because of the spatial separation of the cathode and the anode chemistry, this reaction can be identified straight from the polarity of the cell, which shows that electrons from the NTCDI molecules are ejected into silicon, that is, NTCDI molecules oxidize. Charge separation is supported by the asymmetry of multiplication of the dark current with respect to the bias direction (Figure 8), which cannot be accounted for by the influence of nonpolar excited states. Indeed, regardless of the amplification mechanism, they would not be able to discriminate the bias directions. On the contrary, charge separation explains this asymmetry easily. Since the positive charges in the NTCDI film "reflect" in silicon "mirror", they are accompanied by their countercharged electrostatic images and migrate as trans-surface dipoles. As these dipoles approach the Ag/film/Si junction, they are either attracted into the contact area by parallel or repelled by the antiparallel external field. In agreement with photooxidation mechanism of energy conservation, light harvesting was observed in the thick films of N,N'-dihexyl-naphthalene tetracarboxylic diimide (C6-NTCDI) physadsorbed on the silicon surface, but not in the thick films of NTCDA, because NTCDA is much harder to oxidize. This photooxidation incorporates several events. Absorption of light results in elevation of an electron to the conductance band leaving a vacancy in the valence band. This vacancy can be filled either by back recombination of the electron from the conductance band (unproductive decay) or by transfer of an electron from the film into silicon (reaction 1, Figure 8) since the affinity of this vacancy for an electron is apparently high enough to oxidize a molecule of NTCDI. As a result, similarly to the photochemistry of dye-sensitized cells [76, 77], an extra electron remains in the conductance band of silicon, while the oxidized molecules of NTCDI become cation radicals (Figure 7, inset).

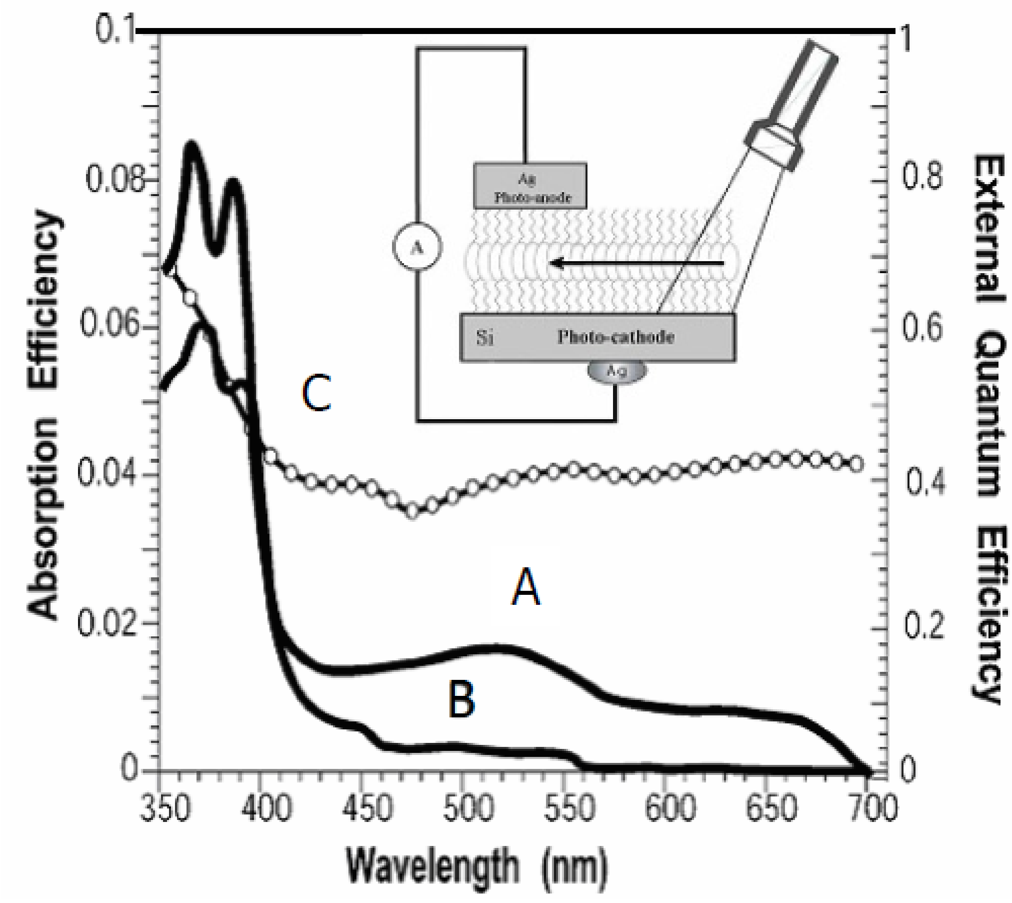

Figure 9. Effect of the surface density of NTCDI on the film spectra and light-harvesting efficiency. Dense film A assembled on glass has a prominent aggregation band in the greenish-orange region. The external quantum efficiency of the corresponding Si cell illuminated by constant nonsaturating light is represented by spectrum C. Sparse film B has no aggregation band in the spectrum. The external quantum efficiency of the corresponding cell was too low to measure. Insert show the measurement setup under continuous illumination.

These radicals combine essential structural motifs of the oxidized forms of two ubiquitous redox cofactors: $NAD^+$ and semiquinone. These features ease oxidation of neutral molecules. The energy of light is conserved in two forms: the electrostatic energy of trans-surface dipoles and the free energy of reduction of cation radicals by silver (reaction 3, Figure 8). The equilibrium of this reaction is shifted toward neutralization of cation radicals, and we could not attain electric currents in the films assembled on the surface of glass because measurements of such currents even over microgaps require very sensitive equipment [78].

To study migration of cation radicals to the photoanode (reaction 2), we used short light pulses focused at different distances from the anode to provide both time and spatial resolution. The photovoltage transients consist of voltage rise and decay (Figure 10). The decay is exponential with $\tau \sim 40$ μs at the given external load. This component represents the discharge of the cell because of both the backflow and the functional current through the load. The voltage rise originates from accumulation of charges at the anode and its kinetics depends on the distance between the illuminated spot and silver (Figure 10).

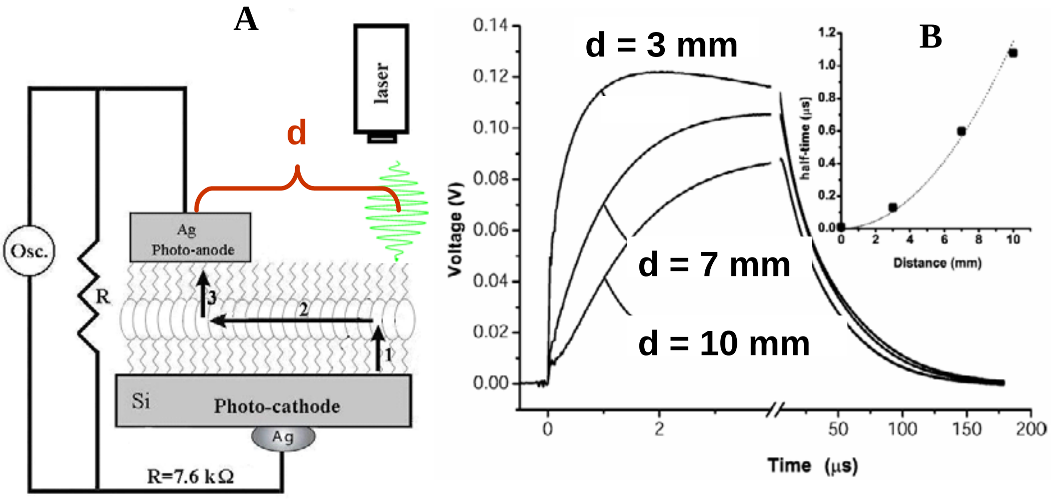

Figure 10. Scanning time-resolved photovoltage probing. A) Measurement setup. Distance *d* is between illumination point and harvesting upper Ag electrode. The transients were induced by pulses centered at different distances apart from the silver electrode. B) Kinetic of photoresponse at different *d*. The inset shows the dependency of the $T_{1/2}$ of the voltage rise on the distance *l* between the bright spot and the silver photoanode. The solid line approximates the points by a parabola $T_{1/2}=l^2/D$ with the parameter $D \sim 10^6$ cm$^2$/s.

To avoid a model bias, we described the kinetics of the voltage rise by its half-time $T_{1/2}$ (Figure 10, inset), which reflects the travel time of the cation radicals. Simple estimate shows that corresponding speed of charge exchange exceeds $10^4$ m/s. Despite some spatial uncertainty due to the finite beam size and a limited number of data points, one can see that the travel time appears to be proportional to the second power of the distance between the illuminated area and the silver electrode rather than to its first power. Since the area (distance quadrate) covered by a random-walking particle is proportional to its travel time, this dependency (Figure 7, reaction 2) is consistent with the random walk fashion of migration of cation radicals within the film during successive self-exchange reactions between the neutral molecules and the cation radicals. It is driven by the spatial gradients of their electrochemical potential, which are present because the anode reduces the cation radicals. Migration of cation radicals requires proximity of the molecules forming the monolayer and acting as redox centers. Such proximity manifests itself as a broad absorbance band in the green-orange region (Figure 9), attributed to formation of closed packed aggregate channel [62]. This migration, that is, time-resolved growth of the photovoltage, was not observed in the sparse monolayers of NTCDI, in the thick films of NTCDA, or without organic film. Only minor signals were observed in these control devices especially with the laser beam incident at the edge of the Ag contact. When the center of the beam was moved away from the edge, these signals disappeared rather than develop slower. The slight decrease of the total charge collected by the anode is probably due to partial recombination of trans-surface dipoles.

The charges formed in the remote-illuminated area have to travel within the film over "gigantic" distances at finite speed. The vast majority of studies of lateral charge transfer in monomolecular structures were limited to the self-assembling and Langmuir-Blodgett monolayers [79, 80, 81]. Some of these studies have revealed that electrochemical activity of the assembling molecules is a requirement for charge transfer within these monolayers [82, 83]. In analogy to that we believe that the efficient delivery of positive charges to the photoanode becomes possible because of the macroscopic connectivity of the network of NTCDI molecules acting as redox centers. This connectivity permits rapid transfer of large net charge through an extremely narrow cross section and originates from assembling NTCDI molecules at the positions predetermined by arrangement of the $NH_2$-groups within the dense interlinked siloxane network [27].

## 2.2. Measurement of Out-of-Plane Charge Recombination in SAM-PVC: Open-Circuit Electrical Measurements

When redox active molecules are covalently tethered to the surface of the n-doped silicon, light induces their oxidation by the semiconductor (*section 2.1*). One particular problem to be solved by the new method originates from our abovementioned results. In principle, the energy can be conserved for further spatial transfer in two ways. First, it can be converted into the energy of the excited state as in the photosynthetic light harvesting antennas. Second, similarly to the dye-sensitized cells, the energy can be conserved as the free energy of charge back recombination (Figures 11 and 12). In the second case, the actual case as we show, the role of the organic molecules in these SAM-PVCs is different from the role of the dye in the dye sensitized cells. The NTCDI molecules do not absorb light but act exclusively as redox couplers and form cation-radicals upon ejection of an electron into the light-induced hole in the valence band of silicon. However, distinguishing between the two possible mechanisms is challenging because adoption of the traditional methods used for the dyes-sensitized cells would make the endeavor prohibitively difficult. Switching to the IR region where silicon is transparent is demanding in terms of the equipment and still cannot help the fact that, the monolayers contain too few molecules for time-resolved spectroscopy and only a small fraction of these molecules actually forms radicals. These molecules react too fast to make single molecule techniques applicable even in principle. Finally, an attempt to produce model nanoparticles would require an adequate adaptation of the existing modification technology and there is now guarantee for the adequacy of the model system studied in the solution compared to the actual element functions in the solid state.

Experimental results of the previous section show that the diffusion time of about 1 μs or less at the given distances is apparently much shorter than the life time of the cation radicals in SAM-PVC. The similar back recombination in the dye-sensitized $TiO_2$ takes milliseconds [84]. Direct measurements in the closed-circuit configuration do not allow answering the question about back charge recombination, because in this configuration a long-time part of the charge transfer kinetics depends on the input impedance of the measurement system and internal impedance of the monomolecular devise, which in turn depends on many other external parameters.

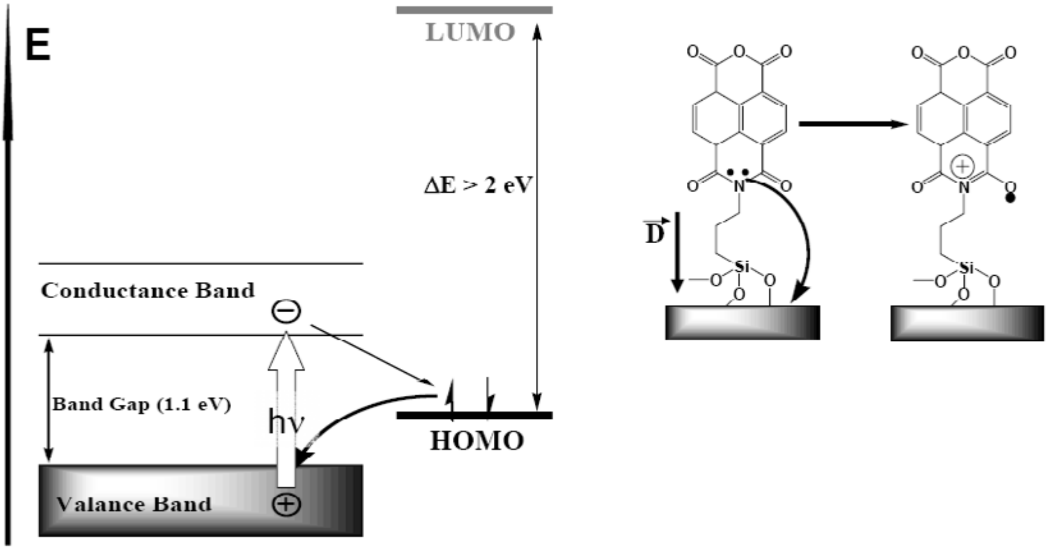

Figure 11. Light indiced charge transfer at the silicon-NTCI(A) interface. The relative arrangement of the energy levels of silicon and NTCI(A) is necessitated by the observed polarity of the photo-induced charge transfer and by the fact that the light is absorbed by silicon. The structure of the putative cation radical is presented on the left. Vector D stands for the induced electric displacement.

Therefore, the purpose of our study became two-fold. The first goal was to find a universal and highly sensitive method to study interfacial charge transfer. The second goal was to prove that illumination of the NTCDI-modified surface of silicon results in formation of cation-radicals at the junction and thus to test the potential of the method. In order to match these goals we have opted to the surface photovoltage technique, which is sensitive to the net charge displacement [85, 86], the very basic property of redox reactions. Since the spatially organized charge transfer inevitably causes electric displacement perpendicular to the junction (Figure 11), we have expected this elegant non-spectroscopic approach to be extremely useful in the studies of the surface redox chemistry.

Here we show that the charge displacement perpendicular to the surface is sufficiently strong for direct measurements. To pick this electrostatic signature we utilize an auxiliary transparent electrode that act as a capacitive probe (Figure 12). This probe proposed by Bergmann in 1932 selectively picks the ac voltage [87]. Previously the transparent auxiliary electrode has been used to study the photovoltage generated by the p-n junctions. This nondestructive no contact method proved to be convenient for the quality control of these junctions before and without equipping them with electrodes [87, 88] or for measurement of the lifetimes of the minority charge carriers [89, 90]. In those measurements the ac photovoltage has been generated by a chopped light beam and its amplitude has been measured. While repetitive laser represents a limit case of the chopped beam, application of short pulses permits time-resolved measurements. Interestingly, a related approach has been utilized in the studies of the photosynthetic reaction centers in the essentially 3D membrane suspension samples [91, 92].

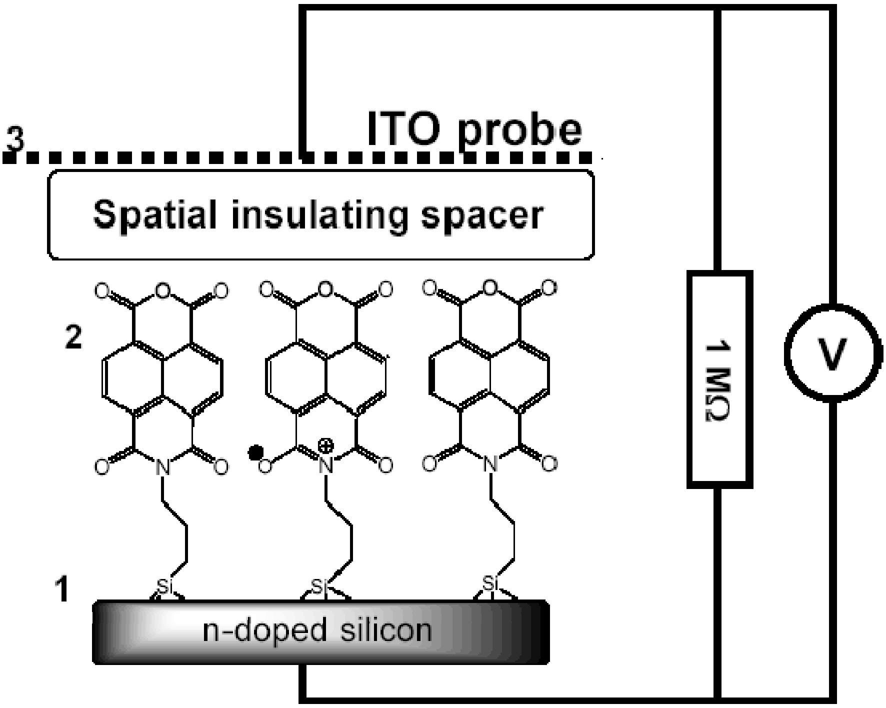

Figure 12. The putative surface electrochemistry and its electrostatic signature. The silicon substrate forms the capacitor plane 1. The neutral NTCDI(A) molecules and the putative cation-radical formed upon illumination form the imaginative plane 2. This organic layer is separated from the tin-doped indium oxide electrode (plane 3) by a 25 micrometer insulating film. The capacitor planes 1 and 3 are connected respectively to the ground and signal input of the oscilloscope (V), which has a standard input resistance of 1 MOhm.

The method measures the transient voltage drop between the plates of the capacitor formed by the semiconductor chip and a probe ITO electrode transparent to the visible light. The photovoltaic response of this device contains two components. The first one is characteristic of capacitor between doped Si and ITO electrodes and the second one is a response from organic heterojunction itself. The relaxation time constant *k* for organic heterojunction is independent on device area and identical to the constant of charge annihilation on the single molecule or cluster. That is in opposite to a capacitor response, which is area dependent.

### 2.2.1. Theoretical Background for the Capacitive Probe Measurements

To proceed further, we need to develop a theory of the capacitive probe response to distinguish between the surface charge transfer dynamics and the instrumental response. Let us denote the silicon surface, the organic film and the probe electrode as planes 1, 2 and 3 respectively (see Figure 12). Charge separation between the organic film and the silicon substrate will cause formation of an electric field between the planes 1 and 2. Under uniform illumination the concentration of the surface dipoles is the same throughout the film plane. The film becomes a surface of equal potential and can be considered as a plate of a complex 3-plate capacitor, which in turn is formed by two serial capacitors: $C_{21}$ (organic film/Si) and $C_{23}$ (organic film/ITO electrode). The voltage jump $U_{21}$ will cause an electric current through the outer circuit formed by the probe capacitor $C_{23}$, cable and internal resistance $R$ of the oscilloscope. The capacities of the organic film and probe electrode were estimated to be $C_{21} \sim 1\ \mu\text{F}$ and $C_{23} \sim 100\ \text{pF}$, respectively. Direct measurement of the cable capacity demonstrated $C = 360$ pF. Input capacity of the oscilloscope $C_S = 13$ pF is much smaller than the cable capacity, and in the following up calculations $C_S$ was included into $C$.

Observed signal (voltage $U_S(t)$ on the oscilloscope) reflects the dynamics related to the charge exchange between capacitors and to the finite lifetime of the dipoles created in organic film and semiconductor surface. Charge annihilation in the film will cause a backward current $I_{21}(t) = kQ_{21}(t)$, where $Q_{21}(t)$ is the charge accumulated in the capacitor $C_{21}$, and $k$ is the rate of the transient charge annigilation. As it was mentioned above, the constant $k$ is defined by electrochemical properties of the sample, and does not depend on the area of illumination.

To analyze the system behavior we consider three time scales: 1) charging the organic film buy the picosecond laser pulse; 2) fast (nanosecond scale) charge redistribution between capacitors $C_{21}$, $C_{23}$, and $C$; 3) discharge of the system (microsecond to millisecond time scale). We assume the $C_{21}$ charging event is much faster than any discharge or charge exchange process, because it is defined by the laser pulse duration ~1 ps. With this assumption, the initial voltage $U_{21}$ is defined by the charge $Q_{21}^0$ generated during the light action: $U_{21}(0) = Q_{21}^0 / C_{21}$. The initial charges of the probe capacitor $C_{23}$ and the cable are supposed to be negligible: $Q_{23}(0) = 0$, $Q_C(0) = 0$.

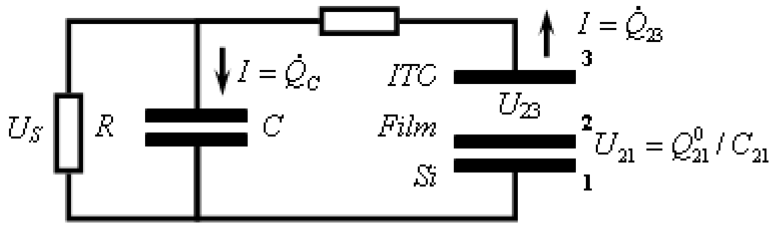

Figure 13. Equivalent circuit for the capacitive probe shown on Figure 12 in the nanosecond time scale.

Fast voltage jump $U_{21}$ causes charge exchange in the system. Now the cable and probe electrode are being charged by the capacitor $C_{21}$. At this step we take into account finite impedance of the cable $Z = 50\ \Omega$. The initial voltage jump is compensated by the voltage drop $U_C = IZ$ , where $I$ is the electric current through the cable. At this time scale we can neglect the current through the oscilloscope, because its input impedance is $R = 1$ MΩ, so that $RC \sim 400$ µs, and $RC >> ZC \sim 20$ ns. At this relatively fast time scale of the charge exchange we also can neglect the $C_{21}$ discharge and consider $U_{21}$ to be constant. (We expect the typical relaxation time of transient dipoles in the organic film to be in the range of 10-100 µs, while time constants $ZC_{23}$ and $ZC$ are in the nanosecond range). Finally, we can describe the second step of the charge exchange by the next system of Kirchhoff's equations according to the equivalent electric circuit shown on Fig 13:

$$\begin{aligned} &U_{21} = U_{23} + U_C + U_S \\ &I = \dot{Q}_{23} = \dot{Q}_C \end{aligned} \tag{2}$$

Taking into account Ohm's low $U_C = IZ$, noting that $U_{21} = Q_{21}^0 / C_{21}$, $U_{23} = Q_{23} / C_{23}$, $U_S = Q_C / C$, and denoting for the simplicity: $k_{23} = 1/ZC_{23}$ and $k_C = 1/ZC$, we can rewrite the system (1) in the next form:

$$\begin{aligned} &k_{23}Q_{23} + \dot{Q}_C + k_C Q_C = \frac{Q_{21}^0}{C_{21}Z} \\ &\dot{Q}_{23} - \dot{Q}_C = 0 \end{aligned} \tag{3}$$

Using a Laplace transform with initial conditions $Q_{23}(0) = 0$, $Q_C(0) = 0$, we can convert the system of differential equations (3) to the system of linear equations, the latter being presented in the matrix form as follows:

$$\begin{pmatrix} k_{23} & s + k_C \\ s & -s \end{pmatrix} \begin{pmatrix} \tilde{Q}_{23} \\ \tilde{Q}_C \end{pmatrix} = \begin{pmatrix} Q_{21}^0 / sC_{21}Z \\ 0 \end{pmatrix} \tag{4}$$

Here, $\tilde{Q}_{23}(s)$ and $\tilde{Q}_C(s)$ are Laplace transforms of $Q_{23}(t)$ and $Q_C(t)$, respectively. The solution for the system (4) is

$$\begin{pmatrix} \tilde{Q}_{23} \\ \tilde{Q}_C \end{pmatrix} = \begin{pmatrix} \dfrac{1}{s + k_C + k_{23}} & \dfrac{s + k_C}{s(s + k_C + k_{23})} \\ \dfrac{1}{s + k_C + k_{23}} & \dfrac{-k_{23}}{s(s + k_C + k_{23})} \end{pmatrix} \begin{pmatrix} \dfrac{Q_{21}^0}{sC_{21}Z} \\ 0 \end{pmatrix} \tag{5}$$

It can be written in the simplified form:

$$\tilde{Q}_{23} = \tilde{Q}_C = \frac{Q_{21}^0}{C_{21}Z} \frac{1}{s(s + k_C + k_{23})} \tag{6}$$

Applying an inverse Laplace transform to (5) we get:

$$Q_{23}(t) = Q_C(t) = \frac{Q_{21}^0}{C_{21}Z(k_C + k_{23})}(1 - e^{-(k_C + k_{23})t}) \tag{7}$$

Equation (7) leads to the quite obvious conclusion. Because the charge exchange on the nanosecond time scale is controlled by the same current $I = \dot{Q}_{23} = \dot{Q}_C$, the cable and probe capacitor are charged equally, and at the time scale $t$ □ $(k_C + k_{23})$ □ 10 ns the charge and voltage distribution are defined just by the capacities of the appropriate elements:

$$\begin{aligned} &Q_{23}^0 = Q_C^0 = \frac{Q_{21}^0 C C_{23}}{C_{21}(C + C_{23})} \\ &U_{23}^0 = \frac{Q_{21}^0 C}{C_{21}(C + C_{23})}, \quad U_C^0 = \frac{Q_{21}^0 C_{23}}{C_{21}(C + C_{23})} \end{aligned} \tag{8}$$

These values may be taken as initial conditions to evaluate the system dynamics on the microsecond time scale. The equivalent electric circuit for the measurement system at this time scale is shown on Figure 14.

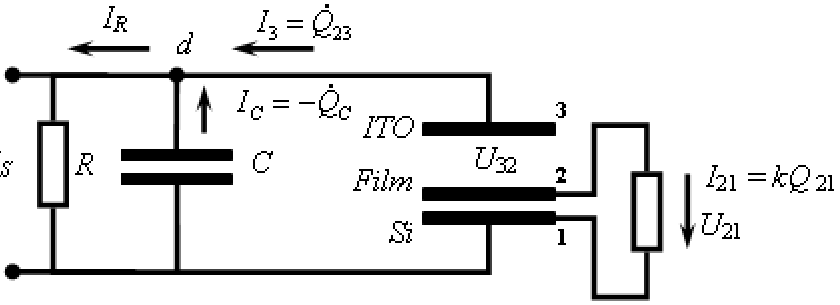

Figure 14. Equivalent circuit for the capacitive probe in microsecond time scale.

Let us consider some additional approximations to simplify the final analysis. After the fast restoration of the balance in the system, we can neglect the voltage drop in the cable. The discharge of the cable is defined now by the input impedance *R* of the oscilloscope, while the cable impedance *Z* = 50 Ω is negligible compared to *R* = 1 MΩ. Another assumption is based on the fact that the faster time constant observed in experiment is in the range of 10 – 20 μs, which is shorter by, at least, the order of magnitude than any time constant related to the electrical discharge through *R*. This fact allows us to conclude, that the discharge of the organic film is mainly caused by the electrochemical annihilation, and like in the previous case we can neglect the current to the outer circuit, so that $I_{21} = -\dot{Q}_{21} = kQ_{21}$. With these assumptions we can write the system of Kirchhoff's equations for equivalent electric circuit presented on Figure 14 as:

$$\begin{aligned} &U_{21} = U_{23} + U_S \\ &I_{21} = -\dot{Q}_{21} = kQ_{21} \\ &I_3 + I_C - I_R = 0 \end{aligned} \tag{9}$$

In the last equation, which represents the currents in the node *d*, we have taken into account that in the shown configuration the current $I_C$ is discharging $C$, while $I_3$ is charging the probe capacitor $C_{23}$, so $I_C = -\dot{Q}_C$, $I_3 = \dot{Q}_{23}$, and $I_C = U_S / R = Q_C / RC$. The voltages $U_{21}$, $U_{23}$ and $U_S$ are defined by the charges accumulated in the appropriate capacitors: $U_{23} = Q_{23}/C_{23}$, $U_S = Q_C/C$, $U_{21} = Q_{21}/C_{21}$. Let as also keep notation $K_{21} = 1/RC_{21}$, $K_C = 1/RC$ and $K_{23} = 1/RC_{23}$. (These constants are much lager than $k_{23} = 1/ZC_{23}$ and $k_C = 1/ZC$). Now the system (9) may be rewritten in the form:

$$\begin{aligned} &K_{21}Q_{21} - K_{23}Q_{23} - K_C Q_C = 0 \\ &\dot{Q}_{21} + kQ_{21} = 0 \\ &-\dot{Q}_{23} + \dot{Q}_C + K_C Q_C = 0 \end{aligned} \tag{10}$$

Applying a Laplace transform with the initial conditions (8), we convert (10) to the system of linear equations presented in the matrix form as:

$$\begin{pmatrix} K_{21} & -K_{23} & -K_C \\ s+k & 0 & 0 \\ 0 & -s & s+K_C \end{pmatrix} \begin{pmatrix} \tilde{Q}_{21} \\ \tilde{Q}_{23} \\ \tilde{Q}_C \end{pmatrix} = \begin{pmatrix} 0 \\ Q_{21}^0 \\ 0 \end{pmatrix} \tag{11}$$

The solution of the system (11) is:

$$\begin{pmatrix} \tilde{Q}_{21} \\ \tilde{Q}_{23} \\ \tilde{Q}_C \end{pmatrix} = \frac{1}{D(s)} \begin{pmatrix} 0 & K_{23}K_C + s(K_{23}+K_C) & 0 \\ (s+k)(s+K_C) & K_{21}(s+K_C) & -K_C(s+k) \\ -s(s+k) & K_{21}s & K_{23}(s+k) \end{pmatrix} \begin{pmatrix} 0 \\ Q_{21}^0 \\ 0 \end{pmatrix}, \tag{12}$$

where $D(s)$ is a discriminant of the matrix presented in (11):

$$D(s) = s^2(K_{23} + K_C) + s(kK_{23} + kK_C + k_{23}K_C) + kK_{23}K_C = \\ = (K_{23} + K_C)(s + k)(s + \frac{K_{23}K_C}{K_{23} + K_C}) \tag{13}$$

The solution for $\tilde{Q}_C\,(s)$ can be found in form:

$$\tilde{Q}_C = \frac{s \cdot K_{21}Q_{21}^0}{D(s)} = \frac{K_{21}Q_{21}^0}{(K_{23} + K_C)} \frac{s}{(s + k)(s + K_\Sigma)} \tag{14}$$

Here we denote $K_\Sigma = K_{23}K_C / (K_{23} + K_C) = 1/(C_{23} + C)R$. Applying the inverse Laplace transform to (13), we can find $Q_C(t)$ and the final signal $U_S\,(t) = Q_C(t)/C$:

$$U_S(t) = \frac{K_{21}Q_{21}^0}{(K_{23} + K_C)(k - K_\Sigma)C}(ke^{-kt} - K_\Sigma e^{-K_\Sigma t}) \tag{15}$$

The last expression can be modified to the simplified form if we denote $1/K_\Sigma = \tau$ and $\frac{K_{21}Q_{21}^0}{(K_{23} + K_C)C} = \frac{C_{23}}{(C_{23} + C)C_{21}}Q_{21}^0 = U_0$:

$$U_S(t) = \frac{U_0}{k\tau - 1}(k\tau e^{-kt} - e^{-t/\tau}) \tag{16}$$

The expression (16) shows that a monodisperse charge recombination gives rise to a bi-exponential signal. Let us consider rapid recombination of the dipoles: $k\tau >> 1$. Now, it is more convenient to discuss the response (16) if it is presented in the form:

$$U_S(t) = U_0 e^{-kt} + \frac{U_0}{k\tau - 1}(e^{-kt} - e^{-t/\tau}) \tag{17}$$

The first additive term in the equation (17) reflects the kinetics of the surface charge displacements. The second term is the deviation of the measured signal from the charge transfer dynamics. It is important that the transient crosses the $U_S = 0$ level before recovering the base line. Such behavior is an intrinsic property of the *RC* chain and reflects the simple fact that the probe *charges and then discharges* during the measurements, while the oscilloscope measures the *current* through its input resistance. So, the second term in equation (17) reflects the input resistance of the oscilloscope and the capacity of the sample/probe capacitor and therefore depends on the size of the sample, length of the cable and other instrumental parameters. However, in the discussed case, $k\tau >> 1$, the amplitude of the instrumental part of the response is considerably smaller than the amplitude of the signal related to charge dynamics in the sample. Therefore, the best condition for the measurements is $k \gg 1/\tau = 1/(C_{23} + C)R$, which may be controlled by increasing the input impedance, capacity of the probe $C_{23}$ (i.e., by increasing the size of the surface, or decreasing the thickness of the spacer) or the cable capacity $C$ (i.e., by increasing the length of the cable). In our experiments the instrumental time constant was in the range 0.2–2 ms.

When $k\tau \ll 1$, the rapidly formed voltage $U_0$ will dissipate as a result of charge redistribution between the plates 1 and 3 through the oscilloscope. Now, the faster component will reflect the instrumental time constant $\tau = R(C_{21} + C) \ll k$. At longer time scale the system dynamics will reflect the dynamics of charge annihilation. Because the amplitude of the first term in Equation (16) becomes small compared to instrumental term, this configuration is not very useful for measurements. However, even in this configuration it is possible to estimate charge annihilation rate $k$.

### 2.2.2. Experimental Results

The functionalized with amino groups silicon chips were prepared and left as is or topped with the either sparse or dense layers of NTCI(A) as described in *step-A* materials and method section. The electrometric measurements have been performed using set up shown schematically on Figure 3, but with uncoupled upper electrode. This electrode was a 200 nm thick ITO (indium tin-oxide) film deposited on a glass plate and separated from the NTCDI(A) film on the silicon surface by a 0.025 mm insulating spacer (Figure 12). The input impedance of the Tectronics TDS 3032 oscilloscope was set to 1 MΩ. In the experiments with an external 1:10 voltage splitter the apparent input resistance was 10 MΩ. In these experiments a 1/10 of the actual voltage has been applied to the input channel of the oscilloscope. The excitation light pulses at 800 nm were generated by the Ti/sapphire laser system. The pulses had 1 ps duration, 10 µJ energy (attenuated with the set of neutral density filters), and 1 kHz or 200 Hz repetition rate. Note that NTCI(A) does not absorb at 800 nm in contrast to 532 nm utilized in the experiments of previous section. The signals were recorded by averaging of 512 oscilloscope traces. The maximum sampling rate was 2.5 GS/second.

A typical photovoltaic signal from the sparse film of the NTCI(A) molecules is shown in the Figure 15. It is complex and includes ~20 ns grouing up part, heterogeneous decay below $V = 0$ and recovery to the base line. The polarity of the signal corresponds to charging the NTCI(A) film positively. This observation perfectly agrees with our previous assumption (*section 2.1*) that silicon photo-oxidizes the neutral NTCI(A) molecules, which form cation-radicals upon ejection of electrons into the semiconductor.

Minor electric responses are observed even in the absence of the NTCI(A) coating. Bare silicon surfaces are often contaminated with electrochemically active impurities. Such “as is” surfaces give highly irreproducible electric responses, which strongly decrease after rinsing the surface with acetonytrile (the data are not shown). This artifact is almost completely gone after $NH_2$-functionalization of the silicon surface (Figure 15). The remaining signal could originate from certain polarization of the silicon waffle due to introduction of the gradient of the minority charge carriers near the surface [72]. Another possibility is the light-induced change of the built-in potential [93]. Regardless of its nature, this artifact is minor. No signal is observed when the surface of silicon is protected by a thick (>200 nm) insulating layer of

$SiO_2$. The insulating oxide layer prevents both the interfacial redox chemistry and band bending.

While the initial charge separation is too fast to be resolved electrometrically, the heterogeneous recombination is time-resolved clearly. The fast and intermediate phases are independent of the input resistance and have a time constant of ~ 10 µsec and ~100 µsec, respectively. The contribution of the slower component into the signal varies among the samples and is about 1/3 of the total amplitude of the signal presented in Figure 13 (spare film of NTCDI(A)). The third, slowest negative component, demonstrates a clear proportionality to the input resistance and stretches 10-fold upon addition of a 9 MΩ additional resistor. Therefore, the baseline recovery likely represents the instrumental function as outlined in equations 16 and 17. This recovery component is difficult to measure because of its small amplitude.

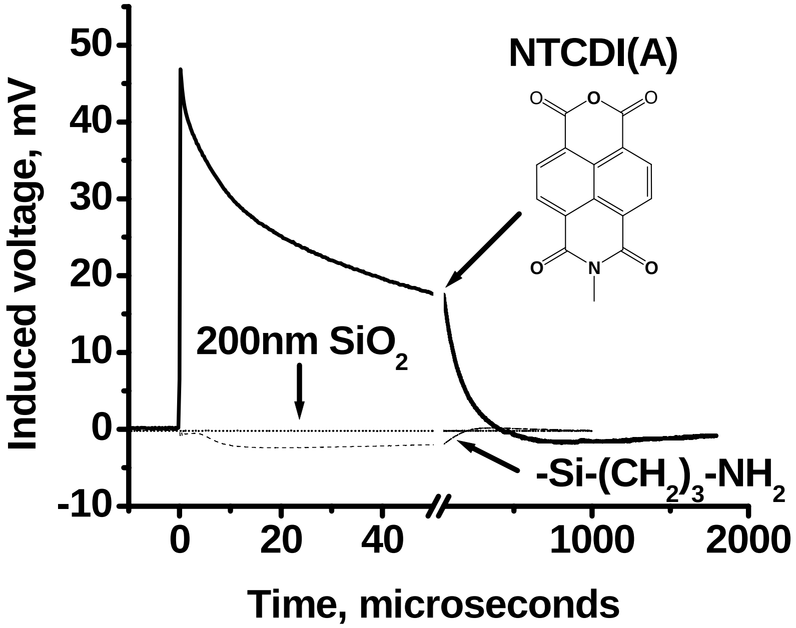

Figure 15. Light-induced voltage transients. Samples were used as capacitor faces separated from the ITO probe electrode by a 25 µm insulating spacer. The voltage transients represent polarization and depolarization of the Si/film junctions: Si/NTCDI(A) (solid line), Si/$SiO_2$ (dotted line), Si surface derivatized with amino groups (dashed line).

It is important to note that in the dense NTCI(A) films the contribution of the slow (~100 µsec) component of the photovoltage decay does not exceed 10% [94] (Figure 14). This observation well agrees with our previous conclusion that in the dense films the molecules rapidly exchange the oxidizing equivalent with their neighbors (*section 2.1*). Therefore, the positive charges formed in the “slow” molecules drain back to the silicon substrate via the two-step process: (i) exchange with the “rapid” molecules within connected redox network and (ii) the following discharge of these “rapid” molecules. Overall this process is apparently faster than the direct discharge of the "slow" molecules. It is also important to note that these "slow" NTCI(A) molecules can be pre-charged in the discontinuous networks with the intense constant light [95]. A strong continuous illumination decreases the total amplitude of the signal, mainly at the expense of the slow component while the fast component remains essentially unchanged. The heterogeneity of the recombination most probably reflects the micro-heterogeneity introduced by the silicon cleaning procedures and/or the microscopically uneven thickness of the siloxane layer. Similar kinetic heterogeneity has been observed in PTCDI-doped SAMs grown on ITO by single molecule fluorescence analysis [96] and has been attributed to the differences in the local environment.

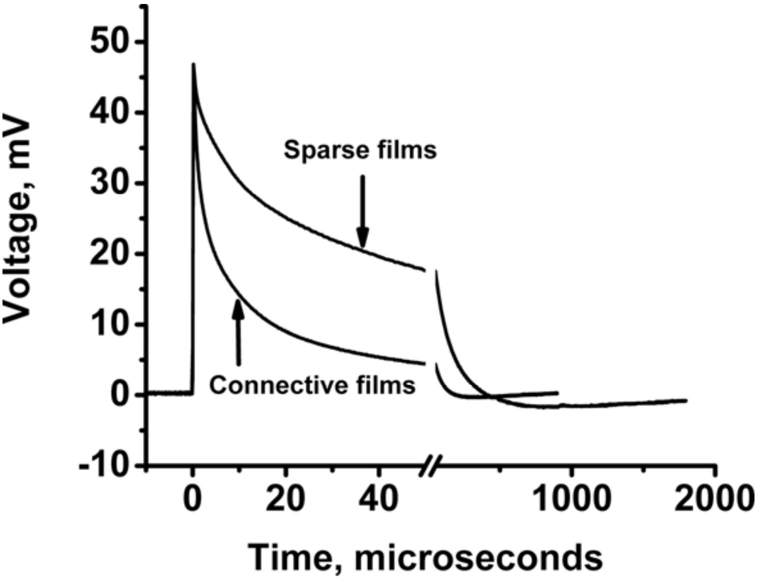

Figure 16. Charge recombination in connective and sparse films.

In contrast to the photosynthetic light-harvesting antennas, the energy of light is conserved by the SAM-PVC via interfacial electron transfer. The silicon/film junction forms an electrochemical capacitor charged by the light. This capacitor stores both the electrostatic energy and the free energy of the back recombination [96]. It is important to be able to measure and control the discharge characteristics of this capacitor in order to utilize it as an energy source. The electric field formed within this capacitor is picked by the auxiliary electrode and can be measured directly.

The time resolution limits of capacitive probing are defined instrumentally. A typical 2G-sample/second oscilloscope is convenient to measure charge transfers that are not much faster than ~ $10^8$ $s^{-1}$. The reactions, which are slower than the instrumental time-constant, are also inconvenient to measure. Therefore, the ideal dynamic range for the capacitive measurements is between $10^3$-$10^8$ $s^{-1}$.

Capacitive probing has lower time-resolution than the pump-probe spectroscopy but is free of certain limitations of the latter. First, it is independent on the optical properties of the semiconductor. Second, it works with flat surfaces which contain much less molecules than suspensions of nano-particles [97]. Indeed, separation of only $5.5 \times 10^9$ charges per $cm^2$ across

~ 20 Å will induce a strong enough signal with amplitude of ~ 1 mV (for $\varepsilon \approx 2$). This number of molecules dissolved in 1 $cm^3$ corresponds to a less than 10 pM concentration which is far below the sensitivity limit of any spectroscopic method except for fluorescent techniques [96]. However, the electrometric approach works with non fluorescent molecules and provides a nanosecond time-resolution. The technique also provides the direction of the charge transfer.

Measurement of interface charge transfer response from ultra-fast spectroscopy is complicated in general case. The interpretation of transfer kinetics is even more challenging. For example, in well-studies Gratzell photovoltaic cells [98], the origin of two charge transfer kinetics in femtosecond range [99] is not clear. Luckily, for SAM-OFET such delicate measurements of interface charge transfer are not required, since the kinetics of charge transport in conductive NTCDI channel is in microsecond range [119]. Nevertheless, in this scale several components of kinetics (~10 μsec and ~100 μsec) have been observed. We tested few control sample devices to discriminate direct charge injection kinetics. We note that thick NTCDIA films measured with capacitor probe showed mostly long type kinetics. This likely can be attributed to trapping of the charge the molecules, which do not have a contact with Si substrate. Exact physics of *long*-component response in thick NTCDI film still have to be proved unambiguously. However, it is clear that *short-component* of decay function (~10 μsec) characterize interfacial back charge transport from NTCDI to the substrate. This component was the main one in pure SAM-devices. Therefore, we can apply developed model to determine kinetics of charge recombination and compare with kinetic of charge transport.

### 2.3. Reversing Conductivity Channel in SAM-PVC (Closed-Circuit Measurements)

The preparation of efficient *n-type* conductive channel in addition to *p-type* conductive channel is another challenge in OFET fabrication. Moreover, it is highly desirable that *n-* and *p*-channel OFET devices were fabricated by technologically comparable methods. Mainstream research direction in OFET is attempting to develop suitable organic materials for *n-type* conductive OFETs. Contrary to this mainstream studies, we are trying to develop switching of type of conductive channel based entirely on type of substrate, which is p- or n-type Silicon. The idea behind this study is the fact that 'static' charge transfer self-assembled monolayer should be greatly affected by type of substrate due to proximity effect. Thus different type of 'Shotkey barrier'-like structure is conceivable. In turn, it could change the type of conductive channel in SAM material. To verify this assumption we perfomed a photophysical study in SAM-PVC devices. The silicon chips functionalized with amino groups were prepared and topped with the dense layers of NTCI(A) on n-type and p-type silicon substrates in the same manner as described in step-A section of materials and methods. Here, p-type silicon substrates (Si(100), 100 Ω·cm, Virginia Semiconductors) were tested in addition to silicon wafers of n-type (Si(100), 500 Ω·cm, Virginia Semiconductors). Both wafers had 20 Å of $SiO_2$ coating. SAM-PVC devices were tested by time-resolved photovoltaic measurements in closed-circuit SAM-PVCs as described in *section 2.1*. Devices were illuminated at the distance 10 mm from collective electrodes.

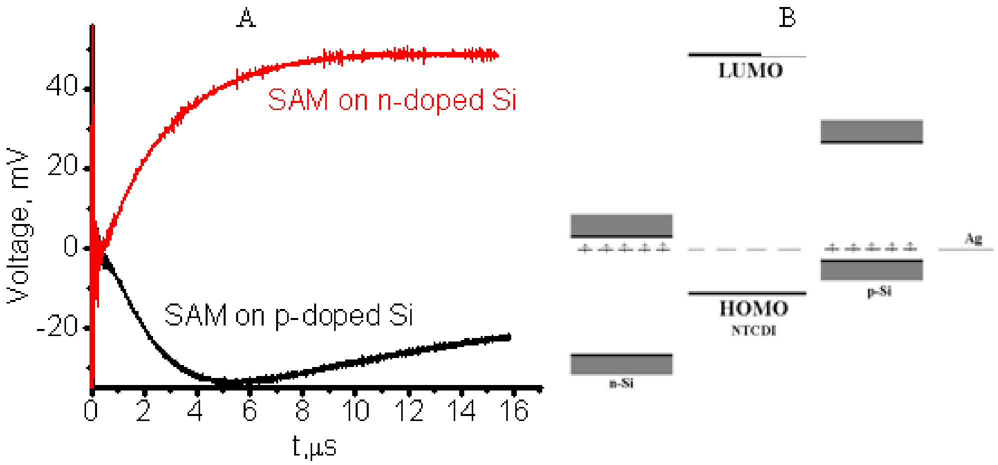

Figure 17. (A) Photoresponse of NTCDI SAM-PVC placed on n-doped and p-doped silicon wafer; (B) possible scheme of molecular level, which explain switching conductivity channel in SAM-NTCDI.

Result of these measurements is shown in Figure 15. The change of the response poliarity clearly indicates the conductivity type in NTCDI conductive channels switches and depends on conductivity type of the substrate. Difference in response kinetics is related to difference in heterostructures, doping level of Si and possible SAM density. Direct SAM-OFET testing of this idea is more complicated. Such test will require development of metal electrodes and surface chemistry to establish chemical bond between metal and organics, which would have requested charge injection ability. Nevertheless, the described experiment could be taken as proof of concept of such approach. Complementary circuit design should be very straightforward once this approach will be developed for SAM-OFET. The simplicity of this approach will be due to the possibility to use the same material (as NTCDI SAM matrix) for different types of conductivity.

## DISCUSSION: POLARON TRANSPORT MECHANICS

This chapter is focused on study of a correlation between dynamic properties and charge mobility in NTCDI SAM systems. This research is connected to similar studies in bulk crystals of N. Karl group [100]. These publications reported a direct time of flight measurements of charge carriers in bulk crystals of organic aromatic compound. It is remarkable that ten years ago, in 1998 N. Karl bring question “Fast electronic transport in organic molecular solids?” in the title of their paper [101]. It has been demonstrated unambiguously that charge transport in the bulk crystals is intrinsic. Therefore, these researches bring a hope for generation of scientists, who developed the field of molecular electronics. In this spirit, in the beginning of this section, the question “Fast electronic transport in SAMs?” will be discussed. We have to note a difference between our experiments and the research of N. Karl group [101]. The time of flight experiments were carried out in thin organic crystals (0.2 to 1 mm thick) by applying electric field across the sample and

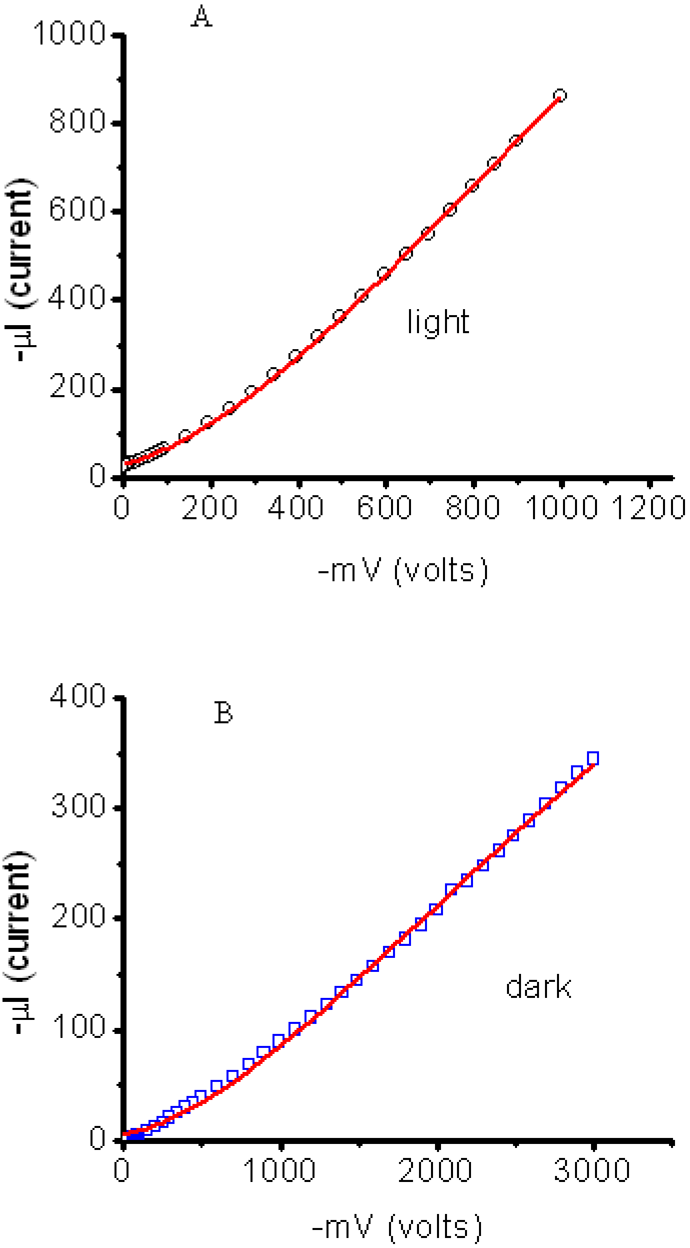

Figure 18. Photoresponse of NTCDI SAM-PVC, as “marked area” at Figure 7 and fit ln *I* ~ $E^{-2/3}$ over experimental data for (A) photocurrent and (B) dark current.

registering the transient electric current created by illumination of the surface of the crystal by a short laser pulse. Karl et al were focused on charge mobility measurements, but simple estimate shows that the speed of charges in the sample achieved $10^3$ m/s (at 300 K) to $5{\cdot}10^4$ m/s (at 40 K) with applied electric field 20-40 kV/cm. In our experiments we did not apply longitude (*in-plane*) or interface (*out-of-plane*) biases to avoid bias polarization phenomena in SAM. In addition, our photovoltaic study was aimed to distinguish between charge transport and charge recombination processes. Nevertheless, we have sown that in SAM the speed of charge diffusion can be as high as $10^4$ m/s at room temperature (Figure 10). One could expect that this speed may be even higher if the bias is applied along the surface. Even more surprising is the capability to initiate an electron or hole conductivity in SAM-NTCDI (Figure 16) by changing type of doping of the Si substrate as it was observed in perylene crystal by applying different polarity of the electric field. Due to technological reason, we could not self-assemble perelene molecules on Si (sublimation temperature of perylene tetracarboxyl dianhydride is 200 °C higher than of NTCDI). However, naphalene and perylene belong to the same class of disc-shaped aromatic compounds with extended π-electron system. Therefore, a certain analogy of transport properties is anticipated, if similar packing is achieved. It is possible to conclude that, despite of the difference between photocurrent measurements in organic crystal and SAM film, the transport phenomena are very similar and velocities of charge waves in crystal and SAM film are roughly at the same range. Moreover the speed of charges in SAM film exceeds the same rate in organic crystal. This observation is an opposite of what could be expected from transport in 3D vs. 2D systems [101]. This discrepancy could be explained by role of Si substrate in NTCDI SAM/ Si heterostruture, as discussed below. Due to barrier structure of this interface, out-of-plane charge transfer from NTCDI to Si could sustain in-plane current. The contribution of this mechanism is absent in crystal.

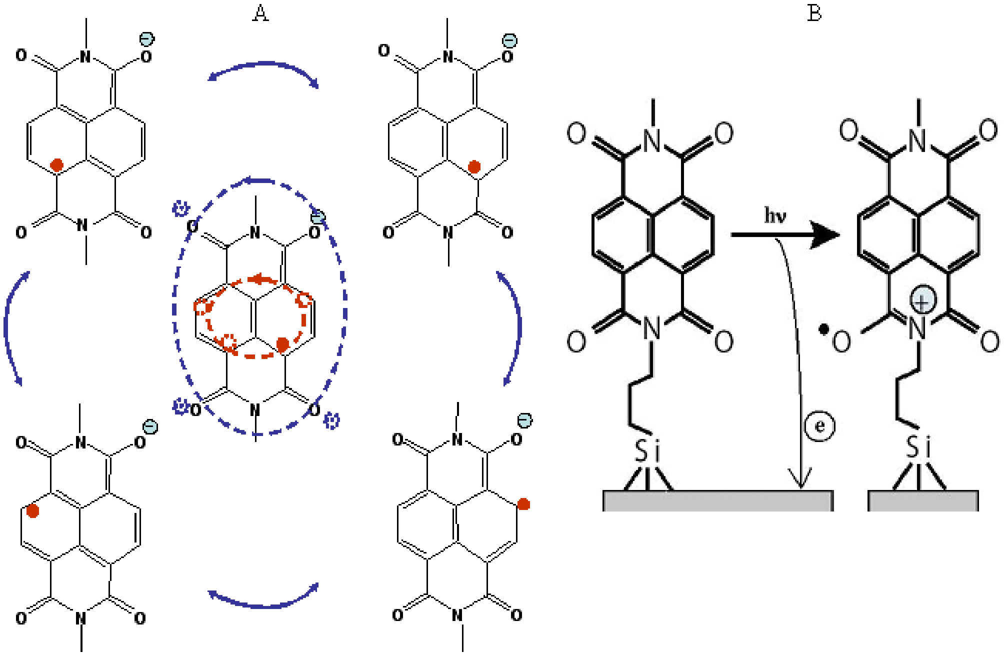

Figure 19. Variety of possible cation-radicals in NTCDI molecules on molecular level. (A) Formation of anion-radical state. (B) Formation of cation-radical state. This redox state could be exchanged extremely fast with neighboring neutral NTCDI molecule and transport a redox state to harvesting electrode thought self-exchange reactions. This transfer of redox state is illustration of polaron transport in SAM-NTCDI on nano-scale level.

Experimental results clearly indicate on the possibility of polaron transport in NTCDI-SAM 2D channel, which is located along the substrate plane. Such possibility was theoretically predicted by Horovitz [102]. He suggested that polarons dominate the photocurrent I due to a novel electric field–assisted tunneling route for which $\ln I \sim E^{-2/3}$. The negative area of our experimental SAM-PVC I-V (Figure 8) taken under illumination and dark conditions is presented at Figure 15 for *in-plane* currents. The Horovitz model ($\ln I \sim -E^{-2/3}$) is used to fit our experimental data.

We take these results as an evidence of possible polaron transport mechanism in SAM-NTCDI conductive channel. Moreover, an estimate of front velocity of electronic wave in SAM-NTCDI system, (Figure 10) result in the diffusion parameter $D\sim10^4$ cm$^2$/s, which is close to speed of the polaron transport. In addition, the photovoltaic studies make possible to discuss a possible type of polaron system in SAM matrix.

This polaron transport is likely realized in SAM-PVC device through random walk mechanism. Excited redox state likely employs percolation-defined random walk [103], which is exemplified in Figure 18.

The set of redox reactions occurring in NTCDI channel (Fig 18) includes three steps:

1. $Si^* + NTCDI \rightarrow (Si^-) + (NTCDI^+)$: photo-oxidation (18)
2. $(NTCDI^+) + NTCDI \rightarrow NTCDI + (NTCDI^+)$: dark self-exchange
3. $(NTCDI^+) + Ag \rightarrow NTCDI + Ag+$: dark harvesting.

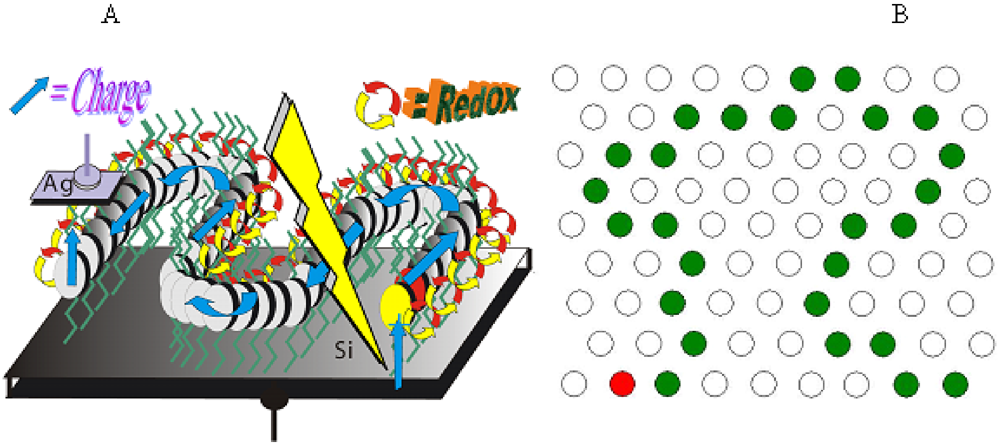

Figure 20. Possible cation-radicals in NTCDI molecules at macroscopic scale. (A) 3D cartoon of random walk transport of redox state from illuminated area to harvesting Ag electrode. (B) Top view of redox transport at macroscopic scale. Note that this system could potentially handle a large current density due to possible multi-channel transport in organic 2D system. Only one conductive channel is shown here for simplicity.

Results of photocurrent measurement in SAM-PVC could rationalize a high mobility measurement in SAM-OFETs. Indeed, assuming initiation of the same redox transport in SAM-OFET, a polaron level mobility might be expected. Assuming polaron nature of transport in SAM-OFET, we could expect to increase the charge mobility, which currently is achieved to be as high as 31.5 $cm^2 V^{-1} s^{-1}$. It is a few orders of magnitude higher than in the bulk organic crystals. This mobility level could bring performance of SAM-OFET on the level of amorphous silicon FETs. This conclusion could be confirmed by photovoltaic response in control devices (defined at materials and method section), which were illuminated by light at the vicinity of contact upon different scope loads: 50 Ohm and 7.6 kOhm (Figure 19). A different scope load in this case define the time-scale and sensitivity of measurement.

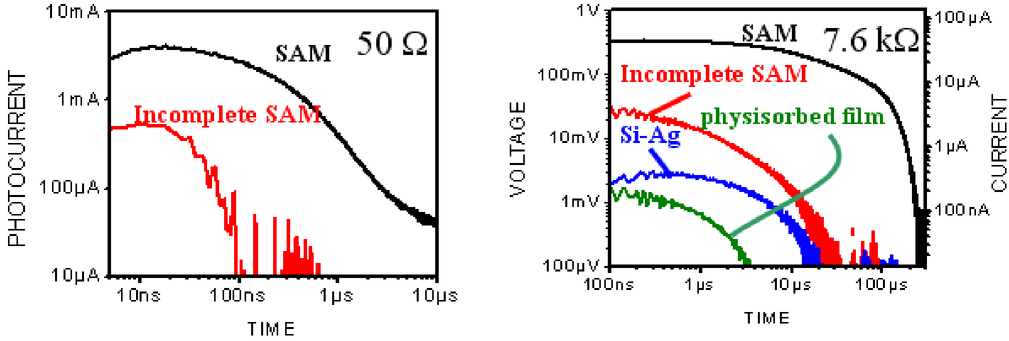

Figure 21. PV response in control devices with illumination at the vicinity of the contact upon different scope loads: 50 Ω and 7.6 kΩ.

In addition to SAM film, a thick (~300 nm) films of NTCDA and $C_6$-NTCDI were prepared by physisorption of NTCDA on the cold functionalized surface of silicon. This sample has been marked above as physisorbed film. Sparse NTCDI films were obtained from thick films of NTCDA by heat desorption of the excess of NTCDA followed by *step c*. This sample has been marked above as incomplete SAM. Response of Si-Ag point contact was included for comparison. Only the sample with complete SAM demonstrates a long-range charge delivery (~ 1 cm illumination from the electrode). The maximum voltage in SAM films exceeds that in incomplete SAM and physisorbed films by 2–3 orders of magnitude. These results clearly demonstrate that any incompleteness and disorder in SAM conductive channel affects redox self-exchange reactions on microscopic level. The time-scale of the SAM device response also demonstrates an ability of complete SAM structure to deliver charges from remote areas, in contrast to other tested devices. It is also notable that only SAM-device and incomplete-SAM-devices give rise to photo-signal at finest time scale-resolution wit 50 Ω input resistance of the oscilloscope. The fact that Si-Ag device has a higher efficiency than the device based on NTCDI-C6 physisorbed film is due to shielding of incoming light by a thick film.

Transport properties of NTDCI SAM OFETs and PVCs clearly point on polaron nature of the transport. The way to prove this hypothesis is to find the way to block cation-radical exchange in the transport channel and observe change in transport properties in these devices. Experiment which addresses this possibility is shown at Figure 20. It proves the importance of redox capability to polaron transport on the molecular level. PV response of ~150 mV was observable in NTCDI-C6 film under illumination 3 mm away from Ag harvesting electrode, while no PV effect was observed in the case of NTCDA film. NTCDA molecules could not be oxidized at normal conditions. Thus, any un-reacted physisorbed molecular cluster will serve as an isolator for polaron transport (‘redox blockade’). It is also known that OFET based on NTCDA molecules shows mobility of $10^{-4}$ cm$^2$ V$^{-1}$ s$^{-1}$ [104], while NTCDI-based OFET routinely demonstrates mobilities, which are higher by factor $10^3$ [105]. Thus, the experiment on Figure 20 demonstrates evidence of polaron transport on the molecular level, in addition to importance of the macroscopic order. It is also notable that OFET based on NTCDA molecules [105] shows mobility of $10^{-4}$ cm$^2$ V$^{-1}$s$^{-1}$, while NTCDI-based OFET [105] routinely demonstrates mobilities, which are by $10^3$ factor higher. Therefore “redox blockade” experimental (Fig 20) and literature data prove the polaron transport in the NTCDI-SAM channel. Thus, any unreacted physisorbed molecular cluster will serve as an isolator and trap for polaron transport.

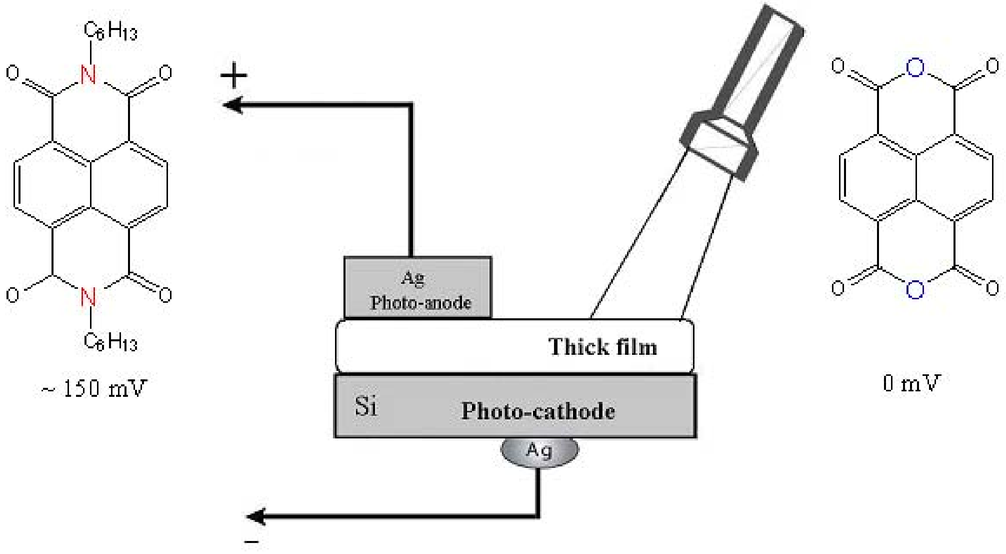

Figure 22. Light harvesting in thick films: molecular redox. Only film composed from C6-NTCDI-C6 molecule, which contains nitrogen atom (red color on the left panel), was active in long-range harvesting. NTCDA molecule with unsubstantiated oxygen (blue color on the right panel) could not sustain long-range any redox transport. We took this fact as an evidence of polaron transport in latent channel in SAM-PVC and SAM-OFET devices.

Polaron conductive mechanism could explain why at the current stage it is so difficult to achieve high mobility in SAM-OFET. Both macroscopic and microscopic orderings are important for polaron transport and this impose strict conditions on quality of SAM conductive channel. Taking into account short range of dipole-dipole interaction, any defect could trap redox state. In addition to that, trapped redox state will form stable charged trap, which will prevent transport not only through the defect point, but also in the vicinity of this defect. Trapped redox state should affect the efficiency of charge transfer more than existence of non-reactive molecular cluster, which not carrying any charge. As the number of such trap exceeds percolation limit, no polaron transport will exist in such a system. Thus, in some analogy to biological systems, a redox active path in SAM matrix and good packing are the pre-condition for an efficient charge transport in the SAM systems.

Based on this assumption, we suggest that switching of conductivity type is possible in conductive channel. It is due to the fact that (i) various forms of cation-radical are possible and (ii) proximity of interface with inorganic semiconductor. Formed anion- and cation radicals as shown at Figure 17 correspond to p- and n-type conductive channel in OFET. Our SAM-PVC measurements indicate that changing doping of substrate could indeed change the current sign and, thus, the type of conductive channel in SAM-PVC. Although this assumption should be confirmed in SAM-OFET system, our observation could result in alternative way to achieve efficient OFETs with tunable type of conductive channel. Moreover, one could conceive the cascade FET devices, which would have variable mobility in conductive channel according to selective doping of substrate.

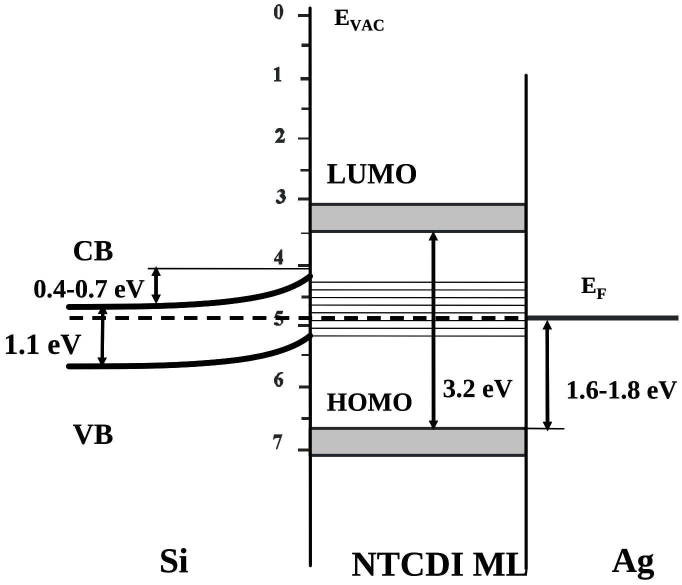

Figure 23. Energy diagram of heterostructure of 2D NTCDI transport channel according to SAM-PVC studies.

Finally, we could summarize results of our SAM-PVC and reported studies [106, 107] at energy diagram, which shows positions of the energy levels at the heterostructure of p-type 2D NTCDI transport channel, at Figure 21. Left part of this diagram shows conductive (CB) and valence (VB) bands in silicon substrate and slope of the bands, as they approach to the interface with SAM NTCDI. Middle panel demonstrate HOMO-LUMO (HOMO = highest occupied molecular orbital, LUMO = lowest occupied molecular orbital) gap and COB (COB = continuum of band, [108]) of NTCDI monolayer. The right part of diagram shows position of Fermi level $E_F$ of Ag electrode.

The Si/NTCDI interface of SAM-PVC (left part of Fig 21) models the interface of conductive channel on silicon in SAM-OFET device. In this interface the *out-of plane* photo-oxidation of NTSDI takes place. Structure of NTCDI SAM is modeled at the middle part of diagram. This part is responsible for the charge transport in SAM-OFET NTCDI 2D system. Set of thin lines in the vicinity of $E_F$ shows continuous of band (COB) of 2D NTCDI system, which is also called sometime “the-states-in-the gap”. Transport through COB is *in-plane* dark self-exchange step in equation 18. Note that SAM-PVC device does not have direct access to HOMO-LUMO levels, neither SAM-OFET. Of course, molecular orbitals change essentially their distribution as the redox undergoes through molecule, but charges do not have to overcome energy barriers, which involve molecular LUMO orbitals. Boundaries of molecular stacks are the only places where tunneling is governing transport mechanism [109, 110, 111]. The right panel of Figure 21 shows the Fermi level of the electrode inside the COB. The possibility of such position of $E_F$ was proven at ref. [113]. This part of SAM-PVC system corresponds to *out-of-plane* dark harvesting (*equation 18*) and should model charge injection into NTCDI channel from Au electrodes in SAM-OFETs. Figure 21 represent the "static" model which describe SAM heterostructure in neutral manifold. While the polarons are propagating along the *in-plane* COB channel, the out-of-plane electronic "pump" (*reaction 1* at Figure 7) could provide an electrical motion force for the charge-delivery. This contribution could explain the higher charge speed in SAM layer than in organic crystal, as discussed in first paragraph of Discussion section.

Therefore, the charge kinetic studies described in *section 2.2* demonstrate that the out-of-plane charge injection can be discriminated. This discrimination is possible through illumination of the SAM-PVC device in different positions. Thus, variable kinetic of in-plane charge transport could be separated from the constant value of charge injection. The whole balance of device kinetics can now be visualized and used for optimization of the SAM-OFET design. Our studies underline the importance of careful comparison of the electrical and optical data to discuss major transport mechanism in SAM system. *Section 2.3* of this chapter demonstrates that a photocurrent study was the only way to split and estimate performance of different OFET component, such as conductive channel and electrodes. Using optic and electronic studies we were able to evaluate the major transport mechanism in SAM-OFET. A complex interplay of the molecular properties and solid-state properties was highlighted by SAM-PVC studies in NTCDI conductive channel.

There are questions about the optimal structure of conductive channel in the OFET, which include determination of what kind of crystal packing (e.g., herringbone versus π-stacking) is most favorable for the charge transport and whether intermolecular electronic cloud overlap can be enhanced by tuning the crystal packing (e.g., the degree of intermolecular ring slip) or by increasing the strength of intermolecular bonding [112,113]. Our results indicate that high charge mobility could be achieved in a herring-bone packing molecules, for example NTCDI molecules, which have one of the highest mobility for organic molecules. Significantly, closing the structure-property knowledge gap on low-dimensional phase transitions in organic solids is required component to get insight into structure-property relationship of SAM-OFETs and other organic devices with epitaxial order.

We also want to note that SAM-OFET was used without any protection layer and demonstrated good device stability, which is perhaps one of the most crucial issues in OFET. SAM-OFETs were studied in an operational regime for two weeks without any protection from the ambient. Two-week check of SAM-OFET does not show any decrease of the semiconductor sensitivity due to $O_2$ and $H_2O$. The I-V characteristics do not show a hysteresis as a function of device operating parameters. This result agrees with previous results on OFET performance based on functionalized NTCDI system, such as NTCDI-$CH_2C_6H_4CF_3$ [4]. These structures offer the best combination of high mobility and air stability.

# CONCLUSION

## 1. Estimating Mobility in NTCDI SAM-OFETs

Photocurrent investigation of transport mechanism in 2D NTCDI-based SAM-OFET demonstrates that a moderately high mobility could be achieved in this device. Mobility which we achieve in NTCDI SAM OFET is roughly 10 times larger than the value reported for NTCDI thick film OFETs. We believe that improvement in mobility has been achieved due to the better packing in OFET conductive channel and better condition for redox exchange transport, as is evident from structure-photoresponse study depicted in Fig 19. Experiment with cation-radical blockade in photovoltaic device (Fig 19) and essentially lower mobility in NTCDA thick film OFET device impose the polaron nature of charge transport in NTCDI based thick film OFETs. The possible ways to improve performance of 2D NTCDI-based SAM OFET are (*1*) proper molecular engineering of a metal-SAM charge injecting interface, (2) better contact between SAM layer on electrodes and contacts, (*3*) usage of more efficient redox transport mechanism, (*4*) usage of smaller gap between electrode to limit possible number of defects and (*5*) optimizaton of macro- and micro-scope structure of organic conductive channel to insure the best connectivity of aromatic rings. However, it is unlikely that charge mobility in 2D SAM OFET devices will exceed electron mobility in amorphous silicon, which is ~ 1000 $cm^2 V^{-1} s^{-1}$. This limitation arises from proposed polaron nature of charge transport in studied organic 2D system.

The better charge mobility in SAM OFET could be achieved using (i) different electrode and device configuration in organic compounds or (ii) materials, which demonstrate higher intrinsic mobilities. The *first solution* could be exemplified by self-assembly of benzene molecule between two Pt electrodes with following hybridization of 3 π–electrons from aromatic core and electrons of electrodes [114]. The result is conductivity, which exceed $G_0$ in tunneling regime in this system. The celebrating example of *second approach* for achieving higher mobility is graphine material. Recently physicists have demonstrated that graphene, a single-atom-thick sheet of graphite, has a greater ability to conduct electricity than any other known material at room temperature ($\mu = 2 \cdot 10^5$ $cm^2 V^{-1} s^{-1}$) [115]. In fact, electrons can travel up to 100 times faster in graphine than silicon, making it a likely candidate for semiconductor material replacement in devices like computer chips and sensors. Graphene also has a resistivity of 1.0 μOhm-cm, which is just 35% less than copper. That figure would also make graphene the lowest resistivity material at room temperature. A first field-effect experiments with graphine demonstrated formation of gap state at low temperatures [116], which is extremely promising for a SAM-OFET application. These two systems, graphene and planar benzene congiguration utilize transport mechanisms, which are different from one that we found in NTCDI-based SAM-OFET system.

## 2. Alternative Pathways for Development of SAM-OFETs

A possible avenue for developing 2D NTCDI-based SAM-OFET systems for electronic devices is an approach comprising “intramolecular circuits”, suggested by C. Joachim at 2002 [117]. Here, instead of pursuing highest performance in three terminal FET devices, the new logic devices based on intermolecular circuits in organic 2D system are introduced. The circuit is assumed to be connected by many electrodes. Development of this concept should result in a different design of a logic or intramolecular gate. Another path, which might be explored in 2D NTCDI-based systems, is spin transport in 2D aggregates. It was noted that weak spin-orbit and hyperfine interaction in organic solids is favorable for spintronic applications. This research could also lead to new logic devices, such as spin-OFETs. The specific feature of these two examples is that high mobilities are not pre-required and special properties of organic solids in 2D are utilized to achieve new electronic devices, which are currently not available. It has been suggested that 2D NTCDI-based systems could be used as an artificial model of charge transfer in a biological membrane [119]. In developing this idea, a new type of biosensor could be developed. A new type of biosensor could utilize in real time latent skin current in SAM–OFET and SAM-PVC as a sensor for probing bio-recognition events on interface of SAM. This assumption is based on the robustness of NTCDI-derived structures, pronounced skin-current in SAM-OFET and SAM-PVC devices and chemical capability to continue self-assembly.

## 3. Photocurrent Study as Tool to Elucidate a Transport Mechanism in 2D NTCDI-Based SAM-OFET

We demonstrated in this chapter the development of adequate analytical tools, and combine electric and opto-electronic studies that are crucial for future progress beyond the current stage of SAM-OFETs. In the current state of the art, a variety of Kelvin probe-derived techniques are widely used to determine electron work function and bend banding in organic-inorganic heterostructures. UV and inverse photoemission spectroscopy (UPS, IPES) are used to determine the position of the highest occupied and lowest unoccupied molecular orbitals (HOMO, LUMO). XPS measurements served to estimate band bending. Comparison of these techniques with measured I-V characteristics enables one to determine the mechanism(s) that control charge transfer in molecular diodes. These methods are static, since probing interfaces in time-scale compared to interface charge transfer is very challenging. Ultra-fast spectroscopy was applied to clarify dynamic of charge transfer in organics. Nevertheless, direct observation of the complete dynamics of charge transfer in the interface is still beyond the scope of these methods. We are suggesting using a photocurrent method in a time-resolved regime as a new tool, supplementary to direct electrical $I_D$-$U_D$ measurements to probe hybrid molecular interfaces. The possibility of studying charge transfer kinetics described in *section 2.2* demonstrates that the charge out-of-plane injection and in-plane transport in an organic channel pathway can be discriminated. Thus, a new photocurrent approach is an important analytical tool for the molecular engineering of SAM OFETs. It should be possible to evaluate and compare the rate of charge injection and charge transport in these hybrid devices to achieve optimal device performance. The application of photophysics studies of SAM devices makes possible the analysis of transport properties in 2D organic systems and should provide future insight into charge transfer in low-dimensional objects.

## Acknowledgments

We thank A. A. Gewirth for the valid suggestions and helpful discussions, A. Bezryadin (Physics Department, UIUC) for the loan of the electrometer and supportive discussions, R. Gennis (Chemistry Department, UIUC) for the use of UV–Vis instrumentation, R. Hash (MRL, UIUC) for XPS measurements, R. Strange (MRL, UIUC) for reflection spectroscopy, and M. Sardela (MRL, UIUC) for XRD measurements. We benefited from useful discussions with L. Woichek, V. Vardeny, A. Rogachev (all of the Physics Department, UU), and J. Wright (Chemistry Department, WMU). We thank M. Zudov (School of Physics and Astronomy, UM) for his review and critical comments of our manuscript.

### Review

This chapter was reviewed by Professor Michael Zudov, School of Physics and Astronomy, University of Minnesota, 116 Church Street S.E., Minneapolis, MN, 55455; email zudov@ physics.umn.edu.

## REFERENCES

[1] Aviram, A.; and Ratner, M.A. *Chem Phys. Lett.* 1974, 29, 277-283.

[2] Katz, H. E.; and Bao, Z. J. *Phys. Chem. B* 2000, 104, 671-678.

[3] Horowitz, G., J. *Mater. Res.* 2004, 19, 1946.

[4] Newman, C. R.; Frisbie, C. D.; da Silva Filho, D. A.; Bredas, J.-L.; Ewbank, P. C.; and Mann, K. R. *Chem. Mater.* 2004, 16, 4436-4451.

[5] Da Silva Pinheiro, C.; and Silva, G. M.E. International *J. Quantum Chem.* 2005, 95, 153–158.

[6] Zelichenok, A.; Burtman, V.; Zenou, N.; Yitzchaik, S.; Di Bella, S.; Meshulam, G.; and Kotler, Z. *J. Phys. Chem. B* 1999**,** 103, 8702-8701.

[7] Moukouri, S.; Allen, S.; Lemay, F.; Kyung, B.; Poulin, D.; Vilk, Y.M.; and Tremblay, M. S. *Phys. Rev. B* 2000, 61, 7887-7892.

[8] Kobayashi, S.; Takenobu, T.; Mori, S.; Fujiwara, A.; and Iwasa, Y. *Appl. Phys. Lett.* 2003, 82, 4581.

[9] Chikamatsu, M.; Nagamatsu, S.; Yoshida, Y.; Saito, K.; Yase, K.; and Kikuchi, K. *Appl. Phys. Lett.* 2005, 87, 203504.

[10] Letizia, J. A.; Facchetti, A. C.; Stem, L.; Ratner, M. A.; and Marks, T. J. *J. Am. Chem. Soc.* 2005, 127, 13476.

[11] Jones, B. A.; Ahrens, M. J.; Yoon, M.-H.; Facchetti, A.; Marks, T. J.; and Wasielewski, M. R. *Angew. Chem., Int. Ed.* 2004, 43, 6363.

[12] Chen, H. Z.; Ling, M. M.; Mo, X.; Shi, M. M.; Wang, M.; and Bao, Z. *Chem. Mater.* 2007, 19, 816.

[13] Ling, M.-M.; Erk, P.; Gomez, M.; Koenemann, M.; Locklin, J.; and Bao, Z. *Adv. Mater.* 2007, 19, 1123.

[14] Chesterfield, R. J.; McKeen, J. C.; Newman, C. R.; Ewbank, P. C.; da Silva Filho, D. A.; Brédas, J.-L.; Miller, L. L.; Mann, K. R.; and Frisbie, C. D. *J. Phys. Chem. B* 2004, 108, 19281.

[15] Sirringhaus, H. *Adv. Mater.* 2005, 17, 2411.

[16] Newman, C. R.; Frisbie, C. D.; da Silva Filho, D. A.; Brédas, J.-L.; Ewbank, P. C.; and Mann, K. R. *Chem. Mater.* 2004, 16, 4436.

[17] Yoo, B.; Jung, T.; Basu, D.; Dodabalapur, A.; Jones, B. A.; Facchetti, A.; Wasielewski, M. R.; and Marks, T. J. *Appl. Phys. Lett.* 2006, 88, 082104.

[18] Jones, B. A.; Facchetti, A.; Marks, T. J.; and Wasielewski, M. R. *Chem. Mater.* 2007, 19, 2703.

[19] Ando, S.; Murakami, R.; Nishida, J.-I.; Tuda, H.; Inoue, Y.; Tokito, S.; and Yamashita, Y. *J. Am. Chem. Soc.* 2005, 127, 14996.

[20] Salomon, A.; Boecking, T.; Chan, C. K.; Amy, F.; Girshevitz, O.; Cahen, D.; and Kahn, A. *Phys. Rev. Lett.* 2005, 95, 266807.

[21] Salomon, A.; Cahen, D.; Lindsay, S.; Tomfohr, J.; Engelkes, V.B.; and Frisbie, C.D. *Adv. Mater. (Weinheim, Ger.)* 2003, 15, 1881-1890.

[22] Zahid, F.; Ghosh, A. W.; Paulsson, M.; Polizzi, E.; and Datta, S. *Phys. Rev. B* 2004, 70, 245317.

[23] Cahen, D.; and Kahn, A.; Umbach, E. *Materials Today*, 2005, *July/August*, 32-41.

[24] Burtman, V.; Hukic, G.; Ndobe, A. S.; Drori, T.; Vardeny, Z. V. *J. of Appl. Phys.* 2007,101, 054502.

[25] Burtman, V.; Ndobe, A. S.; and Vardeny, Z. V. *J. of Appl. Phys.* 2005, 98, 034314.

[26] Ulman, A. *Chem. Rev.* 1996, 96, 1533-54.

[27] Ulman, An Introduction to Ultrathin Organic Films, Academic Press, Boston, 1991.

[28] Lehn, J-M. *Science* 2002, 295, 2400-2403.

[29] Katz, H. E.; Lovinger, A. J.; Johnson, J.; Kloc, C.; Seigrist, T.; Li, W.; Lin, Y.-Y.; and Dodabalapur, A. *Nature* 2000, 404, 478.

[30] Katz, H. E.; Johnson, J.; Lovinger, A. J.; and Li, W. *J. Am. Chem. Soc.* 2000, 122, 7787.

[31] Singh, T. B.; Erten, S.; Günes, S.; Zafer, C.; Turkmen, G.; Kuhan, B.; Teoman, Y.; Sariciftci, N. S.; and Icli, S. *Org. Electron.* 2006, 7, 480.

[32] Kao, C.-C.; Lin, P.; Lee, C.-C.; Wang, Y.-K.; Ho, J.-C.; and Shen, Y.-Y. *Appl. Phys. Lett.* 2007, 90, 212101.

[33] Letizia, J. A.; Facchetti, A.; Stern, C. L.; Ratner, M. A.; and Marks, T. J. *J. Am. Chem. Soc.* 2005, 127, 13476.

[34] Lee, Y-L.; Hsu, H.-L.; Chen, S.-Y.; and Yew, T.-R. *J. Phys. Chem. C*, 2008, 112, 1694 -1699.

[35] Janssen, D. Ph.D. thesis Katholieke University of Leuven , Departement of Chemistry, Belgium June 2006.(on-line: https://repository.libis.kuleuven.be/dspace/bitstream/1979/330/5/thesis+final+color.pdf)

[36] Burtman, V.; Zelichenok, A.; Y and itzchaik, S. *Polym. Prepr.* 1998, 39, 167-8.

[37] Burtman, V.; Zelichenok, A.; Yakimov, A.; and Yitzchaik, S. Yitzchaik, in Semiconductive Polymers: Applications, Properties, and Synthesis; edited by Hsieh, B. R., (ACS Symposium Series 735; American Chemical Society: Washington, DC, 1999) pp. 399-419.

[38] Ofir, Y.; Shwartzglass, O.; Shappir, J.; and Yitzchaik, S. in Organic Thin-Film Electronics, edited by A.C. Arias, N. Tessler, L. Burgi, and J.A. Emerson (Mater. Res. Soc. Symp. Proc. 871E, Warrendale, PA, 2005), I3.22-I3226.

[39] Ofir, Y.; Burtman, V.; and Yitzchaik, S. The 66th Annual Meeting of the Israel Chemical Society, extended abstract (chapter 66/024Ofir) poster # 24, 2001 (on-line http://www.weizmann.ac.il/ICS/chemistry66/024Ofir.html)

[40] Yitzchaik, S. The 66th Annual Meeting of the Israel Chemical Society, 2001. (extended abstract is available on-line:

[41] http://www.weizmann.ac.il/ICS/chemistry66/Yitzchaik.html)

[42] Holstein, T., *Ann. Phys.* (N.Y.) 1959, 8, 343.

[43] Emin, D., *Phys. Today,* 1982, 6, 34-35.

[44] Silinsh, E. A., and V.C Cápek, Organic Molecular Crystals: Interaction, Localization, and Transport Phenomena (AIP, New York). 1994.

[45] Pope, M., and C. E. Swenberg, Electronic *Processes in Organic Crystals and Polymers*, 2nd ed. (Oxford University Press, New York) 1999.

[46] Gershenson, M. E.; Podzorov, V.; Morpurgo, A. F. *Rev. Mod. Phys*. 2006, 78.

[47] Troisi, A., G. Orlandi, and J. E. Anthony, *Chem. Mater*. 2005,17, 5024.

[48] Kenkre, V. M., J. D., Andersen, D. H. Dunlap, and C. B. Duke, *Phys. Rev. Lett.* 1989, 62, 1165.

[49] Wu, M. W., and E. M. Conwell, *Chem. Phys. Lett.* 1997, 266, 363.

[50] Fratini, S., and S. Ciuchi, *Phys. Rev. Lett.* 2003, 91, 256403.

[51] Deng, W.-Q., and W. A. Goddard, *J. Phys. Chem. B* 2004,108, 8614.

[52] Hannewald, K., and P. A. Bobbert, *Appl. Phys. Lett*. 2004,85, 1535.

[53] Hannewald, K., and P. A. Bobbert, in *Physics of Semiconductors*, edited by J. Menendez and C. G. van de Walle, AIP Conf. Proc. No. 772 (AIP, Melville, NY), 2005, p. 1101.

[54] da Silva Filho, D. A., E.-G. Kim, and J.-L. Bredas, *Adv. Mater. (Weinheim, Ger.)* 2005, 17, 1072.

[55] Karl, N., in *Organic Electronic Materials*, edited by R. Farchioni and G. Grosso (Springer-Verlag, Berlin), 2001,pp. 283– 326.

[56] Dodabalapur, A., L. Torsi, and H. E. Katz, *Science* 1995, 268, 270.

[57] Chua, L. L., J. Zaumseil, J. F. Chang, E. C.-W. Ou, P. K.-H. Ho, H. Sirringhaus, and R. Friend, *Nature (London)* 2005,434, 194.

[58] Kiguchi, M., M. Nakayama, T. Shimada, and K. Saiki, *Phys. Rev. B* 2005, 71, 035332.

[59] Panzer M. J., and C. D. Frisbie, *J. Am. Chem. Soc*. 2005, 127, 6960.

[60] Houili, H., J. D. Picon, M. N. Bussac, and L. Zuppiroli, 2005, *e-print cond-mat/*0510751.

[61] Horowitz, G., *J. Mater. Res*. 2004, 19, 1946.

[62] Burtman, V.; Zelichenok, A.; Yitzchaik, S. *Angew. Chem., Int. Ed.* 1999, 38, 2041-2045.

[63] Burtman, V.; Offir, Y.; Yitzhaik, S. *Langmuir* 2000, 17, 2137-2142.

[64] Whitesides, G. M.; Laibinis, P. E. *Langmuir* 1990, 6, 87-96.

[65] Ada, E. T.; Hanley, L.; Etchin, S.; Melngailis, J.; Dressick, W. J.; Chen, M.-S.; Calvert, J. M. *J. Vac. Sci. Technol. B* 1995, 13, 2189-2196.

[66] *Practical Surface Analysis*; Briggs, D., Seah, M. P., Eds.; Wiley: New York, 1990; p 444.

[67] Kallury, K. M. R.; Macdonald, P. M.; and Thompson, M. *Langmuir* 1994, 10, 492-499.

[68] Forrest, S. R. *Chem. Rev.* 1997, 97, 1793 -1896.

[69] Dodabalapur, A.; Katz, H. E.; Tordi, L.; Haddon, R. C. *App. Phys. Lett.* 1996, 69 4227.

[70] Werner, A.; Li, F.; Harada, K.; Pfeiffer, M.; Fritz, T.; Leo, K.; and Machill S. *Adv. Funct. Materials* 2004,14, 255-260..

[71] Burtman, V. *Thin Solid Films* 2008, 516, 3436–3440.

[72] Sze, S. *Semiconductor Devices Physics and Technology*; Wiley: New York, 1985.

[73] Hagfeldt, A.; and Gratzel, M. *Acc. Chem. Res*. 2000, 33, 269-277.

[74] Grätzel, M. *Nature* 2001, 414, 338-344.

[75] Huynh, W. U.; and Dittmer, J. J.; Alivisatos, A. P. *Science* 2002, 295, 2425-2427.

[76] Glazer, A. *N. Annu. Rev. Biochem*. 1983, 52, 125-157.

[77] Di Bilio, A. J.; Crane, B. R.; Wehbi, W. A.; Kiser, C. N.; Abu-Omar, M. M.; Carlos, R. M.; Richards, J. H.; Winkler, J. R.; and Gray H. B. *J. Am. Chem. Soc*. 2001, 123, 3181-3182.

[78] Barry, B. A.; El-Deeb, M. K.; Sandusky P. O.; and Babcock, G. T. *J. Biol. Chem.* 1990, 265, 20139-20143.

[79] Collet, J.; Lenfant, S.; Vuillaume, D.; Bouloussa, O.; Rondelez, F.; Gay, J. M.; Kham K.; and Chevrot C. *Appl. Phys. Lett.* 2000, 76, 1339-1341.

[80] Bryce, M R.; Petty M. C. *Nature (London)* 1995, 374, 771-776.

[81] Bjornholm, T.; Hassenkam, T.; and Reitzel, N. *J. Mater. Chem*. 1999, 9, 1975-1990.

[82] *Advances in Synthetic Metals Twenty Years of Progress in Science and Technology*; Bernier, P., Lefrant, S., Bidan, G., Eds.; Elsevier Science: 1999.

[83] Novàk, P.; Muller, K.; Santhanam, K. S. V.; and Haas, O. *Chem. Rev.*1997, 97, 207-281.

[84] Heath, J. R.; Ratner, M. A. *Phys. Today* 2003, 56, 43-49.

[85] Rehm, J. M.; McLendon, G. L.; Nagasawa, Y.; Yoshihara, K.; Moser, J.; and Grattzel, M. *J. Phys. Chem.* 1996, 100, 9577-9578.

[86] Schroder, D. K. *Meas. Sci. Technol.* 2001, 12, R16-R31.

[87] Bergmann, L. *Phys Z* 1932, 33, 209.

[88] Munakata, C.; and Matsubara, S. *J Phys D Appl Phys* 1982, 16, 1093-1098.

[89] Munakata, C.; Yagi, K.; Warabisako, T.; Nanba, M.; Matsubara, S. *Jpn. J. Appl. Phys.* 1982, 21, 624-632.

[90] Munakata, C.; Honma, N.; Itoh, H. *Jpn J Appl Phys* 1983, 22, L103-L105.

[91] Honma, N.; Munakata, C.; Shimizu, H. *Jpn J Appl Phys* 1988, 27, 1498-1503.

[92] Witt, H. T.; Zickler, A. *FEBS Lett* 1973, 37, 307-310.

[93] Trissl, H. W. *Proc Natl Acad Sci U S A* 1983, 80, 7173-7177.

[94] Cohen, R.; Zenou, N.; Cahen, D.; Yitzchaik, S. *Chem Phys Lett* 1997, 279, 270-274.

[95] Pakoulev, V. Burtman, D. Zaslavsky, prepared for a publication.

[96] Holman, M. W.; Liu, R.; Adams, D. M. *J Am Chem Soc* 2003, 125, 12649-12654.

[97] Raistrick, I. D. Electrochemical Capacitors. In *Electrochemistry of Semiconductors and Electronics - Processes and Devices*; McHardy, J., Ludwig, F., Eds.; William Andrew Publishing/Noyes: Norwich, NY, 1992, pp 297.

[98] Wenger, B.; Gratzel, M.; Moser, J. E. *J Am Chem Soc* 2005, 127, 12150-12151.

[99] M. Grätzel, *Nature* (*London*), 2001, 414, 338.

[100] Hagfeldt and M. Grätzel, *Chem. Rev*., 1995, 95, 49.

[101] N. Karl, K.-H. Kraft, J. Marktanner, M. Munch, F. Schatz, R. Stehle, and H.-M. Uhde, *J. Vac. Sci. Technol*. A 1999, 174**,** 2318.

[102] Meyer, J.R.; Arnold, D. J., Hoffman C. A. and Bartoli F. J. *Phys. Rev B*, 1992, 45, 1295-1304.

[103] Horovitz B.; Pazy, E. *Europhysics Letters*, 2004**,** 65**,** 386-392.

[104] Khondaker, S. I.; Shlimak, I. S.; Nicholls, J. T.; Pepper, M.; and Ritchie D. A. *Phys. Rev. B* 1999, 59, 4580 – 4583.

[105] Laquindanum, J. G.; Katz, H.E.; Dodabalapur, A.; and Lovinger A. J. *J. Am. Chem. Soc.,* 1996, 118, 11331 -11332.

[106] Facchetti, A. *Materials Today*, 2007 10, 28-37.

[107] Hiramoto, M.; Imahigashi T.; and Yokoyama M. *Appl. Phys. Lett.* 1994 64, 187-189.

[108] Hiramoto, M.; Sato, I.; and Yokoyama M. *IEICE Trans. Electront*. 2002 *E*85-*C,* 1253-1255.

[109] Burtman V.; and Vardeny, Z. V. *Japanese J. Applied Phys.* 2008, 47,1165-1172

[110] Reed, M. A.; Zhou, C.; Deshpande, M. R.; Muller, C. J.; Burgin, T. P.; Jones, II, L.;. Tour J. M. *Ann. N.Y. Acad. Sci.* 1998, 852, 133-144.

[111] Holmlin, R.E.; Haag, R.; Chabinyc, M.L.; Ismagilov, R.F.; Cohen, A.E.; Terfort, A.; Rampi, M.A.; and Whitesides, G.M. *J. Am. Chem. Soc.* 2001,123, 5075-5085.

[112] Petta, J. R.; Slater, S. K.; and Ralph, D. C. *Phys. Rev. Lett*. 2004, 93, 136601.

[113] Curtis, M. D.; Cao, J.; and Kampf, J. W. *J. Am. Chem. Soc*. 2004, 126, 4318-4328.

[114] Desiraju, G. R. *J. Mol. Struct.* 2003, 656, 5.

[115] Kiguchi, M.; Tal, O.; Wohlthat, S.; Pauly, F.; Krieger, M.; Djukic, D.; Cuevas, J.C. van and Ruitenbeek, J.M. *Phys. Rev. Lett*. 2008, 101, 046801.

[116] Chen, J.-H.; Jang, C.; Xiao, S.; Ishigami M.; Fuhrer, M. S. *Nature Nanotechnology*, 2008, 3, 206 – 209.

[117] Lin, YM.; Perebeinos, V.; Chen, Z.; and Avouris, P. *http://arxiv.org/abs/*0805.0035 , also: http://physicsworld.com/cws/article/news/34159

[118] Ami S.; Joachim, C. *Phys. Rev. B* 2002, 65, 155419.

[119] Zaslavsky, D.; Pakoulev, A.; and Burtman, V. *J. Phys. Chem. B* 2004, 108, 15815-15819.

In: Integrated Circuits, Photodiodes…
Editors: R. McIntire and P. Donnell, pp. 161-183

ISBN: 978-1-60692-660-4

© 2009 Nova Science Publishers, Inc.

*Chapter 6*

# ELECTRON SPECTROSCOPY AND NEAR INFRARED PHOTOCURRENT MEASUREMENT OF WORKING ORGANIC THIN FILM FETS

***Toshihiro Shimada, Manabu Ohtomo and Tetsuya Hasegawa***
Department of Chemistry, The University of Tokyo
Bunkyo-ku, Tokyo 113-0033, JAPAN

## ABSTRACT

This contribution is intended to provide a combined view of spectroscopic studies on electronic states in working organic thin film FETs based on our experiments. Three kinds of spectroscopic techniques are presented: Ultraviolet Photoelectron Spectroscopy (UPS), Electron Energy Loss Spectroscopy(EELS), and near infrared photocurrent spectroscopy (NIRPCS). Information on energy levels, effective mass, location of field induced carriers and gap states related with traps and off-current of the devices can be obtained from those spectroscopic techniques.

## 1. INTRODUCTION

Understanding charge conduction mechanism in organic FETs is important to improve the performance of the devices. However, the knowledge of conduction mechanism is based only on the theoretical basis, which contains several unsettled questions such as the role of polarons and effect of intermolecular vibrations. Therefore we have developed several in situ spectroscopic analysis techniques for organic FETs as shown in Figure 1. Two kinds of electron spectroscopy, i.e. ultraviolet photoelectron spectroscopy (UPS) and electron energy loss spectroscopy (EELS) measure the energy of electrons emitted or reflected from the device surfaces. It was not certain before our experiments whether it is possible to measure the kinetic energy of the electrons near the high electric field. We developed shielding techniques and succeeded in the measurement. From the UPS, it is possible to detect the field induced charges in n-type OFETs in principle, although the signal to noise ratio is a severe problem which is now being pursued[1]. From the EELS, it is possible to discuss the effective mass in field induced carriers[2]. Another kind of spectroscopy is near infrared photocurrent spectroscopy (NIRPCS). In this technique, photons with the energy less than fundamental excitation of the molecules are irradiated on working organic FETs and the modulation in source-drain current is measured as functions of source-drain and source-gate voltages[3,4]. It is possible to detect the gap states in the organic semiconductors by this technique and the result on pentacene FETs - long-tail gap states induced by the deposition of metal electrodes and impurity states related with the off current - are presented.

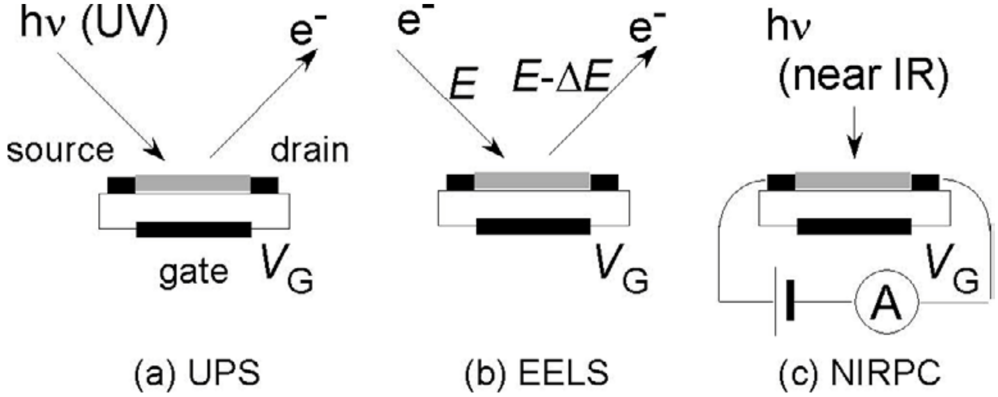

Figure 1. Three kinds of spectroscopy techniques newly applied to OFETs.

## 2. EXPERIMENTAL SETUP

### 2.1. Electron Spectroscopy

Electron spectroscopy (UPS and EELS) measurements were performed in an ultrahigh vacuum chamber equipped with specially designed sample holder for gate electric field shielding. This measurement chamber was directly connected with the sample preparation chamber via a gate valve, and the sample was transferred from the preparation chamber to the measurement chamber keeping ultrahigh vacuum condition. The schematic diagram of the vacuum chamber is shown in Figure 2.

The sample structure is illustrated in Figure 3. The FET had a bottom contact structure, namely, molecule (50nm $C_{60}$ for UPS, 1.5~4.5nm pentacene for EELS)/ Au (50 nm, source(S), drain(D) electrodes) / thermal $SiO_2$(700nm)/ highly doped Si (Gate(G) electrode). Interdigitally patterned source and drain electrodes made of Au (50 nm- thick) were fabricated by a lift-off process using Cr (5 nm- thick) as a sticking layer on the thermal oxide formed upon highly doped Si substrates that work as gate electrodes. The line width and the interval were 20 μm and 100 μm, respectively, and the thickness of the oxide was 700 nm. The substrate with the electrodes was mounted on an alumina-ceramic holder that contains three electrically-shielded connectors.[1] Coaxial shield connectors are used to make connections between the sample holder and manipulator.

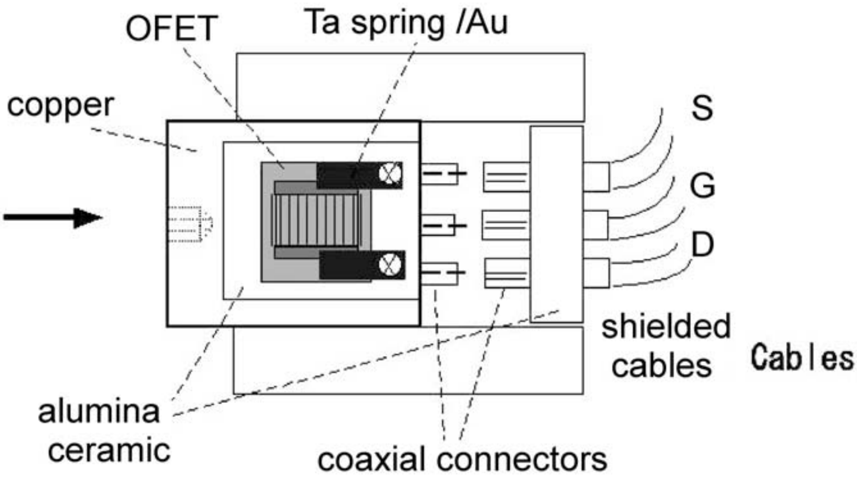

Figure 2. Vacuum system used for UPS and EELS experiments.

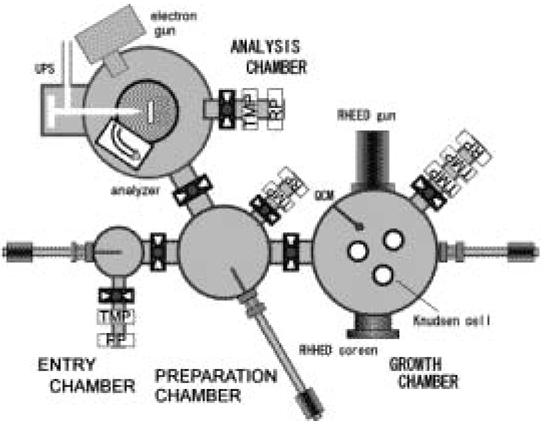

Figure 3. Sample structure for UPS and EELS of OFETs.

The electrical contacts to the S and D electrodes were made with spring plates made of tantalum. The contact to the gate electrode was made from the backside using a Ga-In alloy. The substrate was heated in an ultrahigh vacuum for 6 hours at 80 °C. After cooling, the sample was transferred to the deposition chamber and molecules were deposited at room temperature. The growth rates of the molecules were 1 nm / min and 0.1nm/min in the case of $C_{60}$ and pentacene, respectively. The thickness and the growth rate of the molecules were monitored by a quartz crystal microbalance. After the deposition, the sample was transferred to the analysis chamber where the transport properties, UPS or EELS were measured.

The macroscopic electric field, which disturbs the UPS measurement, was shielded by the source and drain electrodes, conductive molecular semiconductor films and shielded connectors. The use of shielded connectors was essential for the reproducible spectroscopic results under the gate bias. The leakage current of the gate oxide was less than 100 pA throughout the measurement. Kinetic energy of emitted (in the case of UPS) or reflected (in the case of EELS) electrons was measured using a VG ADES 400 angle resolved electron energy analyzer, which was set to detect the electrons emitted along the surface normal. For the UPS, the incident photons from the He discharge lamp were irradiated on the sample at an incident angle of 25 ° off the surface normal. EELS was measured using a monochromatized electron beam (kinetic energy centered at 10 eV, FWHM = 180 meV) and the same analyzer as used for UPS. The electron beam impinged on the surface at the angle 60° off from the surface normal, and the electrons emitting along the surface normal were collected to reduce the possible effect of a stray field.

## 2.2. Near IR Photocurrent Spectroscopy

For the NIRPCS measurement, photocurrent measurement connector was attached to the sample preparation chamber, and wavelength-tunable near IR laser light was introduced to the chamber. A schematic illustration of our photocurrent measurement setup is shown in Figure 4. The OFET sample was kept in a high-vacuum ($<10^{-5}$ Pa) deposition-measurement chamber, and infrared light was directed onto the channel and electrodes through a view port. The laser power was 0.8 mW, and the beam size was 2 mm in diameter, the same size as the channel width. The laser light source was a CW Ti: sapphire laser, which emits infrared light with a wavelength ranging from 700 to 1000 nm. The laser beam was chopped by an optical chopper at 131-137 Hz, and modulated photocurrent flow between the source electrode and the drain electrode was measured with a lock-in amplifier. To minimize electrical noise, we used voltage sources configured with batteries and computer-controlled relays. The noise level was less than 3 pA.

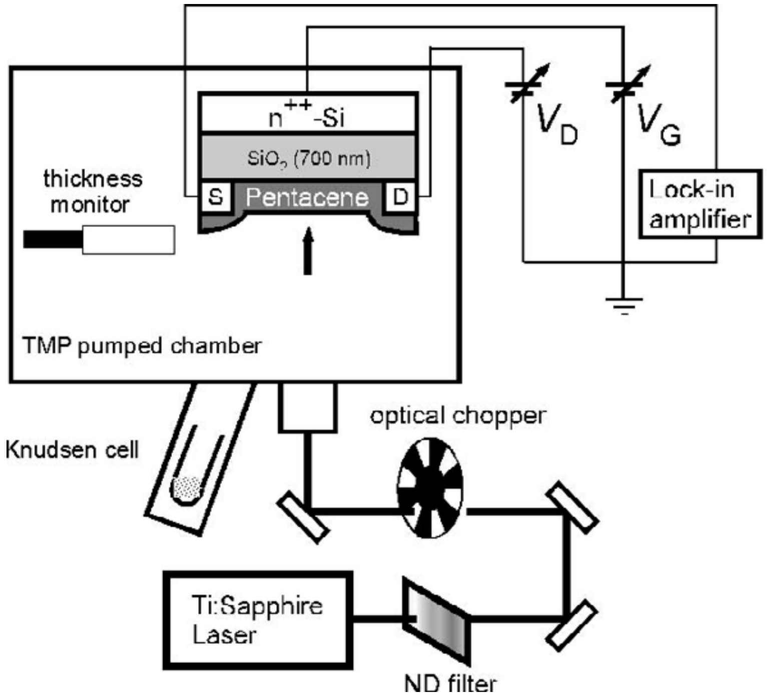

Figure 4. Preparation / measurement chamber for NIRPCS.

## 3. UPS MEASUREMENT OF $C_{60}$ FETS AND ACCELERATION OF PHOTOPOLYMERIZATION

UPS is used to measure the occupied energy levels of materials. It is characterized by the ability of measuring all of the valence electronic states up to 10~20 eV binding energy ($E_B$), the possibility of detecting band structure by angle resolved measurement of single crystalline material, and surface sensitivity (< 1 nm). When applied to working FETs, it might be possible to determine the energy levels and the depth profile of field induced carriers. With this expectation, we started UPS experiment of working organic FETs. It was not known whether it is possible to measure UPS of working FETs with biasing gate voltages.

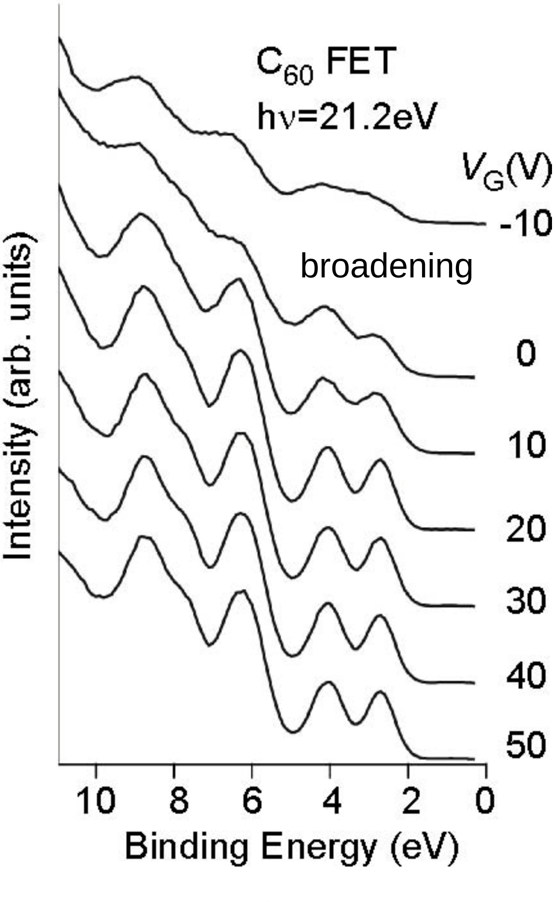

Figure 5. UPS of 50 nm thick C60 FET with various $V_G$.

Figure 5 shows the UPS spectra ($h\nu = 21.2$ eV) of a 50 nm - thick $C_{60}$ FET structure with various gate voltages ($V_G$). The typical photoelectron current was ~ 1 nA. The potentials of the source and drain ($V_S$ and $V_D$) electrodes were zero, equal to that of the electron spectrometer. When $V_G$ was not more than about 10 V, the spectra showed broadening. This is probably because the photoelectron emission induces a not-homogeneous quasi Fermi level in the poorly conductive film when the carriers in the film are depleted by the field effect.

With $V_G$ not less than 20 V, the spectra show the same feature as that of a $C_{60}$ film on a conductive substrate. Without proper shielding of the gate voltages mentioned in section 2, the spectra were deformed and not reproducible. It was proved that it is possible to measure the UPS of working FETs with proper shielding.

To our surprise, it was found that a continuous UPS measurement caused a gradual change in the valence electronic structure. Figure 6 (a) shows the time-dependent UPS spectra of the 50 nm-thick $C_{60}$ FET recorded every three minutes with a $V_G$ of 20 V. The intensity at the valley between HOMO and HOMO-1 (binding energy ($E_B$) 3.5 eV) increases and the shoulder at $E_B$ ~ 7.7 eV shifts to the higher binding energy side. On the other hand, a $C_{60}$ film epitaxially grown on $MoS_2$ (0001) basal plane with the same thickness of 50 nm showed negligible change in the valence structure even after a 1000-min UPS measurement as shown in Figure 6(b).

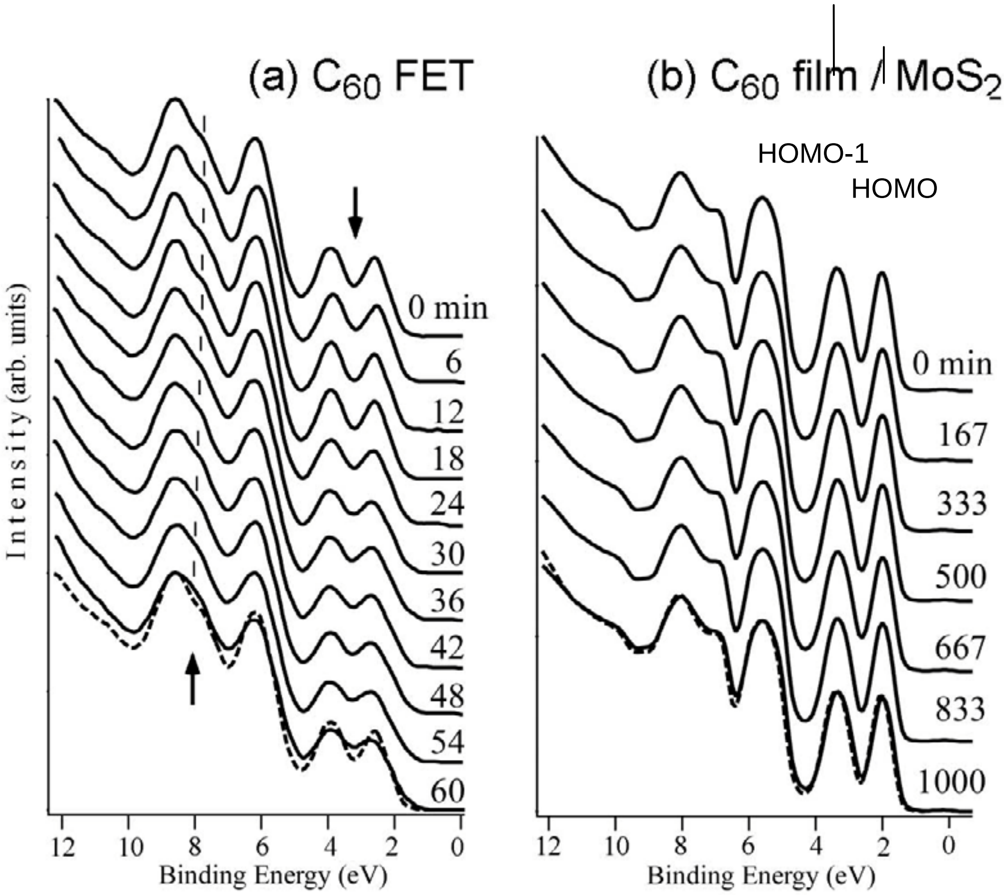

Figure 6. Time evolution of UPS of C60 films (thickness = 50nm) during continuous measurement. (a) $C_{60}$ FET and (b) $C_{60}$ epitaxial film grown on $MoS_2$. The incident photon energy was 21.2 eV.

In order to examine the origin of the changes in the UPS, we have compared it with the photopolymerized $C_{60}$, which was prepared by irradiating a 532 nm CW laser (0.2 W/cm$^2$) in an ultrahigh vacuum for 20 h on a 100 nm- thick $C_{60}$ epitaxial film grown on $MoS_2$ (0001).[5]

Although the UPS measurement of the $C_{60}$ photopolymer can be found in the literature, the polymerization ratio of the samples were not specified. In our sample, the ratio of pristine $C_{60}$ to the polymerized species was determined from the curve fitting of the Raman spectra in the 1400-1500 $cm^{-1}$ region using the spectra in the literature[6,7] and it was less than 2% after laser irradiation. The UPS spectra ($h\nu$ = 40.8 eV) of the pristine $C_{60}$ and photopolymerized $C_{60}$ are shown in Figures 7(a) and 7(b), respectively. The shallowing of the valley at 3.5 eV and the shift in the shoulder at 7.7 eV are observed in Figure 7(b), as compared with Figure 6(b). Thus we concluded that the observed change in Figure 6(a) is due to the photopolymerization of $C_{60}$. We measured the UPS of the $C_{60}$ FET at different values of $V_G$ but could not find a significant difference in the polymerization rate if $V_G$ was high enough to allow the UPS measurements without suffering a photovoltaic effect. We have applied $V_G$ up to 200V without measuring the UPS and found that the polymerization does not occur without UV light irradiation. It should be noted that the UV photon intensity of ordinary UPS measurements is insufficient to polymerize $C_{60}$ films grown on conductive substrates within the time scale of the present experiment.[8]

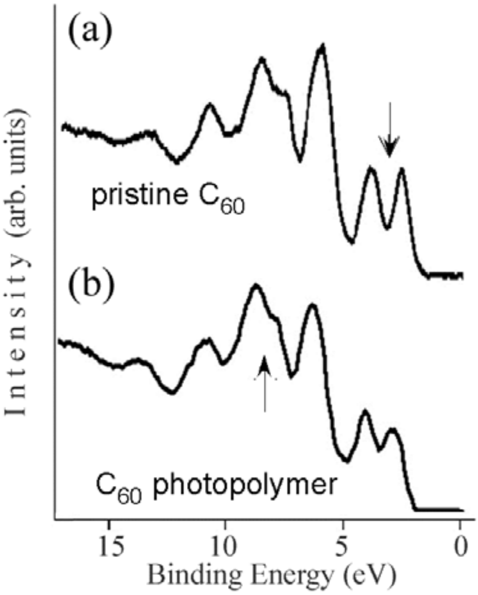

Figure 7. UPS of pristine $C_{60}$ (a) and $C_{60}$ photopolymer (b). The incident photon energy was 40.8 eV.

The FET mobility in the device was initially 0.085 $cm^2\ V^{-1}s^{-1}$ and increased to be 0.22 $cm^2\ V^{-1}s^{-1}$ after UPS polymerization.

The present experiments have revealed several interesting phenomena. First, we discuss the mechanism of the accelerated photopolymerization in an FET structure. It has been reported that the polymerization of pristine $C_{60}$ is triggered by irradiating photons with an energy more than 2 eV[9], by irradiating an intense electron beam [8], or by injecting tunnel electrons by STM[10]. The present result indicates that the FET structure under UV photon irradiation significantly accelerates the polymerization. Since the formation of the $C_{60}$ polymer is basically a photochemical 2+2 addition to form a four-membered ring between unsaturated double bonds, the alignment of the double bonds of adjacent molecules with the appropriate direction and distance is essential for the polymerization. The polymerization rate drastically increases at temperatures above about 250 K [11] where the free rotation of the molecule is allowed[12] because the mutual orientation between the molecules appropriate for the polymerization is different from the most stable one in the crystalline solids. Therefore, it is considered that having a polymerization trigger (an exciton or an electron) in the correctly facing pair is necessary for the polymer bond formation.

Since the UV photons are irradiated equally on the $C_{60}$ FET and the film grown on $MoS_2$, the difference in the polymerization rate must be related with the charge (electron) carrying species. In the present experiment, photoelectrons are emitted from the surface (~1 nA /mm$^2$), which cause the electron flow from the substrate. In the case of a $C_{60}$ film on the conductive substrate, the electron flow just travels the thickness of the film (50 nm), whereas it must travel at most half the distance between the interdigital electrodes (~50 μm).

In this section, we have described the accelerated photopolymerization of $C_{60}$ by orders of magnitudes in a thin film FET compared to that of the film grown on conductive substrates. Charge carriers in organic semiconductors can be regarded as organic radicals, which are recognized as reactive species under ordinary conditions. It was possible to change the chemical reactivity of $C_{60}$ molecules by injecting carriers, and it will find applications in device processing and in field-effect transistor (FET) -based chemical sensors.

## 4. Electron Energy Loss Spectroscopy (EELS) of Pentacene FETs

The measurement setup for EELS was similar to the UPS measurement of $C_{60}$ FETs described in the previous section. During the EELS measurement, the S and D electrodes were connected to ground. The electric field from the gate electrodes was shielded by the coaxial connectors and the conducting channel of the sample itself.

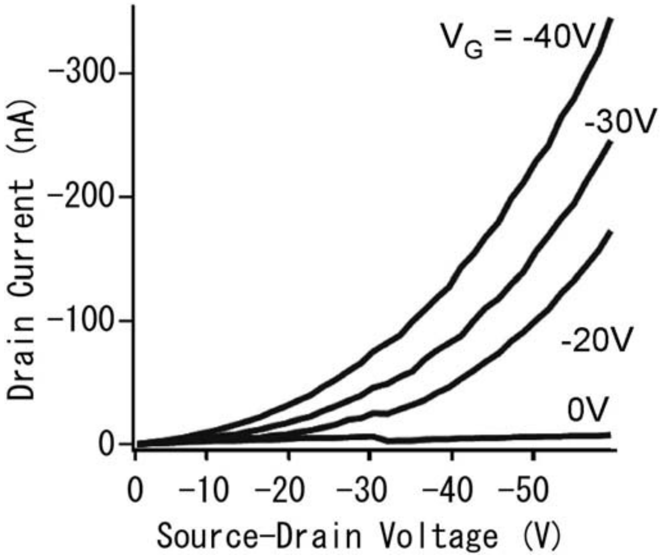

Figure 8. FET characteristics of 1 molecular layer (ML: 1ML=1.5nm) pentacene FET.

Figure 8 shows the FET characteristics of the 1.5 nm- thick pentacene FET. We have confirmed by AFM measurement that the pentacene forms a uniformly covered monolayer film with the longer axis of the molecules aligned perpendicular to the $SiO_2$ surface with this growth condition. The thickness of 1.5 nm corresponds to one standing molecular layer. From Figure 8, it is shown that the FET characteristic is observed even with a one monolayer thickness. The mobility obtained from the linear fit at $V_D$ = - 35 V was 4 x $10^{-3}$ $cm^2/Vs$. The low mobility and the nonlinearity without saturation is a signature of the injection limit at the S and D electrodes. Poor connectivity of the monolayer grains also contribute to the low mobility.

Figure 9 (a)-(d) (circles) shows the EEL spectra of a pentacene 1.5nm- thick FET. When the gate voltage ($V_G$) was 0 V, the spectrum is almost symmetric. Slight tailing is attributed to phonon excitations, which was not separated due to the instrumental resolution. It corresponds to the pure elastic scattering peak without a significant loss feature in this region. When $V_G > 0$, the spectrum is symmetric, but the intensity becomes weak as $V_G$ increases. This is due to the stray field because the p-type pentacene film becomes insulating with a positive gate bias and the shielding effect of the film is accordingly lost. When $V_G < 0$, on the other hand, the spectra show tailing towards the energy loss side ($V_G$ = -20, -40V) and a small shoulder appeared at $V_G$ = -60V. In this case, it is considered that the gate electric field is shielded by the conducting pentacene film. The spectra are composed of an elastic peak and energy loss peaks. In order to extract the energy loss feature, we have deconvolved the elastic peak from the spectra. It was assumed that the spectrum measured at $V_G$ = 0V corresponds to the elastic peak. In the determination of the loss feature, the "energy gain" process was also taken into account,[13] namely, the gain feature was added to the loss feature as follows:

$$L(E) = \begin{cases} L_0(E) & (E < E_p) \\ L_0(E)\exp((E_p - E)/k_B T) & (E > E_p) \end{cases} \tag{1}$$

Here, $E$ and $E_p$ are the kinetic energy of the measured electrons and the primary electrons, respectively. $L$(E) is the loss feature obtained from the deconvolution including the gain feature, and $L_0$(E) is the pure energy loss feature. It turned out that the gain feature is almost negligible in the present experiment. The multiple loss process was neglected because of its low probability. The results are shown in Figure 9(e)-(g). The convolution fit to the raw data is shown in Figure 9 (a)-(d) as solid curves. It is noted that the peak energy in the loss feature increases as the $V_G$ is increased. Since the energy of the two dimensional plasmons ($\hbar\omega_{sp}$) at the interface with vacuum is expressed as

$$\hbar\omega_{sp} = \hbar(\frac{ne^2}{2\varepsilon_0 m^*})^{1/2} \tag{2}$$

and the carrier concentration n in the conducting channel of FET at the gate voltage of $V_G$ is

$$n = \frac{C_0 V_G}{ed} \tag{3}$$

where $C_0$ and d are the gate capacitance per unit area ($C_0 = 5.0 \times 10^{-5}$ F/m$^2$) and the thickness of the channel region ($d$ = 1.5 nm), respectively. The carrier concentration at $V_G$ = -60V is, for example, estimated to be 0.0045 holes per molecule assuming the reported structure of the pentacene monolayer,[14] in which the volume per molecule is estimated to be 0.36 nm$^3$.

Eq. 3 leads to

$$\hbar\omega_{sp} = \hbar\left(\frac{C_o V_G e}{2\varepsilon_0 m^* d}\right)^{1/2} \tag{4}$$

which gives the relation between the plasmon energy and the effective mass. Based on the theoretical calculation, the band mass of pentacene is highly anisotropic and the minimum value for m* is 1.3~1.6 $m_0$, where $m_0$ is the static mass of an electron.[15,16] Assuming m* = 1.3 $m_0$ according to the band calculation and using the above values of $C_0$ and d, the plasmon energies $\hbar\omega_{sp}$ corresponding to $V_G$ = -20, -40 and -60 V are 47, 67, and 81 meV, respectively. The values are indicated by the arrows in Figs. 9 (e)-(g). The experimentally observed peak energies are systematically greater than the value corresponding to $m^*/m_0$ = 1.3, if we take the average value of the two peaks in Figure 9(g). Although the reason is not yet clarified, we speculate that it is due to the nonhomogeneity of the field-induced charge distribution in the films because the connectivity of the monolayer films is not perfect. The electrostatic consideration gives the result that the average charge density is unchanged even if microscopic gaps exist in the pentacene film, provided that the gap sizes are much smaller than the thickness of the gate insulator. The local charge density in pentacene will then be greater than the calculated value, which leads to the larger plasmon energies. It is also noticed that the square-root relation between $V_G$ and $\hbar\omega_{sp}$ (Eq.(4)) is roughly satisfied between $V_G$= -20V and -40V., but not for $V_G$ = -60V. It might be due to the opening of new conductive channels at larger $V_G$. It is also possible that the singularity in the dielectric function due to phonon excitations contribute to the discrepancy, especially at $V_G$ = -60V, in which the energy loss feature seems to show splitting.

Since the probing depth of EELS is on the order of 1 nm due to the mean free path of electrons, we examined the thickness dependence of EELS. Figures 10 (a)-(c) show the EEL spectra of a 3ML-thick pentacene FET. Although the tailing of the curve at $V_G$ = -60V is too weak to allow a reliable deconvolution, the spectrum showed noticeable broadening on the energy loss side at $V_G$ = -100V. The deconvolution result of the spectrum at $V_G$ = -100V is shown in Figure 10(d) and the energy loss peak is located at 40 meV as indicated by the arrow. We compared this value to the plasmon energy calculated using Eq. 4 assuming uniform field-induced charge distribution in the 3ML-thick film volume and $m^*/m_0$ = 1.3. The calculation yields $\hbar\omega_{sp}$ = 61 meV, which is substantially greater than the observed value. This result shows that the carrier concentration within the probing depth of EELS is lower than the value corresponding to the uniform distribution. It means that more carriers are condensed at the interface than at the surface. Considering that the probing depth of EELS is on the order of ~ 1 nm, it is consistent with our experimental estimation of the accumulation layer thickness of the pentacene FETs (~ 1 ML).[17,18]

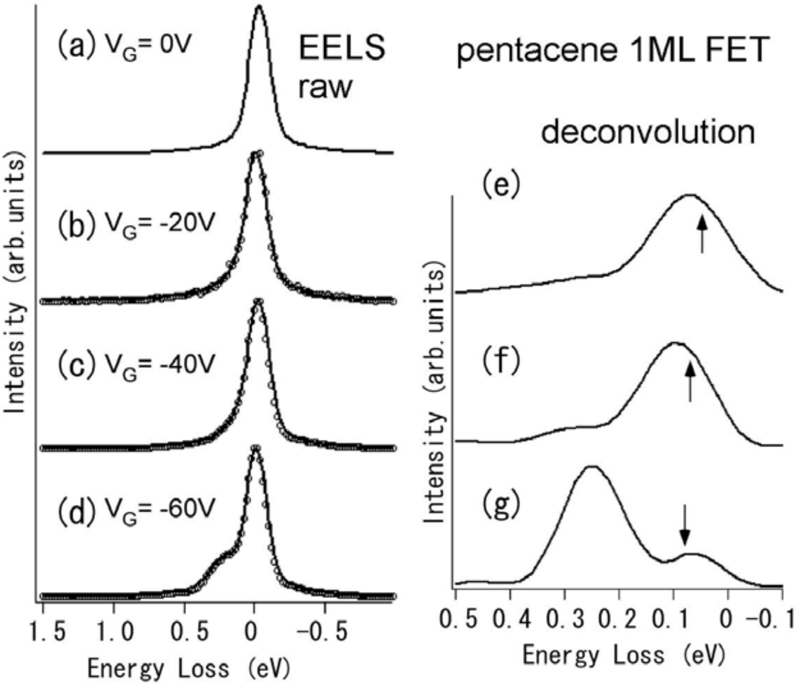

Figure 9. (a)-(d) EELS raw data (circles) and deconvolution fits (solid curves) of 1ML-thick pentacene FET. (e)-(g) Deconvolution assuming (a) as the primary electron profile.

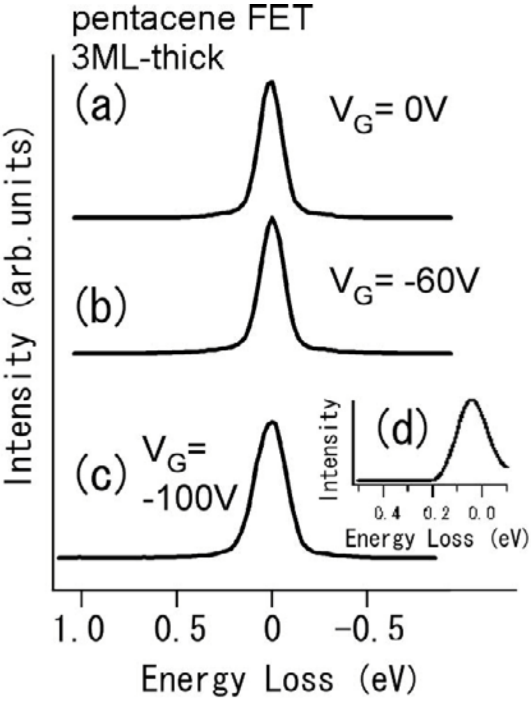

Figure 10. EELS and deconvolution of 3ML (4.5nm) thick pentacene FETs.

It is expected that an interface plasmon should be observed at the interface between field-doped pentacene and nondoped pentacene and it should be compared with the experimental energy loss peak. The excitation energy of this plasmon is given by the following.

$$\hbar\omega_{sp} = \hbar\left(\frac{C_o V_G e}{(1+\varepsilon_{pentacene})\varepsilon_0 m^* d}\right)^{1/2} \tag{5}$$

We could not find the dielectric constant of pentacene in the literature, but we can use Eq. 5 to estimate it from the observed plasmon energy (61meV) and estimation from uniform charge distribution in the film (40meV). The result is

$$\varepsilon_{pentacene} = \frac{2(61\text{meV})^2}{(40\text{meV})} - 1 = 3.7 \, .$$

This value is close to the reported dielectric constant of π-electron semiconductors $C_{60}$ (4.08 ~ 4.4).[19,20] We consider that it supports our model of charge distribution in thin film FET. This effect of overlayer may also contribute to the broadening of the energy loss peaks though inhomogeneous thickness of the films.

To summarize this section, we measured EELS of pentacene thin film FETs with biasing gate voltages. One monolayer-thick pentacene film on the gate dielectric worked as an FET. The EELS of the film showed a significant loss feature and the loss energy of the peak position increased when the gate voltage was increased. The loss energies were on the same order with the predicted energies of the two dimensional plasmon. The plasmon loss energy of 3 ML (4.5nm) -thick FETs were substantially lower than the value estimated from the uniform distribution of the field-induced carriers. This is consistent with our previous results of the thickness of the accumulation layers in the pentacene FETs.

## 5. Sub-band Gap near IR Photocurrent Spectroscopy

### 5.1. Introduction

Gap states of semiconductors play very important role in actual devices. They may act as carrier traps, leak current path and carrier injection mediators depending upon the energy levels and location in the devices. In spite of their importance in organic electronics devices, very few studies can be found in the literature.[21, 22].

A powerful method for investigating the gap states is the photocurrent measurement. The photoconductivity of pentacene films was studied[23], in which the fundamental optical properties were reported. The photoconductivity measurement of the pentacene single crystal revealed that purified pentacene single crystals have exponential band tails broader than in inorganic amorphous materials.[24] The photocurrent spectrum of OFETs was also measured to investigate the photo-induced carrier generation mechanisms.[25] However, little is known about the effects of the source-drain voltage ($V_D$) and gate-source voltage ($V_G$) to the photocurrent, and no photocurrent spectrum in relation to interface gap states has been reported.

In this section, we present our photocurrent measurement experiments on pentacene FETs. First, we will show the photocurrent-voltage characteristics of the pentacene OFET, and propose that the relationship between the photocurrent and $V_D$ or $V_G$ can reveal the carrier generation mechanism. Then we will focus on the metal electrode - organic layer interfaces where gap states are formed only in the top-contact devices. The last part of this section is devoted to the unknown impurity states which determine the off current in the bottom contact FETs. The important device parameters of OFETs include carrier mobility, on/off ratio, subthreshold swing and threshold voltage. Microscopic or molecular origin of these characteristics has not been understood sufficiently although phenomenological studies can be found in large number of publications in this field.

## 5.2. Relationship between near IR Photocurrent and Gate and Drain Voltage of OFETs

In this subsection, we discuss the photocurrent-voltage characteristics of the bottom-contact devices. Figure 11 (a) is the characteristic under a 650 nm (1.91 eV) red light, and Figure 11 (b) is that induced by a 785 nm (1.58 eV) infrared light. The HOMO–LUMO gap energy of the thin solid pentacene has been determined to be 1.97 eV, and the fundamental exciton binding energy of 0.15 eV has been reported[26]. Therefore, red light with a wavelength of 650 nm (1.91 eV) corresponds to photons with an energy almost equal to the band gap, and the 785 nm (1.58 eV) infrared light is a sub-band gap light, i.e., light with an energy considerably smaller than the gap. Under the 650 nm (1.91 eV) red light, the photocurrent-voltage characteristics were similar to the static source-drain current ($I_{SD}$)-$V_G$ characteristic of our OFET (Figure 11(a) inset). This similarity indicates that the motion of the charges is affected in the same manner by the electric field in the device, which means that the hole current dominates the photocurrent-voltage characteristics. The absorption of 1.91 eV photons leads to a transition from the valence band to the conduction band and the formation of an electron-hole pair. Since the mobility of the holes in the pentacene thin film is much greater than that of electrons,[27] it is reasonable that the hole current will prevail over the electron current.

On the other hand, completely different photocurrent-voltage characteristics were observed under the 785 nm (1.58 eV) sub-band gap light (Figure 11(b)). First, the modulated photocurrent under the sub-band gap light was two orders of magnitude smaller than that under the 650 nm light. Second, when $|V_D|$ was higher than $|V_G + 9\ \text{V}|$, the sub-band gap photocurrent decreased as $|V_G|$ increased, while the photocurrent increased as $|V_G|$ increased when $|V_D| < |V_G + 9\ \text{V}|$.

The threshold voltage of the device ($V_{TH}$) was -9 V and the pinch-off occurs when $V_D = V_G + 9$ V. If $|V_D|$ is higher than $|V_G + 9\ \text{V}|$, there is a depletion area (area without hole accumulation) in the channel. In such an area, electrons can move without being captured by the holes. The width of the depletion area changes depending on the source-drain voltage and gate-drain voltage. Figure 11(b) shows that the sub-band gap photocurrent decreases as $|V_G|$ increases and the depletion area width decreases. When the depletion area disappears, the

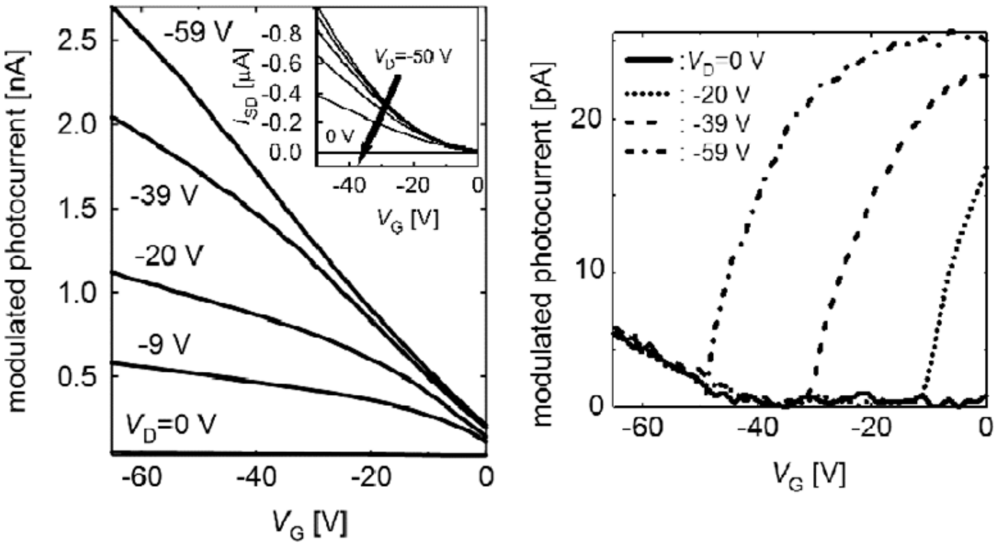

(a) hν = 650 nm (b) hν =785 nm

Figure 11. Photocurrent-$V_G$ characteristics of bottom contact FET. (a) Photon energy was 650nm. (b) Photon energy was 785 nm.

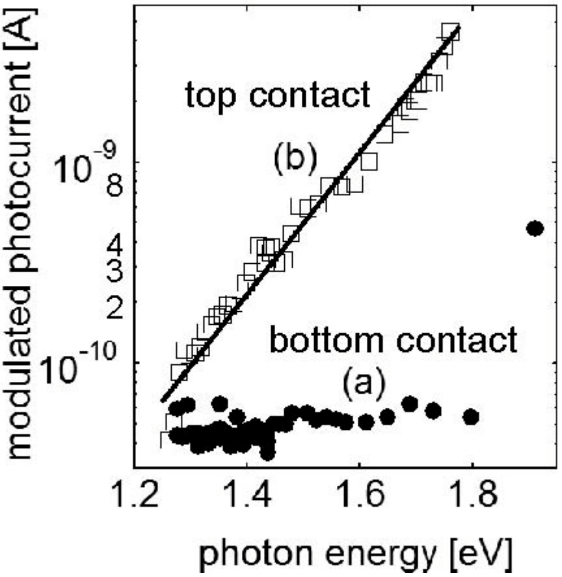

Figure 12. Photocurrent spectra of bottom contact (a) and top contact pentacene FET (b).

sub-band gap photocurrent became almost zero. Thus, the depletion area seems essential for the sub-band gap photocurrent, which means that the major carrier is the electron. The possible carrier generation mechanism for the mobile electron is the optical transition between the empty delocalized band states and occupied localized gap states. This sub-band gap photocurrent was measured even under a 1000 nm (1.24 eV) light illumination. We also investigated the photon energy dependence of the photocurrent. Contrary to the previously reported photocurrent spectrum,[23,24] we found a rather flat energy dependence of the photocurrent (Figure 12(a); (b) is the photocurrent spectrum of the top-contact devices and will be discussed later), except for an absorption peak induced by an exciton at 1.72 eV. This deviation from the reported photocurrent spectrum of the pentacene crystals and films will be discussed later. The observed flat distribution versus photon energy indicates that there are many localized gap states with a constant density of states in the polycrystalline thin film of pentacene. In order to elucidate the nature of the gap states, we fabricated many FETs using purified or as-purchased (Aldrich) pentacene, but the photocurrent intensity was mainly dependent on the pentacene/insulator interface, while the pentacene purity did not seem to play a key role in the gap states formation. The correlation between the interface and gap states needs further investigation, which will be discussed in section 5.4.

## 5.3. Urbach Tail in the Photocurrent of Top Contact Device

We will now discuss the photocurrent-voltage characteristics of the top-contact pentacene FETs. The metal-organic interface in organic field effect transistors (OFETs) is important for the injection and extraction of carriers from electrodes. The electron injection, for instance, requires metals with low work functions, because a large energy level mismatch between the lowest unoccupied molecular orbital (LUMO) and the metal Fermi level causes an injection barrier. However, recent studies revealed that the energy levels in the metal-organic interface deviate from the typical Mott-Schottky theory.[21, 22] An injection barrier lowering was reported at the gold/pentacene interface, and was explained by assuming the presence of in-gap states at the interface. It is said that those interface states are caused by metal-induced damage[28], but no consensus has been reached about the nature of the "damage".

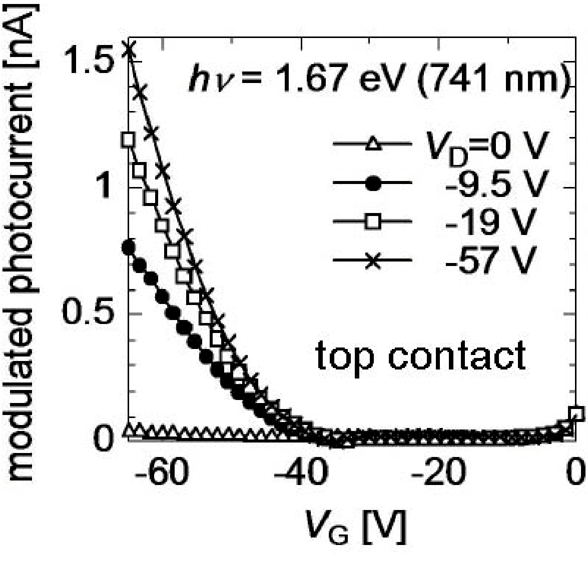

Figure 13. Photocurrent-$V_G$ characteristics of top-contact FET with 741 nm photon irradiation.

Figure 13 shows the characteristics of the top-contact device in the sub-band gap region (741 nm, 1.67 eV). Except for the $V_G$ shift caused by the high threshold voltage of the device, Figure 13 is very similar to Figure 11(a), in which the interband transition is observed. This result strongly suggests that the interband transition and electron-hole pair generation occur in the top-contact devices, even though the irradiated photon energy is smaller than the band gap.

Qualitatively similar characteristics were observed from 1.24 eV to 1.91 eV, except for the photocurrent intensity. The photon energy dependence of the intensity is shown in Figure 12(b), which depicts the sub-band gap photocurrent at $V_G$=-57 V and $V_D$=-64 V in the top-contact OFETs. This absorption edge is excellently fit by the following exponential function:

$$I_{ph} \propto \exp\left(\frac{h\nu - E_g\ [\mathrm{eV}]}{E_0\ [\mathrm{eV}]}\right)$$

where $I_{ph}$ is the photocurrent, hν is the photon energy, $E_0$ is the characteristic width of the absorption edge, and $E_g$ is the optical band gap energy. Here, we chose 1.97 eV for $E_g$,[26] and $E_0$ was found to be 132 meV from the fit. Such absorption edge characteristics are known as Urbach tails, and reported for many inorganic materials with impurities or disorders.[29] The unified theory of the Urbach tail is based on electric microfields resulting in an exciton energy stabilization. The common origin of such a microfield is the electrical charges of the impurities, but there are other causes as well. The exponential Urbach tail of InP:Cu was explained by the presence of microfields induced by Cu precipitates.[30]

In the bottom-contact devices, the sub-band gap photocurrent did not show an exponential dependence (Figure 12(a)), and photoexcitation of the electrons in the localized states was observed in the sub-band gap region. Therefore, Urbach tails in the top-contact devices cannot be attributed to intrinsic defects caused by the low purity of pentacene. It should be noted that the bottom contact devices made from non-purified pentacene did not show the Urbach tails. Another major difference between the top-contact and bottom-contact devices is air exposure. As already mentioned, the top-contact samples were exposed to the atmosphere during the fabrication process. In order to understand the effect of the air exposure, we exposed the bottom-contact samples to the atmosphere for approximately one hour and confirmed that the sub-band gap photocurrent-voltage characteristics indicated the excitation of electrons in the gap states (as in Figure 11(b)), and the spectrum did not show the Urbach tails. Instead, we suggest that the microfield induced by the metal-nanoparticle is responsible for the Urbach tails, just as in InP:Cu. In the top-contact configuration, metal electrodes are deposited after the organic semiconductor films are formed. Thus, metal atoms hit the organic films, penetrate the surface, diffuse into the film, and create metal clusters.[31, 32] In this way, there are large numbers of gold nanoparticles at the gold/pentacene interface of the top-contact devices.

The metal evaporation causes not only the diffusion of metals into the film, but also structural disorders, which can be another mechanism for the Urbach tails. However, we consider that the metal-induced structural disorders are negligible in the present case. We investigated the bottom-contact devices with low hole mobilities (~$10^{-4}$ $cm^2/Vs$) fabricated at room temperature, and qualitatively observed the same photocurrent-voltage characteristics as in Figure 11(b), in which the electrons in the localized states are excited under the sub-band gap light. Since the low mobilities of devices mean a poor crystallinity and many structural disorders, this photocurrent-voltage characteristic indicates that the structural disorders in the films form localized gap states, instead of the Urbach tails.

Unlike highly reactive metals such as Ca, chemically non-reactive materials like gold will not react with organic semiconductors and form interface states.[28, 33] Nevertheless, we can explain the lowering of the injection barriers without such chemical reactions, because microfields in the gold/pentacene interface will lower the energy levels of nearby pentacene molecules. In our top-contact devices, the characteristic energy $E_0$ of the Urbach tail was determined to be 132 meV from Figure 4(b). The microfield E can be roughly estimated from $\mu E=132$ meV, where $\mu$ is the dipole of the Frenkel excitons and the distance between the electron and the hole is the same size as one pentacene molecule. It is reasonable to assume that a similar dipole is formed by a hole (in the pentacene) and an electron (in the electrodes), when holes are injected from the electrodes. That dipole is of the same order of magnitude as the Frenkel exciton dipoles, or even larger. Thus, the hole injection barrier will be lowered by several hundred meVs. This is a possible explanation for the observed lowering of the interface injection barriers. Our hypothesis is reinforced by another example, i.e., ohmic contact formation by metal (Pt) co-deposition with an organic semiconductor.[34] We theorize that this can also be explained by the effect of microfields caused by the Pt nanoparticles embedded in the organic layers.

As mentioned above, gold nanoparticles generated by the gold deposition have complicated effects on the net physical properties. When the photoconductivity of the organic crystals or films is investigated, the top-contact geometry should not be employed. Some of the reported photocurrent measurements were performed using top-contact or sandwich-type devices in which metal electrodes are evaporated onto organic layers. It is suspected that the reported gap states [23,24] may be extrinsic ones arising from the metal nanoparticles near the electrodes deposited for the measurements. Using the bottom-contact configuration, we successfully measured the intrinsic photocurrent spectrum of polycrystalline pentacene films (Figure 12(a)), and observed the flat dependence versus photon energy and the absorption peak of the excitons.

### 5.4. Correlation between Sub-bandgap Photocurrent and Off Current of OFET - Microscopic Origin

We now focus on the bottom contact FETs again, because the sub-band-gap photocurrent of the top -contact device is dominated by an extrinsic Urbach tail induced by metal nanoparticles as described in the previous subsection.

We fabricated many FET samples by changing the surface treatment and growth conditions, and selected FETs with different characteristics. The FET characteristics of two typical samples with low and high off-currents are shown in Figure 14. The mobilities of the devices shown in Figs. 14(a) and 14(b) are $1.1 \times 10^{-2}$ and $8 \times 10^{-4}$ $cm^2V^{-1}s^{-1}$ respectively. The threshold voltage ($V_{TH}$) of the device shown in Figure 14(a) was evaluated from the $I_{SD}$-$V_G$ plot as -4 V. It was impossible to evaluate the $V_{TH}$ of the sample shown in Figure 14(b) because of the large off-current. We do not fully understand the conditions needed to prepare FETs with particular device characteristics in the present setup, but the surface treatment (which depends on UV-ozone, sonication in organic solvents, and other factors) is surely involved.

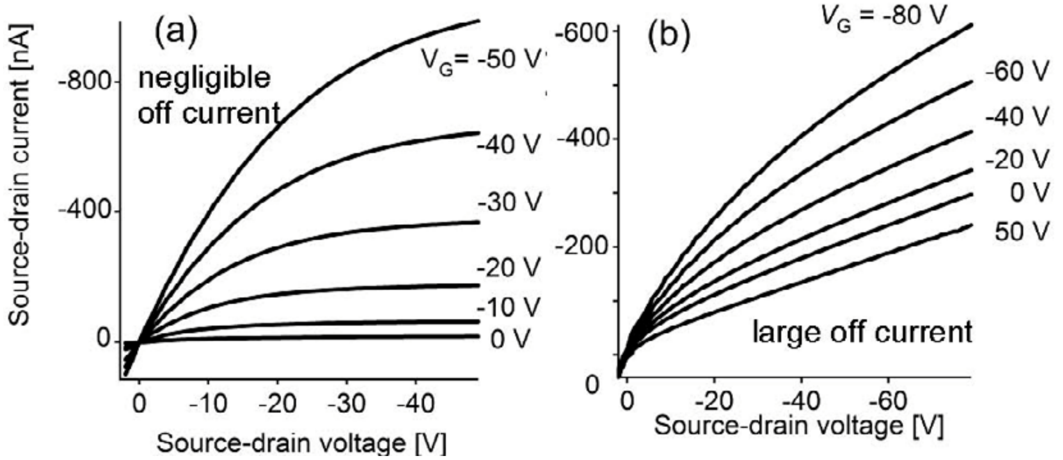

Figure 14. FET characteristics of pentacene FETs with different off-current intensity.

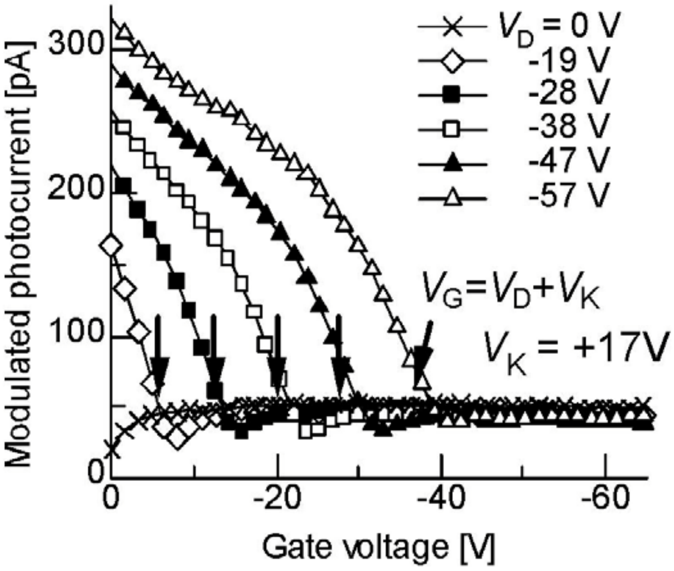

Figure 15. Photocurrent-$V_G$ characteristics of a bottom-contact FET with a large off current.

Figure 15(a) shows the photocurrent-$V_G$ characteristic induced by sub-band-gap light for the sample shown in Figure 14(b). The photon energy (hν) was 1.45 eV (856 nm) and the photocurrent intensity was rather uniform within the measured photon energy range (1.78 ~ 1.24 eV) without pronounced peaks except for those of excitons (1.82 eV).[35] There were kinks in Figure 15(a), which are indicated by arrows. $V_G$ - $V_D$ at the kinks, which we define as $V_K$, was independent of $V_D$. In the case of Figure 15(a), $V_K$ was -17 V for all $V_D$ values. When $V_{TH}$ could be simply evaluated from $I_{SD}$-$V_G$ plot in low off-current devices, $V_K$ was similarly invariant to changes in $V_D$, and was equal to $V_{TH}$ as described in the previous section. We therefore assumed that the $V_{TH}$ of the device can be evaluated from photocurrent-voltage characteristics, even when the off-current is too large to define $V_{TH}$. If $V_K$ is equal to $V_{TH}$, then pinch-off occurs at the kinks. It is noted that this photocurrent-$V_G$ characteristic somewhat resembles the transfer characteristics of ambipolar OFETs.[36] In the case of ambipolar OFETs, electron conduction appears after the holes are depleted by a large negative $V_D$. In this experiment, the modulated photocurrent was almost zero when $|V_G| > |V_D + V_{TH}|$ and it increased when $|V_G| < |V_D + V_{TH}|$. This condition indicates that the photocurrent was not observed when the holes accumulated throughout the channel [Figure 16(a)], while it was observed when pinch-off occurred [Figure 16(b)]. This point is very important for understanding the nature of sub-band-gap excitation. There are three possible origins of the absorption of the sub-band-gap photons (Figure 17): (a) excitation from the filled gap states to the empty part of the conduction band, (b) excitation from the filled part of the valence band to the empty gap states, and (c) excitation from the filled gap states to the empty gap states. Since it is considered that the gap states are not densely distributed and the conduction via partly filled gap states is probably negligible, (c) can be ruled out. In case (a), the conduction occurs via mobile electrons, and in case (b), it occurs via mobile holes. In our result, the modulated photocurrent corresponding to the holes was not observed when the hole conduction dominated [Figure 16(a)], whereas photocurrent corresponding to the electrons was observed in the depletion region after the pinch-off [Figure 16(b)]. Thus, our observation strongly suggests case (a). The photocurrent appears just after the holes are depleted because the mobile electrons are supplied from the photoexcitation of the gap states. Since the photon energy range was larger than half of the band gap and the photocurrent spectrum did not have a pronounced structure in the measured photon energy range as shown in Figure 12(a), we can conclude that the gap states contributing to the photocurrent are widely distributed from the valence band edge towards the midgap.

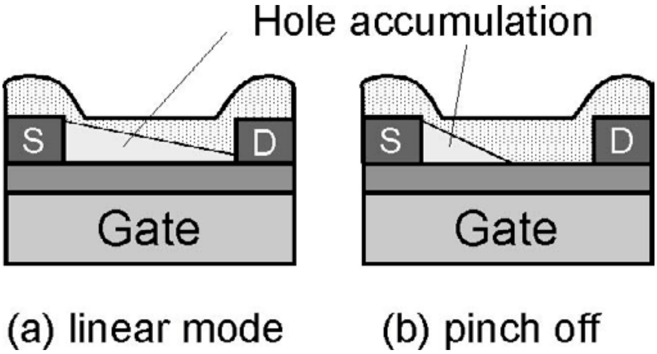

Figure 16. Schematic drawing of hole accumulation region in FET in linear mode (a) in pinch-off mode (b).

With this knowledge, we examined the correlation between the intensity of the sub-band-gap photocurrent and various properties of the devices. Figure 18 depicts the correlation of the intensity of the sub-band-gap ($h\nu = 1.45$ eV) photocurrent with (a) mobility and (b) off-current. The same marks correspond to the same sample. When the sample did not show obvious off-states, $I_{SD}$ at $V_D$=-50V was chosen for the value of the off-current. It is easily noticed that there is an obvious correlation between the off-current and the sub-band-gap photocurrent, whereas the mobility is not related with the photocurrent.

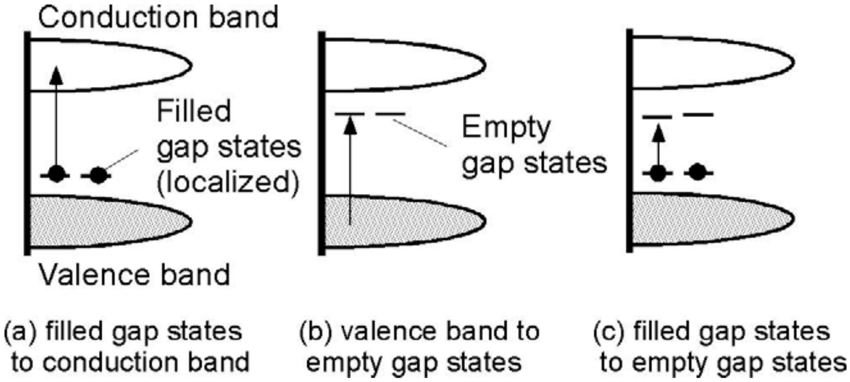
Conduction band
Filled gap states (localized)
Empty gap states
Valence band
(a) filled gap states to conduction band
(b) valence band to empty gap states
(c) filled gap states to empty gap states

Figure 17. Possible origins of electronic transition induced by sub-band gap photons.

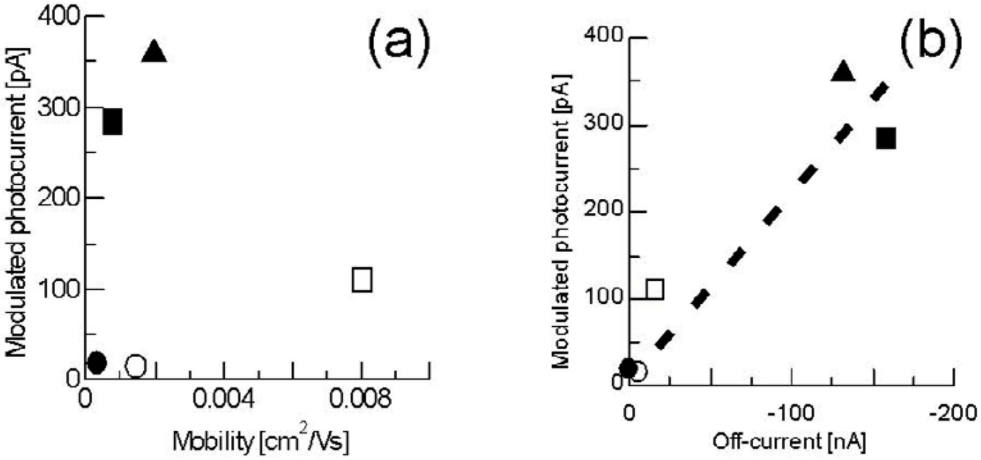

Figure 18. Plots to see the correlations of the intensity of NIRPC (photon energy 1.45 eV). (a) A plot with mobility (b) A plot with off-current. The line in (b) is drawn as a guide to the eyes.

This result is rather surprising, because the gap states close to the valence band can be assumed to be hole traps. The large photocurrent under sub-band-gap light, which corresponds to an electron transition from traps to the conduction band, indicates that there are a large number of traps in the films. We can simply assume that the mobility of that sample is low. One FET sample (marked with a filled triangle) with relatively high mobility showed a large photocurrent, and another one (open circle) showed a small photocurrent, even though its mobility was low. This result suggests the following two possibilities: the gap states that can be observed using the photocurrent method do not trap holes, or the hole mobility in polycrystalline pentacene films is not trap-limited. For the mechanism of the latter case, we can assume that the conduction path in the film is effectively narrow and limits mobilities. Since the mobility shown in Figure 16(b) is rather low, we consider that the latter is more probable.

The present result gives us some insight on the off-current of pentacene FETs. There are very few studies on the microscopic origin of the off-current. Since the off-current is due to conductivity that is not suppressed by the field effect, it should be regarded as a parallel passive resistance path between the source and drain electrodes. The most plausible origin of the parallel resistance is unintentional dopants, which make a continuous "pentacene path" a degenerate semiconductor. However, the experimental result shows that the sub-band-gap photocurrent responded to $V_G$ and $V_D$. This is not expected for a degenerate semiconductor and we must consider that the part of the channel producing the off-current and that producing the sub-band-gap photocurrent are different. We consider that the correlation between the off-current and the sub-band-gap photocurrent is explained by assuming that the molecular origin of these two properties is the same. In a region where the concentration of unintentional dopants is small, they act as photoexcitable gap states located near the valence band. In a region where the concentration is high, it will make the region into a degenerate semiconductor that does not respond to the gate electric field. We have not yet identified the unintentional dopants, but the location of their energy levels was identified through the present experiment. Since the photocurrent spectrum was rather flat between 1.24 and 1.7 eV (Figure 12(a)), the energy levels of the involved gap states are widely distributed from the valence band edge toward the midgap.

To summarize this section, we investigated the photocurrent-$V_G$ characteristics of pentacene FETs, and showed that the photocurrent-$V_G$ characteristics can reveal the origins of the carriers: i.e., the interband transition or excitation of electrons in the localized gap states. We also compared the photocurrent-$V_G$ characteristics of the bottom-contact and top-contact pentacene FET, and proposed that diffused gold particles cause an Urbach tail at the gold/pentacene interface. This is the first observation of the Urbach tail at the metal/organic interface, and we suggest that metal contacts without diffused nanoparticles are necessary for the intrinsic photocurrent measurement. By employing the bottom-contact geometry, we investigated the intrinsic photocurrent spectrum of the polycrystalline pentacene films, and found a flat distribution of energy levels in the sub-band gap region.

Then we compared the modulated photocurrents of various FET samples using sub-band-gap irradiation, and investigated the relationship between gap states and FET parameters. Since the sub-band-gap photocurrent is only observed in the pinch-off region, the energy level of the gap states is located close to the valence band top. The sub-band-gap photocurrent showed a correlation with the off-current, and the molecular origin of the off-current was suggested to be highly concentrated gap states that form degenerate semiconductor paths in the channel.

## 6. CONCLUSION

In this chapter, we introduced three kinds of spectroscopic techniques newly applied to OFETs under gate bias. In electron spectroscopy experiments (UPS and EELS), we showed that the measurement is possible by properly shielding the gate electric field around the sample. We found the reactivity for polymerization is greatly enhanced by introducing charges in $C_{60}$ FETs by UPS measurement and obtained reasonable agreement about the effective mass values in pentacene FETs by EELS measurement.

In the near IR photocurrent spectroscopy of working pentacene FETs, we showed that the origin of the carriers giving photocurrent can be evaluated by changing the drain and gate voltages. We found that strong Urbach tail was observed only in top contact devices and concluded that it was due to the metal nanoparticles penetrating the organic layers. The characteristic energy of the Urbach tail was large enough to account for the formation of the Ohmic contact at "dirty" metal-organic interface. In the bottom contact devices, we found a correlation between the sub-bandgap photocurrent and off current of the OFETs, and the speculated that chemical origin of both phenomena is the same, i.e., formation of some kind of charge transfer complex. The newly introduced measurement techniques will be useful not only for fundamental studies on the conduction mechanism in organic semiconductors but also for the characterization of the devices and their fault analysis.

## Acknowledgments

The present work was partly supported by a PREST-JST grant, a NEDO grant (00B64026c) and Grants-in-Aid from the Ministry of Education, Science, Culture and Sports of Japan. Financial supports from Ogasawara Science Foundation, Mukai Foundation, Shorai Science and Technology Foundation were also essential for the present research. Discussions with Prof. K. Saiki (Univ. Tokyo), Prof. K.Kudo and Prof. M. Nakamura (Chiba University) are gratefully acknowledged.

## REFERENCES

[1] T. Shimada, T. Suetsugu, T. Miyadera, Y. Yamamoto, A. Koma, K. Saiki, and K. Kudo, *Appl. Phys. Lett.* **84**, 2439-2441 (2004).
[2] T.Shimada, K.Saiki, *J. Electron. Spectrosc.Related Phenomena,* **154**, 119-122 (2007).
[3] M. Ohtomo, T. Shimada, K. Saiki, and T. Hasegawa., *J. Appl. Phys.* **102**, 064510(2007) (4 pages)
[4] M. Ohtomo, T. Shimada, T. Hasegawa, *Jpn. J. Appl. Phys.* **46**, L817-L820 (2007).
[5] M. Sakurai, H. Tada, K. Saiki, A. and Koma, *Jpn. J. Appl. Phys.* **30**, L1892 (1991).
[6] A.M. Rao, P. Zhou, K. Wang, G.T. Hager, J.M. Holden, Y. Wang, W.T. Lee, X.X. Bi, P.C. Eklund, D.S. Cornett, M.A. Duncan, and I.J. Amster, *Science,* **259**, 955 (1993).
[7] Y. Wang, J.M. Holden, Z.H. Dong, X.X. Bi, and P.C. Eklund, *Chem. Phys. Lett.* **211**, 341 (1993).
[8] Y.B. Zhao, D.M. Poirier, and R.J. Pechman, *J. Weaver, Appl. Phys. Lett.* **64**, 577 (1993).
[9] Ito, T. Morikawa, and T. Takahashi, *Chem. Phys. Lett.* **211**, 333 (1993).
[10] Y. Nakamura, Y. Mera, and K. Maeda, *Appl. Phys. Lett.* **77**, 2534 (2000).
[11] P. Zhou, Z.H. Don, A.M. Rao, and P.C. Eklund, *Chem. Phys. Lett.* **211**,337 (1993).
[12] P.A. Heiney, J.E. Fischer, A.R. McGhie, W.J. Romanow, A.M. Denenstein, J.P. McCauley Jr., A.B. Smith III, D.E. Cox, *Phys. Rev. Lett.* **66**,2911 (1991)
[13] M. Portail, M. Carrere, J. M. *Layet, Surf. Sci.* **433–435** (1999) 863.

[14] S. E. Fritz, S. M. Martin, C. D. Frisbie, M. D. Ward, and M. F. Toney, *J. Am. Chem. Soc.* **126** (2004) 4084.

[15] G.A. de Wijs, C.C. Mattheus, and R.A. de Groot, T.T.M. *Palstra, Synth. Metals*, **139** (2003) 109.

[16] K. Hummer, C. and Amnrosch-Draxl, *Phys. Rev. B.* **72** (2005) 205205.

[17] M. Kiguchi, M. Nakayama, K. Fujiwara, K.Ueno, T.Shimada, and K. Saiki, *Jpn. J. Appl. Phys.* 42 (2003) L1408.

[18] M. Kiguchi, M. Nakayama, T. Shimada, and K. Saiki, *Phys. Rev. B,* **71** (2005) 035332.

[19] P.C.Eklund,A.M.Rao,Y.Wang,P.Zhou,K-.A.Wang, J.M. Holden, M.S. Dresselhaus, and G. Dresselhaus, *Thin Solid Films*, **257** (1995) 211.

[20] A.F.Hebard, R.C.Haddon, R.M. Fleming, and A.R.Kortan, *Appl. Phys. Lett.* **59** (1991) 2109.

[21] S. C. Veenstra, and H. T. Jonkman, *J. Polym. Sci., Part B, Polym. Phys*. **41**, 2549 (2003).

[22] H. Vazquez, F. Flores, R. Oszwaldowski, J. Ortega, R. Perez, and A. Kahn, *Appl. Surf. Sci.* **234**, 107 (2004).

[23] E. A. Silinsh, A. I. Belkind, D. R. Balode, A. J. Biseniece, V. V. Grechov, L. F. Taure, M. V. Kurik, J. I. and Vertzymacha, I. *Bok, Phys. Stat. Sol. (a)* **25**, 339 (1974).

[24] D. V. Lang, X. Chi, T. Siegrist, A. M. Sergent, and A. P. Ramirez, *Phys. Rev. Lett.* **93**, 086802 (2004).

[25] S. Dutta, and K. S. Narayan, *Synthetic Metals*, **155**, 328 (2005).

[26] Lee, S. S. Kim, K. Kim, J. H. Kim, and S. Im, *Appl. Phys. Lett.* **84**, 1701 (2004).

[27] T. Yasuda, T. Goto, K. Fujita, and T. Tsutsui, *Mol. Cryst. Liq. Cryst.*, **444**, 219 (2006)

[28] P. V. Pesavento, R. J. Chesterfield, C. R. Newman, and C. D. Frisbie, *J. Appl. Phys.* **96**, 7312 (2004).

[29] J. D. Dow, and D. Redfield, *Phys. Rev. B*, **5,** 594 (1972).

[30] R. Adomavicius, A. Krotkus, R. and Leon, C. Jagadish, *Phys. Stat. Sol.* (a) **168**, 475 (1998).

[31] check! 31. A. C. Durr, *J. Appl. Phys.* **93**, 5201 (2003)

[32] Shen, and A. Kahn, *J. Appl. Phys.* **89**, 449 (2001)

[33] V.-E. Choong, M. G. Mason, C. W. Tang, and Y. Gao, *Appl. Phys. Lett.* **72**,2689 (1998).

[34] K. Suemori, M. Yokoyama, and M. Hiramoto, *Appl. Phys. Lett.* **86**, 173505 (2005).

[35] J. Lee, S.S. Kim, K. Kim, J.H. and Kim, S. Im, *Appl. Phys. Lett.* **84**, 1701 (2004).

[36] J. Zaumseil, and H. Sirringhaus: *Chem. Rev.* **107**,1296 (2007).

In: Integrated Circuits, Photodiodes…
Editors: R. McIntire and P. Donnell, pp. 185-207

ISBN: 978-1-60692-660-4
© 2009 Nova Science Publishers, Inc.

*Chapter 7*

# SOLUTION-PROCESSED ORGANIC THIN-FILM TRANSISTORS

***Jeong-In Han, Sung Kyu Park and Yong-Hoon Kim***
Information Display Research Center, Korea Electronics
Technology Institute, Korea

## ABSTRACT

In this chapter, solution-processed organic thin-film transistors (OTFTs) using poly (3-hexylthiohpene) (P3HT) and 6,13-bis(triisopropylsilylethynyl) (TIPS) pentacene are introduced. By properly selecting the organic solvent for semiconductor, adjusting the surface energy of gate insulator and introducing a novel source/drain electrode structure, high performance OTFTs can be realized. This chapter focuses on effect of solvent on the crystallinity, morphology and electrical performances of OTFTs based on P3HT and TIPS pentacene.

## 1. INTRODUCTION

OTFTs have attracted a considerable attention in various display applications due to their potential advantages such as simple device architecture, large-area compatible fabrication and low-temperature process for flexible applications. A vacuum deposited pentacene OTFT exhibits field-effect mobility of 1 ~ 3 $cm^2/Vs$, higher than hydrogenated amorphous silicon TFTs [1-3]. However, the rather poor electrical reliability is the critical problem for practical applications and pentacene may not be a suitable material for large area applications due to rather costly vacuum deposition process.

Recently, OTFT *via* solution process is becoming more important because of its simplicity in device fabrication. With combination of printing techniques such as ink-jet printing, solution-processed OTFT can be a promising candidate for switching device in flexible active-matrix displays. However, the electrical performances of solution-processed OTFTs are still yet much inferior to that of vacuum-deposited OTFTs using pentacene. To enhance the electrical performances of solution-processed OTFTs, several approaches have been introduced; *i)* using novel semiconductor materials, *ii)* surface treatment of gate insulator (modifying the surface energy), *iii)* contact treatment of source/drain electrodes, *iv)* adoption of new device structure, *v)* blending with high boiling point organic solvent *etc*.

In the following sections, the effect of solvent and device structure on the electrical performances of OTFTs will be discussed.

# 2. P3HT BASED OTFTS

## 2.1. Poly (3-hexylthiohpene)

Poly (3-hexylthiophene) (P3HT) is a solution processable polymer semiconductors material which has gathered much attention due to its relatively high mobility (~ 0.1 $cm^2/Vs$) and easy processing. Solution process enables low cost fabrication processes such as spin coating, dip coating [4], ink-jet printing [5] and contact printing [6]. These processes are compatible with roll-to-roll process and also the process temperature can be very low (< 100°C). Because of these reasons solution processed OTFTs can be easily adopted in flexible display fabrication with polymer substrates.

One of the main issues rising in the area of solution processed OTFT is the patterning technique for organic layers. With spin coating and dip coating methods, the polymer solution will cover the entire area and the patterns must be defined by conventional photolithography process or by surface energy control (hydrophilic/hydrophobic). Another possibility is using photo-sensible functional polymers but this could be rather difficult work [7]. Ink jet printing method, currently used in polymer light emitting diode devices, is one another possible way to make patterns with very high speed, but the disadvantage of this method is it requires extra layer with patterned wells or bank structures.

## 2.2. Device Structure

Basically, the device structure of OTFT is very similar to conventional Si based TFTs. Polycrystalline Si TFTs are mostly fabricated as top gate structure [8,9] whereas amorphous Si TFTs are fabricated as bottom gate, bottom contact structure [10]. In the case of OTFTs, bottom gate, bottom contact structure generally is used due to limited physical and chemical endurance of organic semiconductor materials.

In the early stage of OTFT development, top contact structure (which the source and drain electrodes are deposited over the organic semiconductor layer) was used because of its superior electrical characteristics over the bottom contact device and also simple fabrication process [11-13]. However, the top contact structure has limits in realizing transistors with a short channel length (< 20 μm) and also a metallic shadow mask is required to generate the electrode patterns. Because of these reasons, bottom gate, bottom contact structure has now become the most frequently used device structure [14,15].

## 2.3. Fabrication

In Figure 1, a schematic diagram of a bottom contact type P3HT based OTFT device is shown. The gate electrode (usually metals) is deposited on thin substrates such as polymers, glass, quartz and papers. On top of gate electrode, gate insulator is deposited and patterned. The source and drain electrodes which consist of Cr and Au are deposited sequentially by evaporator system without breaking the vacuum. After patterning the source and drain electrodes, surface treatment of gate insulator is usually followed to modify the gate insulator surface from hydrophilic to hydrophobic. In this case, $O_2$ plasma and hexamethyldisilazane (HMDS) treatments were followed to modify the surface property of the $SiO_2$ gate insulator [16].

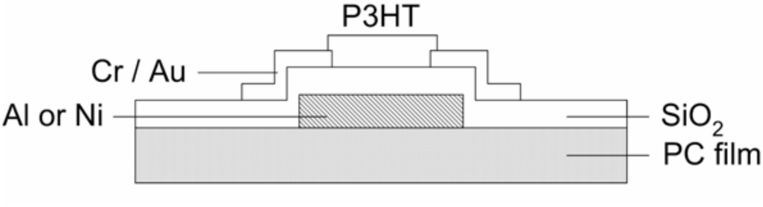

Figure 1. Schematic diagram of a bottom-contact type P3HT organic thin-film transistor fabricated on PC substrate.

After the surface modification of gate insulator, a semiconductor material P3HT is coated as a channel layer. Head-to-tail regioregular P3HT forms a thin layer with self-assembled, two-dimensional (2D) lamellae structures and the transistor characteristics such as field effect mobility and on/off ratio are greatly affected by the microstructure of this layer. According to Sirringhaus et al., spin-coated P3HT layer with edge-on orientation showed enhanced field effect mobility up to 0.1 $cm^2/V{\cdot}s$ [17]. Whereas, P3HT layer with face-on orientation showed mobility of nearly 2 orders lower. This phenomenon is believed to be due to the difference in π-π stacking orientation of channel layer. When the side chain is attached to the oxide surface, the layer is edge-on oriented, which results in π-π stacking orientation parallel to substrate surface, also the direction which the current flows in the device. However, when the side of thienyl ring is attached to the oxide surface, the layer is face-on oriented, which results in π-π stacking orientation normal to substrate surface and direction the current flows [18].

As well as the stacking structure of P3HT film on gate insulator, the regioregularity of P3HT also significantly affects its electrical characteristics. Especially, higher head-to-tail regioregularity exhibits better electrical performance. To increase the regioregularity of P3HT material, a purification process of continuous extraction with tetrahydrofuran (THF) and acetonitrile is usually carried out, using solubility difference between regio-random and regioregular polymers. By this method, the regioregularity of P3HT can be increased from 93% to 98% after the purification which is estimated with $^1H$ NMR by comparing the signal intensity that arises from the aromatic region of the spectrum [19].

P3HT material dissolves in a variety of organic solvents such as chloroform, chlorobenzene, xylene, toluene and hexane. It was revealed that the electrical performances of P3HT OTFTs were varied by the choice of a solvent [20]. Also, the coating method affects the crystallinity and electrical properties of P3HT film. Among several coating methods, a rubber stamp printing method has an advantage of generating patterns without any lithography processes and because the mold used in the rubber stamping process has great flexibility this process can be easily integrated in roll-to-roll process.

The rubber stamp printing method is carried by following steps. At first, to create the rubber stamp, a master structure with rectangular type islands was fabricated on a Si wafer or on a glass substrate using thick photoresist such as SU-8 (MicroChem corp.). The thickness of the photoresist can be controlled from 50 μm to 700 μm by varying the rotation speed of spin coating. After fabricating the master structure, poly (dimethylsiloxane) (PDMS) (DC 184, Dow Chemical) prepolymer is poured and thermally cured in an oven. After the curing process, the rubber stamp is removed from the master structure. Then, a drop of P3HT solution is supplied on the rubber stamp and blown with a stream of nitrogen, leaving a thin film of polymer on the stamp. Finally, the stamp is contacted directly with the substrate to transfer the film onto the substrate forming an active channel layer. Figure 2 shows the optical images of fabricated PDMS rubber stamp and printed P3HT film on a PC substrate. The size of the island pattern is 700 μm x 900 μm and the thickness of the film is approximately 60 nm. The thickness uniformity of the P3HT films was near 80% in 100 island test patterns.

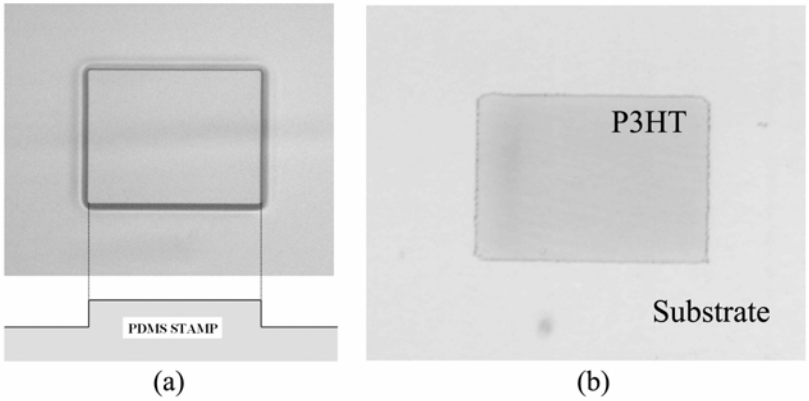

Figure 2. Optical images of (a) a poly(dimethylsiloxane) (PDMS) rubber stamp, and (b) rubber-stamp-printed P3HT film on a polycarbonate substrate. The size of the rectangular pattern is 700 μm x 900 μm and the thickness of printed P3HT film is 60 nm.

## 2.4. Crystallinity

The relationship between the microstructure of P3HT films and the electrical characteristics of field-effect transistor has been intensively studied since after the first investigation by Sirringhaus et al. [17]. This report showed that the field-effect mobility of organic transistor depends on the two-dimensional molecular ordering of P3HT film and the edge-on structure is more favorable in achieving high mobility rather than the face-on structure.

In order to investigate the structural properties of rubber-stamp-printed P3HT films, synchrotron grazing-incident x-ray diffraction (GI-XRD) measurements were carried out on both spin coated and rubber-stamp-printed P3HT films on Si/SiO$_2$ substrates. To minimize the scattering contributions from the substrate during the synchrotron measurements, the grazing incidence angle was fixed at 0.18º which is between the critical incidence angles ($\alpha_c$) of $SiO_2$ (0.20º) and polymers (0.17º). Figure 4 shows diffraction patterns obtained from the samples in out-of-plane mode. The first peak ($2\theta \approx 5.5$º) corresponds to (100) and the second ($2\theta \approx 11$º), third ($2\theta \approx 16$º), fourth ($2\theta \approx 24$º) peaks represent (200), (300), (010), respectively [19,21]. The (100), (200) and (300) reflections correspond to the lamellar type stacking of the two-dimensional conjugated planes (d = 16.7 Å) and (010) reflections correspond to the π-π interchain stacking distance between the polymer chains (d = 3.8 Å) [22].

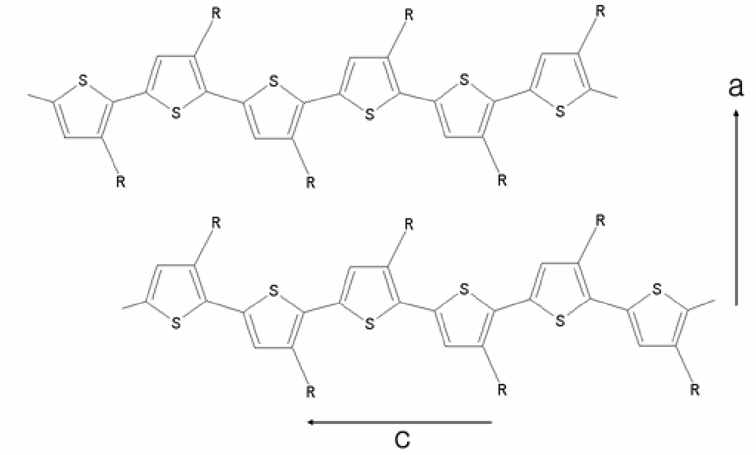

Figure 3. Molecular structure of poly (3-hexylthiophene).

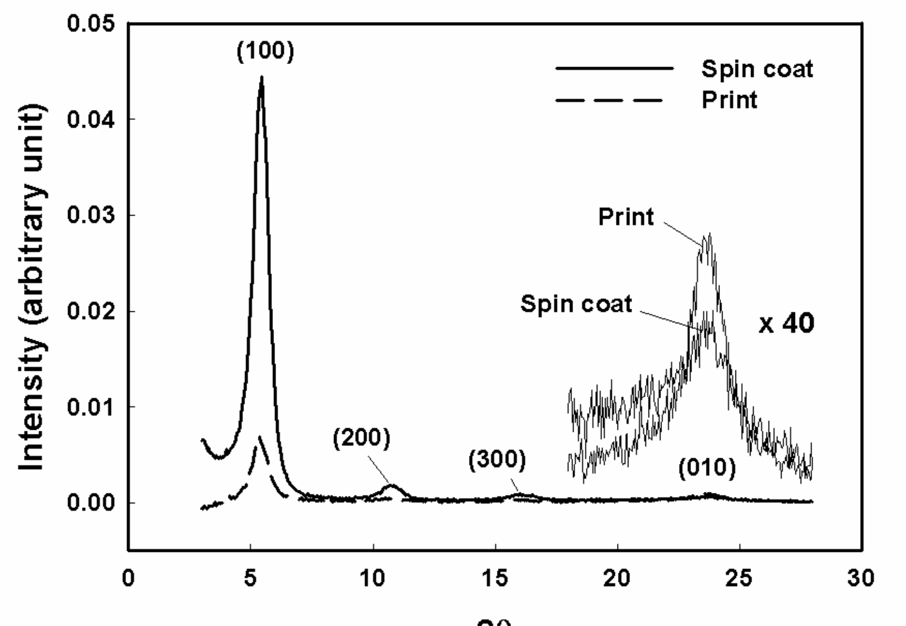

Figure 4. Diffraction patterns of spin coated and rubber-stamp-printed P3HT film obtained by synchrotron grazing-incidence X-ray diffraction (GI-XRD) measurements (out-of-plane mode).

Results show that strong (100) reflections were observed in spin-coated as well as printed P3HT films, whereas (010) reflections were very weak. This implies that the (100)-axis has the preferred orientation normal to the film surface. The difference in the intensity of (h00) (h = 1, 2, 3) reflections in spin coated and printed films may result from the difference in film thickness. However, the intensity of (010) reflections in printed film is higher than spin coated sample, suggesting that printed films have more random structure than spin-coated films. This is due to the different film forming conditions during the rubber stamp printing process. In rubber stamp printing, P3HT film is formed with a very rapid growth rate by a stream of $N_2$ gas and consequently results in more disordered structure than spin coated films. However, despite the fact that the printed films have less ordered structure than spin coated films, it has preferential orientation of (100)-axis normal to the film surface and suggests that the organic transistors with high field-effect mobility can be achieved using the rubber stamp printing.

Figure 5 shows the transfer characteristics of organic transistors fabricated with as-received (93% in regioregularity) and purified (98% in regioregularity) P3HT materials. Here, the active channel was printed using the rubber stamp. With low regioregular material (93%), the field-effect mobility was found to be 0.025 $cm^2/V{\cdot}s$ and the on/off ratio was $10^2 \sim 10^3$ (Figure 5(a)). However with purified material (98%), the field-effect mobility increased to 0.079 $cm^2/V{\cdot}s$ with a maximum value of 0.1 $cm^2/V{\cdot}s$ and the on/off ratio also increased to $10^4 \sim 10^5$ (Figure 5(b)). Consequently, using higher regioregular P3HT, field-effect mobility and on/off ratio were improved by factors of 3 and $10^2$, respectively. The enhancement of field-effect mobility is attributed to more microcrystalline P3HT domains which have preferential orientation of (100)-axis normal to the film surface. In other words, more microcrystalline domains have π-π interchain stacking direction parallel to the charge moving direction in a transistor and consequently enhancing the charge transport in the device.

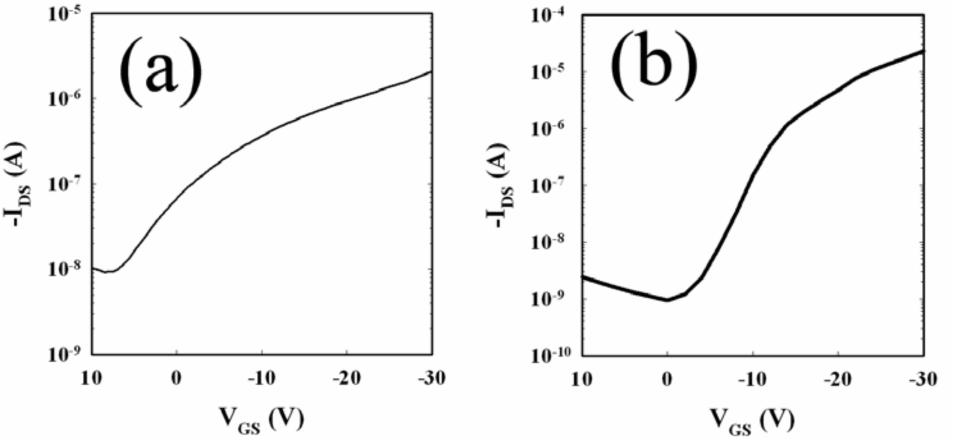

Figure 5. Transfer characteristics of rubber-stamp-printed OTFTs on polycarbonate substrates with; (a) as-received P3HT (93% in HT regioregularity), and (b) purified P3HT (98% in HT regioregularity). (L=25 μm, W=500 μm, $V_{DS}$ = -30V).

## 2.5. Stability

Most of the functional organic materials are very sensitive to air, leading to significant degradation or failure of the device. In order to achieve an air-stable and reliable device, the degradation process by the air must be clarified beforehand. Several physical mechanisms have been proposed for the degradation recently, such as trapping of charges at semiconductor-insulator interface [23] or at the grain boundary [24] and chemical degradation of the organic material. In this section, the stability of P3HT OTFT in various test environment conditions is discussed.

Figure 6 shows the changes in field effect mobility of an OTFT device as a function of time and measured condition. The field effect mobility was calculated in the saturated regime using the follow Eq. 1,

$$I_{DS} = \frac{W}{2L} C_i \mu (V_g - V_t)^2 \tag{1}$$

where $I_{DS}$ is the drain current, $C_i$ the capacitance per unit area of the gate insulator layer, $V_g$ and $V_t$ are the gate voltage and threshold voltage, respectively.

When the device was measured in vacuum, the change in mobility was relatively small, although the mobility constantly decreased. The initial mobility of the device was 4.48 × $10^{-3}$ $cm^2$/V·s and decreased to 1.61 × $10^{-3}$ $cm^2$/V·s after 7 hours in the vacuum chamber. However, when the air was inserted into the chamber, rapid degradation of the device was observed. Typically, after 15 minutes of exposure, the mobility decreased to 1.02 × $10^{-5}$ $cm^2$/V·s.

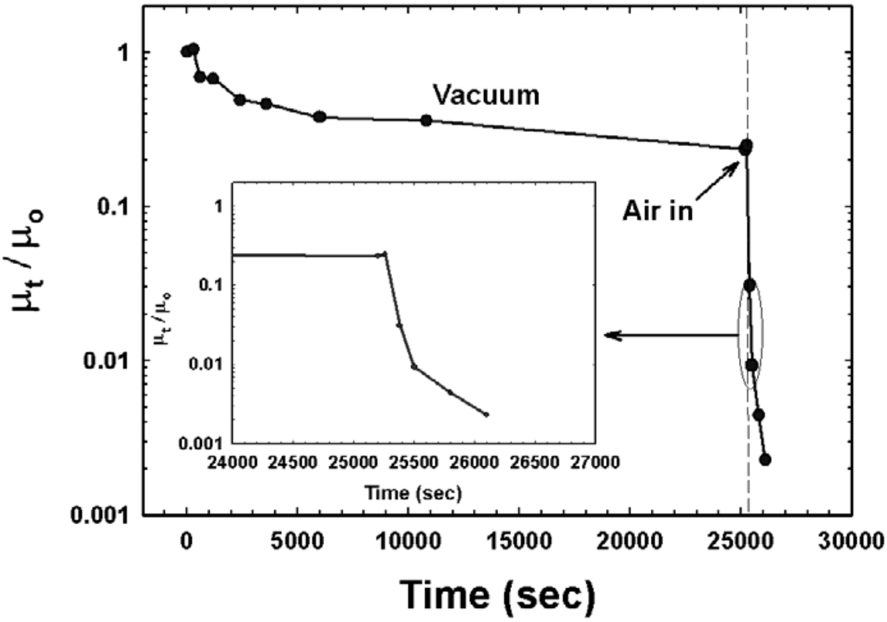

Figure 6. Dependence of field effect mobility on the measured condition (as a function of time).

The changes in the *on* and *off* currents as a function of time and measured condition are shown in Figure 7. The *on* current is the current measured at $V_{GS} = V_{DS} = -40$ V and the *off* current is the current measured at $V_{GS} = 5$ V and $V_{DS} = -40$ V. In the case *off* current, the current initially decreases to about 50% of its original value and saturates. When the air is inserted into the chamber, the off current first increases and then returns to its original value.

In the case of *on* current, the degradation is more significant. The *on* current also decreases first and saturates in vacuum. However, as the air is inserted, the *on* current drops very rapidly. Typically, the initial *on* current is - 0.976 µA and saturated to about - 0.184 µA after 7 hours in vacuum. When the air is inserted, the current decreases down to - 0.013 µA. As a consequence, the on/off ratio was also greatly affected by the exposure to air. After 15 minutes of exposure, the on/off current was changed from $10^3$ to $10^1$.

The observed degradation of the OTFT device is possibly resulted from the fact that P3HT is sensitive to $H_2O$ and $O_2$ molecules present in air. Previously, Zhu et al. [25] reported a humidity sensor based on pentacene thin film transistors. According to this report, the saturation current of the device was vastly affected by the humidity change (the saturation current decreased as the relative humidity increased) and this reaction with humidity change was very fast (within a few tens of minutes). This reaction is due to the effect of humidity on the charge transport properties of pentacene. Since the pentacene film has a relatively open structure, $H_2O$ molecules can easily diffuse into the film and interact with the trapped carriers by altering the electrical field at the grain boundary or change the morphology [26-28]. It is known that P3HT can be p-doped by atmospheric oxygen and charge transfer complexes can be formed by interact with oxygen and light [29,30]. However, when oxygen gas was inserted into the chamber instead of air, a rapid degradation of the device was not observed. Hence, oxygen is not responsible for the rapid degradation. More detailed studies are under investigation to clarify this rapid degradation process, whether the $H_2O$ molecules are responsible for the degradation.

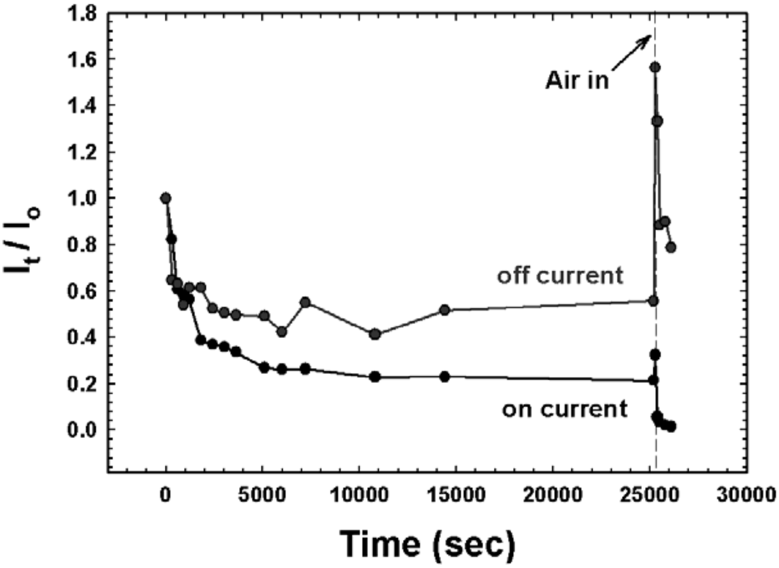

Figure 7. Dependence of *on* and *off* current on the measured condition (as a function of time).

In Figure 8, the threshold voltage shift of the OTFT device under various operating conditions is shown. As well as the field effect mobility and on/off current, the threshold voltage is also dependent on the exposed time and operation conditions. Initially negative threshold shift is observed in every case. This negative threshold shift is attributed to charge trapping when the device is stressed with negative bias [23]. On longer time scales, the device shows positive threshold shift when exposed to air. However, in vacuum, no positive threshold shift can be seen and a saturation point is observed, which suggests that $H_2O$ and $O_2$ molecules are also responsible for the threshold voltage shift. [reproduced from "Jpn. J. Appl. Phys. 43 (2004) 3605"]

In order to reduce the threshold voltage shift, a passivation layer of $SiO_2$ can be deposited on the device, which is widely used as a diffusion barrier for oxygen and water vapor molecules. As shown in the graph, when the passivation layer of $SiO_2$ is deposited on the device, the rate of threshold voltage shift decreases. Thus this implies that the threshold voltage is also affected by the exposure to air and a passivation layer is a prerequisite for an air stable device.

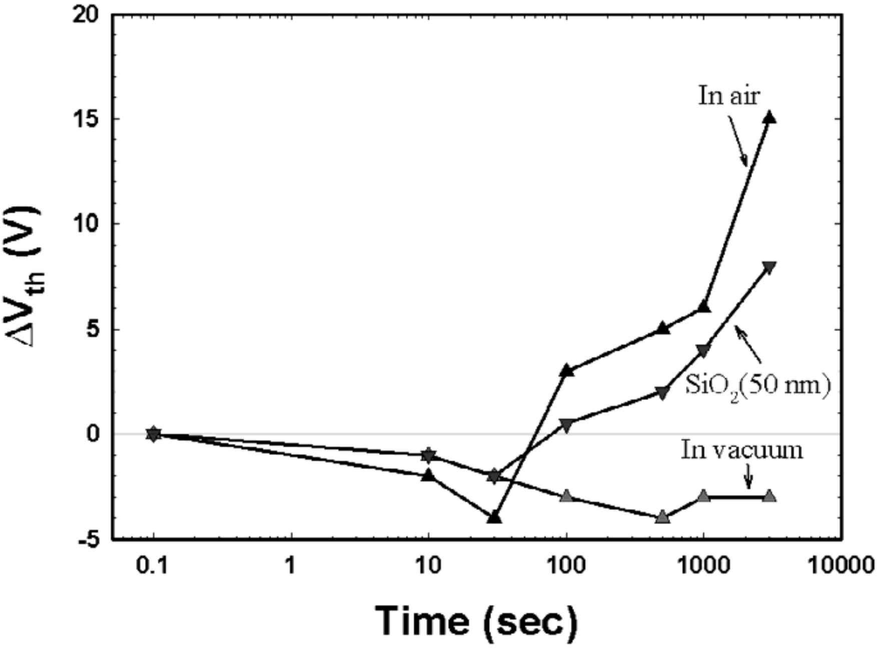

Reproduced from "Y. H. Kim et al., Jpn. J. Appl. Phys. 43, 6A (2004) 3605".

Figure 8. Threshold voltage shift of P3HT OTFT device under various operating conditions. A 50-nm-thick $SiO_2$ passivation layer is applied and measured in air condtion.

Figure 9 shows the changes in the transfer characteristics of an OTFT device as a function of time. When the device is measured in vacuum (Figure 9(a)), the change in the transfer characteristic is relatively small, although the curves show a constant negative shift (Figure 10) and decrease in the drain current. The initial mobility of the device was $4.48 \times 10^{-3}$ $cm^2/V{\cdot}s$ and decreases to $1.61 \times 10^{-3}$ $cm^2/V{\cdot}s$ after 7 hours in the vacuum chamber. Also, the threshold voltage changed from 8 V to 1 V.

When the air is inserted into the chamber, rapid degradation of the device was observed. Typically, after 15 minutes of exposure the mobility decreases from $1.61 \times 10^{-3}$ cm$^2$/V·s to $1.02 \times 10^{-5}$ cm$^2$/V·s. Figure 9(b) shows the changes in the transfer characteristics as a function of time after air is inserted. As the exposed time increases, degradation in the current modulation is significant and after 15 minutes of exposure, the on/off ratio of the device becomes less than 10. The degradation of the on/off ratio is caused by increase in the *off* state current and decrease in the *on* state current. However, interestingly the transfer characteristic of the device returns to the initial state when the device is again set in a vacuum state or instead of air, $N_2$ gas is inserted into the chamber.

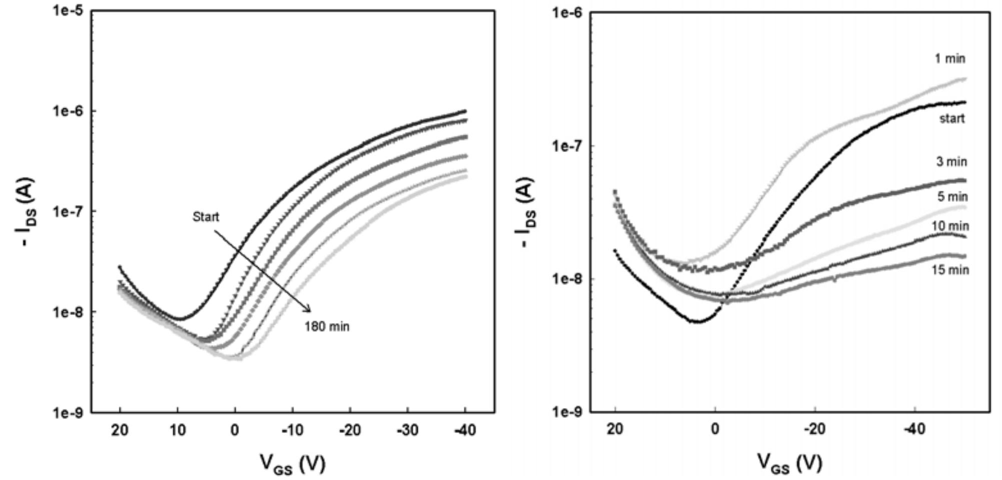

Figure 9. Transfer characteristics of rubber stamp printed thin film transistors as a function of time, (a) when the transistor is in vacuum state, (b) after air is inserted.

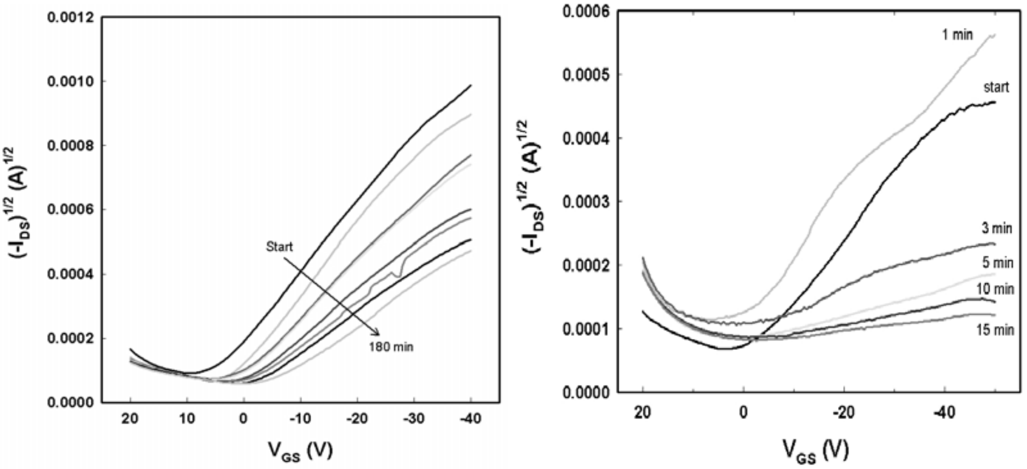

Figure 10. Curves of square root of the drain current vs. gate voltage of rubber stamp printed thin film transistors as a function of time, (a) when the transistor is in vacuum state, (b) after air is inserted.

Figure 11 shows the changes in output characteristics of a transistor in vacuum state. The drain-source voltage was swept from 0 V to – 30 V and the gate-source voltage was 0 V to –

40 V, with – 10 V of step. Along with the negative shift of the threshold voltage, the current flowing in P3HT layer also decreases, suggesting another source of degradation.

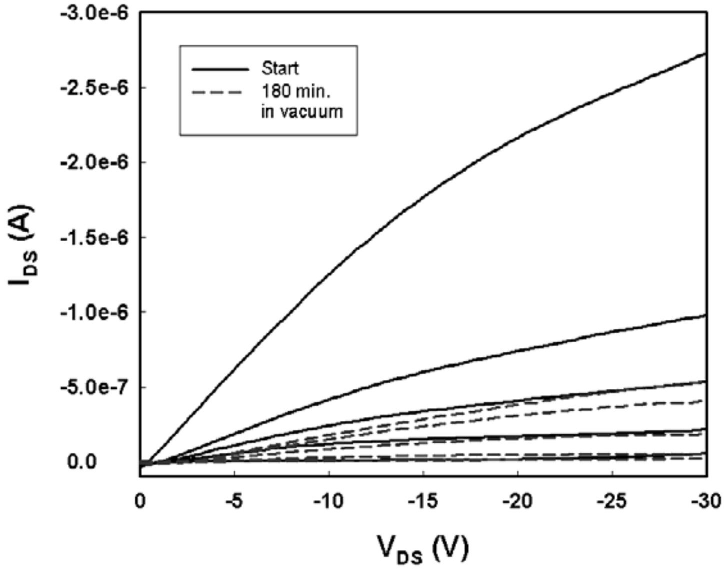

Figure 11. Output characteristics of a rubber stamp printed thin film transistor, (a) at initial state, and (b) after 180 minutes placed in a vacuum chamber.

## 2.6. P3HT OTFT-Driven AMLCD

P3HT based OTFT-LCD was fabricated with PC substrates by employing the rubber stamp printing method. Figure 12 shows the optical images of the OTFT array and the 2” panel fabricated with PC substrates. For the fabrication of a reliable OTFT-LCD, we tested and measured the expansion and contraction ratio of the PC substrate after each process. On the basis of the measured values, we constructed the OTFT-LCD having 32 × 24 pixels and 500 μm pitch within the range of 0.5 to 1 μm alignment error. The channel width and length of the TFT device were 500 μm and 25 μm, respectively. The dimension of the pixel was 850 μm × 850 μm. [reproduced from "Jpn. J. Appl. Phys. 43 (2004) 3605"]

The response of the single OTFT-driven cell made on flexible substrates as a function of dc gate bias is shown in Figure 13. The pixel was switched ON with sufficient negative dc gate bias (> −18 V) and ac wave form (60 ~ 100 Hz) applied to the source electrode. The panel was a twisted nematic (TN) type and normally white (NW) mode was used. The transmission, response time and viewing angles were measured using an LCD characterization system (DMS 501, Autronics). The typical contrast ratio of a single pixel was varied from 30 to 50:1 and the response time was 20 to 30 ms. [reproduced from "Jpn. J. Appl. Phys. 43 (2004) 3605"].

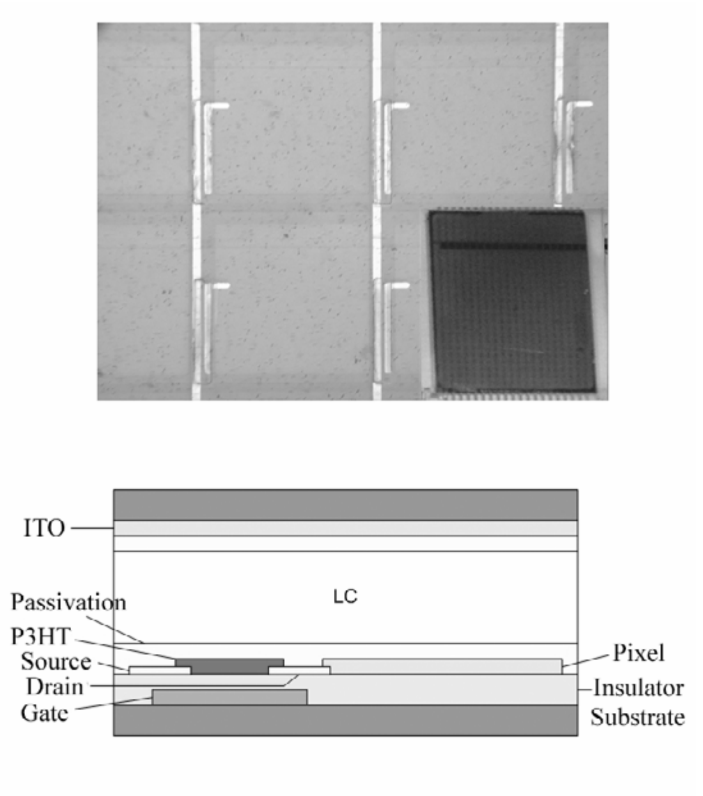

Rreproduced from "Y. H. Kim et al., Jpn. J. Appl. Phys. 43, 6A (2004) 3605".

Figure 12. Optical and schematic images of OTFT-LCD panel (32 x 24 pixels). Inset image shows when the pixels are turned ON when the DC gate bias was -16 V.

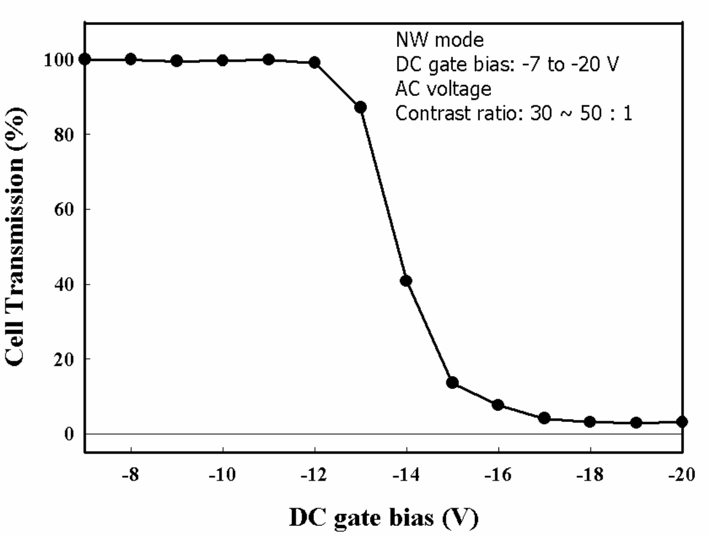

Reproduced from "Y. H. Kim et al., Jpn. J. Appl. Phys. 43, 6A (2004) 3605".

Figure 13. Electro-optical characteristics of P3HT based OTFT-LCD as a function of dc gate bias. The panel was a twisted nematic (TN) type and normally white (NW) mode was used.

# 3. TIPS PENTACENE BASED OTFTS

Previously, most of the organic semiconductors used in the fabrication of OTFT were polymer based materials. However, polymer semiconductors have limited electrical performance of maximum field-effect mobility less than 0.1 cm$^2$/Vs. Although some types of displays can be driven by these low-performance OTFTs but in order to compete with a-Si TFTs, the field-effect mobility must be more than 0.5 cm$^2$/Vs. In order to satisfy this requirement for display applications, pentacene or other oligomer type semiconductors were developed.

Even though the pentacene and oligomers show field-effect mobility more than 1 cm$^2$/Vs (sometimes more than 10 cm$^2$/Vs), these materials are not soluble in common organic solvents. Recently, Anthony et al. synthesized 6,13-bis (triisopropylsilylethynyl) (TIPS) pentacene, which added bulky functional groups at the 6, 13 positions of pentacene molecule [31]. Also, Kuo et al. showed OTFTs using solution processible Triethylsilylethynyl anthradithiophene (TES ADT) with field-effect mobility up to 1 cm$^2$/Vs [32].

In this section, the fabrication process of TIPS pentacene OTFTs and the effect of solvent on the crystallinity, morphology and electrical properties will be discussed. Also, improvement of extrinsic mobility by using suspended source/drain electrode is introduced.

## 3.1. 6,13-Bis (Triisopropylsilylethynyl) (TIPS) Pentacene

The molecular structure of TIPS pentacene is shown in Figure 14. TIPS pentacene has high solubility in organic solvents due to the added bulky functional groups. Also, these functional groups lead to cofacial π-π stacking structure. Because of this arrangement, interplanar spacing of the aromatic ring in TIPS pentacene crystals is 3.47Å [33,34].

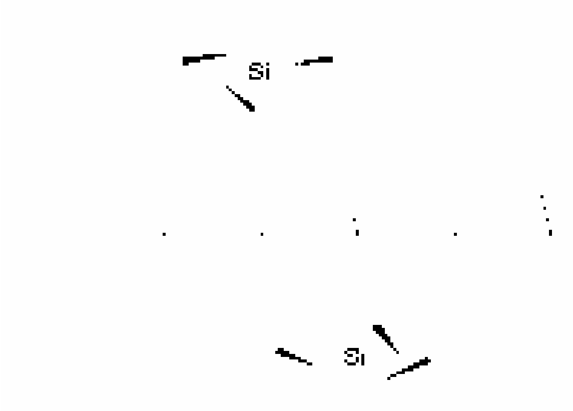

Figure 14. The molecular structure of ,13-bis (triisopropylsilylethynyl) (TIPS) pentacene.

## 3.2. Device Structure and Fabrication

Similar to P3HT OTFTs, TIPS pentacene OTFTs are fabricated with a bottom-gate and bottom-contact source/drain structure (Figure 15). On a patterned metal gate electrode, an organic gate insulator, poly-4-vinylphenol (PVP) is spin-coated and thermally cured. For source/drain electrode, e-beam-deposited Cr with a thermally evaporated Au layer are deposited and patterned. Before spin coating the organic semiconductor, the surface of PVP gate insulator is modified using a self-assembled monolayer or HMDS solution. Then, TIPS pentacene is coated on the channel region by using solution processes such as spin coating, dip coating and ink jet printing.

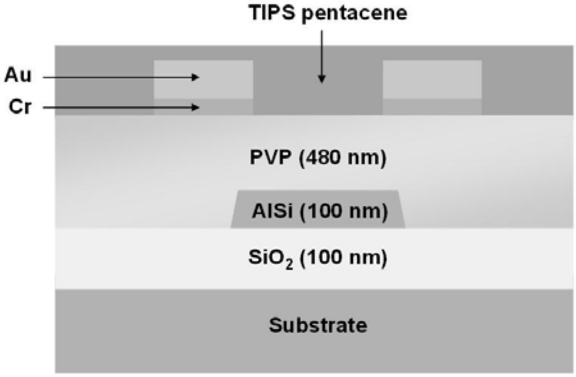

Figure 15. Schematic diagram of a bottom-contact type OTFT with spin-coated TIPS pentacene active layer.

## 3.3. Solvent Effect on Film Morphology

The film morphology, crystallinity and the electrical properties of TIPS pentacene OTFTs are largely affected by choice of a solvent. Various solvents were selected and tested to determine the solvent effect on the film morphology of TIPS pentacene films: the solvents were chlorobenzene, chloroform, xylene and toluene which have boiling points (BPs) of 131.7°C, 61.7°C, 138.4°C and 110.6°C, respectively [35]. The concentration of all TIPS pentacene solution was 1 wt%. After spin coating, the samples were heated on a hotplate to remove the residual solvent. The thicknesses of spin coated TIPS pentacene layers were 50 to 70 nm. However, in the case of toluene, the spin coating was not done uniformly because of the bad wettability of on PVP gate insulator.

The optical microscope images of spin-coated TIPS pentacene films from different solutions are shown in Figure 16. Clearly, the morphology of TIPS pentacene film changes significantly depending on the solvent used. The TIPS pentacene films spin-coated from chlorobenzene and xylene show dendrite-like morphology (Figure 16(a) and 16(b)), whereas the pentacene film spin-coated from chloroform has pores with a diameter of ~ 20 μm (Figure 16(c)). It was relatively difficult to obtain a uniform film from toluene because the wetting property between toluene and PVP layer was not good as other solvents and resulted in a film having discrete crystalline islands as shown in Figure 16(d).

The XRD results of TIPS pentacene films obtained from four different solvents are displayed in Figure 17. Single crystal TIPS pentacene has a triclinic structure with unit cell parameters $a$ = 7.5650 Å, $b$ = 7.7500 Å, $c$ = 16.835 Å, $\alpha$ = 89.15°, $\beta$ = 92.713° and $\gamma$ = 83.63° [33]. Therefore, the peaks observed at 5.4° correspond to intermolecular spacing of 16.8 Å indicating that preferential orientation of (001)-axis normal to the surface. From the XRD results, the degree of crystallinity (peak intensity) increases in the order of chloroform, toluene, xylene and chlorobenzene [35].

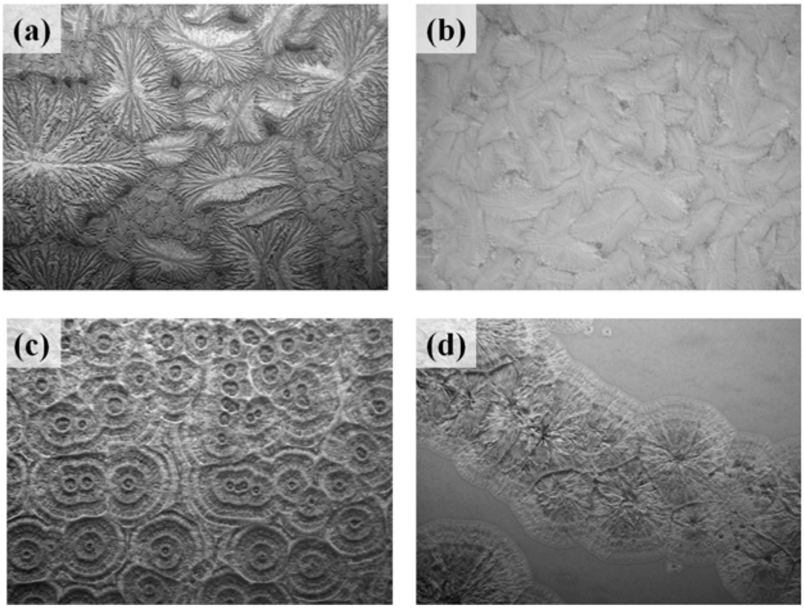

Figure 16. The optical images of spin-coated TIPS pentacene films on HMDS-treated PVP gate insulator using, a) chlorobenzene, b) xylene, c) chloroform and d) toluene as a solvent. The concentration of each solution was 1 wt%.

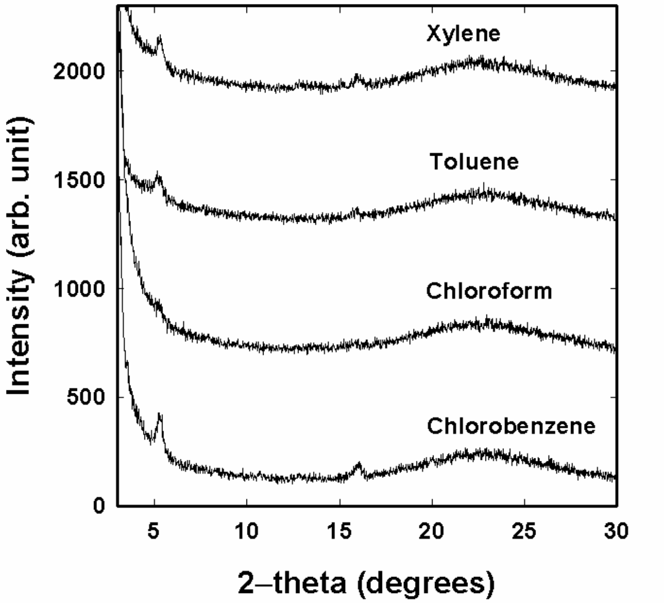

Figure 17. The XRD results of TIPS pentacene films obtained from four different solvents. (Single crystal TIPS pentacene has a triclinic structure with unit cell parameters $a$ = 7.5650 Å, $b$ = 7.7500 Å, $c$ = 16.835 Å, $\alpha = 89.15^{o}$, $\beta = 92.713^{o}$ and $\gamma = 83.63^{o}$)

The strong solvent dependence of morphology and crystallinity of TIPS pentacene films can be explained by the aromaticity and BP of solvent. It has been suggested that the morphology of polymer films is greatly affected by the aromaticity of solvent used in the coating process [36,37]. For aromatic solvents such as dichlorobenzene, chlorobenzene and xylene, the solvent molecules solvate the $\pi$-electron conjugated segments of polymer. As a result, films having better $\pi$-$\pi$ stacking and electrical conduction are obtained. On the other hand, for non-aromatic solvents such as tetrahydrofuran and chloroform, the solvent molecules solvate non-conjugated segments of polymer and therefore films with lower electrical conduction are obtained [36]. Since TIPS pentacene molecule contains five benzene rings ($\pi$-electron conjugated segments) it is expected that the aromaticity of solvent will have a significant effect on its morphology as in polymer systems.

In addition to aromaticity, the BP of solvent can affect the morphology and crystallinity of TIPS pentacene films. It was reported that polymer semiconductor film obtained from a solvent having a higher BP had a better crystallinity compared to the film from a solvent with lower BP [38]. Also, the mobility increased approximately by a factor of 10. The improved crystallinity and mobility can be attributed from the fact that when using a solvent with a higher BP, the evaporation time increases and facilitates the growth of a highly crystalline film. Whereas, when using a solvent having a lower BP rapid evaporation limits the time for crystallization during spin coating process [38]. It is not clear whether the aromaticity or the BP plays a dominant role in determining the morphology and crystallinity of the organic films since most of the aromatic solvents have higher BPs than the non-aromatic solvents [35]. However, it is clear that both aromaticity and BP of solvent have significant effects on the film characteristics and more variety of solvents should be examined to fully understand their effects.

## 3.4. Solvent Effect on Electrical Properties

In this section, the solvent effect on the electrical properties of TIPS pentacene is discussed. To investigate the relationship between the electrical characteristics of OTFT and the crystallinity of TIPS pentacene film, OTFT devices were fabricated by using each solvent. Figure 18 shows the transfer characteristics of fabricated organic transistors.

The OTFT made from chlorobenzene exhibited the highest mobility ranging from 0.01 to 0.1 $cm^2/Vs$, with an average mobility of 0.04 $cm^2/Vs$. On the other hand, the OTFT made from chloroform showed mobility of $10^{-4} \sim 10^{-5}$ $cm^2/Vs$. The average mobilities of OTFTs from xylene and toluene were 0.01 $cm^2/Vs$ and 0.002 $cm^2/Vs$, respectively. These results are consistent with the results from XRD analysis of TIPS pentacene films showing that TIPS pentacene film having higher degree of crystallinity exhibits higher electrical characteristics. The current on/off ratio also was affected by the solvent and the highest on/off ratio was obtained when using chlorobenzene as a solvent ($4.3 \times 10^3$). The device made from chloroform had the lowest on/off ratio due to extremely low on-state current ($4.3 \times 10^2$). Unlike ink-jet printed devices, the spin-coated TIPS pentacene OTFTs have rather large off-state current in the range of $10^{-9}$ A (in ink-jet printed device, the off-state current is in the order of $10^{-11} \sim 10^{-13}$ A). The rather large off-state current observed in spin-coated OTFT is attributed to undefined (not-patterned) organic semiconductor layer and residual impurities present in the solution or extrinsic doping effect could give rise to the off current of the device [38].

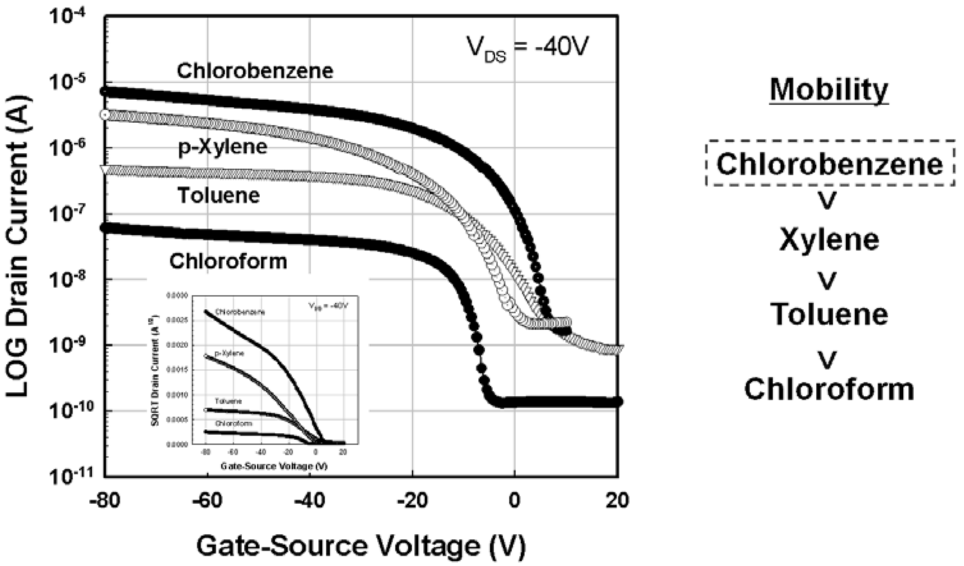

Figure 18. The transfer curves of bottom-contact type TIPS pentacene OTFTs spin-coated with different solvents. The OTFTs were operated in saturation mode where the gate voltage was swept from +20 V to – 40 V with a fixed source-drain voltage of -40 V.

It has been reported that the electrical properties of OTFTs such as mobility, on/off ratio and threshold voltage are affected by the active layer thickness [39]. With a thicker active layer, higher drain current and mobility are obtained while the on/off ratio is decreased due to more leakage current.

The threshold voltage of OTFT was also changed by the choice of solvent. The threshold voltage was extracted from the x-axis intercept of the linear portion of the plot $\sqrt{I_{DS}}$ vs. $V_{GS}$ curve. Using chloroform as a solvent, the threshold voltage of OTFT was around – 8 V (operate in accumulation mode), whereas using chlorobenzene and toluene, the threshold voltages were positively shifted to +6 and +7 V (operate in depletion mode), respectively. The OTFT from xylene shows the lowest threshold voltage of approximately -2 V. The threshold voltage of a transistor is influenced by several factors such as the interface states of semiconductor/insulator, trap states in the bulk and surface potential of the gate insulator [40]. In this case, it is possible that residual impurities which were originally present in the solvent may have affected the interface state of semiconductor/insulator and shifted the threshold voltage. However, to fully understand the threshold voltage shift by the solvent, the roles of residual impurities in semiconductor/insulator interface states and alteration of gate insulator surface by the solvent should be further investigated.

### 3.5. Suspended Source/Drain Electrode Structure

As describe in previous sections, top contact and bottom contact source/drain structures are frequently used in OTFTs. The top contact OTFT exhibits higher field-effect mobility and lower mobility-dependence on channel length compared to bottom contact OTFT due to lower S/D contact resistance [41]. However in top contact OTFT, the channel length is limited by the feature size of a metal shadow mask and is extremely difficult to fabricate transistors having short channel length [42]. In bottom contact OTFT, it is rather easy to fabricate short channel transistors by means of photolithography. But, the high S/D contact resistance in bottom contact OTFT becomes an issue when the channel length is scaled down under 10 μm because the extrinsic field-effect mobility is degraded by more than 2 orders due to the high contact resistance [43].

There have been many attempts to lower the S/D contact series resistance in bottom contact OTFTs[42,44,45]. Previously, a bottom contact OTFT employing a self-assembled monolayer (SAM) as an adhesion layer for Au S/D electrode has been reported [42]. Compared to Cr or Ti adhesion layer, the S/D contact resistance was reduced by more than four orders using SAM adhesion layer. Also, the effect of S/D undercut in pentacene OTFTs has been reported [45]. The S/D undercut with a length of ~ 0.2 μm improved the saturation field-effect mobility by ~ 35% but degraded the mobility in linear region by a factor of 1/9 [45].

To improve the contact between the organic semiconductor and S/D electrodes, a suspended source/drain (SSD) structure is suggested (Figure 19(a)). In SSD structure, the S/D electrode is suspended over gate insulator with a controlled gap. The organic semiconductor fills in this gap forming a channel layer. The SSD OTFT can be fabricated by the conventional bottom contact OTFT process which implies that OTFTs with short channel length can be easily obtained. In addition, because the S/D electrode is suspended over the gate insulator, the SSD OTFT is expected to have a top-contact-like structure. By employing the SSD structure, the OTFT shows very steep subthreshold slope, low threshold voltage as well as higher mobility in linear region compared to bottom contact OTFTs.

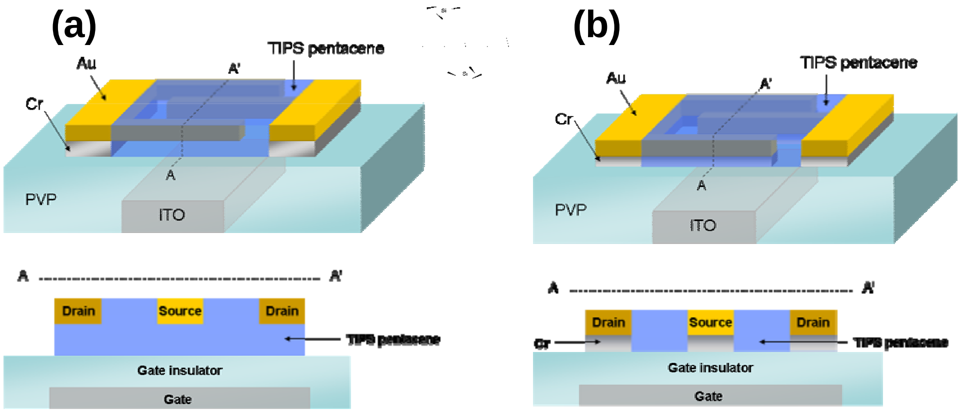

Reprinted with permission from Y. H. Kim et al., Appl. Phys. Lett., 91, 4, 042113, 2007. Copyright 2007, American Institute of Physics.

Figure. 19. Schematic diagrams of (a) a suspended source/drain (SSD) OTFT and (b) a bottom-contact OTFT. From the cross section view, the SSD OTFT shows a top-contact-like S/D structure rather than a bottom-contact S/D structure.

The schematic diagrams of a SSD OTFT are shown in Figure 19(a). The SSD OTFTs are fabricated with the bottom-gate architecture. On a glass substrate, indium-tin-oxide (ITO) gate electrode is deposited and patterned. On the top of the gate electrode, an organic gate insulator, is spin-coated and cured. For SSD electrode, Cr (50 nm-thick) and Au (50 nm-thick) layers are deposited. The Cr sacrificial layer is completely etched in the active area providing a freestanding and suspended Au S/D electrode. Finally, TIPS pentacene is printed using an ink-jet printing machine with a 30 μm piezoelectric-type nozzle. For a comparison bottom contact OTFTs are also fabricated using ITO gate electrode and PVP gate insulator (Figure 19(b)). As S/D electrode, 3 nm-thick Cr and 50 nm-thick Au layers are deposited and patterned by photolithography and wet etching.

The optical microscope image and scanning electron microscope (SEM) images of SSD OTFT are displayed in Figure 20. The channel width and length of the transistor are 125 μm and 10 μm, respectively. The Cr layer under the Au electrode in the active area (top of the gate electrode/insulator stack) is completely wet-etched except the edge regions where much wider Cr lines exist. It was possible to fabricate over 150 μm-long SSD structure using this technique.

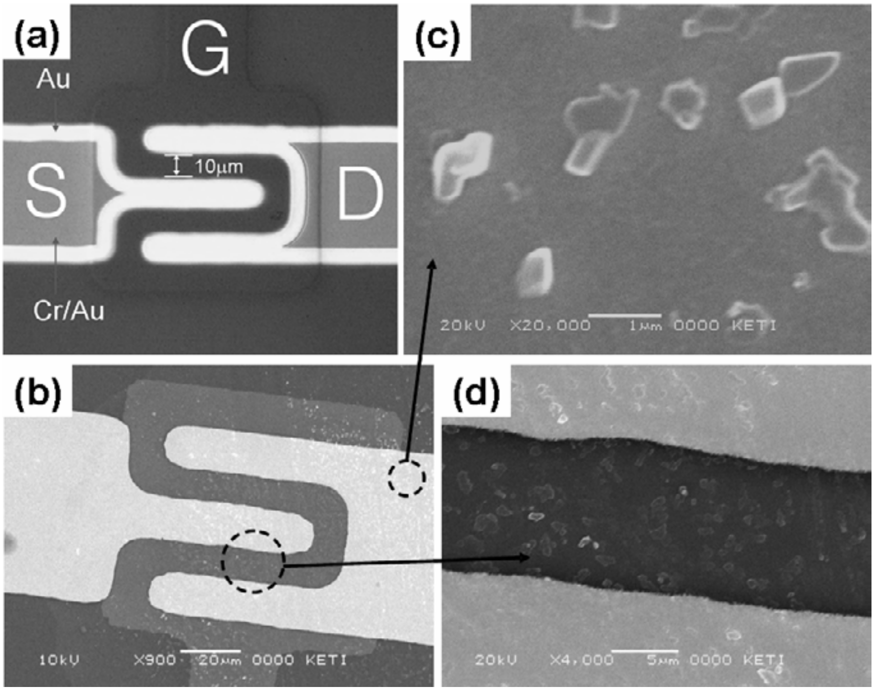

Reprinted with permission from Y. H. Kim et al., Appl. Phys. Lett., 91, 4, 042113, 2007. Copyright 2007, American Institute of Physics.

Figure 20. (a) Optical image of SSD OTFT before printing the organic semiconductor (the image was taken from the backside of the substrate). The channel width and length of the transistor were 125 μm and 10 μm, respectively. (b) Scanning electron microscope (SEM) image of SSD OTFT after printing TIPS pentacene (c) SEM image of SSD OTFT in the channel region showing TIPS pentacene grains (d) SEM image of TIPS pentacene on S/D electrode. The size of the TIPS pentacene grains ranges from 0.5 ~ 1 μm.

The transfer characteristics of ink-jet printed TIPS pentacene OTFTs with conventional bottom contact S/D structure and SSD structure are shown in Figure 21 (both devices had channel width and length of 125 μm and 10 μm, respectively). In the case of bottom contact OTFT, the thickness of Cr adhesion layer was 3 nm in order to minimize the S/D contact resistance. The field-effect mobility in the linear region was obtained from transconductance ($g_m$) by Eq. 2 [46],

$$g_m = \left.\frac{\partial I_{DS}}{\partial V_{GS}}\right|_{V_{DS}=const} = \mu_{EFF} C_i \frac{W}{L} V_{DS} \quad (V_{DS} < V_{Dsat}) \tag{2}$$

where $I_{DS}$ is the drain current, $L$ is the channel length, $W$ is the channel width, $C_i$ is the capacitance per unit area of the gate insulator, $V_{GS}$ is the gate-source voltage and $V_{DS}$ is the drain-source voltage.

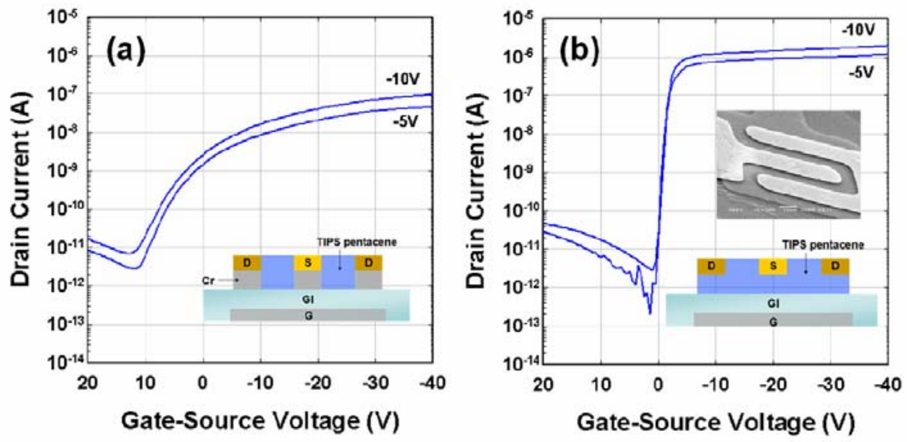

Reprinted with permission from Y. H. Kim et al., Appl. Phys. Lett., 91, 4, 042113, 2007. Copyright 2007, American Institute of Physics.

Figure 21. The transfer curves of ink-jet printed TIPS pentacene OTFTs with conventional bottom contact S/D structure (a) and with SSD structure (b). The field-effect mobility, threshold voltage and subthreshold slope of bottom contact OTFT were 0.007 $cm^2/Vs$, +9 V and 4.5 V/decade, respectively. The SSD OTFT exhibited field-effect mobility, threshold voltage and subthreshold slope of 0.29 $cm^2/Vs$, -3 V and 0.6 V/decade, respectively. The channel length and width of both bottom contact and SSD OTFTs were 125 μm and 10 μm, respectively.

The bottom contact OTFT exhibits field-effect mobility of 0.007 $cm^2/Vs$ and $V_{TH}$ of +9 V, whereas the SSD OTFT shows field-effect mobility of 0.29 $cm^2/Vs$ and $V_{TH}$ of -3 V. The on/off ratio increased from $10^4$ to $10^7$ and the subthreshold slope decreases from 4.5 V/decade to 0.6 V/decade by employing the SSD structure. Surprisingly, the subthreshold slope becomes much steeper in SSD OTFT compared to that of bottom contact OTFT. It is known that the subthreshold slope (S) can be expressed approximately by Eq. 3 [47],

$$S = U_T \ln(10)(1 + \frac{C_d + C_{it}}{C_{ox}}) \tag{3}$$

where $U_T$ is the temperature voltage, $C_d$, $C_{it}$, and $C_{ox}$ are the depletion capacitance, the interface trap capacitance and the gate insulator capacitance, respectively. The interface traps as well as bulk trap states in organic semiconductors are responsible for variation of subthreshold slope. Especially the concentration and energetic position of acceptor-like bulk traps in organic semiconductor have dominant effect on the subthreshold characteristics in organic transistors [48]. In SSD OTFT, the growth of organic semiconductor in the active area is restricted by its geometry (50 nm gap between suspended Au electrodes and PVP gate insulator), whereas in bottom contact OTFT the growth of organic semiconductor is restricted within the narrow S/D electrodes. Therefore, the significant improvement in the subthreshold characteristic of SSD OTFTs reflects that the SSD structure can effectively lower the concentration of insulator-semiconductor interface traps and/or acceptor-like bulk traps in the organic semiconductor. Also, the higher field-effect mobility observed in SSD OTFT shows that the crystallinity of TIPS pentacene is improved using the SSD structure.

## 4. CONCLUSION

This chapter described the device structure, fabrication process and effect of solvent on the morphology, crystallinity and electrical properties of solution-processed OTFTs. In solution-processed OTFTs, selecting a proper solvent for organic semiconductor is essential in realizing high performance OTFTs, as well as optimization of device structure and fabrication processes.

## REFERENCES

[1] Kelley, T. W.; Muyres, D. V.; Baude, P. F.; Smith, T. P.; and Jones, T. D. *Mat. Res. Soc. Symp. Proc.* 2003, 771, L6.5.

[2] Gundlach, D. J.; Kuo, C.-C.; Sheraw, C. D.; Nichols, J. A.; J and ackson, T. N. *Proc. SPIE*, 2001, 4466, 54-64.

[3] Sheraw, C. D.; Nichols, J. A.; Gundlach, D. J.; Huang, ; J. R.; Kuo, C. C.; Ktauk, H.; Jackson, T. N.; Kane M. G. Hill, I. G.; Hammond, M.S.; Campi, J.; Greening, B. K.; Francl, J.; and West, J. *Appl. Phys. Lett.* 2002, 80, 1088-1090.

[4] Ghim, P. J.; Baeg, K. J.; Noh, Y. Y.; Kang, S. J.; Jo, J.; and Kim, D. Y. *Appl. Phys. Lett.* 2006, 89, 202516.

[5] Speakman, S. P.; Rozenberg, G. G.; Clay, K. J.; Milne, W. I.; Ille, A.; Gardner, I. A.; Bresler, E.; and Steinke, J. H. G. *Organic Electronics* 2001, 2, 65-73.

[6] Kim, Y. H.; Park, S. K.; Moon, D. G.; Kim W. K.; and Han, J. I. *Jpn. J. Appl. Phys.* 2004, 43, 3605-3608.

[7] Chen, K. Y.; Hsieh, H. H.; Wu, C. C.; Hwang J. J.; and Chow, T. J. *Chem. Commun.* 2007, 10, 1065-1067.

[8] Voutsas, A. T. *Appl. Surf. Sci.* 2003, 208-209, 250-262.

[9] Young, N. D.; Trainor, M. J.; Yoon, S. Y.; McCulloch, D. J.; Wilks, R. W.; Pearson, A.; Godfrey, S.; Green, P. W.; Roosendaal S.; and Hallworth, E. *Mat. Res. Soc. Symp. Proc.* 2003, 769, H2.1.

[10] Kanoh, H.; Sugiuta, O.; Paul A. B.; and Matsumura, M. *Jpn. J. Appl. Phys.* 1990, 29, 2358-2364.

[11] Park, J.; Kang, S. I.; Jang, S. P.; and Choi, J. S. *Jpn. J. Appl. Phys.* 2005, 44, 648-651

[12] Kim, C. S.; Jo, S. J.; Lee, S. W.; Kim, W. J.; Baik, H. K.; Lee, S. J.; Hwang. D. K.; and Im, S. *Semicond. Sci. Technol*. 2006, 21, 1022-1025.

[13] Zaumseil, J.; Baldwin, K. W.; and Rogers, J. A. *J. Appl. Phys.* 2003, 93, 6117-6124.

[14] Mizukami M.; Hirohata N.; Iseki T.; Ohtawara K.; Tada T.; Yagyu S.; Abe T.; Suzuki T.; Fujisaki Y.; Inoue Y.; Tokito S.; and Kurita T. *IEEE Electron Dev. Lett.* 2006, 27, 249-251.

[15] Yoshihide, F.; Toshiki, A.; Hiroshi, O.; Hirotaka, M.; Yoji, I.; Hideo, F.; Shizuo, T.; and Taiichiro, K. *The Journal of the Institute of Image Information and Television Engineers* 2006, 60, 1428-1434.

[16] Kline, R. J.; McGehee, M. D.; Kadnikova, E. N.; Liu, J.; and FrØchet, J. M. J. *Adv. Mater.* 2003, 15, 1519-1522.

[17] Sirringhaus, H.; Brown, P. J.; Friend, R. H.; Nielsen, M. M.; Bechgaard, K.; Langeveld-Voss, B. M. W.; Spiering, A. J. H.; Janssen, R. A. J.; Meijer, E. W.; Herwig, P.; and de Leeuw, D. M. *Nature* 1999, 401, 685-688.

[18] Sirringhaus, H.; Tessler, N.; Friend, R. H.; *Synth. Met.* 1999, 102, 857-860.

[19] Łużny, W.; Trznadel, M.; and Proń, A. *Synth. Met.* 1996, 81, 71-74.

[20] Bao, Z.; and Dodabalapur, A.; Lovinger, A. J. *Appl. Phys. Lett.* 1996, 69, 4108-4110.

[21] H. J. Fell, E. J. Samuelsen, J. Als-Nielsen, G. Grübel, and J. Mårdalen, Solid State Commun. **71**, 435 (1989).

[22] Sirringhaus, H.; Brown, P. J.; Friend, R. H.; Nielsen, M. M.; Bechgaard, K. ; Langeveld-Voss, B. M. W.; Spiering, A. J. H.; Janssen, R. A. J.; and Meijer, E. W. *Synth. Met.* 2000, 111-112, 129-132.

[23] Zilker, S. J.; Detcheverry, C.; Cantatore, E.; and de Leeuw, D. M. *Appl. Phys. Lett.* 2001, 79, 1124-1126.

[24] Schön, J. H. *Appl. Phys. Lett.* 2001, 79, 4163-4164.

[25] Zhu, Z.; and Mason, J. T.; Dieckmann, R.; Malliaras, G. G. *Appl. Phys. Lett.* 2002, 81, 4643-4645.

[26] Dimitrakopoulos, C. D.; and Mascaro, D. J. *IBM J. Res. Dev.* 2001, 45, 11-27.

[27] Gundlach, D. J.; Jackson, T. N.; Schlon, D. G.; and Nelson, S. F. *Appl. Phys. Lett.* 1999, 74, 3302-3304.

[28] Schön, J. H.; and Batlogg, B. *Appl. Phys. Lett.* 1999, 74, 260-262.

[29] Bao, Z.; Dodabalapur, A.; and Lovinger, A. J. *Appl. Phys. Lett.* 1996, 69, 4108-4110.

[30] Abdou, M. S. A.; Orfino, F. P.; Son, Y.; and Holdcroft, S. *J. Am. Chem. Soc.* 1997, 119, 4518-4524.

[31] Sheraw, C. D.; Jackson, T. N.; Eaton, D. L.; and Anthony, J. E. *Adv. Mater.* 2003, 23, 2009-2011.

[32] Kuo, C-C.; Payne, M. M.; Anthony, J. E.; and Jackson, T. N. *IEDM Technical. Digest* 2004, 373-376.

[33] Anthony, J. E.; Brooks, J. S.; Eaton, D. L.; and Parkin, S. R. *J. Am. Chem. Soc.* 2001, 123, 9842-9483.

[34] Anthony, J. E.; Eaton, D. L.; and Parkin, S. R. *Organic Lett.* 2002, 4, 15-18.

[35] Kim, Y. H.; Lee, Y. H.; Han, J. I.; Han, S. M.; and Han, M. K. *J. Electrochem. Soc.* 2007, 154, H995-H998.

[36] Liu, J.; Shi, Y.; and Yang, Y. *Adv. Funct. Mater.* 2001, 11, 420-424.

[37] Shi, Y.; Liu, J.; and Yang, Y. *J. Appl. Phys.* 2000, 87, 4254-4263.

[38] Chang, J. F.; Sun, B.; Breiby, D. W.; Nielsen, M. M.; Sölling, T. I.; Giles, M.; McCulloch, I.; S and irringhaus, H. *Chem. Mater.* 2004, 16, 4772-4776.

[39] Jia, H.; Gowrisanker, S.; Pant, G. K.; Wallace, R. M.; and Gnade, B. E. *J. Vac. Sci. Technol. A* 2006, 24, 1228-1232.

[40] Pernstich, K. P.; Haas, S.; Oberhoff, D.; Goldmann, C.; Gundlach, D. J.; Batlogg, B.; Rashid, A. N.; and Schitter, G. *J. Appl. Phys.* 2004, 96, 6431-6438.

[41] Klauk, H.; Schmid, G.; Radlik, W.; Weber, W.; Zhou, L.; Sheraw, C. D.; Nochols, J. A.; and Jackson, T. N. *Solid-State Electron.* 2003, 47, 297-301.

[42] Nomoto, K.; Hirai, N.; Yoneya, N.; Kawashima, N.; Noda, M.; Wada, M.; and Kasahara, J. *IEEE Trans. Electron Devices* 2005, 52, 1519-1526.

[43] Hill, I. G. *Appl. Phys. Lett.* 2005, 87, 163505.

[44] Schroeder, R.; Majewski, L. A.; Grell, M.; Maunoury, J.; Gautrot, J.; Hodge, P.; Turner, M. *Appl. Phys. Lett.* 2005, 87, 113501.

[45] Kim, S. H.; and Choi, H. Y.; Jang, J. *Appl. Phys. Lett.* 2004, 85, 4514-4516.

[46] Kagan C. R.; and Andry, P. *Thin-Film Transistors*; Dekker: New York, NY, 2003; Chap. 2, pp 42.

[47] Sze, S. M. *Physics of Semiconductor Devices*; 2nd ed.; Wiley: New York, NY, 1981, Chap. 8, pp. 467.

[48] Scheinert, S.; Paasch, G.; and Doll, T. *Synth. Met.* 2003, 139, 233-237.

In: Integrated Circuits, Photodiodes…
Editors: R. McIntire and P. Donnell, pp. 209-225

ISBN: 978-1-60692-660-4
© 2009 Nova Science Publishers, Inc.

*Chapter 8*

# ORGANIC LUMINESCENCE DEVICE DEGRADATION ANALYSIS AND LIFETIME IMPROVEMENT

***Ke Lin, Ramadas Senthil Kumar, Lai Szu Cheng and Chua Soo Jin***
Institute of Materials Research and Engineering, A*STAR (Agency for Science, Technology and Research), 3 Research Link, Singapore 117602

## ABSTRACT

Organic light emitting device degradation mechanisms have been elaborated. A novel technique to inhibit the growth of dark spots and improve device lifetime have been proposed. The technique involved the development of organic film such as Parylene, Teflon and other suitable high barrier and dielectric organic polymer materials in the device structure which proved to improve device lifetime by 100 folds. A new analytical tool, low frequency fluctuation, has been setup for organic device lifetime characterization. Correlation between the process of device degradation and the low frequency fluctuation was successfully established.

**Keywords:** Dark Spot Formation Mechanism Studies, Organic Device Degradation, Development of Proprietary Dark Spot Inhibition Technology and Device Lifetime Estimation Methodology.

## 1. INTRODUCTION

One of the critical challenges that the OLED industry is facing is the need to improve device lifetime to standards benchmarked by the conventional display technologies. Degradations in OLEDs typically manifest in the forms of non-emissive areas known as dark spots. These dark spots substantially reduce device luminescence and proliferate as the device degrades. In order to improve an OLED's lifetime, it is crucial to investigate the formation of these dark spots so that we can identify the real causes of degradations and devise appropriate measures to mitigate the degradation mechanisms. A real understanding in dark spot formation mechanisms will pave the way for new technologies to increase the lifetime of OLED devices dramatically.

From the earlier studies, there are numerous explanations to account for the formations of dark spots. Some studies conjectured that electrical shorts and the metal diffusion [1,3] into polymers are the main culprits behind dark spots formations. These short circuit points also lead to the formation of pin holes and local fusion of the polymer and the metallic cathode [4]. In addition, it had been suggested that device degradation is largely due to delamination between different layers [5], crystallization of organic materials such as emitting or hole-transport materials, or electrochemical reaction on interfaces. The device lifetime may also be limited by photodegradation of polymer materials mainly due to photo-oxidation caused by either residual oxygen in the polymer itself or by that released from the indium-tin-oxide (ITO) [2]. According to some recent articles, degradation of organic electroluminescent materials and/or metallic cathode is the reason for dark spot formation and final device failure [3]. Despite numerous attempts to explain device degradation process, its understanding is far from being complete and there is still no consensus.

The purpose of our study is to put forward an explanation on the mechanism of dark spot formation. The mechanism as proposed here is that due to metal migration, the indium tin oxide / polymer interface roughens during device operation. The roughening of the interface results in the formation of sharp metal protrusions at which intense current stresses are localized. The intense local current degrades the polymer, causing the growth of the non-emissive dark regions.

Furthermore, based on the above degradation mechanism, the research team proposes a novel technique to inhibit the growth of dark spots. The technique involved the development of organic film such as Parylene, Teflon and other suitable high barrier and dielectric organic polymer materials on the ITO layer prior to deposition process of hole-transport layer. The newly added organic interlayer covers the spikes present in the ITO film and thus, provides a smoother surface to the subsequent organic layer. In the experiment, it is observed that the added Parylene interlayer remains stable and does not experience significant roughening under electrical stress. A smoother ITO interface leads to a more uniform current flow and minimizes the formation of the non-emissive regions. It is also demonstrated in the experiment that by inserting an additional Parylene layer in between the EL polymer and the cathode layer, the device cathode layer can be further stabilize and impede the growth of the dark spots. These experiments serve to further substantiate the dark spot formation mechanisms as proposed by the research team and even more importantly, constitutes to the team's patented technology of the new OLED architecture with organic interlayer enhancement.

Finally, the article shall present an observation on the correlation between the occurrence of dark spots in a degraded OLED device and the low frequency noise exhibited in the device. The experiment showed that the occurrence of dark spots in a device is primarily correlated to current 1/f noise slope: the higher the slope, the poorer the interface, and the more abnormal dark spot growth rate and the shorter lifetime. In addition, the higher the noise magnitude, the larger is the dark spot initial size. These are interesting observations that help to provide a basis for new analytical methodologies to estimate device lifetime by means of noise spectral analysis.

## 2. MECHANISM FOR ORGNIC DEVICE DEGRADATION

### Development of OLED Samples

In the experiment, an organic bilayer device structure is adopted for the study of dark spot formation as the OLED device undergoes electrical stresses. The device under test is developed by depositing the hole-transport layer with polyethylenedioxythiophene (PEDOT) and the emitting layer with MEH-poly (*p*-phenylene vinylene) (PPV). These two layers are developed by means of thermal evaporation in between the Indium-Tin Oxide (ITO) anode and Calcium cathode.

### Observation of Dark Spot Formation under Electrical Stresses

In order to conduct electrical stressing on the test device, a constant voltage source of 6V was connected across the test device in $N_2$ at an ambient temperature of 21 °C and humidity of 60%–70%. In this setup, the stress current was measured to be 2.32mA. Upon duration of 20 minutes, numerous dark spots which developed as a result of electrical stresses could be discerned under a microscope (Figure1a) viewed from the top of the substrate.

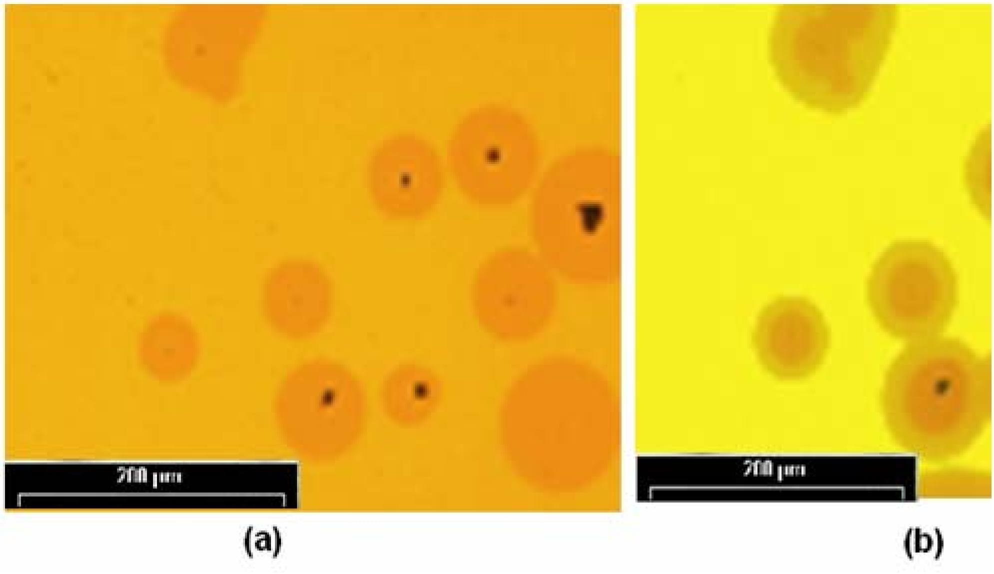

Figure 1. Dark spot seen under the microscope (a): drive voltage at 6 V, current at 52.32 mA; duration of electrical stress is 20 min; (b) drive voltage at 10 V, current is 5.89 mA; duration of electrical stress is 20 m 15 s.

As the drive voltage was increased to 10 V with a current of 5.89 mA, a weak emitting area surrounding the core began to develop as in Figure 1b. The non-emissive area remained circular when they did not overlap with one another. As the stress duration increased, it could be observed that the weakly emitting area enlarged and merged with the adjacent ones while the non-emissive area still remained circular. The dark spot at the center took an irregular dark shape. The dark spot at the center could not be clearly discerned in the beginning, but after some period of time, the dark center appeared, which was confirmed via scanning electron microscopy to contain only carbon and metal particles [7].

## Photoluminescence Spectral

To investigate the causes for the formation of the weak emissive regions, PL spectra were taken at the bright area and the weakly emissive area. As shown in Fig 2, PL intensity dropped to almost zero in the area within the weakly emissive area. It was noted that there were three spectral peaks centered at 510, 550 and 570 nm. After degradation, the peak at 510 nm was totally quenched. This could be due to bond breakage resulting in the elimination of one of the emitting species and, at the same time, restricting carrier flow.

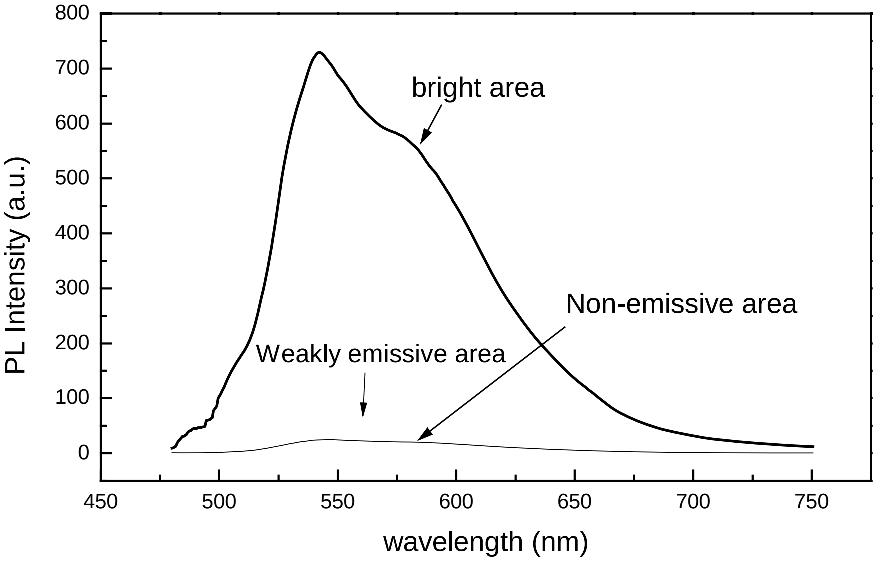

Figure 2. Photoluminescence spectra taken for the bright area and non-emissive area in the electrically stressed device. The peak centered at 510 nm is quenched in the weakly emissive area.

## SIMS Depth Profile

In order to obtain elaborated information on the degradation effects of electrical stresses, SIMS profiles of the Ca and In distributions in the bright, weakly emissive area and non-emissive areas in the stressed device were acquired as in Figure3. The zero point of the abscissa was set at device surface (Ca electrode). It was observed from the SIMS results that the Ca profile was broader within the weakly emissive area compared to the normal bright area. There was also a severe overlap with the In profile in non-emissive area as compared to the normal bright area. In the weakly emissive area, on the other hand, the Ca and In profiles exhibited a transitional status, with a slightly longer sputtering time to reach these layers and a smaller overlap compared with those from the non-emissive area. This strongly suggested that the polymer had degraded in the non-emissive area and caved in towards the glass side [8].

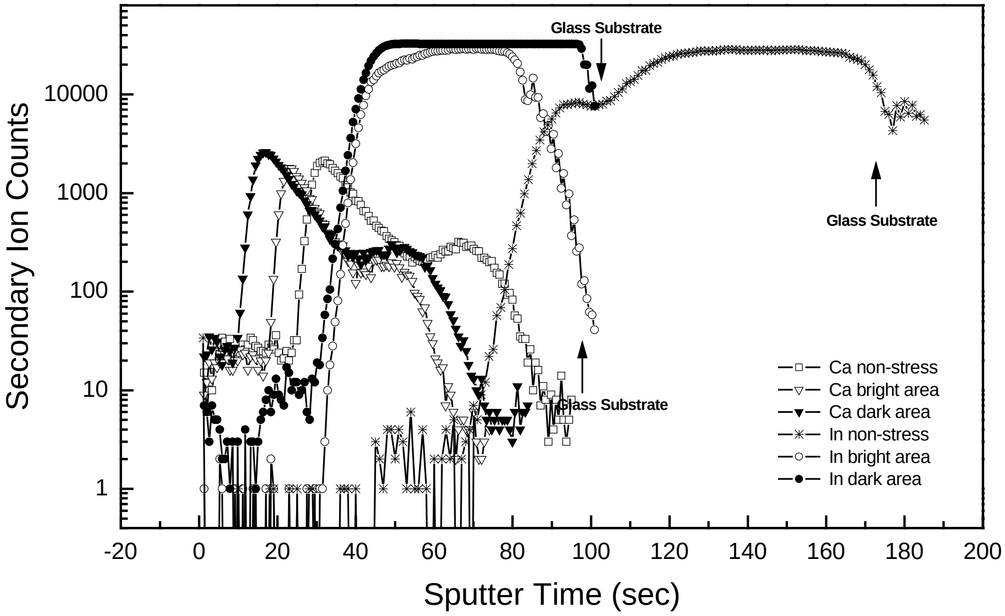

Figure 3. SIMS depth profile for Ca and In on bright area and the weakly emissive area in the electrically stressed device.

Furthermore, there was a reduction in ITO thickness in the non-emissive area as a result of electrical stress. All these observations suggested that the electrochemical or photochemical decomposition of the polymer had taken place in the non-emissive area under electrical stress.

## Deductions on Dark Spot Formation Mechanism

The photoluminescence and SIMS profiles acquired in the experiment could be explained with the newly conjectured theory on OLED degradation mechanisms. As illustrated in Figure 4(a), the ITO polymer interface began to roughen under electrical stress and metal migration, leading to close proximity of materials at the Ca and In protrusion points. A large electric field intensity and current density was thus created at these protrusion points. The enhanced local luminescence and heating led to instability and further growth of local current densities. As the duration of electrical stress continued, the polymer might have broken down and led to short circuit in the device. This led to the formation of the central dark spot at the metal protrusion areas where high electrical current stress was localized.

Subsequent electrochemical, photochemical reactions resulting in polymer decomposition might have occurred in the surrounding polymer under electrical stress. This might result in the formation of volatile species, as illustrated in Figure 4(a) (arrow a), and a large concentration of carbonyl groups which quenched luminescence from the polymer.

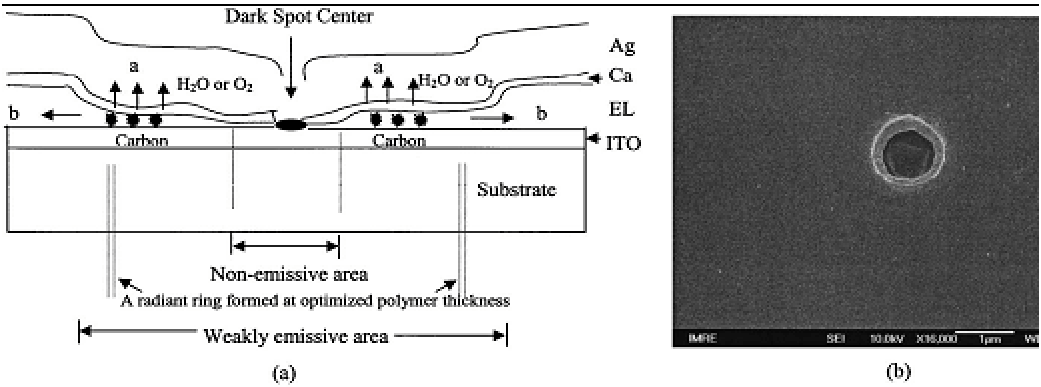

Figure 4 (a). Schematic diagram showing dark spot formation; (b) SEM image of the dark spot.

As the electrical stress continued, the polymer became thinner as it degraded while the edge expanded as shown in Figure 4(a) (arrow b). The residue gas, which remained in the polymer during synthesis, might also evolve into big gas bubbles during current stress. The formation of the gas bubble might be further aided by the volatile species generated from polymer decomposition [8]. With stress time, the polymer at the dark spot center might become ‘‘carbonized’’ and result in a damaged area forming the non-emissive area. The “carbonized” phenomenon was verified via the scanning electron microscopy image of the dark spot center. As in Fig 4 (b), the EDX spectra revealed that the very center of dark spot consisted predominantly of In from the ITO, with a small amount of debris containing C, Ca, Ag, and O.

## 3. DEVELOPMENT OF DARK SPOTS INHIBITION TECHNIQUE

### Proposed OLED Structure

In view of the findings that the presence of cathode imperfection and interface roughness is well correlated to the formation of dark spots, an OLED structure and a suitable processing technology for the effective control of the formation of the non-emissive areas had been formulated. In order to reduce interface roughness between the ITO and hole-transport layer (HTL), a 3 nm thin layer of Parylene was deposited on the ITO glass used for device development. With an energy band gap of about 6 eV, Parylene shows good insulating properties. As the only way for charge carriers to cross the barrier is by tunneling, the layer was kept thin but free of pinholes. The HTL and the EL were subsequently developed with 3,4-ethylene dioxythiophene and Ph-PPV respectively. Finally, a 5-nm thick calcium film covered with a 200 nm thick silver cathode was deposited by means of thermal evaporation. A new OLED structure with polymer interlayer enhancement was thus completed and ready for the experiment.

## SIMS Depth Profiles with and Without Parylene Interlayer

To ascertain that the polymer interlayer enhances the device durability against electrical stresses, the research team had developed another set of device without the Parylene interlayer to serve as the control in the experiment. Prior to electrical stressing, the SIMS depth profiles of the test devices (with and without the Parylene interlayer) were taken to exhibit the distribution of calcium, carbon and indium. These devices were then subjected to an electrical stress of 7 Volts for some times, and the SIMS profiles were again taken.

It could be observed from the SIMS profile of the stressed device without the Parylene interlayer, as in Figure 5, that there was an obvious boundary movement for both the brightly lit area and the non-emissive area. In addition, the distributions were different for both the bright and dark areas. The Ca profile had expanded in the dark spot area as compared with that in the bright area. The indium profile boundary had moved closer to the calcium profile in stressed devices. These phenomena were interpreted as due to the migration of the metals. The relative position of the leading edges of the carbon and calcium profiles remained the same for the dark and bright areas. A wider carbon profile was detected in the dark spot area, signifying that the polymer had spread into the anode and cathode regions.

In the SIMS profile of the device with Parylene interlayer enhancement, as in Figure 6, changes of both In and Ca profiles in the new device structures were insignificant. The In profile for stressed devices remained in the same position as compared to that prior to electrical stressing. It is only in the non-emissive area that the indium had obviously shifted and moved closer to the calcium profile.

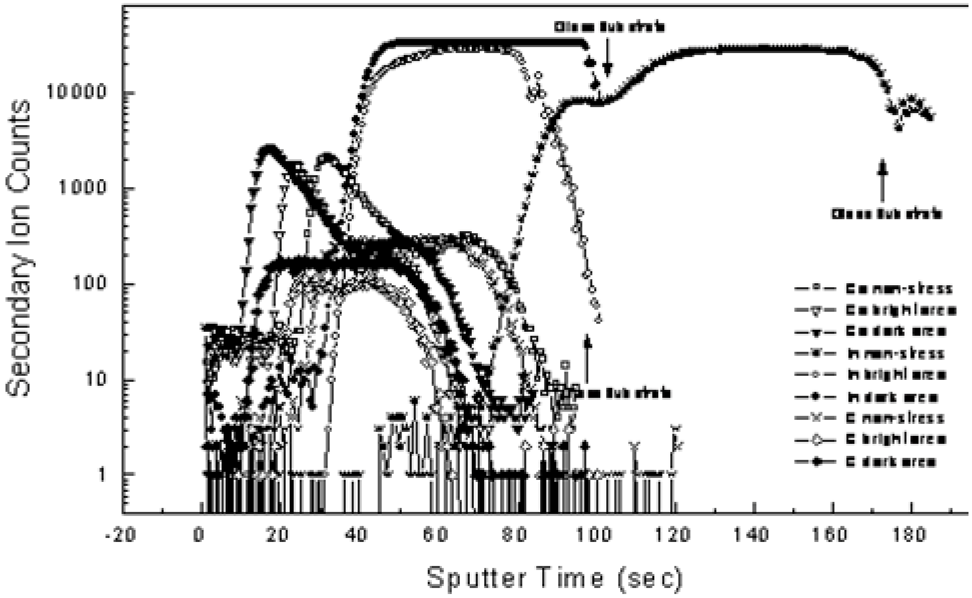

Figure 5. SIMS profiles for device structure of ITO/HTL/EL/Ca/Ag.

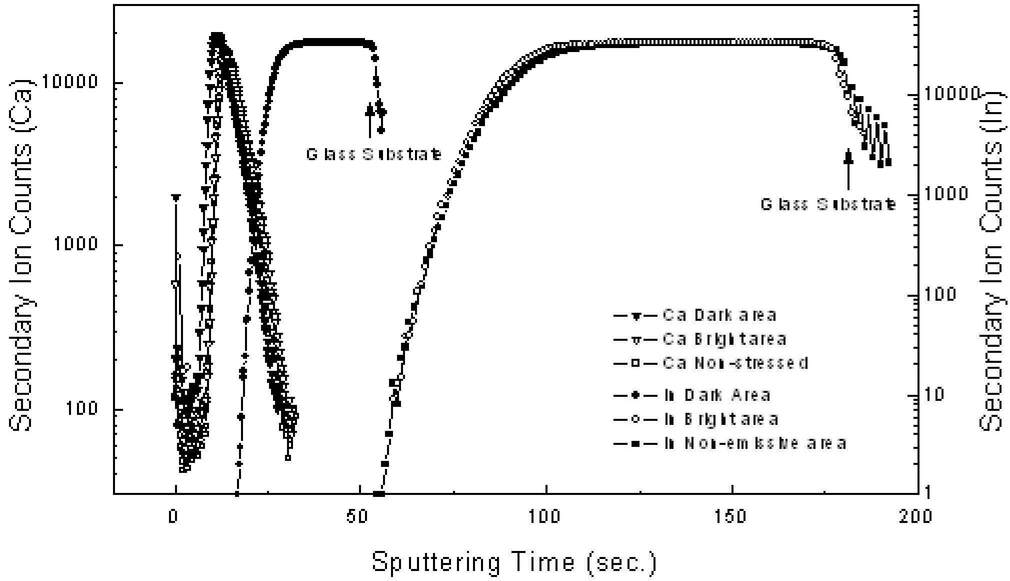

Figure 6. SIMS profiles for device structure of ITO/3 nm parylene/HTL/EL/ Ca/Ag.

From the above observation, it can be deduced that the thin Parylene interlayer in between the ITO and the HTL had effectively stabilized the Ca and In profiles during electrical stressing. In the stressed device with Parylene interlayer, the In profile remained in the same position for the emitting areas as that in the non-stressed case. Only in the non-emissive area did the In and Ca profiles overlap. A distinct feature that is worth noting is that the Ca profile did not exhibit a shoulder where the polymer resided, and for this reason on the Ca ion counts remained high. The slopes of the Ca and In profiles remained the same indicating no roughening of the interfaces at both the anode and cathode surfaces in contact with the PPV polymer. As proposed in the new degradation mechanism, the roughening of the ITO/HTL interface results in the formation of sharp metal protrusions at which intense current stresses are localized and accelerates the growth of the non-emissive dark spots. The Parylene interlayer, thus, serves a very useful purpose in our new OLED architecture in resolving the roughening phenomenon of the ITO/HTL interface and increasing the device lifetime dramatically.

To further ascertain that the Parylene interlayer improves the surface smoothness of the ITO / HTL interface, the device structure had been investigated under the atomic force microscope (AFM). As seen in the comparative images between the Parylene-enhanced and ordinary devices in Figure 7, the addition of the Parylene layer effectively reduced the interface roughness from 1.295 to 0.78 nm. The improved smoothness of the interface was in line with our SIMS result. The improvement was attributed to the Parylene film providing a conformal coverage of the ITO spikes. Furthermore, the smoother Parylene surface provided an organic–organic contact between the ITO/HTL, as compared to the inorganic–organic contact in the ITO/HTL interface of the traditional structure.

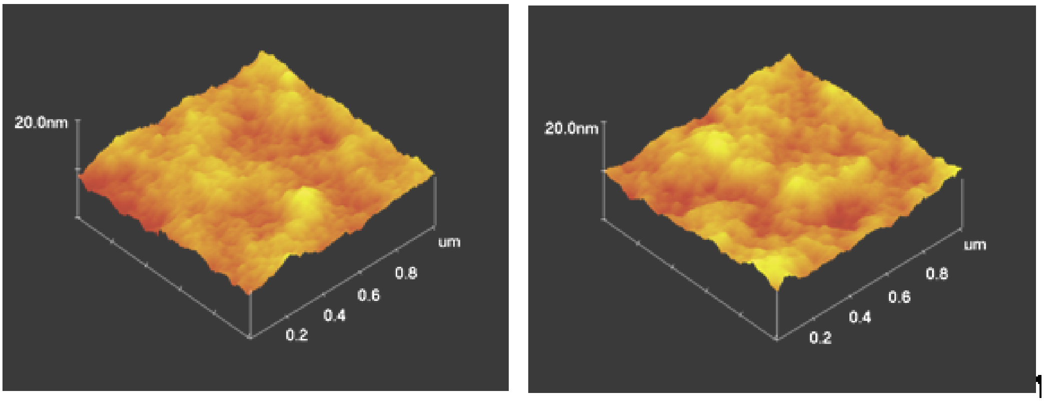

Figure 7. AFM images obtained over an area of 1 mm31 mm on polymer surface with structure (a) ITO/HTL/EL, roughness is 1.295 nm and (b)ITO/3 nm parylene/HTL/EL, roughness is: 0.78 nm.

The enhancement effects of the Parylene interlayer was further studied under optical microscopy. It was observed that the device with the Parylene layer showed not only fewer non-emissive dark spots but also exhibited a slower dark spot formation growth rates. Figure 8 shows the picture of the non-emissive dark areas after the devices, both with and without the Parylene layer, were taken out from the cathode evaporation chamber and stressed for 20 min. It was further noted that failure mode of the device with the Parylene layer was typically associated with the areas growing dimmer rather than the spontaneous appearance of dark spots in the normal devices. From this, it was deduced that the Parylene layer resulted in a more uniform current density. The above observations lead to the conclusion that the addition of the Parylene interlayer is indeed an efficient technique to inhibit the growth of non-emissive dark spots and extend an OLED device lifetime.

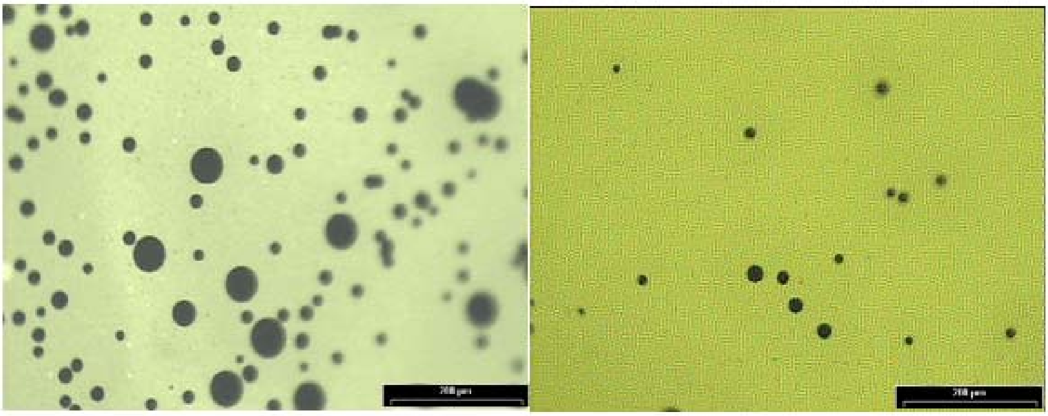

Figure 8. Optical microscopy pictures of dark non-emissive area in the devices after they were taken out from the cathode evaporation chamber and electrically stressed for 20 min. (a) the device without the parylene layer and (b) the device with the parylene layer.

To further explore the possible role of Parylene in prolonging device lifetime, a study was conducted by inserting another Parylene layer in between the organic layer (EL) and cathode layer. A new device structure with dual Parylene layer was thus developed. After subjecting the device to electrical stresses, the SIMS profile was acquired, as in Figure9.

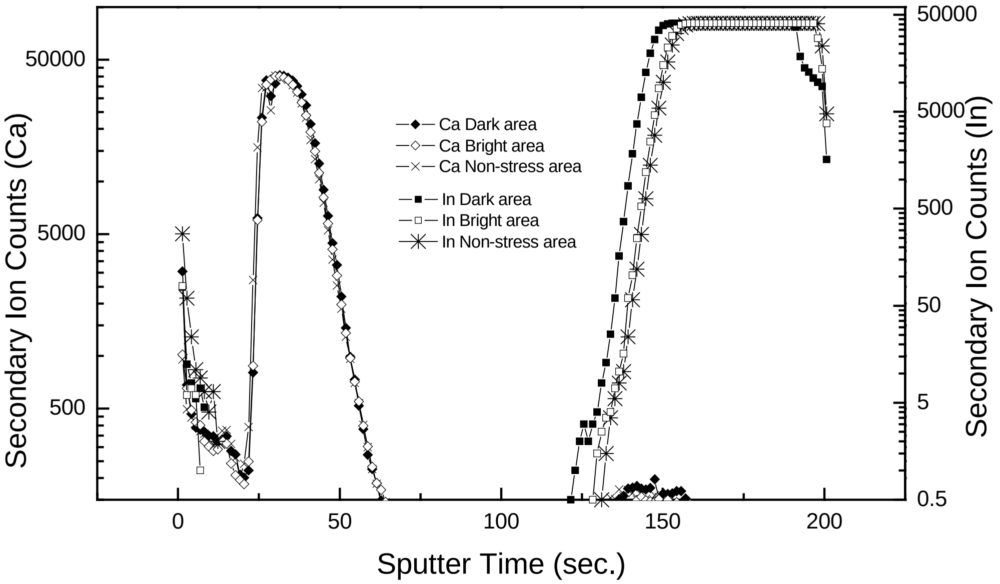

Figure 9. SIMS profiles for device structure of: ITO/3 nm parylene/HTL/EL/3 nm parylene/Ca/Ag.

As observed in the SIMS profile, the Ca and In profiles were clearly separated with no boundary movement even for the non-emissive area. However, the device with dual Parylene layers showed a higher turn-on voltage of 10 V. The formation of non-emissive dark areas and their growth rates were further reduced. The results further substantiate that inhibition in electrode migration is a key to improved device lifetime.

## Patenting the New Device Structure

In lights of the findings on the new device structure that effectively inhibits the growth of dark spots and prolongs device lifetime, a patent was filed by the research team on the device architecture whereby an organic interlayer is deployed in between the Anode / HTL, and/or the HTL/EL, and/or the Anode/EL (as in Figure 10). The organic interlayer as claimed in the patent includes Polyimides, Teflon, Parylene or other kind of high barrier polymer or organic films. It is worth mentioning that the proprietary OLED architecture is capable of reducing the number of pinholes in the cathode by at least a 100 fold and exercising effective control over the growth of the non-emissive areas in the EL polymer and cathode surfaces. In sum, the new architecture provides a cost effective solution to the OLED industry for the development of robust OLED to compete against the qualities of the conventional display products.

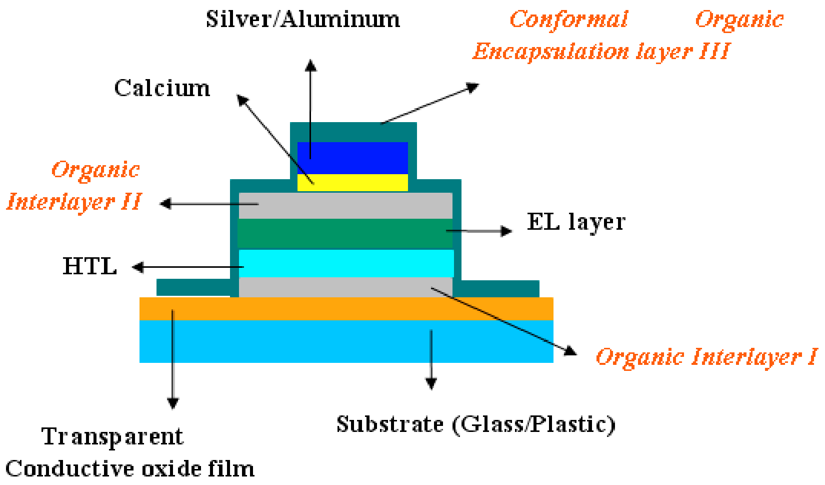
Silver/Aluminum
Conformal Organic Encapsulation layer III
Calcium
Organic Interlayer II
EL layer
HTL
Organic Interlayer I
Transparent Conductive oxide film
Substrate (Glass/Plastic)

Figure 10. Patented Architecture of OLED with organic interlayer enhancement.

## 4. CORRELATION OF CURRENT NOISE BEHAVIOR AND DARK SPOT FORMATION AND DEVICE LIFETIME

During the course of the studies on OLED degradation, it had been observed that the proliferation of dark spots exhibits a strong correlation with the low frequency electrical noise. This led to further research into the correlative behavior between dark spot formation and low frequency noise it was believed that the phenomenon has a far-reaching implication in device degradation analysis and lifetime prediction. There is a strong advantage if an analysis technique uses low frequency noise for degradation studies and computation of lifetime as low frequency noise can be performed instantaneously with a short time of biasing without damaging the test device. Conventional test technique, on the other hand, subjects the test device to accelerated test conditions and induces irreversible damage to the device.

In this chapter, 1/f noise investigation shall be conducted on encapsulated OLED devices. The purpose of the experiment is to show that the dark spot is primarily correlated to current 1/f noise slope. The studies include correlating the low frequency noise slopes of the test devices with the dark spot growth rate and device lifetime. Besides, the correlative relationship between current 1/f noise magnitude and the dark spot initial size shall be investigated. With the results, the research team intends to provide a basis for the low frequency noise measurement method for predicting device lifetime and degradation behavior.

### Experimental Procedures

The OLED devices investigated in this article are typical two-layer small molecular devices with a structure of ITO / NPB (75 nm) / $Alq_3$ (75 nm) / LiF (5 Å) / Al (200 nm), where ITO is indium-tin-oxide, NPB is naphthyl-substituted benzidine derivative and $Alq_3$ is aluminum tris(8-hydroxyquinoline). The devices are fabricated by depositing the NPB, $Alq_3$, LiF and Al layers on ITO-coated glass via thermal evaporation. Finally the devices were encapsulated by a capping glass sealed with epoxy.

The fabricated devices, numbered 1 to 6, are placed in the shielded testing box for the measurement of 1/f noise prior to electrical stressing. Noise measurements were performed by biasing the devices with a low noise DC current source (a stack of Ni–Cd batteries). The noise signal, fluctuations of current *I*, was coupled to a wideband (0.03 Hz–100 kHz) low-noise SR570 current preamplifier. The output of the amplifier was fed to a HP35670A digital signal analyzer in which the power spectral density (PSD) *S(f)* of current *I* was calculated in the range of 1 to 800 Hz. At the same time, the initial luminance for all the devices is measured to be approximately 1000 $Cd/m^2$.

The devices were then subjected to electrical stresses by passing through a constant current of 1mA. The devices were examined for dark spot formation at every 24 hours interval. The images of dark spots were acquired by attaching a CCD camera on an optical microscope and the images obtained by the CCD camera were sent to image processing software for computation of the dark spot areas.

## The Results

The current noise PSD as a function of frequency for Device 1 to 4 is exhibited in Figure 11 (a). The PSD slope value α for the respective devices were computed in accordance to Hooge's theory whereby $S_v = \alpha_H (V_{dc}^2 / N_c f^{\alpha})$ , and indicated in the figure. It can be observed that the computed PSD slope values were larger than 1, implying the existence of poor interfaces, defects and traps in the test devices. Comparing among the four devices, Device 1 and 2 possess considerably higher α values than those of Device 3 and 4. It was further noted that the Devices 1 and 3 possess higher noise magnitude than those of Device 2 and 4.

The areas of dark spots induced in the test devices stressed over times are exhibited in Figure 11 (b). It could be seen that Device 2 and 4 have smaller initial dark spot sizes, and this phenomenon correlates the observation that the two devices have a low noise magnitude as in Figure 11 (a). Under further stressing, it was further observed that the dark spot areas in Device 1 and 2 increases dramatically at about 200 hours. The sudden increase in the dark spot areas indicate device failure and hence, the end of device lifetime. The relatively shorter lifetimes in Device 1 and 2 correlate the observation that the two devices possess considerably higher α values, as in Figure 11 (a).

The correlative behavior between the 1/f noise slope and the lifetime can be explained by the tunneling model, a direct application of McWhorter's potential fluctuation mechanism [26]. It accounted for the magnitude and slope of noise PSD in the low frequency range for high temperature superconductors. The model suggested that the energy barriers resulted from abundant defects should cause fluctuations in number of charge carriers, which would lead to an abnormally high slope level of *1/f* noise. In organic light emitting devices, interface deterioration has been ascertained to play an important role in device degradation [30]. On the other hand, interface deterioration definitely cause energy barrier to increase, resulting in fluctuation of number of charge carriers.

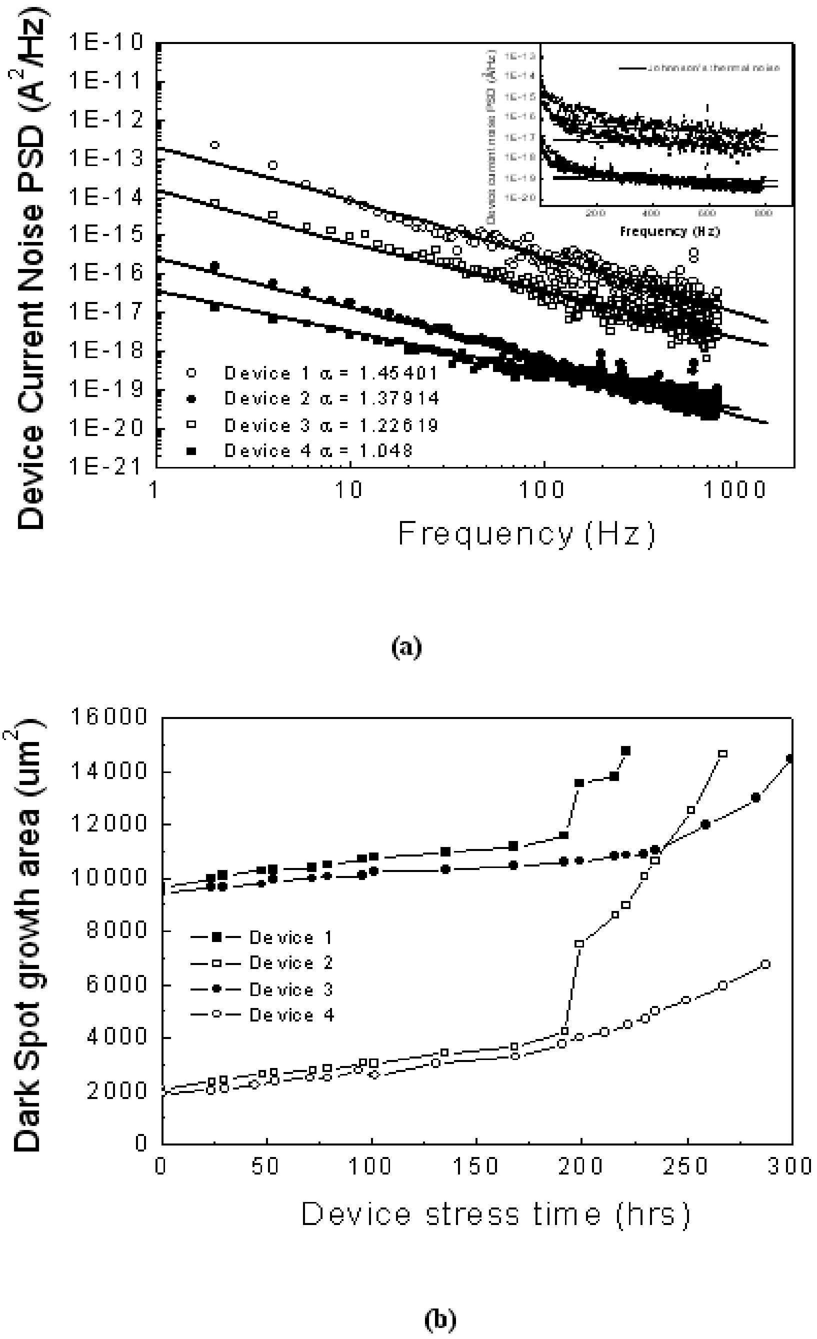

Figure 11. (a) The PSD *S*(*f*) of OLED Devices 1 to 4. Solid lines are linear fits, scatter sample points are experimental data. The inset shows the same PSD curves against a linear frequency axis. The solid lines in the inset are Johnson's thermal noise fitting. (b) Dark spot area as a function of device stress time for the devices 1 to 4.

The above explanation, therefore, substantiates the correlations indicated in Figure 11 (a) and 11 (b). Device 1 and 2, having larger 1/f noise slope than Device 3 and 4, should probably have poorer interfaces. This leads to a higher tendency for dark spots proliferations and shortening of lifetime in Device 1 and 2.

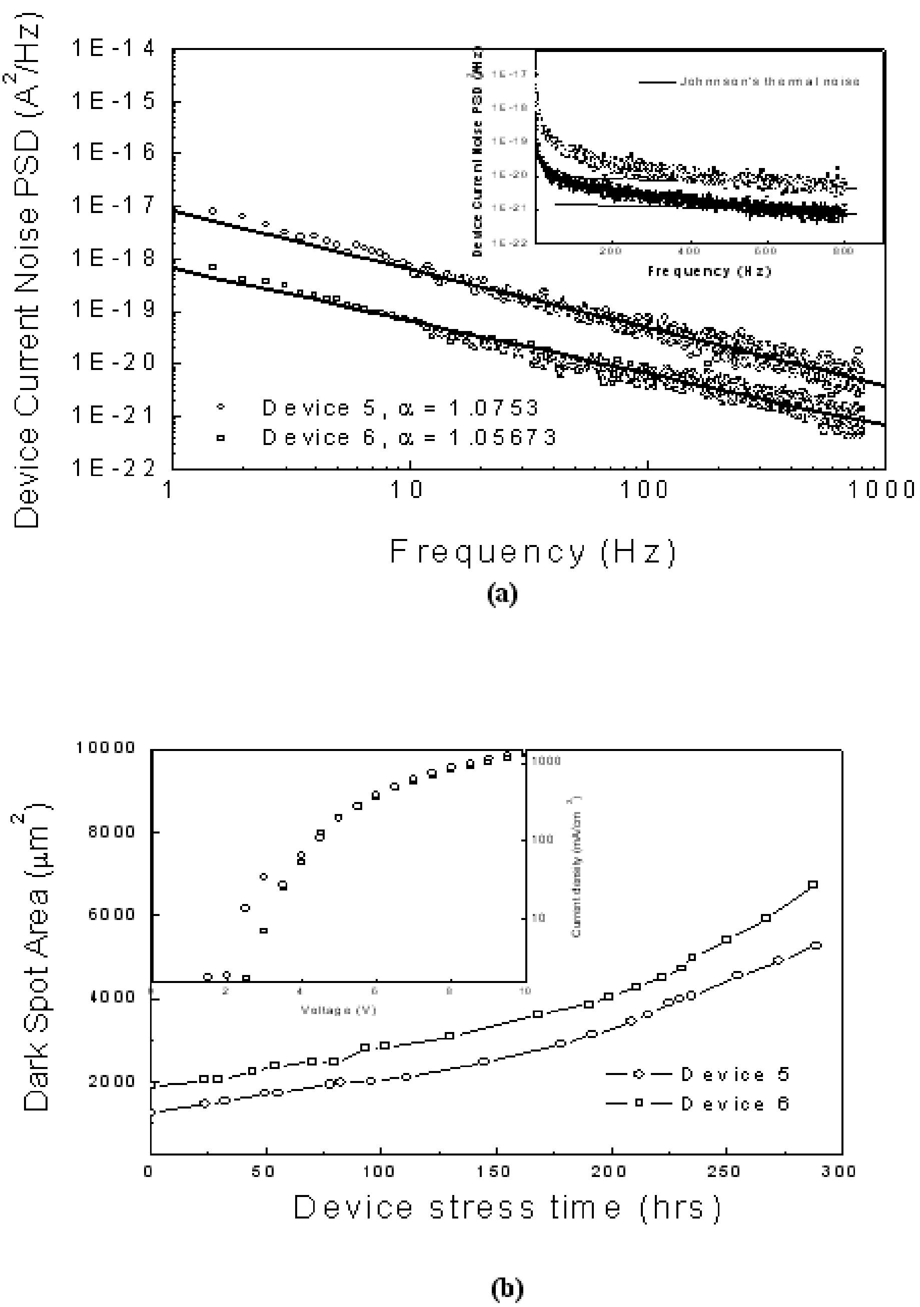

Figure 12. (a) The PSD $S(f)$ of OLED devices 5 and 6. Solid lines are linear fits, scatter sample points are experimental data. The inset shows the same PSD curves against a linear frequency axis. (b) Dark spot growth area as a function of device stress time for devices 5 and 6. The inset shows the I-V curves for OLED device 5 and 6.

The other possible mechanism for carrier number fluctuations is the widely existing material defects and flaws, which are primarily reflected by the magnitude of noise PSD. The electroluminescence material defects could come from the synthesis and purification process, which decrease the carrier injections and cause the much increased low frequency noise level. This accounted for the observation that Devices 2 and 4 have roughly the same dark spot initial size, which is reflected by the close noise magnitude levels of the two. Noise spectral analysis is an effective way to comprehend the device interface (via noise slope) and bulk quality (via noise magnitude).

In order to illustrate the advantages of noise spectral analysis over the conventional method of device I-V analysis in lifetime prediction, the noise spectral and I-V characteristics curves of Device 5 and 6 as fabricated earlier were acquired and the two devices were then subjected to current stress test. As in Figure 12 (b), the I-V characteristics of Device 5 and 6 are almost identical. The PSD profile in Figure 12(a), however, shows that Device 5 has a higher noise slope and magnitude than Device 6. The results from the stress test concurred with the observation on the devices' PSD profile, as Device 5 exhibits a larger initial dark spots areas and slightly faster growth of the dark spots after 250 hours. The test serves to illustrate that one can reliably predict a device degradation based on the noise spectral profiles. On the other hand, the I-V curve only provides a macroscopic description of the device performance and is relatively insensitive to the inherent defects and interface qualities.

In summary, the experiment had illustrated that low-frequency $1/f$ noise is a very sensitive measurement of the quality and reliability of optoelectronic devices and exhibits a strong correlation between current noise and dark spot formation. Based on the results of the experiment, a correlation between 1/f noise slope and the dark spot growth rate and lifetime was thus established. A larger 1/f noise slope generally leads to a faster dark spot growth rate and shorter lifetime. Another correlation was established between the dark spot initial size and the noise magnitude. The higher the magnitude, the larger is the dark spot initial size. These two correlations are significant to device reliability analysts as they provide a basis for developing noise measurement into a powerful tool to predict device lifetime and degradation behavior.

## 5. CONCLUSION

The paper spans across three areas: 1) the new perspectives on dark spots formation mechanism, 2) the proprietary technique to inhibit the growth of dark spots, 3) the proposed methodology to predict the dark spot growth and device lifetime with low frequency analysis.

In the research on dark spot formation, it had been identified that the degradation of the active polymer is the main cause of weakly emissive and non-emissive areas in OLEDs. The mechanism begins with the roughening of the polymer/electrode interface caused by metal migration. The roughening results in the formation of sharp metal protrusions at which intense current stresses are localized. The intense local current degrades the polymer, causing the growth of the non-emissive dark regions.

As it was conjectured that stabilizing and smoothing the polymer/electrode interface is an effective way to minimize the formation of the non-emissive area, the research team had developed a technique to improve the interface by inserting polymer in between the ITO and hole-transport layer. The experiment had proven that the method leads to a more uniform current flow, and is effective in inhibiting the dark spot formation. It had been further shown that by inserting one more polymer layer in between the EL polymer and the cathode layer, the device cathode interface can be further stabilized, thus, minimizing the probability of formation of the non-emissive area.

Finally, the research team had identified a correlation between 1/f noise slope and the dark spot growth rate and lifetime. In the experiment, a larger 1/f noise slope generally leads to a faster dark spot growth rate and shorter lifetime. It had been further identified another correlation between the dark spot initial size and the noise magnitude. The higher the magnitude, the larger is the dark spot initial size. These two correlations are very important for the development of advanced technique for device lifetime predictions based on low frequency noise spectral measurements.

## REFERENCES

[1] B. H. Cumpston and K. F. Jensen “Electromigration of Aluminum Cathodes in Polymer-based Electroluminescent Device”, *Appl. Phys. Lett.* **69** (25) (1996).

[2] B. H. Cumpston and K. F. Jensen “Photo-oxidation of Electroluminescent Polymers”, *Trends in Polymer Science*, **4** (5) (1996).

[3] Hany Aziz , Zoran D. Popovic, Nan-Xing Hu, Ah-Mee Hor and Gu Xu “Degradation Mechanism if Small Molecule-Based Organic Light-Emitting Devices”, *Science,* Vol. 283 (1999).

[4] P. E. Burrow, V. Bulovic, S. R. Forrest, L. S. Sapochak, D. M. McCarty and M. E. Thompson “Reliability and Degradation of Organic Light Emitting Devices”, *Appl. Phys. Lett.* **65** (23) (1994).

[5] J. McElvain, H. Antoniadis, M.R. Hueschen, J.N. Miller, D.M. Roitman, J.R. Sheats and R.L.Moon “ Formation and Growth of Black Spots in Organic Light-Emitting Diodes”, *J. Appl. Phys.* **80** (10) (1996).

[6] Y. F. Liew, H. Aziz, N. X. Hu, H. S. O. Chan, G. Xu and Z. Popovic “ Investigation of the Sites of Dark Sports in Organic Light-Emitting Devices”, *Appl. Phys. Lett.* **77** (17), (2000).

[7] L. Ke, S. J. Chua, K. R. Zhang and N. Yakolev “Degradation and Failure of Organic Light-Emitting Devices”, *Appl. Phys. Lett.* **80** (12) (2002).

[8] L. Ke, K. R. Zhang and N. Yakolev, S. J. Chua, “Secondary Ion Mass Spectroscopy Study of Failure Mechanism in Organic Light Emitting Devices” *Mat. Sci. Eng. B-Solid,* **97** (1) (2003).

[9] L. Ke, S. J. Chua, W. Wang “Degradation Mechanisms in Electrically Stressed Organic Light-Emitting Devices” *Thin Solid Films* **417** (36-39) (2002).

[10] L. Ke, P. Chen, S. J. Chua, “Photoluminescence Degradation in Organic Light-Emitting Devices” *Appl. Phys. Lett.* **80** (697) (2002).

[11] L. Ke, R.S. Kumar, S. J. Chua, A.P. Burden “Degradation Study in Flexible Substrate Organic Light-Emitting Diodes” *Appl. Phys. A* **81** (969-974) (2005).

[12] L. Ke, S. F. Lim, S. J. Chua, “Organic Light Emitting Device Dark Spot Growth Behavior Analysis by Diffusion Reaction Theory” *Journal of Appl. Polymer Science, Part B,* (Polymer physics) Vol. 39, 1697, 2001.

[13] L. Ke, R.S. Kumar, A.P. Burden, S. J. Chua, “Blocking Impurities in Organic Light Emitting Device by Inserting Parylene Interlayer” *Japanese Journal of Applied Physics*, Vol. 44, No. 1A, 2005 pp. 406-409.

[14] Lin Ke, Ramadas Senthil Kumar, Keran Zhang, Soo Jin Chua, A.T.S. Wee Organic Light “Emitting Devices Performance Improvement by Inserting Thin Parylene Layer” *Syn. Metals*. **140** (2004) 295-299.

[15] Lin Ke, Kumar RS, Zhang KR, Chua SJ, Wee ATS “Effect of parylene layer on the performance of OLED” *Microelectronics Journal* **35** (4): 325-328 (2004).

[16] Soo Jin Chua, Lin Ke, Ramadas Senthil Kumar, Keran Zhang “:Stabilization of electrode migration in polymer electroluminescent devices” *Appl. Phys.Lett*. Vol 81, 1119 (2002).

[17] L. Ke, R.S. Kumar and S.J. Chua, Singapore Patent No. 200107343-6 28 Nov 2001,

[18] L. K. J. Vandamme, “Noise as a Diagnostic Tool for Quality and Reliability of Electronic Devices”, *IEEE transactions on electron devices*, Vol. 41, NO. 11, (1994),

[19] X. S. Li and L. K. J. Vandamme, “1/f Noise In MOSFET as a Diagnostic Tool”, *Solid-State Electronics* Vol.35, No.10 pp.1477-1481, (1992).

[20] F. N. Hooge, “1/f Noise Sources”, *IEEE Transactions on Electron Devices*, Vol. 41, No. 11 (1994),

[21] L. Ke, X. Y. Zhao, R. S. Kumar, S. J. Chua Lin, “Low Frequency Noise Measurement and Analysis in Organic Light-Emitting Diodes”, *IEEE Electron Device Letters*, Vol. 27, NO. 7, Jul 2008.

[22] L. Ke, X. Y. Zhao, R. S. Kumar, S. J. Chua, ”Low Frequency Optical Noise from Organic Light Emitting Diode“, *Solid State Electronics*, Vol. 52, No. 8 (2008).

[23] L. Ke, R. S. Kumar, and C. Vijila, “Correlation of Current Noise Behavior and Dark Spot Formation in Organic Light-Emitting Diodes*”, IEEE Electron Device Letters*, Vol. 29, Issue 1 (2008).

[24] L. Ke and W. H. Teng, “Noise Characterization of Light-Emitting Devices Based on Conjugated Copolymers of Fluorene and Thiophene Moieties”, *Journal of Applied Physics* **102**, 063103 (2007).

[25] J. S. Kim and Y. Yamamoto, “Theory of Noise in p-n Junction Light Emitters”, *Physical Review B,* Vol. 55, No. 15 (1997).

[26] Y. Song, A. Misra, P. P. Crooker, and J. R. Gaines, “1/f noise and morphology of $YBa_2Cu_3O_7 - \delta$ single crystals,” *Phys. Rev. Lett*., vol.66, no. 6, pp.825 – 828, Feb.1991.

[27] Vadim N. Savvate’ev, Aharon V. Yakimov, Dan Davidov, Roman M. Pogreb, Ronny Neumann, Yair Avny, ”Degradation of Nonencapsulated Polymer-Based Light-Emitting Diodes Noise and Morphology” *Appl. Phys. Lett*. **71** (23), 8 Dec 1997.

[28] G. Ferrai, D. Natali, M. Sampietro, F.P. Wenzl, U. Scherf, C. Schmitt, R. Günter, G. Leising, “ Current Noise Spectroscopy on mLPPP based Organic Light Emitting Diodes”, *Organic Electronics* **3** (2002) 33-42.

[29] M. Sampietro, G. Ferrari, D. Natali, U. Scherf, K.O. Annan, F.P. Wenzl and G. Leising, “Tracking of Conduction Phenomena and Degradation in Organic Light Emtting Diodes by Current Noise Measurement”, *Applied Physics Letter*, Vol78, NO.21 (2001).

[30] M. Fukuda, T. Hirono and F. Kano “1/f Noise Behavior in Semiconductor laser Degradation” *IEEE Photon. Technol. Lett.* Vol. 5, No. 8 (2002).

In: Integrated Circuits, Photodiodes…
Editors: R. McIntire and P. Donnell, pp. 227-291
ISBN: 978-1-60692-660-4
© 2009 Nova Science Publishers, Inc.

*Chapter 9*

# PHOTODIODES: A POWERFUL TOOL IN HPLC FOR PEAK DETECTION AND IDENTIFICATION

***Victoria F. Samanidou[a], Ioannis N. Papadoyannis[b] and Eftichia G. Karageorgou***
Laboratory of Analytical Chemistry, Department of Chemistry,
Aristotle University of Thessaloniki, Thessaloniki, 541 24 Greece

## ABSTRACT

Photodiodes are semiconductor devices with a p–n or p–i–n structure for the detection of light. When used as an array (a number of diodes placed side by side), they serve as light sensors characterized by excellent linearity with respect to incident light, low noise, wide spectral response and mechanical ruggedness. This advanced type of detection is the most sophisticated UV-Vis detector widely applied in HPLC. In contrast to a conventional single wavelength detector, photodiode array (PDA) detectors are used for monitoring spectra of analytes passing through a sample flow cell over the entire wavelength range. Continous monitoring of the absorbance spectra of eluted components provides a great deal of information for an analysis. One of the most significant advantages of the PDA detector to the HPLC analyst is that it permits the recognition of unknown constituents in a complex matrix. Peak identification is achieved using spectral information and detection is not only based on retention time. Spectral data stored in a computer, can serve as a bank for identifying unknown peaks. PDA detectors can be used both for routine applications and applications such as method development and peak characterization.

Additionally a PDA detector can provide information using the acquisition of spectra to determine peak purity. The latter is of paramount importance in pharmaceutical industry, where it is designated to detect the presence of co-eluting impurities.

Applications of PDA detection can be found in all analytical fields, especially in cases where confirmatory analytical methods are required. In food quality control samples, residual analytes in food of animal origin can be detected so that non-compliant samples can be traced. In clinical analysis, it can be used in pharmacokinetics, metabolism and bioavailability

---

[a] E-mail address: samanidu@chem.auth.gr. Tel:+30231997698, FAX: +302310997719. (Corresponding author)
[b] E-mail address: papadoya@chem.auth.gr. Tel:+30231997793, FAX: +302310997719. (Corresponding author)
Aristotle University of Thessaloniki. GR-54 124 Thessaloniki, Greece

studies. Moreover, drugs can be monitored so that therapeutic levels can be estimated and effective drug doses can be personalized in patients.

In this chapter, the use of PDA detectors as a powerful tool in HPLC will be discussed with emphasis in peak identification and confirmatory analysis. Examples of applications in several analytical fields will be provided.

## 1. INTRODUCTION

The function of the high performance liquid chromatography (HPLC) detector is to examine the solution that elutes from the column and to output an electronic signal proportional to the concentrations of individual components present there. The fact that most analytes absorb light in the UV region (at least to some extent) without needing chemical derivatization makes UV-visible spectrophotometers by far the most widely applied detectors in HPLC. However with regards to the identification of mixture components, simple detectors, which rely only on comparison of retention times, are not sufficient and thus erroneous conclusions may be drawn.

The development of photodiode array (PDA) detectors, which are the most advanced UV/vis detectors, has helped significantly to this direction. In contrast to conventional single wavelength detectors, PDA detectors are used for recording the full UV-Vis absorption spectrum of analytes passing through the sample flow cell. Stored reference spectra are used for comparison with recorded data to confirm identity to a certain degree. Spectral information used for analytes confirmation after separation provides a useful tool comparable to other detection techniques, which are more sophisticated but of significantly higher cost. The popularity of a PDA detector is also complemented from the ease of its use. Numerous publications have been published in recent years as PDA detection has been coupled not only with HPLC, but with capillary electrophoresis, GC and SFC as well.

The advent of a diode array spectrophotometer took place in 1979, when Hewlett Packard introduced the HP 8450A spectrophotometer. James G. was the first who had the pioneering idea to propose the ability of the diode array spectrophotometer to serve as an HPLC detector. The year 1982 appears to be the cut-off point in the development of commercial PDA detectors for HPLC. Since the introduction of the first PDA spectrophotometer by Hewlett Packard, many companies like Shimadzu, Beckman, Hitachi, Waters Associates, Varian, Perkin Elmer and others have followed manufacturing various PDA detectors [1].

Photodiode Array Technology offers to the chromatographer not only the possibility of compound identification by permitting the recognition of unknown constituents in a complex matrix, but also the ability to detect co-elution and peak purity/peak homogeneity.

PDA detectors can be used both for routine applications e.g. in quality assurance as well as for research applications such as method development and peak characterization. Numerous applications of PDA detection can be found in all analytical fields, especially in cases where confirmatory analytical methods are required. In food quality control samples, residual analytes in food of animal origin can be detected, so that non-compliant samples can be traced. In clinical analysis, PDA technology can help in the field of pharmacokinetics, metabolism and bioavailability studies. Moreover, drugs can be monitored so that therapeutic levels can be estimated and effective drug doses can be personalized in patients.

## 2. PRINCIPLE OF OPERATION

Photodiodes make use of the unique properties of semiconductors, such as silicon. Silicon can be doped with impurities to make it either electron rich (an n-type semiconductor) or electron poor (a p-type semiconductor). When an n-type semiconductor is in contact with a p-type semiconductor, electronic changes occur at the boundary, or junction (Figure 1). A photodiode is a p–n junction constructed with the top p layer so thin that it is transparent to light. When used as an array that is a number of diodes placed side by side, they can serve as light sensors characterized by excellent linearity with respect to incident light, low noise, wide spectral response and mechanical ruggedness [2].

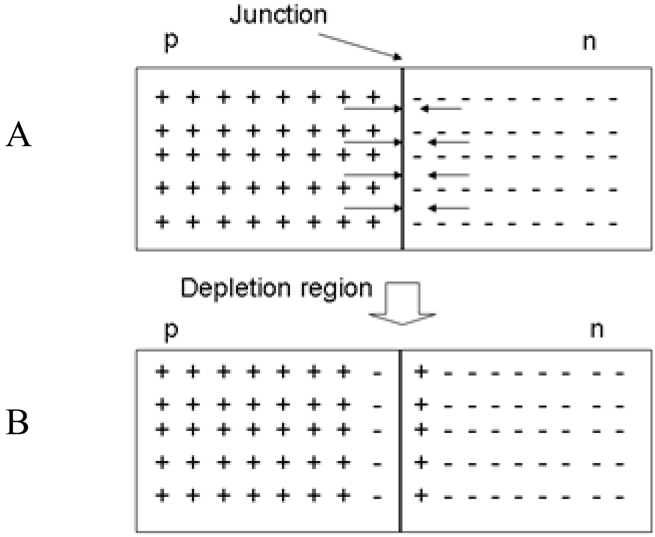

Figure 1. A. Electron and holes migration across the p-n junction when no voltage is applied. B. Formation of barrier potential.

The PDA detector can be equipped with a deuterium ($D_2$) lamp or xenon lamp that emits light over the UV spectrum range and a tungsten halogen (W) lamp for the visible range. Polychromatic light from two lamps is mixed by a half mirror, reflected on a concave mirror, and introduced into a flow cell. The light which has passed through the flow cell is gathered on a slit by another mirror and introduced to spectrophotometer. The light is then dispersed by a quartz prism or a diffraction grating and sprays across an array of photodiodes each of which detects only a narrow wavelength band. A shutter or a filter before the cell is automatically inserted into the light path each at measurement of the dark signal (dark current), and at the automatic wavelength check. The schematic showing the principle of operation of a PDA detector is presented in Figure 2. In the photodiode array, a number of photodiode elements are arranged in a row, with nearly one diode per nm in the range of the UV/Vis spectrum. Each diode receives light of a slightly different wavelength to that received by its neighbor. Light shining through the p layer creates additional free electrons in the n layer that can diffuse to the p layer, thus creating an electrical current that depends on the intensity of the light. This small current is easily amplified and measured [2, 3].

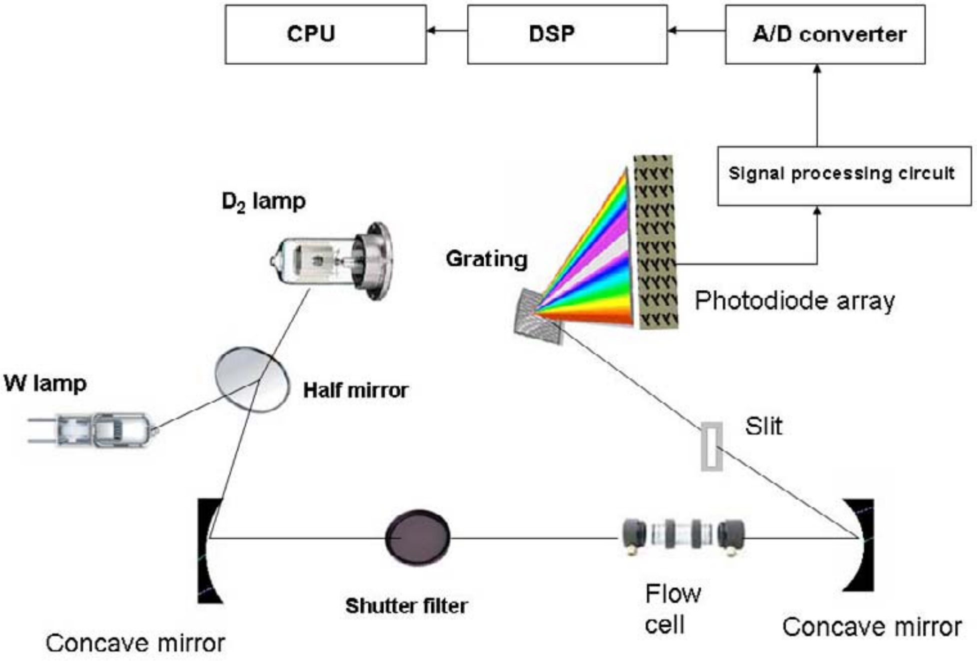

Figure 2. Principle of operation of a PDA detector.

The size of the band of radiation observed is related to the resolution of the instrument. The resolution of the detector ($\Delta\lambda$) will depend on the number of diodes ($n$) in the array, and also on the range of wavelengths covered [4].

The ultimate resolving power of the diode array detector will depend on the semiconductor manufacturer and on how narrow the individual photocells can be commercially fabricated.

The array may contain many hundreds of diodes. At the end of the run, the output from any diode is regularly sampled by a computer and stored on a hard disk. A chromatogram is produced using the UV wavelength that was falling on that particular diode.

Considering the range from 200 to 700 nm, it would take 500 photodiodes to achieve spectral resolution of about 1 nm. The speed of a diode array instrument depends on the speed at which a computer can access, sample, measure and discharge the voltage developed on each diode. The number of diodes sampled affects also the rate at which spectra can be obtained. Current photodiode instruments can obtain spectra with resolutions of 1–3 nm (256–1024 diodes/ 190–1100 nm range) at a rate of up to 2500 spectra $s^{-1}$.

For example in Shimadzu SPD-MXA one element is assigned every 1.2 nm of the spectra in the range of 190 nm to 800 nm. Each of these devices measures independently the intensity of light in the wavelength associated with it and sends the information to the memory unit.

With the light source of a $D_2$ lamp the range 190-600 nm is covered, with only W, the range 371-800 nm and when both are simultaneously illuminated the reange 190-800 nm.

The optical current in the wavelength associated with each element is accumulated for a fixed time (scan period) and read in the high speed at a fixed internal. The signal at each element is then converted into a digital signal by A/D converter, and then sent to the LC workstation via interface board through a Central Processing Unit (CPU).

When the array receives a "start" pulse signal, the scanning circuit turns on and off a metallic Oxide Silicon Field Effect Transistor gate one after another at intervals of 50 µs. Accordingly, 512 signals (spectral data) appear in succession at the output terminals in 25.6 ms.

When light enters the photodiode with the metallic Oxide Silicon Field Effect Transistor gate in the off state, an electrical charge (photoelectron), as can be expressed by the following equation, is accumulated at the p-n junction in the photodiode.

$$Q = K*I*\Delta t \tag{1}$$

where Q = Quantity of electric charge

I = quantity of incident light
T = time needed for accumulating electric charge
K = a constant

So the quantity of the electrical charge (Q) becomes proportional to the incident light (I).

The electrical charge flows out of the output terminal when the metallic Oxide Silicon Field Effect Transistor gate is on.

Actually the quantity of electrical charge measured by the unit is not only due to the incident light, as a certain amount of charge is output even when there is no incident light at all. This is caused by the dark current in the photodiode having been accumulated during the time period t mentioned above. If we take into account the dark current in the photodiode accumulated during period t, the above equitation can be rewritten as:

$$Q = K*I*\Delta t + D_0 \tag{2}$$

The unit measures the electrical charge accumulated when light impinges on the photodiode, and checks for variation in the quantity of light. The value $D_0$ varies according to individual photodiode arrays, and it is temperature dependent. In some instruments the problem of noise due to dark current is solved by maintaining the value $D_0$ at a constant level through the optimal temperature control of the polychromator.

Since the signal transmitted by the PDA is easily affected by variations in ambient temperature the PDA is housed in a thermostatic chamber accurately regulated in temperature

Most instruments will allow at least one diode to be monitored in real time, so that a chromatogram can be generated as the separation develops. The spectrum of the analyte can be obtained by recalling from memory the output of all the diodes at the retention time. This makes the PDA ideal as a versatile detector for HPLC applications.

Spectral evaluation software allows the display of both chromatographic and spectral data in samples. These features are integrated into the chromatographic data system. Most software include automated spectral annotations of $\lambda_{max}$, peak matching, library searches, and peak purity evaluation [5].

A summary of features and functions of modern PDAs are:

- Contour maps and 3-D spectral display, for overall evaluation of the entire sample
- $\lambda_{max}$ annotations, for peak tracking during method development

- Spectral library searches, for peak identification
- Peak purity evaluation, by comparing the upslope, apex and downslope spectra, assessment of UV spectral peak purity can give some limited assurance that there is not an impurity with different characteristics co-eluting with the main peak [6].

Figure 3A shows an example of a chromatogram obtained by PDA concerning the separation of antibiotics. The UV spectrum of a selected peak at 5.07 min is shown in Figure 3B. LC solutions of Shimadzu was used.

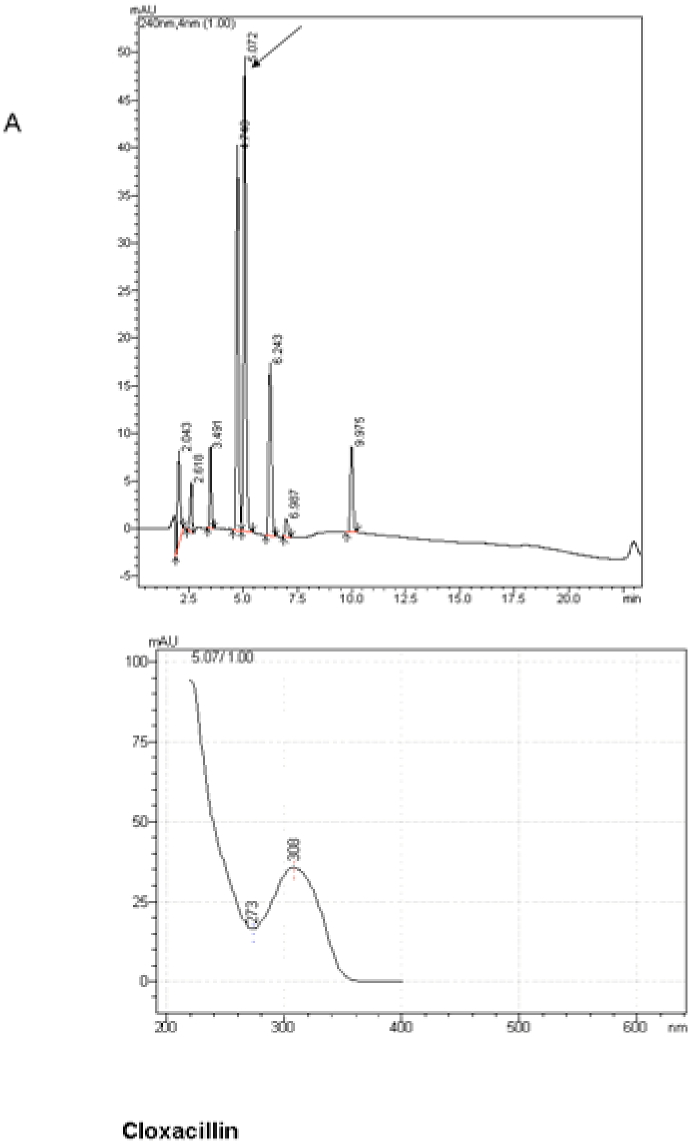

Figure 3. A. Example of a chromatogram of antibiotics. B. UV spectrum of the selected peak of Cloxacilllin at 5.07 min.

The PDA contour view allows data to be viewed in their entirety, while 3D image provides better visual effects in checking the data. Sophisticated spectral evaluation software allows the convenient display of both chromatographic and spectral data along three axes (absorbance versus wavelength, versus retention time). Figures 4A, 4B and 4C show the same chromatogram in a typical view, as 3D image and contour plot respectively. The contour view allows the display of the absorbance of the sample at each time point and wavelength like an aerial photograph. This allows the rapid determination of a wavelength at which the sample can be detected more easily. Specifying a wavelength allows the analyst to obtain the extracted chromatogram and specifying the time allows obtaining the extracted spectrum.

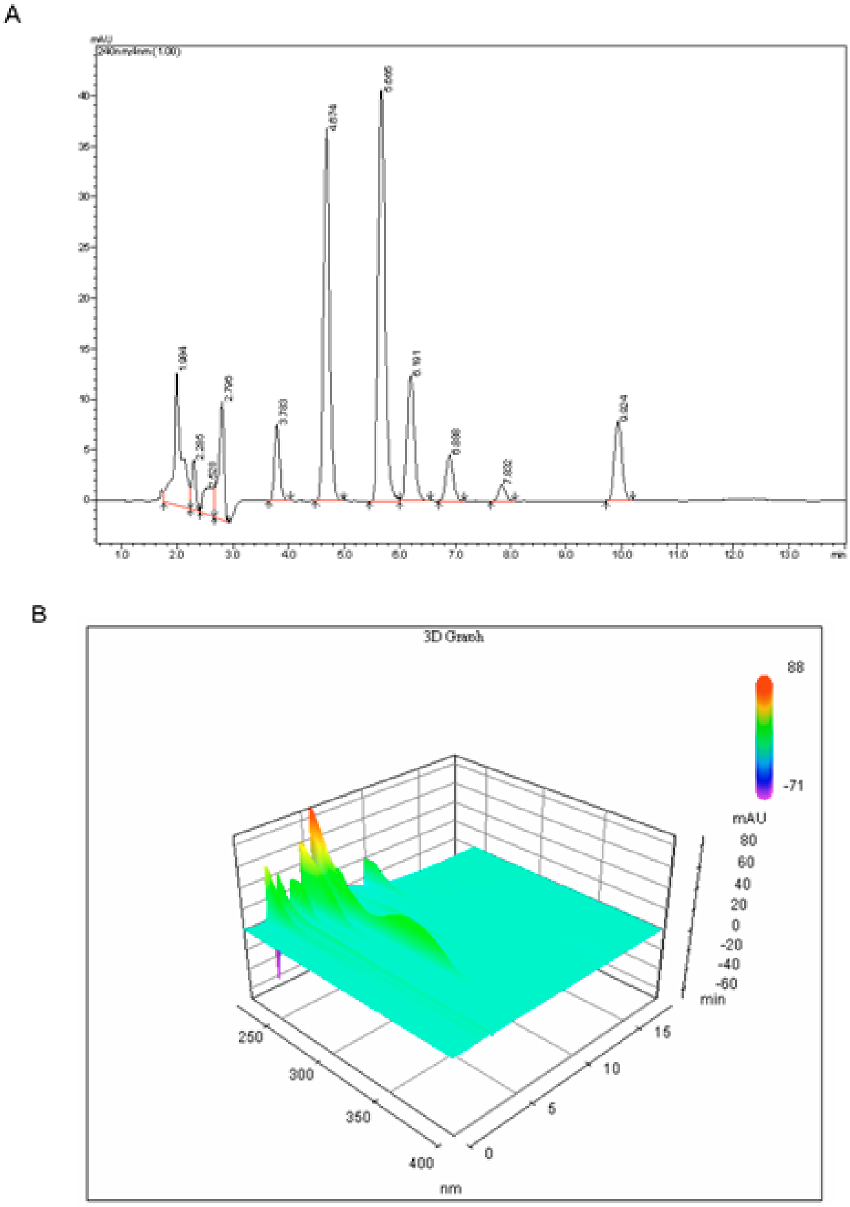

Figure 4. Continued on next page.

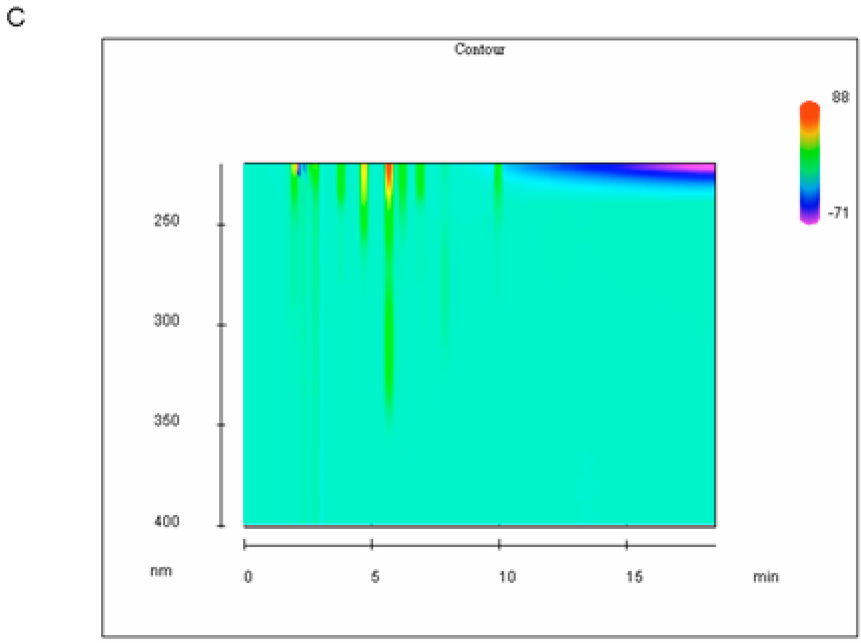

Figure 4. A. Chromatogram in a typical view, B. the same as 3D image and C. as contour plot.

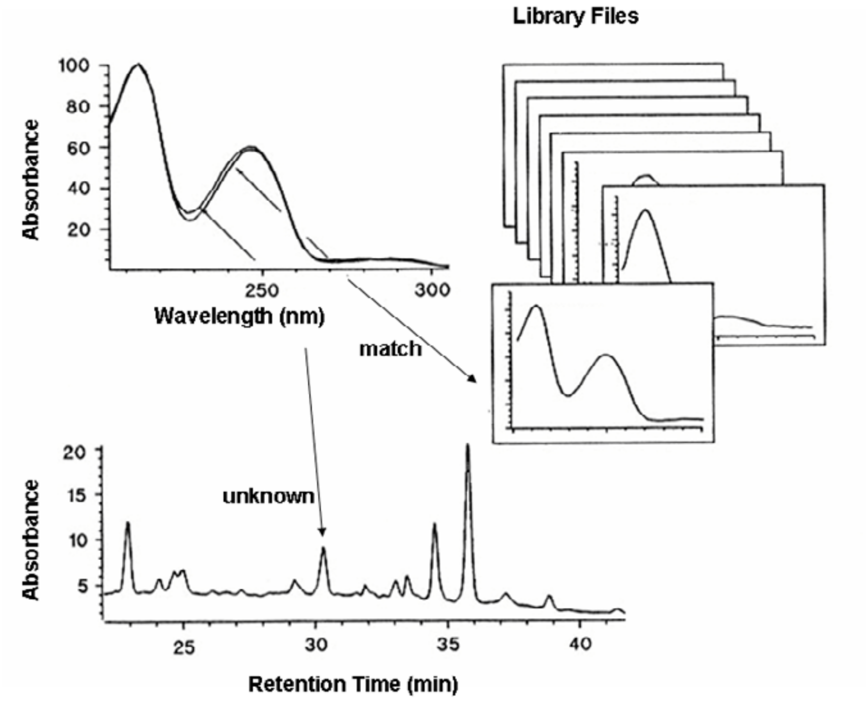

Figure 5. Peak identification by spectral matching.

The spectrum obtained by extracting 3D data collected by the PDA detector at specific time shows a pattern specific to each compound. This means that comparing the extracted spectrum with the spectra of known compounds allows the identification of the component separated by the chromatograph.

By using a PDA detector the chromatographer can generate and maintain a spectrum library for searching for analytes as shown in Figure 5. The library can be created by registering the spectra of known compounds. Then peaks are identified after specifying similarity threshold. When library search is used the list of hits will be created based on the required similarity and the spectra identified as having the same pattern will be displayed in the order of similarity. When the pattern is completely identical the similarity is 1.000. If the similarity is below 1, there is a deviation in the spectrum pattern. Background compensation is sometimes required in some cases e.g. when gradient analysis is performed using THF in the mobile phase, and a baseline drift positive or negative is noticed. These features are discussed in the following paragraphs.

Each HPLC run requires high-powered computation and display technology similar to that needed to process LC/MS data. A drawback of this detector is the array chatter, which limits sensitivity and generally gets worse as the system ages. Another problem is the cost of the detector and associated data-handling and storage computers, although this seems to be improving as technology advances [7].

## 3. PEAK PURITY ANALYSIS WITH PDA DETECTOR

Peak purity analysis is a powerful tool for detecting and/or identifying the presence of co-eluting impurities in HPLC chromatograms. When using a single wavelength UV-visible detector, the chromatographer can suspect the presence of an impurity, only if a shoulder or a valley or excessive tailing on the chromatographic peak are present. However the absence of these features cannot reassure the absence of an impurity or in other words cannot assure peak purity, especially in cases when the chromatographic resolution is poor or the concentration of the impurity is high. Thus a single variable-wavelength detector provides insufficient information for peak purity determination. The PDA detector providing spectral information enables the detection of peak purity by additional acquisition of spectral data. The spectral uniqueness of each compound is used to indicate when there are two or more components present in the peak, to identify peaks and assess purity [8].

Before the chromatographer can proceed with the quantitative information contained in a chromatographic peak, the purity of the peak should be confirmed. Only when the analyst is sure that no co-eluting impurity is present that could have contributed to the peak response, can convert the peak’s area or height into quantitative information based on the equivalent response of a pure standard. Peak purity analysis can also reveal the presence of contamination and prevent the subsequent generation of false analytical data.

Peak purity analysis is a useful addition to routine quality control procedures, especially in the analysis of pharmaceuticals and food products, for which contamination and quality of results are critical. During method development peak purity analysis is very useful to confirm all components which have been chromatographically separated and in quality control to warn the analyst that an unexpected co-eluting impurity has appeared [9,10].

### 3.1. Peak Purity Analysis

Since the PDA detector allows simultaneous collection of chromatograms at different wavelengths during a single run, following the run, a chromatogram at any desired wavelength in the UV/vis region can be displayed. By examining the UV spectrum for a peak from beginning to end, peak purity can be evaluated. If a single component is present in the peak, the UV spectra obtained across the peak should be superimposable. One should keep in mind that the opposite is not necessarily true. If the spectra are identical, the peak can still be impure because:

i) The impurity is present at a much lower concentration than the main compound and therefore not detectable.
ii) The impurity has the same or a very similar spectrum compared to the main compound.
iii) The impurity exhibits the same peak profile, as does the main compound, that is, it completely co-elutes with the main peak.

There are several ways to check for the homogeneity of a peak. One is to compare the UV spectrum of a standard with a sample peak that elutes at the same retention time. Spectra of the analytes peak are shown superimposed for visual observation. If they are identical it is presumed that they comprise the same compound. Peak purity is best evaluated by similarly comparing spectra obtained at the beginning, middle, and end of the band. Peak purity can be also evaluated in terms of ***ratiograms.*** These are plots of the ratio of absorbance collected at two different wavelengths, as illustrated in Figure 6. The wavelengths chosen will depend on the UV absorption characteristics of the substance concerned. If a peak is pure and homogeneous, the ratio of the absorption at two selected wavelengths would remain constant throughout the elution of the entire peak so that a clean rectangular peak is produced. The closer to a rectangle the shape of the ratio chromatogram the higher the purity of the peak is. Any significant distortion of the ratiogram's ideally rectangular form is an indication of differential absorption, and the presence of an impurity. This is because if an impurity e.g. with higher absorbance is present, the ratiogram changes from negative to positive during the transition from pure compound to mainly impurity.

The chromatographer yet should bear in mind that tests for peak purity are equivocal, because sample components are often chemically related and have the same or similar UV spectra (e.g., impurities, degradation products, homologs and oligomers, or metabolities). Only when the UV spectra of the two peaks between the compound of interest and potential interferants differ significantly the PDA detector can confirm the presence of an overlapping peak successfully; the relative concentration of one of the two peaks must fall within about 5 to 95% of the other. The resolution of the two peaks must be greater than 0.3. The presence of an impurity is confirmed unambiguously by the difference in the spectra obtained for the leading and trailing edges of the peak. It must be emphasized that use of a DAD alone is by no means definite in establishing peak purity. Peak collection, followed by other qualitative analysis techniques, such as infrared (IR), nuclear magnetic resonance (NMR), mass spectroscopy, and so on, are often used to increase assurance of peak purity.

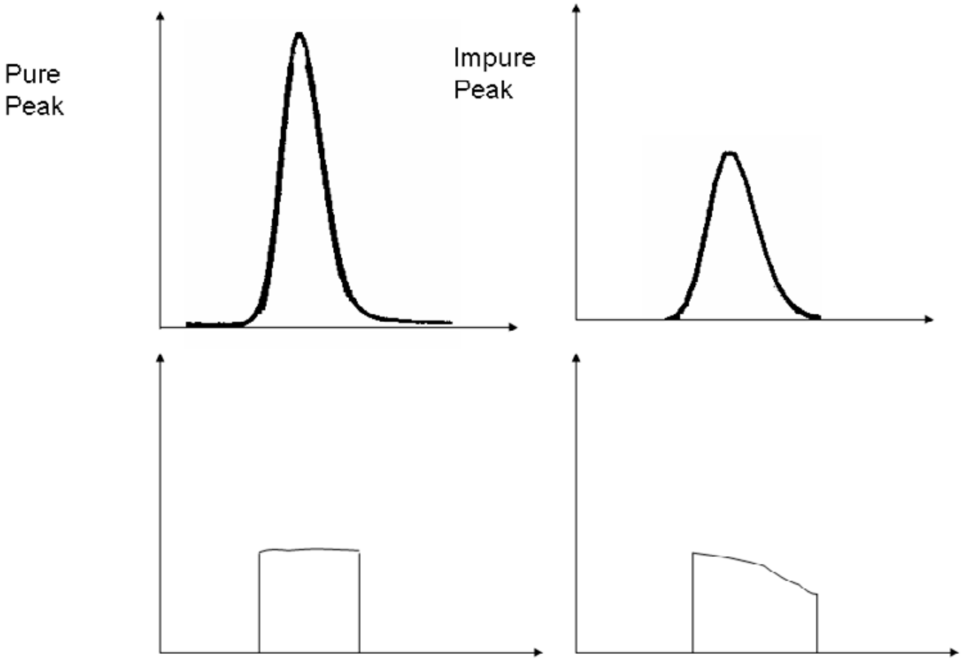

Figure 6. Ratiograms taken from (a) an impure and (b) a pure peak.

The use of a PDA detector is also important for ***peak tracking*** or the matching of peaks that contain the same compound between different experimental runs during method development. However, for accurate trace analyses, the S/N ratio must be reasonably high for such cross-checks to be meaningful.

## 3.2. Similarity Index and Peak Purity Index

The peak purity of the integrated chromatogram can be displayed in a graph and numerically. The more sophisticated way to evaluate the purity of the peaks detected is based on Peak purity curve. Three spectra (in the up slope, the peak top and the down slope) are simultaneously displayed.

The peak purity curve is created based on the similarity between the spectrum at the top of the target peak and the spectra at each point on that peak. If there is any part where this curve deflects toward the negative side, some impurities are considered to be included at that part [8,9].

## 3.3. Peak Purity Using Spectral Data

Comparison of spectra is the most popular method of peak purity determination. The primary advantage of this approach is that prior knowledge of component spectra is not required. Information derived using these techniques, however, is not sufficient for determining the kind, number, and level of impurities present. A number of selection criteria and data manipulation techniques can be applied prior to analysis to improve the quality of the analytical result. These include setting different spectrum acquisition modes, background correction, normalization and threshold settings.

Peak purity analysis software versions provided by various manufacturers allow users to sample spectra at equidistant points across an HPLC peak. Generally the poorer the resolution between potentially co-eluting peaks, the greater numbers of data should be used to detect the impurity. The most common procedure is to sample spectra up-slope, at the apex and down-slope of the eluted peak. This selection pattern may overlook the presence of impurities near the peak extremes. On the other hand, acquisition of many spectra may increase calculation and display time without adding significant information.

Background correction is often required before labeling a peak as impure as spectral subtraction increases the noise of a spectrum and there by lowers the ideal match factor. Background correction is not necessary when the instrument is balanced properly. In this case, for isocratic separations the solvent background will be eliminated by the built-in automatic subtraction of the solvent spectrum, as present at the beginning of the analysis, from all recorded spectra. For gradient separations, background corrections will have to be applied after the analysis. Different methods for correction are possible and depend on the availability of spectra resulting from specific modes of spectral storage for different instruments.

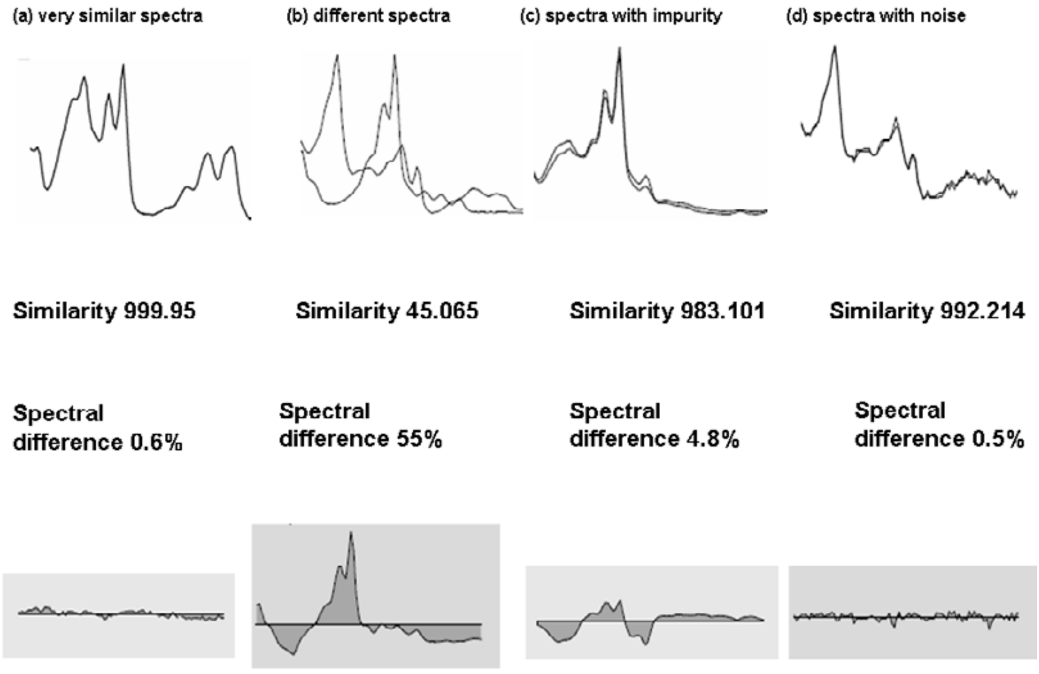

Figure 7. Graphical display of similarity factors for different pairs of normalized spectra of peaks with different concentration of impurities.

In the simplest case, a single baseline spectrum is subtracted from all analytes spectra. This will work only for the elimination of constant spectral impurities. If several baseline spectra are available, linear combinations of those spectra can be used to generate a synthetic background spectrum at any point in the chromatogram. Ideally, the two spectra should be close to the beginning and end of the peak analyzed. If this is not possible due to incomplete separation of the peak from its neighbours, baseline spectra could be taken from the beginning and end of a peak group.

Spectra used for comparison in peak purity determination should be normalized to compensate for differences in concentration. Normalization can be based on setting equal absorbance maxima or maximum wavelength ranges, on setting equal area of spectra or spectral region of interest or on using a matching algorithm that minimizes area differences by shifting and scaling spectra.

Impurity concentrations in the 0.1-1 % range may be detected when the spectra are dissimilar. However if the spectra of the different components are highly similar and the HPLC peaks are not well resolved the impurity detection limit is of the order of 5% (Figure 7).

In the case when the impurity is not present at significant concentration levels statistical software is available for automated spectral comparisons. In these cases peak purity determination and analysis of spectral differences is achieved using vector analysis algorithms. The more similar the spectra are, the closer the value is to 0.0 degrees, the more spectrally different, the larger the value. All the spectra, data points, across the peak are analyzed; the data is converted into vectors, compared and graphically plotted so that the results can be visualized. That software provides both numerical results and graphical representations like similarity and threshold curves.

**Similarity curves** are plots of retention times versus similarity factors computed by comparing spectra across an eluted peak with one or more selected spectra. Similarity curves improve the sensitivity of detecting impurities because they extract and highlight subtle impurity-generated anomalies in an analyte spectrum that might otherwise go unnoticed.

The mathematical fundamentals used in the similarity curve calculations are those used for the purity factor, however they are displayed in another format. All spectra from a peak are compared with one or more spectra selected by the operator, an apex spectrum for example. The degree of match or spectral similarity is plotted over time during elution. An ideal profile of a pure peak is a flat line at 1000 as demonstrated in Figure 8A.

At the beginning and end of each peak, where the signal-to-noise ratio decreases, the contribution of spectral background noise to the peak's spectra becomes important. The contribution of noise to the similarity curve is shown in Figure 8B.

The **threshold curve** is a plot of retention time versus a similarity factor threshold below which the presence of an impurity cannot be distinguished from spectral noise. The threshold trace may be computed automatically from the standard deviation of a number of user selected pure noise spectra. The threshold may also be set at a fixed value. Similarity and threshold curves tend to rise at the edges of the eluted peak even when no impurity is present. As signal strength decreases, a larger proportion of the spectral response is caused by noise. The determination of noise threshold is performed automatically based on the standard deviation of pure noise spectra at a specified time with a user selectable number of spectra. The threshold curve gives the range for which spectral impurity lies within the noise limit. Above this threshold, spectral impurity exceeds the spectral background noise and the similarity curve intersects the threshold curve indicating an impurity providing the reference and noise parameters have been sensibly chosen (Figure 8C).

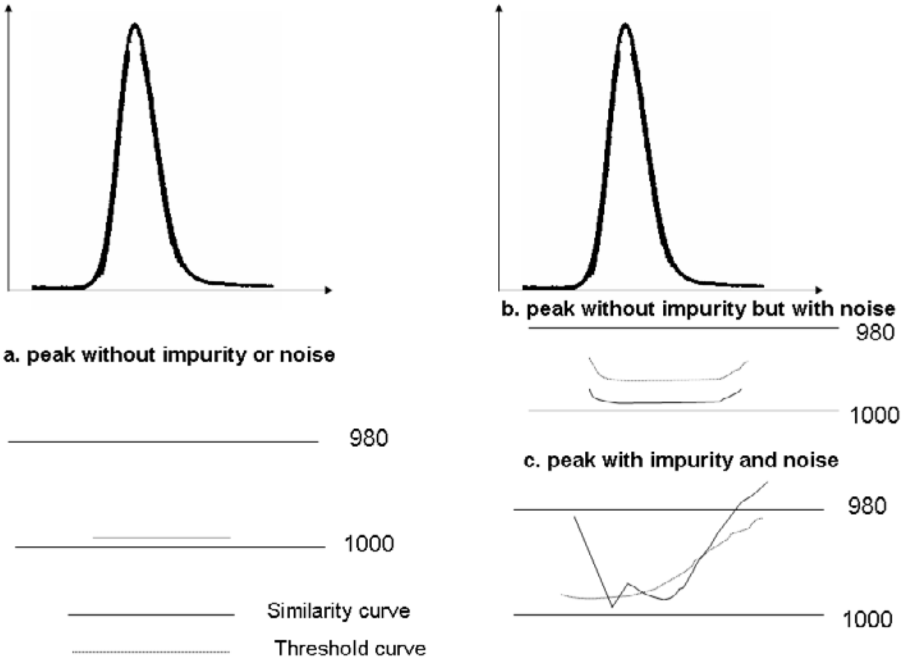

Figure 8. Effect of impurity and noise on similarity and threshold curves of A. A pure peak, B. A peak without impurity but with noise, C. A peak with impurity and noise.

Three modes to display the similarity and threshold curves are: (1) without any transformation; (2) as the natural logarithm, ln, with the advantage of more detail for the peak apex in the lower part of the graphic; and (3) as a ratio 1000 – similarity ratio = 1000 – threshold. For a spectral pure peak the ratio values are below unity and for spectral impure peaks the values are above unity. The advantage of this mode is that only one line is displayed, instead of two which facilitates interpretation.

The spectra overlay, the residual spectra and even the ratiogram do not provide sensitive enough information to uncover the impurity. The similarity curve and threshold curve functions improve the sensitivity and reliability of the peak purity evaluation by using all the spectra acquired during the elution or migration of a peak [11].

## 4. PEAK IDENTIFICATION

Peak identification refers to the data processing used to identify a specific acquired peak among the separated peaks in the analysed sample. Peak identification is a feature especially beneficial in method development as well as in the quality assurance laboratory. It provides the analyst a tool for the identification of unknown constituents in a sample of a complex matrix. This mode of identification is also useful when retention times shift due to changing chromatography for similar sample runs.

By using a PDA detector peak identification is achieved using spectral information so that detection is not only based on retention time. UV spectrum is very reproducible and its full shape is much more compound-specific than generally assumed. Analytes' spectra can be acquired automatically for each peak during the analysis. Spectral comparison may be performed one by one or by using a library. In the latter case the standard sample is analyzed and the spectrum of the target compound is registered in a library. Stored spectral data can serve as a bank for identifying unknown peaks. Comparison can be performed either interactively on the computer display or mathematically with the help of microprocessors.

The best match of spectra is the closest to the correct identification. It is obvious that complete automation is required, however software have been designed to take advantage of the benefits offered by this advanced detection technique.

When performing peak identification substance's name, retention time and concentration are reported in a table. Then the acquired chromatogram peak values and compound table's set values are compared. If the retention time of the analyte peak falls within the identification allowance width, the substance is identified as the target substance. All spectra from the set of possible candidates that fall in the window are compared to the unknown spectrum. The candidate with the best match factor above a certain threshold level is then used to identify the compound for the peak. Another possibility is to weigh both the match factor and the similarity in retention times and use the combined information for identification [3].

If the instrument parameters that determine how spectra are acquired are matched suitably, the spectral match of an unknown to a known spectrum can be used as strong indication of compound similarity or confirmation of identity. Combinatorial estimation of retention time and spectra comparison results will give more specific conclusions [12].

## 4.1. Spectral Libraries

The UV spectra employed in HPLC can change for the same compound depending on the mobile phase environment at the time of elution. To have any success in applying similar approaches to compound identification, the separation system used to acquire spectra for standards and unknown compounds needs to be well defined.

Two primary approaches to the use of spectral libraries in HPLC can be described:

1. In the **forward library search**, an attempt is made to identify each compound in an unknown sample from a large library of standard compounds, recorded under defined chromatographic conditions. Each compound spectrum from the sample, analyzed under the same conditions, is searched against the library for identification. In case this is not possible it may be classified by comparison with similar compounds from the library. Since the unknown sample may contain compounds that are not present in the library it is desirable to obtain, at least, a list of likely matches for each unknown. In some cases pre-selection of spectra is employed based on the retention time indexing or on rough comparison of spectral features such as number and position of the primary absorbance maxima. This is done primarily to reduce the time needed to search the full compound library. This feature is particularly helpful in toxicological screening and drug testing applications.

2. **For reverse library searching**, a limited library of standard compounds, all of which are expected to be present in the sample, is searched against the unknown spectra in the current analysis. Each peak of interest in a sample should be characterized through analysis of a standard. The spectral library, consequently, contains spectra for a limited number of compounds. In this case, the best match for each standard spectrum in the library can be found by searching against all compound spectra identified in the current analysis [12].

## 4.2. Spectral Matching

Spectral matching can be defined as the process of comparing two spectra with the intention of determining their similarity. Mathematically spectral matching is a procedure whereby the digital information available for a pair of spectra, each typically consisting of numerous discrete data points, is reduced to a single number indicative of the similarity between the two spectra. Ideally, this reduction in the number of data points does not involve any reduction in the information contained in the relationship of two spectra to each other. More specifically, most matching procedures are based on a point-by-point comparison of the two spectra in question to establish the presence or absence of significant differences.

Generally there are three ways of performing spectra comparison: 1) Overlay of spectra and visual determination, 2) Evaluation with spectral differences between the reference spectrum and the unknown spectrum using the appropriate software, 3) Use of sophisticated software to calculate a numerical value that mathematically defines the closeness of the match.

The most common mathematical approaches used through spectra matching software are described.

### 4.2.1. Vectorial Approach to Spectra Matching

One approach that facilitates the comparison of various matching procedures is to view each spectrum as a vector in N-dimensional space. A spectrum data is considered as the group of the absorbance at each wavelength and it is represented with the vector.

$(a\ (\lambda_1),\ a\ (\lambda_2),\ a\ (\lambda_3),\ \ldots\ldots\ldots,\ a\ (\lambda_n))$where $a\ (\lambda_i)$ is the absorbance at the wavelength $\lambda_i$

One spectrum corresponds to one vector: $\vec{S} = (a\ (\lambda_1),\ a\ (\lambda_2),\ a\ (\lambda_3),\ \ldots\ldots\ldots\ldots,\ a\ (\lambda_n))$

If there are two spectra, spectrum $S_1$ corresponds to $\vec{S}_1$ and spectrum $S_2$ corresponds to $\vec{S}_2$

$$\vec{S}_1 = (a_1\ (\lambda_1),\ a_1\ (\lambda_2),\ a_1\ (\lambda_3),\ \ldots\ldots\ldots\ldots,\ a_1\ (\lambda_n))$$

$$\vec{S}_2 = (a_2\ (\lambda_1),\ a_2\ (\lambda_2),\ a_2\ (\lambda_3),\ \ldots\ldots\ldots\ldots,\ a_2\ (\lambda_n))$$

These vectors are simplified to two-dimensional vector as shown in Figure 9. The matching procedure can then be based either on determining the angle between the two vectors or on finding the distance between their tops. The first approach would seem to be independent of the relative magnitude of $\vec{S}_1$ and $\vec{S}_2$; the later definition definitely implies normalization of $\vec{S}_1$ and $\vec{S}_2$ prior to the calculation of the distance.

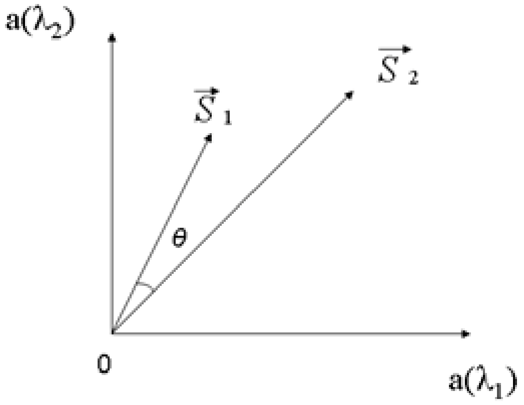

Figure 9. Vectorial definitions of spectral matching.

If these spectra are derived from the same compound, the ratio between corresponding elements in $S_1$ and $S_2$ is constant and these vectors have the same direction. In that case, the angle θ between the spectral vectors (Figure 9) becomes zero. Generally the more the angle approaches zero the greater the similarity between the two spectra is considered. The degree to which the two spectra correspond (similarity index) on the basis of the cosine of the angle of their component vectors formed at each point of measurement is described by the equation:

$$\mathrm{SI} = \frac{\vec{S}_1 \cdot \vec{S}_2}{\left|\vec{S}_1\right| \cdot \left|\vec{S}_2\right|} = \cos\theta \tag{3}$$

or

$$\text{Matching r= } \mathrm{SI} = \frac{\sum_{\lambda i} a_1(\lambda_i) \cdot a_2(\lambda_i)}{\sqrt{\sum_{\lambda i} a_1(\lambda_i)^2} \cdot \sqrt{\sum_{\lambda i} a_2(\lambda_i)^2}} \tag{4}$$

As similarity index (SI) or r approaches 0, the pattern matching becomes poor (the angle θ between the vectors approaches $90^o$) and conversely, as it approaches 1, the pattern approaches a perfect match.

For easier manipulation, especially in the case of very similar spectra where differences may exist only in the third or fourth decimal, the spectral match factor can further be multiplied by 1000.

### 4.2.2. The Similarity Factor

ChemStation's from Agilent Technologies special peak purity software calculates a numerical value to characterize the degree of dissimilarity of the peak spectra, a so-called similarity factor, based on the match of the peak spectra to one another [11].

Several statistical techniques are available for comparison of spectra. Since UV-Visible spectra contain only a small amount of fine structure, the least-square-fit coefficient of all the absorbances at the same wavelength gives the best result. The similarity factor used in the ChemStation is defined as: Similarity = 1000 x $r^2$, where r is defined as:

$$r = \frac{\sum_{i=1}^{i=n}\left\{\left(A_i - A_{av}\right)\times\left(B_i - B_{av}\right)\right\}}{\sqrt{\sum_{i=1}^{i=n}\left(A_i - A_{av}\right)^2 \times \sum_{i=1}^{i=n}\left(B_i - B_{av}\right)^2}} \tag{5}$$

and where $A_i$ and $B_i$ are measured absorbances in the first and second spectrum respectively at the same wavelength; n is the number of data points and $A_{av}$ and $B_{av}$ the average absorbance of the first and second spectrum respectively. At the extremes, a similarity factor of 0 indicates no match and 1000 indicates identical spectra. Generally, values very close to the ideal similarity factor (greater than 995) indicate that the spectra are very similar, values lower than 990 but higher than 900 indicate some similarity and underlying data should be observed more carefully.

### 4.2.3. Measures of Dissimilarity

Reliant on the ultimate relationship of trigonometry: $\cos^2 + \sin^2 = 1$ (6) we can define a factor of dissimilarity of spectra. Thus, the sine squared multiplied by 1000, could serve as an indicator of spectra dissimilarity.

Another possible measure of spectral dissimilarity, the Euclidean distance $e$ between the tips of the two vectors as shown in Figure 9 can also be related to sine and cosine:

$$e = S_1\text{-}S_2 = \sqrt{\sin^2(S_1 - S_2) + [1 - \cos(S_1, S_2)]^2} \tag{7}$$

$$e = \sqrt{\sin^2(S_1 - S_2) + 1 - 2\cos(S_1 - S_2) + \cos^2(S_1 - S_2)} \tag{8}$$

$$e = \sqrt{2 - 2\cos(S_1, S_2)} \tag{9}$$

$$e = \sqrt{1 - \left|\cos(S_1, S_2)\right|} \tag{10}$$

All the mathematical approaches, mentioned above, differ in the degree of change observed for spectra differences, most noticeably for angles below $15^{o}$. Between 0 and $10^{o}$ $\sin^2$, $\cos^2$ and cosine do not change very much, making it more difficult to differentiate among spectra with strong similarity. The rate of change varies, complicating the task of assessing the variability of the match score for different degrees of dissimilarity.

### 4.3. Example of Application

The identification of an unknown peak in a chromatographic analysis, performed by the Shimadzu SPD-M10A UV/Vis Photodiode Array Detector complied with data acquisition software LC Solutions is presented in Figure 10. Spectrum file of the selected peak is compared against reference spectra in a user built library. Data processing through the mathematical approach mentioned above defines the best match. The numerical value of similarity index (SI) indicates the spectrum of oxacillin as the better match since in this case

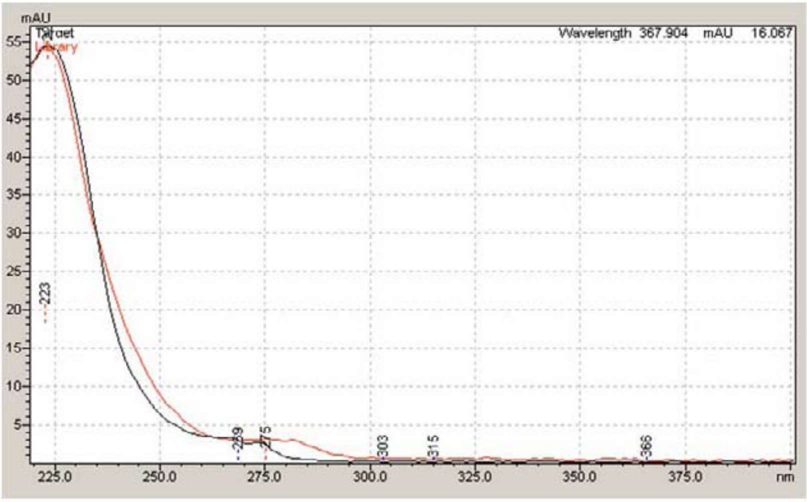

A. Similarity index 0.996164

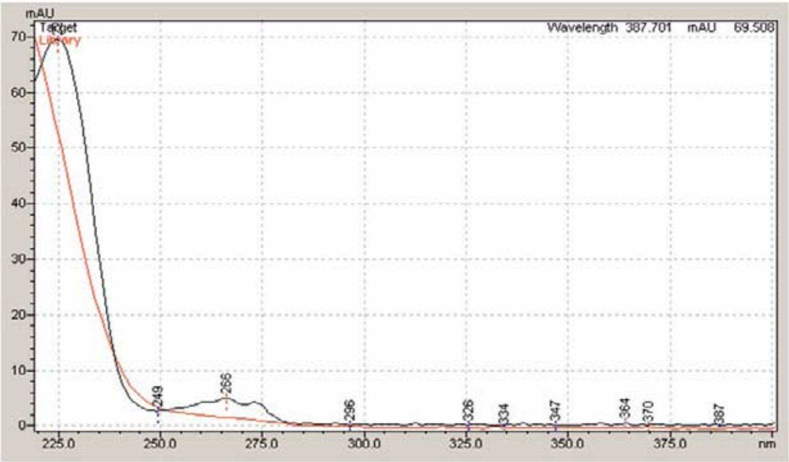

B. Similarity Index 0.976412

Figure 10. Identification of penicillin antibiotics by Shimadzu LC Solutions using the SPD-M10A photodiode array detector. The similarity index indicates the closest match.

is close to unity. The comparison is also made by visual evaluation through the overlaid spectra. The created spectral sublibrary is consisted of a number of penicillins spectra, which are those of interest in this application. Thus, the chromatographic peak assuming that belongs to oxacillin can be identified among other related compounds by its UV spectrum, allowing even more accurate qualitative analyses.

## 5. FIELDS OF APPLICATIONS

Numerous of applications of PDA detection in HPLC can be found in literature. Examples of a broad range of applications include:

- **In clinical analysis**: the determination of water and fat soluble vitamins in biological fluids, caffeine metabolism products: methylxanthines and methyluric acids in human biological fluids, iodotyrosines and iodothyronines in biological samples, methadone and its main metabolite EDDP in biological fluids, 1,4 benzodiazepines and tricyclic antidepressants in human biological fluids etc.
- **In pharmaceutical analysis**: the determination of antibiotics, vitamins, antidepressants, etc in pharmaceutical formulations for human and veterinary medicine.
- **In food analysis:** the identification of free phenolic acids in wines and wine vinegar, the detection of fluoroquinolones, penicillins, sulphonamides and tetracyclines residues in tissues of various food producing animals, and products like milk and eggs.
- **In forensic science:** the identification of ballpoint pen ink Components and application to the study of Their Decomposition on Aging.
- **In environmental analysis:** the monitoring of anthracene and its oxidation products in surface waters.

These applications among other cited in literature are briefly discussed in the following paragraphs.

It is not the intended scope of this review to describe all applications in detail, but to give the reader as many indications to apply the PDA technology in the HPLC analysis and take advantage of all its features.

### 5.1. Method Development

High performance liquid chromatography (HPLC) is a technique widely applied in routine analysis in many areas, such as pharmaceutical, biological, environmental and food analysis. In the majority of the cases, it can efficiently provide the separation of all compounds of interest. However, when a complex sample is analyzed, the overlap of the analytes with sample interferences is frequently observed, and great effort may be necessary to optimize the chromatographic conditions of the separation.

Diode array detection (DAD) has given growth to a number of new methods of data analysis applying chemometrics’ potential for extracting hidden information. Moreover in

HPLC method development one of the largest challenges is the necessity for tracking the movement of peaks as separation conditions are deliberately or randomly changed. Achievement of the optimal separation becomes an important factor for successful identification or quantitation. In such a case, the optimization may be based on assigning peaks of the same component chosen from different experiments to each other. This means that mutual peak matching between the HPLC runs is required. Bogomolov and McBrien have used diode array detection to develop a new method for mutual peak matching in a series of HPLC analyses of the same unknown mixture acquired at varying separation conditions [13].

Lindholm et al in their study applied the detailed guidelines by FDA for bioanalytical method validation to a typical biotechnological process: the enzymatic synthesis of 9a-hydroxyprogesterone in *E. coli* using progesterone as substrate. The process liquid was extracted and analyzed using an HPLC–DAD system. The DAD made it possible to acquire spectra of all peaks in the chromatogram. The UV spectra and 3D spectro-chromatograms were recorded from 190 to 400 nm [14].

The analysis of data from analytical equipment is an important factor in the execution of metabolomics. Self-modeling curve resolution (SMCR) is one of the theoretical techniques of chemometrics and has recently been applied to the data of hyphenated chromatography techniques.

Alternating least squares (ALS) is a classical SMCR method. Independent component analysis (ICA) is a comparatively new method and has been discussed very actively by information science researchers, but has still been applied only in very few cases to curve resolution problems in chemometrics studies. Yamamoto et al applied regularized version of ALS (RALS) with a normalized constraint and ICA to the HPLC-DAD data of *Haematococcus pluvialis* metabolites and obtained a high accuracy of peak detection, suggesting that these curve resolution methods are useful for identification of metabolites in metabolomics. ICA was used to resolve the HPLC-DAD data in cases where several important metabolites are coeluted because samples derived from living organisms contain many complex metabolites. These curve resolution methods are useful for peak detection of metabolites in HPLC-DAD data [15].

Ferreiros, et al applied DAD to study extraction efficiency of several process variables of four angiotensin II receptor antagonist drugs: eprosartan, telmisartan, irbesartan and valsartan from urine and thus they constructed a D-optimal design [16].

HPLC with DAD constitutes a valuable tool for the simultaneous determination of pesticide residues in complex samples. However, it has been shown that the presence of interference in the sample may constitute a serious problem. When HPLC-DAD is applied, the choice of a selective wavelength is sometimes difficult or impossible, since the UV spectra generally are constituted of wide bands. In these cases, second-order calibration models can be an alternative due to the possibility of mathematical separation of the instrumental signals, making determinations in the presence of unknown interferences possible; a property known as the second-order advantage.

Braga, et al used the models parallel factor analysis (PARAFAC) and the recently introduced bilinear least squares (BLLS) to develop second-order calibration methods to high performance liquid chromatography with diode array detection (HPLC-DAD) data, where overlap of interferences with the compounds of interest was observed, making the determination and resolution of the analytes possible. The simultaneous determination of five pesticides and two metabolites in red wine samples by HPLC-DAD was performed, using the second-order advantage [17].

Carneiro et al proposed a variable selection methodology based on genetic algorithm (GA) was applied in a bilinear least squares model (BLLS) with second-order advantage, in three distinct situations, for determination by HPLC–DAD of the pesticides carbaryl (CBL), methyl thiophanate (TIO), simazin (SIM) and dimethoate (DMT) and the metabolite phthalimide (PTA) in wine [18].

## 5.2. Clinical Analysis

The use of photodiode array detection in HPLC has implemented the determination of drugs and their metabolites during therapy as well as during drug development. Analytical methods necessary for monitoring drugs and their metabolites in biological fluids are complimented by the advantages of DAD. It can be applied both for quantification and confirmatory identification purposes. UV spectra from 190 to 600 nm are recorded and used for peak purity assessment and as well as for the identification of drugs and their metabolites through the comparison with libraries created for that purpose. The toxicity of the drugs besides the effective therapeutic level can also be studied.

Chatzimichalakis et al applied DAD to the identification of eight fat-soluble vitamins: retinol, menadione, menaquinone, a-tocopherol, cholecalciferol, d-tocopherol, a-tocopherol acetate and phylloquinone, in biological fluids blood serum and urine [19].

The identification, separation and quantitation of iodoaminoacids, is essential for the biological research and the clinical diagnosis of thyroid gland disease. Gika et al applied DAD for the determination thyroid gland hormones and some of their primary metabolites, 3,3’,5,5’-tetra-iodo-l-thyronine (l-thyroxine), 3,3’,5-tri-iodo-l-thyronine, 3,5-di-iodo-l-thyronine, l-thyronine, 3,5-di-iodo-l-tyrosine, 3-iodo-l-tyrosine and l-tyrosine in commercial pharmaceuticals and biological samples (serum, urine and tissue) [20].

Penicillins have been the most widely used antimicrobial drugs for more than 80 years and still are considered as one of the most important groups of antibiotics. They are broad-spectrum antibiotics, clinically used against Gram positive and Gram negative bacteria. Samanidou et al applied DAD to the determination of four penicillin antibiotics: amoxicillin, oxacillin, cloxacillin and dicloxacillin, in pharmaceuticals and human biological fluids blood plasma and urine. The objective of such a method development was its applicability to routine analysis in pharmacokinetic studies as well as in the quality control of pharmaceutical samples [21].

Benzodiazepines belong to a group of substances known for their sedative, anti-depressive, muscle relaxant, tranquilizer, hypnotic, and anticonvulsant properties. They have become the most worldwide commonly prescribed medicines in the therapy of anxiety, sleep disorders, and convulsive attacks as being relatively safe with mild side effects. Since benzodiazepines are widely seen in clinical and forensic cases, for the bio-pharmacological, clinical, and toxicological studies of these drugs, the availability of rapid, sensitive, and selective analytical methods for their determination in biological fluids and pharmaceutical formulations is essential. Nasir Uddin et al developed an HPLC-DAD method for the determination of six 1,4-benzodiazepines (alprazolam, bromazepam, clonazepam, diazepam, flunitrazepam, lorazepam) in pharmaceuticals and human biological fluids [22].

The same authors applied DAD to the simultaneous determination of six benzodiazepines: bromazepam, clonazepam, diazepam, flunitrazepam, alprazolam, and lorazepam and four tricyclic antidepressants: amitriptyline, clomipramine, imipramine, and doxepin in biological fluids (human blood plasma and urine) [23].

### 5.2.1. Metabolism Studies

Georga et al used DAD to identify caffeine and its eight primary metabolites: xanthine, 7-methylxanthine, 3-methylxanthine, 1-methylxanthine, isocaffeine, theobromine, paraxanthine and theophylline in human biological fluids: blood serum and urine [24].

Schmidt et al applied HPLC-DAD to describe the discovery of a new major endogenous vitamin A metabolite with particularly high hepatic concentrations. This metabolite was isolated from mouse livers and was characterized as 9-cis-4-oxo-13,14-dihydro-retinoic acid (RA) based on mass spectral, ultraviolet, and nuclear magnetic resonance analyses. It was also detected in one human liver. UV spectra were checked in the mobile phase within the HPLC detector cell via the stopped flow method, after injection of standard solutions (of all-trans-4-OH-RA, 13- cis-4-OH-RA, 9-cis-4-OH-RA, all-trans-18-OH-RA, all-trans- 3-OH-RA, 13-cis-3-OH-RA, all-trans-4-oxo-ROH) or after rechromatography of the isolated metabolite. A few UV spectra (all-trans-4-oxo-RA, 13-cis-4-oxo-RA, all-trans-5,6-epoxy-RA) were recorded under the same chromatographic conditions with the DAD detector of the HPLC system used for the analysis of the serum samples. Only retinoids with a keto-group at C4 of the cyclohexenyl ring showed a characteristic secondary minor maximum at lower wavelengths. This minor maximum was also found in the UV spectrum of the newly detected metabolite [25].

Selective serotonin reuptake inhibitors (SSRIs), serotonin noradrenergic reuptake inhibitors (SNRIs) and noradrenergic and specific serotoninergic antidepressant are widely used in the treatment of depression. An increase in antidepressant intoxications has lead to the development of reliable analytical methods for their analysis. Labat et al applied DAD to the determination of milnacipran, venlafaxine, desmethylvenlafaxine, mirtazapine, desmethylmirtazapine, citalopram, desmethylcitalopram, fluvoxamine, paroxetine, sertraline and fluoxetine, by HPLC and MEKC. The methods were useful for the determination of new antidepressants in post-mortem cases. DAD was used to identify the different antidepressants in the toxicological screening [26].

Bugamelli et al proposed a rapid and simple liquid chromatographic method with photodiode array detection for the simultaneous determination of six antiepileptic drugs (oxcarbazepine, carbamazepine, lamotrigine, phenobarbital, primidone and phenytoin) and two metabolites (10,11-dihydro-10,11-epoxycarbamazepine and 10,11-dihydro-10-hydroxycarbamazepine, the main active metabolites of carbamazepine and oxcarbazepine, respectively) in human plasma. The HPLC-DAD method was suitable for the plasma level determination of simultaneously administered antiepileptic drugs [27].

Caubet et al applied HPLC- DAD to the selective and rapid analysis of caffeine and 14 of its metabolites in urine taken from 20 healthy subjects, men and women, smokers and non-smokers and women taking or not taking oral contraceptives [28].

Tarbah et al applied DAD to investigate kavain metabolism in humans. In the present study an HPLC–DAD assay method for the simultaneous determination of kavain and its main metabolites (*p*-hydroxykavain, *p*-hydroxy-5,6-dehydrokavain and *p*-hydroxy-7,8-

dihydrokavain) in serum and urine was developed and validated. The metabolites were mainly excreted in the form of their conjugates. The UV spectra for kavain and the known metabolites were compared with available reference substances [29].

Anthocyanins are suggested to be responsible for protective effects against cardiovascular diseases and certain forms of cancer. Keppler and Humpf investigated the microbial deglycosylation and degradation of six anthocyanins exhibiting three different aglycones with mono- or di-b-D-glycosidic bonds using HPLC-DAD and GC–MS [30].

Wille et al detrmined 13 ‘new’ antidepressants (venlafaxine, fluoxetine, viloxazine, fluvoxamine, mianserin, mirtazapine, melitracen, reboxetine, citalopram, maprotiline, sertraline, paroxetine and trazodone) together with eight of their metabolites (*o*-desmethylvenlafaxine, norfluoxetine, desmethylmianserine, desmethylmirtazapine, desmethylcitalopram, didesmethylcitalopram, desmethylsertraline and *m*-chlorophenylpiperazine) in plasma using HPLC-DAD as monitoring system [31].

Frassanito et al proposed a selective and sensitive methodology, mainly based on reversed-phase HPLC coupled both to photodiode array detection and to atmospheric pressure mass spectrometric techniques (HPLC–DAD-APIMS) to the analysis and identification of a wide range of secondary metabolites biosynthesized by different algal taxa and cyanobacteria [32].

Fernandez et al used HPLC–DAD for the simultaneous determination of morphine, codeine, 6-acetylmorphine (6AM), cocaine, benzoylecgonine (BEG), cocaethylene, methadone and its metabolite, 2-ethylidene-1,5-dimethyldiphenylpyrrolidine (EDDP), in plasma. The analytes were identified from their retention times and UV spectral data [33].

de Castro et al used HPLC-DAD as a screening method in routine analysis of 14 antidepressants and their metabolites in plasma in authentic samples from clinical cases which were further analysed by LC-/MS/MS. The results of both methods were compared qualitatively [34].

Flubendazole, methyl ester of [5-(4-fluorobenzoyl)-1*H*-benzimidazol-2-yl] carbamic acid, belongs to the group of benzimidazole anthelmintics, which are widely used in veterinary and human medicine. In order to understand some important aspects of *phase I* flubendazole metabolism, the *in vitro* biotransformation studies of this compound with microsomal and cytosolic fractions of cells from various sources, various species and performed under various incubation conditions were designed. The bioanalytical support of these xenobiochemical experiments consisted in the identification and determination of flubendazole and its principal *phase I* metabolites (decarbamoylated flubendazole, reduced flubendazole) in the incubation mixtures. Milan Nobilis et al developed two bioanalytical HPLC methods for the determination of flubendazole and its metabolites in biomatrices: pig and pheasant hepatic microsomal and cytosolic fractions. Flubendazole is a prochiral drug. A racemic mixture is formed during non-stereoselective reductions at the carbonyl group. The individual analytes had very characteristic UV spectra, thus the identification of flubendazole, its metabolites and albendazole (I.S.) could be based not only on the retention times, but also on the UV spectra obtained from spectrochromatograms [35].

Mertens et al combined HPLC with diode array and tandem mass spectrometry detection (LC–DAD–MS/MS) for the simultaneous quantitative determination of fenofibric acid, pravastatin and its main metabolites in human plasma: 3-hydroxy isomeric metabolite (3-OH metab), pravalactone.

The developed LC–DAD–MS/MS procedure was used to investigate the bioavailability of fenofibrate and pravastatin after multiple oral dose of one formulation of fenofibrate, one formulation of pravastatin and one new capsule containing both fenofibrate and pravastatin, in 36 healthy subjects [36].

Xie et al applied DAD to determine Paeonol, a principal bioactive component of the Chinese herb Moutan Cortex with anti-inflammatory and analgesic effects, in order to determine its pharmacokinetic behavior and metabolic profile in rat following oral administration of the pure paeonol alone and an herbal preparation “Qingfu Guanjieshu” (QFGJS) containing paeonol. An HPLC–DAD method was developed and validated for determining the concentration of paeonol in rat plasma. The method was applied to a pharmacokinetic study of paeonol in rats using two administrative protocols, *i.e.*, an oral administration of the pure paeonol alone, and oral dosing of QFGJS containing approximately equivalent paeonol [37].

Nasir Uddin et al applied HPLC-DAD to the determination of six 1,4-benzodiazepines: Bromazepam (BRZ), Clonazepam (CLZ), Diazepam (DZP), Flunitrazepam (FNZ), Lorazepam (LRZ), Alprazolam (APZ) and two metabolites: α-hydroxyalprazolam (HALZ) and α-hydroxytriazolam (HTZL) in human plasma, urine and saliva [38].

## 5.3. Pharmaceutical Industry

PDA detection can provide the required specification from regulatory agencies like performance verification tests required by major pharmacopoeias. The required performance tests include wavelength accuracy, stray light, resolution, and photometric accuracy. An appropriate computer system is needed to provide system control, data acquisition, and accurate and precise integration and quantification of chromatographic peaks. Generally, it is accepted that proper operation is confirmed by obtaining satisfactory results from operational qualification testing of the complete computer system. Basic research and product development in pharmaceutical companies are often concerned with the purity of the compounds developed or produced. A PDA detector can provide information using the acquisition of spectra to determine peak purity. The latter is of paramount importance in pharmaceutical industry, where it is designated to detect the presence of co-eluting impurities.

Quality control and stability testing laboratories bring their own demands to analytical instruments. Stability laboratories are responsible for determining the expiration date of the product and to determine the conditions under which the product degrades to the point of not meeting the expected concentration levels. In this section the applied capabilities of PDA detector to meet the demands of product development in pharmaceutical companies will be discussed.

### 5.3.1. Drug Monitoring

The photodiode array detection allows obtaining full UV spectral data for the analytes and this in turn allows identifying chromatographic peaks with a higher degree of confidence with respect to normal spectrophotometric detection. This is particularly important when analysing drugs which have a high potential for abuse and when monitoring patients who have a history of drug abuse.

Colombo et al used DAD for the assay of amprenavir, ritonavir, indinavir, saquinavir, nelfinavir, lopinavir, atazanavir, nevirapine and efavirenz and the novel non-peptidic HIV protease inhibitor tipranavir in human plasma [39].

Vermeij and Edelbroek applied DAD to the simultaneous determination of seven antiepileptic drugs, including primidone, phenobarbital, phenytoin, carbamazepine, with its two major metabolites carbamazepine-10,11-epoxide and carbamazepine-10,11-(*trans*)-dihydrodiol and the new antiepileptic drugs: lamotrigine, hydroxycarbazepine (active metabolite of oxcarbazepine) and zonisamide in serum. Since heptobarbital and phenacemide elute very close to each other and may interfere with analysis of carbamazepine-10,11-(*trans*)-dihydrodiol, the use of a diode array detector is a useful aid in diminishing the chance on interferences by checking peak purity. Identity of each analyte is further confirmed by matching UV-spectra with references in the spectral library [40].

Desrivot et al developed an HPLC/DAD method for the in vivo monitoring of three new antileishmanial 2-substituted quinolines for the development of an oral treatment. Three phase I metabolites were included in this work for the optimization of the method. The method, allowed the quantification of examined analytes in rat plasma. The objective of this work was also to allow the detection of putative metabolites, and to confirm the in vivo formation of the metabolites identified in vitro. It allowed defining the physico-chemical parameters of three antileishmanial quinolines under pre-clinical study for the development of an oral treatment of VL. This method was also optimized to allow the determination of more hydrophilic derivatives, expected to be in vivo phase I metabolites. It can be also used to characterize the extent of plasma protein and albumin binding of the three drug candidates which will be further used for the establishment of essential pharmacokinetic parameters [41].

Methadone and buprenorphine are two of the drugs most frequently used for abstinence from illicit opioids and in the treatment of pain. Mercolini et al developed a sensitive and selective high-performance liquid chromatographic method with diode array detection for the simultaneous determination of methadone, buprenorphine and norbuprenorphine in biological fluids for therapeutic drug monitoring (TDM) purposes [42].

Lancelin et al developed an HPLC-DAD method for the quantification of aripiprazole and dehydro-aripiprazole, in human plasma for the therapeutic drug monitoring of aripiprazole-treated patients. The method validation was performed according to the Food and Drug Administration (FDA) guidelines for the analytical Methods. Acquisition from 200 to 350 nm was performed to allow the drug identification by its ultraviolet absorption spectrum and for the study of the peaks' purity [43].

Musenga et al used DAD to develop of two methods, based on the use of capillary electrophoresis (CE) and HPLC, respectively, for the analysis of the atypical antipsychotic aripiprazole in human plasma of schizophrenic patients for therapeutic drug monitoring purposes [44].

### 5.3.2. Pharmacokinetic Studies

Lee et al described a rapid, simple and sensitive isocratic high-performance liquid chromatography with diode array UV detection for micro-sample analysis of paclitaxel in mouse plasma. Peak purity was determined over a UV wavelength range of 200 to 400 nm. HPLC methods have been most frequently used in pharmacokinetic studies of paclitaxel because of their simplicity, sensitivity and selectivity [45].

Samanidou et al applied DAD to the determination of ten quinolone antibiotics: enoxacin, ofloxacin, norfloxacin, ciprofloxacin, danofloxacin, enrofloxacin, sarafloxacin, oxolinic acid, nalidixic acid, and flumequine in pharmaceutical formulations destined either for human or for veterinary use [46].

Küçük et al used DAD for the investigation of the pharmacokinetics of tramadol in rabbit plasma. PDAD was applied to validate the whole analytical method, according to international guidelines in order to obtain an efficient tool for further pharmacokinetic studies in rabbit plasma [47].

Jacobson et al applied PDA to the pharmacokinetic study of Ceftiofur sodium, which is a third generation broad-spectrum cephalosporin, formulated as an intramuscular injection, used to treat respiratory diseases in swine, ruminants and horses. In addition to retention time, diode-array detection was used to confirm peaks based on wavelength with neighbouring peaks possessing significantly different UV spectra [48].

Yang et al applied PDA to characterize the pharmacokinetic and metabolic properties of 1,5-Dicaffeoylquinic acid (1,5-DCQA) in rats following single intravenous administration (160 mg/kg), which is a potentially important HIV-1 integrase inhibitor widely distributed in many plants. The metabolites formed in urine were identified by liquid chromatography–mass spectrometry (LC–MS) in parallel to diode-array detection [49].

Zhang et al applied PDA to the pharmacokinetic study of dihydromyricetin and myricetin in rat plasma after orally administrating the decoction of *Ampelopsis grossedentata* [50].

Mertens et al developed a sensitive and selective method based on liquid chromatography combined with diode array and tandem mass spectrometry detection (LC–DAD–MS/MS) for the simultaneous quantitative determination of fenofibric acid, pravastatin and its main metabolites in human plasma. The developed LC–DAD–MS/MS procedure was used to investigate the bioavailability of fenofibrate and pravastatin after multiple oral doses of different formulations of fenofibrate, pravastatin, a mixture of fenofibrate and pravastatin in 36 healthy subjects [51].

Liang et al applied photodiode array detection to the pharmacokinetic study of five bufadienolides in rat plasma after oral administration of Chansu extract (*Venenum Bufonis*) [52].

### 5.3.3. Peak Purity Analysis- Determination of Impurities

In a typical analysis of chromatographic purity in the pharmaceutical industry, the chromatogram consists of one major peak, which is the active ingredient, and several much smaller peaks, consisting of the impurities. The analysis to test the purity of drugs is mainly performed by HPLC, using DAD or mass spectrometric detection. The aim of purity analysis is to separate possible impurities from the main component and then, if possible, to identify them.The origin of organic impurities implies that their molecular structures are usually very similar and also closely related to the molecular structure of the main compound. Therefore, most separation methods do not provide sufficient resolution for drug impurity profiling. To solve this problem hyphenated methods may be used [53].

Görög et al used HPLC-DAD for the impurity profiling of several drugs [54].

Nicolas and Scholz described the use of HPLC-DAD for spectral matching. Impurities could be characterised without isolating them, when retention times vary and standards are not available. Therefore, this method is particularly useful for unknown impurities [55].

The analytical search for impurities in drugs is complicated, because the standards are not always available and because unexpected impurities are produced by new mutants during fermentation. Due to this it is useful to check the purity of the peaks in the chromatogram even when it is obtained with an optimized analytical technique. De Braekeleer et al used HPLC with diode array detection for the analysis of a tetracycline hydrochloride sample (TC-HCl). Data obtained with hyphenated techniques, such as high-performance liquid chromatography coupled with a diode array detector (HPLC–DAD), are analysed with chemometric methods such as the orthogonal projection approach and the fixed size moving window evolving factor analysis approach for this purpose [56].

The growing interest in combinatorial chemistry has led to a new source of compounds from which a large number of leads has emerged over recent years. Parallel synthesis, in particular, allows a quick production of a wide number of individual compounds. A rapid analytical control is needed to determine their quality. Dulery et al developed a strategy using automated, fast reversed-phase HPLC with diode-array detection (LC–DAD) followed by atmospheric pressure chemical ionisation mass spectrometry (APCI–MS) and NMR has been developed for their characterisation and purity control [57].

The application of HPLC coupled with DAD is becoming more and more important for the analysis of multicomponent systems. In spite of the high separation efficiency of the technique, the occurrence of overlapped peaks is often unavoidable. In difficult cases chemometrics can help in peak purity analysis. Garrido Frenich et al used DAD to the Simple to use interactive self-modelling mixture analysis (SIMPLISMA), orthogonal projection (OPA) and Needle Search (NS) approaches which have been applied to the determination of a number of compounds present in a complex multicomponent system [58].

van Zomeren et al applied HPLC-DAD for the identification and quantification of impurities in drug impurity profiling. Real and simulated high-performance liquid chromatography diode array detection (HPLC-DAD) data were obtained for drug mixtures containing one main compound and two impurities. The performance of five curve resolution methods was compared systematically. HPLC-DAD data were simulated for six impurity levels (30, 10, 3, 1, 0.3, and 0.1%), three main compounds (first, second, and last eluting peak), and four resolutions [59].

Related organic impurities generally have approximately similar molar absorption coefficients ($\varepsilon$) due to their structural similarities. On the assumption that all peaks in an impurity profiling chromatogram have approximately the same maximum molar absorption coefficients ($\varepsilon$max) and the chromatogram contains one major peak and several much smaller ones, all of which are completely separated, integration of the summed score vectors from the principal component analysis (PCA) decomposition of high-performance liquid chromatography–diode array detection (HPLC–DAD) data will give areas that are quantitatively proportional to the actual content of the compounds [53].

Wiberg et al proposed DAD for the determination of chromatographic peak purity by means of principal component analysis (PCA) of high-performance liquid chromatography with diode array detection (HPLC–DAD) data. The method is exemplified with analysis of binary mixtures of lidocaine and prilocaine with different levels of separation. Lidocaine and prilocaine have very similar spectra and the chromatograms used had substantial peak overlap. The peak purity determination was made by examination of relative observation residuals, scores and loadings from the PCA decomposition of DAD data over a chromatographic peak. As a reference method, the functions for peak purity analysis in the chromatographic data system used were applied.

DAD with absorbance measured as a function of retention time and wavelength provides greater scope for analysing peak purity compared to single wavelength detection. Different methods of peak purity determination utilising DAD data have been developed, and modern chromatographic data systems generally have some functions for the analysis of peak purity in their software. By performing PCA of DAD data for a chromatographic peak with an investigation of relative observation residuals, scores and loadings, peak purity can be determined [60].

Burini and Coli developed an HPLC-DAD method to identify and quantify formaldehyde in spirits. Formaldehyde was quantified with DAD after derivatization. Purity of formaldehyde derivative peak was confirmed by comparing of UV-Vis spectra of the derivative of formaldehyde as a standard with that of a real sample. The use of a diode-array detector ensured peak identify and purity of the formaldehyde derivative [61].

Vuletic et al used HPLC-DAD to detect unknown impurities in simvastatin substance and tablets at a 0.2% level. The impurity structures were elucidated by a direct hyphenation of liquid chromatograph to high-resolution mass spectrometer with electrospray ionisation interface. Peak tracking was performed using the column-switching technique. The impurity from tablets was synthesized and its structure confirmed by LC–UV, LC–MS/MS, and NMR techniques [62].

Fiori et al developed HPLC-DAD and LC-ESI-MS methods for the analysis of doxycycline, including the identification of the related impurities metacycline and 6-epidoxycycline and its determination in a medicated premix [63].

Identification of the unresolved peaks is a challenging task for analysts. In the use of DAD spectral library, when peaks overlap, searching a standard spectra library could produce varying qualitative results due to the extraction of sample spectra with the peaks at different positions in the chromatogram. In the use of spectral correlative chromatography, one chromatogram is only compared with one standard spectrum to find the highest points of every curve, so the process has to be performed many times for identification of all peaks in the chromatogram.

Advances in computer application techniques and instrumentation for HPLC coupled to diode array detection (DAD) and to mass spectrometry (MS) provide more information and make qualitative analysis accurate and faster. Li and Hu developed a novel qualitative analytical method for peak tracking in impurity profiling control by the correlation of spectra was established. Two-dimensional (2D) standard spectrochromatographic data produced by high-performance liquid chromatography with diode array detection (HPLC-DAD) were compared with sample data to develop two-dimensional chromatographic spectral correlative maps. With 2D chromatographic spectral correlative maps, all unresolved components and their elution order could be recognized in a new chromatographic system, with only a single run.

The comparison of spectra was expanded to three-dimensional space and developed two-dimensional chromatographic spectral correlative maps.

Making the most of the separation ability of HPLC and spectral specificity, 2D chromatographic correlation spectroscopy is a powerful method for the identification and is successfully applied to a recognition system for peak tracking in impurity profiling control in quinolones. The main advantages of the method are rapidly and simultaneously identifying multi-components without reference substances, accurately distinguishing the elution orders of the unresolved peaks, and testing the peak purity at the same time [64].

Salicylaldehyde isonicotinoyl hydrazone (SIH) is an iron-chelating aromatic hydrazone with promising pharmacological properties. However, it suffers from relatively short biological half-life. Hence, two novel derivates of SIH, HAP-INH 2'-hydroxyacetophenone isonicotinoyl hydrazone and HPP-INH 2'-hydroxypropiophenone isonicotinoylhydrazone (HPP-INH) were synthesized in order to overcome this pharmacokinetic drawback. Kovăříková et al applied HPLC-DAD and HPLC–MS/MS methods to investigate the identity of the putative impurities of these newly prepared substances, which are being formed in aqueous environment. At first, it was shown that their retention times as well as UV spectra did not correspond to any expected synthetic precursor, by-product or degradation product. HPLC-DAD analysis confirmed purity of peaks and revealed close but not identical UV spectra of putative impurities and corresponding hydrazones. In order to obtain more information about the origin and identity of the unknown impurities, HPLC-DAD analysis was performed. The peak purity of all peaks in the study was initially documented, thus excluding the possibility of co-elution. Thereafter, DAD spectra of the putative impurity were compared with those of the parent compounds [65].

*Eleutherine americana* originates from tropical America, where its elongated red roots have been used by the indigenous population for centuries as a herbal remedy. The plant, belonging to the Iridaceae family, is now widely cultivated in China for ornamental and medicinal purposes. The bulb is used for the treatment of coronary diseases, and as diuretic, emetic and purgative. In Thailand, in pure form it is a traditional carminative, as mixture with galangal it is applied externally on the forehead to treat cold and nasal congestion in children. Previous research on the chemical constituents of *E. americana* resulted in the isolation of several naphthalene derivatives such as hongconin, elecanacin, eleuthoside B, isoeleutherin, eleutherin and eleutherol. Pharmacological studies indicated significant anti-HIV activity of isoeleutherin, and cardio protective activity of hongconin. Eleutherin revealed inhibition of human topoisomerase II (anticancer activity), and antibacterial activity against *Pycococcus aureus, Streptococcus haemolyticus A*, and *Bacillus subtilis.* Paramapojn et al applied DAD for the determination of a new naphthopyrone, eleutherinoside A, together with the known bioactive compounds eleuthoside B, isoeleutherin, eleutherin and eleutherol in *Eleutherine americana* [66].

## 5.4. Food Analysis

HPLC has been increasingly applied to the analysis of food samples for additives, contaminants, antibiotic residues, ferilizers or pesticide residues, adulterants etc.

Because of the need to determine these analytes at low concentration levels in complex matrices, sensitive and selective detectors are required. Spectral capabilities of a DAD enable a compound's identity to be confirmed. The identity of separated compounds can be confirmed by library search. Such instruments provide the required identification of analytes according to legislation e.g. 657/2002/EC directive. According to this directive Confirmation can be also achieved by full scan DAD [67].

Confirmatory methods shall provide information on the chemical structure of the analyte. When more than one compound gives the same response, then the method cannot discriminate between these compounds. Methods based only on chromatographic analysis without the use of spectrometric detection are not suitable on their own for use as confirmatory methods.

LC with UV/VIS detection (single wavelength) is not suitable on its own to be used as a confirmatory method. LC-full-scan DAD Group B Specific requirements for absorption in UV spectrometry have to be met. In the case computer-aided library searching and matching are used, the comparison of the spectral data in the test samples to that of the calibration solution has to exceed a critical match factor. This factor shall be determined during the validation process for every analyte on the basis of spectra for which the criteria described above are fulfilled. Variability in the spectra caused by the sample matrix and the detector performance shall be checked.

### 5.4.1. Residue Analysis

Antibiotics are widely used in veterinary medicine for the treatment of diseases as well as in the form of nutritional supplements. The abundant and in some cases improper use of antibiotics may result in the presence of residues in edible animal tissues. Despite their beneficial usage, the misuse of antibiotics results in the development of nonpathogenic and pathogenic organisms' resistance. Moreover, the long-term use of antibiotics is dangerous for human health and potentially causes allergic reactions. In order to protect human health, the European Union has banned or enacted permitted limits (PL) or maximum residue levels (MRLs) for the presence of TCs in animal products. The use of veterinary drugs in the EU is regulated through Council Regulation. Council Directive 96/23/EC describes the procedure for the establishment of MRLs for veterinary medicinal products in foodstuffs of animal origin and regulates the residue monitoring of pharmacologically active compounds in products of animal origin [68]. This Directive divides all residues into Group A compounds, which comprises prohibited substances, and Group B compounds, including all registered veterinary drugs in conformity with Annexes I and III of 2377/90/EC and other residues [69]. The performance of analytical methods and the interpretation of results is regulated by 657/2002/EC directive of the European Union [67].

Dommarco et al applied HPLC-DAD to the multi-residue method for simultaneously determining ten urea and three benzoylurea pesticides residues in drinking water with quantitation limits below the European regulatory limit. In conclusion, the present procedure can be considered sufficiently sensitive and reliable for routine analysis of drinking water [70].

Martínez-Galera et al developed an HPLC-DAD method for the determination of imidacloprid and its main metabolite 6-chloronicotinic acid (two very polar compounds) in the resolution of pesticide mixtures. The combination of advanced computational capability with the DAD technology applied in HPLC offers a powerful approach for the resolution of highly overlapping peaks when resolution of the mixture is not possible by modifying the mobile phase, it not being necessary to change the column [71].

Koole et al applied HPLC-DAD to the analysis and identification of 20 substances with anabolic properties that are considered as potential growth promoters, to be used for the analysis of extracts of calf urine samples. For the identification, a retention parameter and the UV spectrum were used. The combination of the information provided by the retention parameter obtained with the HPLC and the UV spectrum recorded with the DAD may be sufficient for an unequivocal identification of the anabolics. For routine operation, the software can be programmed to collect data at those five wavelengths (multichromatogram mode). Spectra were saved for detected peaks in this mode.

The HPLC–DAD system was used for the analysis of extracts of urine samples from calf taken during fattening of the animals for the presence of residues of illegal anabolics [72].

Cinquina et al [73] applied a high-performance liquid chromatography–diode array detection method (HPLC–DAD) combined with liquid chromatography–mass spectrometry for the determination of residues enrofloxacin and its metabolite ciprofloxacin in goat milk. The HPLC–DAD method validation was compliant with the ‘‘DG SANCO 1805/2000’’ European regulation, and it was capable to detect and quantify enrofloxacin residues and its metabolite ciprofloxacin in milk [74].

Cinquina et al also applied HPLC–DAD to the multiresidue determination of tetracyclines in bovine milk and tissues [75].

Chromatographic techniques are the most suitable to identify and quantify pesticides residues in grapes, in particular gas chromatography (GC) equipped with selective and sensitive detectors. Nevertheless, some pesticides can not be determined directly by GC due to their lack of thermal stability and/or their insufficient volatility without further derivatization (e.g. benomyl, carbendazim or thiophanate-methyl). In these cases the use of high-performance liquid chromatography (HPLC) is particularly useful for determining these residues in grapes. Rial Otero et al applied HPLC–DAD to the multi-residue analysis of 14 fungicides in white grapes for vinification [76].

The increasing interest in the study of pesticides in grapes is justified from an enological point of view, since some pesticides can interfere with fermentative microflora used in wine production, as well as, with the consumer’ safety. Considering that washing grapes before consumption is the standard procedure, the study of the effect of washing on the residue concentration is required to assess real consumer exposure. Teixeira et al developed an HPLC-DAD method to study pesticide mobility in grapes, by comparing their residual concentration in the skin with that of the whole grape. The method was applied to 14 fungicides and insecticides mostly used in grapevines, and was accepted by Integrated Pest Management procedures. The efficiency of water washing to remove pesticides from grape skins was also evaluated. A new analytical methodology to analyse is reported, employing liquid chromatography with diode array detection (LC-DAD) [77].

Garcinuño et al used DAD for the simultaneous determination of the fungicide maneb and its main metabolites (ethylenethiourea—ETU, ethylenebis (isothiocyanate) sulfide—EBIS, and ethyleneurea—EU) in tomatoes. The identity of EBIS, one of the main UV degradation products of maneb, was verified by both DAD UV detection and mass spectrometry [78].

Marazuela et al used UV-DAD for the simultaneous determination of ciprofloxacin, enrofloxacin, marbofloxacin, danofloxacin and sarafloxacin residues in milk, using norfloxacin as internal standard. Focus was given on the analysis of marbofloxacin, danofloxacin and enrofloxacin, which are administered to milk-producing animals, and ciprofloxacin and norfloxacin, which are exclusively applied in human medicine [79].

Topuz et al applied HPLC-DAD method to the simultaneous determination of four fungicides (folpet, chlorothalonil, quinomethionat, tetradifon) and one herbicide (trifluralin) in fruit juices. [80]

Vinas et al applied HPLC-DAD to the determination of chloramphenicol chloramphenicol residues in animal feeds. Specificity was demonstrated by the retention characteristics, UV spectra and peak purity index [81].

Gratacos-Cubarsı et al proposed an HPLC method with diode array detection (DAD) for the detection of sulphamethazine residues in pig and cattle hair. The identification of sulphamethazine peak in hair extracts was made comparing both retention time and spectra (collected between 240 and 400 nm) with those of the sulphamethazine pure standard solutions. The suitability of this method was verified on spiked and incurred hair samples. Residues of sulphamethazine were detected, at ng/mg level, in hair samples of both calves and pigs supplied with therapeutic doses of sulphamethazine [82].

Within the EU, the use of nitrofurans is prohibited in food production animals. For this reason detection of these compounds in feedingstuffs, at whatever limit, constitutes an offence under EU legislation. Jorge Barbosa et al applied HPLC-DAD to confirm the identity of the suspected presence of any of the nitrofuran compounds. In routine analysis, the HPLC-DAD method can be used to screen samples for the possible presence of the four nitrofurans analyzed and the LC-MS/MS method can be used to confirm any positive finding [83].

Vinas et al applied UPLC-DAD for the sensitive, selective and solvent-free determination of six oxazole fungicide residues (hymexazol, drazoxolon, vinclozolin, chlozolinate, oxadixyl and famoxadone) in wine and juices. The peaks were identified again using the DAD detector to continuously measure the spectrum while the solute passed through the flow-cell, thus confirming the identity and the purity of the peaks. Good agreement was found between the UV spectra of the different peaks obtained for the standards, the samples and the spiked samples [84].

Nozal et al applied HPLC-DAD to the determination of fumagillin residues in honey [85].

### 5.4.2. The Use of DAD for Residue Confirmation According to European Union Directive 657/2002/EC

Pecorelli et al implemented DAD in a simple multiresidue method for assaying 10 sulphonamides (SAs): sulfadiazine, sulfathiazole, sulfapyridine, sulfamerazine, sulfamethazine, sulfamonomethoxine, sulfachlorpyridazine, sulfamethoxazole, sulfaquinoxaline and sulfadimethoxine) in muscle samples. The method was validated according to the directive 657/2002/EC [86].

The use of the two macrolides antibiotics Spiramycin (S) and Tylosin (T) as growth promoters in animal feeding has been recently withdrawn in the European Union due to a concern about the outbreaks of farmacoresistance fenomena as a possible hazard for humans. For feed additives monitoring purposes, Civitareale et al developed an analytical method has been for their extraction, purification and identification in different animal feedingstuffs (pelleted beef, pig, poultry feeds and calves milk replacer) at the minimum performance required limit (MRPL). DAD was applied to identify the illegal presence of spiramycin and tylosin in different feedingstuffs. As verification, the overlapping of UV spectra in the range 220–350 nm between analytical standards and the compounds in the matrix were considered.

By the comparison of the spectral data (DAD) in the test sample to that of the calibration solution, HPLC method can be used as a simpler preliminary confirmatory mean method of verification than LC/MS(MS) able to use on official controls. This method can be considered as a multi-drug method since it can distinguish the molecules of the same drug family such as erythromycin and oleandomycin [87].

Posyniak et al developed a liquid chromatography-diode array detection (LC-DAD) procedure for the determination of chlortetracycline and its 4- epimer (4-epi-chlortetracycline) residues in pig kidneys. The identification criteria of decision 2002/657/EC for full scan UV–vis detection were accomplished for all analysed solutions [88].

Quinolones comprise an interesting group of antibacterials whose action is based on their anti-DNA activity. All quinolone antibiotics possess a carboxylic group in position 3 and a carbonyl group in position 4. The introduction of 6-fluoro and 7-piperazinyl moiety gave rise to the production of second-generation quinolones, known as fluoroquinolones. The addition of these two moieties has increased the activity against Gram-positive and Gram-negative organisms. Samanidou et al applied DAD to the determination of five fluoroquinolones (enoxacin, ofloxacin, norfloxacin, ciprofloxacin, and enrofloxacin) in edible animal tissues (muscle tissue, liver, kidney, and eggs). Peaks in real samples were identified by means of a photodiode array detector. The applicability of the method was examined using real samples from a chicken treated orally with the five studied fluoroquinolones [89].

Tetracycline antibiotics (TCs) are broad-spectrum agents, exhibiting activity against infections caused by both Gram-positive and Gram-negative bacteria, as well as chlamydia, mycoplasmas, rickettsiae, and protozoan parasites. TCs were first discovered in 1945 and since then they have been extensively used to control bacterial infections in both humans and animals. Tetracycline, oxytetracycline, chlortetracycline, doxycycline, and minocycline are five members of this antibiotics group that are commonly used in food-producing animals. TCs are given to animals destined for human consumption not only to prevent and treat certain diseases but also to fraudulently promote growth. Different MRL values have been set for TCs in different target tissues. Samanidou et al applied HPLC-DAD to the determination of five tetracyclines (TCs): minocycline, tetracycline, oxytetracycline, chlortetracycline, and doxycycline in bovine muscle. The procedure was validated according to the European Union decision 2002/657/EC determining selectivity, stability, decision limit, detection capability, accuracy, and precision. Decision limits (CCa) and detection capability (CCb) were determined for all compounds. In compliance with the 2002/657/EC decision, the validation procedure includes the determination of two novel criteria, CCa (limit of decision) and CCb (capability of detection), defined respectively as “the limit at and above which it can be concluded, with an error probability of a, that a sample is noncompliant” (greater than the MRL for group B substances), and “the smallest content of the substance that may be detected, identified, and/or quantified in a sample with an error probability of b.” For group B substances, errors must be *a* 5%. The results of the validation process demonstrate that the method can be readily applied to European Union statutory veterinary drug residue surveillance programmes [90].

Ortiz et al applied DAD detection to the determination of chlortetracycline in milk. The method was validated according to 657/2002/EC [91]. Corticosteroids, such as dexamethasone, have been illegally used as growth promoting agents to obtain an economical benefit from increased muscle development. These substances remain in meat and other animal products and may have negative toxic consequences for consumers. Reig et al developed a screening and confirmatory method for dexamethasone detection in feed and drinking water in livestock has been developed and validated. This method is based on immunoaffinity chromatography followed by reverse-phase high- erformance liquid chromatrography (IAC–HPLC) with diode array detection (DAD). The performance criteria for liquid-chromatography with DAD detection, as fixed in the EC decision were accomplished. DAD was necessary for confirmatory purposes by comparing the spectrum of the analyte at the dexamethasone elution time with the spectrum of the pure dexamethasone.[92]

García et al used DAD to determine six sulfamides: sulfadiazine, sulfamethazine, sulfamethoxypyridazine, sulfamethoxazole, sulfadimethoxine and sulfaquinoxaline, in kidney and the method was validated according to 657/2002/EC [93].

Berrada et al applied a simple multiresidue HPLC-DAD to the determination of seven macrolide antibiotics in samples of liver and kidney animals at concentrations lower than those allowed by current legislation. The method was validated in accordance with the European Commission Decision 657/2002 [94].

Milk is one of the products from food-producing animals that may be contaminated by residues of drugs. The consumption of antibiotics through milk may generate allergic reactions to sensitive individuals. Different MRL values have been set by the European Union for quinolones in milk. In order to accomplish the European Union's requirements for the MRLs, sensitive multiresidue screening methods for quinolones in milk are required.

Samanidou and Christodoulou applied DAD to develop a sensitive and simple multiresidue HPLC method for the determination of ten quinolones' residues in milk: enoxacin, ofloxacin, norfloxacin, ciprofloxacin, danofloxacin, enrofloxacin, sarafloxacin, oxolinic acid, nalidixic acid, and flumequine. Among these quinolones, only for danofloxacin, enrofloxacin, and flumequine, MRLs have been established in milk, according to the Council Directive (EEC) no. 2377/90. The proposed method is validated according to the performance criteria of European Decision 2002/657/EC. The method was subsequently applied to various milk samples available in Greek market: full cream, low fat and skimmed pasteurized milk, full cream and reduced fat evaporated milk, full cream and low fat high pasteurized milk, and milk treated at ultrahigh temperature [95].

DAD was also applied by Samanidou et al to the determination of seven tetracyclines (TCs) in milk: minocycline, tetracycline, oxytetracycline, methacycline, demeclocycline, chlortetracycline, and doxycycline. The procedure was validated according to the European Union decision 2002/657/EC determining selectivity, stability, decision limit, detection capability, accuracy, and precision [96].

Christodoulou et al used DAD for the simultaneous determination of ten quinolones: enoxacin, ofloxacin, norfloxacin, ciprofloxacin, danofloxacin, enrofloxacin, sarafloxacin, oxolinic acid, nalidixic acid, and flumequine, in various tissues of food-producing animals [97], as well as in chicken muscle and egg yolk, [98] and in bovine liver and porcine kidney [99]. All three methods were fully validated according to the criteria of European Union Decision 2002/657/EC determining linearity, selectivity, decision limit, detection capability, accuracy, and precision.

Sulphonamides (SAs) are a group of synthetic antibacterial agents widely used in veterinary practice for the treatment of infections and growth promotion of food producing animals. There is a risk of SA residues remaining in animal products if these drugs have been improperly administered or if the withdrawal period has not been observed. Improper use of these sulphonamides in lactary cows has caused, for example, the presence of sulphonamide residues in milk, so that monitoring of such residues in products designated for human consumption and in slaughtered animals has become one of the most important duties for public health agencies. Drug residues may cause allergic or toxic reactions to consumers and promote occurrence of antibiotic resistant bacteria.

Samanidou et al used DAD for the determination of four sulphonamides: sulphadiazine, sulphaquinoxaline, suplhamethazine, and sulphadimethoxine. Two of them: sulphaquinoxaline and sulphadimethoxine, were determined in cow's milk. PDA detection was performed for the detection and confirmation of separated analytes with monitoring at 260 nm. Validation of the method was based on the Commission Decision 2002/657/EC. The method was applied to the analysis of twenty two milk samples from the local market. Eight different types of milk samples, purchased from the local market were analyzed following the proposed method in order to investigate the presence of the examined SAs. Milk samples included full cream pasteurized (3.5%), low fat pasteurized (1.5%), skimmed pasteurized (0.0%), full cream evaporated (7.5%), reduced fat evaporated (1.5%), high pasteurized full cream (3.5%), high pasteurized low fat (1.5%), and ultra high temperature treated (1.5%) and (0.3%). Identification of antibiotics was performed by means of a PDA detector. Sulphaquinoxaline was identified in seven of these samples. The similarity factors were greater than 0.9149 [100].

Nikolaidou et al used diode-array detection for the determination of seven tetracyclines in chicken muscle and egg yolk: minocycline, tetracycline, oxytetracycline, methacycline, demeclocycline, chlortetracycline, and doxycycline [101], as well as in liver and kidney muscle tissues [102], and in bovine and porcine muscle tissues [103]. All procedures were validated according to the Decision 2002/657/EC, determining selectivity, stability, decision limit, detection capability, accuracy, and precision.

### 5.4.3. Food Characterisation

The analysis of phenolic compounds in wines is of considerable commercial importance, since they are known to play the major role in defying the sensorial characteristics of wines, such as astringency, flavor, and color, as well as in the browning process, causing product deterioration.

Samanidou et al applied DAD to the determination of five phenolic acids: caffeic, ferulic, vanillic, salicylic, and p-hydroxy-benzoic acid in wine and wine vinegar samples. The identification of phenolic compounds was performed by comparing their retention time values and UV spectra in the 190- 300 nm range with authentic standards stored in a data bank [104].

de Melo Abreu et al applied DAD to determine Azoxystrobin, kresoxim-methyl, trifloxystrobin, pyraclostrobin, famoxadone and fenamidone which are permitted Qo Inhibitor (QoI) fungicides applied to vine in some European countries for the treatment of downy and powdery mildews. The method was validated for the analysis of these fungicides in grapes and wine [105].

Lai et al successfully applied a Diode array detector hyphenated with atmospheric pressure chemical ionization/mass spectrometry (LC/DAD-APCI/MS) to the identification and characterization of the main flavonoids and caffeoylquinic acids (CQAs) of three common *Compositae* plants (*Chrysanthemum morifolium* Raman, *Artemisia annua*, and *Chrysanthemum coronarium*), which have been used as herbal medicine. Identification was performed by comparing the retention time, UV and mass spectra of samples with standards or/and earlier publications. Although there exist some similarities in the flavonoidic content of the leaf and flower of *C. morifolium*, significant variations in their varities and concentrations were observed. *Artemisia annua* processes substantial amount of alkylated derivatives of flavones and *Chrysanthemum coronarium* contains only CQAs. These findings suggest that although all the plants studied are from the same *Compositae* family, their flavonoids and phenolic compositions are markedly different. The proposed method is useful for further chromatographic fingerprinting of plant flavonoids [106].

Curcuma xanthorrhiza and Zingiber zerumbet are two of the most commonly used ingredients in Indo-Malaysian traditional medicines, health supplements and tonics. Lately, a number of products derived from the aqueous extracts of these species have appeared in the market in the form of spray-dried powder packed in sachet or bottle. Ruslay et al used on-line high performance liquid chromatography, coupled with diode array detection and electrospray ion trap tandem mass spectroscopy (HPLC–DAD–ESI–MSn), to analyze the components in the antioxidant-active fractions from the rhizomes of these species. Three components were identified from C. xanthorrhiza, including bisdemethoxycurcumin, demethoxycurcumin and curcumin. To confirm their identities, the components from *Z. zerumbet* were isolated conventionally and were analyzed by spectroscopic techniques as well as by comparison with literature data [107].

Netzel et al investigated twelve native Australian fruits for their antioxidant capacity and presence of phenolic compounds, anthocyanins and ascorbic acid by HPLC-DAD/ESI/MS-MS which revealed profiles with simple anthocyanin composition (one to four individual pigments) with cyanidin as the dominating type. Australian native fruits investigated in this study are shown to be a novel rich source of antioxidant compounds. Identification of anthocyanins was performed by HPLC-DAD/ESI/MS-MS [108].

Kang et al developed an HPLC/DAD/ESI-MS*n* method for the chromatographic fingerprint analysis and characterization of furocoumarins in the roots of *Angelica dahurica* for the first time. Nine “common peaks” were identified by comparing with the retention time, UV and MS spectra of reference furocoumarins. Moreover, a total of 20 furocoumarins were identified or tentatively characterized from the roots of *A. dahurica* by HPLC/DAD/ESI-MS*n* technique. The wavelength for the detection of compounds in the roots of *A. dahurica* was selected by DAD. It appeared that the chromatograms at 270 nm and 320nm could represent the profile of the extract [109].

Anthocyanins, which belong to the flavonoid phenolic group of compounds, are natural pigments which are widely distributed in plants that are consumed in the human diet such as crops, beans, vegetables and fruits. A large amount of anthocyanins from plants is ingested every day. In particular these anthocyanins are associated with a wide range of biological activities including antioxidant, anti-inflammatory, anticancer and a-glucosidase inhibition. Additionally these pigments may reduce the risk of coronary heart disease through modulation of arterial protection, inhibition of platelet aggregation or endothelial protection. For this reason, the food and medicinal industries are increasingly interested in fruits and vegetables with a high content of bioactive anthocyanins for the manufacture of supplements with preventative and therapeutic uses. Numerous studies have revealed that the beneficial health effects of black soybean are due to the several phytochemicals, such as isoflavones, saponin, and anthocyanins. It should be noted, however, that the anthocyanins isolated from black seed coated soybean can be expected to possess various biological activities. Lee et al isolated, identified and characterised the anthocyanins in the black seed coated soybean using HPLC with diode array detection and electro spray ionization/mass spectrometry (DAD ESI/MS) analysis [110].

Salad vegetables could be relevant as dietary sources of natural antioxidants. A better knowledge of their composition can be useful for understanding their potential bioavailability and biological activities. The antioxidant compounds, polyphenols and vitamin C, have been determined in five varieties of lettuce (iceberg, romaine, continental, red oak leaf, lollo rosso) and one variety of escarole (frissé). Rafael Llorach et al studied the phenolic contents of these salad vegetables by HPLC-DAD and significant differences in the content of polyphenols between green varieties, red varieties and escarole were detected. The method allowed the identification of two compounds previously not reported in lettuce; quercetin and luteolin rhamnosyl-hexosides. Qualitative and quantitative differences were observed between the polyphenol profiles. Caffeic acid derivatives were the main phenolics in green varieties, while flavonols were detected in higher quantities in red varieties and escarole, and anthocyanins were only present in red-leafed varieties. The highest total phenolic content was observed in red-leafed varieties while the highest level of vitamin C was detected in the continental variety. The red varieties showed the highest antioxidant activity by all the methods assayed [111].

## 5.5. Stability Studies

Bilia et al used DAD as a part of their investigations on the stability of tinctures. They have evaluated 40 and 60% v/v tinctures of Calendula flower, Milk-thistle fruit and Passionflower. These preparations are widely employed in phytotherapy, thus Calendula is used externally for anti-inflammatory properties, Milk-thistle and Passionflower are employed for hepatic injuries and in tenseness with difficulty in falling asleep, respectively. Aim of this work was to assess the chemical stability of their active or marker constituents from accelerated and long-term testing by using HPLC. Thermal stability of the constituents from accelerated and long-term testing was determined by HPLC-DAD and -MS analyses and was related both to the class of flavonoids and water content of the investigated tinctures. The purity of peaks was checked by DAD, comparing the UV spectra of each peak with those of authentic reference samples and/or by examination the MS spectra [112].

Escarpa et al. applied HPLC-DAD to the study of the analytical performance of the main phenolic classes (benzoic and cinnamic acids and flavan-3-ols, flavonols and flavones as subclass of flavonoids) contained in legume samples. (+)-catechin, (−)-epicatechin and luteolin as flavonoids as well as caffeic and coumaric acids were definitely identified by comparison of retention time and UV spectra against those found in standards. The phenolics contained in extract solutions were successfully separated and they showed high stability in their retention times and peak area [113].

Amoxicillin is widely used in veterinary medicine. Perez-Lozano et al described an HPLC-DAD methodology (by VICH guidelines) for the stability evaluation of amoxicillin in granular premixes. The method monitors amoxicillin as well as the degradation products formed during the stability study. It also proved to be suitable as a rapid and reliable quality control method. The stability study of premix, by monitoring the degradation products by the HPLC method proposed, indicates that the estimated shelf life during which it keeps its initial quality attributes is of 21 months [114].

Berries and red fruits are dietary sources of polyphenols with reported health benefits. As part of the diet, polyphenols are ingested as complex mixtures immersed in a food matrix which is digested in the gut. To understand the effects of dietary polyphenols on human gut health it is essential to determine their stability and fate in the lumen. Bermudez-Soto et al investigated the effects of an in vitro gastric and pancreatic digestion on the stability and composition of the major polyphenols in chokeberry juice. Samples taken after gastric and pancreatic digestion were analyzed by HPLC-DAD and HPLC-MS/MS to determine the composition and recovery of soluble phenolics. Phenolic compounds were identified by their UV spectra, by their molecular weight and molecular fragments and, wherever possible, by chromatographic comparisons with authentic synthetic standards [115].

St John's wort is a medicinal plant with a long history of use in traditional medicine all over Europe. The presence of the characteristic polyprenylated acylphloroglucinol derivatives, namely hyperforin and analogs are instead related to the oil's therapeutic activity. Isacchi et al evaluated five different samples of SJW oils by HPLC-DAD-MS analysis to verify the variability and stability of the constituents according to the following factors: different harvesting time, fresh or dried plant material, use of sunlight or heating systems during extraction. The stability of the oils over a 1-year period was also tested by HPLC-DAD-MS analysis. The authors reported a comparison of HPLC analysis of the constituents of *Oleum Hyperici* prepared by traditional method and other procedures to find the best condition of extraction of the phytocomplex in order to obtain a maximum concentration of constituents [116].

Xie et al developed a selective and efficient quality consistency assessment system for monitoring the manufacturing processes of a Chinese herbal preparation, Qingfu Guanjieshu (QFGJS) capsule, and for assessing its stability over time. This system is based on quantitative determination of four marker compounds, i.e., sinomenine, paeoniflorin, paeonol, and curcumin, and on qualitative fingerprinting analysis of QFGJS using HPLC-DAD. This could be used both for quantitative determination of four bioactive compounds and for fingerprinting analysis to evaluate the quality consistency of QFGJS during its stability testing.

By comparing both the retention times and the UV spectra of the reference standards, four marker compounds (sinomenine, paeoniflorin, paeonol, and curcumin) in QFGJS were well identified.

The peak purity was confirmed by studying the DAD data with all peaks of interests in which no indication of impurities of peaks was found [117].

The chemical composition of virgin olive oil may be influenced by genotype and different agronomic (i.e. fruit ripeness degree, water supply) and technological factors. Baccouri et al reported the evaluation of the influence of the olive ripening stage on the quality indices, the major and the minor components and the oxidative stability of the two main monovarietal Tunisian cultivars (cvv. Chétoui and Chemlali) virgin olive oils. Moreover, the olives cv. Chétoui were tested in a rain-fed control and an irrigation regime. The oils sampled at five different ripeness stages were submitted to HPLC-DAD/MSD determination of their quali-quantitative phenolic and tocopherolic profiles. Moreover, the triacylglycerol and fatty acid compositions, and minor components such as squalene, pigments and their relation with the oil oxidative stability were evaluated [118].

## 5.6. Identification Studies

Though HPLC–MS is a powerful tool for identification, the methods based on it are usually more sophisticated so that the laboratories that are not well equipped cannot easily perform them. In contrast, methods based on HPLC-DAD such as the maximum absorbance at a certain wavelength, multiple absorbance ratios, which are not reliable, are employed to identify substances, and it is reported that DAD spectral library and spectral correlative chromatography were applied to identification of peaks in chromatograms.

Brolis et al used PDA for the identification of flavonoid, naphthodianthrone and phloroglucinol constituents of *Hypericum perforatum,* a medicinal plant, which has been known in traditional medicine as an anti-inflammatory and healing agent. The alcoholic extract of its aerial parts finds wide application for its antidepressant activity. The purity of the peaks was also checked by photodiode array detection. The UV spectra of a peak at three different points (upslope, top and downslope) were compared with the UV spectrum of the authentic reference sample. The method was found to be specific and suitable for routine analysis because of its simplicity, specificity, accuracy and reproducibility [119].

Arnoldi et al used DAD to distinguish between ‘poisonous’ and ‘non-poisonous’ chemotypes of *Ferula communis.* The two chemotypes showed different fingerprints. The identification of five coumarins and eleven daucane derivatives was performed by HPLC-diode array detection (HPLC-DAD) and HPLC-MS. A coumarin, not yet described, was detected. The HPLC-DAD-UV fingerprint of the ‘poisonous’ chemotype of *F. communis* was totally different from that of the ‘non poisonous’ chemotype.

The developed HPLC method allowed a simple and rapid identification of the two different and morphologically indistinguishable chemotypes of *F. communis* growing in Sardinia [120].

Horvath et al developed a method of analysis of eight flavones using HPLC-DAD in root and aerial tissues of the medicinal plant *Scutellaria baicalensis.* The identity of the analytes was confirmed using retention time, UV–vis and mass spectral comparisons to commercial standards. By combining HPLC, DAD, and MS for medicinal plant analysis, the identification and quantification of bioactive and marker compounds in complex matrices can be realized even with structurally similar natural products. The ethod was used for subsequent quantitative analysis of two different *S. baicalensis* plant types, including greenhouse and in vitro-grown plants, to establish potential differences of flavone concentrations between the two plant types [121].

Wu et al developed an HPLC-PDA method for the analysis of the major alkaloids in *Huperzia serrata*, a traditional Chinese medicine herb.

With the help of multi-dimensional information of HPLC-DAD-ESI-MS-MS the alkaloid compounds in *H. serrata* could be identified in a single run successfully. The chromatogram acquired using this method can serve as a fingerprint of the alkaloid components for the quality control of *H. serrata* and its alkaloid extracts [122].

Blanc et al applied DAD to the separation and identification of natural dyes in historical maps. The authors introduced a new methodology for the chemical analysis of historical documents, text and graphic, based on HPLC-DAD. The method is useful for librarians and archivists because knowledge of the nature or type of dyes within the artefacts is essential to classify and to use the adequate procedure to restore and preserve them. It has been successfully applied to historical maps from The Royal Chancellery Archives in Granada [123].

High performance liquid chromatography coupled with a photodiode-array detector and a mass spectrometry (HPLC-DAD-MS) provides a powerful tool for polyphenol analysis in crude plant extracts. HPLC DAD provides extensive information on polyphenol structures, while HPLC–MS provides information about the polyphenol molecular weight and the molecular structure from its fragmentation data. Fang et al used DAD for the qualitative analysis of the ethyl acetate extracts from three bayberry cultivars, Xiangshan, Biqi and Dongkui, performed by means of a hyphenated technique of HPLC coupled to photodiode array detection and electrospray ionization mass spectrometry. Three phenolic compounds were identified (gallic acid, protocatechuic acid, and quercetin 3-glucoside) and seven others partially identified. Spectral measurements were made over the range 200–600 nm. Contents of gallic acid, protocatechuic acid and flavonol glycosides were determined by the HPLC-DAD. The method was successfully used in determination of phenolic compounds from bayberry cultivars of Xiangshan, Biqi and Dongkui [124]. Flos Lonicerae, a traditional herbal medicine, has been used in China to treat some inflammatory disease. Several different classes of compounds have been separated from the herb to assess their pharmacological activities. Among these classes, flavonoids, iridoid glycosides and saponins have been well studied and may be responsible for its clinical application. Therefore, quality control of Flos Lonicerae is an important issue for drug safety and validity evaluations. Chen et al developed a quantitative method of capillary HPLC–DAD/ESI-MS for the simultaneous assay of 24 compounds in Flos Lonicerae. The method was demonstrated to be a powerful tool for comprehensive analysis of herbal medicines, owing to its exclusive selectivity and excellent sensitivity.

Iridoid glycosides and flavonoids could be simultaneously detected at 250 nm and flavonoids could be monitored at 350 nm by DAD. As saponins do not contain strong chromophores, HPLC–MS was the method of choice for their determination [125].

Various analytical methods based on the HPLC-DAD technique were used to determine 38 phenolic compounds in red wines. García-Falcon et al proposed used DAD to establish the phenol composition of Mencía and Brancellao, two varietal young red wines, and its influence on colour stability during storage in bottles for one year. Phenolic compounds in wines are usually identified by standard HPLC. By virtue of their high concentrations in red wines, anthocyanins can be determined simply by direct injection of samples into an HPLC-DAD instrument. Phenolic compounds in wine were identified from their UV-Vis spectra and, wherever possible, by chromatographic comparison with authentic markers. Anthocyanins and hydroxycinnamic acids in the two varietal wines studied were successfully determined by direct injection into an HPLC-DAD instrument. All other phenolic compounds, however, required some pretreatment for analysis [126].

Lin et al applied LC-DAD-ESI/MS to identify 23 flavonoids in the extract of Mexican oregano (Lippia graveolens H.B.K.), a spice and herb, used in the USA and Mexico. The identification was made by detailed analysis of their UV and mass spectral data. Of these flavonoids, 20 are reported for the first time in this plant [127].

Carmona et al analysed the flavonoid fraction in saffron spice, by LC-DAD-MS/MS ESI and five kaempferol derivatives have been found. Compounds such as kaempferol-3-sophoroside, kaempferol-3-sophoroside-7-glucoside and kaempferol-3,7,40-triglucoside were tentatively identified, whereas other compounds, such as kaempferol tetrahexoside and kaempferol-3-dihexoside were detected. Differences in the flavonoid contents of samples from various geographical origins were also studied in order to know whether they could be used as biomarkers for the determination of saffron origin. Spectral data from all peaks were accumulated in the range of 240–400 nm. Five flavonol compounds were tentatively identified by combination of the UV and mass spectra by HPLC-DAD-ESI-MS/MS [128].

## 5.7. Authenticity-Adulteration Studies

Food adulteration is considered the act of intentionally debasing the quality of food offered for sale either by the admixture or substitution of inferior substances or by the removal of some valuable ingredient. Adulteration of foods is a serious economic problem concerning most food commodities.

All types of adulteration are difficult to detect and lead to a deterioration of product quality. For consumer protection and to avoid unfair competition, it is of essential importance to guarantee both authenticity and compliance with the product specification [129].

### 5.7.1. Fruit Juices and Jams

The advent of diode array detection has enhanced the profile characterization and phenolics identification; in fact, many phenolics show similar UV absorption spectra and, on the other hand, co-elution of phenolic acids with flavonoids and cinnamic acids may occur. Versari et al reported the analysis results of dihydrochalcone glycosides (phloretin glucoside and phloretin xyloglucoside) by direct RP-HPLC/DAD in several commercial juices, nectars and mashes in order to investigate the presence of marker compounds that could be useful in the characterization and differentiation of fruit-based beverages. Some phenolic compounds, (+) catechin, (–) epicatechin, chlorogenic acid, phloretin glucoside (phloridzin) and phloretin xyloglucoside, in several juice samples were separated and identified. Dihydrochalcones were identified as ‘markers’ in apple samples, their content was calculated and a ‘threshold concentration’ for detectable addition was evaluated.

Phenolics identification was based on retention times and UV spectra. As evidenced by their characteristic UV spectrum recorded with diode array detection the spectrum of phloretin standards overlaps completely with those of the dihydrochalcones found in the samples and this can be considered as an indication of the relevant peak purity. In pear and strawberry samples, dihydrochalcones eluted close to flavonol compounds (quercetin derivatives); in these cases, diode array detection is required for peak identification [130].

Due to the similar texture and rheological properties of apple (Malus communis Lamk) and pear (Pirus communis Lin.), quince products are easily adulterated by these fruits. The stronger odour of quince masks the sweet flavours of both fruits, their presence being very difficult to detect by sensory evaluation. Silva et al determined the phenolic profiles of 12 samples of Portuguese commercial and one home-made quince jelly by HPLC/DAD in order to evaluate their authenticity. These analyses showed that all samples presented a similar profile composed of at least eight identified phenolic compounds. The conclusion was that none of the samples were fraudulently adulterated by the addition of pear or apple, since they did not contain arbutin, the characteristic compound of pear, nor phloretin 20-xylosylglucoside and phloretin 20-glucoside, considered the chemical markers of apple. All samples exhibited 5-HMF, a sugar derivative, as the major compound. This work represents a contribution to the definition of quince jelly phenolic profile, allowing the determination of its authenticity. The different phenolic compounds were identified by chromatographic comparisons with authentic standards and UV/vis spectra in the 200±400 nm range [131].

Stintzing et al used DAD for anthocyanins and betalains that are mutually exclusive in nature to investigate their potential synergism for food colouring purposes. An official HPLC method providing fingerprints of common fruit juices to detect adulterations among anthocyanic or with red beet extracts has also been published. Finally, the proposed HPLC method may be applied for authenticity evaluation of such mixtures [132].

Kurz, et al quantified the predominant free carotenoids in apricots by HPLC with diode array detection. In contrast to previously published data, a-carotene could not be detected in apricots. Although the pumpkins showed significant differences in their free carotenoid profiles, major unesterified compounds different from those found in apricots could be determined. However, due to the natural heterogeneity, authentication of the apricot products cannot be accomplished exclusively using the profile of free carotenoids. Therefore, the investigations were extended to carotenoid esters. The xanthophyll ester profiles in pumpkins significantly differed from those in apricots in that the latter also contained both saturated and unsaturated fatty acids, whereas in pumpkins exclusively saturated fatty acids were detected. Admixtures of lower cost pumpkins could be detected in quantities of P5% by increased contents of lutein and zeaxanthin, and by the appearance of antheraxanthin and a-carotene, respectively, depending on the added pumpkin cultivar, as well as the presence of characteristic lutein and antheraxanthin esters. However, pronounced differences in the carotenoid profiles of the investigated pumpkins and the partly minor amount of characteristic compounds lead to limitations of the detection of 5% level of admixture of pumpkin to apricot and of the method in general.

One analytical technique is usually insufficient to detect all kinds of adulteration commonly practised. Therefore, in most cases only combined analyses allows reliable authenticity assessment of a product. Hence, the objective of the present study was to evaluate the potential of the carotenoid profile for authenticity studies of apricot purees and jams.

The identification of the carotenes and xanthophylls investigated in the present study (antheraxanthin, lutein, lycopene, zeaxanthin, a-carotene, b-carotene, c-carotene and b-cryptoxanthin) was based on the comparison of retention times, UV/vis and mass spectrometric data of reference standards. b-Carotene Z-isomers were identified according to a former investigation by their retention time and their UV/vis spectral characteristics in comparison with the isomers obtained by iodine-catalysed conversion of all-E-b-carotene. Xanthophyll esters were characterised based on their retention times, UV/vis spectra and fragmentation patterns in LC–MS experiments [133].

### 5.7.2. Medical Plants

Worldwide traditional herbal medicines are gaining popularity as a source of complementary and alternative remedies. In contrast to conventional pharmaceuticals, herbal medicines are generally presumed as safe, harmless and without side effects, because of their natural origin. Common problems affecting the safety of herbal medicines include contamination, adulteration, toxicity, lack of standardization, incorrect preparation or dosage and inappropriate labeling. According to the source of the plant materials, herbal medicines can contain excessive or even banned pesticides, heavy metals and microbial contaminants. The presence of these contaminants as well as adulteration with conventional pharmaceuticals can lead to acute or chronic toxicity, severe side effects and drug interactions. Over the past several years, there have been many reports on adulterations of traditional herbal medicines by synthetic therapeutic substances [134].

Chromatographic fingerprint with marker compounds can be used as a mean of identification and standardization of FAHF-5 herb product. Chinese herbal formula is a complex mixture of chemical components. Chromatographic fingerprint has been suggested to be a practical and comprehensive approach for identifying authenticity and evaluating the quality, consistency and the stability of raw herbal materials and herbal extracts. Zou et al generated a simplified anti-food allergy herbal formula FAHF-5. This study was undertaken to establish the chromatographic fingerprint HPLC analysis of FAHF-5 by RP-HPLC with DAD detection (scan from 200 to 400 nm). From the chromatographic fingerprint of FAHF-5, 31 diagnostic peaks were observed [135].

High pressure liquid chromatography coupled with a photodiode-array detector (HPLC-DAD) provides extensive information on polyphenol structures in crude or semipurified plant extracts. Knowledge of the precise composition of apple varieties may contribute to a better understanding of their influence in the quality and diversity of apple products such as apple juice and cider. For this reason, characterisation studies based on the polyphenolic profiles have been carried out with dessert and cider apple cultivars. The main classes of polyphenols found in apple fruit are flavan-3-ols (catechins (monomeric flavan-3-ols) and procyanidins (polymeric flavan-3-ols)), dihydrochalcones (phloretin glycosides), flavonols (quercetin and isorhamnetin glycosides), hydroxycinnamic acids and anthocyanins (cyanidin glycosides). LC-DAD with postcolumn addition of UV shift reagents afforded precise structural information about the position of the free hydroxyl groups in the polyphenolic nucleus. Alonso-Salces et al characterised apple polyphenols by means of hyphenated techniques such as HPLC coupled to UV photodiode array detection (LC-DAD) and to mass spectrometry (LC–MS). Five isorhamnetin glycosides, two hydroxyphloretin glycosides and quercetin were reported in apple peel for the first time. Postcolumn addition of UV shift reagents in LC-DAD analysis confirmed the presence of isorhamnetin glycosides and not the isomeric glycosides of rhamnetin. Moreover, isorhamnetin-3-*O*-rhamnoglucoside was identified unambiguously by comparison with a standard. These results are relevant not only from a chemotaxonomic point of view, but also in the control of authenticity of fruit derived products in order to detect fraudulent admixtures [136].

Jung et al applied HPLC-DAD to the identification of the ingredients, a urine sample as well as a sample of the Chinese herbal medicine ‘‘LiDa’’ capsule. This case demonstrates a common problem with herbal medicines. Besides contamination with excessive or even banned pesticides, heavy metals and microbial products, adulteration with synthetic therapeutic substances are one of the greatest risks using herbal medicines. Adulteration can lead to severe side effects or potentially fatal interactions with conventional drugs [137].

Problems with identification and labeling of medicinal plants, as well as substitution/adulteration of non-toxic plants by toxic ones have previously led to cancer, renal failure and even deaths. The non-toxic *Stephania tetrandra* (Fangji) has been known to be substituted by *Aristolochia fangchi* (Guang fangji), which contains the nephrotoxic and carcinogenic aristolochic acid (AA). Koh et al in their study compared HPLC-DAD chromatographic fingerprints of each methanol extract from 10 samples of “Fangji” bought from local medicinal shops with those of *A. fangchi* and *S. tetrandra*, using aristolochic acid I (AAI), tetrandrine and fangchinoline as marker compounds. Nine of the samples were found to be similar to *A. fangchi*. The roots of *S. tetrandra* and *A. fangchi* are usually sold in the form of slices and look similar in appearance. Despite the similarity in appearance of both herbs and the presence of toxic AA in *A. fangchi*, to date, no method for the simultaneous detection of AAI, tetrandrine and fangchinoline is available for the purpose of differentiating between the two roots. DAD was used for the rapid identication and differentiation of both *A. fangchi* and *S. tetrandra*, using AAI, tetrandrine and fangchinoline as marker compounds. All but one of the samples resembled *A. fangchi*. The marker compounds, tetrandrine and fangchinoline, could not be found in all the 10 herbal samples. Instead, AAI was found to be present in the nine samples that resembled *A. fangchi*. AAI was identified by comparisons of the RT and UV profiles, as well as spiking the samples with AAI. The profiles were similar but the match factor was only 743. The fingerprints were very similar. The low concentration of the peak, suspected to be AAI, may have given rise to the low match factor [138].

### 5.7.3. Wine

Wine is a product that can be easily adulterated, and for this reason wine authenticity is guaranteed by strict guidelines laid down by responsible national authorities, and includes sensory evaluation, chemical analyses, and examination of the records kept by wine producers.

Matějíček et al applied HPLC-DAD to determine the concentrations of derivatives of benzoic and cinnamic acids and furaldehyde during maturing of a red wine (a mixture of Cabernet Sauvignon and Merlot) in barrique barrels (Quercus robur). The influence of degree of toasting of the wood on the amount of phenolic compounds in barrique wine was also investigated. Gallic, protocatechuic, p-hydroxybenzoic, vanillic, caffeic, syringic, p-coumaric, ferulic, benzoic and ellagic acids and p-hydroxybenzaldehyde, vanillin, 2-furaldehyde, 5-methoxy-2-furaldehyde and 5- methyl-2-furaldehyde were identified in the extracts of natural and toasted wood chips and in the extracts of the wine. Syringaldehyde was identified only in the extracts of the toasted wood chips. Ellagic acid can be regarded as a characteristic compound of barrique wine ageing and its constant level during some periods could become a marker of maturity of barrique wines. Due to the absence of furaldehydes in natural wines, these compounds can be considered as typical components of barrique wines and so they can serve as a marker of authenticity of barrique wines.

In this study, time-dependent changes in the spectrum of phenolic compounds and furaldehydes in one natural red wine (an 80:20 v/v mixture of Cabernet Sauvignon and Merlot) matured in middle- and highly toasted oak-barrels were investigated. Two oak species (Quercus robur and Quercus alba) were compared in a model experiment in order to characterize the kinetics of extraction of these compounds from the toasted wood to wine. The peak identity was confirmed by comparing the retention times and UV-spectra of individual compounds (match factors greater than 995) stored in a user's library [139].

Makris et al used HPLC-DAD to determine nineteen major polyphenolic phytochemicals including hydroxycinnamate derivatives, flavanols, flavonols, and anthocyanins, in 40 experimental red wines. All wines analysed were young (non-aged), produced, and stored under identical conditions, in an effort to minimize the effect of oak wood and vinification technology.

The scope of this study was the utilization of several major polyphenolic components as critical parameters for categorizing young, non-aged, and varietal wines according to region of origin and cultivar, thus eliminating the impact of oak wood, as well as the reactions that might take place during ageing in an oak barrel. Furthermore, vinification and storage of all samples were carried out under identical conditions, to ascertain minimal influence deriving from implementation of techniques or conditions that could substantially alter the polyphenolic composition, thereby resulting in misleading conclusions. Identification was based on comparing retention times of the peaks detected with those of original compounds, and on UV–vis on-line spectral data. The examination was based on the determination of characteristic, predominant polyphenols, which could be very well separated and quantified, employing routine HPLC analysis with conventional diode array detection [140].

### 5.7.4. Meat

Wissiack et al used DAD to determine hemoglobins in meat samples. After cation exchange chromatographic separation and diode array detection, different peak patterns for extracted hemoglobins of cow, lamb or pork meat are obtained. Other heme-group containing proteins like myoglobin or cytochrome C, which could be also detected with diode array detection at 416 nm, were chromatographically separated from the hemoglobins. By the use of these characteristic peak patterns, the species of the meat can be specified permitting the qualitative assessment of meat adulteration with the proposed screening method [141].

## 5.8. Toxicological Studies-Forensic Applications

Forensic drug and toxicology laboratories have an on-going need for rapid, simple assays for screening biological samples suspected of containing drugs and metabolites of toxicological interest.

HPLC is a versatile technique used in this area. DAD is a low cost compromise compared to LC-MS. Spectral information increase the reliability of this technique bringing into use a second criterion besides that of the retention time. HPLC–DAD is broadly used as identification tool in forensic and in emergency toxicology, particularly for detection of drugs of abuse. Compared to LC-MS which is typically used as confirmatory method HPLC-DAD is much less expensive and relatively simple to use [142].

Etorphine is a synthetic narcotic analgesic usually used in veterinary medicine. Elliott and Hale described a method for detecting and quantifying etorphine using HPLC with UV diode array detection (HPLC–DAD) and demonstrated the advantage of the technique for the detection of Immobilon at low doses. This paper describes a method for the detection and quantitation of etorphine in postmortem blood by HPLC–DAD, from a forensic case involving a suspected Large Animal Immobilon overdose.

Post mortem blood specimens from the femoral vein and the heart were analysed and only etorphine and an acepromazine metabolite previously unidentified in humans were detected. Etorphine was identified by retention index value) and by UV spectral matching [143].

Dumestre-Toulet et al applied DAD to investigate a case study of a 43 year old man who was found dead in a hotel during a sexual relation with a colleague. He was treated both for cardiovascular disease and for erectile dysfunction with Viagra. A pillbox was found in the room with several tablets of verapamil, trimetazidine, yohimbine and bromazepam.

Sildenafil and yohimbine were screened with LC/MS and trinitrine with head space injection HS/GC/MS. Verapamil and trimetazidine were identified and quantified with LC/DAD [144].

A fast liquid chromatographic method with tandem diode array–fluorescence detection for the simultaneous determination of in total 17 opium alkaloids and opioids in blood and urine was presented by Dams et al. After solid-phase extraction, based on weak cation exchange, the extracts were examined by HPLC–DAD–FL. Furthermore, the dual detector system allowed to simultaneously perform a general (by diode array detection, for all opiates) and a more specific (by fluorescence detection, only nine opiates) analysis [145].

Fenarimol (Rubigan1) is a pyrimidine ergosterol biosynthesis inhibitor used as a systemic fungicide. Proença et al presentd a fatal fenarimol intoxication case analysed in the Forensic Toxicology Service of the National Institute of Legal Medicine. The results were used to compare two different HPLC techniques, regarding selectivity and sensitivity: an HPLC system with a diode array detector (DAD) and an HPLC system with a DAD and a mass spectrometry detector with an electrospray interface, for the determination of fenarimol concentrations in liver, kidney and gastric content samples. Identification of the analytes was performed through spectral matching.

In the HPLC chromatogram obtained from a postmortem liver specimen spiked with fenarimol followed by DAD detection at 225 nm. The UV spectrum of fenarimol and ethirimol was compared to a user-built library containing a standard spectrum of the same compound.

The ability of DAD to provide information on peak homogeneity combined with mass spectral information such as the pseudo-molecular ion of the molecule simplifies the identification of unknowns and increases confidence in chromatographic peak identification [146].

Duverneuil et al proposed an original liquid chromatography method with photodiode-array detection (DAD) for the determination of strychnine in blood. A case report of fatal strychnine intoxication was reported to demonstrate the suitability of the method [147].

Clobazam (Castillium1, Urbanil1), a benzodiazepine often used as an anxiolytic and in the treatment of epilepsy, is considered a relatively safe drug. Proença et al presented a fatal case with a 49-year-old female, found dead at home. She had been undergoing psychiatric treatment and was a chronic alcoholic. A high-performance liquid chromatography (HPLC)/diode array detector (DAD)/mass spectrometry detection (MSD) with electrospray method was developed in order to detect, confirm and quantify clobazam and its metabolite in the post-mortem samples [148].

Stoll et al developed a method for the detection of drugs of abuse in biological samples based on fast gradient elution liquid chromatography coupled with diode array spectroscopic detection (LC-DAD for screening samples for regulated intoxicants. The method proved that fast gradient chromatography can be used as an effective screening method for drugs of abuse in blood and urine [149].

Porter et applied the chemometric method of target factor analysis (TFA) to the chromatograms of reference 149. The ability to resolve highly overlapped peaks using the spectral data afforded by the DAD is what distinguishes the present method from conventional library searching methods. Herein LC-DAD was proved to be a fast and robust method for screening biological samples in conjunction with a library search algorithm to quickly identify those samples that require confirmatory testing. Because a DAD can collect an entire spectrum at each time point in a chromatogram, the resultant data are information rich and more selective than single wavelength chromatograms. The LC-DAD screening test is fast enough that a second LC analysis on an “orthogonal” stationary phase would be quite feasible, which would further improve the selectivity of the method. The data obtained when using hyphenated instruments are multivariate data. A single LC-DAD experiment produces two way data. All chromatograms were collected on one of the fast LC-DAD systems described in Part I. Using the data obtained on the fast LC-DAD method described in Part I in combination with a TFA algorithm facilitates the identification of those samples that require confirmatory testing [150].

### 5.8.1. Ink Analysis-Ink Dating

The discrimination of different ink components is of great interest in forensic science. Authenticity and ink dating have occupied scientific interest for many years. However, the questions have not yet been fully answered.The composition of inks is complex. Except for the dyes other materials such as solvents (or carriers), fatty acids, resins, surface active agents, corrosion control ingredients, or conductivity salts may be present. Dyes used as coloring materials for inks include different classes as defined by the Color Index. The ability to determine the date when a document was written would be a major breakthrough in forensic science. Many efforts have been expended to determine the actual age of a document by examination of the ink. The exact determination of the absolute age of a document by examination of the ink has been the subject of several studies since more than 30 years. However, the results obtained have not been very promising. The most successful of these include the effect of time on the relative solubility of the ink in different solvents, changes in the relative concentrations of dyestuffs and solvents in the ink as determined by chromatographic and or spectroscopic methods and changes in the IR absorbance spectrum of the ink over time. Initially, methods of ink dating aimed to detect backdating by proving that the ink entry on the document was not available at the time that the document was written. Later on, attempts were made for the absolute or relative determination of age of writing. Several factors are supposed to affect the written line. Among them are the pen-mechanism and ink, writing speed, point load, writing angle, writing direction, and writing surface. Except for the first, all others are controlled by the writer. Moreover, storage lighting conditions might cause differences even with entries of the same age.

Samanidou et al applied an HPLC-PDAD Method for the identification of ballpoint pen ink components (blue violet, fuchsin, pararosaniline, crystal violet, and victoria blue) study of their decomposition on aging for forensic science applications the method can be used in order to characterize ink entries from different suppliers over different time intervals [151].

## 5.9. Environmental Analysis

PDA detector meets to a great extent the requirements needed for environmental samples, which are usually characterized by extremely low concentrations, a wide polarity range of complex matrices.

Lacorte et al used DAD for the monitoring of of terbuthylazine in river water. Identification was by retention time and spectral comparison with a library search. One of the main advantages of the system was that allowed the results to be confirmed by retention time and by comparison with data in a library, without having to use more sophisticated techniques such as MS [152].

Fernandez-Alba et al applied HPLC-DAD to the determination of a selected group of insecticides and fungicides in ground water samples [153].

E. Rodríguez et al applied HPLC/DAD to the determination of the pesticide diflubenzuron (DFB) and its main metabolites: 2, 6-diflurobenzamide (2,6- DFBA), 4-chlorophenylurea (4-CPU), 4-chloroacetanilide (4-CAA), 4-chloroaniline (4-CA) and N-methyl-4-chloroaniline (NM-4-CA) in forestry matrices. The DAD detector was set at 245 and 260 nm, where the compounds show secondary maxima of absorbance which do not interfere with the matrix.

DAD takes advantage of the possibility that the software of this equipment offers to make an accurate chromatographic diagnosis by evaluating match factors of peak purity and identifying the peaks by spectral analysis [154].

Liquid chromatography with photodiode array detection (LC–DAD) and liquid chromatography with mass spectrometry (LC–MS) are two techniques that have been widely used in monitoring pesticides and their degradation products in the environment. Jeannot et al in their study, compared these methods for the multi-residue analysis of forty-eight pesticides belonging to eight different classes (triazine, amide, phenylurea, triazole, triazinone, benzimidazole, morpholine, phenoxyalkanoic), along with some of their degradation products, which were monitored on a regular basis in the surface waters collected from the central and southeastern regions of France, and from the St. Lawrence River in Canada. There was good correlation between the LC–DAD and LC–MS techniques for 60 samples [155].

Garrido Frenich et al described the use of HPLC-DAD for analysing and sampling imidacloprid and its metabolite 6-chloronicotinic acid in greenhouse air. Diode-array detection (DAD) provided spectral confirmation capability required to eliminate false positives [156].

As with many other pesticide metabolites, high-performance liquid chromatography is needed for the analysis of chloroacetanilide herbicide metabolites because they are ionic compounds and are not sufficiently volatile for analysis by gas chromatography. HPLC-diode array detection/DAD is very useful in determining metabolite concentrations, especially when the water sample is relatively free of humic materials and ionic surfactants that can cause chromatographic interference. Hostetler and Thurman applied HPLC-DAD to the analysis of chloroacetanilide herbicide metabolites of ethanesulfonic acid and oxanilic acid metabolites of alachlor, acetochlor, and metolachlor in surface water and ground water. Information about the fate and transport of the chloroacetanilide herbicides alachlor, acetochlor and metolachlor in water can be acquired from the analysis of field-runoff water and ground water from nearby wells. The method also can be useful for water-quality determinations and analytical verification in toxicological studies [157].

López de Alda and Barceló used DAD for the determination of six estrogens (17b-estradiol, estriol, estrone, ethynylestradiol, mestranol, and diethylstilbestrol) and four progestogens (progesterone, levonorgestrel, norethindrone and ethynodiol diacetate) in several types of water bodies, including sewage influents and effluents, surface water and drinking water. Diethylstilbestrol and levonorgestrel, and ethinylestradiol and estrone, are partially coeluted, making it difficult to use the UV detector. All steroid hormones as well as the synthetic analogues have in common the cyclopentanophenanthrene nucleus. With the exception of diethylstilbestrol, which is a non-ster oidal compound, all analytes possess one methyl group (an ethyl group in the case of levonorgestrel) at position C-13, one or two substituents at position C-17, and an oxygen atom in the form of either a hydroxyl group or a carbonyl group, at C-3. However, estrogens and progestogens differ in their ring. A structure, which is fully unsaturated (aromatic) in the former whereas in the later has only one alkene-ype double bond (C=C) at 4.5-position, and this difference is responsible for their distinctive UV spectra [158].

Martins et al used HPLC-DAD to study the degradation and ecotocity of sulfonylurea herbicide rimsulfuron and its major metabolites in batch samples of an alluvial sandy loam in freshwater. The method was adapted to simultaneously identify and quantify rimsulfuron and its metabolites. The chemicals were identified with a DAD on the basis of their UV spectra [159].

Papadoyannis et al applied DAD to the determination of anthracene and its oxidation products, anthraquinone, and 1-hydroxyanthraquinone in surface waters river and lake water samples from Northern Greece [160].

Bobeldijk et al used DAD for the identification of environmental pollutants e.g. pesticides, like phenylurea herbicides, in raw surface water as well as infiltrated and drinking water [161].

Filipkowska et al applied DAD to the determination of Polycyclic Aromatic Hydrocarbons (PAHs) in marine samples of various types, i.e. seawater, sediment and mussel homogenate samples [162].

Gatidou et al proposed HPLC-DAD for the simultaneous determination of two antifouling booster biocides, diuron (1-(3,4 dichlorophenyl) 3,3 dimethyl urea) and irgarol 1051 (2-methylthio-4-*tert*-butylamino-6-cyclopropylamino-*s*-triazine), and their metabolites, DCPMU (1-(3,4 dichlorophenyl)-3 methyl urea), DCPU (1-(3,4 dichlorophenyl) urea), DCA (3,4 dichloroaniline) and M1 (2-methylthio-4-*tert*-butylamino-*s*-triazine) in seawater. The identification of the six substances in the samples was accomplished on the basis of their retention times and by comparison between the UV spectrum of the compounds in the standard solutions and the UV spectrum of the detected peak in the sample. A match equal or higher than 99% was fixed to confirm identification between both spectra for all the compounds [163].

Sanchez-Ortega et al used LC-DAD for the analysis of the insecticide fenitrothion and its two main environmental metabolites, fenitrooxon and 3-methyl-4-nitrophenol metabolites in a water matrix [164].

Benito-Pena et al developed a novel and simple method for the simultaneous determination of beta-lactam antibiotics (BLAs) (penicillin G, amoxicillin, ampicillin, penicillin V, oxacillin, cloxacillin, dicloxacillin and nafcillin) in wastewater by HPLC-DAD [165].

## 5.10. Fuel

HPLC analysis methods for the separation of crude oils and oil fractions into component groups (saturates, aromatics, polars) are widely used. Varotsis et al investigated the applicability of the evolving factor analysis (EFA) in the characterization of the non-saturated fraction of petroleum mixtures by high performance liquid chromatography coupled with UV diode array detection (HPLC-UV-DAD). EFA was used to interpret the signal obtained from the analysis of fluids, the aromatic peaks of which overlap to a great extent.

The EFA method provides satisfactory estimations of the spectra patterns present in the ultraviolet diode array detection (UV-DAD) signal, as well as of the elution profiles of the components. The data matrix produced by a UV-DAD consists of rows and columns which store the spectra taken at different times and the chromatograms measured at different wavelengths respectively. It can be reproduced by multiplying the spectra patterns by the concentration profiles. The mathematical basis for the spectrum pattern identification is the singular value decomposition of time segments in the original data matrix. Each singular value corresponds to a different pattern present in the current time segment. This analysis has already been applied successfully for the peak purity control in HPLC by identifying the presence of irrelevant spectra patterns which correspond to the impurities 9-11. It can also provide an estimation of the impurity concentration in the original sample.

The EFA method was firstly applied to the UV-DAD signal obtained from the HPLC analysis of a synthetic mixture prepared from three aromatic components. The chromatographic conditions were selected so that the eluted components strongly overlapped. The developed method determined both the initial and final elution times of each component. These times were subsequently used to deconvolve the UV-DAD signal of the mixture in three clearly defined elution profiles and to perform quantitative analysis.

Subsequently, the method was applied to the UV-DAD signal obtained from the analysis of lubricant base oil [166].

Kaminski et al developed an HPLC-DAD methhod for the determination of class composition of gasoline and its components including saturated hydrocarbons, alkenes and aromatic compounds in gasoline meeting modern quality standards. A DAD signal integrated over the 207–240 nm range was used to determine alkenes. This eliminates the necessity of separating alkenes from saturates, because the latter do not absorb UV radiation above 200 nm. The content of aromatic hydrocarbons is determined by means of a refractive index detector [167].

## 6. CONCLUSION

The PDA detector is generally considered as the most versatile and useful detector for everyday use in liquid chromatographic analysis. It provides UV spectra of eluting peaks in addition to monitoring the absorbance of the HPLC eluent. It is the detector of choice for method development and for monitoring impurities. Low sensitivity which was conidered to be a drawback in earlier models has been improved significantly in recent years. So, modern PDAs have sensitivity performance close to the benchmark level of $\pm 1 \times 10^{-5}$AU for UV/Vis detectors. Further sensitivity enhancement is due to the advanced flow cell design using fiber-optics technology to extend the path length without increasing noise or chromatographic band dispersion. This type of flow cell is especially important in micro HPLC for samples of limited availability. Another noteworthy development is a programmable slit design, which allows the user to select for either high detector sensitivity (wider slit) or high spectral resolution (narrower slit) [6].

The diode array detector is likely to continue as the 'workhorse' detector for liquid chromatography for many years to come. The design of the PDA detector has changed over the last decade and its performance has been only significantly improved especially when compared to single UV detectors. Changes that may appear likely in the future, concern improved sensitivity and cell design. In addition, software has been designed to evaluate peak purity with diode array-generated data.

Before the introduction of the DAD in HPLC analysis, mass spectrometry was the sole domain in peak identification for gas or liquid chromatography (GC-MS or LC-MS). This can now be achieved as part of the HPLC analysis and at a lower cost. Benefits of LC-MS are provided at lower cost. However integrated PDA with Mass Detector enforces PDA benefits, enables PDA peak purity to investigate peak homogeneity UV and mass spectral information to be used from the same run for positive compound identification UV monitoring of separation for diagnostic purposes and quantitation.

Taken all the above into consideration is perfect justified why there are numerous applications of HPLC-DAD in all analytical fields.

## REFERENCES

[1] Huber, L and George S. Diode Array Detection in HPLC. Chromatographic Science Series. Marcel Dekker Inc. New York; 1993.

[2] Kenkel, J. Analytical Chemistry for Technicians. Third Edition. CRC Press, LLC; 2003.

[3] UV/Vis Diode Array Detector Model SPD-M10Avp, Instruction Manual. Shimadzu Corporation, Kyoto Japan.

[4] Jones, K. Affinity Separation, Freeport, Ballsall, Isle of Man, UK, Affinity Chromatography Ltd; 2000.

[5] Ahuja S. and Jespersen N. (Eds) Comprehensive Analytical Chemistry Volume 47**.** Elsevier, 2006.

[6] Dong, M.W. Modern HPLC for Practicing Scientists. John Wiley & Sons Inc. Hoboken, New Jersey; 2006.

[7] McMaster, M.C. HPLC A Practical User's Guide, Second Editon. John Wiley & Sons Inc. Hoboken, New Jersey; 2007.

[8] Papadoyannis, I; and Gika, H. Peak Purity Determination with a Diode Array Detector *Journal of Liquid Chromatography & Related Technologies*, 2004 27(6), 1083 – 1092.

[9] Papadoyannis, I; and Gika, H. Peak Purity Determination with a Diode Array Detector *Encyclopedia of Chromatography: Second Edition*, 2005, 1198 – 1202.

[10] Snyder, L.R., Kirkland, J.J. and Glajch, J.L. Practical HPLC Method Development, John Wiley & Sons Inc. Hoboken, New Jersey; 1997.

[11] Hewlett Packard, Peak purity analysis in HPLC and CE using diode- array technology, Product note. 1993

[12] Papadoyannis, I.; and Gika, G. Peak Identification with a Diode Array Detector *Encyclopedia of Chromatography: Second Edition*, 2005, 1192 – 1197.

[13] Bogomolov, A.; and McBrien, M. Mutual peak matching in a series of HPLC–DAD mixture analyses. *Analytica Chimica Acta* 2003 490, 41–58.

[14] Lindholm, J.; Johansson, M.; and Fornstedt T. Guidelines for analytical method development and validation of biotechnological synthesis of drugs Production of a hydroxyprogesterone as model. *Journal of Chromatography B* 2003 791, 323–336.

[15] Yamamoto, H.; Hada, K.; Yamaji, H.; Katsuda, T.; Ohno, H.; and Fukuda, H. Application of regularized alternating least squares and independent component analysis to HPLC-DAD data of Haematococcus pluvialis metabolites. *Biochemical Engineering Journal* 2006 32, 149–156.

[16] Ferreiros, N.; Iriarte, G.; Alonso, R.M.; and Jimenez, R.M. Development of a solid phase extraction procedure for HPLC–DAD determination of several angiotensin II receptor antagonists in human urine using mixture design. *Talanta* 2007 73, 748–756.

[17] Braga, J.W.B.; Bottoli, C.B.G.; Jardim, I.C.S.F.; Goicoechea, H.C.; Olivieri, A.C.; and Poppi, R.J. Determination of pesticides and metabolites in wine by high performance liquid chromatography and second-order calibration methods. *Journal of Chromatography A* 2007 1148, 200–210.

[18] Carneiro, R.L.; Braga, J.W.B.; Bottoli, C.B.G.; and Poppi, R.J. Application of genetic algorithm for selection of variables for the BLLS method applied to determination of pesticides and metabolites in wine. *Analytica Chimica Acta* 2007 595, 51–58.

[19] Chatzimichalakis, P.F.; Samanidou, V.F.; and Papadoyannis, I.N. Development of a validated liquid chromatography method for the simultaneous determination of eight fat-soluble vitamins in biological fluids after solid-phase extraction. *Journal of Chromatography B* 2004 805, 289–296.

[20] Gika, H.G.; Samanidou, V.F.; and Papadoyannis, I.N. Development of a validated HPLC method for the determination of iodotyrosines and iodothyronines in pharmaceuticals and biological samples using solid phase extraction. *Journal of Chromatography B* 2005 814, 163–172.

[21] Samanidou, V.; Evaggelopoulou E.; and Papadoyannis, IN. Development of a validated HPLC method for the determination of four penicillin antibiotics in pharmaceuticals and human biological fluids. *Journal of Separation Science* 2006 29 (11), 1550-1560.

[22] Uddin, M.N.; Samanidou, V.F.; and Papadoyannis, I.N. Development and Validation of an HPLC Method for the Determination of Six 1,4-Benzodiazepines in Pharmaceuticals and Human Biological Fluids. *Journal of Liquid Chromatography & Related Technologies* 2008 31, 1258–1282.

[23] Uddin, M.N.; Samanidou, V.F.; and Papadoyannis, I.N. Development and validation of an HPLC method for the determination of benzodiazepines and tricyclic antidepressants in biological fluids after sequential SPE. *Journal of Separation Science* 2008 31, 2358 – 2370.

[24] Georga, K. A.; Samanidou, V. F.; and Papadoyannis, I. N. Improved micro-method for the HPLC analysis of caffeine and its dimethylated metabolites in human biolofical fluids after SPE. *Journal of Liquid Chromatography & Related Technologies* 2000 23(10), 1523–1537.

[25] Schmidt, C.K.; Volland, J.; Hamscher, G.; and Nau, H. Characterization of a new endogenous vitamin A metabolite. *Biochimica et Biophysica Acta* 2002 1583, 237–251.

[26] Labat, L.; Deveaux, M.; Dallet, P.; and Dubost, J.P. Separation of new antidepressants and their metabolites by micellar electrokinetic capillary chromatography. *Journal of Chromatography B* 2002 773, 17–23.

[27] Bugamelli, F.; Sabbioni, C.; Mandrioli, R.; Kenndler, E.; Albani, F.; and Raggi, M.A. Simultaneous analysis of six antiepileptic drugs and two selected metabolites in human plasma by liquid chromatography after solid-phase extraction. *Analytica Chimica Acta* 2002 472, 1–10.

[28] Caubet, M.-S.; Elbast, W.; Dubuc, M.-C.; and Brazier, J.-L. Analysis of urinary caffeine metabolites by HPLC-DAD: the use of metabolic ratios to assess CYP1A2 enzyme activity. *Journal of Pharmaceutical and Biomedical Analysis* 2002 27, 261–270.

[29] Tarbah, F.; Mahler, H.; Kardel, B.; Weinmann, W.; Hafner, D.; and Daldrup, T. K inetics of kavain and its metabolites after oral application. *Journal of Chromatography B* 2003789, 115–130.

[30] Keppler, K.; Humpf, H.-U. Metabolism of anthocyanins and their phenolic degradation products by the intestinal microflora. *Bioorganic & Medicinal Chemistry* 2005 13, 5195–5205.

[31] Wille, S.M.R.; Maudens, K.E.; Van Peteghem, C.H.; and Lambert, W.E.E. Development of a solid phase extraction for 13 ‘new’ generation antidepressants and their active metabolites for gas chromatographic–mass spectrometric analysis. *Journal of Chromatography A* 2005 1098, 19–29.

[32] Frassanito, R.; Cantonati, M.; Tardıo, M.; Mancini, I.; and Guella, G.; On-line identification of secondary metabolites in freshwater microalgae and cyanobacteria by combined liquid chromatography–photodiode array detection-mass spectrometric techniques. *Journal of Chromatography A* 2005 1082, 33–42.

[33] Fernandez, P.; Morales, L.; Vazquez, C.; Bermejo, A.M.; and Tabernero, M.J. HPLC–DAD determination of opioids, cocaine and their metabolites in plasma. *Forensic Science International* 2006 161, 31–35.

[34] de Castro, A.; del Mar Ramirez Fernandez, M.; Laloup, M.; Samyn, N.; De Boeck, G.; Wood, M.; Maes, V.; Lopez-Rivadulla, M. High-throughput on-line solid-phase extraction–liquid chromatography–tandem mass spectrometry method for the simultaneous analysis of 14 antidepressants and their metabolites in plasma. *Journal of Chromatography A* 2007 1160, 3–12.

[35] Nobilis, M.; Jira, T.; Lısa, M.; Holcapek, M.; Szotakova, B.; Lamka, J.; and Skalova, L. A chiral and chiral high-performance liquid chromatographic determination of flubendazole and its metabolites in biomatrices using UV photodiode-array and mass spectrometric detection. *Journal of Chromatography A* 2007 1149, 112–120.

[36] Mertens, B.; Cahay, B.; Klinkenberg, R.; and Streel, B. An automated method for the simultaneous determination of pravastatin, 3-hydroxy isomeric metabolite, pravalactone and fenofibric acid in human plasma by sensitive liquid chromatography combined with diode array and tandem mass spectrometry detection. *Journal of Chromatography A* 2008 1189, 493–502.

[37] Xie, Y.; Zhou, H.; Wong, Y.-F.; Xu, H.-X.; Jiang, Z.-H.; and Liu, L. Study on the pharmacokinetics and metabolism of paeonol in rats treated with pure paeonol and an herbal preparation containing paeonol by using HPLC–DAD-MS method. *Journal of Pharmaceutical and Biomedical Analysis* 2008 46, 748–756.

[38] Nasir Uddin,M; Samanidou,V; and Papadoyannis, IN. Validation of SPE-HPLC determination of 1,4-benzodiazepines and metabolites in blood plasma, urine and saliva. *Journal of Separation Science* 2008 31, 3704 – 3717.

[39] Colombo, S.; Beguin, A.; Marzolini, C.; Telenti, A.; Biollaz, J.; and Decosterd, L.A. Determination of the novel non-peptidic HIV-protease inhibitor tipranavir by HPLC–UV after solid-phase extraction. *Journal of Chromatography B* 2006 832, 138–143.

[40] Vermeij, T.A.C.; and Edelbroek, P.M. Robust isocratic high performance liquid chromatographic method for simultaneous determination of seven antiepileptic drugs including lamotrigine, oxcarbazepine and zonisamide in serum after solid-phase extraction. *Journal of Chromatography B* 2007 857, 40–46.

[41] Desrivot, J.; Moussa, F.; Champy, P.; Fournet, A.; Figadere, B.; and Herrenknecht, C. Development of a SPE/HPLC/DAD method for the determination of antileishmanial 2-substituted quinolines and metabolites in rat plasma. *Journal of Chromatography B* 2007 854, 230–238.

[42] Mercolini, L.; Mandrioli, R.; Conti, M.; Leonardi, C.; Gerra, G.; Raggi, M.A. Simultaneous determination of methadone, buprenorphine and norbuprenorphine in biological fluids for therapeutic drug monitoring purposes. *Journal of Chromatography B* 2007 847, 95–102.

[43] Lancelin, F.; Djebrani, K.; Tabaouti, K.; Kraoul, L.; Brovedani, S.; Paubel, P.; Piketty, M.-L. Development and validation of a high-performance liquid chromatography method using diode array detection for the simultaneous quantification of aripiprazole and dehydro-aripiprazole in human plasma. *Journal of Chromatography B* 2008 867, 15–19.

[44] Musenga, A;. Addolorata Saracino, M.; Spinelli, D.; Rizzato, E.; Boncompagni, G.; Kenndler, E.; and Raggi, M.A. Analysis of the recent antipsychotic aripiprazole in human plasma by capillary electrophoresis and high-performance liquid chromatography with diode array detection. *Analytica Chimica Acta* 2008 612, 204–211.

[45] Lee, S.-H.; Yoo, S.D.; and Lee, K.-H. Rapid and sensitive determination of paclitaxel in mouse plasma by high-performance liquid chromatography. *Journal of Chromatography B* 1999 724, 357–363.

[46] Samanidou,V; Christodoulou, E.; and Papadoyannis, IN. Validation of a novel HPLC sorbent material for the determination of ten quinolones in human and veterinary pharmaceutical formulations. *Journal of Separation Science* 2005 28 (18), 2444-2453.

[47] Kucuk, A.; Kadıoglu, Y.; and Celebi, F. Investigation of the pharmacokinetics and determination of tramadol in rabbit plasma by a high-performance liquid chromatography–diode array detector method using liquid–liquid extraction. *Journal of Chromatography B* 2005 816, 203–208.

[48] Jacobson, G.A.; Martinod, S.; and Cunningham, C.P. Determination of ceftiofur in bovine plasma by HPLC-DAD. *Journal of Pharmaceutical and Biomedical Analysis* 2006 40, 1249–1252.

[49] Yang, B.; Meng, Z.Y.; Yan, L.P.; Dong, J.X.; Zou, L.B.; Tang, Z.M.; and Dou, G.F. Pharmacokinetics and metabolism of 1,5-dicaffeoylquinic acid in rats following a single intravenous administration. *Journal of Pharmaceutical and Biomedical Analysis* 2006 40, 417–422.

[50] Zhang, Y.-s.; Zhang, Q.-y.; Li, L.-y.; Wang, B.; Zhao, Y.-y.; and Guo, D.-a. Simultaneous determination and pharmacokinetic studies of dihydromyricetin and myricetin in rat plasma by HPLC-DAD after oral administration of *Ampelopsis grossedentata* decoction. *Journal of Chromatography B* 2007 860, 4–9.

[51] Mertens, B.; Cahay, B.; Klinkenberg, R.; and Streel, B. An automated method for the simultaneous determination of pravastatin, 3-hydroxy isomeric metabolite, pravalactone and fenofibric acid in human plasma by sensitive liquid chromatography combined with diode array and tandem mass spectrometry detection. *Journal of Chromatography A* 2008 1189 , 493–502.

[52] Liang, Y.; Liu, A.-h.; Qin, S.; Sun, J.-h.; Yang, M.; Li, P.; and Guo, D.-a. Simultaneous determination and pharmacokinetics of five bufadienolides in rat plasma after oral administration of Chansu extract by SPE-HPLC method. *Journal of Pharmaceutical and Biomedical Analysis* 2008 46, 442–448.

[53] Wiberg, K. Quantitative impurity profiling by principal component analysis of high-performance liquid chromatography–diode array detection data. *Journal of Chromatography A* 2006 1108, 50–67.

[54] Görög, S.; Babják, M.; Balogh, G.; Brlik, J.; Csehi, A.; Dravecz, F.; Gasdag, M.; Horváth, P.; Laukó, A.; and Varga, K. Drug impurity profiling strategies. *Talanta,* 1997 44, 1517-1526.

[55] Nicolas EC; and Scholz TH. Active drug substance impurity profiling: Part I. LC/UV diode array spectral matching. *J. Pharm. Biomed. Anal.* 16 (1998), *813-824.*

[56] De Braekeleer, K.; De Juan, A.; and Massart, D.L.; Purity assessment and resolution of tetracycline hydrochloride samples analysed using high-performance liquid chromatography with diode array detection. *Journal of Chromatography A* 1999 832, 67–86.

[57] Dulery, B. D.; Verne-Mismer, J.; Wolf, E.; Kugel, C.; and Van Hijfte, L. Analyses of compound libraries obtained by high-throughput parallel synthesis: strategy of quality control by high-performance liquid chromatography, mass spectrometry and nuclear magnetic resonance techniques. *Journal of Chromatography B* 1999 725, 39–47.

[58] Frenich, A.G.; Torres-Lapasio, J.R.; De Braekeleer, K.; Massart, D.L.; Martınez Vidal, J.L.; and Martınez Galera, M. Application of several modified peak purity assays to real complex multicomponent mixtures by high-performance liquid chromatography with diode-array detection. *Journal of Chromatography A* 1999 855, 487–499.

[59] van Zomeren, P.V.; Darwinkel, H.; and Coenegracht, P.M.J.; de Jong, G.J. Comparison of several curve resolution methods for drug impurity profiling using high-performance liquid chromatography with diode array detection. *Analytica Chimica Acta* 2003 487, 155–170.

[60] Wiberg, K.; Andersson, M.; Hagman, A.; and Jacobsson, S.P. Peak purity determination with principal component analysis of high-performance liquid chromatography–diode array detection data. *Journal of Chromatography A* 2004 1029, 13–20.

[61] Burini, G.; and Coli, R. Determination of formaldehyde in spirits by high-performance liquid chromatography with diode-array detection after derivatization. *Analytica Chimica Acta* 2004 51, 155–158.

[62] Vuletic, M.; Cindric, M.; Dogan and Koruznjak, J. Identification of unknown impurities in simvastatin substance and tablets by liquid chromatography/tandem mass spectrometry. *Journal of Pharmaceutical and Biomedical Analysis* 2005 37, 715–721.

[63] Fiori, J.; Grassigli, G.; Filippi, P.; Gotti, R.; and Cavrini, V. HPLC-DAD and LC-ESI-MS analysis of doxycycline and related impurities in doxipan mix, a medicated premix

for incorporation in medicated feedstuff. *Journal of Pharmaceutical and Biomedical Analysis* 2005 37, 979–985.

[64] Li, W.; and Hu, C.-q. Spectral correlation of high-performance liquid chromatography-diode array detection data from two independent chromatographic runs. Peak tracking in pharmaceutical impurity profiling. *Journal of Chromatography A* 2008 1190, 141–149.

[65] Kovaříková, P; Vávrová, K; Tomalová, K; Schöngut, M; Hrušková,K; and Hašková, P; Klimeš, J. J. HPLC-DAD and MS/MS analysis of novel drug candidates from the group of aromatic hydrazones revealing the presence of geometric isomers. *Journal of Pharmaceutical and Biomedical Analysis* 2008 48(2) 295-302.

[66] Paramapojn, S.; Ganzera, M.; Gritsanapan, W.; and Stuppner, H. Analysis of naphthoquinone derivatives in the Asian medicinal plant *Eleutherine americana* by RP-HPLC and LC–MS. *Journal of Pharmaceutical and Biomedical Analysis* 2008 47, 990–993.

[67] 2002/657/EC: Commission Decision of 12 August 2002 implementing Council Directive 96/23/EC concerning the performance of analytical methods and the interpretation of results, *Off. J. Eur. Commun.* 2002, L221, 8-36.

[68] Council Directive 96/23/EC of April 1996 on measures to monitor certain substances and residues thereof in live animals and animal products and repealing Directives 85/358/ EEC and 86/469/EEC and Decisions 89/18/EEC and 91/664/ EEC, *Off. J. Eur. Commun.* 1996, L125, 10–18.

[69] Council Regulation (EEC) No 2377/90 of 26 June 1990 laying down a Community procedure for the establishment of maximum residue limits of veterinary medicinal products in foodstuffs of animal origin. *Off. J. Eur. Commun.* 1990, L 224, 1-8.

[70] Dommarco, R.; Santilio, A.; Fornarelli, L.; and Rubbiani, M. Simultaneous quantitative determination of thirteen urea pesticides at sub-ppb levels on a Zorbax SB-$C_{18}$ column. *Journal of Chromatography A* 1998 825, 200–204.

[71] Martınez Galera, M.; Garrido Frenich, A.; Martınez Vidal, J.L.; and Parrilla Vazquez, P. Resolution of imidacloprid pesticide and its metabolite 6-chloronicotinic acid using cross-sections of spectrochromatograms obtained by high-performance liquid chromatography with diode-array detection. *Journal of Chromatography A* 1998 799, 149–154.

[72] Koole, A.; Franke, J.-P.; and de Zeeuw, R.A. Multi-residue analysis of anabolics in calf urine using highperformance liquid chromatography with diode-array detection. *Journal of Chromatography B* 1999 724, 41–51.

[73] Cinquina, A.L.; Roberti, P.; Giannetti, L.; Longo, F.; Draisci, R.; Fagiolo, A.; and Brizioli, N.R. Determination of enrofloxacin and its metabolite ciprofloxacin in goat milk by high-performance liquid chromatography with diode-array detection. Optimization and validation. *Journal of Chromatography A* 2003 987, 221–226.

[74] Commission of the European Communities, Draft SANCO/1805/2000 Rev. 1, Laying down performance criteria thereof in live animals and animal products according to Council Directive 96/23/EC.

[75] Cinquina, A.L.; Longo, F.; Anastasi, G.; Giannetti, L.; and Cozzani, R. Validation of a high-performance liquid chromatography method for the determination of oxytetracycline, tetracycline, chlortetracycline and doxycycline in bovine milk and muscle. *Journal of Chromatography A,* 2003 987, 227–233.

[76] Rial Otero, R.; Cancho Grande, B.; Simal and Gandara J. Multiresidue method for fourteen fungicides in white grapes by liquid–liquid and solid-phase extraction followed by liquid chromatography–diode array detection. *Journal of Chromatography A* 2003 992, 121–131.

[77] Teixeira, M.J.; Aguiar, A.; Afonso, C.M.M.; Alves, A.; and Bastos, M.M.S.M. Comparison of pesticides levels in grape skin and in the whole grape by a new liquid chromatographic multiresidue methodology. *Analytica Chimica Acta* 2004 513, 333–340.

[78] Garcinuño, R.M.; Fernández-Hernando, P.; and Cámara, C. Simultaneous determination of maneb and its main metabolites in tomatoes by liquid chromatography using diode array ultraviolet absorbance detection. *Journal of Chromatography A* 2004 1043, 225–229.

[79] Marazuela, M.D.; and Moreno-Bondi, M.C. Multiresidue determination of fluoroquinolones in milk by column liquid chromatography with fluorescence and ultraviolet absorbance detection. *Journal of Chromatography,* A 2004 1034, 25–32.

[80] Topuz, S.; Ozhan, G.; and Alpertunga, B. Simultaneous determination of various pesticides in fruit juices by HPLC-DAD. *Food Control* 2005 16, 87–92.

[81] Vinas, P.; Balsalobre, N.; and Hernandez-Cordoba, M. Determination of chloramphenicol residues in animal feeds by liquid chromatography with photo-diode array detection. *Analytica Chimica Acta* 2006 558, 11–15.

[82] Gratacos-Cubarsı, M.; Castellari, M.; and Garcıa-Regueiro, J.A.; Detection of sulphamethazine residues in cattle and pig hair by HPLC–DAD. *Journal of Chromatography B* 2006 832, 121–126.

[83] Barbosa, J.; Moura, S.; Barbosa, R.; Ramos, F.; and da Silveira, M.I.N. Determination of nitrofurans in animal feeds by liquid chromatography-UV photodiode array detection and liquid chromatography-ionspray tandem mass spectrometry. *Analytica Chimica Acta* 2007 586, 359–365.

[84] Vinas, P.; Aguinaga, N.; Campillo, N.; and Hernandez-Cordoba, M. Comparison of stir bar sorptive extraction and membrane-assisted solvent extraction for the ultra-performance liquid chromatographic determination of oxazole fungicide residues in wines and juices. *Journal of Chromatography A* 2008 1194, 178–183.

[85] Nozal, M.J.; Bernal, J.L.; Martın, M.T.; Bernal, J.; Alvaro, A.; Martın, R.; and Higes, M. Trace analysis of fumagillin in honey by liquid chromatography-diode array–electrospray ionization mass spectrometry. *Journal of Chromatography A* 2008 1190, 224–231.

[86] Pecorelli, I.; Bibi, R.; Fioroni, L.; and Galarini, R. Validation of a confirmatory method for the determination of sulphonamides in muscle according to the European Union regulation 2002/657/EC. *Journal of Chromatography A* 2004 1032, 23–29.

[87] Civitareale, C.; Fiori, M.; Ballerini, A.; and Brambilla, G. Identification and quantification method of spiramycin and tylosin in feeding stuffs with HPLC–UV/DAD at 1 ppm level. *Journal of Pharmaceutical and Biomedical Analysis* 2004 36, 317–325.

[88] Posyniak, A.; Mitrowska, K.; Zmudzki, J.; and Niedzielska, J. Analytical procedure for the determination of chlortetracycline and 4-epi-chlortetracycline in pig kidneys. *Journal of Chromatography A* 2005 1088, 169–174.

[89] Samanidou,V; Christodoulou, E; Papadoyannis, IN. Determination of fluoroquinolones in edible animal tissues samples, by High Performance Liquid Chromatography, after Solid Phase Extraction. *Journal of Separation Science* 2005 28(6) 555-565.

[90] Samanidou, V.; Nikolaidou K.; and Papadoyannis I. N. Development and validation of an HPLC confirmatory method for the determination of tetracycline antibiotics residues in bovine muscle according to the European Union regulation 2002/657/EC. *Journal of Separation Science* 2005, 28(17), 2247–2258.

[91] Ortiz, M.C.; Sarabia, L.A.; Garcıa, I.; Gimenez, D.; and Melendez E. Capability of detection and three-way data. *Analytica Chimica Acta* 2006 559, 124–136.

[92] Reig, M.; Mora, L.; Navarro, J.L.; and Toldra, F. A chromatography method for the screening and confirmatory detection of dexamethasone. *Meat Science* 2006 74, 676–680.

[93] Garcıa, I.; Ortiz, M.C.; Sarabia, L.; and Aldama, J.M. Validation of an analytical method to determine sulfamides in kidney by HPLC-DAD and PARAFAC2 with first-order derivative chromatograms. *Analytica Chimica Acta* 2007 587, 222–234.

[94] Berrada, H.; Borrull, F.; Font, G.; Molto, J.C.; and Marc, R.M. Validation of a confirmatory method for the determination of macrolides in liver and kidney animal tissues in accordance with the European Union regulation 2002/657/EC. *Journal of Chromatography A* 2007 1157, 281–288.

[95] Samanidou, V; and Christodoulou, E. Multi-residue HPLC analysis of ten quinolones in milk after solid phase extraction- Validation according to the European Union decision 2002/657/EC. *Journal of Separation Science* 2007 30(15), 2421 – 2429.

[96] Samanidou, V; Nikolaidou, K; and Papadoyannis, I.N. Development and validation of an HPLC confirmatory method for the determination of seven tetracycline antibiotics residues in milk according to the European Union decision 2002/657/EC. *Journal of Separation Science* 30 (15) 2007, 2430 – 2439.

[97] Christodoulou, E; Samanidou, V; Papadoyannis, I.N. Development and Validation of an HPLC confirmatory method for residue analysis of ten quinolones in tissues of various food producing animals, according to the European Union Decision 2002/657/EC. *Journal of Separation Science* 30 (16), 2676 – 2686 (2007).

[98] Christodoulou, E; Samanidou, V; and Papadoyannis, I.N. Validation of an HPLC-UV method according to the European Union Decision 2002/657/EC for the simultaneous determination of ten quinolones in chicken muscle and egg yolk. *Journal of Chromatography B* 2007 859(2) 246-255.

[99] Christodoulou, E; Samanidou, V; and Papadoyannis, I.N. evelopment of an HPLC multi-residue method for the determination of ten quinolones in bovine liver and porcine kidney according to the European Union Decision 2002/657/EC. *Journal of Separation Science* 2008 31, 119 – 127.

[100] Samanidou, V.; Tolika, E; and Papadoyannis, I.N. Development and validation of an HPLC confirmatory method for the residue analysis of four sulphonamides in cow's milk according to the European Union Decision 2002/657/EC. *Journal of Liquid Chromatography & Related Technologies*. 2008 31(9): 1358 – 1372.

[101] Nikolaidou, K; Samanidou, V; and Papadoyannis, I.N. Development and validation of an HPLC method for the determination of seven tetracycline antibiotics residues in chicken muscle and egg yolk according to 2002/657/EC. *Journal of Liquid Chromatography & Related Technologies,* 2008 31(14) 2141–2158.

[102] Nikolaidou,K; Samanidou, V; and Papadoyannis, IN. Development and validation of an HPLC multi-residue method for the determination of seven tetracycline antibiotics residues in bovine liver and kidney according to the European Union Decision 2002/657/EC. *Journal of Liquid Chromatography & Related Technologies,* 2008 31(17): 2523–2540.

[103] Nikolaidou,K; Samanidou, V; and Papadoyannis, I.N. Development and validation of an HPLC confirmatory method for the determination of seven tetracycline antibiotics residues in bovine and porcine muscle tissues according to 2002/657/EC. *Journal of Liquid Chromatography & Related Technologies*, 2008 31(19) 3032–3054.

[104] Samanidou, V.; Antoniou C.; and Papadoyannis, I. Gradient RP-HPLC Determination of free phenolic acids in wines and wine vinegar samples after SPE, with Photodiode Array Identification. *Journal of Liquid Chromatography & Related Technologies* 2001, 24(14) 2161-2176.

[105] de Melo Abreu, S.; Caboni, P.; Cabras, P.; Luigi Garau, V.; and Alves, A. Validation and global uncertainty of a liquid chromatographic with diode array detection method for the screening of azoxystrobin, kresoxim-methyl, trifloxystrobin, famoxadone, pyraclostrobin and fenamidone in grapes and wine. *Analytica Chimica Acta* 2006 573–574, 291–297.

[106] Lai, J.-P.; Lim, Y.H.; Su, J.; Shen, H.-M.; and Ong, C.N. Identification and characterization of major flavonoids and caffeoylquinic acids in three *Compositae* plants by LC/DAD-APCI/MS. *Journal of Chromatography B* 2007 848 , 215–225.

[107] Ruslay, S.; Abas, F.; Shaari, K.; Zainal, Z.; Maulidiani; Sirat, H.; Ahmad Israf, D.; and Lajis, N.H. Characterization of the components present in the active fractions of health gingers (Curcuma xanthorrhiza and Zingiber zerumbet) by HPLC–DAD–ESIMS. Food Chemistry 2007 104, 1183–1191.

[108] Netzel, M.; Netzel, G.; Tian, Q.; Schwartz, S.; and Konczak, I. Native Australian fruits- a novel source of antioxidants for food. *Innovative Food Science and Emerging Technologies* 2007 8, 339–346.

[109] Kang, J.; Zhou, L.; Sun, J.; Han, J.; and Guo, D.-A. Chromatographic fingerprint analysis and characterization of furocoumarins in the roots of *Angelica dahurica* by HPLC/DAD/ESI-MS*n* technique. *Journal of Pharmaceutical and Biomedical Analysis* 2008 47, 778–785.

[110] Lee, J.H.; Kang, N.S.; Shin, S.-O.; Shin, S.-H.; Lim, S.-G.; Suh, D.-Y.; Baek, I.-Y.; Park, K.-Y.; and Ha, T.J. Characterization of Anthocyanins in the Black Soybean (Glycine max L.) by HPLC-DAD-ESI/MS Analysis. *Food Chemistry* 2008, doi: 10.1016/j.foodchem.2008.05.056

[111] Llorach, R.; Martınez-Sanchez, A.; Tomas-Barberan, F.A.; Gil, M.I.; and Ferreres, F. Characterisation of polyphenols and antioxidant properties of five lettuce varieties and escarole. *Food Chemistry* 2008 108, 1028–1038.

[112] Bilia, A.R.; Bergonzi, M.C.; Gallori, S.; Mazzi, G.; and Vincieri, F.F. Stability of the constituents of Calendula, Milk-thistle and Passionflower tinctures by LC-DAD and LC-MS. *Journal of Pharmaceutical and Biomedical Analysis* 2002 30, 613–624.

[113] Escarpa, A.; Morales, M.D.; G and onzález, M.C. Analytical performance of commercially available and unavailable phenolic compounds using real samples by high-performance liquid chromatography–diode-array detection. *Analytica Chimica Acta* 2002 460, 61–72.

[114] Perez-Lozano, P.; Garcıa-Montoya, E.; Orriols, A.; Minarro, M.; Tico, J.R.; and Sune-Negre, J.M. Stability evaluation of amoxicillin in a solid premix veterinary formulation by monitoring the degradation products through a new HPLC analytical method. *Journal of Pharmaceutical and Biomedical Analysis* 2006 42, 192–199.

[115] Bermudez-Soto, M.-J.; Tomas-Barberan, F.-A.; and Garcıa-Conesa, M.-T. Stability of polyphenols in chokeberry (Aronia melanocarpa) subjected to in vitro gastric and pancreatic digestion. *Food Chemistry*, 2007 102, 865–874.

[116] Isacchi, B.; Bergonzi, M.C.; Carnevali, F.; van der Esch, S.A.; Vincieri, F.F.; and Bilia, A.R. Analysis and stability of the constituents of St. John's wort oils prepared with different methods. *Journal of Pharmaceutical and Biomedical Analysis* 2007 45, 756–761.

[117] Xie, Y.; Jiang, Z.-H.; Zhou, H.; Cai, X.; Wong, Y.-F.; Liu, Z.-Q.; Bian, Z.-X.; Xu, H.-X.; and Liu, L. Combinative method using HPLC quantitative and qualitative analyses for quality consistency assessment of a herbal medicinal preparation. *Journal of Pharmaceutical and Biomedical Analysis* 2007 43, 204–212.

[118] Baccouri, O.; Guerfel, M.; Baccouri, B.; Cerretani, L.; Bendini, A.; Lercker, G.; Zarrouk, M.; and Ben Miled,D.D. Chemical composition and oxidative stability of Tunisian monovarietal virgin olive oils with regard to fruit ripening. *Food Chemistry* 2008 109, 743–754.

[119] Brolis, M.; Gabetta, B.; Fuzzati, N.; Pace, R.; Panzeri, F.; and Peterlongo, F. Identification by high-performance liquid chromatography–diode array detection–mass spectrometry and quantification by highperformance liquid chromatography–UV absorbance detection of active constituents of *Hypericum perforatum. Journal of Chromatography A* 1998 825, 9–16.

[120] Arnoldi, L.; Ballero, M.; Fuzzati, N.; Maxia, A.; Mercalli, E.; and Pagni, L. HPLC-DAD-MS identification of bioactive secondary metabolites from *Ferula communis* roots. *Fitoterapia* 2004 75, 342–354.

[121] Horvath, C.R.; Martos, P.A.; and Saxena, P.K. Identification and quantification of eight flavones in root and shoot tissues of the medicinal plant Huang-qin (*Scutellaria baicalensis* Georgi) using high-performance liquid chromatography with diode array and mass spectrometric detection. *Journal of Chromatography A* 2005 1062, 199–207.

[122] Wu, Q.; and Gu, Y. Quantification of huperzine A in *Huperzia serrata* by HPLC-UV and identification of the major constituents in its alkaloid extracts by HPLC-DAD-MS-MS. *Journal of Pharmaceutical and Biomedical Analysis* 2006 40, 993–998.

[123] Blanc, R.; Espejo, T.; Lopez-Montes, A.; Torres, D.; Crovetto, G.; Navalon, A.; and Vılchez, J.L. Sampling and identification of natural dyes in historical maps and drawings by liquid chromatography with diode-array detection. *Journal of Chromatography A* 2006 1122, 105–113.

[124] Fang, Z.; Zhang, M.; and Wang, L. HPLC-DAD-ESIMS analysis of phenolic compounds in bayberries (Myrica rubra Sieb. et Zucc.). *Food Chemistry* 2007 100, 845–852.

[125] Chen, J.; Song, Y.; and Li, P. Capillary high-performance liquid chromatography with mass spectrometry for simultaneous determination of major flavonoids, iridoid glucosides and saponins in Flos Lonicerae. *Journal of Chromatography A* 2007 1157, 217–226.

[126] Garcıa-Falcon, M.S.; Perez-Lamela, C.; Martınez-Carballo, E.; and Simal-Gandara, J. Determination of phenolic compounds in wines: Influence of bottle storage of young red wines on their evolution. *Food Chemistry* 2007 105, 248–259.

[127] Lin, L.-Z.; Mukhopadhyay, S.; Robbins, R.J.; and Harnly, J.M. Identification and quantification of flavonoids of Mexican oregano (Lippia graveolens) by LC-DAD-ESI/MS analysis. *Journal of Food Composition and Analysis* 2007 20, 361–369.

[128] Carmona, M.; Sanchez, A.M.; Ferreres, F.; Zalacain, A.; Tomas-Barberan, F.; and Alonso, G.L. Identification of the flavonoid fraction in saffron spice by LC/DAD/MS/MS: Comparative study of samples from different geographical origins. *Food Chemistry* 2007 100, 445–450.

**[129]** Fügel, R., Carle, R. & Schieber, A. Quality and authenticity control of fruit purées, fruit preparations and jams—a review. *Trends in Food Science & Technology* 2005 16(10), 433-441.

[130] Versari, A.; Biesenbruch, S.; Barbanti D.; and Farnell, P.J. Adulteration of Fruit Juices: Dihydrochalcones as Quality Markers for Apple Juice Identification. *Lebens m.-Wiss. u.-Technol.* 1997 30, 585–589.

[131] Silva, B.M.; Andrade, P.B.; Valentao, P.; Mendes, G.C.; Seabra, R.M.; and Ferreira, M.A. Phenolic prole in the evaluation of commercial quince jellies authenticity. *Food Chemistry* 2000 71, 281-285.

[132] Stintzing, F.C.; Trichterborn, J.; and Carle, R. Characterisation of anthocyanin–betalain mixtures for food colouring by chromatic and HPLC-DAD-MS analyses. *Food Chemistry* 2006 94, 296–309.

[133] Kurz, C.; Carle, R.; and Schieber, A. HPLC-DAD-MS characterisation of carotenoids from apricots and pumpkins for the evaluation of fruit product authenticity. *Food Chemistry* 2008 110, 522–530.

[134] Jung, J.; Hermanns-Clausen, M.; and Weinmann, W. Anorectic sibutramine detected in a Chinese herbal drug for weight loss. *Forensic Science International* 2006 161. 221–222.

[135] Zou Z. M**.**; Zhang, H. W.; Srivastava, K. D.; Sampson H. A,; and Li, X. M. Identification and Standardization of Anti Food Allergy Chinese Herbal Formula FAHF-5 by HPLC Chromatographic Fingerprint. *Journal of Allergy and Clinical Immunology*, 2004, S154.

[136] Alonso-Salces, R.M.; Ndjoko, K.; Queiroz, E.F.; Ioset, J.R.; Hostettmann, K.; Berrueta, L.A.; Gallo, B.; and Vicente, F. On-line characterisation of apple polyphenols by liquid chromatography coupled with mass spectrometry and ultraviolet absorbance detection. *Journal of Chromatography A* 2004 1046, 89–100.

[137] Jung, J.; Hermanns-Clausen, M.; and Weinmann, W. Anorectic sibutramine detected in a Chinese herbal drug for weight loss. *Forensic Science International* 2006 161, 221–222.

[138] Koh, H.L.; Wang, H.; Zhou, S.; Chan, E.; Woo, S.O. Detection of aristolochic acid I, tetrandrine and fangchinoline in medicinal plants by high performance liquid chromatography and liquid chromatography/mass spectrometry. *Journal of Pharmaceutical and Biomedical Analysis* 2006 40, 653–661.

[139] Matejıcek, D.; Mikes, O.; Klejdus, B.; Sterbova, D.; and Kuban, V. Changes in contents of phenolic compounds during maturing of barrique red wines. *Food Chemistry* 2005 90, 791–800.

[140] Makris, D.P.; Kallithraka, S.; and Mamalos, A. Differentiation of young red wines based on cultivar and geographical origin with application of chemometrics of principal polyphenolic constituents. *Talanta* 2006 70, 1143–1152.

[141] Wissiack, R.; de la Calle, B.; Bordin, G.; and Rodriguez, A.R; Screening test to detect meat adulteration through the determination of hemoglobin by cation exchange chromatography with diode array detection. *Meat Science* 2003 64, 427–432.

[142] Bogusz, M.J. Hyphenated liquid chromatographic techniques in forensic toxicology, Review. *Journal of Chromatography B* 1999 733, 65–91.

[143] Elliott, S.P.; and Hale, K.A. Analysis of etorphine in postmortem samples by HPLC with UV diode-array detection. *Forensic Science International* 1999 101, 9–16.

[144] Dumestre-Toulet, V.; Cirimele, V.; Gromb, V.; Belooussooff, T.; Lavault, D.; Ludes, B.; and Kintz, P. Last performance with Viagra: post-moderm identification of sildenafil and its metabolites in biological specimens including hair sample. *Forensic Science International* 2002 126, 71-76.

[145] Dams, R.; Benijts, T.; Lambert, W.E.; and De Leenheer, A.P. Simultaneous determination of in total 17 opium alkaloids and opioids in blood and urine by fast liquid chromatography–diode array detection–fluorescence detection, after solid-phase extraction. *Journal of Chromatography B* 2002 773, 53–61.

[146] Proenca, P.; Pinho Marques, E.; Teixeira, H.; Castanheira, F.; Barroso, M.; Avila, S.; and Vieira, D.N. A fatal forensic intoxication with fenarimol: analysis by HPLC/DAD/MSD. *Forensic Science International* 2003 133, 95–100.

[147] Duverneuil, C.; de la Grandmaison, G.L.; de Mazancourt, P.; and Alvarez, J.-C. Liquid chromatography/photodiode array detection for determination of strychnine in blood: a fatal case report. *Forensic Science International* 2004 141, 17–21.

[148] Proenca, P.; Teixeira, H.; Pinheiro, J.; Marques, E.P.; and Vieira, D.N. Forensic intoxication with clobazam: HPLC/DAD/MSD analysis. *Forensic Science International* 2004 143, 205–209.

[149] Stoll, DR.; Li,X.; Wang,X; Carr, PW; Porter, S; and Rutan, S. Fast, comprehensive two-dimensional liquid chromatography. *Journal of Chromatography A*, *2007 1168 (1-2) 3-43.*

[150] Porter, S.E.G.; Stoll, D.R.; Paek, C.; Rutan, S.C.; and Carr, P.W. Fast gradient elution reversed-phase liquid chromatography with diode-array detection as a high-throughput screening method for drugs of abuse II. Data analysis. *Journal of Chromatography A* 2006 1137, 163–172.

[151] Samanidou, V. F.; Nikolaidou, K. I.; and Papadoyannis, I. N. Development and Validation of a Gradient- HPLC-PDAD Method for the Identification of Ballpoint Pen Ink Components: Study of Their Decomposition on Aging for Forensic Science Applications. *Journal of Liquid Chromatography & Related Technologies.* 2004 Vol. 27, No. 2, 215–235.

[152] Lacorte, S.; Vreuls, J.J.; Salau, J.S.; Ventura, F.; and Barcelo, D. Monitoring of pesticides in river water using fully automated on-line solid-pase extraction and liquid chromatography with diode array detection with a novel filtration device. *Journal of Chromatography A* 1998 795, 71–82.

[153] Fernandez-Alba, A.R.; Aguera, A.; Contreras, M.; Penuela, G.; Ferrer, I.; and Barcelo, D. Comparison of various sample handling and analytical procedures for the monitoring

of pesticides and metabolites in ground waters. *Journal of Chromatography A* 1998 823, 35–47.

[154] Rodriguez, E.; Barrio, R.J.; Goicolea, A.; and Gomez de Balugera, Z. Determination of diflubenzuron and its main metabolites in forestry matrices by liquid chromatography with on-line diode-array and electrochemical detection. *Analytica Chimica Acta* 1999 384, 63-70.

[155] Jeannot, R.; Sabik, H.; Sauvard, E.; and Genin, E. Application of liquid chromatography with mass spectrometry combined with photodiode array detection and tandem mass spectrometry for monitoring pesticides in surface waters. *Journal of Chromatography A* 2000 879, 51–71.

[156] Garrido Frenich, A.; Egea Gonzalez, F.J.; Martınez Vidal, J.L.; Parrilla Vazquez, P.; and Mateu Sanchez, M. Determination of imidacloprid and its metabolite 6-chloronicotinic acid in greenhouse air by high-performance liquid chromatography with diode-array detection. *Journal of Chromatography A* 2000 869, 497–504.

[157] Hostetler, K.A.; and Thurman, E.M. Determination of chloroacetanilide herbicide metabolites in water using high-performance liquid chromatography-diode array detection and high-performance liquid chromatography/mass spectrometry. *The Science of the Total Environment* 2000 248, 147-155.

[158] Lopez de Alda, M.J.; and Barcelo, D. Determination of steroid sex hormones and related synthetic compounds considered as endocrine disrupters in water by liquid chromatography–diode array detection–mass spectrometry. *Journal of Chromatography A* 2000 892, 391–406.

[159] Martins, J.M.F.; Chevre, N. S.; Pack, L.; Tarradellas, J.; and Mermoud, A. Degradation in soil and water and ecotoxicity of rimsulfuron and its metabolites. *Chemosphere* 2001 45, 515-522.

[160] Papadoyannis, I. N.; Zotou, A.; and Samanidou, V. F. Development of a solid phase extraction protocol for the simultaneous determination of anthracene and its oxidation products in surface waters by RP-HPLC. *Journal of Liquid Chromatography & Related Technologies.* 2002 Vol. 25, No. 17, 2635–2653.

[161] Bobeldijk, I.; Stoks, P.G.M.; Vissers, J.P.C.; Emke, E.; van Leerdam, J.A.; Muilwijk , B.; Berbee, R.; Noij, and Th.H.M. Surface and wastewater quality monitoring: combination of liquid chromatography with (geno)toxicity detection, diode array detection and tandem mass spectrometry for identification of pollutants. *Journal of Chromatography A* 2002 970, 167–181.

[162] Filipkowska, A.; Lubecki, L.; and Kowalewska, G. Polycyclic aromatic hydrocarbon analysis in different matrices of the marine environment. *Analytica Chimica Acta* 2005 547, 243–254.

[163] Gatidou, G.; Kotrikla, A.; Thomaidis, N.S.; and Lekkas, T.D. Determination of the antifouling booster biocides irgarol 1051 and diuron and their metabolites in seawater by high performance liquid chromatography–diode array detector. *Analytica Chimica Acta* 2005 528, 89–99.

[164] Sanchez-Ortega, A.; Sampedro, M.C.; Unceta, N.; Goicolea, M.A.; and Barrio, R.J. Solid-phase microextraction coupled with high performance liquid chromatography using on-line diode-array and electrochemical detection for the determination of fenitrothion and its main metabolites in environmental water samples. *Journal of Chromatography A* 2005 1094, 70–76.

[165] Benito-Pena, E.; Partal-Rodera, A.I.; Leon-Gonzalez, M.E.; and Moreno-Bondi, M.C. Evaluation of mixed mode solid phase extraction cartridges for the preconcentration of beta-lactam antibiotics in wastewater using liquid chromatography with UV-DAD detection. *Analytica Chimica Acta* 2006 556, 415–422.

[166] Varotsis, N.; Pasadakis, N.; and Gaganis, V. A novel approach for the characterization of aromatics in petroleum fractions using HPLC-UV-DAD and evolving factor analysis. *Fuel* 1998 Vol. 77 No. 13, 1495-1502.

[167] Kaminski, M.; Kartanowicz, R.; and Przyjazny, A. Application of high-performance liquid chromatography with ultraviolet diode array detection and refractive index detection to the determination of class composition and to the analysis of gasoline. *Journal of Chromatography A* 2004 1029, 77–85.

In: Integrated Circuits, Photodiodes…
Editors: R. McIntire and P. Donnell, pp. 293-342

ISBN: 978-1-60692-660-4

© 2009 Nova Science Publishers, Inc.

### *Chapter 10*

# PHOTODIODES: CHARACTERISTICS AND APPLICATIONS IN TEXTILE INDUSTRY AND BIOMEDICINE

***V. Carvalho*[*], *G. Minas, F. Soares, M.R. Vasconcelos*[1] *and M. Belsley*[2]**
Department of Industrial Electronics,
[1]Department of Textile Engineering
[2]Department of Physics, Minho University, Guimarães, Portugal

## ABSTRACT

This chapter presents the main characteristics and properties of photodiodes, discussing also their applications in the Textile Industry and Biomedicine.

In the Textile Industry photodiodes can be used to characterize both yarn diameter and hairiness using a coherent optical signal processing technique based on Fourier analysis. The characterization of the degree of hairiness using a high-pass spatial Fourier filter introduces several advantages in the hairiness measurement compared to other conventional approaches. These advantages include a signal reference for 0 % yarn hairiness, the elimination of contributions from the yarn contours, a measurement technique which is largely independent of the specific yarn diameter, yarn shape or orientation in the plane perpendicular to the optical axis. On the other hand, a reliable measurement of yarn diameter can be made using the same optical set-up but employing a low-pass spatial filter to eliminate yarn hairiness contribution, increasing the final measurement precision. In both measurements, a single projection direction is sufficient for a correct characterization, as both hairiness and yarn irregularities tend to be uniformly distributed over a full rotation of the yarn. These characteristics are fundamental for a reliable and precise characterization of yarn, introducing a superior level of yarn parameterization in Textile Industry.

In Biomedicine photodiodes can be used, as the detection element, in biochemical analysis of body fluid samples based on spectrophotometry (interaction of electromagnetic radiation with biochemical compounds). They can be used to read the light intensity that is absorbed, emitted or reflected by a sample and therefore determine the concentration, activity, amount and structure of a compound. They can also be used in CMOS (Complementary

---

[*] E-mail address: vcarvalho@dei.uminho.pt

Mosfet Oxide Semiconductor) imagers for X-ray detection or for being integrated in endoscopic capsules. They benefit from their wide availability, reduced component and costs and, more importantly, the capacity to accommodate multi-functional circuitry on-chip, all functions available in CMOS processes. All these applications take advantage of the fact that absorption of light in silicon and other semiconductor materials is wavelength dependent, which causes the penetration depth of light to be wavelength dependent. Therefore, selecting both the suitable junction depth and the oxide layers on top, photodiodes can be programmed to have their quantum efficiency increased at a particular wavelength.

## INTRODUCTION

Regarding yarn hairiness determination, a coherent optical signal processing technique based on Fourier analysis to characterize yarn hairiness using a singular projection has been developed[1]. This approach overcomes the drawbacks of other methods as it employs a signal reference for 0 % of yarn hairiness, it does not consider yarn contours, the optical configuration is not dependent on the hairiness orientation and the yarn diameter, the shape and alignment are not relevant as there is a considerable safe area of detection in the implemented hairiness sensor. Moreover, the signal obtained is proportional to the overall integrated length of hairs. These characteristics are fundamental for a reliable and precise characterization of yarn hairiness. Although one might think that a full hairiness classification should require several different and simultaneous projections, it was verified that, as hairiness is randomly distributed over the yarn, there is a high probability, considering the length of the yarn analyzed in a test, that on average, the amount of hairiness is uniformly distributed over a full rotation of the yarn; it was confirmed that the results obtained using two orthogonal projections give nearly identical results. As a consequence, a single projection is sufficient for the correct determination of yarn hairiness.

Following the analysis of the techniques employed by commercial systems for yarn diameter variation determination, it was observed that all systems include the yarn hairiness in the diameter measurements [1], leading to higher diameter values. To overcome this drawback, like in the hairiness determination approach, it was used a coherent optical signal processing technique based on Fourier analysis to characterize yarn diameter using a single projection. This method filters the yarn hairiness using a low-pass spatial filter, increasing the measurement precision. A signal proportional to the yarn diameter is also obtained. Moreover, as in hairiness measurement, the study undertaken shows that the results obtained using two orthogonal projections give nearly similar results and as a consequence, a single projection is sufficient for the correct determination of diameter variation. Likewise, it was used a laser source in order to define a linear saturation zone with high directionally which enables a superior system sensibility. The use of an incoherent light source would compromise these assumptions.

The biomedical sector is nowadays extremely dynamic and where the novelty is a strategic and operational imperative. The possibility of increasing the quantity and quality of clinical analysis, performed with instantaneous results and outside the clinical laboratories, contributes to a better quality in the health care services and also a better efficiency in the clinical and administrative processes [2]. The biomedical sector is under pressure to provide better service at a lower price. Therefore, more cost-efficient practices are needed. One of the places to improve the efficiency is at the physician's office. When the physician is confronted with an ill patient he will start looking for symptoms. However, when these symptoms lead to a wrong diagnosis, there is a problem for the physician, the patient and the society. A wrong diagnosis can lead to a wrong treatment that ultimately brings further harm to the patient and increases society expenses. The best way of increasing the diagnosis quality is to give the physician more precise information about the state of the patient. Presently, this information is often based on the measurement of biochemical substances in body fluids, such as blood, urine, cerebrospinal fluid and saliva. Most diseases leave a molecular fingerprint in those fluids and by measuring that fingerprint in the right way, the precision of the diagnostic can be increased [2]. Usually, this kind of analyses is carried out in clinical laboratories and the results become available after several hours, sometimes days. As a consequence a reliable diagnosis cannot be performed within the consultation time. Mistakes in the logistics, such as lost samples and mislabelling, may further delay the diagnosis. The automated equipment used in a state-of-the-art laboratory reduces errors, but use high sample and reagent volumes, making the analysis systems expensive and does not contribute to patient comfort. Outside the laboratory environment, reagent strips for colorimetric detection are commercially available. They provide a colour when a fluid sample contacts the strip. However, such strips are intended for a limited set of substances to be analyzed and provide a qualitative result in the form of colour readout (by visual inspection).

The need for rapid and on-line measurements with low sample volumes has led to the development of lab-on-a-chip devices with the fluidic, detection and readout systems integrated in a single chip. The great interest in lab-on-a-chip technology stems from the inherent performance gains that arise when most analytical systems are downsized to the micron scale. The advantages associated with shrinking clinical analyses systems include: reduced sample size, higher degree of integration and hence enhanced potential for automation, shortened response time, potential for improved analytical performance, reduced chemicals storage and hence laboratory safety and a considerable reduction in the samples handling, logistics and costs [3].

Regarding biochemical analysis of body fluids samples, it was developed an on-chip integrated CMOS optical detection microsystem for being used in lab-on-a-chip devices, especially in the measurement of several biochemical substances in body fluids by spectrophotometric analysis [4-8]. Its measurement is based on colorimetric detection by the optical absorption in a part of the visible spectrum defined by the reaction of the specific biochemical substance with a specific reagent. The device was designed to be integrated in a lab-on-a-chip device, allowing low-cost instantaneous results at any location, with small quantities of reagents and samples. To fulfil those requirements, the highly accurate optical detection microsystem includes photodiodes, programmed to have their quantum efficiency increased at a particular wavelength, and a light-to-frequency converter for readout, both fabricated using a standard CMOS process. Signals proportional to the intensity of the light transmitted through the fluid are available at the output in the form of bit streams, which allows simple computer interfacing. This microsystem avoids the need of expensive readout optics and opens the door to low-cost disposable devices.

# TEXTILE INDUSTRY: YARN HAIRINESS MEASUREMENT

This section describes the methodology employed to characterize yarn hairiness based on a single photodiode considering a coherent signal processing technique. Here are reported the electronic and optical setups for a single direction projection, the system calibration procedure, the development of the non invasive minimum statistical reference method and finally the yarn hairiness determination considering two orthogonal directions. The results obtained during the referred studies proved that, using a singular projection, it is possible to obtain a reliable characterization of yarn hairiness.

## Development of One Direction Projection Hairiness Analysis Methodology

In this approach a pair light emitter (laser)/receiver (photodiode), with an optical setup, is employed for yarn hairiness analysis using a coherent optical signal processing technique [1][9-17]. Using this procedure, a dark and red image is created in the final image plane, where the red contrast gives information about the yarn hairiness and can easily be converted in an electrical signal (current intensity) by a photodiode.

This method quantifies with high accuracy, the mass variation (%) caused by hairiness, considering as reference, the yarn mass linear density. This is a very precise method as it is not influenced by the yarn position, considering a linear range measurement field, as will be demonstrated later in this section. However, this method is more expensive and complex than the LED/photocell method, in spite of being more efficient and accurate.

### Optical and Electronic Hardware

The experimental determination of hairiness requires an electronic and an optical rig. In the electronic hardware, a photodiode (S1227-1010BR) [18] from Hamamatsu was chosen as a receiver. It is a low cost photodiode, with a high sensitivity for red wavelengths (for the emitter used, laser, 0.39 A/W), a large active measurement area (10 mm x 10 mm), a low dark current (maximum of 50 pA), a high shunt resistance (2 GΩ), a noise equivalent power (NEP) of $3.1 \times 10^{-15}$ W/Hz$^{1/2}$ and a low terminal capacitance (3000 pF). A conditioning circuit was designed. It includes a current to voltage (I-V) converter (transimpedance amplifier) and an instrumentation amplifier [19] to eliminate the offset and the noise, introduced by the operational amplifiers of the circuit. The instrumentation amplifier output is connected to an analogue channel of the data acquisition board and the software developed in LabVIEW® from National Instruments [20] was used to acquire and process the data (Figure 1).

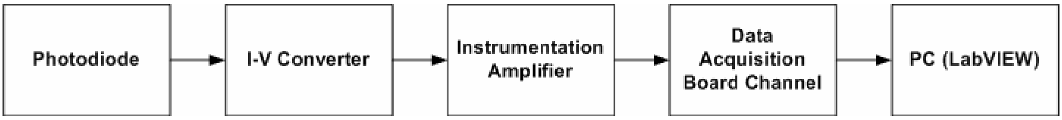

Figure 1. First approach of the electronic setup for the hairiness determination system.

Figure 2 presents the first approach to the optical system for the hairiness determination.

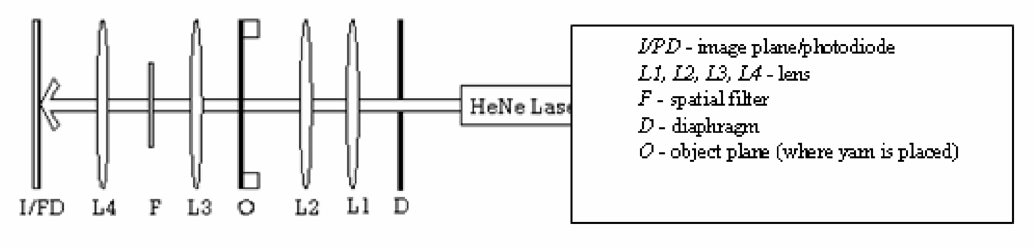

Figure 2. First approach of the experimental setup of the optical system.

The objective of this setup is to quantify yarn hairiness, as the brighter elements of the final image (I) (position of the photodiode PD). The setup includes the optical devices needed to obtain the image of yarn hairiness placed in the object plane (O). Coherent light from a helium-neon (HeNe) laser from Mells/Griot with 15 mW of output power, emitting at a red wavelength of 632.8 mm is first spatially filtered by a diaphragm (D), with an aperture of 1.25 mm limiting the laser beam to its core, guaranteeing a smooth transverse spatial profile. After the diaphragm, the laser beam passes through a two plano-convex lens beam expander telescope (L1 and L2 with a focal length of 60 mm) to produce a beam diameter of roughly 1 cm which is then directed to the yarn placed in the object holder (O). The size of the object image is controlled by the plano-convex lenses, L3, that have a focal length of 65 mm and which obtain a spatial Fourier transform of the object in its principal focal plane, and L4 with a focal length of 60 mm. By placing a custom fabricated spatial filter (F) in the Fourier plane of L3, we can select which spatial frequencies in the image are allowed to propagate to the detector. A filter with roughly 1 mm of opaque target (F) placed in the Fourier plane, blocks all spatial frequencies below 11 $mm^{-1}$, corresponding to a characteristic size of 91 microns or larger in the object plane. Textile yarns typically have diameters ranging from a few hundred microns up to millimetres, while the small hairs protruding from the yarn are single fibres with diameters typically less than 10 microns. As there is a clear separation in the characteristic length scales of the yarns, this filter allows only the high spatial frequencies in the image to propagate further. Essentially, this is a high-pass spatial Fourier filter [10][11][13][21] (Figure 3).

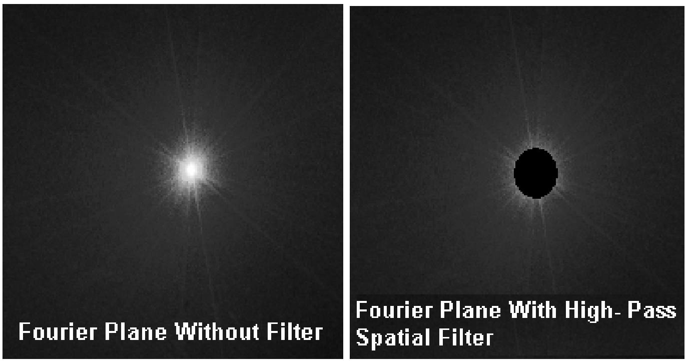
Fourier Plane Without Filter
Fourier Plane With High- Pass Spatial Filter

**a)** **b)**

Figure 3. Application of the high-pass spatial filter in the Fourier plane.

Observing Figure 3 a), it is verified that the Fourier plane resulting from the yarn is a well defined circular point of light, where the spatial frequency distribution varies from the centre (low spatial frequencies) to the outside (high spatial frequencies). The use of the high-pass spatial filter (opaque circular filter, to block the area of the Fourier plane where are the low spatial frequencies Figure 3 b) results in the contours of the edges of the yarn and associated hairs being highlighted while simultaneously eliminating the constant background (Figure 4 a and b) associated with the portion of the laser beam that was not obstructed by the sample. Through this method a higher portion of the processed optical signal is associated with the presence of yarn hairs [22].

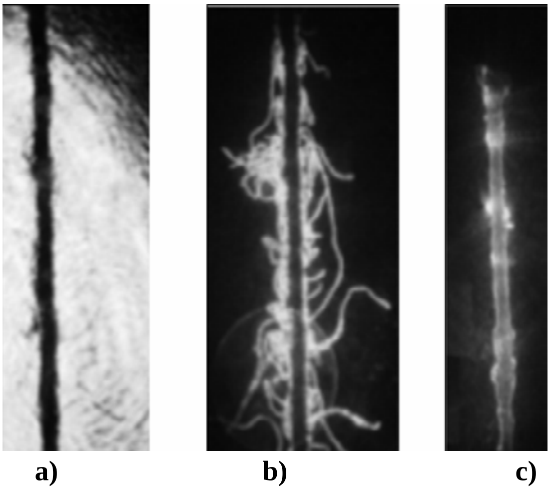

Figure 4. Figure a) and b) present the image of the yarn without and with the application of the high spatial frequency optical filter, respectively. Figure c), corresponds to a photograph of the same yarn using the optical filter, but in this case the hairiness was greatly reduced by wetting the yarn with water and by increasing the exposition time of the digital camera.

In Figure 4 a), it is difficult to identify yarn hairiness, because they are very thin, compared to the yarn. The resulting shadows are lost as a background in the high intensity of the unobstructed laser beam. Figure 4 b), taken using the same section of yarn but employing the coherent optical filter, clearly highlights the previously hidden yarn hairiness. Figure 4 c) is the yarn image, using water droplets to smooth the yarn hairiness. By doing this, the optical effect of the yarn itself is seen, without the visualization of the yarn hairiness. In fact, the signal from the yarn itself, in the absence of hairiness, is much reduced - the exposure time was increased significantly to obtain the image. These preliminary tests showed that it was possible to develop an automated, robust and precise, hairiness measurement procedure. In addition, regarding hairiness analysis, there is a relation between the dimension of the filter employed in the setup and the frequency limit allowed. A technique to calibrate this signal, allowing the determination of the ratio of hairiness mass compared to yarn mass, should be taken into consideration.

In order to obtain a voltage proportional to the brightness of the final image, a conditioning circuit was developed for yarn hairiness quantification. A high precision current to voltage converter based on a Burr-Brown [23] operational amplifier OPA277P was used (Figure 5). Some of the main features of the operational amplifier are: ultra low offset voltage

(10 µV), high open-loop gain (134 dB), high common-mode rejection (140 dB), low bias current (1 nA maximum) and a bandwidth of 1 MHz.

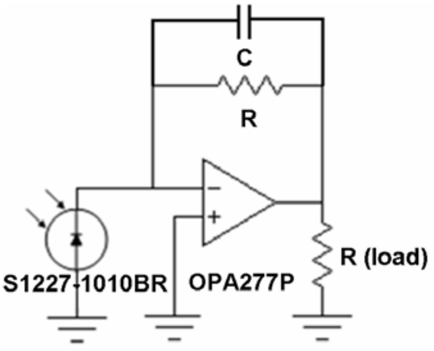

Figure 5. Transimpedance amplifier.

As the operational amplifier offset and dark photodiode current are extremely low, they can be neglected, compared to the signal magnitude involved in the system. This particularity allows one to eliminate the instrumentation amplifier from the conditioning circuit as initially designed . Moreover, provided that the saturation of both the photodiode and the operational amplifier are avoided, a direct proportionality can be obtained between the photodiode current and the output voltage by (1).

$$V_{Rload} = -R.I_{photodiode} \tag{1}$$

Subsequently, the output of the transimpedance amplifier is read by an analogue channel of the USB-6251 Data Acquisition Board (DAQ), from National Instruments [20]. Some of the main features are [24]:

16 bit of resolution;
Maximum acquisition rate of 1.25 MS/s;
Maximum range of ± 10 V;
A ± 1 least significant bit (LSB).

A custom software application was developed in LabVIEW® to manage and acquire the data obtained from the output of the transimpedance amplifier [21]. Figure 6 presents the final schematic of the developed electronic yarn measurement hardware.

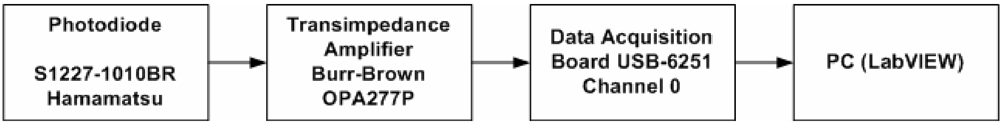

Figure 6. Custom developed electronic yarn measurement hardware.

The measurement hardware causes a significant variation of the yarn signal with and without hairiness and without yarn, establishing three well defined voltage levels and allowing one to infer yarn quality, considering hairiness. However, to assure a higher measurement precision, a polarizer in the optical setup was included before the image plane. This optical device reduces significantly the voltage without yarn (DC component), increasing subsequently the absolute variation between the three signals levels identified [25].

## Hairiness Measurement Length Calibration

This section describes the methodology employed to obtain the signal output voltage associated with the length of hairs, in order to establish a calibration reference value for the hairiness module.

### Experimental Procedure

This study was performed isolating one single hair in the yarn with a diameter of 0.64 mm (Figure 7) [21].

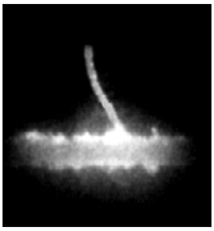

Figure 7. Hair isolation.

To isolate the hair silicone was used to eliminate all the other yarn hairs. Silicone was used instead of water to avoid the problem associated with drying, which would have allowed undesired hairiness to appear during the test.

The isolated hair was stretched and oriented perpendicular to the yarn. However, to ensure that the signal received by the photodiode was due to the hair itself, a “window” was built using an opaque card placed in front of the photodiode. The “window” was positioned to block the signal from the yarn’s borders. It was observed that this signal became enhanced due to the light scattering from the silicone (high refractive index). The “window” used had an adjustable aperture, to allowing one to measure the variation of the output voltage as a function of the hair length (Figure 8).

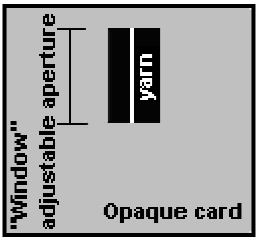

Figure 8. Window aperture in the maximum position.

The hair had an actual length of 2.67 mm. The projection of the hair on the photodiode had a length of 1.50 mm. This means that a 44 % reduction of the actual hair length occurred due to the optical elements needed to image the signal on the photodiode.

The measurement process was performed reducing the aperture in steps of 250 μm. Starting with the window fully opened and then gradually reducing the aperture until it was fully closed, seven separate readings were obtained. Afterwards, the hair was taken out and the window was gradually opened to register the background signal at each aperture setting, which was then subtracted from the corresponding values obtained with the hair. The operational amplifier offset signal (value measured with no light signal) was also subtracted from all measurements. .

## Experimental Results

Figure 9 presents the results obtained considering the previously described procedure.

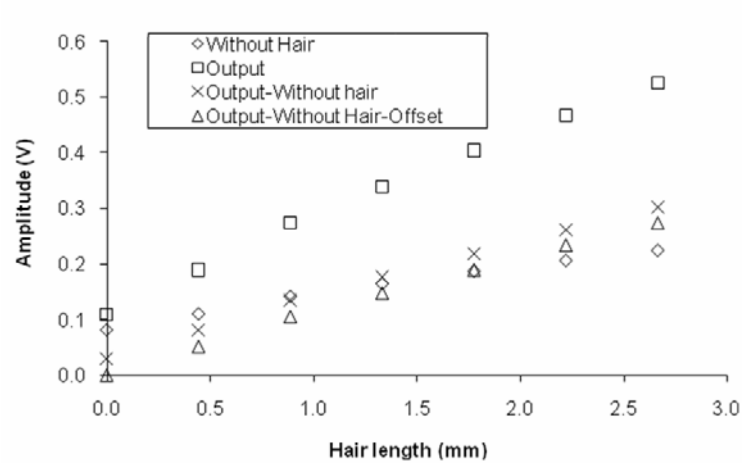

Figure 9. Measured results for system calibration.

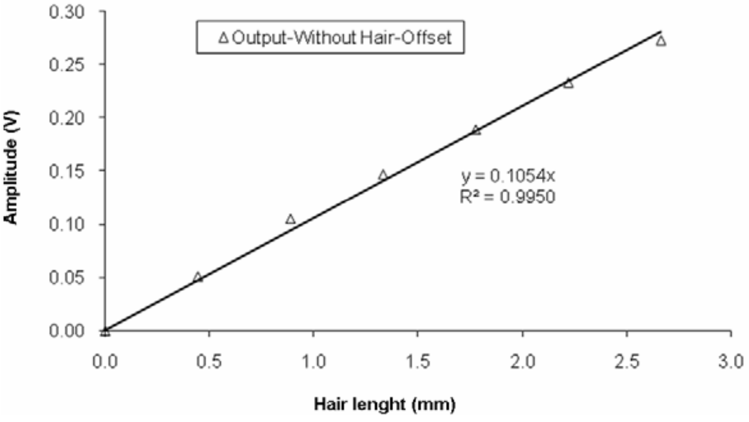

Figure 10. Linear correlation for final output.

A linear correlation for the final curve (Output-Without Hair-Offset) was tested (Figure 10). The determination coefficient ($R^2$) is close to the unity and it is possible to reliably claim that the signal obtained from a single hair is directly proportional to its length. In fact, the fit allows one to calibrate the system. In this case the output signal (y) is related to the hair length (x) by the expression y = 0.1054x, which implies that for each millimetre of hair length, the output increases by 105.4 mV for the gain used in these tests.

As the system calibration fit presented in Figure 10 was determined for a specific yarn (295.00 g/km - 0.64 mm), its reliability has to be assured when using other yarns. This analysis was carried out observing 50 μm electron microscope pictures of several yarns (Figure 11).

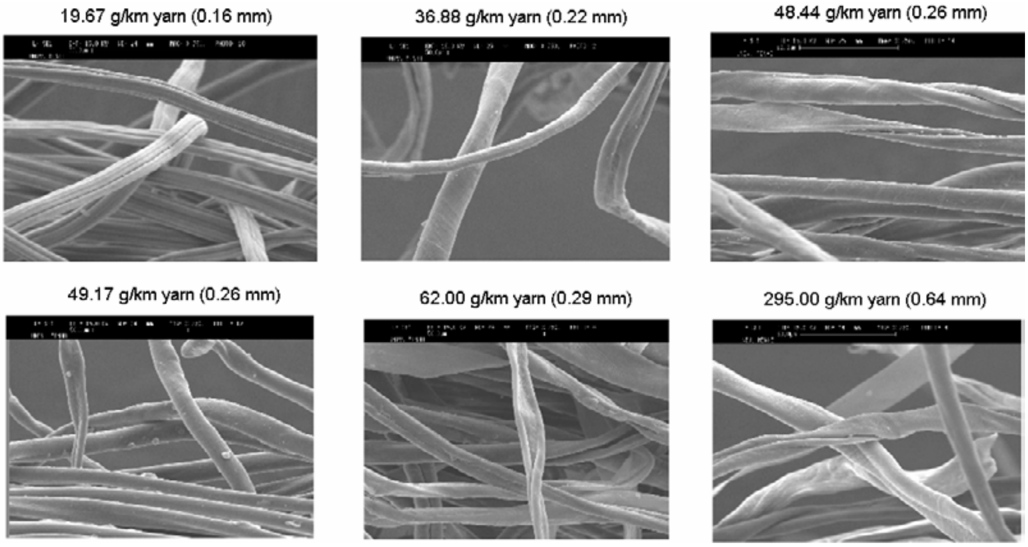

19.67 g/km yarn (0.16 mm)

36.88 g/km yarn (0.22 mm)

48.44 g/km yarn (0.26 mm)

49.17 g/km yarn (0.26 mm)

62.00 g/km yarn (0.29 mm)

295.00 g/km yarn (0.64 mm)

Figure 11. Yarns electron microscope pictures.

The individual cotton fibres are not round, but rather ribbon-like with a cross-section that can be much smaller in one direction. However, the linear mass of each fibre should be approximately uniform. The method of detecting hairiness is not sensitive to the actual cotton fibre diameter (as should be the case in the methods based on diffraction).

Regarding the variation of hair diameter (fibres) between the yarns tested and even in the same yarn, it is observed that they present very small variations (only a few microns) (Figure 11). Subsequently, their influence (opacity) comparatively to the influence of the hair length can practically be neglected. So, the study performed can be used as a correlation between the hairiness length and the system output voltage.

## Minimum Statistical Reference Method

This section presents the algorithm to statistically determine the yarn reference value.

## Method Description

As stated before, the water droplets reference method is simple to implement and does not cause extra hairiness. Nevertheless, with the addition of water, there is a slight increase of the scattering level of the yarn. Also, it needs to be performed offline, which implies stopping the yarn test. So, a new mathematical method was developed: the minimum statistical reference [26].

This method is based on the fact that, if the yarn is analyzed using samples of 1 mm, even for hairy yarns, a considerable number of observations will correspond to sections of yarn without hairiness. Figure 12 presents an electron microscope picture that confirms this statement for a particular case of a yarn with rather high hairiness. It is possible to verify that there is a 1 mm length region where no hairiness is observed.

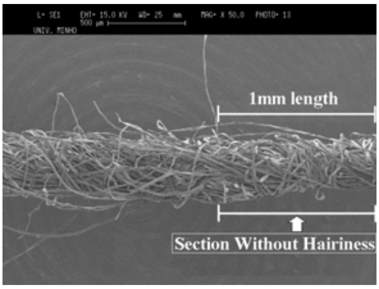
L= SE1 EHT= 15.0 KV WD= 25 mm MAG= X 50.0 PHOTO= 13
500 µm
UNIV. MINHO
1mm length
Section Without Hairiness

Figure 12. Example of an image showing a region of 1 mm length without hairiness.

As the photodiode used has a signal area more stable (9 x 10 mm$^2$) and it was intended to measure yarn samples of 1 mm length, a mask using an opaque card, with a 9 mm x 1 mm aperture was built and placed in front of the photodiode (Figure 13). Using this configuration, measurements in steps of 1 mm could be performed.

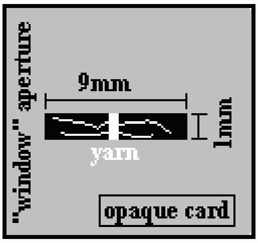

Figure 13. Photodiode mask.

The algorithm for implementing the statistical reference method consists of:

1. Determine the minimum value, the average value and the standard deviation (SD), of all samples;
2. Determine the number of 1 % increases, step by step, above the minimum to reach the average value;
3. Determine, for each increase up to the average, the number of samples and their values, in the interval [minimum; increased value];

4. Determine the average value of the elements which belongs to each tested interval and their corresponding standard deviation;
5. Calculate the median of the average values obtained in step 4, the step where it is located and also the inferior median and superior median.
6. If the yarn tested has: low level of hairiness ($SD \leq 0.1$) - the reference is the linear interpolation between the superior median and the average; high level of hairiness ($SD \geq 0.2$) - the reference is the inferior median; medium level of hairiness ($SD > 0.1$ and $SD < 0.2$) - the reference is the superior median.

This procedure was designed to obtain reference values similar to those obtained using the water method. To do so, it was necessary to divide the interval of steps at the median point into lower and upper segments. We refer to the median of the lower interval as the inferior median, while the superior median is the corresponding value of the upper segment. Afterwards, a software application using the described algorithm was developed.

## Method Validation

To validate the method, we performed a test using a 100 % cotton yarn with a linear mass of 4.20 g/km which is characterized by a very low level of hairiness (Figure 14).

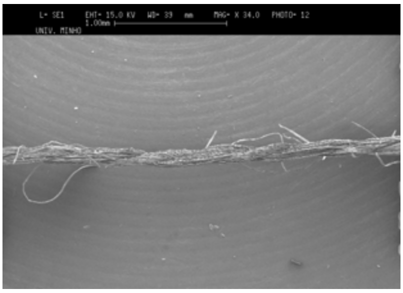

Figure 14. Image of an 100 % cotton yarn with a 4.20 g/km linear mass.

The total yarn length tested was one metre; water droplets were added to eliminate the hairiness in the first 20 cm and no alteration of yarn was performed over the last 80 cm. The objective of the test was to verify that the signal levels measured in the first part (reference with water droplets), are reproduced in some parts of the last 80 cm (similar to the reference with water droplets). The main parameters of the acquisition module were: yarn speed of 6 m/min, yarn length of 1 m and sample length of 1 mm, which corresponds to an acquisition frequency of 100 Hz. Figure 15 presents the acquired signals.

Figure 15 shows that the amplitude values measured in the first 20 cm of the yarn (corresponding to the reference level using water droplets) are reproduced several times in the following 80 cm of yarn. These sections correspond to zones without hairiness, showing that using the statistical reference method it is possible to obtain a valid reference value.

After confirming the viability of the reference method, 6 m of six different 100 % cotton yarns were analyzed. The other input parameters were not altered. Table 1 lists the linear mass (g/km) and the theoretical diameter (mm) [27][28] for each yarn tested.

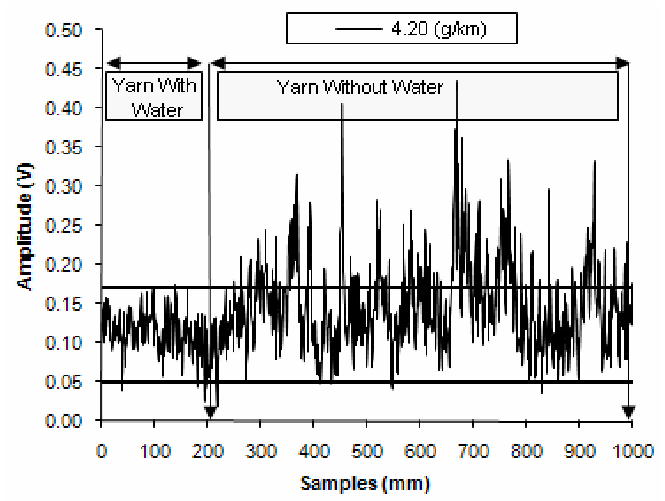

Figure 15. Analysis of 1 m of the 4.20 g/km yarn in samples of 1 mm - first 200 mm using the water droplets reference method.

**Table 1. Description of the yarns used in the test**

| Yarn linear mass (g/km) | Yarn theoretical diameter (mm) |
|---|---|
| 4.20 | 0.08 |
| 19.67 | 0.16 |
| 36.88 | 0.22 |
| 49.17 | 0.26 |
| 62.00 | 0.29 |
| 295.00 | 0.64 |

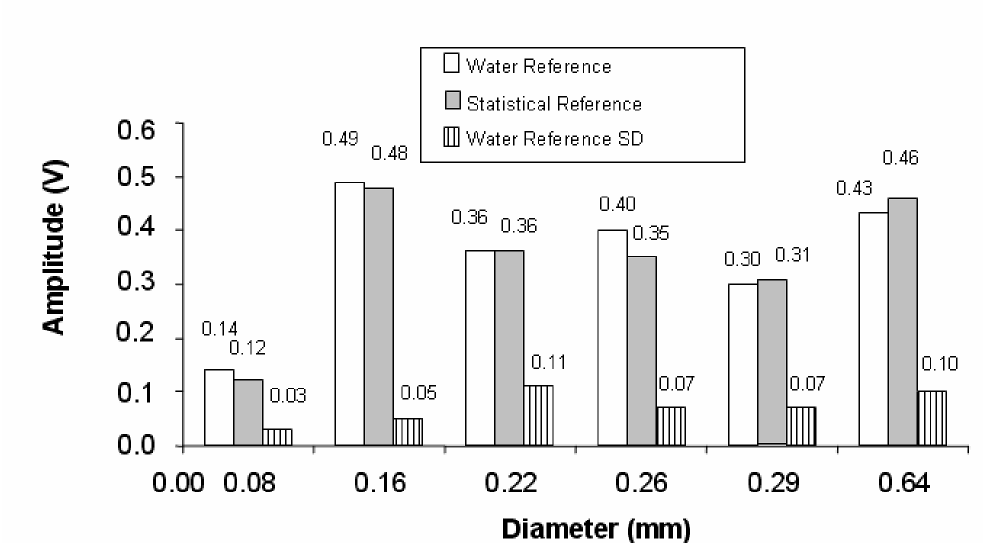

Figure 16. Reference methods comparison.

For each test, the output signal without yarn (0.14 V) was deducted from the original signal. Subsequently, a comparison between the water reference method (using droplets to smooth the hairiness) and the minimum statistical reference was performed using exactly the same section of yarn, for each of the yarns tested. Figure 16 presents the results obtained.

Observing Figure 16, it is possible to state that the water references are very similar to the minimum statistical references. In all cases the difference between the two methods is less than the uncertainty (SD) associated with the water method. So, the method can be considered as a reliable and convenient reference procedure.

The minimum statistical reference method showed reliable and consistent results. It is a non invasive procedure, as opposed to the water reference method. Moreover, the determination of the reference does not require stopping the line test, as it can be implemented online. These two important advantages allow establishing this method as the most consistent and suitable for hairiness analysis, in comparison to the water droplets.

## Orthogonal Projections Directions Statistical Analysis

This section presents the studies undertaken to support the characterization of yarn hairiness analysis using a single direction projection, based on the statistical similarity obtained between orthogonal projections directions.

### Mathematical Description

As verified in the previous sections, it was possible to develop and implement a reliable and valid system which measures yarn hairiness. However, this hairiness determination is performed only in a single projection direction and a full 360º yarn hairiness analysis requires several different projection directions. But, an open question remains as to whether it is possible to obtain a valid characterization of the yarn properties using a single projection direction [29].

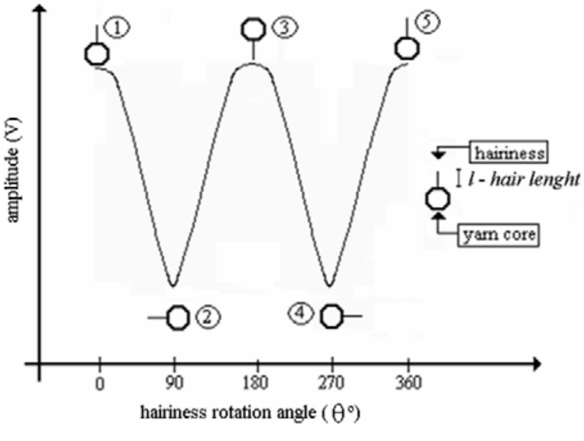

Figure 17. Example of the absolute cosine signal, resulting from a 360º projection of one straight hair of length *l*, using a single photodiode.

Considering a single coherent imaging system, if a yarn containing a single straight fibre hair of length *l*, thrusting out from the core is rotated over 360º, an absolute cosine signal with amplitude of the length of the hairiness is obtained (Figure 17).

Essentially, the system would record a signal proportional to the cosine of the angle between the direction of the hair fibre and the plane perpendicular to the incident light direction. Maximum projections are obtained at orientations referenced by 1, 3 and 5 in Figure 17. In contrast, a minimum signal would be obtained for orientations referenced by 2 and 4, when the hair is aligned along the incident light's propagation direction (the hair is not projected into the photodiode).

Mathematically, for an arbitrary direction of a given hair segment, the signal S1 recorded by a photodiode PD1 will be proportional to the absolute cosine of the hair's direction (2).

$$S_1 \sim l\left|\cos(\theta)\right| \tag{2}$$

For an arbitrary hair orientation, the signal acquired by a single photodiode corresponds to the following average (3). This signal is calculated between 0º and 90º (π/2), as in this angular range the full amplitude variations of the sampled signal are then repeated over the following 270º.

$$S_1 \sim l\frac{2}{\pi}\int_0^{\pi/2}\cos(\theta)d\theta = \frac{2l}{\pi}\left[\sin(\theta)\right]_0^{\pi/2} = \frac{2l}{\pi} \approx 0.64l \tag{3}$$

A similar calculation also holds for the hairiness detected by a photodiode in the orthogonal direction of the first photodiode. On average, assuming a random distribution of protruding hairs, the total amount of hairiness ($S_t$) will be π/2 (1 / 0.64) times larger than that detected along a single projection (4).

$$S_t = \frac{\pi}{2}S_1 \approx 1.57S_1 \tag{4}$$

Provided the distribution of protruding hairs is random in direction and the area of "intersecting hair projections" is negligible, the above relation should always prove valid.

## Yarn Hairiness Characterization

This section is focused on obtaining the yarn hairiness characterization using only one direction projection. A test, considering two photodiodes oriented along orthogonal directions is undertaken to allow a correlation analysis between both acquisition results.

A double coherent imaging setup was implemented to characterize the yarn hairiness simultaneously along two orthogonal directions. In this case, if a second coherent imaging system is placed along a direction orthogonal to the first system (Figure 18), a complementary signal to the absolute cosine (absolute sine) is obtained (Figure 19). The effective length of the protruding fibre (*l*) is, in this case, proportional to the absolute sine of the angle between the hair's direction and the plane perpendicular to the incident direction of the initial light beam [24].

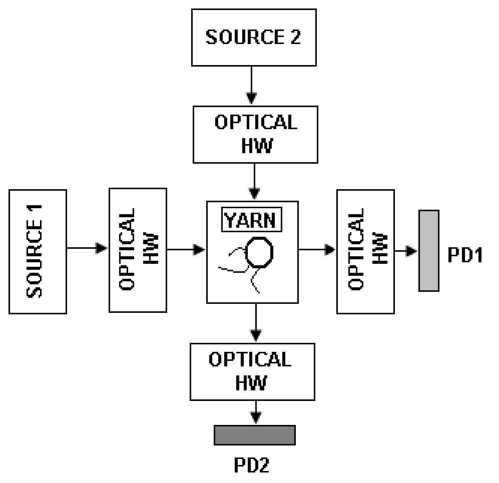

Figure 18. Configuration of a system to quantify yarn hairiness using two orthogonal directions, where SOURCE 1 and SOURCE 2 are light sources (lasers), OPTICAL HW represents the optical elements used to obtain the yarn hairiness projections, PD1 and PD2 are optical sensors (photodiodes) and YARN is the yarn sample to be analyzed.

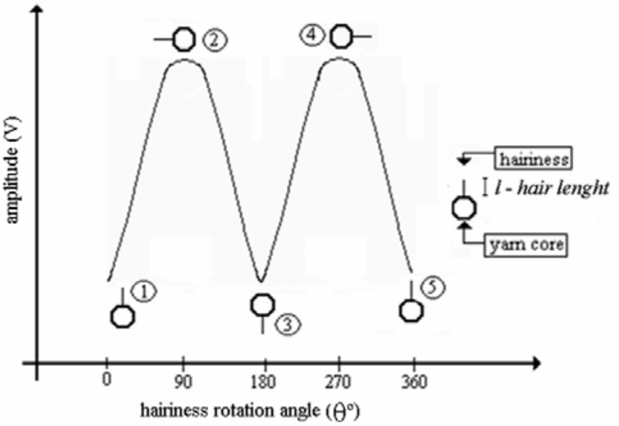

Figure 19. Example of the absolute sine signal resulting from a 360º projection of one straight hair of length *l*, for a second photodiode positioned orthogonally relatively to the first photodiode.

Furthermore, if the yarn has several hairs with different angular displacements, the two systems register signals corresponding to the net projections of the illuminated hairs in the two planes perpendicular to the incident light directions.

Mathematically, for the orthogonal direction of S1 in a given hair segment, the signals (S2) recorded by the second photodiode (PD2) will be proportional to the absolute sine of the hair's direction relative to the detection plane of the first photodiode (5) .

$$S_2 \sim l|\sin(\theta)| \tag{5}$$

With the aim of analyzing yarn hairiness simultaneously along two orthogonal directions, the electronic and optical hardware employed in the single direction hairiness analysis system referred in the previous sections was duplicated. As a second radiation source a diode laserwhich emits in both single transverse and single longitudinal mode was used. The optical elements used in this new setup had an anti-refelction coating allowing one to eliminate the polarizer, as the background signal is low in comparison to the hairiness signal. Moreover, they permit a reduction in the length of this system, which is an important factor considering the portability desired for the final system. Figure 20 presents the optical hardware used for a single direction yarn hairiness measurement system in this experiment [24].

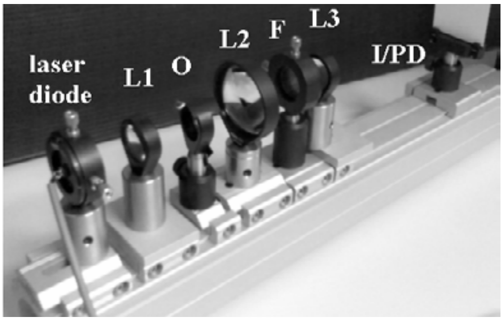

Figure 20. New custom developed optical yarn measurement hardware for a single direction.

The coherent optical imaging technique is employed to obtain an optical signal proportional to the amount of hairiness present on the yarn being sampled. The main components of this new optical system are, as in the first configuration approach, a collimated coherent illumination source, aperture lens used to form the Fourier transform image of the sample yarn under study, a custom made high-pass spatial filter and a second lens to create a final image in the detector plane (position of the photo detector in Figure 20) (I/PD).

For the illumination source it is use a diode laser (Eudyna FLD6A2TK) that emits light at 685 ± 10 nm in both a single transverse and single longitudinal mode, with an especially low aspect ratio of 1.3. Emitting in a single longitudinal mode, the coherence length of the laser light is expected to be greater than several tens of metres. The light from this laser was collimated using a single plano-convex lens of 40 mm focal length (L1). After illuminating the sample under study (O), the light passes through a 60 mm focal length, 50 mm diameter plano-convex lens (L2) used to obtain the spatial Fourier transform of the object in its principal focal plane. A roughly 1 mm diameter opaque target (F) placed in the Fourier plane, blocks all spatial frequencies below 10 mm$^{-1}$, corresponding to a characteristic size of 100 microns or larger in the object plane. As in the first optical setup, the filter is chosen to let pass through the information regarding the small fibres, while eliminating almost entirely the nearly constant background light due to laser light that is not incident on the sample. However, the amount of light transmitted by the spatial filter is relatively small, roughly 3 to 4 orders of magnitude less than the full power emitted by the laser. A third plano-convex lens of 60 mm focal length (L3) is used to form a final filtered image which then highlights the sharp transitions in the object, basically the core boundary of the fibre and any small protruding hairs from the yarn core. In this main setup all the lenses have a broadband anti-reflective coating. In addition, an interference filter centred at 680 nm with a bandpass (full width at half maximum) of 10 nm and a peak transmission of 50 % (Thorlabs FB680-10) can be placed directly in front of the detector to limit the amount of stray ambient light detected.

Due to equipment limitations, the elements in the second optical arm have slightly different characteristics; the lenses used have different focal lengths and the laser sources operate at different wavelengths and powers. Nonetheless, the operation principle is identical, while the associated electronic hardware is exactly reproduced. Moreover, to ensure that the beam area incident on photodiode is precisely the same, two similar windows with 5 mm height (final beam area of 5 mm x 10 mm) were built and placed on the active area of the photodiodes. To obtain approximately the same output signal amplitude in both setups, the gains used in the transimpedance amplifiers were adjusted, in order to compensate the differences in the optical hardware and light sources (source 1 - HeNe laser with a wavelength of 632.8 nm, with a polarization contrast of more than 100:1; source 2 - Laser diode with a wavelength of approximately 685 nm, with a polarization contrast of more than 100:1). The output power of the sources (lasers) can be considered stable, as during measurements the variations are less than 1 %. Figure 21 presents a schematic of the overall optical hardware set up for two directions.

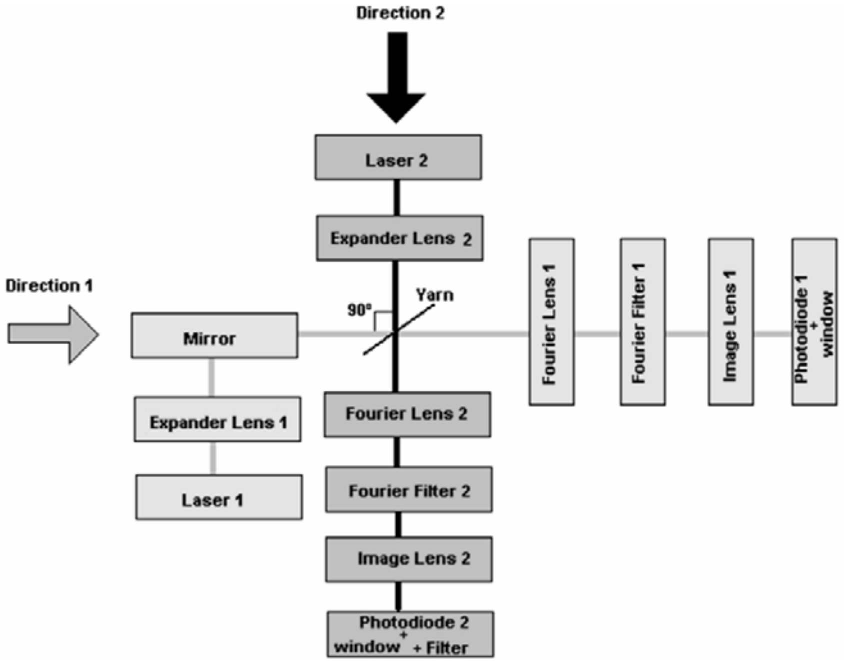

Figure 21. Experimental configuration of the orthogonal yarn hairiness analysis.

## Test Description and Implementation

In the several experimental tests performed, the results showed that the majority of the signal detected by photodiode 1 was due to light originating from laser source 1. However, a small component of the light from laser source 2 is also scattered and detected by photodiode 1. This indirect or cross signal was reduced, in the case of photodiode 2, by placing a narrowband interference filter in front of the photodiode which rejects the vast majority of light that propagates to photodiode 2 from laser source 1 (Figure 21).

A small amount of light from laser source 1 is transmitted, since the interference filter has a limited acceptance angle. To take into account the small cross-signals, each experiment was repeated using the following three different scenarios:

a) Laser 1 on - laser 2 off, the signal in photodiode 1 is directly transmitted and the signal registered by photodiode 2 is due to the light scattered from laser source 1;
b) Laser 1 off - laser 2 on, the signal observed using photodiode 2 is the directed transmitted signal while the signal detected by photodiode 1 is due to light scattered from laser source 2;
c) Lasers 1 on - laser 2 on, both photodiodes registered the directly transmitted signal from the respective source together with a scattered signal from the other laser source.

A 62.00 g/km yarn, with a high level of hairiness, was analyzed in 4.8 k samples of 5 mm each, corresponding to a total of 24 m of yarn, for each tested laser configuration.

In each arm a small and constant background signal exists, mainly due to the quality of the optical elements used in the setup. This background can be easily measured by acquiring the signals without the presence of yarn. The signals without yarn are, for channel 1 (photodiode 1), 0.134 V and for channel 2 (photodiode 2), 0.014 V. There is no reflection if no yarn is placed in the object plane. So, these values refer only to the signal transmission of the direct laser beam for each photodiode. The voltage values without yarn were subtracted from the acquisition yarn sample signals.

Moreover, subtracting the influence on the non direct source in each acquisition signal considering both sources (0.14 V of source 2 influence in channel 1 and 0.01 V of source 1 influence in channel 2, measured using the first two scenarios a) and b)) there are obtained Figure 22 and Figure 23, respectively, for channel 1 and 2.

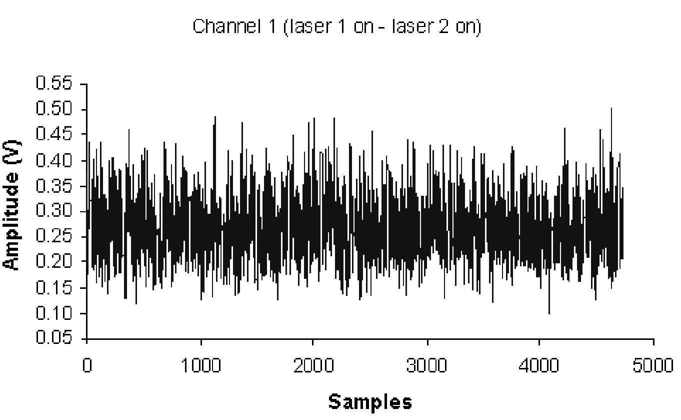

Figure 22. Acquisition signal for channel 1 considering scenario c) (laser 1 on - laser 2 on).

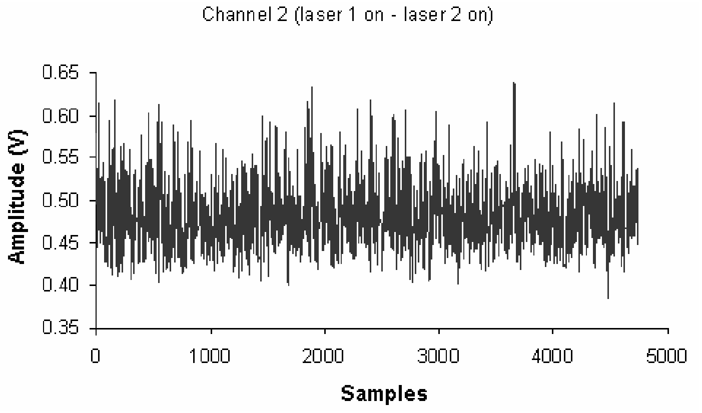

Figure 23. Acquisition signal for channel 2 considering scenario c) (laser 1 on - laser 2 on).

Analysing Figure 22 and Figure 23, it is possible to verify that due to their higher amplitudes, the signals of channels 1 and 2 are directly transmitted. The differences verified in amplitude are related to the different source powers and slightly different gains of the amplifiers.

Table 2 presents the results of the reference values (0 % of hairiness), average and SD of Figure 22 and Figure 23.

**Table 2. Statistical reference, mean and SD of Figure 22 and Figure 23**

| Channel | Reference (V) | Mean (V) | SD (V) |
|---|---|---|---|
| 1 | 0.23 | 0.27 | 0.058 |
| 2 | 0.46 | 0.48 | 0.035 |

As expected, comparing the values from Table 2 to those obtained for scenarios a) and b) considering the direct source for each specific channel, the reference and the mean values are equal, while the SD values are very close.

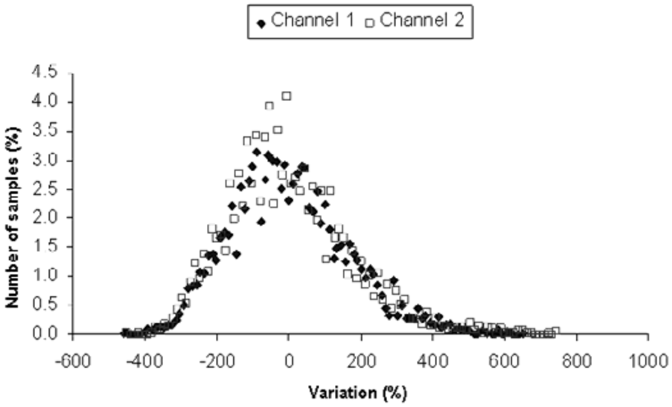

Figure 24. Frequency diagrams of channels 1 and 2 for scenario c) (laser 1 on - laser 2 on).

Using a frequency hairiness variation diagram as presented in Figure 24, it was performed a correlation between both signals, considering the hairiness percentage variation over the average.

Analysing Figure 24, it can be verified that both signals are highly correlated regarding their number of samples obtained for each tested interval. Considering the hairiness reference value, the percentage variation over average SD, for Figure 22 and Figure 23, also confirmed this conclusion, as their values are almost similar (162.83 % for channel 1 and 168.06 % for channel 2). The differences in the amplitudes (%) in the number of samples between channels 1 and 2, obtained at each singular variation interval (%) considered in the frequency diagram of Figure 24, are presented in Figure 25.

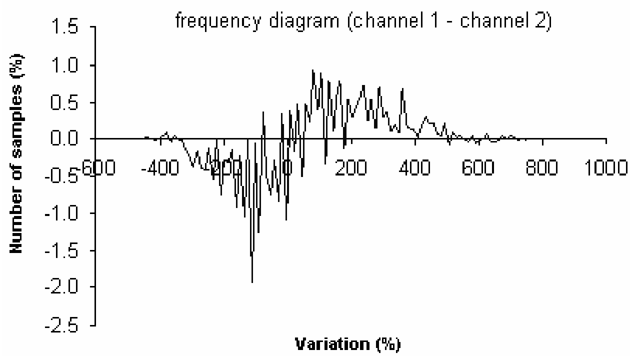

Figure 25. Amplitude differences in each interval of 24.

Observing Figure 25, the amplitude variations over each interval in the number of samples are in the range [-1.9 %; 0.9 %] and so represent very low variations. A SD of 0.45 %, a mode of -0.50 % and an absolute mean of 0.22 % was obtained.

From the high level of statistical significance, between the signals obtained for orthogonal projection directions, it can be concluded that acquiring data along a single projection direction is sufficient to correctly characterize the yarn hairiness. That is, the direction of hairs protruding from the yarn tested appears to be sufficiently random, yielding almost identical results in both orthogonal projections. Furthermore, the single projection data can be corrected by the factor of $\pi/2$ to obtain a reliable overall characterization of yarn hairiness provided a sufficient number of samples are acquired.

## TEXTILE INDUSTRY: YARN DIAMETER MEASUREMENT

This section describes a method to measure yarn diameter variations using coherent optical signal processing based on a single photodiode. This approach enables to quantify yarn irregularities associated with variations in diameter which are linearly correlated with yarn mass variations. A robust method of system auto-calibration, eliminating the need for a standard atmosphere (20 ºC and 65 % of humidity), is also demonstrated. Moreover, a diameter characterization was carried out for three types of yarns.

## Approach Description

The variation in the yarn linear mass and irregularities, are a key quality parameter in the textile industry. Yarn irregularities are usually evaluated using capacitive measurements [30]-[32]. However, optical methods have several possible advantages, including, better resolution and lower sensitivity to environmental factors such as humidity and temperature.

The coherent optical signal processing system, described in section 1.2, can be easily adapted to measure yarn diameter and consequently infer yarn irregularities [33]. However, in this case it is measured the diameter variation and not the mass variation itself.

A typical image without spatial filtering is shown in Figure 4 a) [21]. Looking closely to the image, in addition to the main shadow caused by the yarn core, several small protruding fibres that also block a significant fraction of the laser light can be identified. A low-pass spatial filter allowing only the low spatial frequencies to propagate to the detector plane is used to obtain the main shadow due to the yarn core with the elimination of the signal from the small protruding fibres. Figure 26 show the intensity distribution in the Fourier plane of lens L3 with a low-pass spatial filter.

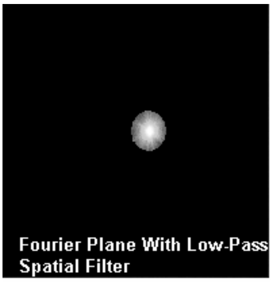

Figure 26. Fourier plane image with a low-pass spatial filter.

Observing Figure 26, it is verified that the low-pass spatial filter corresponds to the “mask” of the high-pass spatial (Figure 3 a), blocking the Fourier plane area where are located the high spatial frequencies.

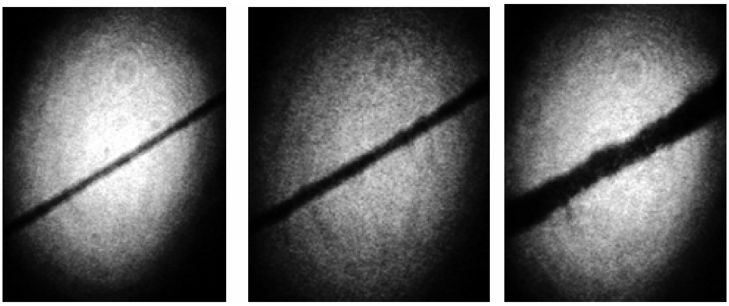

Figure 27. Examples of images resulting from the application of the low-pass spatial filter.

Resulting from the application of a low-pass spatial filter with a circular aperture of 1 mm, images from yarns of different diameters are presented in Figure 27. This filter eliminates all spatial frequencies above 11 $mm^{-1}$, corresponding to a characteristic size of 91 microns or less in the object plane. As expected, the hairiness signal is almost completely absent.

However, as the intensity of the laser light that is not blocked by the yarn, caused the saturation of the photodiode of the electronic system setup, a linear polarizer was placed before the photodiode (image plane) to attenuate the laser light signal. The polarizer should be adjusted assuring that the signal without any yarn will be in the linear response range of the photodiode.

The fundamental transverse spatial mode of the HeNe laser is Gaussian in shape rather than being spatially uniform. To overcome this drawback a detailed study was performed regarding the Gaussian nature of the incident laser beam described in the next section.

## The Gaussian Nature of the Incident Laser Beam

Figure 28 shows that the light intensity is approximately uniform near the centre but drops steeply in the spatial wings [34]. The best approximation for linearity is obtained in the centre of the beam and in its close surroundings.

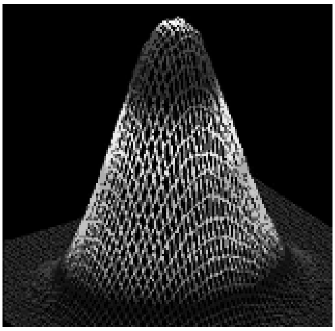

Figure 28. 3D Gaussian distribution of a laser beam [34].

A projection along a single dimension of a typical Gaussian intensity distribution is presented in Figure 29 [35].

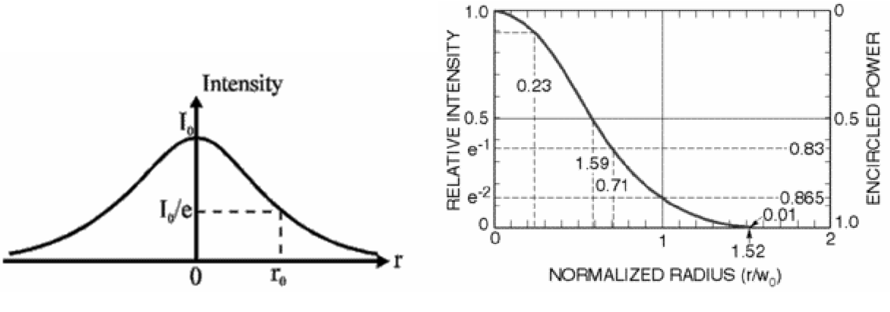

Figure 29. A Gaussian intensity distribution typical of a HeNe laser [35].

Mathematically, the Gaussian intensity distribution of the laser beam is given, as a function of the radius (r), by (6).

$$I(r) = I_0 e^{\left[\frac{-2r^2}{w_0^2}\right]} \tag{6}$$

where, the parameter $w_0$, normally called the Gaussian beam radius, is the distance from the optical axis for which the intensity is reduced by $1/e^2$ (0.135). At $r = 0.59w_0$, the intensity drops to 50 % of its maximum, while at $r = 2w_0$, the intensity is only 0.0003 of its maximum value.

Figure 27 shows that the presence of yarn in the object plane provokes a localized shadow in the image plane. The goal of this study is to correlate the signal reduction caused by this shadow with the yarn diameter. In order to calibrate the variation response of the photodiode to a localized change in the laser beam illumination, it was placed in front of the photodiode, a “window” with a vertically variable aperture. The “window” is adjustable in steps of 250 μm, using a micrometer stage to translate a movable card. Fully open, the maximum aperture has an area of 7.5 mm x 2 mm, as presented in Figure 30.

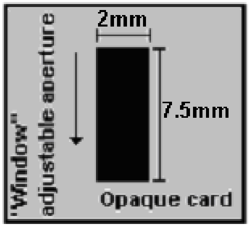

Figure 30. “Window” with variable aperture used in the photodiode.

The photodiode signal over 30 different steps, as the window changes from fully open to fully close, was measured. The resulting signals are displayed in Figure 31.

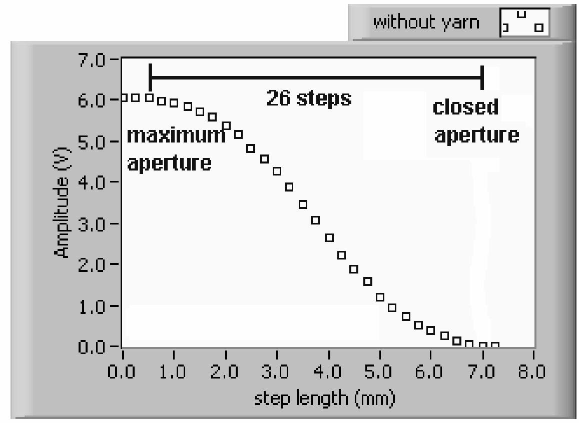

Figure 31. Photodiode signal variation as the window aperture was changed without the presence of yarn in the object plane.

Although the full aperture has a height of 7.5 mm, only 26 steps are necessary to go from a maximum signal to a null signal. Steps numbered 0 and 1 did not block the incident laser light, as an equal signal level is observed as for step number 2. On the other limit, the incident beam blocked completely at step number 28, being redundant step number 29. Only 25 steps are necessary to close totally the aperture, considering that the initial point, maximum aperture, is taken as the reference, meaning that the effective height of the illuminated area on the photodiode is between 6 mm and 6.25 mm. An approximately linear variation in the signal is observed for the aperture distances ranging between 2.5 mm and 5 mm, which correspond to the region of maximum laser intensity (zone 1). Alternatively, in Figure 32, it is displayed the signal difference between adjacent steps.

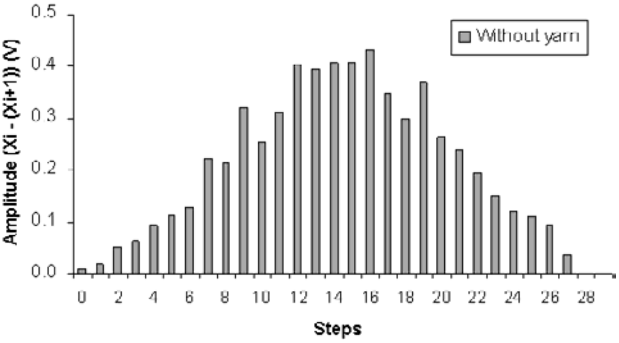

Figure 32. Signal difference between adjacent steps.

**Table 3. Identification of the laser beam illumination zones from Figure 32**

| Majority zone signal | Step variation intervals |
|---|---|
| 1 | [12-16] |
| 2 | [10-11; 17-18] |
| 3 | [8-9; 19-20] |
| 4 and other zones | [2-7; 21-27] |

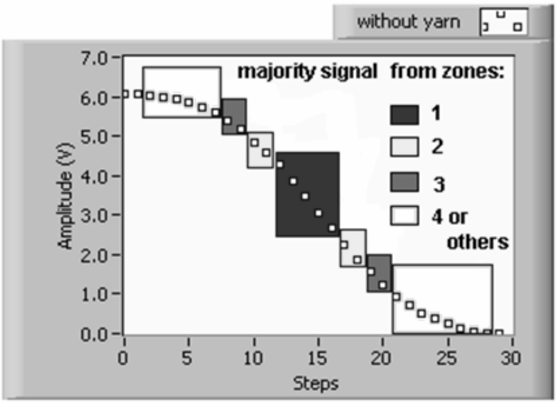

Figure 33. Identification of the laser beam illumination zones.

As expected, an approximately Gaussian distribution was achieved. The centre steps, between 12 and 16, produce an almost constant signal, corresponding to illumination zone 1

(Figure 33). The corresponding assignments between aperture steps and laser beam illumination zones are shown in Table 3 and Figure 33.

Zone 1 presents a linear variation as a function of the blocked vertical distance (Figure 34).

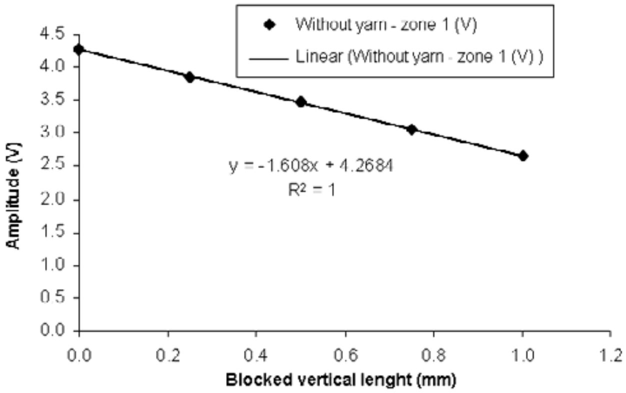

Figure 34. Linear fit to the signal measured as the translating window passed through the zone 1 of the laser illumination.

The determination coefficient ($R^2$) obtained supports the system linearity. Moreover, the system sensitivity can be estimated using the slope value obtained (-1.608 V). In this setup, a reduction of 1 mm in the vertical window, corresponding to 2 $mm^2$ of illumination area, decreases the signal output by 1.608 V. Taking into account the optical reduction factor of 66 % relative to the object plane, a variation of 2 $mm^2$ in the image plane would have an actual area of 3.03 $mm^2$, yielding an overall system sensitivity of 0.531 V/$mm^2$.

In continuous measurements, the yarn can have small deviations from the exact centre of the laser beam illumination, provoked by the traction system. In order to study the influence of such deviations, it was analyzed the signal variation in zones 1 and 2 (Figure 35).

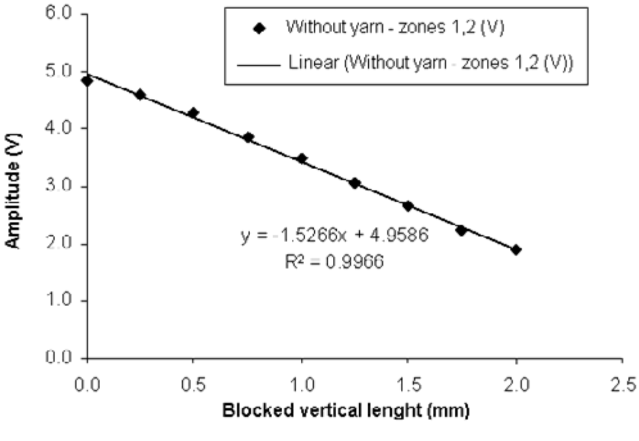

Figure 35. Signal variation over zones 1 and 2 from Figure 34.

The difference obtained in the slopes of Figure 34 (-1.608 V) and Figure 35 (-1.5266 V) is less than 6 %, suggesting that even if the yarn moves as much as ± 2 mm in the object plane (corresponding to less than ± 1.3 mm in the image plane), the diameter measurements uncertainty will be less than 6 %.

## Auto-Calibration, Diameter Determination and Irregularities Classification

In order to establish an auto-calibration procedure in the presented yarn diameter measurement system, avoiding the necessity of a standard atmosphere, the following algorithm was developed [33]:

1. Measure the signal without yarn, $V_{sf}$ (V);
2. Measure the signal with yarn, $V_{cf}$ (V), during the tested yarn length with a determined frequency of acquisition;
3. Determine the average of signal with yarn, $V_{cfa}$ (V), which considers the average diameter;
4. Calculate the average signal blocked by the yarn, $V_f = V_{sf} - V_{cfa}$ (V);
5. Estimate the yarn average theoretical diameter, $d = 4.44 * 10^{-2} \sqrt{(tex / \rho)}$ (mm) [27][28], where $\rho$ is the yarn material density (g/cm$^3$);
6. Determine the area which is on average blocked by the yarn, $A_{fsj} = sl * d$ (mm²), where *sl* is the sample length of the system (mm);
7. Determine the attenuation ratio for the tested yarn, $S_a = V_f / A_{fsj}$ (V/mm²).

Then, after the calibration process, the yarn diameter in each sample is determined by the following steps:

1. Determine the area blocked in each sample, $A_i = (V_{sf} - V_{cf}) / S_a$ (mm²);
2. Determine the diameter in each sample, $d_i = A_i / sl$ (mm).

With the diameter average, it is possible to determine yarn irregularities by calculating the percentage variation in diameter of each sample compared to the average diameter. However, if it is only necessary to characterize yarn irregularities, it is possible to use a simpler process:

1. Measure the signal without yarn, $V_{sf}$ (V);
2. Measure the signal of each sample with yarn, $V_{cf}$ (V), during the tested yarn length with a determined frequency of acquisition;
3. Determine the average for all the measured samples, $V_{cfa}$ (V);
4. Determine the yarn reference voltage, $V_r = V_{sf} - V_{cfa}$ (V);
5. Determine the percentage variation of each sample with yarn,

$$d_{i\,(\%)} = 100\,(V_{sf} - V_{cf}) / V_r.$$

## Yarn Diameter Characterization Results

This section presents the experimental results obtained with several yarns with the diameter characterization setup for a continuous acquisition in a defined length.

Three 100 % cotton yarns with different linear masses of 49.17 g/km, 62.00 g/km and 295.00 g/km were analyzed [36].

To ensure a 1 mm analysis, a window aperture, in the photodiode, with an area of 1 mm x 4 mm, was built. Although, as the optical hardware produced a reduction of 34 % in the image plane, a 1 mm height window in the image plan corresponds to an effective height of 1 mm / 0.66 = 1.52 mm in the object plane. A 4 mm wide window was used to allow a possible oscillation of the sample yarn. As the yarn position was very stable, the system acquired a high percentage of samples in the centre of the laser beam where the window was placed, allowing reliable measurements (laser zone with high linearity).

A total of 6k samples, in steps of 1 mm, were acquired for each yarn. The calibration value corresponding to the signal without yarn was 2.63 V. In order to obtain the effective signal blocked by the yarn, the difference between the acquisition signal and the value without yarn was calculated. Figure 36 presents the results obtained.

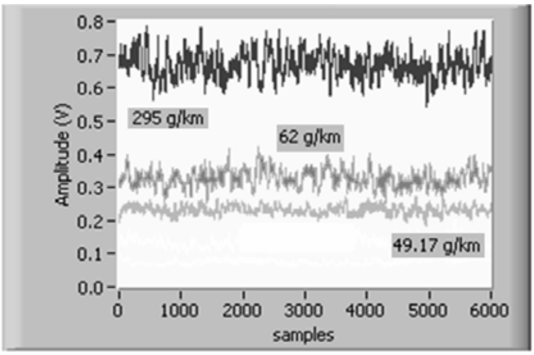

Figure 36. Yarn blocked signals for each analyzed yarn.

Figure 36 shows, as expected, that higher linear mass yarns and consequently larger diameter yarns, produce a greater amount of blocked signal. Table 4 presents the maximum and minimum yarn diameters, determined using images from an electron microscope and the average value of their blocked signals.

**Table 4. Relationship between yarn diameters and average signals**

| Yarn linear mass (g/km) | Average signal (V) | Maximum diameter (mm) | Minimum diameter (mm) |
|---|---|---|---|
| 49.17 | 0.2320 | 0.384 | 0.314 |
| 62.00 | 0.3265 | 0.518 | 0.460 |
| 295.00 | 0.6687 | 1.210 | 0.940 |

As stated before and now confirmed by Table 4, yarn linear masses are correlated with the yarn diameter. Furthermore, Table 4 also shows that the average signal obtained has a direct proportionality with the yarn diameters.

Figure 37 presents the average diameter as a function of the average signal voltage for each yarn, where is observed a clear tendency for a linear relationship between yarn diameter and the average signal blocked by the yarns under test, with the least squares linear fit having an $R^2$ of 0.995.

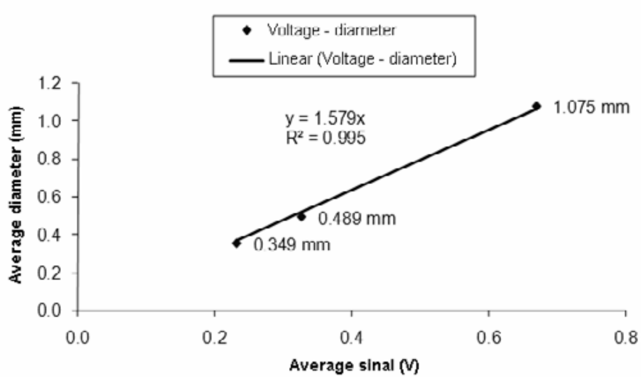

Figure 37. Linear distribution of the system yarn diameter characterization.

## Yarn Diameter Analysis Using Two Orthogonal Projections

A test was performed using two measurement systems disposed orthogonally (two directions) and the results were correlated. As the experimental methods and configurations used in this section have similar theoretical background to the ones presented in section 0 [21], except for the use of low-pass filters instead of high-pass filters, only the experimental results [37] are shown.

In sample lengths of 5 mm, 19 m of the 62 g/km yarn were analyzed, registering the signal received by each photodiode by two analogue channels of the National Instruments USB-6251 data acquisition board [20]. The experimental setup is presented in Figure 21 using low-pass filters instead of high-pass filters.

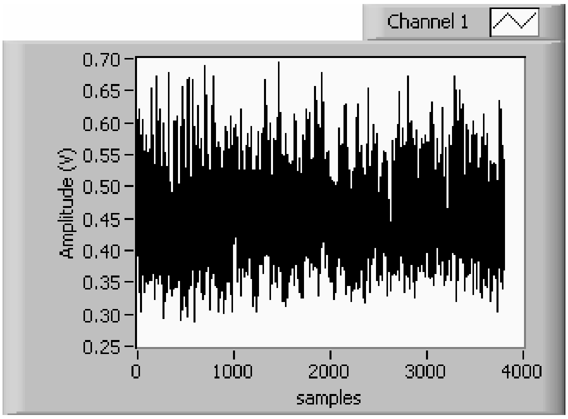

Figure 38. Blocked yarn signal for channel 1.

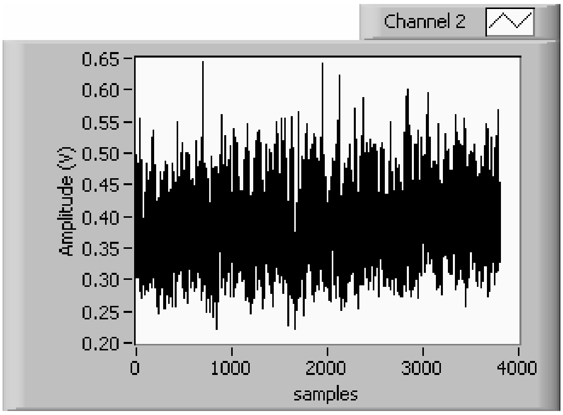

Figure 39. Blocked yarn signal for channel 2.

The signal without yarn for channel 1 was 7.85 V and for channel 2 was 7.46 V. The blocked yarn signal, from each photodiode, was determined by subtracting from the signals without yarn, the acquisition signals. Figure 38 and Figure 39 present, respectively, the blocked yarn signals obtained for channel 1 and channel 2.

It was obtained an average of 0.450 V and a SD of 6.3 % for channel 1 and an average of 0.381 V and a SD of 5.8 % for channel 2. As expected, the average signals are close but not equal. The gains of the transimpedance amplifiers were adjusted to give approximately the same reference level. However, as the laser power was different in each channel, this resulted in different gains for the two channels. Nevertheless, the SD results should be close, as verified. On average, the pattern deviation for the two signals should be close, provided that the irregularities are randomly distributed over the yarn and having an equal probability of taking on any orientation over the 360º about the yarn's axis. But to correctly correlate the signals, their percentage variation over the average must be analyzed. Figure 40 and Figure 41 present respectively, the percentage variation signal obtained for channel 1 and 2, where it was obtained a SD deviation result of 14.1 % and 15.2 %. Although these signals look different, they are in fact statistically very similar, as confirmed by the results obtained.

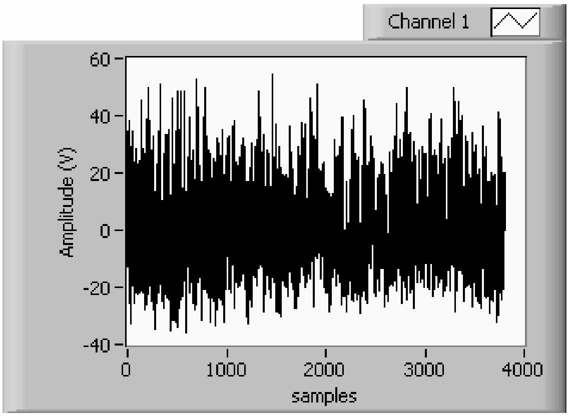

Figure 40. Percentage variation over average for blocked yarn signal from channel 1.

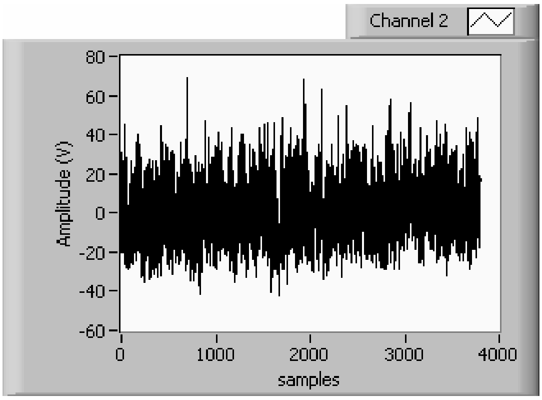

Figure 41. Percentage variation over average for blocked yarn signal from channel 2.

Furthermore, for a detailed analysis of the signals, it were determined their frequency diagrams considering 100 intervals, as presented in Figure 42.

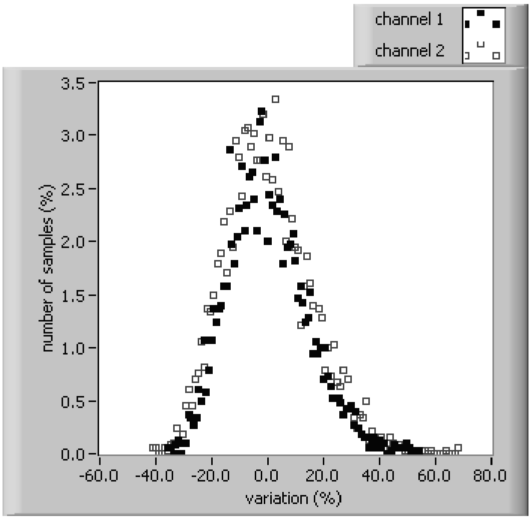

Figure 42. Frequency diagrams of channels 1 and 2 for the percentage variation signals.

Observing Figure 42 it is verified that, regarding the number of samples obtained for each tested interval, both signals are highly correlated. The amplitude differences obtained at each interval are presented in Figure 43, where it is observed that the variations are in a low level of number of samples range of [-0.9 %; 1.18 %]. A SD of 0.33 %, a mode of 0.11 % and a mean of 0.22 % were obtained. The high level of statistical significance between the signals, confirms the mathematical deduction presented in the hairiness measurement approach, where a single direction projection is sufficient to correctly characterize the yarn, in this case, in terms of irregularities [30]-[32].

The experimental results presented in this section demonstrated that the orthogonal results confirmed that for the number of samples used in the test, the variation between the results of each direction is reduced (absolute value of approximately 2 %).

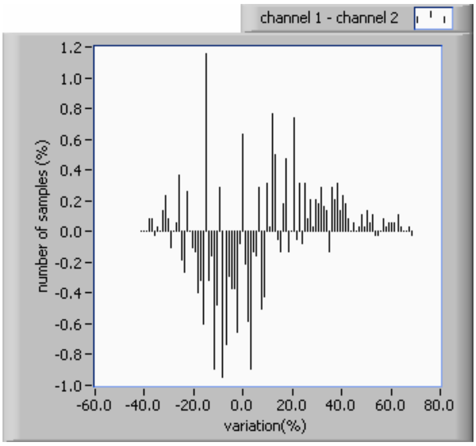

Figure 43. Amplitude differences in each interval of Figure 42.

These facts support that for the high number of samples used in yarn evaluation, using only a single projection is possible to quantify the total amount of yarn irregularities with a good level of confidence, by using a factor of 1.57 to account for the single projection hairiness results. This permits the use of a less complex system at a lower cost.

## BIOMEDICINE: BIOCHEMICAL ANALYSIS OF BODY FLUID SAMPLES

This section describes the methodology employed to develop a CMOS optical detection microsystem that uses photodiodes as the detection element for reading the light intensity that is absorbed by a specific biochemical substance present in a body fluid sample and, therefore, determine its concentration in that fluid sample. Those photodiodes are programmed to feature highly accurate and selective detection. Their relatively simple readout circuits and their compliance with a standard CMOS process (without extra masks) allow addition to an existing CMOS design, and makes them the election detection element in lab-on-a-chip devices based on spectrophotometry.

In the following sub-sections some generic features for the measurement technique are addressed and the major characteristics and properties for the design of the CMOS photodiodes and its readout electronics are discussed. The obtained results are also presented, which allow concluding that the CMOS optical detection microsystem can be used in lab-on-a-chip devices for spectrophotometric analysis of body fluids samples.

### Background of Spectrophotometric Analyses

In biochemical analysis of body fluids samples, one of the most commonly used analytical techniques is the spectrophotometric analysis (the study of the interaction of electromagnetic radiation with biochemical substances). Spectrophotometry by optical absorption is often used to determine the activity, structure, concentration and/or amount of a particular analyte in body fluids samples [38]. An analyte is the substance (element, ion, compound or molecule) being analyzed. The absorbance detection will be briefly reviewed in the following paragraph. More detailed information can be found in books such as [39].

In absorbance detection, the sample is excited by a light source of intensity, $I_0$. The light intensity that passes through the sample is measured, $I$. The ratio of the two previous quantities is denominated as the absorbance, $A$, and is linked to the concentration of the analytes according to the Lambert-Beer's law [39]:

$$A = -\log \frac{I}{I_0} = \alpha\, c\, d \tag{7}$$

where $d$ is the pathlength, $c$ is the concentration of the analyte in the sample and $\alpha$ its corresponding molar absorption coefficient. The Lambert-Beer's law, as written above, is not directly applicable to circular microchannels. Diffraction and reflection effects strongly modify the pathlength, and therefore a correction factor must be applied.

The spectrophotometric measurement used in the lab-on-a-chip presented in this section is based on colorimetric detection by the optical absorption in a part of the visible spectrum defined by the analytes present in the sample. These analytes have an absorption maximum at a specific wavelength, which is directly proportional to their concentration in the samples. However, many of the analytes of interest for clinical analysis do not have chromophores that absorb light in a useful part of the visible range. Specific chemical reactions are available (reagents) to transform these analytes into coloured products that do have adequate absorbance [38]. In addition, in colorimetric analyses, a fluid sample is mixed with a specific reagent, proper for the biochemical substance being analyzed, and, from that mixture, a coloured product is obtained. The intensity of that colour is directly proportional to the concentration of the biochemical substance in analysis and the absorption spectra of the mixture show a maximum peak at a specific wavelength [38]. As an example, for determining the magnesium concentration in a blood sample the mixture has an absorption maximum at 550 nm (Figure 44).

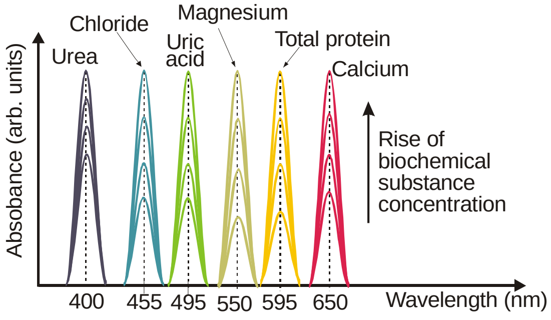

Figure 44. Absorption spectra shape for some biochemical substances with different concentrations in blood.

Shrinking of clinical analysis systems is fundamentally limited by the amount of molecules available in the sample volume (i.e. the product of the cross-sectional area of the channel and the illuminated channel length) and thus by the concentration of the desired analyte. Common body fluids analyses require the reproducible measurement of analyte concentrations between $10^5$ and $10^{12}$ molecules per picoliter. Consequently, a picoliter sample volume is realistic only if the detection system can measure the detection limit of

$10^5$ molecules. For example, in human urine, albumin is the protein that has the lowest target molecules (in average 1 μmol in 1 liter of urine) and also the lowest concentration (less than 15 mg/dl). For a low concentration of albumin in urine, for example 5 mg/dl, there are still $3.35 \times 10^5$ molecules per picoliter. Whether actual shrinking to the picoliter range is feasible also depends on practical aspects, such as the channel height (or optical pathlength) required to achieve measurable absorption (which depends on the analytes absorption coefficient ($\alpha$), for example, $\alpha = 0.27\ \text{m}^{-1}$ for an albumin concentration of 5 mg/dl), as well the minimum channel width and the photodiode area, which are both set by lithographic constraints. Typical minimum dimensions for the optical pathlength is 500 μm. The reduction of this optical pathlength makes solutes with poor absorption coefficients difficult to detect, even with a high-accurate detection system.

## CMOS Photodiodes as the Detection Element

### Absorption of Light In Silicon

The absorption of light in silicon in the visible part of the electromagnetic spectra is wavelength dependent. Radiation with short-wavelengths (high-energy photons) is quickly absorbed near the surface and radiation with long-wavelengths (low-energy photons) penetrates deeper in silicon before being absorbed. This effect is due to the strong wavelength dependence of the silicon absorption coefficient $\alpha$, which causes the penetration depth of light in silicon, $d(\lambda)$, to be wavelength dependent and expressed by [40].

$$d(\lambda) = \frac{1}{\alpha(\lambda)} \tag{8}$$

Selecting the suitable junction depth allows to set a maximum peak at a specific wavelength. An optimal photodiode structure for a particular application might require a special processing of the silicon wafer with several non-standard steps, which usually involves high-costs and the need for easily adaptable and suitable equipped semiconductor facilities. Consequently, most silicon photodiodes structures comply with the possibilities of the standards foundries.

### Photodiodes Available in CMOS

The photodiodes convert the light intensity that reaches its active area into a photocurrent. In the case of the reported application, this light is the light transmitted through the coloured mixture (which is related to the mixture absorbance by equation (1.7)), but, it also can be the light emitted or reflected by the mixture. In a standard n-well CMOS process, three photosensitive structures are possible as vertical junction photodiodes: n-well/p-epilayer, p+/n-well and n+/p-epilayer (see Figure 45). In the CMOS process used, the thickness of the n-well is 2900 nm, the n+ layer is 350 nm, the p+ layer is 500 nm and the depth of the epilayer is 12 μm, with a doping concentration of $10^{16}$ atoms/cm$^3$. At a particular wavelength, the photodiodes quantum efficiency varies according to their junction depth.

The quantum efficiency of a photodiode reveals how well it collects the incident light [41]. In the visible spectrum, the blue light (of about 450 nm) is more efficiently collected by a shallower junction (p+/n-well and n+/p-epilayer) and the red light (of about 650 nm) by a deeper junction (n-well/p-epilayer). Moreover, despite the shallower junction of the n+/p-epilayer photodiode, it has the higher quantum efficiency in the wavelengths of about 500 nm, due to the different doping concentration between the *n* and the *p* side, which extends the *p* side depletion area more deeply. Therefore, according to the biochemical substance maximum absorbance, emission or reflection wavelength, it is chosen one of these three photosensitive structures for the photodiode. When the same lab-on-a-chip is developed to analyse several biochemical substances, ranging from the 400 nm to the 700 nm, the device would benefit of include those three photodiodes. In that case, the readout electronics will be programmed to select the photodiode that better fits the biochemical substance in analysis.

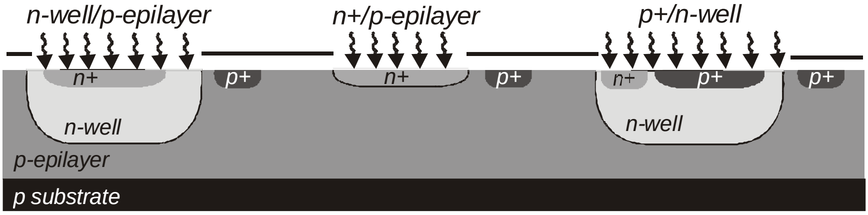

Figure 45.The three vertical junction photodiodes in a standard n-well CMOS process: n-well/p-epilayer, p+/n-well and n+/p-epilayer.

The quantum efficiency is determined by intrinsic and extrinsic parameters. Intrinsic parameters are type of semiconductor, junction depth, depletion width and carrier diffusion length. However, there is little room to play with these parameters in standard CMOS: the junction depth is fixed. The most common extrinsic parameters are the stack of dielectric layers possibly left on top of the photodiode pn-junction and the pixel effective area (fill factor). Therefore, the alternative for improving the quantum efficiency at a certain wavelength is to use a combination of these dielectric layers. They act as a thin-film stack and influence the optical transmittance for each wavelength independently. In addition, the photodiode quantum efficiency can be programmed by design. For that, the thickness and the optical properties of those layers have to be stable and well known for all batches of the standard process [42].

## Optimization of Photodiodes Quantum Efficiency

In the standard CMOS process used there are three dielectric layers above the photodiode pn-junction (see Figure 46). The first oxide (BPSG – Boron Phosphor Silicate Glass) thickness above the photodiode is measured as 650 nm and the second ($SiO_2$) as 700 nm. The silicon nitride layer (the overlayer), used for scratch protection, is 800 nm thick. Since technology rules from the standard CMOS process have to be met, the design of the optical path is restricted to combinations of those three dielectric layers above the pn-junction. The simulated optical transmissions of those combinations are shown in Figure 47. The simulations are done with an optics software package TFCalc 3.4, supplied by Software Spectra, Inc., USA.

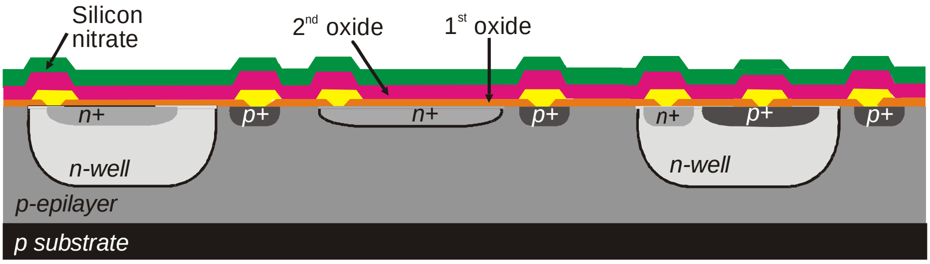

Figure 46. Cross-section of the basic structure of the photodiodes, fabricated in a standard n-well CMOS process.

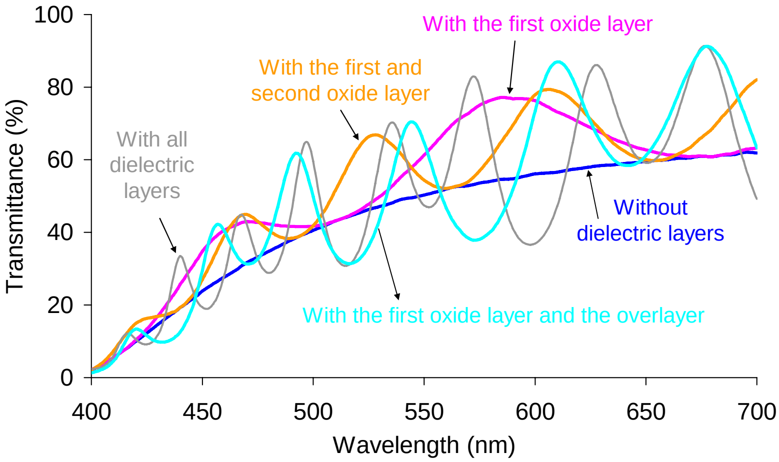

Figure 47. Simulated spectral responses of some typical combinations of the dielectric layers above the photodiode pn-junction.

The simulations indicate that when no dielectric layer is present, the air-silicon interface represents a great transmission loss. An oxide layer, with a thickness around 650 nm, can increase the transmittance from 50% to 60%, but also introduces wavelength dependence.

A properly designed anti-reflective coating can optimize the transmittance. However, this represents a post-processing step to the standard CMOS, which would damage economically the microsystem. In some cases, the best choice would be the removal of all dielectric layers from the top of the silicon surface. This process is performed at the design level, using the same masks designed for the metal contacts and for the overlayer (without additional masks or steps). However, in the used standard CMOS process, when etching the dielectric layers the metal layers are used as etch stops, and so, the etch time does not need to be very accurately controlled. This might represent a problem if the process steps are kept standard, because the removal of the dielectric layers etches the under adjacent layer (see Figure 48). Consequently, from the practical point of view, the removal of the first oxide layer is not feasible, because it may damage the pn-junction. A visible effect is the roughness (like bubbles) in the photodiode active area (see Figure 49). This random surface-rough interferes, also randomly, in the photocurrent response. Therefore, using the standard CMOS process, the first oxide layer should be left over. Thus, the best photodiodes structure for the related application is the one presented in Figure 50. It is desirable to have the minimal wavelength dependence for suiting this optical detection microsystem to the spectrophotometric analysis of several biochemical substances and several body fluids.

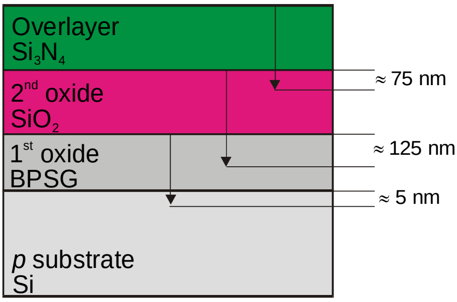

Figure 48. Etched layers when etch masks are applied.

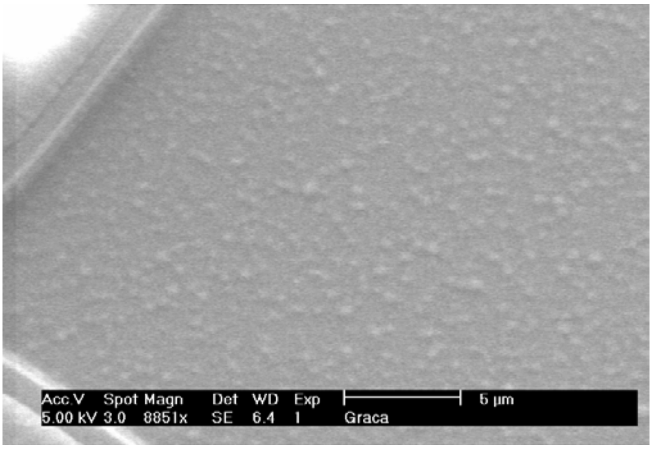
Acc.V Spot Magn Det WD Exp 5 µm
5.00 kV 3.0 8851x SE 6.4 1 Graca

Figure 49. A SEM photograph of the CMOS photodiode without the first oxide.

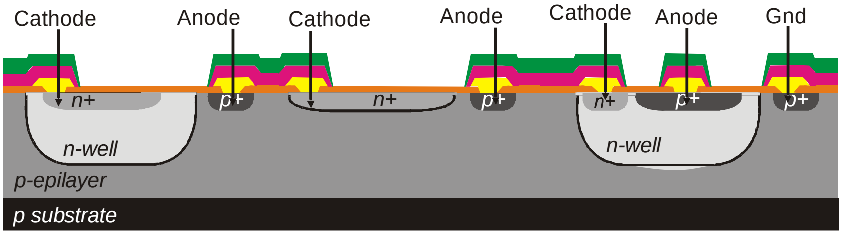

Figure 50. Cross-section of the fabricated CMOS photodiodes.

## Photodiodes Operation and Characterization

The photodiodes operation and characterization is demonstrated by their measured spectral responsivity, quantum efficiency and dark current. All photodiodes have an active area of $250 \times 10^3$ µm$^2$. Those measurements were performed using a Keithley 487 picoamperemeter (full-scale range from 10 fA to 2 mA and a resolution of $5^{1/2}$ digit), and a 250 W quartz tungsten halogen lamp with the ORIEL Cornerstone 130$^{TM}$ monochromator used as light source. The measurements were calibrated with a calibrated commercially available photodiode as reference (Hamamatsu S1336-5BQ). Figure 51 shows the spectral responsivity and the quantum efficiency for the three photodiodes structures presented in Figure 50 (all with only the first oxide on top of the pn-junction). It can be concluded that each photodiode structure is suitable for a certain range of wavelengths, fulfilling the exposed theory of the 1.4.2.2 section.

Figure 52 shows the spectral responsivity and the quantum efficiency for the n+/p-epilayer photodiode with two different combinations of the dielectric layers above the photodiode pn-junction (with only the first oxide and with all dielectric layers). Once again, the measured results agree with the simulated ones presented in Figure 47.

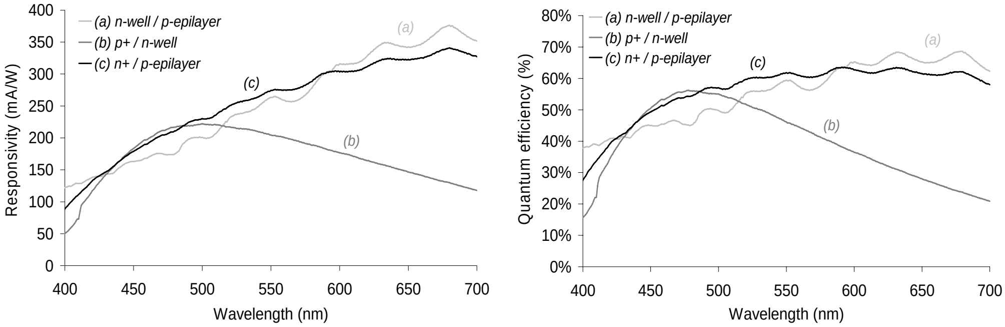

**(A)** **(B)**

Figure 51. Measured (a) spectral responsivity and (b) quantum efficiency of the three photodiodes structures.

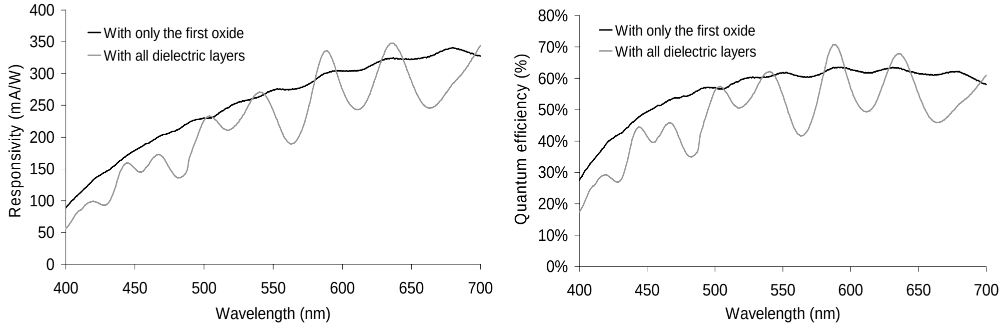

**(A)** **(B)**

Figure 52. Measured (a) spectral responsivity and (b) quantum efficiency of the n+/p-epilayer photodiode with two combinations of the dielectric layers above the photodiode pn-junction.

In Figure 53 it can be shown the n+/p-epilayer photodiode dark current, with only the first oxide and with all dielectric layers, for several reverse bias voltages. A dark current of 0.27 pA ($1.08 \times 10^{-18}$ A/$\mu$m$^2$) and of 0.63 pA ($2.52 \times 10^{-18}$ A/$\mu$m$^2$) at 0 V was measured for a photodiode active area of $250 \times 10^3$ $\mu$m$^2$ with only the first oxide and with all dielectric layers, respectively. From these results it can be concluded that the dielectric layers, not only introduce wavelength dependency, but also increase the dark current.

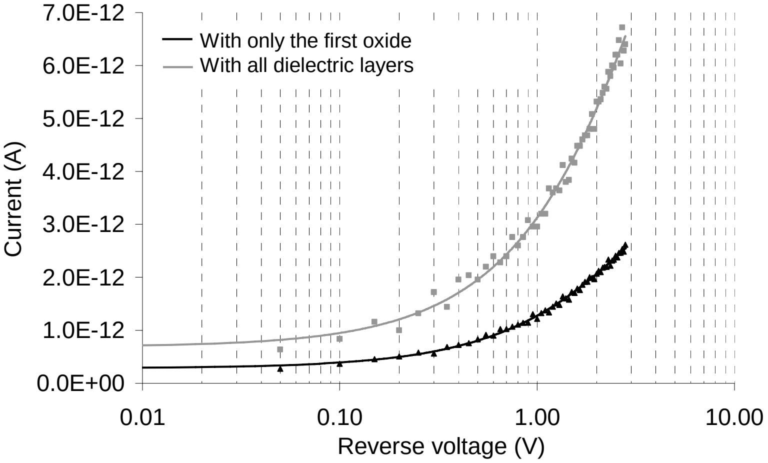

Figure 53. Measured dark current as a function of the reverse bias voltage of the n+/p-epilayer photodiode with two combinations of the dielectric layers above the photodiode pn-junction.

## Photodiodes Readout Electronics

It is desirable to integrate the analog to digital conversion and the photodiodes in the same silicon die. For that, a CMOS light-to-frequency converter was designed (see Figure 54). It produces a bit stream signal with a frequency proportional to the photodiode current and hence proportional to the intensity of the light that reaches the photodiode active area.

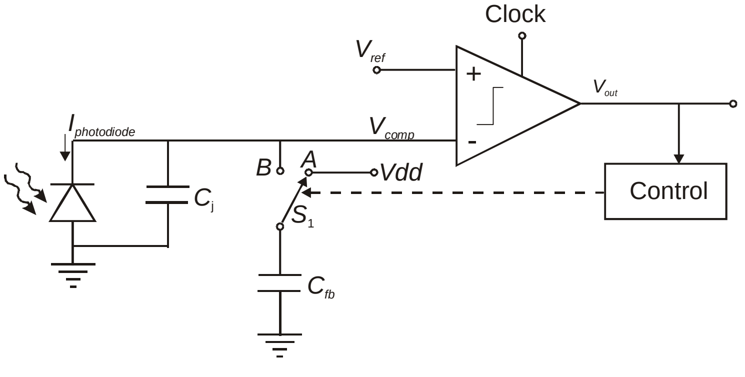

Figure 54. Block diagram of the photodiode readout circuit.

The reverse biased junction capacitance of the photodiode $C_j$ and capacitor $C_{fb}$ are used as storage elements. At the voltage $V_{comp}$ lower than $V_{ref}$, the comparator output $V_{out}$ remains at a high logic level. After synchronization with a clock pulse, the analog switch $S_1$, is changed for the *A* position, which forces the capacitor $C_{fb}$ to be quickly charged during one clock period with the voltage *Vdd*. After that period, this switch is changed again to the *B* position and the comparator output voltage commutes to the low logic level ($Vdd > V_{ref}$). Thus, the photocurrent discharges the capacitor $C_{fb}$ until the comparator detects $V_{comp} < V_{ref}$, which causes $V_{out}$ to change to the high logic level again and the cycle to repeat (see Figure 55). The bit stream frequency of the output converter is a function of the charge change in the capacitor, $\Delta Q$, which is directly proportional to the input photocurrent and hence to the biochemical substance concentration,

$$f_{bitstream} = \frac{I_{photodiode}}{\Delta Q} \tag{9}$$

The logic and the analog switches $S_{2a}$ though $S_{2d}$ select the channel to be measured. These switches are identical complementary PN-MOS switches. The comparator is a clocked high-speed regenerative comparator with a rail-to-rail input circuit. For reliable operation a two-phase non-overlapping clock is used for the analog switch $S_1$ and for the comparator. It is possible to use a digital counter for counting the bit stream output pulses of the comparator during a fixed time period, producing the digital value correspondent to the photocurrent intensity. Alternatively, a microcontroller can substitute the counter, generating all the control logic and performing additional calculations too.

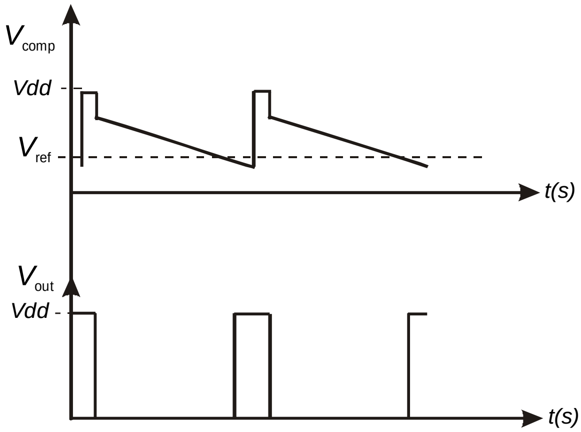

Figure 55. Comparator input and output voltages.

In the reported application, four photodiodes, placed underneath the fluids chambers (see 1.4.5.3 section, Figure 62) should be used in each measurement for fulfil the requirement of portability (Figure 56). The first photodiode is for the reagent (without the biochemical substance) and it is needed to obtain the baseline reference; the second is for the body fluid that is being analyzed; the third is for measuring the photodiode dark current; and the fourth is for the calibrator (a standard sample with a well-known concentration of the biochemical substance that is being analyzed) and it is needed to calibrate the microsystem and to compensate the incident light oscillations (see section 1.4.5). The dark current is the current that flows in a photodiode when there is no optical radiation incident on it. It is usually measured and then subtracted from the flux. As the dark current is temperature dependent, one measurement at the beginning of the experiment is usually not sufficient. Thus, in the reported circuit, a dark current compensation channel is implemented using the photodiode 3. This photodiode is completely covered with metal.

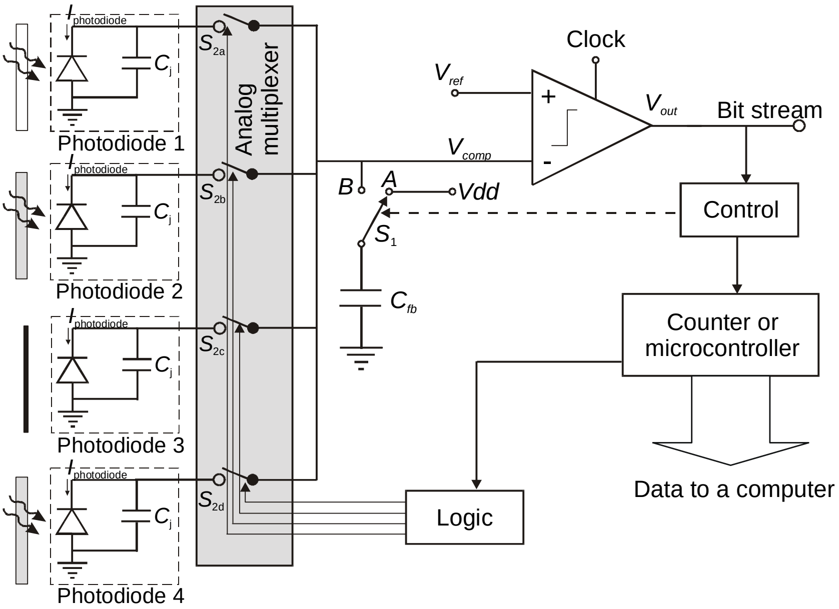

Figure 56. Block diagram of the photodiodes readout circuit used in each biochemical substance concentration measurement.

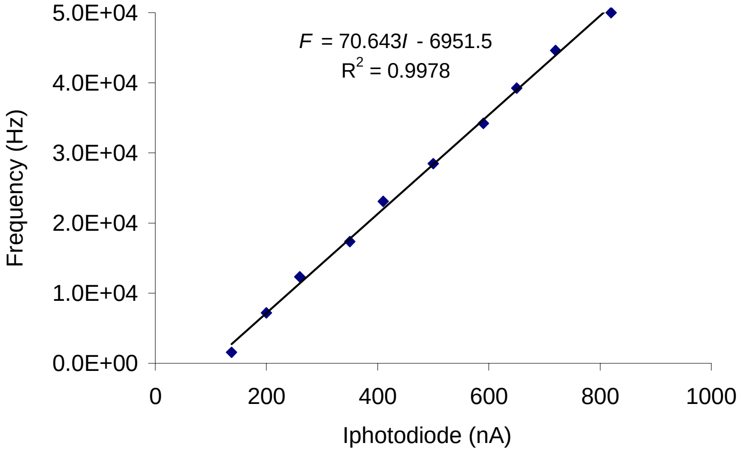

Figure 57. Output frequency of the light-to-frequency converter for different photodiode currents (*F* – frequency, *I* – Photodiode current, R – Pearson product moment correlation coefficient).

The power supply of the light-to-frequency converter circuit is 5 V. The reference voltage of the comparator ($V_{ref}$) is 2 V and the clock frequency is 1 MHz. The monochromator light source is used for testing the performance of the converter. This light is approached and removed from the photodiodes. Figure 57 shows the output frequency of the light-to-frequency converter for different photodiode currents, which corresponds to different intensities of the light source. In Figure 58 samples of the oscilloscope traces, when the light source is at 5 cm (corresponding to a photodiode current of 820 nA) and at 50 cm (corresponding to a photodiode current of 137 nA) from the photodiode, were photographed, respectively. It can be seen that the output frequency of the comparator is proportional to the light intensity. The optical system sensitivity achieved is 1 kHz/Wm$^{-2}$ at $\lambda = 670$ nm (using the TLS230 from Texas Instruments as reference). Further, the comparator output is used as a clock signal for a counter, which counts pulses during a fixed time period, producing the digital readout correspondent to the light intensity.

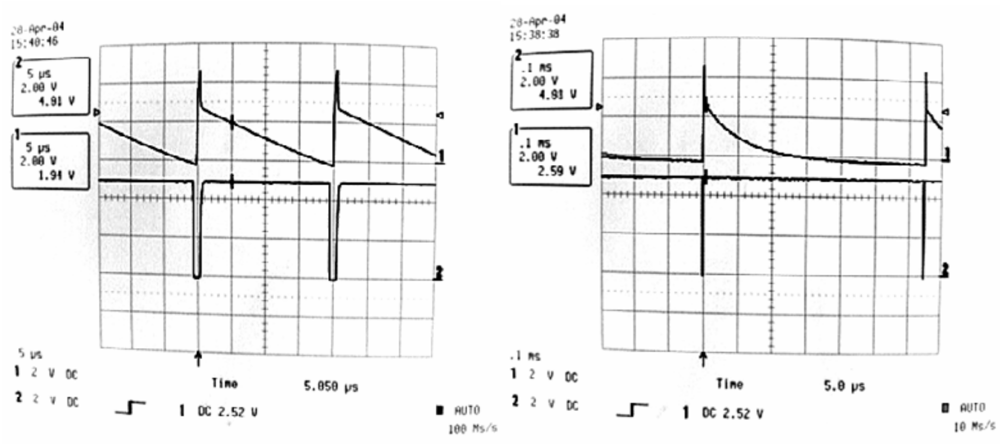

**(A)** **(B)**

Figure 58. Oscilloscope capacitor voltage (1) and comparator output voltage (2) when the light source is at: (a) 5 cm from the photodiode; and (b) 50 cm from the photodiode.

## CMOS Optical Detection Microsystem Fabrication

The CMOS photodiodes and readout circuits have been fabricated through a double-metal, single-polysilicon, 1.6 µm n-well CMOS process. The area of each photodiode is 500 µm × 500 µm. Figure 59 shows a photograph of the fabricated optical detection microsystem. The photodiode for measuring the dark current is point out with the letter ‘B’. A metal layer covered its active area. This microsystem has been packaged in a “Dil 40” package (see Figure 60).

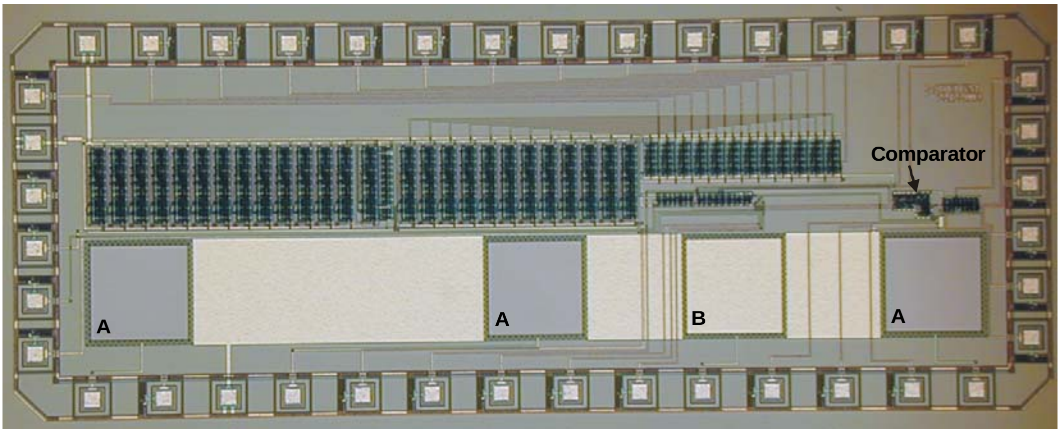

Figure 59. A photograph of the optical detection microsystem.

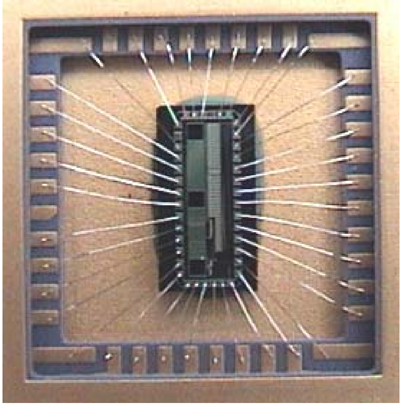

Figure 60. A photograph of the packaged optical detection microsystem.

## CMOS Optical Detection Microsystem Operation Integrated in a Lab-on-a-Chip

### Lab-on-a-Chip Concept

The reported CMOS optical detection microsystem was integrated in a lab-on-a-chip device for measure, by optical absorption in a part of the visible spectrum, the concentration of several biochemical substances in body fluids. The complete device allows the measurement with a regular white light illumination, thus avoiding the use of complex and expensive analysis systems like the ones that comprise spectrophotometers, for example. This feature highly facilitates portability and ensures analysis within consultation time, at a patient house (allowing a first trial) and in clinical laboratories or hospitals. Despite its small dimensions, low energy consumption and the use of small quantities of reagents and samples, it has the same reliability and precision of the body fluids analysis systems by spectrophotometry available, nowadays, in clinical laboratory analyses.

### Lab-on-a-Chip Operation

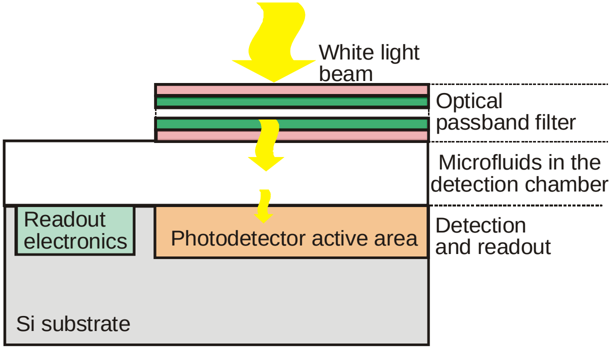

Figure 61. Cross-section of the lab-on-a-chip structure.

The lab-on-a-chip operation (see Figure 61) is based on topside illumination with a white light beam that is transmitted through the detection chambers containing the samples to analyze. The impinging light is filtered, by optical filters, to a narrow spectral band centred at the wavelength for which the coloured mixture has its absorption maximum. The intensity of the selected spectral component transmitted through the fluid is measured using the underlying photodiodes integrated in the reported CMOS optical detection microsystem.

## Lab-on-a-Chip Structure

The lab-on-a-chip combines in a multichip module the microfluidic system, the optical filtering system and the reported CMOS optical detection microsystem (Figure 62a). The microfluidic system contains the microchannels and the detection chambers. The main channel is 500 µm wide, 70 mm long and 500 µm deep, with a liquid volume quantity of 20 µl. Each detection chamber is 2 mm wide, 3 mm long and 500 µm deep. The high depth is crucial for the optical absorption measurements (see section 1.4.1). The microchannels are fabricated in SU-8 photoresist (Figure 62b). Therefore, they have a deep rectangular vertical profile, which is suitable for optical absorption measurement. Moreover, the SU-8 based fabrication is a low-cost process, UV lithography semiconductor compatible and does not require expensive masks, a regular transparency foil, like the one used in printed circuit boards, is enough. In addition, the microfluidic system can be a disposable die, which minimize the cost associated with cleaning and avoids the contamination between analyses [43].

The optical filters are based on highly selective Fabry-Perot thin-films optical resonators fabricated using a stack of dielectric layers ($TiO_2$ and $SiO_2$). These films are deposited on top of the detection chambers by Ion Beam Deposition. They are designed to yield a narrow passband around the wavelength for which the coloured mixture has its absorption maximum. This characteristic enables the selective measurement of the light intensity, at the desired wavelength, transmitted through the mixture. Further information about its design can be found in [44].

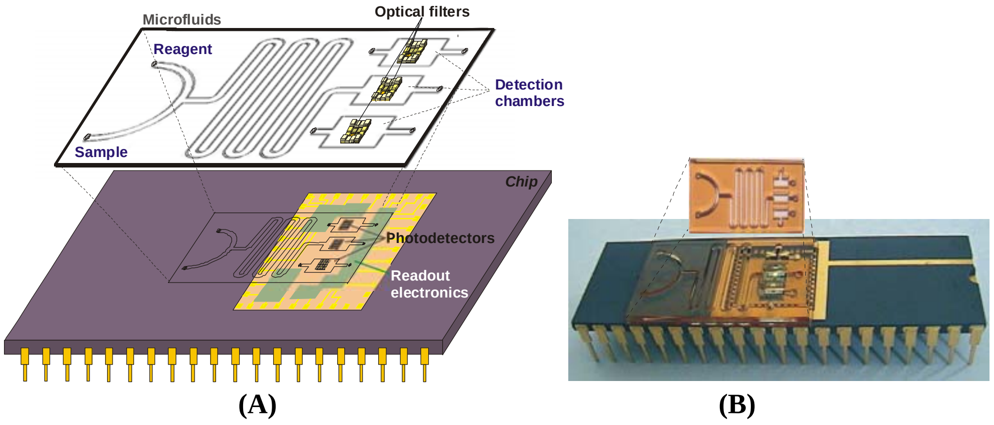

Figure 62. (a) Schematic of the lab-on-a-chip structure; (b) photograph of the lab-on-a-chip. The microfluidic system is glued to the CMOS chip.

## Lab-on-a-Chip Biochemical Measurements

After testing that the use of small quantities of samples remains compatible with the prescribed procedures that are described in the reagent protocol, which are based on 3 ml of sample volume, proper operation of the lab-on-a-chip is confirmed using a set of experiments that involve the quantitative measurement of uric acid and total protein in urine. The complete and homogeneous mixing of the urine sample with the specific reagent for the quantitative measurement of the biochemical substance concentration was performed in about 40 s. The reagents used are from Sigma-Aldrich. They react with a sample of urine in a 50:1 ratio. Measurements were performed comprising the range of normal and typical abnormal biochemical substances concentration values in a human being.

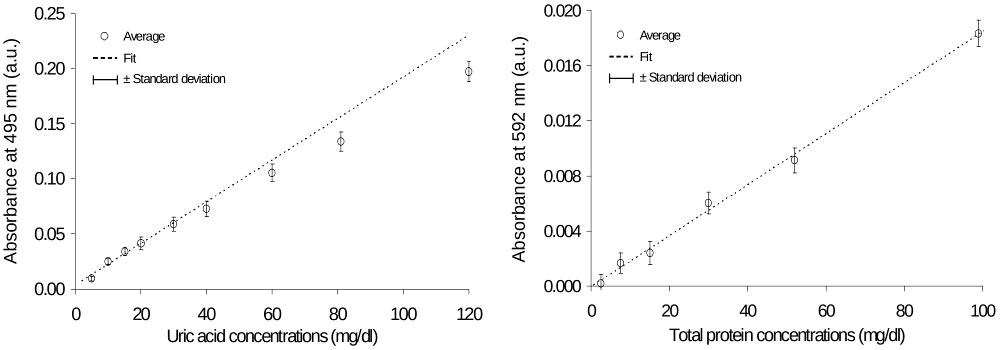

**(A)** **(B)**

Figure 63. Absorbance as a function of the analytes concentration using only a white light source as the lab-on-a-chip illumination (average ± standard deviation, samples number = 10).

**Table 5. Result of linear fit from absorbance calibration plot measured using a white light as light source (a 200 W halogen lamp)**

| Analytes (measured conc. range (mg/dl)) | λ(abs max) (nm) | Linear conc. range (mg/dl) | Slope (a. u.) dl/mg | Intercept (a. u.) | Correlation coefficient ($R^2$) |
|---|---|---|---|---|---|
| Uric acid (0-120) | 495 | 0 – 30 | (1.9 ± 0.4)×10-3 | (3 ± 2)×10-3 | 0.98016 |
| Total protein (0-100) | 592 | 0 – 100 | (1.9 ± 0.2)×10-4 | (-0.5 ± 2)×10-4 | 0.99665 |

The obtained results (Figure 63 and Table 5) allowing the following conclusions: (1) with correlation coefficients above 0.980 the method presents a linear behaviour for the concentration range described in the table (for higher concentrations the sample should be diluted and re-assayed multiplying the result by the dilute factor); (2) the intensity of the colour produced by the mixture is directly proportional to the biochemical substance concentration, once it obeys to Lambert-Beer's law; (3) the uric acid and the total protein absorption spectra show a maximum peak at the wavelength $\lambda$ = 495 nm and $\lambda$ = 592 nm, respectively; (4) the reproducibility mean coefficient variation of 10 replicate analyses for each concentration were less than 10%; (5) the minimum detection of the lab-on-a-chip is 0.5 mg/dl and the achieved sensitivity is 5 mg/dl for both analytes, which corresponds to a relative resolution of 3.3%, enough for human being urine values.

## CONCLUSION

This section presents the main conclusions obtained in photodiode application in Textile Industry and Biomedicine considering the studies and approaches previously described.

### Textile Industry Applications

Concerning the yarn hairiness measurement approach developed, the following achievements were obtained:

1. With the setup proposed it was possible to infer qualitatively the level of yarn hairiness;
2. There is no relationship between yarn diameter and reference values, as the system is only sensible to yarn hairiness and yarn borders (contours);
3. The signal output is directly proportional to the length of the hairs causing the signal;
4. As the hair diameter (fibres) have variations of only a few microns, their influence comparatively to the influence of hair length, is minor and can be ignored;
5. The minimum statistical reference method showed reliable results in comparison to the water method, with the advantage of being a non invasive procedure and can be performed online;
6. A high level of statistical similarity between the signals obtained with orthogonal projections directions was obtained and so a single projection data can be simply corrected by the factor of $\pi/2$ to get a reliable overall characterization of yarn hairiness, provided that a sufficient number of samples is acquired;

Based on the described achievements it is concluded that the developed setup, using a single direction projection, proves to be an accurate method to measure yarn hairiness reducing the system cost and complexity.

Subsequently, analyzing the studies undertaken throughout the yarn diameter measurement approach, it was verified that:

1. A direct relationship between the yarn diameter and the output voltage of the system is obtained for the zones 1 and 2, which correspond roughly to a full laser saturation zone;
2. The use of coherent signal processing increases the precision and resolution of the system measurements as the hairiness is eliminated in the image plane measured by the photodiode;
3. The system is capable of auto-calibration and, as a consequence, do not require a standard atmosphere;

4. A single projection direction analysis is sufficient to correctly characterize the yarn irregularities considering a factor of π/2 (1.57), reducing the complexity and the cost of the apparatus;

Based on the results obtained it is concluded that the system approach is suitable to determine yarn diameter variation, being capable of accurately quantifying the level of yarn irregularity [30]-[32].

## Biomedicine Applications

With the CMOS optical detection microsystem described, it was possible to determine the concentration of some biochemical substances that are present in body fluids. The obtained results confirm the direct proportionality between intensity of the colour produced by the mixture and the biochemical substance concentration. They agree with macroscopic measurements performed with well known uric acid and total protein standards and using state-of-the-art laboratory equipment. In conclusion, it has been obtained the same performance, precision, reliability and sensibility of the analysis performed, nowadays, in clinical analysis laboratories. Although this microsystem was presented for determining the concentration, by optical absorption, of biochemical substances in body fluids, it can also be used for applications that require not only the absorbance measurement, but also the fluorescence or reflectance measurements. Generally, it can be applied when it is needed a colour intensity determination of a fluid sample, in areas such as environmental, food testing, air and water analysis, forensic laboratories.

The same CMOS photodiodes presented here can be used in CMOS imagers for X-ray detection or for being integrated in endoscopic capsules for fluorescence detection of cancer tissue.

Regarding to X-ray detection it would benefit if the analogue to digital (A/D) conversion of the image sensors could be integrated in a single chip, which is difficult using CCD (Charge Coupled Device) imagers. Advantages of such integration are lower power consumption, cost reduced, reliability improved and data conversion speed up. A single chip require that all the components of an image sensor system are integrated on the same substrate, e. g., clock devices, image sensor, A/D conversion, control and signal processing. These requirements can be achieved by using a CMOS process [45]. Besides being widely available, a standard CMOS process is generic, supports several photosensitive structures, favours the integration of multiple electronics functions with a high yield and it is, currently, the cheapest of the competing technology. If a standard technology for the fabrication of the image sensor system has to be followed, CMOS is a more sensible option due to its wide availability, reduced component and packaging costs and, more important, its capacity to accommodate multi-functional circuitry on-chip. Therefore, it stands as a reasonable choice for X-ray detection the use of the reported CMOS photodiodes as the image sensor [46].

Regarding to endoscopic capsules for gastrointestinal applications, human tissues show autofluorescence emission spectra when excited by ultraviolet or short-wavelength visible light. The intensity and shape of these spectra depends of the tissues pathologic state: the emission spectrum of cancer tissue is different from the one of the healthy tissue, and, it is dependent on the cancer development stage. Therefore, its measurement can give information about the degree of malignant transformations that could lead to cancer. CMOS photodiodes can be used and optimized for exploiting those emission spectra differences, by measuring the fluorescence intensity at specific spectral bands [47][48]. Once they are small and easily integrated with readout electronics for data processing, they can be integrated in an endoscopic capsule used for monitoring physiological parameters of the gastrointestinal tract. The complete system will innovate the way of physicians diagnose the gastrointestinal diseases.

## REFERENCES

[1] V. Carvalho, “Automatic Yarn Characterization System”, PhD Thesis, Minho University, Guimarães, 2008.

[2] SK Strasinger, and MS Di Lorenzo - Urianalysis and Body Fluids. F. A. Davis Company Press, Philadelphia, 2001.

[3] AJ Tüdos, GAJ Besselink, and RBM Schasfoort - Trends in miniaturized total analysis systems for point-of-care testing in clinical chemistry. *Lab-on-a-Chip*, Vol 1 (2001) p.83-95.

[4] G. Minas, J. S. Martins, and J. H. Correia – Highly Selective Optical Detection in a Lab-on-a-Chip for Biological Fluids Analysis. In Sensors and Materials, MYU Tokyo, Vol. 14, N. 2 (2002), p. 77-89.

[5] G. Minas, J. S. Martins, J. C. Ribeiro, R. F. Wolffenbuttel, and J. H. Correia – Biological microsystem for measuring uric acid in biological fluids. In *Sensors and Actuators A*, Elsevier, Vol. 110 (2004), p. 33-38.

[6] G. Minas, R. F. Wolffenbuttel, and J. H. Correia – A Lab-on-a-Chip for Spectrophotometric Analysis of Biological Fluids. In *Lab-on-a-Chip*, The Royal Society of Chemistry, Vol. 5, (2005), p. 1303-1309.

[7] G. Minas, R. F. Wolffenbuttel, and J. H. Correia - An array of highly selective Fabry-Perot optical-channels for biological fluids analysis by optical absorption using white light source for illumination. In Journal of Optics A: pure and applied optics, *Institute Of Physics*, Vol. 8 (2006), p. 272-278.

[8] G. Minas, G. de Graaf, R. F. Wolffenbuttel, and J. H. Correia - A MCM-based Microsystem for Colorimetric Detection of Biomolecules in Biological Fluids. In *IEEE Sensors Journal, IEEE*, Vol. 6, N. 4 (2006) p. 1003-1009.

[9] URL: business.vsnl.com/balasubramanian/hairiness.html (access in September 2008)

[10] J. Goodman, “Introduction to Fourier Optics”, McGraw-Hill, Greenwood Village, 1996.

[11] E. Steward, “Fourier Optics: An Introduction”, Dover Publications, New York, 2004.

[12] P. Duffieux, “The Fourier Transform and its Applications to Optics “, 2nd Edition, Jonh Wiley & Sons, New York, 1983.

[13] C. Madsen, “Optical Filter Design and Analysis: A Signal Processing Approach”, Wiley-Interscience, New York, 1999.

[14] J. Stover, “Optical Scattering: Measurement and Analysis”, McGraw-Hill, Washington, 1990.

[15] C. Davis, “Lasers and Electro-optics, Fundamentals and Engineering”, Cambridge University Press, Cambridge, 1996.

[16] M. Born and E. Wolf, “Principles of Optics: Electromagnetic Theory of Propagation, Interference and Diffraction of Light”, Cambridge University Press, Cambridge, 1999.

[17] E. Hecht, “Optics”, Addison Wesley, Redwood, 2001.

[18] url: www.hamamatsu.com (access in September 2008)

[19] S. Franco, “Design with Operational Amplifiers and Analogue Integrated Circuits”, 3rd Edition, McGraw-Hill, Greenwood Village, 2001.

[20] url: www.ni.com (access in September 2008)

[21] V. Carvalho, P. Cardoso, M. Belsley, R. Vasconcelos and F. Soares, “Yarn Hairiness Parameterization Using a Coherent Signal Processing Technique”, *Sensors and Actuators A: Physical,* Vol. 145, Issue 1, January 2008, p.217-224.

[22] V. Carvalho, P. Cardoso, M. Belsley, R. Vasconcelos and F. Soares, “Development of a Yarn Evenness Measurement and Hairiness Analysis System”, *IECON06*, 7-10 November, Paris, France, 2006.

[23] url: www.burr-brown.com (access in September 2008)

[24] V. Carvalho, P. Cardoso, M. Belsley, R. Vasconcelos and F. Soares, “Yarn Hairiness Characterization Using Two Orthogonal Directions”, (accepted for publication in IEEE Transactions on Instrumentation and Measurement).

[25] V. Carvalho, P. Cardoso, M. Belsley, R. Vasconcelos and F. Soares, “Determination of Yarn Hairiness Using Optical Sensors”, *EUROSENSORS* XX, 17-19 September, Gothenburg, Sweden, 2006.

[26] V. Carvalho, P. Cardoso, M. Belsley, R. Vasconcelos and F. Soares, “A New Statistical Reference Method for Yarn Hairiness Quantification”, ISIE’2007, 4-7 June, Vigo, Spain, 2007.

[27] url: business.vsnl.com/balasubramanian/YarnCloth.html#DC (access in September 2008)

[28] M. Castro and M. Araújo, “Manual de Engenharia Têxtil - Vol. II”, Gulbenkian, Lisbon, 1986.

[29] V. Carvalho, P. Cardoso, M. Belsley, R. Vasconcelos and F. Soares, “Optical Quantification of Yarn Hairiness Using Projections Along a Single Direction”, 9th IASTED Control and Applications, 30 May - 1 June, Montreal, Canada, 2007.

[30] V. Carvalho, “Parametrização de Fio Têxtil Baseada na Análise de Massa”, Msc Thesis, Minho University, Guimarães, 2004.

[31] R. Furter, “Evenness Testing in Yarn Production: part I”, The Textile Institute and Zellweger Uster AG, Manchester, 1982.

[32] J. Neves, “A Irregularidade dos Fios Têxteis, sua Origem, Medição e Análise”, Oporto, 1968.

[33] V. Carvalho, P. Cardoso, M. Belsley, R. Vasconcelos and F. Soares, “Yarn Diameter Measurements Using Coherent Optical Signal Processing”, (accepted for publication in *IEEE Sensors Journal*).

[34] url: www.thorlaser.com/Dosage.htm (access in September 2008)

[35] url: www.newport.com/servicesupport/Tutorials/default.aspx?id=112 (access in December 2007)

[36] V. Carvalho, P. Cardoso, M. Belsley, R. Vasconcelos and F. Soares, “Yarn Irregularity Parameterization Using Optical Sensors”, (submitted for publication in Fibres and Textiles on Eastern Europe).

[37] V. Carvalho, P. Cardoso, M. Belsley, R. Vasconcelos and F. Soares, “Yarn Diameter Characterization Using Two Orthogonal Directions”, (submitted for publication on Journal Dynamic Systems, Measurement and Control).

[38] SK Strasinger, and MS Di Lorenzo - Urianalysis and Body Fluids. F. A. Davis Company Press, Philadelphia, 2001.

[39] DA Skoog, DM West, FJ Holler - *Fundamentals of analytical chemistry*. Saunders College Publishing, Orlando, Florida, (1996) p. 497-524.

[40] H. R. Philip and E. A. Taft, “Optical constants of silicon in the region 1 to 10 eV,” *Physics Review*, vol. 120 p. 37-38, 1960.

[41] S. M. SZE, *Physics of semiconductors devices*, 2nd ed., John Wiley &Sons, New York, 1981, p. 74-79.

[42] D. P. Poenar and R. F. Wolffenbuttel, “Optical properties of thin-films silicon-compatible materials,” *Applied Optics*, vol. 36, n. 21, p. 5122-5128, 1997.

[43] J. C. Ribeiro, G. Minas, P. Turmezei, R. F. Wolffenbuttel, and J. H. Correia – A SU-8 Fluidic Microsystem for Biological Fluids Analysis. In *Sensors and Actuators A*, Elsevier, Vol. 123-124 (2005), p. 77-81.

[44] G. Minas, R. F. Wolffenbuttel, and J. H. Correia - An array of highly selective Fabry-Perot optical-channels for biological fluids analysis by optical absorption using white light source for illumination. In Journal of Optics A: pure and applied optics, *Institute Of Physics*, Vol. 8 (2006), p. 272-278.

[45] Fernandes, J. G. Rocha, and G. Minas - Smart-Pixel Array for Imaging Sensors. In "Proceedings of ICECS – The 14th International Conference on Electronics, Circuits and Systems”, Marrakech, Morocco, 11-14 December 2007, p. p. 395-398.

[46] J. G. Rocha, G. Minas, and S. Lanceros-Mendez - Optical coupling between scintillators and standard CMOS detectors. In *Nuclear Instruments and Methods in Physics Research A*, Elsevier, Vol. 556, (2006), p. 281-286.

[47] R. A. Dias, J. H. Correia, and G. Minas - CMOS optical sensors for being incorporated in endoscopic capsule for cancer cells detection. In “Proceedings of ISIE 2007”, Vigo, Spain, 4-7 June 2007, p. 2747- 2751.

[48] R. A. Dias, J. H. Correia, and G. Minas - On-Chip Integrated Optical Sensors for Fluorescence Detection of Cancer Tissue: Application to Capsule Endoscopy. In "Proceedings of ICECS – The 14th International Conference on Electronics, Circuits and Systems”, Marrakech, Morocco, 11-14 December 2007, p. 423-426.

In: Integrated Circuits, Photodiodes…
Editors: R. McIntire and P. Donnell, pp. 343-365
ISBN: 978-1-60692-660-4
© 2009 Nova Science Publishers, Inc.

***Chapter 11***

# CARDIAC OPTICAL MAPPING: BIOMEDICAL RESEARCH APPLICATION OF PHOTODIODES

***Herman D. Himel IV[1], Joseph Savarese[1], Vikram Lakireddy and Nabil El-Sherif[1,2]***
[1]VA New York Harbor Healthcare System, Brooklyn, NY, USA
[2]Downstate Medical Center, State University of New York, Brooklyn, NY, USA

## BRIEF HISTORY OF CARDIAC OPTICAL MAPPING

The human heart pumps oxygenated blood to the organs and extremities in order to maintain normal physiologic function. Coordinated contraction of individual cardiac myocytes provides the mechanical force necessary to produce sufficient pressure and ensure that the more distant organs and extremities remain oxygenated. Before cardiac myocytes may contract, they must first be stimulated in order to begin the sequence of events which results in an intracellular calcium ($Ca_i$) rise, which in turn precipitates actin-myosin binding and results in contraction. The electrical signature of this series of events is reflected in the cardiac action potential (AP), a segment of a transmembrane voltage ($V_m$) recording which indicates electrical excitation (depolarization) and relaxation (repolarization) of the myocardium.

The morphology, duration, and amplitude of the cardiac AP are important markers of electrical activity in the heart. Studies of the cardiac AP have provided important insights into the mechanisms which drive the transition from a normal, healthy heartbeat toward a deadly cardiac arrhythmia.

Early recordings of the cardiac AP were obtained using microelectrodes [1-6]. Although this method was highly effective in tracking temporal changes in the $V_m$ of individual cells, the method could not be easily applied to the problem of tracking excitation over a region of tissue. Extracellular electrode mapping offered a partial solution to this problem and was sufficient to determine activation times in regions of tissue, but with this method the details of repolarization were lost and had to be estimated using indirect indicators. And for practical purposes, this method required that the electrodes be in direct contact with the tissue. This made defibrillation studies difficult since large amplitude defibrillation shocks typically obscure the details of activation during electrical recordings. Monophasic action potential (MAP) recordings were capable of elucidating the details of repolarization without damaging tissue, and have even been recorded in the beating human heart using a cardiac catheter [7]. However they too were restricted by having little or no spatial resolution and could not be placed in close contact with each other. As with extracellular electrodes, MAP recordings require that the electrodes be placed in contact with the tissue.

With the emergence of $V_m$-sensitive dyes in the 70's, it became possible to interrogate cardiac tissue optically [8], and soon afterward optical methods were developed to interrogate multiple spots simultaneously in a small (~$cm^2$) region of tissue. Since then the field of cardiac optical mapping (COM) has greatly expanded in scope, from relatively simple early recordings using one or relatively few spots [8, 9] to highly complex optical systems. These include high spatiotemporal resolutions systems [10], panoramic systems [11, 12], and systems which are capable of interrogating electrophysiological activity beneath the surface [13]. In addition, several labs have used photodiode-based optical mapping systems to map $V_m$ and $Ca_i$ simultaneously, on both the whole heart [14-17] and in monolayer cell cultures of cardiac myocytes [18-20].

Cardiac optical mapping systems have greatly increased our understanding in nearly all areas of cardiac electrophysiology, from basic studies of conduction patterns [21, 22] and effects of fiber geometry [23-26] to more clinical studies of defibrillation [27-30] and ablation therapy [31, 32]. Although COM has not yet led to a widely accepted method of three-dimensional cardiac tissue interrogation, there have been significant advances in this area as well. Investigators have successfully used optical surface recordings to determine wavefront orientation beneath the surface [33, 34], and also to interrogate deeper layers of tissue using transillumination methods [35] and near-infrared fluorescing dyes [36-38].

Photodiode sensors were used in some of the earliest optical recordings of cardiac APs [8, 39], and continue to be used today [40, 41]. Photodiodes function by transferring incoming photonic energy to bound electrons in a semi-conductive material in a transistor configuration. These energized electrons may then cross from one side of the transistor to the other, creating a voltage difference between the two sides. If a wire is connected from one side of the photodiode to the other while the photodiode is receiving photonic energy, current will flow in a very linear fashion with respect to the input intensity of the collected light [42]. This makes photodiodes an excellent choice as a detector in COM systems, and this fact has been reflected by their widespread use over the past 30 years. Examples of optical APs and activation maps recorded with a photodiode array-based system are shown in figure 1.

Although other technologies such as CMOS and CCD cameras have recently gained popularity due to their higher spatial resolution, photodiode systems remain in use due to their ruggedness, high signal-to-noise ratios, excellent temporal resolution, versatility, and low cost. Recently, for example, photodiodes and photodiode arrays (PDAs) have been used in the construction of optrodes, a novel technique used to record optical signals from deeper intramural regions within the ventricular wall [13, 43-45].

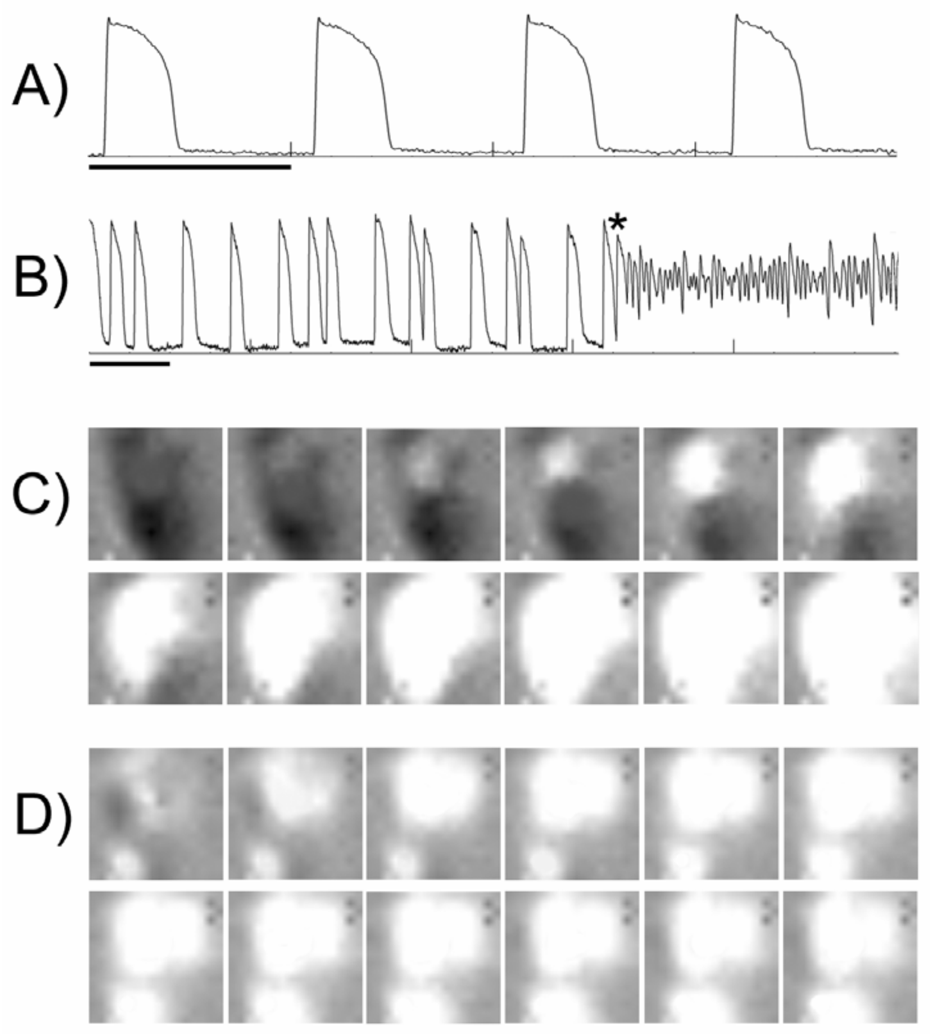

Figure 1. APs and activation maps for normal and irregular rhythms. For rows A and B, the horizontal bar beneath each recording indicates 1 second. Row A shows APs recorded during basic rhythm. Row B shows APs occurring with irregular diastolic intervals, followed by a long run of a ventricular tachyarrhthmia, triggered by the AP marked with an asterisk. The two rows in section C show a sequence of activation during basic rhythm, while the two rows in section D show a sequence of activation which took place during a premature beat which precipitated a sustained ventricular tachyarrhythmia (note the presence of two distinct activation sites). Frames are read from left to right, and then top to bottom. Each successive frame is 1 ms apart. Lighter areas on the map indicate tissue undergoing activation.

## BASIC PRINCIPLES OF CARDIAC OPTICAL MAPPING

Epi-illumination occurs when the fluorescence emission detector is placed on the same side of the tissue as the excitation source, whereas with trans-illumination the detector and excitation source are placed on opposite sides. For monolayer mapping systems, both epi and trans-illumination are possible since cardiac monolayers are typically only a few tens of micrometers thick, permitting the passage of light. For whole-heart mapping systems which map excitation on the surface of the intact heart, epi-illumination is the preferred method since very little fluorescence is transmitted through the myocardial wall.

The tissue being mapped must be illuminated using an excitation source, which excites at least one parameter-sensitive dye in order to elicit a fluorescent signal. Changes in a targeted physiological parameter cause changes in the properties of the dye (e.g., a conformational change in the dye molecules). This results in a change in the emission spectrum of the dye, which is then recorded by a detector (e.g., a PDA), digitized, and stored on a PC for post-experimental analysis.

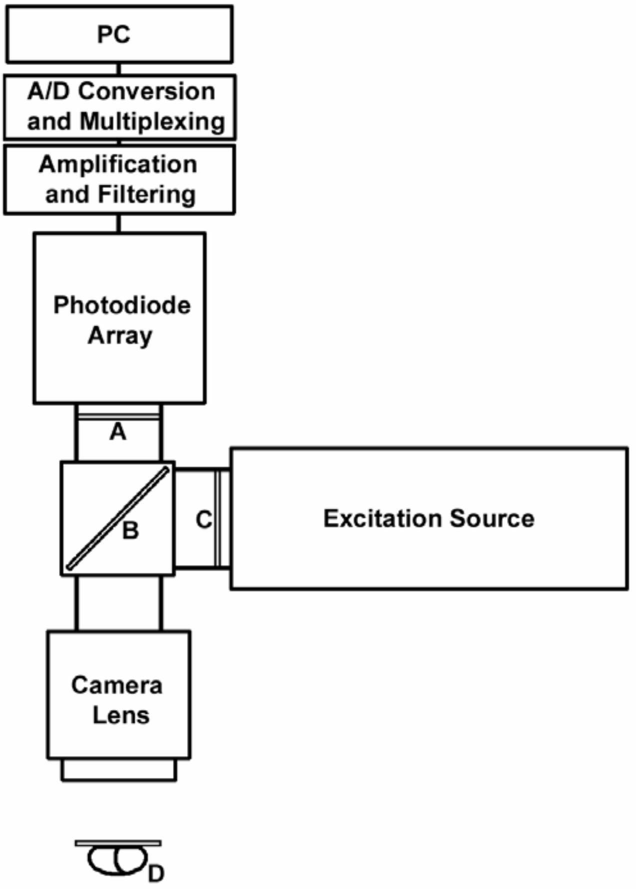

Figure 2. Top-down view of a typical PDA-based optical mapping system. The thin rectangular boxes marked A, B, and C represent fluorescence band pass, long pass, and excitation band pass filters, respectively. The long pass filter B is housed in an optical cube. The oval-like shape marked D represents the heart, which is pressed against a flat plate in order to create a two-dimensional surface so that the entire mapped region lies on the focal plane. Electrically connected components are separated by a thin solid line, while optically connected components are separated by hollow rectangles.

Changes in fluorescence due to changes in the physiological parameter are often measured as a fraction of the baseline fluorescence. This is an important parameter in optical mapping, and is known as fractional fluorescence ($\Delta F/F$). Fractional fluorescence is useful because it is a measure the effectiveness of a particular dye in transducing a physiological signal into recordable fluorescent emission. Fractional fluorescence also indicates the general effectiveness of the system, and higher ΔF/F values are typically accompanied by higher signal-to-noise ratios. Transmembrane voltage is the most commonly studied physiological parameter in optical mapping, but intracellular calcium transients ($Ca_iT$) have also been studied extensively.

There are several variations of the COM system, however there are basic components that are common to all systems. These basic components include an excitation source, detector, and electronic components used for digitization, filtration, and multiplexing. A schematic for a typical whole-heart mapping system is shown in figure 2.

## Excitation Source

The excitation source may be either focused (i.e. laser light) or broadfield illumination (using halogen or tungsten sources). Laser light sources have sufficiently narrow bands so as not to interfere with the fluorescence emission, however broadfield sources should be pre-processed using optical filters in order to decrease the width of their wavelength spectrum before illuminating the target (i.e., the heart). In general, brighter excitation sources lead to higher ΔF/F values, however the intensity of the excitation source cannot be increased without regard for *photobleaching*, which occurs when the dye emission decreases in intensity due to overexposure of dye molecules to excitation light [46, 47].

## Detector

There are several types of detectors that are currently in use for COM, however the focus of this review is upon those detectors which are photodiode-based. Other detector types will be discussed for the purpose of comparison.

Current alternatives to PDAs include photomultiplier (PMT) systems, charge-coupled device (CCD) cameras, and complimentary metal-oxide semiconductor (CMOS) cameras. PMT systems have an extremely high gain (up to $10^8$ increase in intensity), and can even be used in a process call "photon counting" whereby the release of individual photons may be recorded. PMT systems are capable of extremely high sensitivity, and typically have a quicker response time than photodiode systems. However for typical optical mapping applications, the sensitivity and response time of photodiodes is more than sufficient. Typically, PMT systems employ sequential rather than simultaneous recordings of adjacent spots. However, due to their rapid response time they may be coupled with a laser scanner to produce acquisition rates equivalent to those seen in photodiode-based systems. For example, a laser scanner which scans at 256 kHz with a 256-spot grid is essentially equivalent to a PDA-based 256-spot system which scans at a rate of 1 kHz. For this example, there will be a time difference of ~1 ms between the 1st and 256th spots scanned.

Cameras using CCD technology typically have impressive spatial resolution, however these systems have not been able to achieve the same temporal resolution as PDA-based systems until recently. The CardioCCD-SMQ (RedShirt Imaging, Decatur, GA) currently offers a spatial resolution of 80x80 while achieving a temporal resolution of 2000 frames per second (fps). The CCD camera may achieve higher temporal resolution and/or higher signal-to-noise ratios by a process known as “binning,” however this process decreases the spatial resolution of the camera, the major advantage of CCD technology. When using the CCD camera for cardiac mapping experiments, light saturation may be an issue and thus gain must be carefully controlled. Typically this is less of a problem with PDA systems.

Although more costly than either CCD cameras or PDAs, the CMOS camera boasts exciting technology that has recently become capable of delivering extremely high spatiotemporal resolution. RedShirt Imaging lists the CardioCMOS-128f as being capable of recording 128x128 spots at an acquisition rate of 10,000 fps (RedShirt Imaging, LLC, Decatur, GA).

The PDA, as well as the individual photodiode, remains a cost-effective and rugged solution to a wide variety of problems within the field of COM. Photodiode arrays boast a wide spectral response, high dynamic range, and high temporal resolution. The PDA is typically a rugged device and can operate in high-light conditions typical in most laboratory experiments, while still delivering a high signal-to-noise ratios. Due to their robust nature and versatility in a wide variety of applications, photodiode-based systems remain the “workhorse” detector in COM.

## Filtration, Digitization and Multiplexing

Optical signals are subject to several types of noise which must be removed in order to study the details of the cardiac AP. We will briefly review the types of noise most relevant to COM systems. Various types of white noise are ubiquitous throughout all types of electronics, and are typically of frequencies well above those of cardiac signals. Thus low pass filters are frequently used to help remove white noise. Sixty-cyle is another type of noise that is often encountered when collecting optical signals. This noise may contaminate signals by way of electromagnetic waves from power outlets, or may be introduced if equipment used in optical mapping experiments is powered using AC power (i.e., if the equipment is not isolated). It may be alleviated by the use of a Faraday cage and/or the use of a band-stop (i.e., notch) filter centered at 60-Hz. Mechanical vibrations may also affect optical signals, and can range from fluctuations in air current to vibrations due to foot traffic. Sources of mechanical vibrations are highly varied in nature, and must be dealt with on a case-by-case basis. A research-grade optical table with active isolation should be sufficient to suppress most sources of mechanical noise. Optical recordings may also contain drifts in basline voltage due to several sources. These include photobleaching, dye washout, and dye internalization in the inner leaflet of the cell membrane. One way to reduce the impact of these noise sources is to employ the technique of ratiometry [46], which will be discussed in the following section.

Many optical devices, including photodiodes and photomultiplier tubes, record analog signals that must be digitized before being stored on a PC. Digitization equipment must have sufficient speed and throughput in order to follow the high spatiotemporal resolution required for modern optical mapping applications. A recent article by Entcheva et al. summarizes the state of the art in this sub-field of COM [48].

When data is recorded from a two-dimensional grid of sites simultaneously, the most intuitive storage method is a two-dimensional matrix of values. However, prior to storage on a PC, this data must be routed from the digitization equipment to the PC. This requires arranging the data in a sequential fashion, a process known as multiplexing. For a 16x16 element PDA, data for a single millisecond might be arranged from sites 1 to 256 and then be sequentially sent to the PC for storage. Following this, the data could then be demultiplexed and arranged in matrix form, a more logical form for creating activation maps and other graphics to assist with visualizing the data.

## Pre/Post-Conditioning of Optical Data

In contrast to electrical signals, optical signals are highly sensitive to heart motion. Various methods have been developed in order to reduce the "motion artifacts" which are often present in optical signals. These motion artifacts are thought to be the result of a change in the location of the mapped region on the heart surface, where a fluorescence gradient typically exists [49]. Methods to reduce motion artifact include physically restraining the heart [50, 51], the use of electromechanical uncouplers [52-55], and the technique of ratiometry [43, 46, 47]. Physically restraining the heart reduces motion artifacts simply by limiting the extent to which the heart can move during contraction, thus limiting the amount by which the mapped region moves with respect to its original position on the heart. Electromechanical uncouplers work by a variety of methods, but most have an effect upon the actin-myosin cytoskeleton which is responsible for contraction. Electromechanical uncouplers should be used with care, as some studies have shown that these agents can affects various parameters of the cardiac AP and may also effect the dynamics of ventricular fibrillation (VF) [56-59].

Ratiometry is a signal processing method that requires the use of two recorded optical signals, each of a different wavelength spectrum. We will refer to the longer wavelength signal as "red" and the shorter wavelength signal as "green". When a $V_m$-sensitive dye is excited, the peak of the emission spectrum of the dye shifts toward shorter wavelengths (green). Thus the green signal would show an increase in fluorescence intensity while the red signal would show a corresponding decrease in intensity. Using this method, an upright cardiac AP would be recorded in the green signal while an inverted (or "upside-down") AP would be recorded in the red signal. The important thing to consider is that the emission signal corresponding to $V_m$ is emitted at a relatively narrow frequency band. Contrastingly, emission due to motion is not heavily wavelength-dependent, and will cause the change in fluorescence signals in the same direction regardless of the signal type. Since the motion signals are common to both collected wavelengths, we may reduce motion artifacts by simply taking the ratio of the green signal to the red on a point-by-point basis. This will cause a significant reduction in the motion artifact, and will allow us to study the electrical behavior alone. This technique could be achieved in the laboratory by using dual PDAs and separating fluorescence emission into two wavelength bands, one above and one below the peak emission wavelength of the dye of interest. In addition to motion artifact removal, ratiometric signals have also been used to study movement artifacts optically. This may be achieved by subtracting the electrical signal from the signal containing both electrical and motion components [49].

Since fibrillation (both ventricular and atrial) is a topic of great clinical and theoretical interest, considerable effort has been expended in order to analyze data recorded from the fibrillating heart. This data is challenging to interpret, since recordings of fibrillation often have a chaotic appearance when viewed with time as the horizontal axis. Thus a variety of alternate methods have been used to gain insight into the nature of fibrillation, including dominant frequency analysis [60-67] and mutual information [68, 69]. More recently the use of a metric known as spatiotemporal entropy has been used to analyze oscillatory dynamics in cardiac and neural systems [70, 71].

Dominant frequency analysis involves use of the Fourier transform to examine the frequency content of fibrillation recordings. Some groups have used dominant frequency analysis to support the theory of a “mother rotor” (i.e., a high-frequency region of the heart that drives fibrillatory activity) [52, 72, 73], however this issue remains controversial [74]. Others believe that fibrillation is maintained by the constant creation and annihilation of wavelets which occur due to functional and anatomical heterogeneities [75-79]. More recently, some groups have concluded that fibrillatory activity may be driven by both mechanisms, depending on the conditions in the heart [80-83].

Mutual information techniques have been used to examine the relationship between $V_m$ and $Ca_i$. Algorithms assign a numerical value for individual signals in order to quantify the degree of similarity between $V_m$ and $Ca_i$ during fibrillation and to give insight into the mechanisms of arrhythmogenesis and the maintenance of fibrillation; however, mutual information must be calculated for individual signal pairs and by itself does not indicate spatiotemporal heterogeneities in $V_m/Ca_i$ relationships.

Spatiotemporal entropy has been used to quantify the degree of uncertainty in both time and space by considering them as lumped parameters, and analyzing activations in the context of space-time cubes (i.e., stacked two-dimensional optical maps with time as the third dimension). Spatiotemporal entropy has been used to analyze neural simulations as well as oscillatory dynamics in cultured cell monolayers [70, 71]. Spatiotemporal entropy analysis is appealing when analyzing optical mapping data, since one of the major strengths of optical data is its spatial resolution.

## Recent Advances in Cardiac Electrophysiology Research Using Photodiode Arrays

This section will showcase three recent optical mapping studies from this lab which examine cardiac arrhythmia mechanisms [17, 84, 85]. We first discuss a study which examines APs in the context of an animal model of Long QT syndrome, and then move on to discuss two studies which examine the relationship between $V_m$ and $Ca_i$ during ischemia. The first study [84] used a single 12x12 PDA to record transmembrane potential, while the last two studies [17, 85] used a photodiode-based system which simultaneously records $V_m$ and $Ca_i$ with two separate 16x16 PDAs (see figure 3 for a schematic of the simultaneous dual-measurement system). For all three studies, the whole-heart guinea pig (GP) Langendorff model was used, where the heart is suspended to freely hang on a small cannula by its aorta. Heated (~37° C), oxygenated Tyrode’s solution is pumped retrogradely through the aorta in order to nourish and oxygenate the heart via the coronary arteries. The first study [84] we discuss uses the Anthopleurin-A (AP-A) neurotoxin to simulate the effects of a genetic disorder, the long QT syndrome 3. The following two studies [17, 85] simulated the condition of global ischemia (i.e., oxygen deprivation) by temporarily interrupting perfusion into the coronary arteries. These studies used the guinea pig animal model, which is similar to humans in terms of AP morphology and calcium handling in cardiac myocytes.

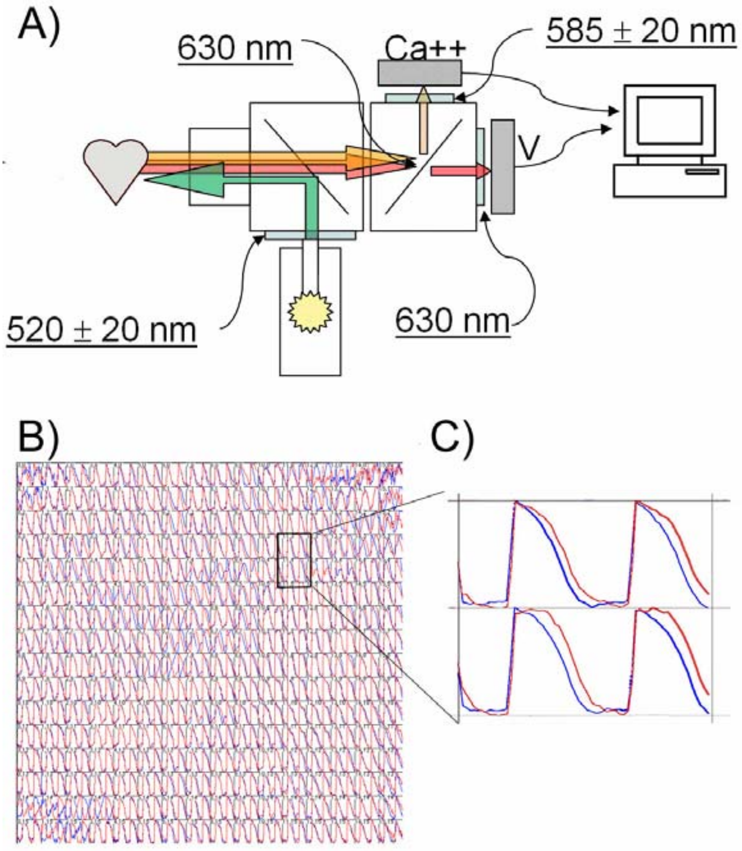

Figure 3. Optical mapping diagram for simultaneous $V_m$ and $Ca_i$ measurements. For panel A), the position of each filter is indicated by thin curved lines with arrowheads, and the characteristics of the filters are underlined (high pass filters are indicated by a single number, whereas band pass filters have number ± band). The calcium and voltage PDAs are shaded gray. The large color-filled lines indicate the path of the given color of light. The excitation source is the bottom component in panel A). Panel B) shows an map of optical signals, and panel C) shows enlarged traces of the indicated pixels. The blue signal in panel C) represents $V_m$, whereas the red signal indicates the $Ca_i$.

Study 1: Long QT syndrome (LQTS) may be either genetic or acquired. LQTS typically occurs due to an alteration of normal transmembrane ion channel structure in the cardiac cell membrane. This causes changes in ionic currents which are modulated by these channels, giving rise to a prolongation of the APD. On a clinical electrocardiogram, this is manifested as an increase in the duration between the QRS complex and the T wave, hence the name long QT syndrome.

It is known that both the congenital and acquired forms of LQTS are commonly associated with the occurrence of polymorphic ventricular tachycardia, also known as Torsades de Pointes. Experimental evidence shows that in LQTS, there is an increase in the tridimensional spatial dispersion of repolarization in the ventricles [86]. Spatial dispersion of repolarization occurs when tissue in various regions of the heart recover at different times.

Whenever there is dispersion of repolarization, a premature AP can result in functional conduction block and set the stage for the development of reentrant tachyarrhythmias [86, 87]. With the use of optical mapping, it is possible to evaluate epicardial spatial dispersion of action potential duration (APD), i.e. spatial dispersion of repolarization.

The purpose of this study was to examine the contribution of spatial dispersion of repolarization to arrhythmogenesis in an experimental guinea pig heart model of LQT3. The neurotoxin AP-A, derived from the sea anemone *Anthopleura xanthogrammica*, was used to simulate the effects of LQT3. AP-A works by interacting with sodium channels to alter the channel inactivation kinetics, leading to continuous sodium current and lengthening of the AP plateau phase and hence prolongation of the APD. The potentiometric fluorescent dye di-4-ANEPPS was used to measure optical APs. In a subset of animals, liquid nitrogen was used to ablate the subendocardial layer of the heart, in order to determine the role of this layer in arrhythmogenesis in the context of an LQT3 model.

The study confirmed that the AP-A GP model of LQT3 is in fact an appropriate surrogate model for investigating the electrophysiologic consequences of nonuniform APD distribution along the epicardial wall. A quantitative description was made of the spatial changes in AP characteristics in response to the rate at which the heart was paced (i.e., cycle length). Results showed that the differences in epicardial APD along the ventricular wall were dramatic (see figures 4 and 5). Results also indicate that APD differences along the ventricular wall are important to the genesis of ventricular tachyarrythmias associated with LQT3. Further, it was found that although endocardial ablation halted spontaneous ventricular tachyarrhythmias, the heart remained vulnerable to a premature stimulus due to the presence of a substrate of spatial dispersion of repolarization.

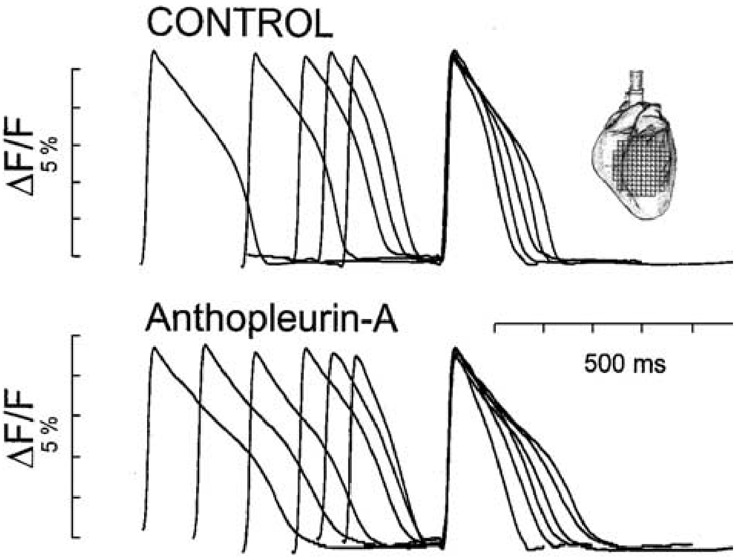

Reproduced with permission from Restivo et al., 2004.

Figure 4. Cycle length (CL) dependence of APD for control vs. experimental LQT3 model (Antopleurin-A). Control APs were taken at 200, 250, 300, 400, and 600 ms CLs while the anthopleurin-A APs were taken at 200, 250, 300, 400, 500, and 600 ms. The approximate position of the optical grid on the heart is shown to the right of the top trace.

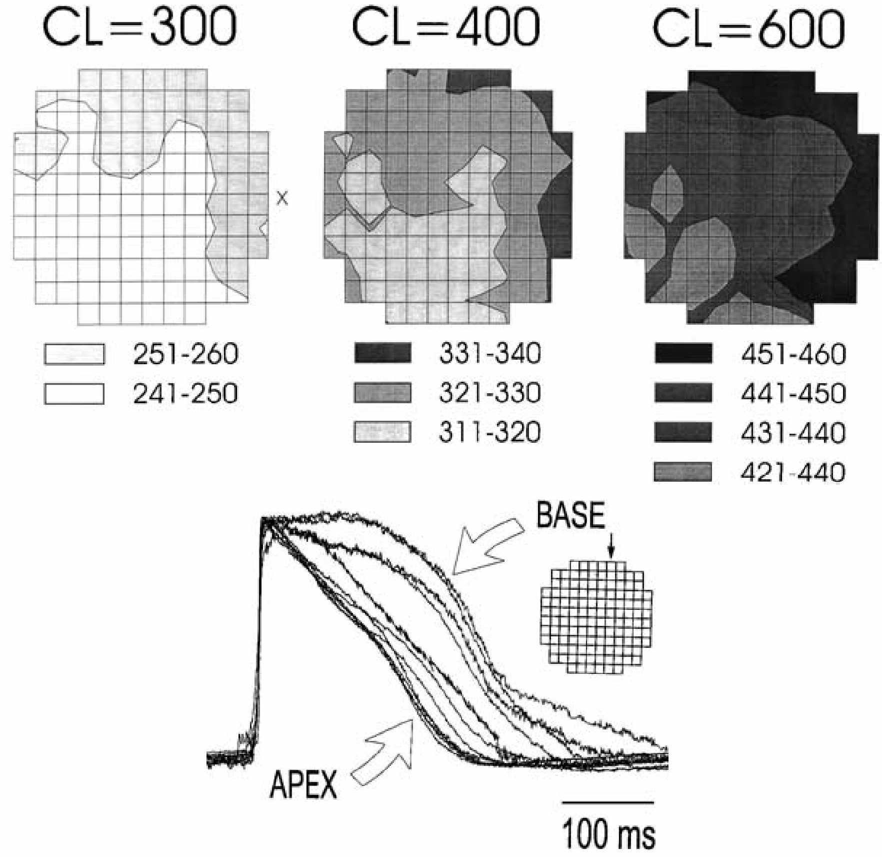

Reproduced with permission from Restivo et al., 2004.

Figure 5. Cycle length-dependent spatial dispersion of repolarization. The top three maps show how increased pacing cycle lengths result in increasingly greater spatial dispersion of repolarization. The bottom panel shows superimposed APs recorded from the base to the apex of the heart, demonstrating the changes in APD that occur over the surface of the heart. For the grid to the right of the bottom panel, the top of the optical map (base of the heart) is indicated by the straight arrow.

Study 2: This study examines spatial dispersion of repolarization in the context of global ischemia, and also the role spatial dispersion plays in the development of electrical alternans. Electrical alternans is a term used to describe beat-to-beat alterations in AP morphology. For example, a one-to-one APD alternans occurs when a normal AP is followed by a short-duration AP, which is then followed by normal AP, short-duration AP, and so on. Electrical alternans are considered to be a strong marker of electrical instability, and often precede malignant arrhythmias such as ventricular tachycardia (VT) and VF [88-94]. In this study, we examine another example of the importance of spatial dispersion, but this time in the context of global ischemia.

In this study by Lakireddy et al. [85], ischemia-induced changes in APD and intracellular calcium transient duration ($Ca_iT$-D) were determined, and their relationship with electrical alternans was investigated. Recordings show that ischemia resulted in a significant decrease in APD, but resulted in a significant increase in $Ca_iT$-D. In addition, changes in APD were spatially heterogeneous while changes in $Ca_iT$-D were relatively homogeneous (see figure 6).

Sites with less shortening of APD displayed alternans in both Ca$_i$T-D and APD, while sites with more shortening of APD displayed Ca$_i$T-D alternans but little or no APD alternans, leading to a condition of significant spatial dispersion of the APD. The condition of increased spatial dispersion due to ischemia is thought to account for the vulnerability of the heart to alternans.

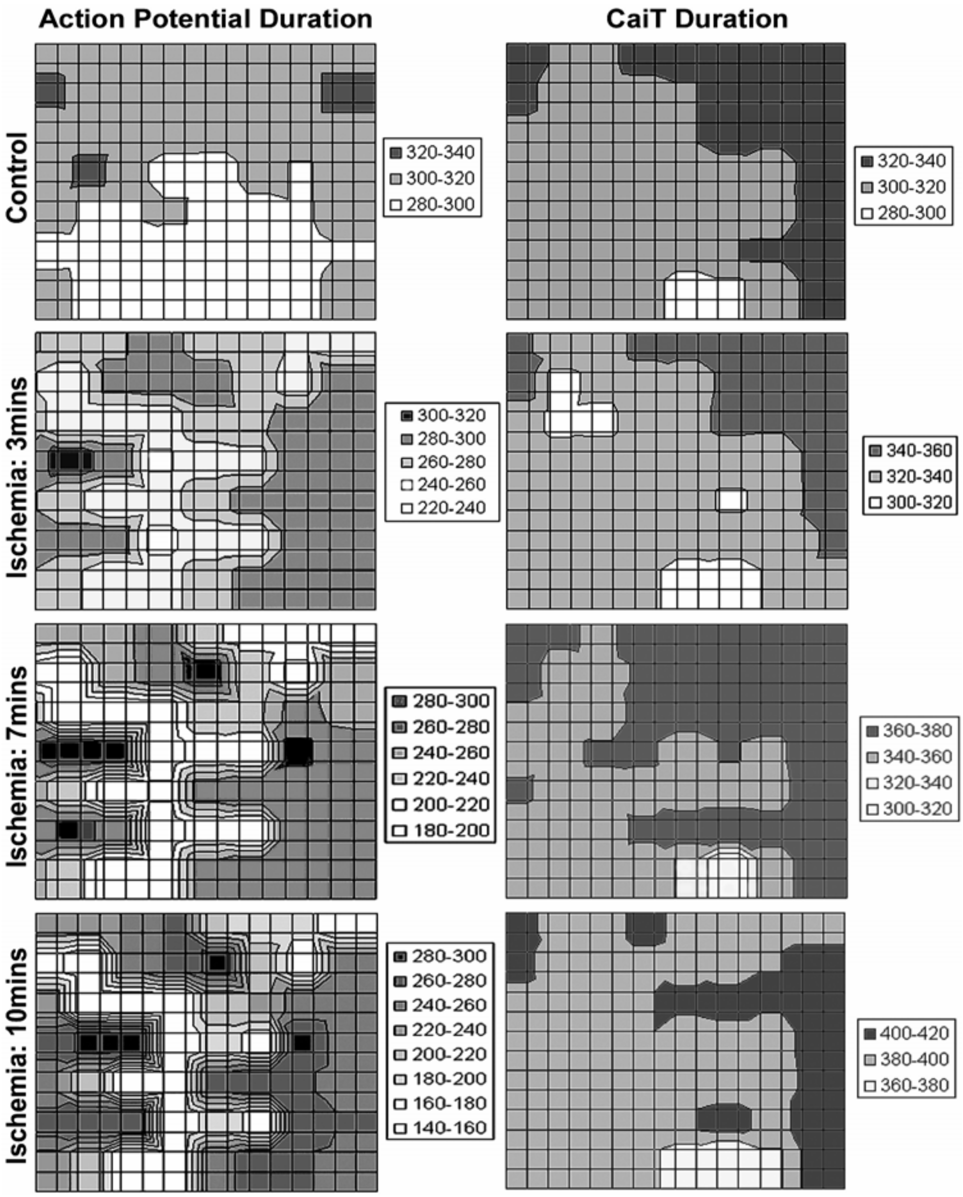

Reproduced with permission from Lakireddy et al., 2005.

Figure 6. APD and Ca$_i$T-D during normal perfusion and into ischemia. Scales to the right indicate the shade of a given APD or Ca$_i$T-D.

Study 3: In a second study by Lakireddy et al. [17], the association between arrhythmogenesis and spontaneous calcium oscillations (S-CaOs) was examined in the intact heart. It is known that ischemia/reperfusion leads to elevated $Ca_i$ and an alteration in $Ca_i$ kinetics [95-97]. This alteration in normal $Ca_i$ kinetics can lead to S-CaOs. Under such conditions, the normal master/slave relationship between $V_m/Ca_iT$ signals is reversed (i.e., calcium signals precede and drive $V_m$).

The goal of this study was to investigate the correlation between S-CaOs and arrhthmogenesis using an experimental GP model with 15 minutes of no flow ischemia followed by 15 minutes of reperfusion. Changes in $Ca_i$ and Vm in a limited zone of the epicardial surface of the GP heart were simultaneously recorded and carefully examined. The study provided evidence of a linkage between S-CaOs and arrhythmogenesis in the setting of ischemia/reperfusion (I/R). In the intact heart during I/R, spontaneous premature beats (PBs) occurred and were ubiquitous. Some PBs initiated a VT or VF (see figure 7), while others remained confined to their site of origin and did not result in an arrhythmia (see figure 8).

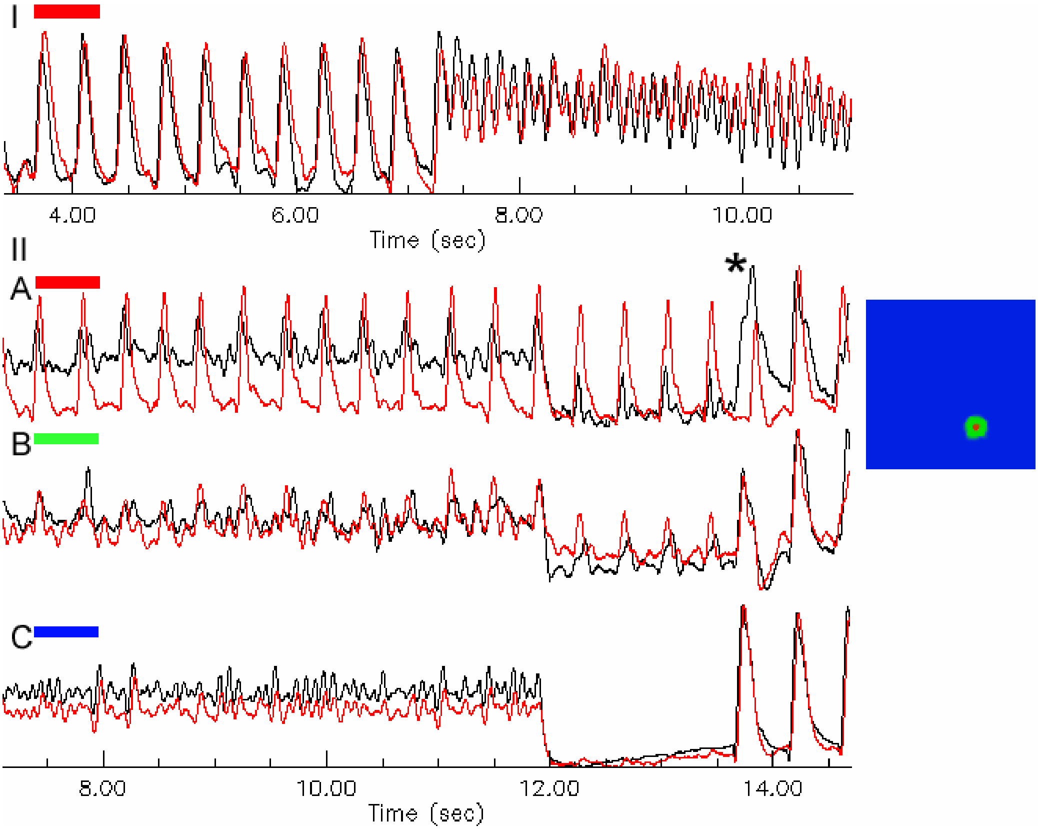

Reproduced with permission from Lakireddy et al., 2006.

Figure 7. Concealed spontaneous calcium oscillations (S-CaOs). Recordings were obtained from an experiment in which localized S-CaOs developed during an episode of self-terminating VF and continued uninterrupted after the resumption of spontaneous cardiac rhythm. Panel I illustrates the initiation of VF. Panel II shows recordings from three representative pixels (marked by different colors in the map of the optical field, seen to the right of the traces). After the self-termination of VF (at approximately 12 seconds), the majority of the optical field showed a pause with no electrical activity (trace C of panel II), while the localized S-CaOs continued.

Two important observations had to be made in order to link an arrhythmia to S-CaOs in the experimental model. First, the beginning of S-CaOs preceded the onset of the simultaneously recorded membrane depolarization by 2-15 ms at a very restricted site in the optical field. In recordings obtained further away from the focal site of origin, the relative amplitude of the S-CaOs gradually decreased and the start of membrane depolarization preceded the onset of S-CaOs. Second, the presence of some degree of conduction block, which by definition is the failure of S-CaOs to trigger a fully propagated response, was essential for the localization of the focal site of origin. In conclusion, this study demonstrated that S-CaOs may remain concealed (and hence benign) or may manifest as PBs, VT or VF.

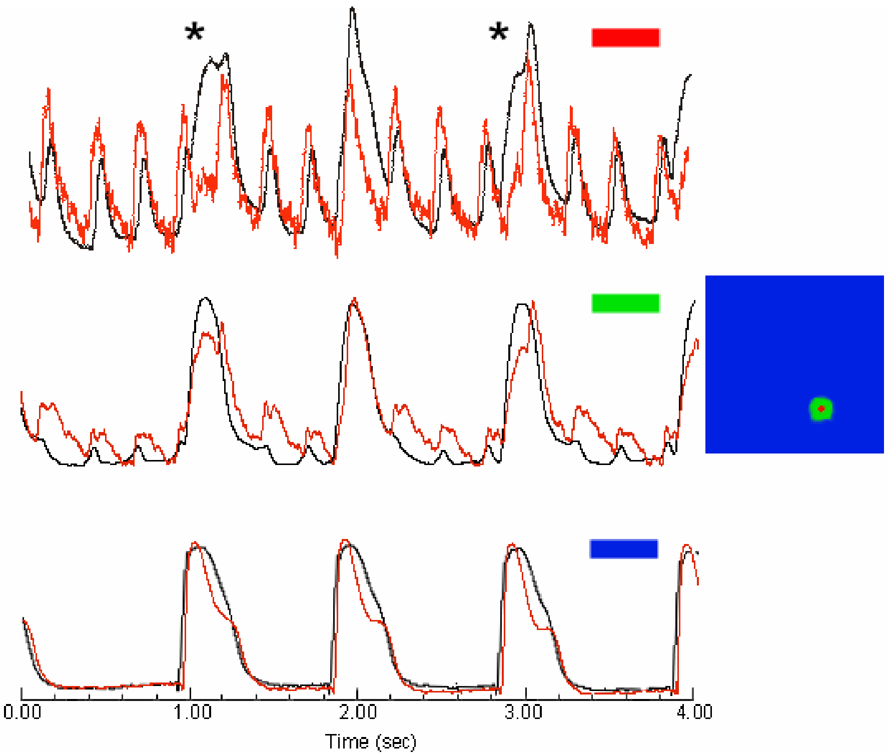

Reproduced with permission from Lakireddy et al., 2006.

Figure 8. Calcium oscillations confined to a site within the mapping field. The top, middle, and bottom traces show recordings from the red, green, and blue regions of the mapping field, respectively. The top trace shows regular calcium oscillations driving $V_m$. The middle trace shows the presence of calcium oscillations which are significantly depressed with respect to those in the top trace, and do not precede $V_m$. The bottom row shows that the calcium transients are being driven by voltage, implying that the calcium oscillations in the red region of the map have failed to escape the red/green region of the map and propagate through to the blue region.

## Recent Advances in Cardiac Optical Mapping

We will now turn to briefly discuss a few of the important recent advances in COM. Optrodes are bundles of microscopic fiberoptic cables which are inserted into cardiac tissue in order to interrogate intramural activation patterns. They are similar to plunge needle electrodes in their usage; however optrodes are capable of measuring complete APs, including the repolarization phase, whereas plunge electrodes measure extracellular potentials only. It is thought that in the future optrodes will play an important role in more carefully examining transmural dispersion of repolarization, an important factor in arrhythmogenesis in a variety of cardiac diseases [86, 98-100]. Optrodes may also be important in the study of the dynamics of arrhythmic circuits, since they are often present deeper in the myocardial wall [101-103]. However, like plunge electrodes optrodes must also be inserted into the tissue and therefore cause damage which may by itself alter activation patterns. Thus the effects of this insertion must be carefully considered when interpreting intramural data [104]. Photodiodes have played a critical role in the construction of optrodes [13, 44, 45].

Several groups have recently begun to use multiple cameras to simultaneously interrogate multiple viewpoints of the epicardial ventricular wall [11, 12, 105-107]. In addition, some of these groups use additional cameras to recreate the geometry of the heart in order to properly orient optical maps from several cameras on the epicardial surface [11, 107]. Most Panoramic optical mapping systems are based on CCD technology, however systems have also been built using multiple PDAs [108]. Panoramic optical mapping does not address the problem of lost depth information, but does provide a significant improvement over traditional optical mapping which only maps a limited region on the epicardial surface.

The use of monolayer cell cultures in COM also represents an important advance, allowing for highly controlled studies of basic conduction as well as studies to elucidate fundamental arrhythmic mechanisms [18, 29, 109-112]. An appealing aspect of the cardiac monolayer is that it allows us to study conduction in cardiac tissue without the complexity associated with the three-dimensional whole-heart Langendorff model. Since the cardiac monolayer is essentially two-dimensional (only tens of micrometers thick while being tens of millimeters in diameter), the entire monolayer may be mapped; therefore data interpretation is not complicated by the absence of missing depth information. And although the monolayer is technically three-dimensional, typical optical mapping systems interrogate at sufficient depths so that no information is lost beneath the surface [113]. Despite being similar to whole-heart mapping in many respects, the actual practice of monolayer mapping carries with it significant challenges, and is in many respects more difficult than whole-heart mapping [48].

In conclusion, photodiodes have played an essential role in the development of the field of COM. They were used in the earliest COM systems and continue to have widespread use today, both in rudimentary applications as well as more advanced designs such as optrodes and panoramic systems. Applications for photodiodes within COM continue to emerge, and will likely remain a vital part of this important and ever-expanding branch of cardiac electrophysiology research.

## LIST OF ABBREVIATIONS

AP – action potential
AP-A – anthopleurin-A
APD – action potential duration
$Ca_i$ – intracellular calcium
$Ca_iT$ – intracellular calcium transient
$Ca_iT$-D – intracellular calcium transient duration

CCD - charge-coupled device
CMOS - complimentary metal-oxide semiconductor
COM – cardiac optical mapping
CL – cycle length
GP – guinea pig
I/R – ischemia/reperfusion
LQTS – long QT syndrome
LQT3 – long QT syndrome 3
PB – premature beat
PDA - photodiode array
PMT - photomultiplier tube
TdP – Torsades de Pointes
VF – ventricular fibrillation
$V_m$ – transmembrane voltage
VT – ventricular tachycardia

## REFERENCES

[1] Coraboeuf E, and Weidmann S. Potentiels d'action du muscle obtenus à l'aide de microélectrodes intracellulaires. Présence d'une inversion de potential. *CR Soc Biol.* (Paris) 1949;143:1360-1360.

[2] Coraboeuf E, and Weidmann S. Potentiels de repos et potentials d'action du muscle cardiaque, mesurés á l'aide d'électrodes intracellulaires. *CR Soc Biol.* (Paris) 1949; 143:1329-1331.

[3] Draper MH, and Weidmann S. Cardiac resting and action potentials recorded with an intracellular electrode. *J Physiol.* 1951;115:74-94.

[4] Weidmann, S. Effect of current flow on the membrane potential of cardiac muscle. *J Physiol.* 1951;115:227-236.

[5] Sano T, Takayama N, and Shimamoto T. Directional difference of conduction velocity in the cardiac ventricular syncytium studied by microelectrodes. *Circ Res.* 1959;7:262-267.

[6] Sano T, Ohtsuka E, and Shimamoto T. "Unidirectional" atrioventricular conduction studied by microelectrodes. *Circ Res.* 1960;8:600-608.

[7] Shabetai R, Surawicz B, Hammill W. Monophasic Action Potentials in Man. *Circulation,* 1968;38:341-352.

[8] Salama G. Merocyanine 540 as an optical probe of transmembrane electrical activity in the heart. Science 1976;191:485-487.

[9] Morad M, and Dillon S. A new laser scanning system for measuring action potential propagation in the heart. *Science,* 1981; 214:453-456.

[10] Choi BR, Jang W, Salama G. Spatially discordant voltage alternans cause wavebreaks in ventricular fibrillation. *Heart Rhythm,* 2007; 4:1057–1068.

[11] Kay M, Amison PM, Rogers JM. Three-dimensional surface reconstruction and

[12] panoramic optical mapping of large hearts. *IEEE Trans Biomed Eng.* 2004;51:1219-1229.

[13] Rogers JM, Walcott GP, Gladden JD, Melnick SB, and Kay MW. Panoramic optical mapping reveals continuous epicardial reentry during ventricular fibrillation in the isolated swine heart. *Biophys J.* 2007;92:1090-1095.

[14] Byars JL, Smith WM, Ideker RE, and Fast VG. Development of an optrode for intramural multisite optical recordings of Vm in the heart. *J Cardiovasc Electrophysiol*. 2003;14:1196-1202.

[15] Choi BR, and Salama G. Simultaneous maps of optical action potentials and calcium

[16] transients in guineapig hearts: mechanisms underlying concordant alternans. *J Physiol.* 2000;529:171-188.

[17] Laurita KR, and Singal A. Mapping action potentials and calcium transients simultaneously from the intact heart. *Am J Physiol Heart Circ Physiol.* 2001;280: H2053–H2060.

[18] Pruvot EJ, Katra RP, Rosenbaum DS, Laurita KR. Role of calcium cycling versus restitution in the mechanism of repolarization alternans. *Circ Res.* 2004;94:1083-1090.

[19] Lakireddy V, Bub G, Baweja P, Syed A, Boutjdir M, and El-Sherif N. The kinetics of spontaneous calcium oscillations and arrhythmogenesis in the in vivo heart during ischemia/reperfusion. *Heart Rhythm,* 2006;3:58-66.

[20] Fast VG, and Ideker RE. Simultaneous optical mapping of transmembrane potential and intracellular calcium in myocyte cultures. *J Cardiovasc Electrophysiol*. 2000;11:547-556.

[21] Fast VG. Simultaneous optical imaging of membrane potential and intracellular calcium. *J Electrocardiol* 2005;38:107-112.

[22] Lan DZ, Pollard AE, and Knisley SB. Optical mapping of Vm and Cai 2+ in a model of arrhythmias induced by local catecholamine application in patterned cell cultures. *Eur J Physiol*. 2007;453:871–877.

[23] Cabo C, Pertsov AM, Baxter WT, Davidenko JM, Gray RA, and Jalife J. Wave-front curvature as a cause of slow conduction and block in isolated cardiac muscle. *Circ Res.* 1994;75:1014-1028.

[24] Knisley SB, and Hill BC. Effects of bipolar point and line stimulation in anisotropic rabbit epicardium: assessment of the critical radius of curvature for longitudinal block. *IEEE Trans Biomed Eng*, 1995;42:957-966.

[25] Knisley SB, Hill BC, and Ideker RE. Virtual electrode effects in myocardial fibers. *Biophys J.* 1994;66:719-728.

[26] Neunlist M, and Tung L. Spatial distribution of cardiac transmembrane potentials around an extracellular electrode: Dependence on fiber orientation. *Biophys J.* 1995;68:2310-2322.

[27] Knisley SB, and Baynham T. Line stimulation parallel to myofibers enhances regional uniformity of transmembrane voltage changes in rabbit hearts. *Circ Res.* 1997;81:229-241.

[28] Knisley SB, Trayanova N, and Aguel F. Roles of electric field and fiber structure in cardiac electric stimulation. Biophys J 1999;77:1404-1417.

[29] Al-Khadra A, Nikolski V, and Efimov IR. The role of electroporation in defibrillation. *Circ Res*. 2000;87:797-804.

[30] Fast VG, Sharifov OF, Cheek ER, Newton JC, and Ideker RE. Intramural virtual electrodes during defibrillation shocks in left ventricular wall assessed by optical mapping of membrane potential. *Circulation*, 2002;106:1007-1014.

[31] Tung L, and Cysyk J. Imaging fibrillation/defibrillation in a dish. *J Electrocardiol.* 2007;40:S62-S65.

[32] Fedorov VV, Kostecki G, Hemphill M, and Efimov IR. Atria are more susceptible to electroporation than ventricles: Implications for atrial stunning, shock-induced arrhythmia and defibrillation failure. *Heart Rhythm*, 2008;5:593-604.

[33] Perez FJ, Wood MA, and Schubert CM. Effects of gap geometry on conduction through discontinuous radiofrequency lesions. *Circulation,* 2006;113:1723-1729.

[34] Himel HD, Dumas JH, Kiser AC, and Knisley SB. Translesion stimulus-excitation delay indicates quality of linear lesions produced by radiofrequency ablation in rabbit hearts. *Physiol. Meas*. 2007;28:611–623.

[35] Hyatt CJ, Mirinov SF, Vetter FJ, Zemlin CW, and Pertsov AM. Optical Action Potential Upstroke Morphology Reveals Near-Surface Transmural Propagation Direction. *Circ Res.* 2005;97:277-284.

[36] Zemlin CW, Bernus O, Matiukas A, Hyatt CJ, and Pertsov AM. Extracting intramural wavefront orientation from optical upstroke shapes in whole hearts. *Biophys J.* 2008;95:942-950.

[37] Baxter WT, Mirinov SF, Zaitsev AV, Jalife J, and Pertsov AM. Visualizing excitation waves inside cardiac muscle using transillumination. Biophys J 2001;80:516-530.

[38] Salama G, Choi BR, Azour G, Lavasani M, Tumbev V, Salzberg BM, Patrick MJ, Ernst LA, and Waggoner AS. Properties of new, long-wavelength, voltage-sensitive dyes in the heart. *J. Membrane Biol*. 2005;208:125–140.

[39] Matiukas A, Mitrea BG, Pertsov AM, Wuskell JP, Wei M, Watras J, Millard AC, and Loew LM. New near-infrared optical probes of cardiac electrical activity. *Am J Physiol Heart Circ Physiol*. 2006;290: H2633–H2643.

[40] Matiukas, A, Mitrea BG, Qin M, Pertsov AM, Shvedko AG, Warren MD, Zaitsev AV, Wuskell JP, Wei M, Watras J, and Loew LM. Near-infrared voltage-sensitive fluorescent dyes optimized for optical mapping in blood-perfused myocardium. *Heart Rhythm*, 2007;4:1441-1451.

[41] Morad M, and Salama G. Optical probes of membrane potential in heart muscle. *J Physiol*. 1979;292:267-295.

[42] Cheng Y. Optical mapping of shock-induced arrhythmogenesis in the rabbit heart with healed myocardial infarction: fluorescent imaging with a photodiode array. *Methods Mol Med.* 2006;129:149-61.

[43] Sakai T. Optical mapping analysis of the spatiotemporal pattern of experimental tachyarrhythmia in improved isolated rat atrium preparation. *J Physiol Sci.* 2008;58:87-97.

[44] Scherz P. Practical Electronics for inventors. Second edition. New York, NY: McGraw-Hill; 2007.

[45] Hooks DA, LeGrice IJ, Harvey JD, S and maill BH. Intramural multisite recording of transmembrane potential in the heart. *Biophys J*. 2001;81:2671-2680.

[46] Caldwell BJ, Legrice IJ, Hooks DA, Tai D, Pullan AJ, and Smaill BH. Intramural measurement of transmembrane potential in the isolated pig heart: Validation of a novel technique. *J Cardiovasc Electrophysiol.* 2005;16:1001-1010.

[47] Kong W, Fakhari N, Sharifov OF, Ideker RE, Smith WM, and Fast VG. Optical measurements of intramural action potentials in isolated porcine hearts using optrodes. *Heart Rhythm*, 2007;4:1430-1436.

[48] Knisley SB, Justice RK, Kong W, and Johnson PL. Ratiometry of transmembrane voltage-sensitive fluorescent dye emission in hearts. *Am J Physiol Heart Circ Physiol*. 2000; 279: H1421–H1433.

[49] Kong W, Walcott GP, Smith WM, Johnson PL, and Knisley SB. Emission ratiometry for simultaneous calcium and action potential measurements with coloaded dyes in rabbit hearts: reduction of motion and drift. *J Cardiovasc Electrophysiol*, 2003;14:76-82.

[50] Entcheva E, and Bien H. Macroscopic optical mapping of excitation in cardiac cell networks with ultra-high spatiotemporal resolution. *Progress in Biophysics and Molecular Biology*, 2006;92:232–257.

[51] Himel, H.D., IV; and Knisley, S.B. Imaging of cardiac movement using ratiometric and nonratiometric optical mapping: effects of ischemia and 2, 3-butaneodione monoxime. *IEEE Trans Med Imaging*, 2006;25:122-127.

[52] 50. Efimov IR, Ermentrout B, Huang DT, and Salama G. Activation and repolarization patterns are governed by different structural characteristics of ventricular myocardium: Experimental study with voltage-sensitive dyes and numerical simulations. *J Cardiovasc Electrophysiol*. 1996;7:512-530.

[53] Girouard SD, Pastore JM, Laurita KR, Gregory KW, and Rosenbaum DS. Optical mapping in a new guinea pig model of ventricular tachycardia reveals mechanisms for multiple wavelengths in a single reentrant circuit. Circulation 1996;93:603-613.

[54] Jalife J, Berenfeld O, Skanes A, and Mandapati R. Mechanisms of atrial fibrillation: mother rotors or multiple daughter wavelets, or both? J Cardiovasc Electrophysiol 1998;9:S2-12.

[55] Wu J, Biermann M, Rubart M, and Zipes DP. Cytochalasin D as excitation-contraction uncoupler for optically mapping action potentials in wedges of ventricular myocardium. *J Cardiovasc Electrophysiol*. 1998;9:1336-1347.

[56] Fedorov VV, Lozinsky IT, Sosunov EA, Anyukhovsky EP, Rosen MR, Balke W, and Efimov IR. Application of blebbistatin as an excitation– contraction uncoupler for electrophysiologic study of rat and rabbit hearts. *Heart Rhythm*, 2007;4:619-626.

[57] Li D, and Nattel S. Pharmacological elimination of motion artifacts during optical imaging of cardiac tissues: Is blebbistatin the answer? *Heart Rhythm*, 2007;4:627-628.

[58] Biermann M, Rubart M, Moreno A, Wu J, Josiah-Durant A, and Zipes DP. Differential effects of cytochalasin D and 2,3 butanedione monoxime on isometric twitch force and transmembrane action potential in isolated ventricular muscle: implications for optical measurements of cardiac repolarization. *J Cardiovasc Electrophysiol*. 1998;9:1348-1357.

[59] Lee MH, Lin SF, Ohara T, Omichi C, Okuyama Y, Chudin E, Garfinkel A, Weiss JN, Karagueuzian HS, and Chen PS. Effects of diacetyl monoxime and cytochalasin D on

[60] ventricular fibrillation in swine right ventricles. *Am J Physiol Heart Circ Physiol*. 2001;280: H2689–H2696.

[61] Hayashi H, Miyauchi Y, Chou CC, Karagueuzian HS, Chen PS, and Lin SF. Effects of cytochalasin D on electrical restitution and the dynamics of ventricular fibrillation in isolated rabbit heart. *J Cardiovasc Electrophysiol*. 2003;14:1077-1084.

[62] Baker LC, Wolk R, Choi BR, Watkins S, Plan P, Shah A, and Salama G. Effects of mechanical uncouplers, diacetyl monoxime, and cytochalasin-D on the

electrophysiology of perfused mouse hearts. *J Physiol Heart Circ Physiol*. 2004;287:H1771-H1779.

[63] 60. Choi BR, Liu T, Lavasani M, and Salama G. Fiber orientation and cell-cell coupling influence ventricular fibrillation dynamics. *J Cardiovasc Electrophysiol.* 2003;14:851-860.

[64] Zaitsev AV, Guha PK, Sarmast F, Kolli A, Berenfeld O, Pertsov AM, de Groot JR, Coronel R, and Jalife J. Wavebreak formation during ventricular fibrillation in the isolated, regionally ischemic pig heart. *Circ Res*. 2003;92:546-553.

[65] Wu TJ, Lin SF, Baher A, Qu Z, Garfinkel A, Weiss JN, Ting CT, and Chen PS. Mother rotors and the mechanisms of D600-induced type 2 ventricular fibrillation. *Circulation,* 2004;110:2110-2118.

[66] Joel SE, and Hsia PW. Discovery of gradient pattern in dominant frequency maps during fibrillation: implication of rotor drift and epicardial conduction velocity changes. *J Electrocardiol*. 2005;38:159-165.

[67] Moreno J, Zaitsev AV, Warren M, Berenfeld O, Kalifa J, Lucca E, Mironov S, Guha P, and Jalife J. Effect of remodelling, stretch and ischaemia on ventricular fibrillation frequency and dynamics in a heart failure model. *Cardiovasc Res*. 2005;65:158-166.

[68] Choi BR, Hatton WJ, Hume JR, Liu T, and Salama G. Low osmolarity transforms ventricular fibrillation from complex to highly organized, with a dominant high-frequency source. *Heart Rhythm*, 2006;3:1210-1220.

[69] Wu TJ, Lin SF, Hsieh YC, Ting CT, Chen PS. Ventricular fibrillation during no-flow global ischemia in isolated rabbit hearts. *J Cardiovasc Electrophysiol*. 2006;17:1112-1120.

[70] Caldwell J, Burton FL, Smith GL, and Cobbe ST. Heterogeneity of ventricular fibrillation dominant frequency during global ischemia in isolated rabbit hearts. *J Cardiovasc Electrophysiol*. 2007;18:854-861.

[71] Omichi C, Lamp ST, Lin SF, Yang J, Baher A, Zhou S, Attin M, Lee MH, Karagueuzian HS, Kogan B, Qu Z, Garfinkel A, Chen PS, and Weiss JN. Intracellular Ca dynamics in ventricular fibrillation. *Am J Physiol Heart Circ Physiol*. 2004;286: H1836–H1844.

[72] Wu S, Weiss JN, Chou CC, Attin M, Hayashi H, and Lin SF. Dissociation of membrane potential and intracellular calcium during ventricular fibrillation. *J Cardiovasc Electrophysiol*. 2005;16:186-192.

[73] Jung P, Wang J, Wackerbauer R, and Showalter K. Coherent structure analysis of spatiotemporal chaos. *Physical Review E,* 2000;61:2095-2098.

[74] Bub G, Shrier A, and Glass L. Global organization of dynamics in oscillatory heterogeneous excitable media. *Physical Review Lett.* 2005;94:028105.

[75] Chen J, Mandapati R, Berenfeld O, Skanes AC, and Jalife J. High-frequency periodic sources underlie ventricular fibrillation in the isolated rabbit heart. *Circ Res*. 2000;86:86-93.

[76] Zaitsev AV, Berenfeld O, Mirinov SF, Jalife J, and Pertsov AM. Distribution of excitation frequencies on the epicardial and endocardial surfaces of fibrillating ventricular wall of the sheep heart. *Circ Res.* 2000;86:408-417.

[77] Berenfeld O, Pertsov AM, and Jalife J. Letter to the editor: What is the organization of waves in ventricular fibrillation. *Circ Res*. 2001;89:e22.

[78] Moe GK. On the multiple wavelet hypothesis of atrial fibrillation. *Arch Int Pharmacodyn Ther*. 1962;140:183–188.

[79] Lee JJ, Kamjoo K, Hough D, Hwang C, Fan W, Fishbein MC, Bonometti C, Ikeda T, Karagueuzian HS, and Chen PS. Reentrant wave fronts in wiggers' stage II ventricular fibrillation. *Circ Res.* 1996;78:660-675.

[80] Rogers JM, Huang J, Smith WM, and Ideker RE. Incidence, evolution, and spatial distribution of functional reentry during ventricular fibrillation in pigs. *Circ Res*. 1999;84:945-954.

[81] Choi BR, Burton F, and Salama G. Cytosolic Ca2+ triggers early afterdepolarizations and

[82] torsade de pointes in rabbit hearts with type 2 long QT syndrome. *J Physiol*. 2002;543:615-631.

[83] 79. Valderrábano M, Yang J, Omichi C, Kil J, Lamp ST, Qu Z, Lin SF, Karagueuzian HS, Garfinkel A, Chen PS, and Weiss JN. Frequency analysis of ventricular fibrillation in swine ventricles. *Circ Res*. 2002;90:213-222.

[84] Wu TJ, Lin SF, Weiss JN, Ting CT and Chen PS. Two types of ventricular fibrillation in isolated rabbit hearts: Importance of excitability and action potential duration restitution. *Circulation,* 2002;106:1859-1866.

[85] Chen PS, Wu TJ, Ting CT, Karagueuzian HS, Garfinkel A, Lin SF, and Weiss JN. A tale of two fibrillations. *Circulation*, 2003;108:2298-2303.

[86] 82. Liu YB, Pak HN, Lamp ST, Okuyama Y, Hayashi H, Wu TJ, Weiss JN, Chen PS, and Lin SF. Coexistence of two types of ventricular fibrillation during acute regional ischemia in rabbit ventricle. *J Cardiovasc Electrophysiol*. 2004;15:1433-1440.

[87] Nash MP, Mourad A, Clayton RH, Sutton PM, Bradley CP, Hayward M, Paterson DJ, and Taggart P. Evidence for multiple mechanisms in human ventricular fibrillation. *Circulation,* 2006;114:536-542.

[88] Restivo M, Caref EB, Kozhevnikov DO, and El-Sherif N. Spatial dispersion of repolarization is a key factor in the arrhythmogenicity of long QT syndrome. *J Cardiovasc Electrophysiol*. 2004;15:323-331.

[89] Lakireddy V, Baweja P, Syed A, Bub G, Boutjdir M, and El-Sherif N. Contrasting effects of ischemia on the kinetics of membrane voltage and intracellular calcium transient underlie electrical alternans. *Am J Physiol Heart Circ Physiol*. 2005; 288:400-407.

[90] El-Sherif N, Caref EB, Yin H, and Restivo M. The electrophysiological mechanism of ventricular arrhythmias in the long QT syndrome. *Circ Res*. 1996;79:474-492.

[91] El-Sherif N. Mechanism of ventricular arrhythmias in the long QT syndrome: on hermeneutics. *J Cardiovasc Electrophysiol*. 2001;12:973-976.

[92] Rosenbaum DS, Jackson LE, Smith JM, Garan H, Ruskin JN, and Cohen RJ. Electrical alternans and vulnerability to ventricular arrhythmias. *N Engl J Med*. 1994;330:235-241.

[93] Hohnloser SH, Klingenheben T, Li YG, Zabel M, Peetermans J, Cohen RJ. T wave alternans as a predictor of recurrent ventricular tachyarrhythmias in ICD recipients: Prospective comparison with conventional risk markers. *J Cardiovasc Electrophysiol*. 1998;9:1258-1268.

[94] Pastore JM, Girouard SD, Laurita KR, Akar FG, and Rosenbaum DS. Mechanism linking T-wave alternans to the genesis of cardiac fibrillation. *Circulation,* 1999;99:1385-1394.

[95] Gold MR, Bloomfield DM, MD, Anderson KP, El-Sherif N, Wilber DJ, Groh WJ, Estes M, Kaufman ES, Greenberg ML, and Rosenbaum DS. A comparison of T-wave alternans, signal averaged electrocardiography and programmed ventricular stimulation for arrhythmia risk stratification. *JACC*, 2000;36:2247-2253.

[96] Pham Q, Quan KJ, and Rosenbaum DS. T-wave alternans: marker, mechanism, and methodology for predicting sudden cardiac death. *J Electrocardiol*. 2003;36:75-81.

[97] Rashba EJ, Osman AF, Macmurdy K, Kirk MM, Sarang SE, Peters RW, Shorofsky SR, and Gold MR. Enhanced detection of arrhythmia vulnerability using T wave alternans, left ventricular ejection fraction, and programmed ventricular stimulation: A prospective study in subjects with chronic ischemic heart disease. *J Cardiovasc Electrophysiol.* 2004;15:170-176.

[98] 94. Ikeda T, Yoshino H, Sugi K, Tanno K, Shimizu H, Watanabe J, Kasamaki Y, Yoshida A, and Kato T. Predictive value of microvolt T-wave alternans for sudden cardiac death in patients with preserved cardiac function after acute myocardial infarction. *JACC,* 2006;48:2268-2274.

[99] Steenbergen C, Murphy E, Levy L, London RE. Elevation in cytosolic free calcium concentration early in myocardial ischemia in perfused rat heart. *Circ Res.* 1987;60:700-707.

[100] Marban E, Kitakaze M, Koretsune Y, Yue DT, Chacko VP, and Pike MM. Quantification of [Ca2+]i in perfused hearts: critical evaluation of the 5F-BAPTA and nuclear magnetic resonance method as applied to the study of ischemia and reperfusion. *Circ Res.* 1990;66:1255-1267.

[101] Bers DM. Calcium and cardiac rhythms: physiological and pathophysiological. *Circ Res.* 2002;90:14-17.

[102] Shimizu W, and Antzelevitch C. Sodium channel block with mexiletine is effective in reducing dispersion of repolarization and preventing torsade de pointes in LQT2 and LQT3 models of the long-QT syndrome. *Circulation*, 1997;96:2038-2047.

[103] Milberg P, Reinsch P, Wasmer K, Mönnig G, Stypmann P, Osada N, Breithardt G, Haverkamp W, and Eckardt L. Transmural dispersion of repolarization as a key factor of

[104] arrhythmogenicity in a novel intact heart model of LQT3. *Circ Res.* 2005;65:397-404.

[105] Antzelevitch C. Role of spatial dispersion of repolarization in inherited and acquired sudden cardiac death syndromes. *Am J Physiol Heart Circ Physiol.* 2007;293:H2024–H2038.

[106] Valderrábano M, Lee MH, Ohara T, Lai AC, Fishbein MC, Lin SF, Karagueuzian HS, and Chen PS. Dynamics of intramural and transmural reentry during ventricular fibrillation in isolated swine ventricles. *Circ Res*. 2001;88:839-848.

[107] Allison JS, Qin H, Dosdall DJ, Huang J, Newton JC, Allred JD, Smith WM, and Ideker RE. The transmural activation sequence in porcine and canine left ventricle is markedly different during long-duration ventricular fibrillation. *J Cardiovasc Electrophysiol.* 2007;18:1306-1312.

[108] Li L, Jin Q, Huang J, Cheng KA, and Ideker RE. Intramural foci during long duration fibrillation in the pig ventricle. *Circ Res.* 2008;102:1256-1264.

[109] El-Sherif N. The challenge of cardiac tridimensional mapping. *Heart Rhythm,* 2007;4:1437-1440.

[110] Kay MW, and Rogers JM. Epicardial rotors in panoramic optical maps of fibrillating swine ventricles. *Conf Proc IEEE Med Biol Soc*. 2006;1:2268-2271.

[111] Kay MW, Walcott GP, Gladden JD, Melnick SB, and Rogers JM. Lifetimes of epicardial rotors in panoramic optical maps of fibrillating swine ventricles. *Am J Physiol Heart Circ Physiol*. 2006;291:1935-1941.

[112] Evertson DW, Holcomb MR, Eames MDC, Bray MA, Sidorov VY, Xu J, Wingard H, Dobrovolny HM, Woods MC, Gauthier DJ, and Wikswo JP. High-resolution high-speed panoramic cardiac imaging system. *IEEE Trans Biomed Eng*. 2008;55:1241-1243.

[113] Qu F, Ripplinger CM, Nikolski VP, Grimm C, and Efimov IR. Three-dimensional panoramic imaging of cardiac arrhythmias in rabbit heart. *J Biomed Opt.* 2007;12:044019.

[114] Bub G, Glass L, Publicover NG, and Shrier A. Bursting calcium rotors in cultured cardiac myocyte monolayers. *Proc Natl Acad Sci USA*, 1998;95:10283-10287.

[115] Entcheva E, Lu SN, Troppman RH, Sharma V, and Tung L. Contact fluorescence imaging of reentry in monolayers of cultured neonatal rat ventricular myocytes. *J Cardiovasc Electrophysiol*. 2000;11:665-676.

[116] Iravanian S, Nabutovsky Y, Kong CR, Saha S, Bursac N, and Tung L. Functional reentry in cultured monolayers of neonatal rat cardiac cells. *Am J Physiol Heart Circ Physiol.* 2003;285:H449–H456.

[117] Tung L, and Zhang Y. Optical imaging of arrhythmias in tissue culture. *J Electrocardiol*. 2006;39:S2-S6.

[118] Ding L; Splinter, R.; and Knisley, S.B. Quantifying spatial localization of optical mapping using Monte Carlo simulations. *IEEE Trans Biomed Eng.* 2001;48:1098-1107.

# SHORT COMMUNICATIONS

In: Integrated Circuits, Photodiodes…
Editors: R. McIntire and P. Donnell, pp. 369-382

ISBN: 978-1-60692-660-4
© 2009 Nova Science Publishers, Inc.

***Short Communication A***

# BASAL GANGLIA CIRCUIT AND BLADDER FUNCTION: CLINICAL IMPLICATION TO PARKINSON'S DISEASE

***Ryuji Sakakibara***[*]
Neurology, Internal Medicine, Sakura Medical Center,
Toho University, Tokyo, Japan

## ABSTRACT

Bladder dysfunction (urinary urgency / frequency) is a common non-motor disorder in Parkinson's disease (PD), which significantly affects quality of life in the patients. According to the animal studies and the clinical imaging studies, basal ganglia circuit influences not only motor but also bladder function. Bladder (detrusor) overactivity is the major cause of bladder dysfunction, which considered an exaggerated micturition reflex in PD. The net effect of the basal ganglia on micturition is thought to be inhibitory. Functional neuroimaging during bladder filling resulted in activation in the globus pallidus of normal volunteers and in the putamen in patients with PD. In contrast, dopamine transporter imaging was decreased in PD patients with urinary dysfunction than in those without it. Bladder overactivity can be reproduced in experimental parkinsonism. Electrical stimulation of the substantia nigra pars compacta (SNc) inhibited the micturition reflex, and striatal dopamine levels *in situ* significantly increased in the urinary storage phase. The micturition reflex is under the influences of dopamine (both inhibitory in D1 and facilitatory in D2) and GABA (inhibitory). Both the SNc neuronal firing and the released striatal dopamine seem to activate the dopamine D1-GABAergic *direct pathway*, which not only inhibits the basal ganglia output nuclei, but also may inhibit the micturition reflex via GABAergic collateral to the micturition circuit. Intracerebroventricularly administered dopamine inhibits the micturition reflex, and high frequency stimulation in the subthalamic nucleus results in bladder inhibition. In patients with PD, disruption of this pathway may lead to bladder overactivity and resultant urinary urgency/frequency. Manifestation of the disrupted basal ganglia circuit on bladder function in patients with Parkinson's disease and its clinical management are reviewed briefly.

**Key words:** basal ganglia; bladder function; dopamine; Parkinson's disease; autonomic nervous system.

---

[*] E-mail address: sakakibara@sakura.med.toho-u.ac.jp. Telephone: +81-43-462-8811. FAX: +81-43-462-8820. Correspondence to: Ryuji Sakakibara, MD, PhD, Associate Professor, Neurology Division, Department of Internal Medicine, Sakura Medical Center, Toho University, 564-1 Shimoshizu, Sakura, 285-8741 Japan

## INTRODUCTION

Parkinson's disease (PD) is a common movement disorder associated with the degeneration of dopaminergic neurons in the substantia nigra (1). In addition to the movement disorder, patients with PD often show non-motor disorders. The non-motor problems of PD include neuropsychiatric disorders, sleep disorders, sensory symptoms, and autonomic disorders (2). The autonomic disorders in PD include bladder dysfunction, constipation, erectile dysfunction, drooling, dysphagia, postural hypotension, decreased sweating, seborrhea, and weight loss, among which bladder dysfunction is the most common (3,4). Studies have shown that the bladder dysfunction has greater significance when assessed by quality-of-life measures, early institutionalization, or health economics (5,6). It is particularly important to note that, in contrast to motor disorder, bladder dysfunction is often non-responsive to levodopa, suggesting that it occurs through a complex patho-mechanism (7,8,9), and for this reason, add-on therapy is required to maximize the patients' quality of life. This chapter reviews the current concepts of basal ganglia and bladder function, with particular reference to bladder dysfunction in Parkinson's disease.

## NORMAL MICTURITION AND DETRUSOR OVERACTIVITY

The lower urinary tract (LUT) consists of two major components, the bladder and urethra. The bladder is abundant with muscarinic M2,3 receptors and adrenergic beta 3 receptors, and is innervated by cholinergic (parasympathetic pelvic nerve; contraction) and noradrenergic (sympathetic hypogastric nerve; relaxation) fibers, respectively (10). The urethra is abundant with adrenergic alpha 1A/D receptors and nictonic receptors, and is innervated by noradrenergic (sympathetic hypogastric nerve; contraction) and cholinergic (somatic pudendal nerve; contraction) fibers, respectively (Figure 1). The LUT performs two opposite functions, storage and emptying of urine, both of which need an intact neuraxis that involves almost all parts of the nervous system (Sakakibara and Fowler, 2001). This is in contrast to postural hypotension, which arises due to lesions below the medullary circulation center (11).

Normal urinary storage is dependent on the autonomic reflex arc of the sacral spinal cord segments (10,12). The storage reflex is thought to be tonically facilitated by the brain, particularly the pontine storage center (13,14). The pontine storage center lies just ventrolateral to the pontine micturition center (PMC). In addition to the pontine storage center, the storage function is facilitated by the hypothalamus, cerebellum, basal ganglia, and frontal cortex. These areas have been shown to be activated during urinary storage by functional neuroimaging (15). In contrast, normal micturition is dependent on the autonomic reflex arc of the brainstem and the spinal cord (10). The micturition reflex is called the spino-bulbo-spinal reflex, particularly involving the midbrain periaqueductal gray (16,17,18,19) and the PMC (10,13). The PMC is located in or adjacent to the locus coeruleus (20,21,22). The PMC is thought to facilitate the sacral bladder preganglionic nucleus by glutamate (23), while inhibiting the sacral urethral motor nucleus (the Onuf's nucleus) by γ-amino-butyric acid (GABA) and glycine (24). The voiding function seems to be initiated and facilitated by the higher brain structures, e.g., the hypothalamus and prefrontal cortex, which seem to lie in close vicinity to, or overlap, the storage-facilitating area (15, 25).

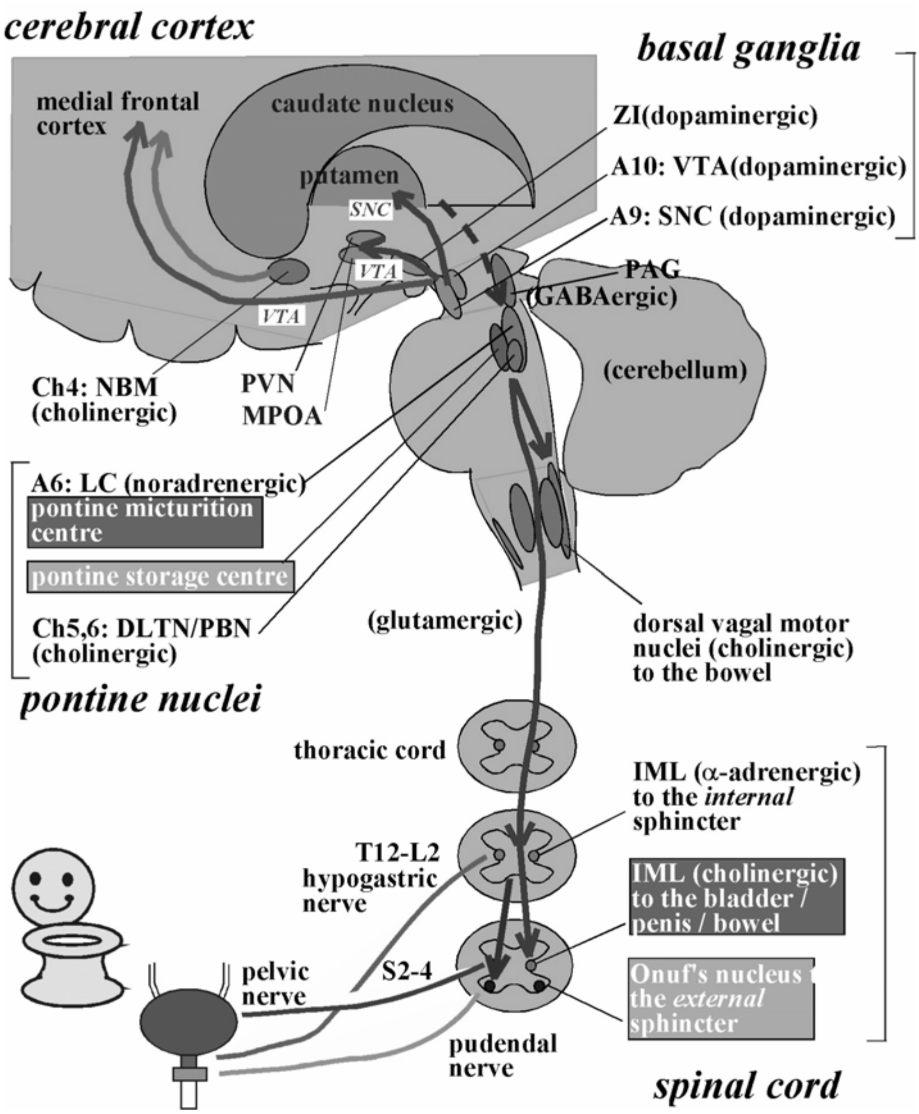

The lower urinary tract consists of two major components, the bladder and urethra. The bladder is mainly innervated by parasympathetic pelvic nerve. The urethra is innervated by sympathetic hypogastric nerve and somatic pudendal nerve, respectively. Urinary storage is dependent on the reflex arc of the sacral spinal cord. The storage reflex is thought to be tonically facilitated by the brain, particularly the pontine storage center. The storage function is thought to be further facilitated by the hypothalamus, cerebellum, basal ganglia, and frontal cortex. Central cholinergic fibers from the nucleus basalis Meynert (NBM, also called as Ch4 cell group) seem to facilitate urinary storage. Micturition is dependent on the reflex arc of the brainstem and the spinal cord, which involves the midbrain periaqueductal gray (PAG) and the pontine micturition center (located in or adjacent to the locus coeruleus [LC]). The voiding function is thought to be initiated by the hypothalamus and prefrontal cortex, which overlap the storage-facilitating area.

PVN: paraventricular nucleus, MPOA: medial preoptic area, A: adrenergic/noradrenergic, ZI: zona incerta, VTA: ventral tegmental area, SNC: substantia nigra pars compacta, DLTN: dorsolateral tegmental nucleus, PBN: parabrachial nucleus, IML: IML cell column, GABA: γ-aminobutyric acid, T: thoracic, L: lumbar, S: sacral

Figure 1. Neural circuitry relevant to micturition.

Bladder (detrusor) overactivity (DO) is the major cause of urinary urgency/frequency and incontinence (26). In lesions above the brainstem, the micturition reflex arc is intact, where DO is considered an exaggerated micturition reflex (26,27). This is in line with the fact that the DO appearing after experimental stroke requires mRNA synthesis in the PMC (28). The exaggeration of the micturition reflex might be brought about not only by decreased inhibition of the brain, and might be further facilitated by glutamatergic and D2 dopaminergic mechanisms (29).

## BASAL GANGLIA CIRCUIT AND DOPAMINE

The net effect of the basal ganglia on micturition is thought to be inhibitory **(**Figure 2**)** (10,30,31), whereas in PD, in which the basal ganglia is affected, the bladder becomes hyperactive. Functional neuroimaging during bladder filling resulted in activation in the globus pallidus of normal volunteers (32) and in the putamen in patients with PD (33). In contrast, dopamine transporter imaging (indicating brain dopamine neurons) was decreased in PD patients with urinary dysfunction than in those without it (34,35). DO can be reproduced in experimental 1-methyl-4-phenyl-1,2,3,6- tetrahydropyridine (MPTP) (36) or 6-OH-dopamine (31)-induced parkinsonism. Electrical stimulation of the substantia nigra pars compacta (SNc, the A9 cell group) inhibited the micturition reflex (37,38), and striatal dopamine levels *in situ* significantly increased in the urinary storage phase by a microdialysis technique (39). Although the details of the link between the basal ganglia circuit and the micturition circuit remain uncertain, the micturition reflex is under the influences of dopamine (both inhibitory in D1 and facilitatory in D2) and GABA (inhibitory) (10,30). Both the SNc neuronal firing and the released striatal dopamine seem to activate the dopamine D1-GABAergic *direct pathway* (Figure 2), which not only inhibits the basal ganglia output nuclei (e.g., the internal glubus pallidus etc.), but also may inhibit the micturition reflex via GABAergic collateral to the micturition circuit (39,40,41). This notion is in line with the fact that intracerebroventricularly administered dopamine inhibits the micturition reflex (36), and the fact that high frequency stimulation in the subthalamic nucleus results in bladder inhibition (41,42). In patients with PD, disruption of this pathway may lead to DO and resultant urinary urgency/frequency.

In addition to the nigrostriatal dopaminergic fibers, the ventral tegmental area (VTA, the A10 cell group)-mesolimbic dopaminergic fibers are thought to be involved in the higher control of micturition **(**Figure 1**)**. In 6-OH-dopamine-treated animals, the VTA lesions induced more severe bladder overactivity than SNc lesions did (43). Electrical or chemical stimulation of VTA elicited both facilitation and termination of the micturition reflex (38,44). Therefore, DO in PD might depend, at least in part, on the degeneration of the VTA-mesolimbic neurons in PD.

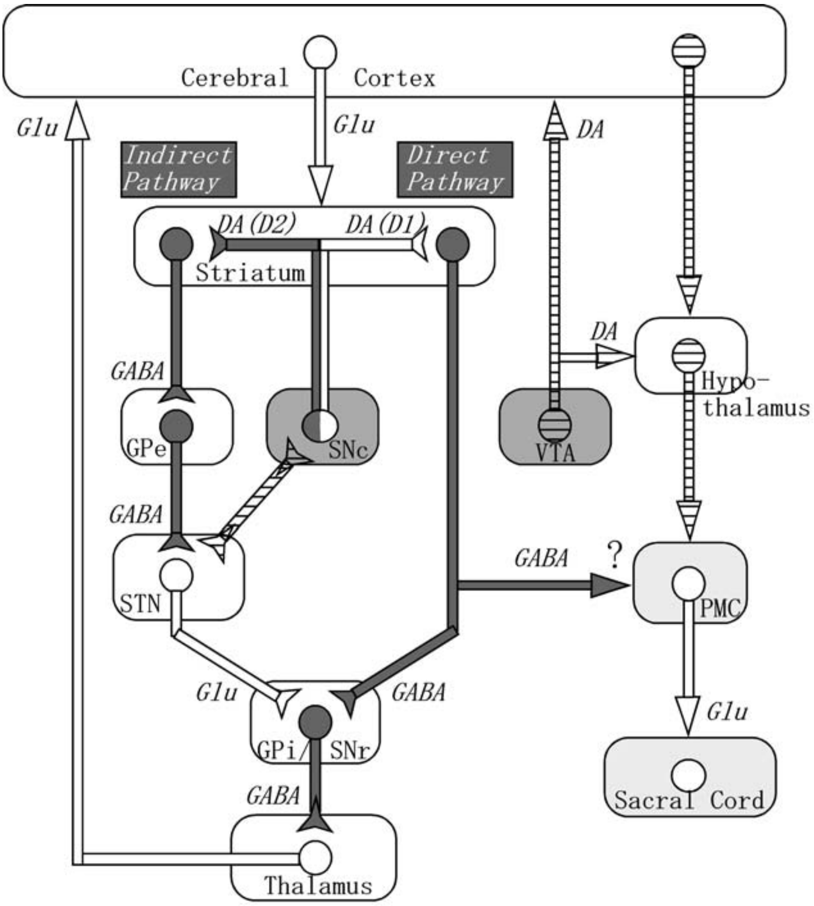

Cited from ref. 39 and 41; modified from Alexander et al. 1990.

The micturition reflex (right-side pathway) is under the influences of dopamine (DA) (both inhibitory in D1 and facilitatory in D2) and gamma-aminobutyric acid (GABA) (inhibitory). The substantia nigra pars compacta (SNc) neuronal firing and the released striatal dopamine seem to activate the dopamine D1-GABAergic *direct pathway*, which not only inhibits the basal ganglia output nuclei (e.g., the globus pallidus internus [GPi], substantia nigra pars reticulata [SNr]), but also may inhibit the micturition reflex via GABAergic collateral to the micturition circuit. High frequency stimulation (leading to inhibition) in the subthalamic nucleus (STN) also results in bladder inhibition.

GPe: globus pallidus externus, VTA: ventral tegmental area, PMC: pontine micturition centre, Glu: glutamate; Black line: inhibitory neurons; White line: excitatory neurons; Hatched line: neurons of undetermined property.

Figure 2. Possible relationship between basal ganglia circuit (left-side) and micturition circuit (right-side).

# BLADDER DYSFUNCTION IN PD

## Lower Urinary Tract Symptoms

The reported prevalence of LUT symptoms (LUTS) in patients with PD ranges from 38% to 71% (45,46,47). However, it has been difficult to determine to what extent PD is contributing to the LUTS. This is because not only PD patients, but also men older than 60 years of age may have an obstruction component to their urinary symptoms brought about by benign prostate hyperplasia. Women may have stress urinary incontinence. Similarly, “idiopathic DO” (12) may occur in men and women older than 65 years due in part to latent brain ischemia (48) In the above studies, most of the data were collected from patients who visited a urology, gynecology or internal medicine clinic because of their symptoms. Furthermore, some of the studies were published before the diagnosis of multiple system atrophy (MSA) (49) was recognized.

In recent studies of PD patients who were diagnosed according to modern criteria (6,50,51,52), the prevalence of LUTS was found to be 27-63.9% using validated questionnaires (50,51,52), or 53% in men and 63% in women using a nonvalidated questionnaire that includes a urinary incontinence category (6), with all of these values being significantly higher than the incidence rates in healthy controls. The majority of patients had onset of the bladder dysfunction after appearance of motor disorder. In one study, urinary incontinence in PD frequently occurred in conjunction with fecal incontinence, whereas no significant relation was observed between bladder and sexual dysfunction (6). Also, it is of particular importance to note that that bladder dysfunction substantially affects the quality of life in patients with PD (6). There has been shown a correlation between bladder dysfunction in patients with PD and neurological disability (50), and a correlation to stage of disease (6), both suggesting a relationship between dopaminergic degeneration and LUTS. LUTS was more common in a group of PD patients with older age than that with younger age, as it is seen in healthy populations (6). Among storage and voiding types of LUTS, storage symptoms are most common. Storage symptoms include nocturia (nighttime urinary frequency), which is the most prevalent symptom reported by patients with PD (>60%) (6,50,51,52). Patients also complain of urinary urgency (33-54%) and daytime frequency (16-36%). Urinary incontinence is a marker for the severity of storage dysfunction, and this symptom was present in 26% of their male and 28% of their female patients with PD (6).

Although less common than storage symptoms, PD patients also show voiding symptoms. In the study by Sakakibara and colleagues, the PD patients had significantly higher rates of retardation in initiating urination (44% of men only), prolongation/poor stream (70% of men only), and straining (28% of women only) compared with the control group (6). However, despite the voiding symptoms, PD patients have low post-void residuals. Therefore, it seems reasonable to say that overactive bladder (urgency/frequency syndrome) is a feature of bladder dysfunction in PD.

## Videourodynamics, Pressure-Flow Analysis and Sphincter Electromyography

### Bladder (Detrusor) Overactivity

The storage phase urodynamic abnormalities in PD included reduced bladder capacity together with detrusor overactivity (DO), which is an involuntary phasic detrusor contraction (12), in 45-93% (45,46,53,54,55) and uninhibited external sphincter relaxation, which is an involuntary decrement of the sphincter electromyogram activity usually accompanying DO, in 33% (55) of patients, respectively. These findings represent the suprasacral type of parasympathetic and somatic dysfunction. Therefore, DO can be the major contributing factor to overactive bladder in PD, which was equally found in both men and women. There is a correlation between DO and stage of disease (56). It is likely that these urodynamic abnormalities are relevant to the pathological lesions in PD, which result in neuronal loss of neuromelanin-containing cells in the nigrostriatal and VTA-mesolimbic system.

### Mild Weak Detrusor and Sphincter Obstruction

Detailed pressure-flow analysis (12,56,57) of the voiding phase in PD has shown weak detrusor on voiding (40% of men; 66% of women) (55). There is a correlation between weak detrusor and stage of disease (56). A subset of PD patients had DO during storage but weak detrusor on voiding. This condition is known as detrusor hyperactivity with impaired contractile function (DHIC) (58), and has recently been estimated to occur in 18% of patients with PD (59). Although little is known about the pathophysiology of DHIC, it seems to be caused by multiple factors rather than a single factor. One possible mechanism for DHIC in PD is that not only bladder-inhibitory, but also bladder-facilitatory brain regions, such as PMC, are affected in this disorder. On the other hand, some older studies described detrusor-external sphincter dyssynergia or pseudo-dyssynergia in PD, and these findings were attributed to PD by analogy of bradykinesia of the limbs (60). However, in our patients with PD, detrusor-external sphincter dyssynergia was rare (55). In contrast, a pressure-flow analysis in PD revealed that half of the patients with PD showed mild urethral obstruction (55). The exact reason for the obstructive pattern in PD is uncertain. However, patients with PD are reported to have high resting urethral pressure, probably as a result of medication—i.e., levodopa and its metabolites, such as norepinephrine, which may contract the internal sphincter via alpha 1A/D-adrenergic receptors. Mild weak detrusor and sphincter obstruction underlie the voiding symptoms in PD. However, in one study, average volume of post-void residuals in PD was 18 ml and none of the patients had post-void residuals of more than 100 ml (55).

### Differential Diagnosis of Parkinsonism by Bladder Dysfunction

DO is not disease-specific, and is commonly seen in other types of degenerative and cerebrovascular parkinsonism. In the differential diagnosis of PD and MSA, large post-void residuals, open bladder neck, and neurogenic change in sphincter motor unit potentials are all common in MSA (55,61), whereas they are rarely seen in clinically typical PD, suggesting relative sparing of the lumbosacral PGN and sacral sphincter motoneurons in PD. However, recent evidences suggest that PD with dementia, or dementia with Lewy bodies (62), may have large post-void residuals and neurogenic change in the sphincter motor unit potentials (63), both of which mimic MSA.

## Drugs and Bladder Function

### Dopaminergic Drugs

It is possible that levodopa and other antiparkinson medication may affect bladder function in PD. Aranda and colleagues (64) studied the effects of subcutaneous injection of 3-

8 mg apomorphine on the storage function in 2 *de novo* PD patients (patients who have not had antiparkinsonian medication previously), and found that the bladder capacity increased. They gave oral levodopa to one of the patients, and the bladder capacity increased. We compared the frequency of bladder dysfunction in *de novo* PD and well-controlled PD with levodopa without the on-off phenomenon. In that study LUTS were fewer in the treated group, although the rates of DO were the same (56). In another study, after 3 months of treatment with levodopa, the storage urodynamic parameters were slightly improved in *de novo* PD (65). Based on these findings, we are currently following overactive bladder in *de novo* PD patients with levodopa or dopamine agonist alone.

In contrast, in non-*de novo* patients, studies concerning the effect of dopaminergic drugs on micturition have produced conflicting results. Regarding overactive bladder, some reports have shown a storage-facilitating effect of dopaminergic drugs as follows. A questionnaire study has shown that in non-*de novo* patients, voiding symptoms (intermittency and sensation of residual urine) were more common in those taking levodopa and bromocriptine (D2-selective agonist) than in those taking levodopa alone (6). In contrast, Kuno and colleagues showed that change of bromocriptine to pergolide (D1<2 agonist) brought lessening of nocturia (66), and Yamamoto described improvement of DO by pergolide (67). Both studies suggested that D1 receptor stimulation is an option for the treatment of overactive bladder. Benson and colleagues (68) studied the effects of 2000 mg of levodopa on LUT function in 2 longstanding PD patients, and found that bladder capacity increased. However, after discontinuation of levodopa, the bladder capacity further increased in one of the patients, but decreased in the other. Other reports have shown a voiding-facilitating effect of dopaminergic drugs as follows. Christmas and colleagues (69) have studied the effects of subcutaneous injection of 3-8 mg apomorphine on the evacuating function in 10 'PD' patients (although some of them had post-void residuals of more than 500 ml), and found that acontractile bladder became normal in 2, and post-void residuals was ameliorated in 6 of these patients. Fitzmaurice and colleagues (70) have described that, in advanced PD with the on-off phenomenon, DO worsened with levodopa in some patients and lessened in others. Winge and colleagues (71) found that the outcome of treatment with dopaminergic drugs on micturition in PD was unpredictable. Recent studies have shown that in early PD (72) and advanced PD with the on-off phenomenon (9), a single-dose of levodopa exacerbates DO in the filling phase, but also improves bladder emptying through increased detrusor contractility. We still do not know the exact reasons for the discrepancy.

There are several factors underlying the complex bladder behavior in non-*de novo* PD patients. Post-synaptic dopamine D1 (excitatory) and D2 (inhibitory) receptors have a millimolar affinity to dopamine, whereas dendritic D2 (inhibitory) autoreceptors have a picomolar affinity to dopamine (73). Therefore, when levodopa is administered externally, it may first stimulate dendritic D2 autoreceptors, which might suppress the NSDN and facilitate the micturition reflex. In cases of PD under long-term treatment with levodopa, dopamine receptors are down-regulated and potential hypersensitivity might occur (74). Bladder hyperactivity might also involve an activation of D2 receptors in the spinal cord (75), which receive dopaminergic fibers from the hypothalamic A11 cell group. Peripheral dopamine D1 and D2 receptors also exist in the bladder (76), although their exact role has not been delineated.

### Cholinergic Drugs

Anticholinergics (77) are generally used as a first-line treatment for overactive bladder. However, it is important to balance the therapeutic benefits with the adverse effects of these drugs. When the dose of drug increased, post-void residuals may appear (77). Dry mouth due to the blocking of M3 receptors in the salivary gland, and constipation due to the blocking of both M2 and M3 receptors in the bowel are common (78). Cognitive adverse events by anticholinergics are a concern particularly in the elderly. For example, trihexyphenidyl (for PD) and oxybutynin (for overactive bladder) proved to have central side effects (79,80). Factors contributing to the central effects of drugs may include receptor subtype-selectivity and blood-brain barrier (BBB) penetration (81). The cerebral cortex is abundant with muscarinic M1 receptors. Whereas most anticholinergics are receptor-nonselective, darifenacin has selective M3 agonistic action and is less apt to block central M1 receptors. Among factors of BBB penetration, diffusion is facilitated by smaller molecular size (<450-500Da), neutrality or smaller polar surface area (<90A), and lipophilicity or smaller partition coefficient of water versus oil (logP<3) (27). Whereas most anticholinergics have neutrality, trospium is ionic and less apt to penetrate the BBB. Particularly in elderly patients who have hallucination or cognitive decline (PD with dementia/ dementia with Lewy bodies) (62,63), anticholinergics should be used with caution.

## CONCLUSION

This article reviewed the current concepts of basal ganglia and bladder function, and the manifestation of basal ganglia dysfunction on the bladder in PD. The net effect of the basal ganglia on micturition is thought to be inhibitory. In PD, disruption of this pathway may lead to bladder overactivity and resultant urinary urgency/frequency. Levodopa seems to alter bladder function in patients with PD, although it is still unpredictable in each case. Longstanding cases with marked bladder overactivity may need peripheral anticholinergic agents, which are beneficial in maximizing patients’ quality of life.

## REFERENCES

[1] Hornykiewicz O, and Kish SJ. (1986). Biochemical pathophysiology of Parkinson’s disease. *Adv Neurol* **45**: 19-34.

[2] Chaudhuri KR, Healy DG, Schapira AHV, National Institute for Clinical Excellence. (2006). Non-motor symptoms of Parkinson’s disease: diagnosis and management. *Lancet Neurol.* **5**: 235-245.

[3] Jost WH. (2003). Autonomic dysfunction in idiopathic Parkinson’s disease. *J Neurol.* 250 Suppl 1: I28-30.

[4] Magerkurth C, Schnitzer R, and Braune S. (2005) Symptoms of autonomic failure in Parkinson’s disease: prevalence and impact on daily life. *Clin Auton Res.* **15**: 76–82.

[5] McGrother CW, Jagger C, Clarke M, and Castleden CM. (1990) Handicaps associated with incontinence: implications for management. *J Epidemiol Commun Health* **44**: 246–248.

[6] Sakakibara R, Shinotoh H, Uchiyama T, Sakuma M, Kashiwado M, Yoshiyama M, and Hattori T. (2001). Questionnaire-based assessment of pelvic organ dysfunction in Parkinson's disease. *Auton Neurosci*. **92**: 76-85.

[7] Levein NG, Thorn E, Lindberg G, and Wattwil M. (1999). Dopamine reduces gastric tone in a dose-related manner. *Acta Anaesthesiol Scand*. **43**: 722.725.

[8] Levein NG, Thorn SE, Wattwil M (1999). Dopamine delays gastric emptying and prolongs orocaecal transit time in volunteers. *Eur J Anaesthesiol.* **16**: 246-250.

[9] Uchiyama T, Sakakibara R, Hattori T, and Yamanishi T (2003). Short-term effect of a single levodopa dose on micturition disturbance in Parkinson's disease patients with the wearing-off phenomenon. *Mov Disord.* **18**: 573-578.

[10] de Groat WC (2006). Integrative control of the lower urinary tract: preclinical perspective. *BJP*, **147**: S25-S40.

[11] Sakakibara R, and Fowler CJ (2001). Brain disease (Chapter 9). In: *Seminars in Clinical Neurology* (by World Federation of Neurology). Neurologic bladder, bowel, and sexual function. Edited by Fowler CJ, Elsevier, Boston, 229-243.

[12] Abrams P, Cardozo L, Fall M, Griffiths D, Rosier P, Ulmsten U, van Kerrebroeck P, Victor A, Wein A; Standardisation Sub-committee of the International Continence Society. (2002). The standardization of terminology of lower urinary tract function: report from the standardization sub-committee of the International Continence Society. *Neurourol Urodynam*. **21**: 167-178.

[13] Blok BF, and Holstege G (1999). The central control of micturition and continence: implications for urology. *Br J Urol Int*. **83** Suppl 2: 1-6.

[14] Sakakibara R, Nakazawa K, Shiba K, Nakajima Y, Uchiyama T, Yoshiyama M, Yamanishi T, and Hattori T (2002). Firing patterns of micturition-related neurons in the pontine storage centre in cats. Auton Neurosci **99**: 24-30.

[15] Kavia RBC, Dasgupta R, and Fowler CJ (2005). Functional imaging and the central control of the bladder. *J Comp Neurol*. **493**: 27-32.

[16] Sakakibara R, Hattori T, Yasuda K, Yamanishi T, Tojo M, and Mori M (1997). Micturitional disturbance in Wernicke's encephalopathy. *Neurourol Urodynam.* **16**: 111-115.

[17] Matsuura S, Downie JW, Allen GV (1998). Volume-evoked micturition reflex is mediated by the ventrolateral periaqueductal gray in anesthetized rat. *Am J Physiol*. **275**, R2049-R2055.

[18] Liu Z, Sakakibara R, Nakazawa K, Uchiyama T, Yamamoto T, Ito T, and Hattori T (2004). Micturition-related neuronal firing in the periaqueductal gray area in cats. *Neuroscience,* **126**: 1075-1082.

[19] Yaguchi H, Soma H, Miyazaki Y, Tashiro J, Yabe I, Kikuchi S, Sasaki H, Kakizaki H, Moriwaka F, and Tashiro K (2004). A case of acute urinary retention caused by periaqueductal grey lesion. *J Neurol Neurosurg Psychiatry,* **75**; 1202-1203.

[20] Betts CD, Kapoor R, and Fowler CJ (1992). Pontine pathology and voiding dysfunction. *Br J Urol.* **70**: 100-102.

[21] Sakakibara R, Hattori T, Yasuda K, and Yamanishi T (1996). Micturitional disturbance and pontine tegmental lesion; urodynamic and MRI analyses of the vascular cases. *J Neurol Sci*. **141**: 105-110.

[22] Sasaki M (2005). Role of Barrington’s nucleus in micturition. *J Comp Neurol.* **493**: 21-26.

[23] Matsumoto G, Hisamitsu T, and De Groat WC (1995). Role of glutamate and NMDA receptors in the descending limb of the spinobulbospinal micturition reflex pathway of the rat. *Neurosci Lett*. **183**: 58-61.

[24] Blok BF, de Weerd H, and Holstege G (1997). The pontine micturition center projects to sacral cord GABA immunoreactive neurons in the cat. *Neurosci Lett*. **233**: 109-112.

[25] Fowler CJ (2006). Integrated control of lower urinary tract: clinical perspective. *BJP*, **147**: S14-S24.

[26] Steers WD (2002). Pathophysiology of overactive and urge urinary incontinence. *Rev Urol 4 Suppl*. **4:** S7-S18.

[27] Andersson KE (2004). Mechanisms of disease: central nervous system involvement in overactive bladder syndrome. *Nat Clin Pract Urol*. **1,** 103-108.

[28] Yokoyama O, Yotsuyanagi S, Akino H, Moriyama H, Matsuta Y, and Namiki M (2003). RNA synthesis in pons necessary for maintenance of bladder overactivity after cerebral infarction in rat. *J Urol*. **169**: 1878-1884.

[29] Yokoyama O, Yoshiyama M, Namiki M, and de Groat WC (2002). Changes in dopaminergic and glutamatergic excitatory mechanisms of micturition reflex after middle cerebral artery occlusion in conscious rats. *Exp Neurol*. **173**, 129-135.

[30] Seki S, Igawa Y, Kaidoh K, Ishizuka O, Nishizawa O, and Andersson KE (2001). Role of dopamine D1 and D2 receptors in the micturition reflex in conscious rats. *Neurourol Urodyn*. **20**: 105-13.

[31] Yoshimura N, Kuno S, Chancellor MB, de Groat WC, and Seki S (2003). Dopaminergic mechanisms underlying bladder hyperactivity in rats with a unilateral 6-hydroxydopamine (6-OHDA) lesion of the nigrostriatal pathway. *Br J Pharmacol*. **139**: 1425-1432.

[32] Nour S, Svarer C, Kristensen JK, PaulsonOB, and Law I (2000). Cerebral activation during micturition in normal men. *Brain*, **123**: 781-789.

[33] Kitta T, Kakizaki H, Furuno T, Moriya K, Tanaka H, Shiga T, Tamaki N, Yabe N, Sasaki H, and Nonomura K (2006). Brain activation during detrusor overactivity in patients with parkinson’s disease: a PET study. *J Urol*. **175**: 994-998.

[34] Sakakibara R, Shinotoh H, Uchiyama T, Yoshiyama M, Hattori T, and Yamanishi T (2001). SPECT imaging of the dopamine transporter with [$^{123}$I]-beta-CIT reveals marked decline of nigrostriatal dopaminergic function in Parkinson's disease with urinary dysfunction. *J Neurol Sci*. **187**: 55-59.

[35] Winge K, Friberg L, Werdelin L, Nielsen KK, and Stimpel H (2005). Relationship between nigrostriatal dopaminergic degeneration, urinary symptoms, and bladder control in Parkinson's disease. *Eur J Neurol*. **12**: 842-850.

[36] Yoshimura N, Mizuta E, Yoshida O, Kuno S (1998). Therapeutic effects of dopamine D1/D2 receptor agonists on detrusor hyperreflexia in 1-methyl-4-phenyl-1,2,3,6-tetrahydropyridine- lesioned parkinsonian cynomolgus monkeys. *J Pharmacol Exp Therapeutics* **286**: 228-233.

[37] Yoshimura N, Sasa M, Yoshida O, Takaori S (1992). Dopamine D-1 receptor mediated inhibition of micturition reflex by central dopamine from the substantia nigra. *Neurourol Urodyn* **11**: 535-545.

[38] Sakakibara R, Nakazawa K, Uchiyama T, Yoshiyama M, Yamanishi T, Hattori T (2002). Micturition-related electrophysiological properties in the substantia nigra pars compacta and the ventral tegmental area in cats. *Auton Neurosci* **102**: 30-38.

[39] Yamamoto T, Sakakibara R, Hashimoto K, Nakazawa K, Uchiyama T, Liu Z, Ito T, Hattori T (2005). Striatal dopamine level increases in the urinary storage phase in cats: an *in vivo* microdialysis study. *Neuroscience,* **135**: 299-303.

[40] Smith Y, Bevan MD, Shink E, and Bolam JP (1998). Microcircuitry of the direct and indirect pathways of the basal ganglia. *Neuroscience,* **86**:353-387.

[41] Sakakibara R, Nakazawa K, Uchiyama T, Yoshiyama M, Yamanishi T, and Hattori T (2003). Effects of subthalamic nucleus stimulation on the micturation reflex in cats. *Neuroscience,* **120**: 871-875.

[42] Dalmose AL, Bjarkam CR, Sorensen JC, Djurhuus JC, and Jorgensen TM (2004). Effects of high frequency deep brain stimulation on urine storage and voiding function in conscious minipigs. *Neurourol Urodyn.* **23**: 265-272.

[43] Hashimoto K, Oyama T, Ukay Y, Kimura K, Sugiyama T, Park YC, and Kurita T (1997). Selective destruction of dopamine neurones of the ventral tegmental area, but not the substantia nigra, impairs reflex micturition in rats. *Neurourol Urodyn.* **16**: 470-471.

[44] Hashimoto K, Oyama T, Sugiyama T, Park YC, and Kurita T (2003). Neuronal excitation in the ventral tegmental area modulates the micturition reflex mediated via the dopamine D(1) and D(2) receptors in rats. *J Pharmacol Sci.* **92**: 143-148.

[45] Murnaghan GF (1961). Neurogenic disorders of the bladder in Parkinsonism. *Br J Urol.* **33**, 403-409.

[46] Hattori T, Yasuda K, Kita K, Hirayama K (1992). Voiding dysfunction in Parkinson's disease. *Jpn J Psychiatry Neurol* **46**: 181-186.

[47] Gray R, Stern G, and Malone-Lee J (1995). Lower urinary tract dysfunction in Parkinson's disease: changes relate to age and not disease. *Age Ageing,* **24**: 499-504.

[48] Sakakibara R, Hattori T, Uchiyama T, and Yamanishi T (1999). Urinary function in the elderly with and without leukoaraiosis; in relation to cognitive and gait function *J Neurol Neurosurg Psychiatry,* **67**; 658-660.

[49] Gilman S, Low PA, Quinn N, Albanese A, Ben-Shlomo Y, Fowler CJ, Kaufmann H, Klockgether T, Lang AE, Lantos PL, Litvan I, Mathias CJ, Oliver E, Robertson D, Schatz I, and Wenning GK (1998). Consensus statement on the diagnosis of multiple system atrophy. *J Auton Nerv Syst.* **74**: 189-192.

[50] Araki I, Kuno S (2000). Assessment of voiding dysfunction in Parkinson's disease by the international prostate symptom score. *J Neurol Neurosurg Psychiatry,* **68**: 429-433.

[51] Lemack GE, Dewey RB, Roehrborn CG, O'Suilleabhain PE, and Zimmern PE (2000). Questionnaire-based assessment of bladder dysfunction in patients with mild to moderate Parkinson's disease. *Urology,* **56**: 250-254.

[52] Campos-Sousa RN, Quagliato E, da Silva BB, De CR Jr, Ribeiro SC, and de Carvalho DF (2003). Urinary symptoms in Parkinson's disease: prevalence and associated factors. *Arq Neuropsiquiatr.* **61**: 359-363.

[53] Stocchi F, Carbone A, Inghilleri M, Monge A, Ruggieri S, Berardelli A, and Manfredi M (1997). Urodynamic and neurophysiological evaluation in Parkinson's disease and multiple system atrophy. *J Neurol Neurosurg Psychiatry,* **62**: 507-511.

[54] Araki I, Kitahara M, Oida T, and Kuno S (2000). Voiding dysfunction and parkinson's disease: urodynamic abnormalities and urinary symptoms. *J Urol.* **164**: 1640-1643.

[55] Sakakibara R, Hattori T, Uchiyama T, and Yamanishi T (2001). Videourodynamic and sphincter motor unit potential analyses in Parkinson's disease and multiple system atrophy. *J Neurol Neurosurg Psychiatry,* **71**: 600-606.

[56] Uchiyama T, Sakakibara R, and Hattori T (2006). Lower urinary tract dysfunctions of Parkinson’s disease model rat (6-hydroxydopamine treated rat) and effects of drugs. *Autonom Nerv Syst* **43**: 302-308 (in Japanese, review with clinical data).

[57] Griffiths D (1995). Basics of pressure-flow studies. *World J Urol.* **13**: 30–33.

[58] Resnick NM, and Yalla SV (1987). Detrusor hyperactivity with impaired contractile function. *JAMA*, **257**: 3076-3081.

[59] Yamamoto T, Sakakibara R, Uchiyama T, Liu Z, Ito T, Awa Y, Yamanishi T, and Hattori T (2006). Neurological diseases that cause detrusor hyperactivity with impaired contractile function *Neurourol Urodynam*, **25**; 356-360.

[60] Pavlakis AJ, Siroky MB, Goldstein I, and Krane RJ (1983). Neurourologic findings in Parkinson's disease. *J Urol*. **129**: 80-83.

[61] Chandiramani VA, Palace J, and Fowler CJ (1997). How to recognize patients with parkinsonism who should not have urological surgery. *Br J Urol*. **80**: 100-104.

[62] McKeith IG, Dickson DW, Lowe J, Emre M, O'Brien JT, Feldman H, Cummings J, Duda JE, Lippa C, Perry EK, Aarsland D, Arai H, Ballard CG, Boeve B, Burn DJ, Costa D, Del Ser T, Dubois B, Galasko D, Gauthier S, Goetz CG, Gomez-Tortosa E, Halliday G, Hansen LA, Hardy J, Iwatsubo T, Kalaria RN, Kaufer D, Kenny RA, Korczyn A, Kosaka K, Lee VM, Lees A, Litvan I, Londos E, Lopez OL, Minoshima S, Mizuno Y, Molina JA, Mukaetova-Ladinska EB, Pasquier F, Perry RH, Schulz JB, Trojanowski JQ, Yamada M; and Consortium on DLB. (2005). Diagnosis and management of dementia with Lewy bodies: third report of the DLB Consortium. *Neurology*. **65**: 1863-1872.

[63] Sakakibara R, Ito T, Uchiyama T, Asahina M, Liu Z, Yamamoto T, Yamanaka Y, and Hattori T (2005). Lower urinary tract function in dementia of Lewy body type (DLB). *J Neurol Neurosurg Psychiatry*, **76**: 729-732.

[64] Aranda B, and Cramer P (1993). Effect of apomorphine and l-dopa on the parkinsonian bladder. *Neurourol Urodynam.* **12**: 203-209.

[65] Sakakibara R, Uchiyama T, Hattori T, and Yamanishi T (2001). Urodynamic evaluation in Parkinson’s disease before and after levodopa treatment. 9th International Catechecholamine Symposium, Kyoto, Japan.

[66] Kuno S, Mizuta E, Yamasaki S, and Araki I (2004). Effects of pergolide on nocturia in Parkinson fs disease: three female cases selected from over 400 patients. *Parkinsonism Related Disord* **10**: 181-187.

[67] Yamamoto M (1997). Pergolide improves neurogenic bladder in patients with Parkinson's disease. *Mov Disord.* **12**: 328.

[68] Benson GS, Raezer DM, Anderson JR, Saunders CD, and Corrierie JN Jr (1976). Effect of levodopa on urinary bladder. Urology **7**: 24-28.

[69] Christmas TJ, Chapple CR, Lees AJ, Kempster PA, Frankel JP, and Stern GM. (1998). Role of subcutaneous apomorphine in parkinsonian voiding dysfunction. *Lancet*; Dec 24/31: 1451-1453..

[70] Fitzmaurice H, Fowler CJ, Rickards D, Kirby RS, Quinn NP, Marsden CD, Milroy EJ, and Turner-Warwick RT (1985). Micturition disturbance in Parkinson's disease. *Br J Urol.* **57**: 652-656.

[71] Winge K, Werdelin LM, Nielsen KK, Stimpel H (2004). Effects of dopaminergic treatment on bladder function in Parkinson's disease. *Neurourol Urodyn* **23**: 689-696.

[72] Brusa L, Petta F, Pisani A, Miano r, Stanzione P, Moschella V, Galati S, and Agro EF (2006). Central acute D2 stimulation worsens bladder function in patients with mild Parkinson's disease. *J Urol*. **175**: 202-206.

[73] Cooper JR, Bloom FE, and Roth RH (2003). *The biochemical basis of neuropharmacology*, Eighth ed, Chapter 9, Dopamine. Oxford University press, Oxford, 225-270.

[74] Obeso JA, Olanow CW, and Nutt JG (2000). Levodopa motor complications in Parkinson’s disease. *Trend Neurosci*. **23**: S2-S7.

[75] Ishizuka O, Mizusawa H, and Nishizawa O (2002). Roles of dopaminergic receptors in bladder and erectile function at the spinal level. *Asian J Androl*. **4**: 287-290.

[76] El-Masu MM, Elmallah AI, amal g. Omar AG, and Sharabi F (1999). Dopamine modulates peripheral purinergic neurotransmission through multiple presynaptic receptors: tissue-dependent effects. *Pharmacol Res.* **39**: 11-19.

[77] Wein AJ, and Rackley RR (2006). Overactive bladder: a better understanding of pathophysiology, diagnosis and management. *J Urol* **175**: S5-S10.

[78] Abrams P, Andersson KE, Buccafusco JJ, Chapple C, de Groat WC, Fryer AD, Kay G, Laties A, Nathanson NM, Pasricha PJ, and Wein AJ (2006). Muscarinic receptors: their distribution and function in body systems, and the implications for treating overactive bladder. *Br J Pharmacol.* **148**: 565-578.

[79] Todorova A, Vonderheid-Guth B, and Dimpfel W (2001). Effects of tolterodine, trospium chloride, and oxybutynin on the central nervous system. *J Clin Pharmacol.* **41**: 636-644.

[80] Kay GG, Abou-Donia MB, Messer WS Jr, Murphy DG, Tsao JW, and Ouslander JG (2005). Antimuscarinic drugs for overactive bladder and their potential effects on cognitive function in older patients. *J Am Geriatr Soc*. **53**: 2195-2201.

[81] Scheife R, and Takeda M (2005). Central nervous system safety of anticholinergic drugs for the treatment of overactive bladder in the elderly. *Clin Ther.* **27**: 144-153.

In: Integrated Circuits, Photodiodes…
Editors: R. McIntire and P. Donnell, pp. 383-393
ISBN: 978-1-60692-660-4
© 2009 Nova Science Publishers, Inc.

*Short Communication B*

# CHARGE INJECTION AND SURFACE MODIFICATION ROUTE FOR PENTACENE -BASED AMBIPOLAR FIELD-EFFECT TRANSISTORS

***Chih-Wei Chu***
Research Center for Applied Sciences, Academia Sinica, Taipei 11529, Taiwan
Department of Photonics, National Chiao-Tung University, Hsinchu 30010, Taiwan

## ABSTRACT

The complexity of the device fabrication process for the complementary metal-oxide-semiconductor (CMOS) technology could greatly be reduced by the utilization of ambipolar thin film transistors. Wide variety of techniques was employed for the realization of such ambipolar TFTs. One such method which is simple and robust is discussed herein. The contribution to the occurrence of ambipolar conduction of a pentacene-based field-effect transistor can be realized by dual interface engineering, which occurs at the dielectric/semiconductor and electrode/semiconductor interface. The former utilized a hydroxyl-free interfacial modified layer, and the latter was made feasible by the use of appropriate metal source/drain electrodes and ultra-thin nano-scale chemical compound insertion layer. For a hydroxyl-free interfacial modified layer, polymethylmethacrylate (PMMA) and Polyvinyl Alcohol (PVA) are appropriate candidates, and one can use alkali halogen materials (e.g. LiF, CsF) or carbonate (e.g. $Cs_2CO_3$) or metal oxide (e.g. MgO) or ultra-thin low work function metal (e.g. Ca) or polymer insulator (e.g. PMMA) etc for the enhancement of the carrier injection. The field-effect hole and electron mobility of around 0.02 $cm^2$/V-s and 0.002 $cm^2$/V-s, respectively, were extracted from the transfer characteristics of pentacene organic field-effect transistors (OFETs) utilizing PMMA as the trap-reduction interfacial modified layer and Al as the source and drain (S/D) electrodes. In addition, the mobility values for hole and electron are estimated as 0.01 and 0.009 $cm^2$/V-s, which were measured from pentacene organic field-effect transistors (OFETs) utilizing PMMA as the trap-reduction interfacial modified layer and LiF as the ultra-thin nano-scale chemical compound. One of the applications of the ambipolar transport is the organic light-emitting transistors, and light emitting transistors combine the light emission properties of an organic light-emitting diode and the switching properties of an organic field-effect transistor. Hence, the organic light-emitting transistors can further offer a new opportunity to the development of organic optoelectronic integrated circuit. Keeping in view of such window of applications, the present article describes the fabrication routes and the demonstration of the ambipolar TFTs and their complementary circuits.

## INTRODUCTION

Organic thin-film transistors (OTFTs) are currently an attractive research area because they can be fabricated at low temperatures with a simple fabrication process. Furthermore, a reduced processing temperature allows a wide range of materials for the flexible substrates, which makes OTFTs attractive for use in numerous low cost electronics applications [1-5]. Substantial progress has been made in developing OTFTs, whose electrical characteristics have already reached the level of hydrogenated amorphous silicon (a-Si:H) [6]. For next generation electronics and circuits, organic field-effect transistors (OFETs) are the key elements because of their extraordinary advantages, such as low cost, large area coverage, mechanical flexibility, and low temperature fabrications. Ambipolar FETs employing double layer scheme and bulk heterojunction configuration have been utilized to achieve complementary-like inverters [7-9]. However, it requires an additional deposition step and critical fabrication conditions [10,11]. Thus, ambipolar FETs with single organic semiconductor have to be addressed for ease of circuit design and simplification of the fabrication process. In general, pentacene FETs have been recognized as p-type devices, even with the low work function metal as source/drain (S/D) electrodes. In this present work, we demonstrate that ambipolar pentacene FETs can be achieved by an interfacial-modified layer made of PMMA. The presence of a PMMA layer significantly reduces the electron traps between pentacene and $SiO_2$ interface and makes the ambipolar FETs feasible for practical applications.

It has been reported that engineering of the organic/electrode interfacial properties is crucial for achieving the balanced hole and electron injection for high performance ambipolar operations [12]. Incorporation of an injecting interlayers at organic/electrode interface has been widely used to approximate the “ideal” electrodes [13]. Recently, there have been various attempts made to improve the electron injection from an Al cathode to an emitting layer by inserting a thin layer of alkali metal halides [14] and carboxylates [15]. Actually, those interlayers not only enhance the fraction of injected electrons, but also allow the top electrode to contact with the organic semiconductor, maintaining a symmetric device structure. Thus, in such a symmetric device structure, it is expected that both holes and electrons could be efficiently injected by inserting a thin interlayer. Although numerous research groups have inserted interlayer to enhance n-channel conduction for OTFTs [16], no reports were conducted wherein they function as bi-functional electrodes for ambipolar transport in organic semiconductors.

In this communication, the importance of dual interface modification to facilitate ambipolar conduction has been investigated. The improved performance is primarily attributed to the reduced electron traps at $SiO_2$/semiconductor interface by incorporating an interfacial-modified layer made of polymethyl methacrylate (PMMA). Additionally, the metal with a suitable work function as source/drain (S/D) electrodes also helps to inject sufficient holes and electrons for effective observation of p- and n-channels in OFETs. For further enhancing the n-type behavior, the ultra-thin nanoscale LiF insertion layer is introduced and utilized as bi-functional source/drain electrodes. The presence of ultra-thin nano-scale LiF insertion layer between semiconductor and S/D electrodes would equilibrate the hole and electron transport in ambipolar pentacene TFTs.

## EXPERIMENTAL

The heavily doped p-type silicon ($p^+$-Si) wafer and a 300 nm thermally oxidized $SiO_2$ film were used as the gate and insulator of our ambipolar transistor devices, respectively. The substrates were cut to 2 cm × 2 cm in size through mechanical scribing. Prior to the deposition, the substrates were cleaned by acetone and isopropanol in an ultrasonic bath followed by UV-ozone cleaning for 15 min. The crucial interfacial-modifying layer was prepared by spin-coating a solution of PMMA (2 wt%) in tetrahydrofuran at 1000 rpm and with a thickness of around 150 nm. The PMMA-coated substrates were baked at 70 $^{o}$C for 30 min to remove the residual solvent. Then the wafers were quickly transferred to a vacuum chamber for the deposition of active layer. The semiconductor layer, consisting of a 50 nm thick pentacene layer, was then deposited at a growth rate of 0.2 Å/sec, a substrate temperature of 60 $^{o}$C, and a base pressure of $6 \times 10^{-6}$ Torr. Pentacene was used without further purification from Sigma-Aldrich. Finally, the 50 nm thick aluminum film was thermally evaporated onto the pentacene film through a shadow mask to form the S/D electrodes. In addition, Au, Ag, and Ca were also investigated as alternatives to the Al as S/D contacts. The role of LiF on the performance of ambipolar TFT is also investigated. Ultra-thin LiF layer was then deposited using thermal evaporation onto the pentacene film and the thickness of the LiF layer was varied from 0 to 30 Å. The length and width of channel were 100 μm and 2 mm, respectively. The electrical measurements of the devices were performed at room temperature in a nitrogen environment inside a glove box by using HP 4156C and Keithley 4200 semiconductor parameter analyzer.

## RESULTS AND DISCUSSION

In the operation of ambipolar FETs, charge carrier transport strongly depends on two factors: (1) semiconductor/dielectric interface, where the charge transport takes place in the semiconductor layer, and (2) metal/semiconductor interface, where the charge injection occurs from the electrode into semiconductor. For the realization of ambipolar pentacene FETs, the devices were first fabricated on the $SiO_2$ gate dielectric and later on a PMMA-capped $SiO_2$ (PMMA/$SiO_2$) as the dielectric with Al as S/D electrodes. However, the devices fabricated on a $SiO_2$ dielectric only exhibit a p-type behavior, even at a positive bias of 100 V to the gate and drain electrodes. The output and transfer characteristic of pentacene-based FETs fabricated on $SiO_2$ is shown in figures 1 (a) and 1 (b). In contrast, the devices fabricated on a PMMA/$SiO_2$ exhibit an ambipolar behavior for a gate voltage $V_G \geqq |40|$ V. According to Chua et al’s report [17], the reason why n-type behavior has previously been so elusive is the trapping of electrons at the semiconductor-dielectric interface by hydroxyl groups. Therefore, we use PMMA as the interfacial modification layer to reduce the silanols of the commonly used $SiO_2$ dielectric. PMMA contains no or minimal hydroxyl groups and the presence of PMMA layer will decrease electron traps at the interface and facilitate the accumulation of electrons. Figure 2 shows the plots of $|I_{DS}|$ and $|I_{DS}|^{1/2}$ versus $V_G$. It can be observed that these devices exhibit strong field-effect modulations of channel conductance in the ambipolar operation with a threshold voltage ($V_T$) of -27 and 42 V for p- and n-type operations, respectively. The saturated drain current ($I_{DS,sat}$) is close to $7 \times 10^{-8}$ A at $V_G = 100$ V for n-type operation and $5.5 \times 10^{-6}$ A at $V_G = -100$ V for p-type operation. The field-effect mobility (μ) are extracted from the measured transfer curves by comparing it to the standard transistor's current-voltage equation in the saturation regime:

$$I_{DS,sat} = (WC_i/2L)\mu(V_G - V_T)^2,$$

where W and L are the width and length of channel, respectively, and $C_i$ is the gate dielectric capacitance. The μ values for hole and electron are estimated as 0.026 and 0.0023 cm$^2$/V-s, respectively.

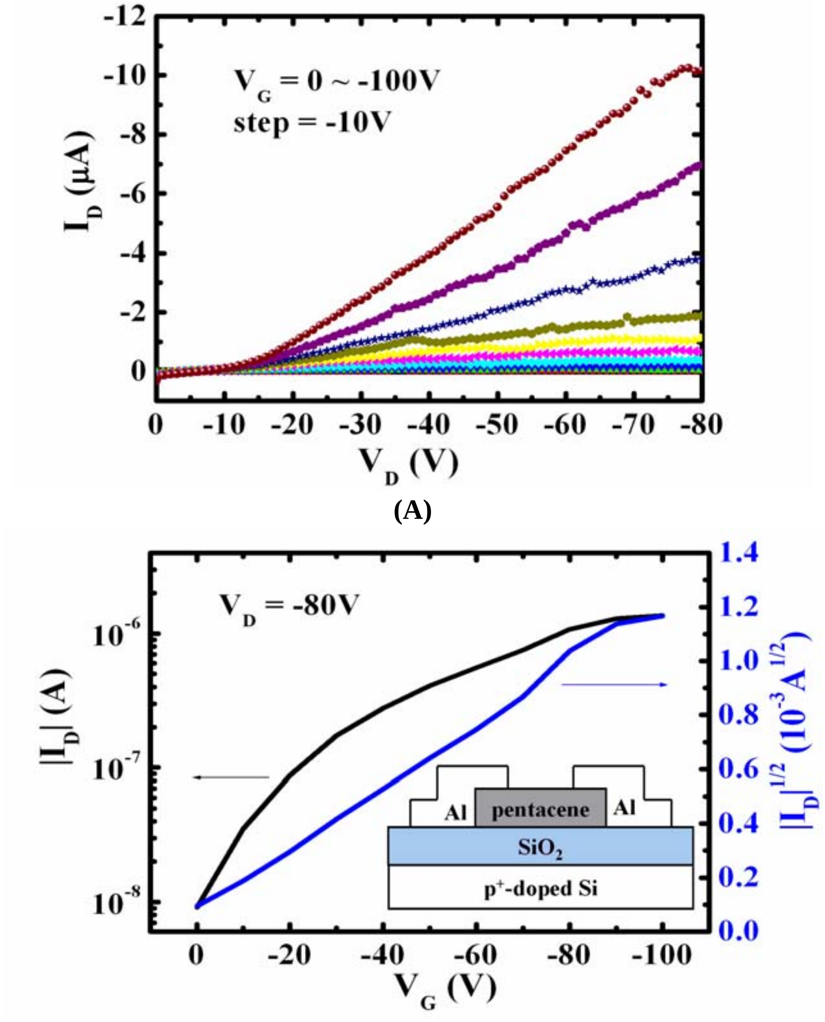

(A)

(B)

Figure 1. (a) Output and (b) transfer characteristic of our pentacene-based field-effect transistors fabricated on bare $SiO_2$.

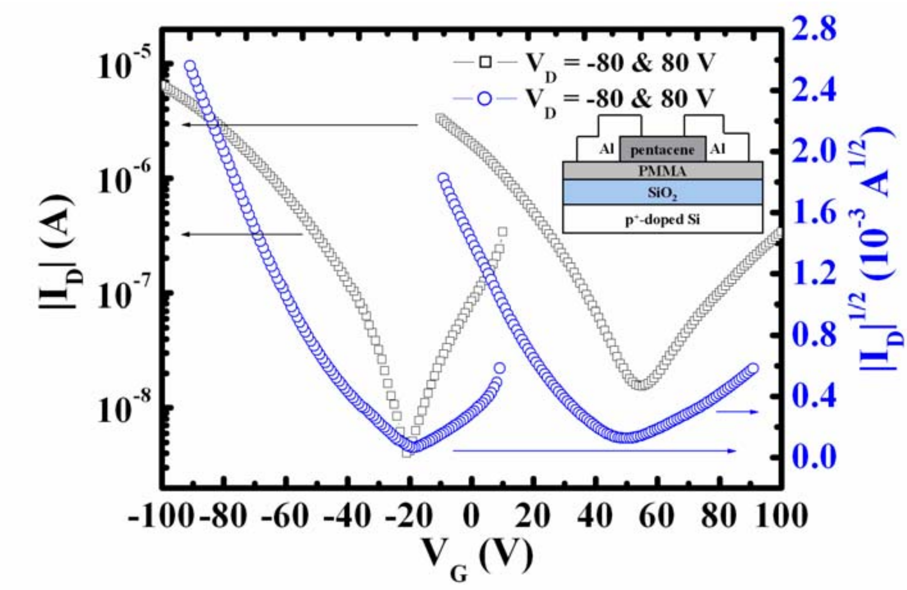

Figure 2. Transfer characteristics of $|I_D|$ and $|I_D|^{1/2}$ vs. $V_G$ for ambipolar pentacene field-effect transistor in p- and n-channel operations.

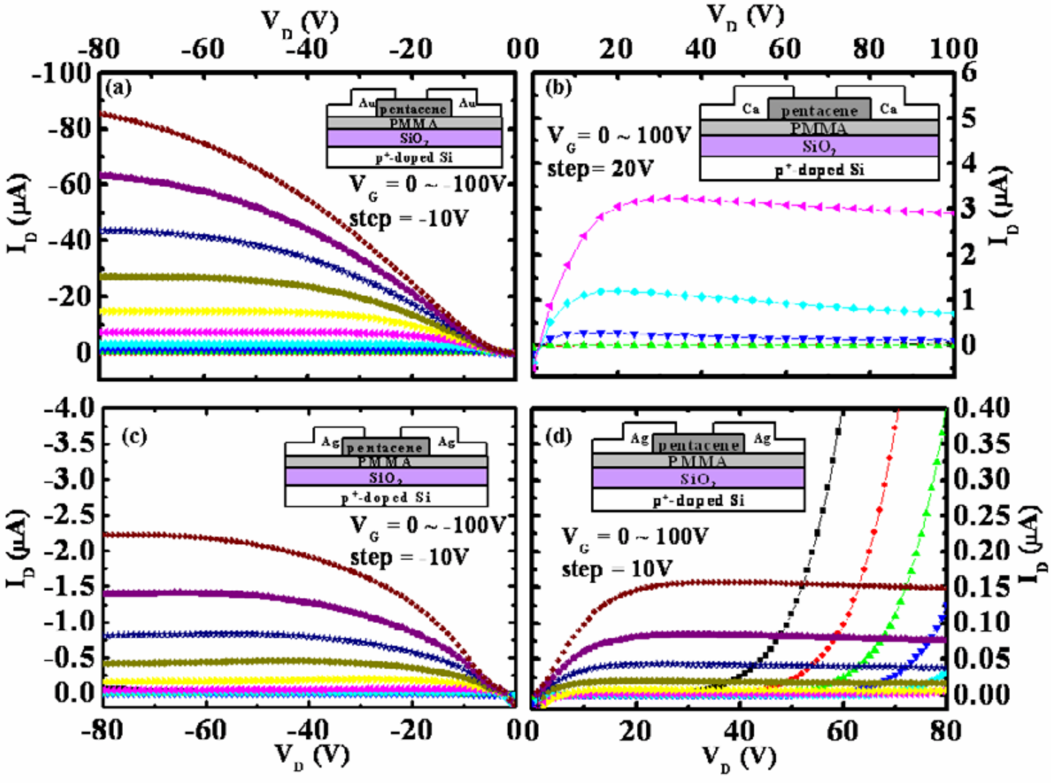

Figure 3. Output characteristic of ambipolar pentacene field-effect transistors with different S/D metal electrodes (a) Au (b) Ca (c)(d) Ag.

The influence of the interface between semiconductor and metal for the pentacene FETs can be ascertained by varying the S/D electrodes. In this case, three different metal electrodes, Ag, Au, and Ca, are used as the S/D contacts to vary the barrier height for hole and electron injection into the pentacene layer. All these devices show ambipolar characteristics as well. Figures 3(a) ~ 3(d) show the transfer characteristics for different metals as the S/D electrodes. The devices with Au as electrodes show the enhancement of p-type behavior, but poor n-type behavior. Since the work function of Au is 5.1 eV, which is very close to the highest occupied molecular orbital of pentacene, it is much easier for a hole than for the electrons to inject from the metal electrode into semiconductor. Using Ca as S/D electrodes, the results obtained are vice versa, i.e., the enhancement of n-type behavior but poor p-type behavior is observed. Al and Ag metals, when used as S/D electrodes, possess a suitable work function to balance the hole and electron injection into the highest occupied and the lowest unoccupied molecular orbital of pentacene. Although the charge injection barriers are balanced in both polarities, the increase of potential drop at organic/metal interface will increase the $|V_T|$ as compared to Au in p-channel operation and Ca in n-channel operation [18]. The summary of ambipolar pentacene FETs with different metals as S/D electrodes is given in Table 1. These results demonstrate that the choice of the suitable metal in pentacene FETs also plays an important role to reveal the ambipolar characteristics.

**Table 1. Summary of parameters extracted from the ambipolar pentacene field-effect transistors using different metals as source and drain electrodes**

| S/D Metal | Mobility (cm2/Vsec) | | On/Off Current Ratio | | Subthreshold Slope | | $V_T$ (V) | |
|---|---|---|---|---|---|---|---|---|
| | n | p | n | p | n | p | n | p |
| Ca | $8.5 \times 10^{-3}$ | $7.5 \times 10^{-3}$ | $1 \times 10^{4}$ | $1 \times 10^{4}$ | 0.4 | 1.1 | 31 | -47 |
| Al | $2.3 \times 10^{-3}$ | $2.6 \times 10^{-2}$ | $1 \times 10^{2}$ | $1 \times 10^{3}$ | 1.0 | 0.4 | 42 | -27 |
| Ag | $2.1 \times 10^{-3}$ | $2.2 \times 10^{-2}$ | $1 \times 10^{3}$ | $1 \times 10^{4}$ | 0.7 | 0.4 | 37 | -35 |
| Au | $1.0 \times 10^{-4}$ | $9.0 \times 10^{-2}$ | $1 \times 10^{2}$ | $1 \times 10^{4}$ | 1.1 | 0.3 | 55 | -15 |

The schematic cross section of device with LiF insertion layer is shown in Figure 4(a). Since the range of thicknesses of LiF thin film employed lies in the sub-nanometer regime, the film surface presumed to be discrete with discontinuous islands (Figure 4(b)). This results in the formation of two different junctions at metal/organic semiconductor interface, which are pentacene/LiF/Al and pentacene/Al. The energy band diagram of pentacene with LiF/Al for electrons and pentacene with Al for holes is shown in the inset of Figure 6. The presence of discontinuous LiF islands leads to a lowering of the energy barrier for electrons from Al to the lowest unoccupied molecular orbital (LUMO) of pentacene resulting in an increase of electron injection via tunneling [19]. Meanwhile, holes can be readily injected to the highest occupied molecular orbital (HOMO) of pentacene from Al. Figure 5 shows the dependence of hole and electron mobilities on the LiF film thickness. As shown in Figure 5, the device with bare Al as S/D electrodes exhibited unbalanced bipolar conduction, with the mobility of holes one order in magnitude higher than that of electrons. However, the effective contact area of the pentacene/LiF increase with increase in LiF thickness, which intern enhances the injection capability for electrons. As a result, the electron mobility is marginally enhanced and the p-type behavior is partially inhibited rather than being totally sacrificed. Further increase in the LiF layer thickness beyond 3 nm leads to the diminishing of balanced bipolar conduction. This could be attributed to the high resistivity of the LiF layer, which leads to slow down the tunneling probability for electrons and to reduce the effective contact area of pentacene/Al. Therefore, the thicker LiF layer makes the electron and hole injections difficult for the ambipolar conduction.

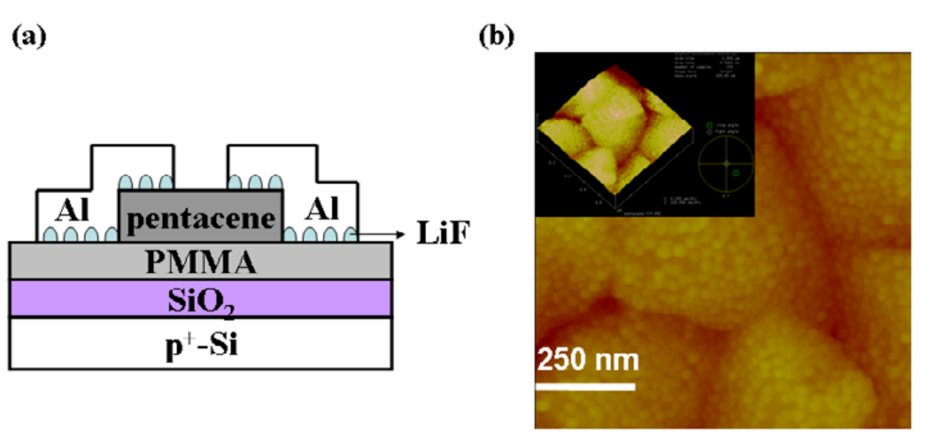

Figure 4. (a) A schematic cross-section configuration of our top-contact OTFTs with insertion layer LiF. (b) The atomic force microscope image of $p^+$-Si/SiO$_2$/pentacene/LiF (0.3 nm).

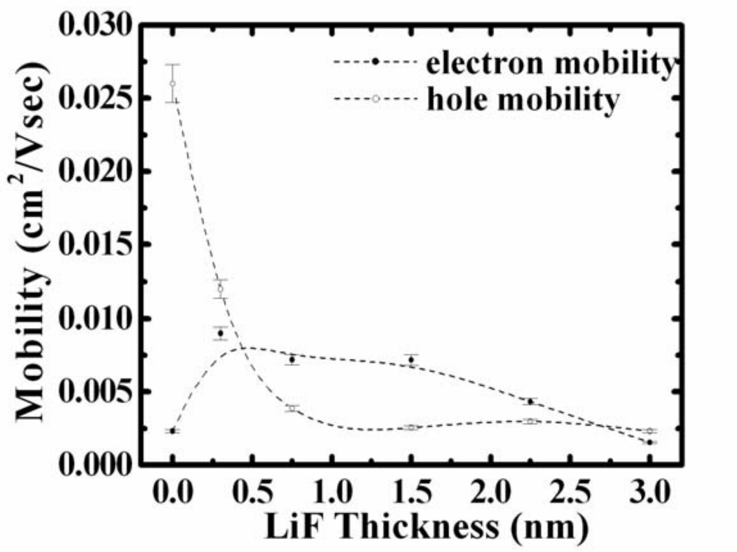

Figure 5. Electron and hole mobilities as a function of LiF layer thickness for the ambipolar pentacene organic field-effect transistors.

Figure 6 shows the drain-source current ($I_{DS}$) as a function of drain-source voltage ($V_{DS}$) of ambipolar pentacene FETs with LiF (3 Å)/Al as bi-functional electrodes at various gate voltages. The devices show an apparent ambipolar transport behavior at a gate voltage of larger than |40| V. It can be noted that both the n- and p-channel output characteristics exhibit significant saturation which behaves quadratically as a function of gate bias. Inset of figure 6 represents the corresponding plots of $|I_{DS}|$ and $|I_{DS}|^{1/2}$ as a function of $V_G$ for the ambipolar pentacene FETs with LiF (3 Å)/Al as bi-functional electrodes. The threshold voltage ($V_T$) and carrier mobility can be extracted from the intercept and slope of the curve of $|I_{DS}|^{1/2}$ versus $V_G$. These devices exhibit strong field-effect modulations of channel conductance in the ambipolar operation with a threshold voltage of -17 and 39 V for p- and n-type operations, respectively. In addition, the mobility values for hole and electron are estimated as 1.2 x $10^{-2}$ and 9 x $10^{-3}$ $cm^2/V$-s, respectively. Such a balanced electron and hole mobilities makes the feasibility of ambipolar transport in pentacene TFTs.

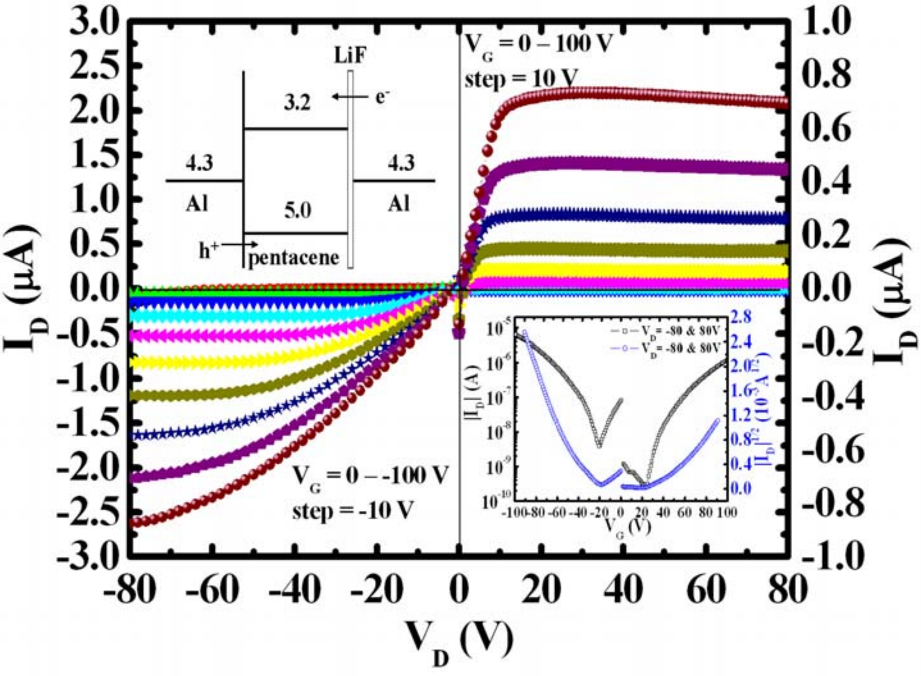

Figure 6. Drain-source current ($I_{DS}$) as a function of drain-source voltage ($V_{DS}$) of ambipolar pentacene FETs with LiF/Al as bi-functional electrodes at various gate voltages in p- and n-channel operations. The left-top inset is the energy band diagram in equivalent of pentacene/LiF/Al and pentacene/Al. The unit of energy level is in electronvolt. The right-bottom inset is the plots of $|I_{DS}|$ and $|I_{DS}|^{1/2}$ as a function of $V_G$ for the ambipolar pentacene FETs with LiF (3 Å)/Al as bi-functional electrodes.

One of the most essential and important building blocks of a logic circuit is the inverter, and these pentacene-based OFETs mentioned above are suitable for the feasibility of an inverter. A complementary-like inverter circuit is shown in the inset of Figure 7. Because of the unique ambipolar characteristics, the inverter is capable of operating in both the first and third quadrants. Figures 7 (a) - 7 (d) show the typical transfer characteristics of such an inverter. A sharp inversion is observed in both quadrants. When the supply voltage ($V_{DD}$) and input node ($V_{IN}$) are biased positively, the ambipolar transistors can be operated as p-channel and n-channel FETs, the inverter works in the first quadrant with the maximum voltage gain for the device without LiF insertion layer of 8 and for the device with LiF insertion layer of

11.5; whereas the supply voltage ($V_{DD}$) and input node ($V_{IN}$) are biased negatively, the ambipolar transistors can be operated as n-channel and p-channel FETs, and the inverter works in the third quadrant with the maximum voltage gain for the device without LiF insertion layer of 11 and for the device with LiF insertion layer of 9.5. The inverter made by LiF inserted ambipolar transistors exhibit a superior performance such as high gain and the inversion point more closer to 1/2 $V_{DD}$.

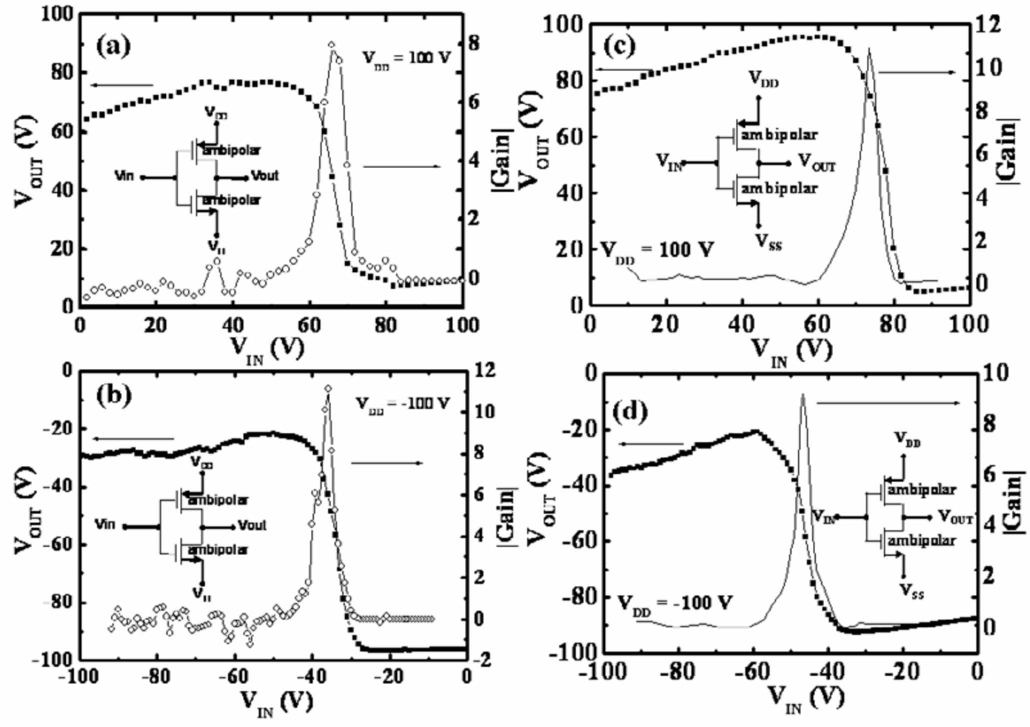

Figure 7. Transfer characteristics of complementary-like ambipolar pentacene inverter in (a) & (b) without LiF insertion and (c) & (d) with LiF insertion and their corresponding gains. The insets show the scheme of the complementary-like inverter circuit, which is composed of two identical pentacene transistors.

## CONCLUSION

In summary, the ambipolar pentacene field-effect transistors have been demonstrated through interface engineering. Incorporation of PMMA layer helps in reducing the surface traps and hence acts as an interfacial-modified layer, thereby promotes ambipolar transport in pentacene TFTs. Meanwhile, using a suitable work-function metal electrode can balance the carrier injection of both polarities thereby leading to the ambipolar conduction. For further enhancing the performance of ambipolar FETs, the insertion of a LiF interlayer between pentacene and Al electrode was carried out and a significant improvement in the performance of ambipolar pentacene TFTs was observed. As compared to the OTFTs with pristine Al electrodes, the devices with an LiF interlayer exhibit an enhanced electron mobility without scarifying a great deal of hole mobility.

## REFERENCES

[1] Dimitrakopoulos, C. D. and Malenfant, P. R. L. (2002). Organic Thin Film Transistors for Large Area Electronics. *Adv. Mater. (Weinheim, Ger.),* **14**, 99-117.

[2] Huitema, H. E. A. Gelinck, G. H. Bas, J. van der Putten, P. H. Kuijk, K. E. Hart, K. M. Cantatore, E. & de Leeuw, D. M. (2002). Active-Matrix Displays Driven by Solution-Processed Polymeric Transistors. *Adv. Mater. (Weinheim, Ger.),* **14**, 1201-1204.

[3] Sheraw, C. D. Zhou, L. Huang, J. R. Gundlach, D. J. & Jackson, T. N. Organic thin-film transistor-driven polymer-dispersed liquid crystal displays on flexible polymeric substrates. *Appl. Phys. Lett.*, **80**, 1088-1090.

[4] Drury, C. J. Mutsaers, C. M. J. Hart, C. M. Matters, M. & de Leeuw, D. M. (1998). Low-cost all-polymer integrated circuits. *Appl. Phys. Lett.*, **73**, 108-110.

[5] Eder, F. Klauk, H. Halik, M. Zschieschang, U. Schmid, G. & Dehm, C. Organic electronics on paper. (2004). *Appl. Phys. Lett.*, **84**, 2673-2675.

[6] Lin, Y. Y. Gundlach, D. J. Nelson, S. F. & Jackson, T. N. (1997). Pentacene-based organic thin-film transistors *IEEE Trans. Electron Devices*, **44**, 1325-1331.

[7] Meijer, E. J. de Leeuw, D. M. Setayesh, S. Van Veenendaal, E. Huisman, B. H. Blom, P. W. M. Hummelen, J. C. Scherf, U. & Klapwijk, T. M. (2003). Solution-processed ambipolar organic field-effect transistors and inverters. *Nat. Mater*. **2,** 678-682.

[8] Kitamura, M. & Arakawa, Y. (2007). Low-voltage-operating complementary inverters with $C_{60}$ and pentacene transistors on glass substrates. *Appl. Phys. Lett.*. **91**, 053505.

[9] Shi, J. Wang, H. Song, D. Tian, H. Geng, Y. & Yan, D. (2007). n-Channel, Ambipolar, and p-Channel Organic Heterojunction Transistors Fabricated with Various Film Morphologies. *Adv. Funct. Mater. (Weinheim, Ger.)* **17**, 397-400.

[10] Klauk, H. Halik, M. Zschieschang, U. Eder, F. Rohde, D. Schmid, G. & Dehm, C. (2005). Flexible organic complementary circuits. *IEEE Trans. Electron Devices,* **52**, 618-622.

[11] Gundlach, D. J. Pernstich, K. P. Wilckens, G. Grüter, M. Haas, S. & Batlogg, B. (2005). High mobility *n*-channel organic thin-film transistors and complementary inverters. *J. Appl. Phys*. **98**, 064502.

[12] Cho, S. Yuen, J. Kim, J. Y. Lee, K. & Heeger, A. J. (2006). Ambipolar organic field-effect transistors fabricated using a composite of semiconducting polymer and soluble fullerene. *Appl. Phys. Lett*. **89**, 153505.

[13] Chu, C. W. Li, S. H. Chen, C. W. Shrotriya, V. & Yang, Y. (2005). High-performance organic thin-film transistors with metal oxide/metal bilayer electrode. *Appl. Phys. Lett.* **87**, 193508.

[14] Wakimoto, T. Fukuda, Y. Nagayama, K. Yokoi, A. Nakada, H. & Tsuchida, M. (1997). Organic EL cells using alkaline metal compounds as electron injection materials. IEEE Trans. *Electron Devices,* **44**, 1245-1248.

[15] Chen, S. Y. Chu, T. Y. Chen, J. F. Su, C. Y. & Chen, C. H. (2006). Stable inverted bottom-emitting organic electroluminescent devices with molecular doping and morphology improvement. *Appl. Phys. Lett*. **89**, 053518.

[16] Chu, C. W. Sung, C. F. Lee, Y. Z. & Cheng, K. (2008). Improved performance in n-channel organic thin film transistors by nanoscale interface modification. *Org. electron.* **9**, 262-266.

[17] Chua, L. L. Jaumseil, J. Chang, J. F. Ou, E. C. W. Ho, P. K. H. Sirringhaus, H. & Eriend, R. H. (2005). General observation of n-type field-effect behaviour in organic semiconductors. *Nature*, **434**, 194-199.

[18] Yan, X. Wang, J. Wang, H. Wang, H. & Yan, D. (2006). Improved *n*-type organic transistors by introducing organic heterojunction buffer layer under source/drain electrodes. *Appl. Phys. Lett.* **89**, 053510.

[19] Masenelli, B. Berner, D. Bussac, M. N. Nuesch, F. & Zuppiroli, L. (2001). Simulation of charge injection enhancements in organic light-emitting diodes. *Appl. Phys. Lett.* **79**, 4438.

In: Integrated Circuits, Photodiodes…
Editors: R. McIntire and P. Donnell, pp. 395-403
ISBN: 978-1-60692-660-4
© 2009 Nova Science Publishers, Inc.

***Short Communication C***

# THE COUPLING OF THE MRS PHOTODIODE WITH COATED EXTRUDED SCINTILLATOR USING Y7 AND Y11 WLS FIBERS

***D. Beznosko[1,*], A. Dyshkant[2], C.K. Jung[1], C. McGrew[1], A. Pla-Dalmau[3] and V. Rykalin[2]***

[1] Stony Brook University, Stony Brook, NY 11794 USA
[2] Northern Illinois University, DeKalb, IL 60115 USA
[3] A. Pla-Dalmau is with Fermilab, Batavia, IL 60510 USA

## ABSTRACT

Extruded scintillator with co-extruded hole and reflective coating will be used both in MINERvA and T2K experiments. We have studied WLS (wavelength shifting) fibers (Y11 and Y7) for different shapes of the extruded scintillator readout using MRS (Metal/Resistor/Semiconductor) photodiode. The Y7 fiber was considered because of its lower then Y11 cost. The purpose was to find out which fiber performs better in above configurations. First, the responses for both types of fibers, with and without optical grease, were measured by PMT (Photomultiplier Tube). The PE (photoelectron) yield from cosmic rays for different scintillator shapes and both fiber types, as seen by MRS photodiode, are reported. The attenuation lengths of Y11 and Y7 were measured using MRS Photodiode. Y7 fiber shows somewhat better performance at short distances from the photo detector, while Y11 performs better at larger lengths.

## I. INTRODUCTION

To take the full advantage of the physics potential of the currently planned e+e- linear collider detector [1] [2], and the T2K neutrino beam near detector [3], the presence of the strong magnetic field will be required.

---

[*] E-mail address: dima@dozory.org. Phone: 347 992 6486.

The performance requirement of the photodetectors in the magnetic field has directed our attention to the MRS photodiode that is known to be insensitive to the magnetic fields of 9T [4]. As silicon based device, MRS has a different spectral sensitivity then PMT. Using this photodiode, we studied the properties of two Kuraray [5] multiclad wavelength shifting (WLS) fibers: Y7 and Y11; and the coupling of the photodiode to the extruded [6] scintillator via those fibers. Attenuation length, light yield of the scintillator used, and effect of optical grease in the co-extruded hole on scintillator-fiber coupling were studied. These results are useful for any detector using WLS fibers.

## II. DESCRIPTIONS AND SCHEMATICS

### A. MRS Photodiode Description and Operational Principle

The MRS photodiode is a multi-pixel solid-state device with every pixel operating in the limited Geiger multiplication mode. A resistive layer on the sensor's surface accomplishes avalanche quenching. The devices used were of round shape, and they had ~ 1000 pixels per 1.1mm diameter photosensitive area, with quantum efficiency (QE) of the device reaching ~25% at 500nm, and reaching peak QE of approximately 30% at ~550nm [7]. In addition, MRS is found to be non-sensitive to the magnetic fields of up to 9T [4].

### B. Types of Scintillator Used

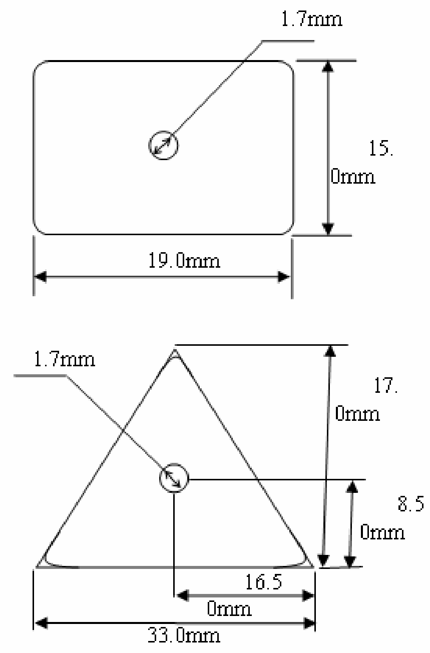

Figure 1. MINERvA rectangular (top) and triangular (bottom) shaped extruded scintillator with co-extruded hole and coating.

The following types and shapes of the scintillator were used: extruded scintillator with co-extruded hole and coating for the MINERvA [8] (both triangular and rectangular shaped) (Figure 1), and the K2K SciBar [9] 1.3x2.5cm$^2$ rectangular extruded scintillator, also with co-extruded hole and coating.

## C. Schematics of PMT Measurements

Light output measurements for different WLS fiber diameter with and without optical grease in the co-extruded hole for Y11, and for 1.2mm outer diameter Y7 fiber were conducted using the Hamamatsu PMT R580 [10]. The PMT was readout by Keithley [11] 6485 picoammeter. The Y11 fibers with different diameters were tested to see the light yield change for each diameter in the same sized co-extruded hole; the Y7 fiber was 1.2mm outer diameter only. Fibers were cut from a reel. All fibers were 16cm in length; this is 2cm longer then the scintillator piece used in this setup. The fibers' ends in contact with PMT were polished using a fly-diamond technique. The other ends of the fibers were cut at 45$^o$ and painted black to prevent reflections.

The attenuation length of scintillator without fiber was measured using same PMT-picoammeter setup. The triangular shaped extruded scintillator bar with co-extruded coating was tested. The setup schematics of these measurements are given in Figure 2.

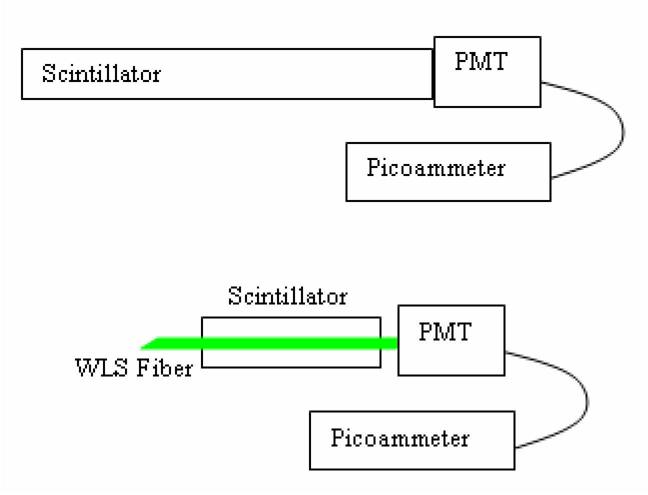

Figure 2. Setup for scintillator attenuation length measurements (top), and for measurements with WLS fibers (bottom).

For attenuation length measurements, the radioactive source was placed on the center of the 33 mm base of triangular scintillator with an accuracy of approximately 3 mm and was not collimated. In addition, the attenuation measurement was repeated using a Bivar [12] LED5-UV-400-30 T1 3/4 5mm UV LED with peak emission at 400nm, to see how the results may change with a different way to excite a scintillation light.

## D. Measurements Using MRS Photodiode

For the measurements with cosmic rays, the ~14cm long pieces of SciBar and MINERvA scintillators were used in conjunction with 1.2mm pieces of Y11 and Y7 WLS fibers. The fibers were ~16cm long, polished at one end and cleaved at 45° and painted black on the other because option of using mirrored fiber was unavailable at that time. There was ~1 cm between the sensor's cap (that held the fiber in alignment with photosensitive are of MRS) and the scintillator. For top and bottom triggers, the 1x2x10cm pieces of extruded [6] scintillator with co-extruded coating were used, coupled directly to the PMT face using optical grease.

For the fiber attenuation length measurements, the 1.2mm outer diameter 3m long Y11 and Y7 fibers were used. In both samples, the concentration of dopant was 175ppm. Both fibers were polished at one end, and cleaved at 45° and painted black at the other. As a light source, a Bivar [12] UV LED coupled to 2x2x3cm extruded [6] scintillator with co-extruded hole was used. The pulse generator was providing the gate signal as well as 15ns wide square pulses for LED.

The schematics for both setups are presented in Figure 3.

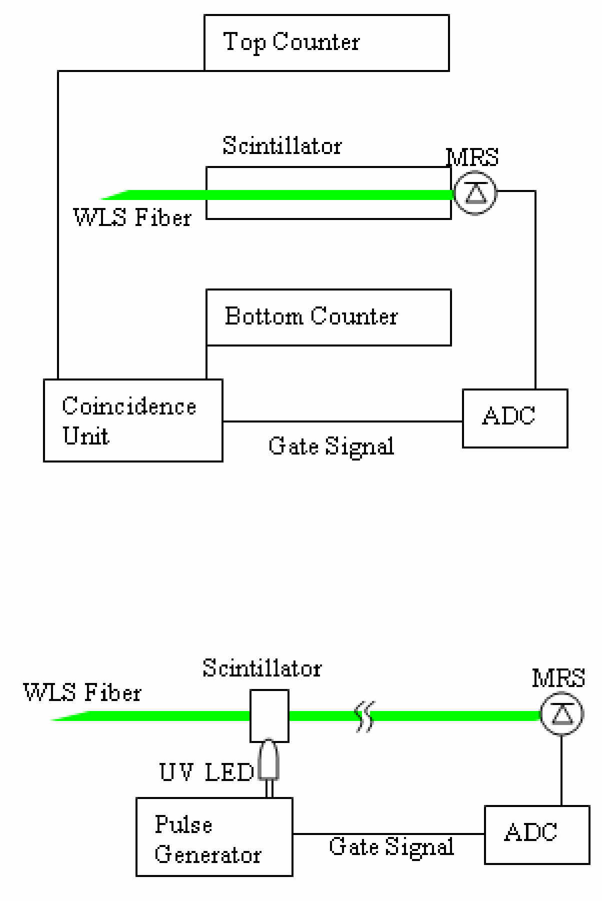

Figure 3. The setup for cosmic rays (top), and for fiber attenuation length (bottom) measurements.

## III. EXPERIMENTAL RESULTS

### A. PMT Measurements

The results for the light output for different diameter fibers (Y11), and 1.2mm Y7, with and without optical grease, are presented in Figure 4. For these measurements, the R580 PMT was biased at 1300V and directly connected to the picoammeter. The scintillator was illuminated by UV LED. Special care was taken to prevent LED light from reaching the PMT directly. A non-transparent cap was placed on the PMT to provide this needed light insulation and to hold fiber in place. All tested fibers were placed in front of the same photocathode area during this measurement. The Bicron BC-630 [13] optical grease was used.

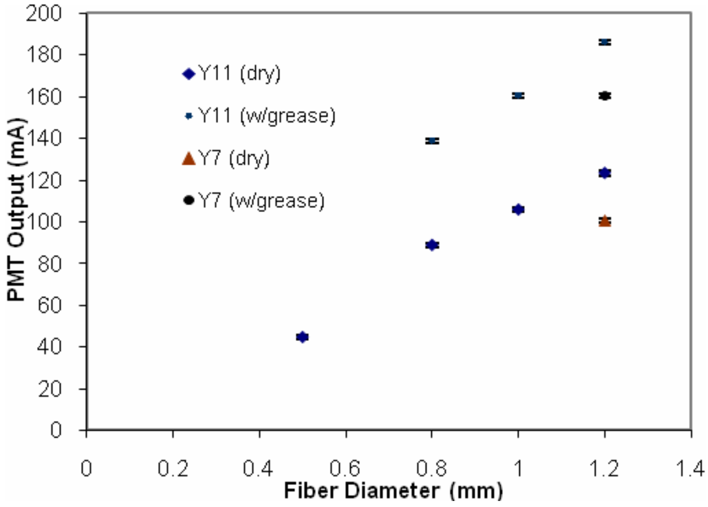

Figure 4. The PMT output for various WLS fibers (with and without optical grease for each fiber tested).

From Figure 4 we see the ~53% increase in light yield when the optical grease is used in the case of co-extruded hole. It indicates that gluing WLS fiber will provide similar increase in light output. The light yield of the 1.2mm outer diameter Y7 WLS fiber, as measured by PMT, is lower than that of the 1.2mm outer diameter Y11 WLS fiber.

The results for the bulk scintillator light attenuation length of the triangular shaped MINERvA bar is shows in Figure 5. Measurements were conducted using $^{137}$Cs and UV LED, yielding similar results. For technical reasons, the zero position in radioactive source measurements is defined at the PMT, and at the end farthest from the PMT for LED measurements. A ~60cm long scintillator bar was used. For this test, a casing with ~1mm diameter hole for light output was built for the LED. Such LED light source was better collimated then the radioactive source. A wand configuration of gamma source without additional collimator was used.

The tests yield results of ~10.1cm for UV LED measurement and ~10.2cm for $^{137}$Cs. The difference between results is ~1% indicating that UV LED in the attenuation length measurement performs similar to the radioactive source.

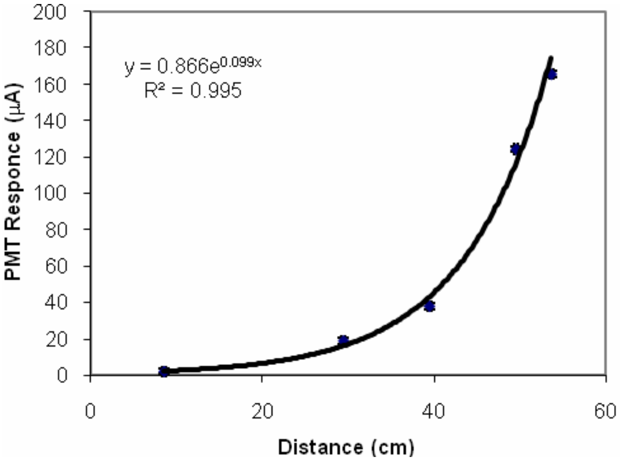

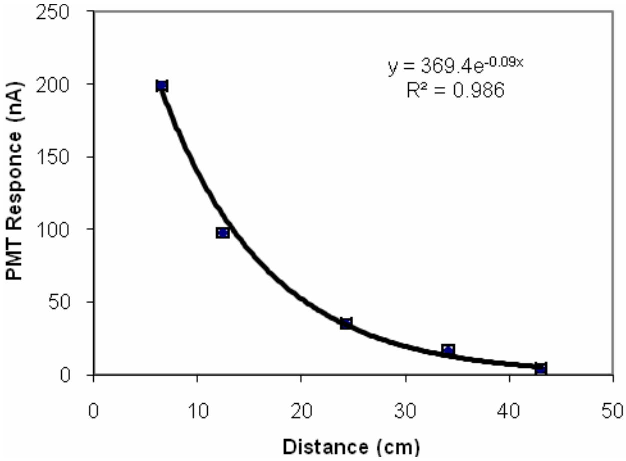

Figure 5. PMT response to UV LED position (top) and radioactive source position (bottom) along the bulk triangular shape scintillator without WLS fiber, yielding attenuation lengths of ~10.1cm and ~10.2 cm respectively.

## B. Measurements Using MRS Photodiode

The measurements conducted using the MRS photodiode include light yield from cosmic rays for various scintillator coupled to the sensor with Y11 and Y7 WLS fibers, and the attenuation lengths for both of these fibers.

The schematic for cosmic rays measurements is in Figure 3 (top). MRS photodiode was calibrated using the procedure described in [14]. The optimal operating bias voltage was found to be 27.84V. From calibration, one PE corresponded to ~8.15 ADC (analog-to-digital converter) channels.

Results are displayed in Table I. The ADC channels mean values and the PE conversions are indicated and are rounded off to first digit after decimal point. For MINERvA triangular scintillator, two results are quoted: "center" and "side". For "side" measurements, top trigger was turned 90° (thus becoming 1cm wide) and placed over the edge of the triangular scintillator. In all results quoted, the position of pedestal is subtracted.

**Table I. light yield from cosmic rays for various scintillator coupled to the sensor with Y11 and Y7 WLS fibers**

| Scintillator | Fiber 1.2mm) | MRS Response ADC Channels) | MRS Response (PE) |
|---|---|---|---|
| MINERvA Rectangular | Y11 | 159.2 | 19.5 |
| SciBar | Y11 | 139.2 | 17.1 |
| MINERvA Rectangular | Y7 | 179.4 | 22.0 |
| SciBar | Y7 | 159.7 | 19.6 |
| MINERvA Triangular (center) | Y7 | 138.2 | 17.0 |
| MINERvA Triangular (side) | Y7 | 48.9 | 6 |

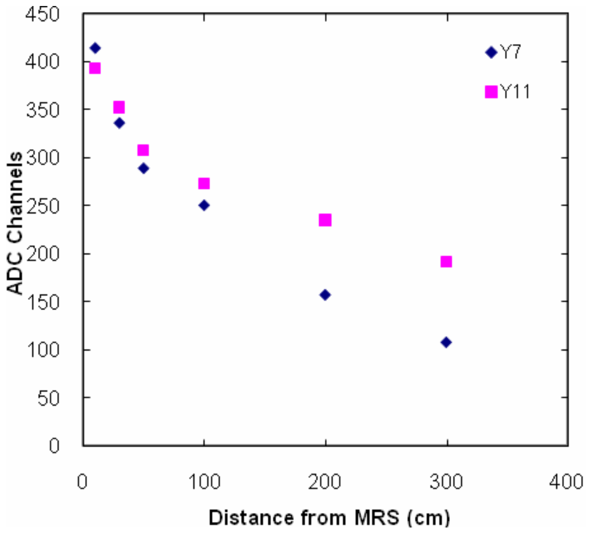

Figure 6. Response of Y11 and Y7 WLS fibers vs. distance from photodetector. The respective error bars are smaller then size of markers and are not shown.

Out of all recorded data, the lower signals discernable from noise were ~47 ADC channels (~5.8PE). In MINERvA "side" test, this value is indicative of the measurable response of the scintillator edge.

The schematic for the light attenuation measurements in Y7 and Y11 fibers is shown in Fig 3 (bottom). A small 2x2x3cm piece of scintillator without coating and with co-extruded [6] hole was used in conjunction with UV LED as a light source. The results of these measurements are presented in Figure 6. As seen, Y7 performs better at rather short distance whereas Y11 is better at larger distances away from photodiode. The fitting with double exponent yields the following results: for Y11 get 35.5±0.3cm and 463.4±1.2cm for short and long components, and for Y7 we get 11.2±0.3cm and 293.1±5.6cm.

## IV. CONCLUSION

The comparison of the Y7 and Y11 WLS fibers is important for the R&D of the T2K project, for which both types of fibers were considered initially. Even though that Y7 fiber yields more light for a short distance from photo detector (as seen by MRS photodiode), for the length of fibers over 2m, as needed for T2K project, Y11 is preferable.

The ~53% increase in light output was detected for WLS fibers of different diameters when optical grease was used in co-extruded hole. Two geometries of the MINERvA scintillator bar were tested, triangular and rectangular. For triangular case, the lower response to cosmic rays measured at the bar side was ~6PE (near photo detector), whereas at the center that value was ~17PE. The attenuation length for the bulk triangular scintillator was found to be ~10.1cm and ~10.2cm by using UV LED and radioactive source respectively.

### Acknowledgment

The authors would like to thank Daniel Ruggiero for his valuable support.

## REFERENCES

[1] H. Weerts., " ILC Detector Design and R&D", *ILC Meeting at Fermilab*, October 27, 2004.

[2] Dyshkant, D. Beznosko, G. Blazey, D. Chakraborty, K. Francis, D. Kubik et al., "Towards a Scintillator-Based Digital Hadron Calorimeter for the Linear Collider Detector", *IEEE* vol. 51, no. 4, pp.1590-1595, Aug. 2004.

[3] S. Bellavia et al. [T2K US B280 Collaboration], "Proposal for Participation in the T2K Long-baseline Neutrino Oscillation Experiment".

[4] D. Beznosko, G. Blazey, A. Dyshkant, V. Rykalin, J. Schellpffer, V. Zutshi, "Modular Design for Narrow Scintillating Cells with MRS Photodiodes in Strong Magnetic Field for ILC Detector", accepted to NIM A, Apr 16 2006, NIMA-D-05-00459.

[5] Kuraray America Inc., 200 Park Ave, NY 10166,USA; 3-1-6, NIHONBASHI, CHUO-KU, TOKYO 103-8254, JAPAN.

[6] D. Beznosko, A. Bross, A. Dyshkant, A. Pla-Dalmau V. Rykalin, "FNAL-NICADD Extruder", FERMILAB-PUB-05-344, Jul 29, 2005.

[7] M. Golovin, A. V. Akindinov, E. A. Grigorev, A. N. Martemyanov, P.A. Polozov, “New Results on MRS APDS”, *Nucl. Instrum. Meth.***A387** 231-234, 1997.

[8] D. Drakoulakos et al. [the MINERνA collaboration], “Proposal to Perform a High-Statistics Neutrino Scattering Experiment Using a Fine-grained Detector in the NuMI Beam”. http://www.pas.rochester.edu/minerva/

[9] K. Nitta, E. Aliu, S. Andringa, S. Aoki, S. Choi, U. Dore et al., "The K2K SCiBar Detector", arXiv:hep-ex/0406023 v1 7 Jun 2004.

[10] Hamamatsu Corporation, 360 Foothill Road, PO Box 6910, Bridgewater, NJ 08807-0919,USA.

[11] Keithley Instruments, Inc., 28775 Aurora Road, Cleveland, OH 44139,USA.

[12] Bivar Inc., 4 Thomas, Irvine, CA 92618, USA

[13] Saint-Gobain (Bicron), 12345 Kinsman Road, Newbury, OH 44065, USA.

[14] D. Beznosko, G. Blazey, D. Chakraborty, A. Dyshkant, K. Francis, D. Kubik et al., "Investigation of a Solid State Photodetector", *NIM A*, **545** (2005) 727-737.

In: Integrated Circuits, Photodiodes... ISBN 978-1-60692-660-4
Editors: R. McIntire and P. Donnell, pp. 405-420 © 2009 Nova Science Publishers, Inc.

***Short Communication D***

# AVALANCHE PHOTODIODE AS AN ELECTRON DETECTOR

***Keiichi Ogasawara***
Tsukuba, Japan

## Abstract

Compared to normal photodiodes, an avalanche photodiode (APD) has internal gain. With a large reverse bias voltage on diodes, the electric field in the active region can exceed a critical value. There, signal carriers are accelerated to a certain velocity and create other electron-hole pairs in the active region. Then the avalanche-like multiplication of the signals can occur incrementally. APDs offer fascinating properties in terms of the detection of minute signals and fast response. The high electric field makes signal carriers fast when passing through the active region. Although APDs are widely used for photo-electronic devices, they are also applicable for ionizing particles. Because of these properties, APD makes it possible to detect extremely low energy particles even under the environment of high temperature. Thanks to technological improvements of the semiconductor process in recent days, excellent APDs for electrons are available. In this chapter, the mechanism of APDs as a particle detector and its latest results are reviewed.

## Introduction

An avalanche Photodiode (APD) has very attractive properties in terms of fast response and high energy resolution in direct measurements of ionizing radiations. Because of the avalanche multiplication of carriers, APD can detect lower energy radiations accompanied by small signal charges. Inside of the APDs, there is an avalanche layer where the electric field is so high that carriers are multiplied in an avalanche way. Typically, the rise time of the output pulse can be as short as a sub-nanosecond [e.g. Kishimoto *et al.*, 2003]. In general, APDs are often used for photoelectronic devices [e.g. Sze, 1981; Laird *et al.*, 2005]. The process of avalanche multiplication in a semiconductor was first reported by McKay [1954]. APDs were widely introduced in the 1960s and the device has been operated in a number of usages because of its high quantum efficiency, compactness, low power consumption, and so on. Recently, the APD has been applied to soft X-ray detection [e.g. Pansart, 1997;

Moszyński *et al.*, 2002a; Kishimoto *et al.*, 2003]. Also APDs were used combined with CsI scintillator for X-rays [e.g. Yang *et al.*, 2003; Ikagawa *et al.*, 2003; Ikagawa *et al.*, 2005; Kataoka *et al.*, 2005], resulting in an excellent energy resolution. For particle detectors, APDs were expected to be applied for the read-out of the light pulses from scintillators under the extremely high magnetic field conditions where photomultiplier tubes are not able to work [Pansart, 1997]. APDs were also applied to beta-decay electrons from tritium ($<$ 18.6 $keV$), converted to characteristic X-rays through the interaction with a metal target [Surette, 1994].

Naturally, attempts have been made to apply APDs as direct particle detectors including electrons as an analogy to semiconductor radiation detectors. In this context, ’direct’ denotes that the particles are detected directly by the detector. Because of the recent improvement of a ’reach-through’ type APDs, APDs have become increasingly sophisticated in terms of particle detection. APDs offer low threshold, high resolution and fast measurement with extremely high and stable detection efficiency for every problem of electron observation. In this chapter, working mechanisms and applications of APDs as direct electron detectors are reviewed. Sometimes ’APD’ is denoted as ’AD’ (Avalanche Diode) focusing on particles in some articles. Instead of AD, ’APD’ is used in this chapter in order to prevent confusion.

# 1. How APD Works

## 1.1. Solid-State Detectors

In terms of the detection mechanism, the APD is basically similar to that of a semiconductor detector, or a solid-state detector (SSD), against ionization radiations. This section starts with the explanation of this SSD. The SSD is a diode device composed of a semiconductor junction between thick n-type material and a thin p-type material. Around a p-n junction, there is a region empty of free carriers called the depletion region, where there is an electric field due to the charge density created by the ionized atoms of the lattice. The charge density is positive in the donor n-type region and negative in the accepter p-type. If a voltage is applied to a diode, the depletion region widens and may even reach the extremities of the diode. If the kinetic energy of an incident electron is larger than the width of the forbidden gap, it can make an electron jump from the valence band to the conduction band creating an electron-hole (e-h) pair. If an e-h pair production occurs in the depletion region, the electron and the hole drift in opposite directions under the influence of the electric field, and a current is created. Once pairs were created, electrons will diffuse or respond to the electric field until they are collected, trapped, or annihilated by recombination with a hole. Like any other ionizing particles or photons, electrons can produce e-h pairs with an average rate of one e-h pair per $\epsilon$ $eV$ of ionization energy ($\epsilon \sim$ 3.61 in the case of silicon photodiode [e.g. Knoll, 2001]). The mean number of produced e-h pairs is then given by $N_{eh} = E/\epsilon$. Thus the incident energy of electrons can be measured with an SSD alone.

Several fundamental parameters of SSDs will govern their performances. Firstly, noise in the SSD can severely limit the low-energy threshold for detection of electrons. Sources of intrinsic SSD noise include the dark current due to the thermal promotion of carriers across the depletion region, and leakage current which becomes significant if large bias is applied to the detector. Second, the energy resolution of the SSD is limited by the statistical variation of the total number $N_{eh}$ of e-h pairs produced. The variance in $N_{eh}$ limits the energy resolution $\Delta E$ in FWHM to $2.35E\sqrt{f_n/N_{eh}}$ where $f_n$ denotes the Fano factor [Knoll, 2001]. For $f_n$ = 0, every incident particle produces the same number of e-h pairs. For $f_n$ = 1, interactions of the incident electron within the solid are completely random, so the variance follows Poisson statistics. A value of $f_n < 1$ implies that sequential interactions of an incident electron in the detector are correlated (not independent as in Poisson statistics). A typical value of $f_n$ in silicon SSDs is about 0.1 [Knoll, 2001; Zullinger *et al.*, 1971].

A normal SSD has a dead layer on the surface where the created e-h pairs cannot be collected as the output, and are annihilated by recombinations. The dead-layer causes a decrease in the SSDs' detection efficiency for lower energy electrons. However, if the thickness of the inlet dead layer is thin enough, the internal quantum efficiency of SSDs, such as silicon photodiodes, can be almost 100% for electrons with energies over 1 $keV$ [Funsten *et al.*, 1997]. That fact has the potential of a lower energy detection limit with silicon based SSDs.

## 1.2. APD Structure

Except for its internal gain, APD works on the same principle as SSDs which are composed of p-n juction diodes. With a large reverse bias voltage on diodes, the field in the depletion region can be made to exceed a critical value (about 200 $kV/cm$ in silicon), then the 'avalanche' multiplication can occur. Once electrons are created in the depletion region, they will drift to the region where there is a strong electric field. That region is called the 'avalanche region'. In case of silicon diode, electrons of the primary e-h pairs will be fully accelerated by the ambient electric field in the avalanche region. If electrons get enough kinetic energy to create another e-h pair in turn by the Augér process, carrier pairs multiply proliferously. This amplification gives an internal gain, which increases the S/N ratio significantly even under a room temperature. In that way, the detection limit of the lowest energy falls down lower. For the semiconducting material, Si, Ge, and GaAs are commonly used for fabricating APDs. Because of the stability of the multiplication factor and low excess noise [e.g. Su *et al.*, 1978], Si is often chosen for the electron detector.

Figure 1 shows three typical APD structures: (a) 'beveled-edge', (b) 'reach-through', (c) 'reverse' type from top to bottom [e.g. Pansart, 1997; Moszyński *et al.*, 2002b; Kataoka *et al.*, 2005]. Early designs of APDs utilized the beveled-edge type to prevent from premature avalanche breakdown in order to achieve a high gain with the simplest structure. It consists of a p$^+$-n junction with a high resistivity n type layer which increases the breakdown voltage up to kilovolt range. The breakdown at the edge is prevented by beveling structure and making the junction very deep ($\sim$ 50 $\mu m$) in order to reduce the edge electric field profile. Therefore the dead-layer in the p$^+$ region is usually etched away to increase the collection efficiency [Webb *et al.*, 1974; Moszyński *et al.*, 2002b]. The beveled-edge device has a wide depletion region ranging up to hundreds of microns, which mainly extends to the n-type region where electrons are more likely to be multiplied than holes. That mechanism relatively decreases the dark current, because the dark current was mostly generated by the hole current [Saleh *et al.*, 1991]. The disadvantage is that the working reverse bias voltage is extremely high. Additionally, the multiplication factor depends highly on the position

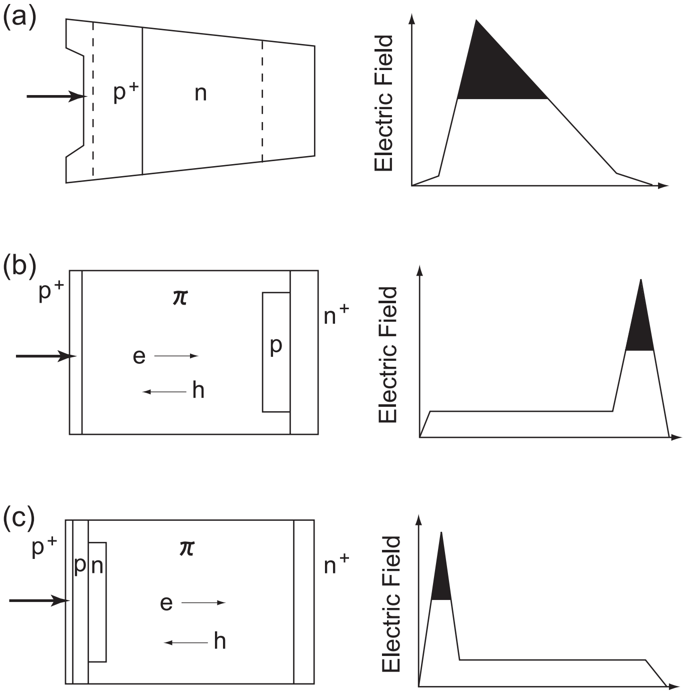

Figure 1. Typical internal structures of three types of APDs: (a) 'beveled-edge', (b) 'reach-through', (c) 'reverse' type from top to bottom. Particles inject from the left side. The electric field profile is also shown in the bottom panels. The avalanche multiplication occurs in the filled part of the electric field profile.

where e-h carrier pairs are produced because there exists the gradient of the electric field in the wide avalanche region.

The most remarkable property of the reach-through device (b) is that the avalanche region is separated from an absorption region. In the absorption region, the p $^+$ layer at the active surface is followed by the an intrinsic depletion layer, which increases the particle absorption depth. As for the thickness of this absorption region, 10 to 200 $\mu m$ is commercially available. Electrons of the carrier pairs generated by an injected particle experience first a region of low electric field, and drift to a narrow region of high electric field where avalanche multiplication occurs [Webb *et al.*, 1974; Webb *et al.*, 1984; Refaat *et al.*, 2000]. The reach-through device needs relatively low voltage (several hundreds of volts) for full depletion due to the narrow avalanche region. The response is so fast that reach-through APDs are sometimes chosen as a fast counting detector. The linearity of the output signals to the injected particles is expected to be good because almost all of the created carriers can be multiplied uniformly.

The device (c) is similar to the reach-through APD, however, the avalanche region has turned over to the front edge, with the peak field lies only about several $\mu m$ from the surface of the device. In the reverse device, carrier electrons are first multiplied, then all the secondary electrons drift toward the diode end [Lecomte *et al.*, 1999; Kataoka *et al.*, 2005]. This type is used specifically coupled with scintillators. Since typical plastic scintillators emit at wavelengths of 500 nm or less, most of the light pulses from scintillators are absorbed within the first 1 to 3 $\mu m$ of the depletion layer and carriers undergo full multiplication. Most of the dark current, on the other hand, undergoes only hole multiplication, that is seldom seen in silicon APDs, and the noise could be relatively reduced significantly.

Though all types are able to be applied for electron measurements, the reach-through type is the best option because of the three reasons: the thin dead-layer, the needlessness of the high reverse voltage, and the existence of the absorption region where the output signals are proportional to the incident electron energy.

## 1.3. Avalanche Multiplication

In any APDs, ionization coefficient, the coefficient to make other carrier pairs for electrons, will increase roughly in proportion to the electric field strength. As a consequence, the gain will initially rise exponentially with the applied bias voltage. Hence the rise is significantly faster than exponential at higher gains, and then the gain rises uncontrollably around break-down voltage. This rapid rise is a consequence of positive feedback inherent in the avalanche process and is mostly caused by ionization produced by holes as well as by electrons [Tapan *et al.* 1997]. In silicon, the hole-induced ionization coefficient $\alpha_h$ is less than the coefficient for electrons ($\alpha_e$). The ratio $k = \alpha_h/\alpha_e$ increases toward unity with increasing field strength. Every ionization event which occurs within an avalanche region will release a hole as well as an electron. Then as the field strength increases, it becomes more likely that some of these holes will cause ionization. As soon as it becomes probable that a hole will ionize the semiconductor and start another avalanche, then the process tends to become self-sustaining and the diode will break down. This is evident in the standard expression for the break down in a depletion region of width $W$ [e.g. McIntyre, 1966; McIntyre 1972; Sze, 1981]

$$\int_0^W \alpha_e \exp\left(-\int_x^W (\alpha_e - \alpha_h)dx'\right) dx = 1. \tag{1}$$

In the extreme case where $\alpha_e = \alpha_h$ the hole and electron ionization are the same and then

$$\int_0^W \alpha_e dx = 1. \tag{2}$$

Under this circumstance, if the bias is high enough to produce ionization by electrons, it is also likely that any hole released will in turn cause further ionization as it makes its way back across the high-field avalanche region and the diode will break down.

Avalanche multiplication is a random process leading to fluctuations in addition to those due to signal statistics. These fluctuations are characterized by the excess noise factor $F$. At high gain $F$ can be approximated by the expression [McIntyre, 1972]

$$F(M) \simeq M\left[1 - (1-k)\left(\frac{M-1}{M}\right)^2\right]. \tag{3}$$

The $k$ value typically equals $\sim$0.04 for silicon. At a gain of M = 50 the APDs have an excess noise factor of 2.

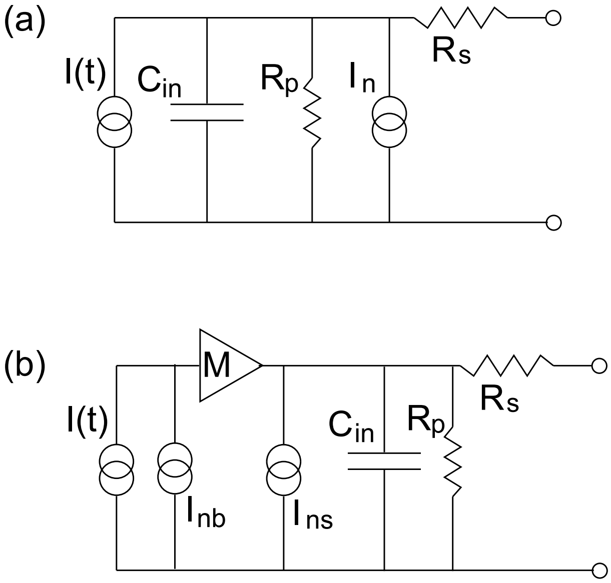

Figure 2. Equivalent circuit of non-avalanching detectors (a) and avalanche photodiodes (b).

### 1.4. Noise Evaluation

The equivalent circuit of the system is shown in Figure 2. Panel (a) shows the case of non-avalanching photodiode, and (b) shows the avalanche photodiode in the figure, where each circuit component expresses: $I(t)$, signal current electrons; $C_{in}$, equivalent input capacitance; $R_p$, equivalent parallel resistance; $I_n$, leakage current of the circuit; $R_s$, equivalent series resistance, $I_{ns}$, surface leakage current of APD; $I_{nb}$, inner leakage current of APD; $M$, gain of the avalanche multiplication. Then, APDs or SSDs work as circuit elements with internal resistance and internal capacity at the same time. The panel (a) in Figure 2 indicates that signal pulses just after the pre-amplifier contains following noise sources in a differential frequency width

$$\overline{V_P}^2 = \left( \frac{4kT}{\omega^2 C_{in}^2 R_p^2} + 4kTR_s + \frac{2eI_n}{\omega^2 C_{in}^2} + \frac{const.}{f} \right) \Delta f, \tag{4}$$

where the first and the second terms on the right-hand side denote the thermal noise, the third denotes the shot noise, the fourth denotes the $1/f$ noise. $\omega$ indicates a frequency of the noise. If the shaping time constant is set to $\tau_s$ and we choose $\omega/2\pi = f \sim \Delta f \sim 1/\tau_s$ for the simplicity, the noise after the shaping amplifier is written in the form

$$\overline{V_S}^2 = \frac{1}{C_{in}^2} \left[ \frac{1}{2\pi^2} \left( \frac{2kT}{R_p} + eI_n \right) \cdot \tau_s + 4kTR_s C_{in}^2 \cdot \frac{1}{\tau_s} + c. \cdot C_{in}^2 \right]. \tag{5}$$

Here both right and left hands are bracketed off by $1/C_{in}^2$, since the object for the measurement is in the unit of charge. The first term of the right-hand side in Eq. 5 has little effect on the result, considering $R_p$ is adequately large. The second and the third terms of the right-hand side suggest that $C_{in}$ is significant and decisive for the noise of the detector, especially because the $R_s$ is considerably large. Note that in the case of solid-state detectors, $C_{in}$ depends on the reverse-bias voltages.

**Table 1. The comparison of the noise coefficient between avalanche and non-avalanching photodiodes.**

| | non-APD | APD |
|---|---|---|
| A | $1.3 \times \left(\frac{2kT}{R_p} + eI_n\right)$ | $1.3 \times \left(\frac{2kT}{R_p} + e\left(I_{ns} + I_{nb}FM^2\right)\right)$ |
| B | $1.3 \times 2kTR_sC_{in}^2$ | $1.3 \times 2kTR_sC_{in}^2$ |
| C | $c. \cdot C_{in}^2$ | $c. \cdot C_{in}^2$ |

Next let us consider the circuit noise for a measurement system with an APD. As is introduced thus far, the APD has an internal gain, represented by $M$. Referring to the panel (b) in Figure 2 and Eq. 5, the noise after the shaping amplifier is written correspondingly in the form

$$\overline{V_{S2}}^2 = \frac{1}{C_{in}^2}\left[\frac{1}{2\pi^2}\left(\frac{2kT}{R_p} + e\left(I_{ns} + I_{nb}FM^2\right)\right)\cdot\tau_s + 4kTR_sC_{in}^2\cdot\frac{1}{\tau_s} + c.\cdot C_{in}^2\right]. \tag{6}$$

After doing some algebra for Eq. 5 and Eq. 6, the equivalent noise charge (ENC) can be divided into three part in accordance with the dependence on $\tau_s$ as follows

$$\overline{ENC}^2 = (\overline{V_S}\cdot C_{in})^2 = A\cdot\tau_s + B\cdot\frac{1}{\tau_s} + C \tag{7}$$

where $C$ represents the $1/f$ noise, and $A$, $B$ are given in the Table 1. $A \cdot \tau_s$ is called the current noise, while $B \cdot \frac{1}{\tau_s}$ is called the capacitance noise.

$F$ is called excess noise factor as a function of $M$ defined in Eq. 3 ($F > 1$). This suggests that the shot noise within the depletion region of APD increases incrementally by the avalanche multiplication. Considering that the power of the signal increases in proportion to $M^2$, the noise source is able to be divided into two parts: the noise that can be reduced by the avalanche gain and the noise that would be multiplied by the avalanche gain. Reflection on the Table 1, the thermal noise and the surface leakage current are able to be cut down by the avalanche gain, while the inner leakage current increases faster than the signal by the avalanche process. That limits the working bias voltage at the optimum value. Figure 3 shows schematically the way the optimum bias voltage is chosen.

## 1.5. Technical Properties for Application

As has been reported so far, the multiplication factor depends on the temperature [e.g. Ochi *et al.*, 1996; Dorokhov *et al.*, 2003; Fernandes, 2004; Yatsu *et al.*, 2006]. The multiplication factor gets higher when the temperature goes down typically by minus several $\%/K$. This temperature dependence of the multiplication factor is due to the temperature

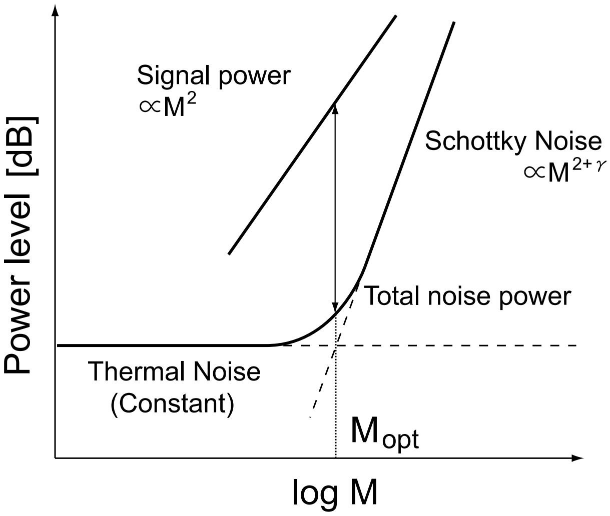

Figure 3. Power levels of noises and signals through a stage of avalanche multiplication.

dependence of the ionization coefficients of electrons and holes. The carrier electrons lose part of their energy with the interactions against optical phonons, and the mean free path of that electron-phonon interaction decreases with increasing temperature [Su *et al.*, 1978]. This dependence on temperature of output signals indicates a necessity of the countermeasure against temperature when we are focused on the energy determination from the output pulse height.

Radiation hardness has been tested by many researchers for $\alpha$ particles [Anzivino *et al.*,1999], for neutrons [Reucroft *et al.*,1997; Baccaro *et al.*,1999], for $\gamma$-rays [Kirn *et al.*, 1997] and for protons [Kotoku *et al.*, 2006]. In almost all case, both the increase of the leakage current and the degradation of the multiplication factor are seen after irradiations. However, some results indicate that APDs are hardly affected by radiations as long as working at low multiplication factors ($\sim$ 15) for $\alpha$ particles [Anzivino *et al.*,1999] or for protons [Kotoku *et al.*, 2006]. Those radiation effects must be tested for the usages of spacecraft applications, accelerators, or other radiological environments.

## 2. Dynamic Range of APD

### 2.1. Detectable Energy Range

The limit of the detection is decided by the thickness of the dead-layer and the depletion layer. Incident electrons are randomly scattered passing through the APD, some penetrate into a deeper part, others stop at a shallower part. The average depth of e-h pair production largely varies with the incident energy. Figure 4 shows the probability at what depth the energy loss occurs in the bulk silicon. Those probabilities were calculated from the montecarlo numerical modeling of the interaction between a bulk of the solid silicon and incident electrons. This figure also represents the distribution of initial e-h pairs because almost all energies lost in the depletion region are expected to be used for creations of e-h pairs. Ob-

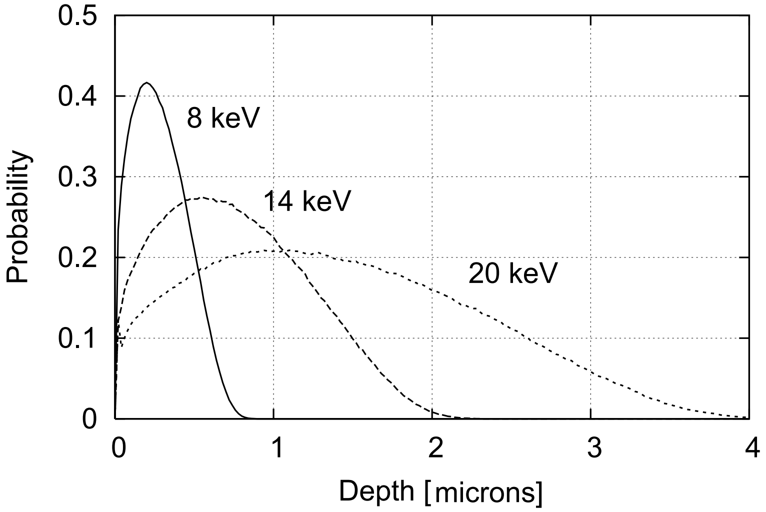

Figure 4. Probability curve of the energy loss of electrons inside the bulk silicon.

viously, the output signals are affected by the structure of the shallower part if the electron energy is low, and by the structure of the deeper part if the electron energy is high.

Assuming that the output charge amount is proportional to the incident energy of electrons, the pulse height distribution (PHD) of the output pulses from APD should have one clear peak when the incident electrons are monochromatic. The formation of the PHD peak is expected to be related to the energy loss process of incident electrons in the dead-layer on the surface of the device. If the incident energy is low, its range in a solid is short and then most of the energy is absorbed in the dead-layer (Figure 5, a). Those e-h pairs created in the dead-layer would be scattered by lattice oscillations or captured by lattice defects, so that they would not contribute to the signal pulse. If the incident electron fortunately penetrate straightforward to the depletion region, the signal charge will be large. Thus the amount of the signal charge differs vastly in every incident electron if the electron range is comparable to the depth of the dead-layer (see the output PHD for 6 $keV$ in Figure 6). Therefore, the proportionlality relation between the incident energy and the output charge becomes ambiguous. Then no clear peak in the pulse height distribution may be formed. In the marginal energy range, the signal charge varies case by case because the trajectory is full of turns and twists. That case, characteristic tailing features will appear (8 $keV$ in Figure 6). The dead-layer also affects the efficiency for the lower energy electrons. If the incident energy is enough high compared to the dead-layer thickness, the intrinsic efficiency of the APD are degraded only by backscatter electrons. Then, the efficiency is expected to be more than 80 %.

On the other hand, higher energy electrons have a larger range in solid and are able to enter deep inside the APD (Figure 5, c). If the incident energy is too high, the pulse hight distributions no longer have clear peaks, and the distribution was deteriorated in comparison with the lower energy case (see the output PHD for 30 $keV$ in Figure 6). As the beam energy increases, the primary peak becomes obscure: the pulse height distribution consequently becomes almost flat at higher part. Instead, a lower new peak appears at the lower side

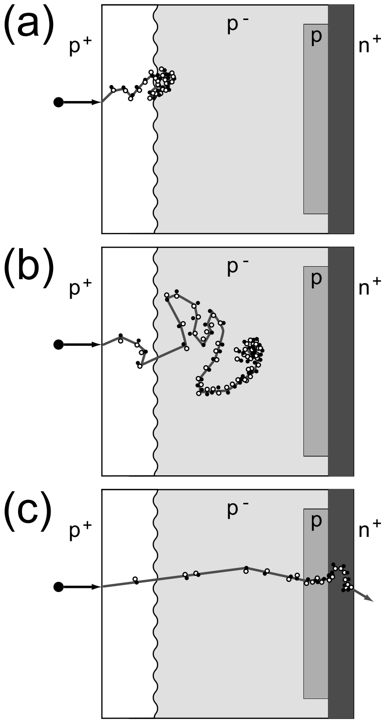

Figure 5. Typical trajectories of electrons with (a) low energy, (b) appropriate energy, and (c) high energy in a reach-through APD. The dead-layer locates above the wiggle lines. Produced e-h pairs are schematically drawn on the trajectory.

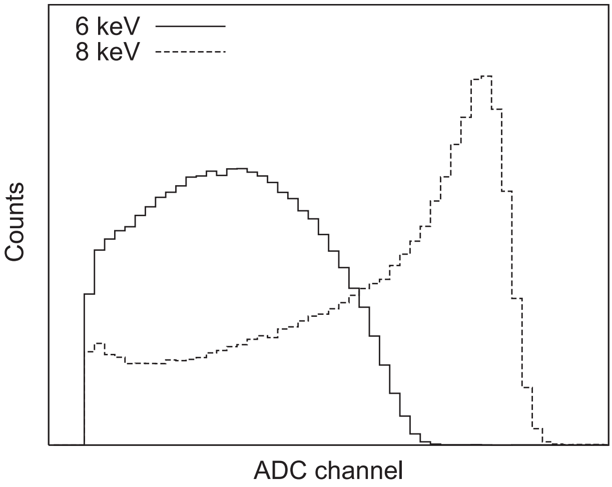

Figure 6. Pulse height distributions of APD output signals for incident 6 $keV$ and 8 $keV$ electrons. The dead-layer thickness of this APD is about 0.3 $\mu m$. The reverse bias voltage was set to 150 $V$ where $M$ $\sim$20. The temperature of the device was 15 $^oC$.

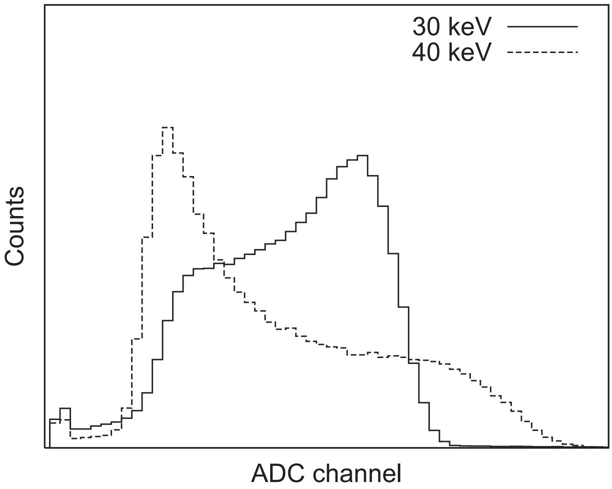

Figure 7. Pulse height distributions of APD output signals for incident 30 $keV$ and 40 $keV$ electrons. The depletion region thickness of this reach-through APD is about 10 $\mu m$. The reverse bias voltage was set to 150 $V$ where $M$ ~20. The temperature of the device was 15 $^oC$.

and becomes more distinct with increasing energy. For primary electrons with energies high enough to transmit through the depletion layer including the avalanche region, the produced e-h pairs would be no longer collected as a signal. Then the pulse hight of the main peak would decrease (40 $keV$ in Figure 6).

The electron range divided by density for a bulk silicon is shown in Figure 8. Roughly speaking, keV electrons are affected by the structure such as the dead-layer at a depth of 0.1 $\mu m$. 100 keV of incident electrons are expected to transmit the whole APD active area with a depth of about 100 $\mu m$. In Ogasawara *et al.* [2008], the APD with 140 $\mu m$ absorption reagion is studied and it was working with clear peaks from 3 $keV$ to 100 $keV$. The linearity was also well throughout the whole energy range.

### 2.2. Count Rate

Due to the strong electric field inside the avalanche region, the rising time of the APD output pulse is extremely fast in the nano-second level. For this reason, APD is also promising as a fast counting device. Though the result is not for the electrons, Kishimoto *et al.* [2001] reports that the APD with 130 $\mu m$ of active layer worked at the counting rate higher than $10^6$ $s^{-1}$ in X-rays spectroscopy keeping good energy resolutions.

## 3. Applications

### 3.1. Hybrid Photodetectors

A hybrid photodetector (HPD) is a single-photon detector consisting of a photocathode and APDs [e.g Suyama *et al.*, 2004; Fukasawa *et al.*, 2008]. Photoelectrons from the pho-

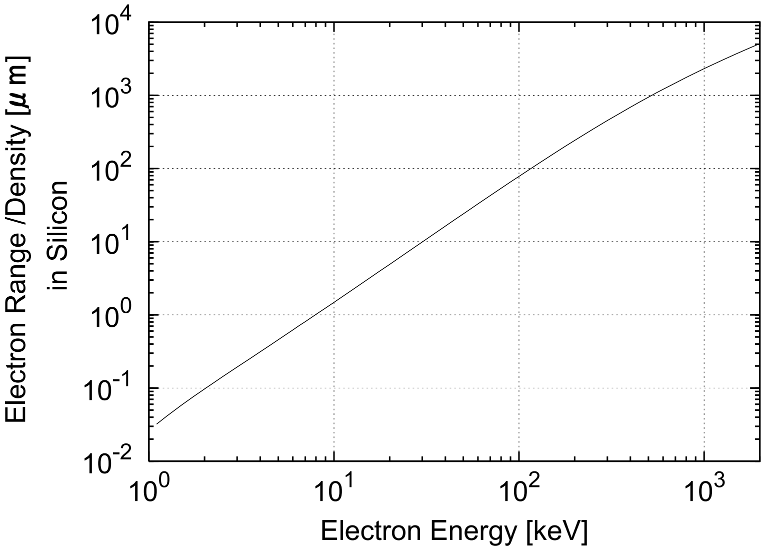

Figure 8. Electron range divided by density for a silicon. The ranges were calculated based on Berger *et al.* [1998].

tocathode are accelerated up to around 10 $keV$ and detected by APDs fixed in the vacuum tube. These HPDs have been recently used to detect extremely weak or fast optical signals at the single photon level. A photomultiplier tube (PMT) is one of the most conventional detectors of weak photon detectors with a large effective area, high gain, and fast response. HPD shows better photon resolution and even faster response, 15 $ps$ of timing resolution with stable and high quantum efficiency [Fukasawa *et al.*, 2008]. Furthermore, HPDs can be used even under the high magnetic field condition. HPDs are expected to be applied for LIDAR (light detection and ranging), TCSPC (time-correlated single photon counting), and PET scanning in nuclear medicine.

## 3.2. Experimental Physics

In order to meet the requirement of fast time resolutions for particle detections, APDs are often used in physics experiments. Here two remarkable examples are reviewed.

In Hauger *et al.* [1994], APDs were applied as a time of flight detector with sub-100 $ps$ precision. They selected $\beta^-$ electrons from $^{160}$Ru source with the end point energy of 3.5 $MeV$, analyzed the pulses from electrons transmitted through two 140 $\mu m$ reach-through APDs. According to their report, the risetime of the signal equaled 2.5 $ns$ and the falling time was 9 $ns$, due to the avalanche multiplication of all the primary electrons and the drift time of the all secondary holes coming from the avalanche respectively.

Kishimoto *et al.* [2000] reports that a reach-through APD was employed to observe the probability of the nuclear excitation by electron transition in $^{197}$Au. Owing to the sub-ns time resolution, APDs enabled to distinguish weak internal-conversion electrons from the intense prompt radiation with a short attenuation time of 5 $ns$.

### 3.3. Space Sciences

Micro Channel Plates (MCPs) and Channeltron Electron Multipliers (CEMs) have been used for the detection of low-energy particles with energies lower than $\sim$20 keV [e.g. Paschmann *et al.,* 1970]. The detection efficiency gradually decreases toward higher energies than 1 $keV$, and the magnification of statistical errors and insufficient time resolution was difficult at this energy range. In addition, MCPs or CEMs are also sensitive to penetrating energetic particles and photons or secondary electrons, which cause background noise. SSDs have been used to measure energetic particles in space [e.g. Willken *et al.,* 2001]. In case of electrons with energies lower than several tens of keV. However, the energy losses in the dead layer near the surface is significant, and the small number of created electron-hole pairs makes it very difficult to measure the electrons under the influence of electric noises. These technical problems have kept us away from the reliable measurements of electrons ranging from 1 $keV$ to 100 $keV$ in space. APDs are expected to be appied as the electron detector instead of the conventional SSDs and MCPs. Ogasawara *et al.* [2006] reports the successful observation of auroral electrons using APDs by a sounding rocket experiment. As for the observation onboard spacecraft, verification test has been planned targetting particles over 30 $keV$ for the first time by a Japanese pico-satellite project [Kotoku *et al.,* 2006]. It is possible that APDs are used widely as a very powerful, light and power saving monitor for the space environment in the near future, if utilized in the space station or spacecraft.

## Conclusion

APD is a promising device for fast, low noise applications in electron observations. The APD is a kind of p-n junction semiconductor with an internal gain due to the avalanche multiplication of signal electrons or holes in the strong electric field within its depletion region. Compared to the normal semiconductor detectors, this strong electric field and internal gain enables low threshold, high resolution measurements and fast time resolution in cases of electron measurements. The thickness of the dead-layer on the surface of the APD determines the low energy limit, while the whole thickness of the depletion region is crucial to the high energy limit. There are wide variations of combinations of the dead-layer and the depletion region depending on the intended use. Continuing developments and experiments are actively being done for future applications. For instance, the pixilation of APDs will provide us with versatile usages for imaging applications or the necessity of a large active area. Geiger-mode APDs [e.g. Renker, 2006] can be applied to electron observations when a strong and extremely fast output is necessary.

## References

### Articles in Journals

Anzivino, G.; Bai, J.; Bencheikh, B.; Contin, A.; DeSalvo, R.; Fagen, S.; He, H.; Liu, L.; Lundin, M.; Madden, R.M.; Mondardini, M.R.; Szawlowski, M.; Wang, K.; Xia, X.; Yang, C.; Zhao, M. *Nucl. Instr. and Meth.* 1999, A 430, 100-109.

Baccaro, S.; Bateman, J.E.; Cavallari, F.; Da Ponte, V.; Deiters, K.; Denes, P.; Diemoz, M.; Kirn, Th.; Lintern, A.L.; Longo, E.; Montecchi, M.; Musienko, Y.; Pansart, J.P.; Renker, D.; Reucroft, S.; Rosi, G.; Rusack, R.; Ruuska, D.; Stephenson, R.; Torbet, M.J. *Nucl. Instr. and Meth.* 1999, A 426, 206–211.

Dorokhov, A.; Glauser, A.; Musienko, Y.; Regenfus, C.; Reucroft, S.; Swain, J. *Nucl. Instr. and Meth.* 2004, A 504, 58–61.

Fernandes, L.M.P.; Lopes, J.A.M.; Dos Santos, J.M.F. *Nucl. Instr. and Meth.* 2004, A 531, 566–568.

Fukasawa, A; Haba, J.; Kageyama, A.; Nakazawa, H.; Suyama, M., *IEEE Trans. Nucl. Sci.* 2008, 55, 758–782.

Funsten, H.O.; Suszcynsky, D.M.; Ritzau, S.M.; Korde, R. *IEEE Trans. NS* 1997, 44, 2561–2565.

Hauger, J.A.; Choi, Y.; Hirsh, A.S.; Scharenberg, R.P.; Stringfellow, B.C.; Tincknell, M.L.; Porile, N.T.; Rai, G.; Garbarino, J.; McIntyre, R.J. *Nucl. Instr. and Meth.* 1994, A 337, 362–369.

Ikagawa, T.; Kataoka, J.; Yatsu, Y.; Kawai, N.; Mori, K.; Kamae, T.; Tajima, H.; Mizuno, T.; Fukazawa, Y.; Ishikawa, Y.; Kawabata, N.; Inutsuka, T. *Nucl. Instr. and Meth.* 2003, A 515, 671–679.

Ikagawa, T.; Kataoka, J.; Yatsu, Y.; Saito, T.; Kuramoto, Y.; Kawai, N.; Kokubun, M.; Kamae, T.; Ishikawa, Y.; Kawabata, N. *Nucl. Instr. and Meth.* 2005, A 538 640–650.

Kataoka, J.; Saito, T.; Kuramoto, Y.; Ikagawa, T.; Yatsu, Y.; Kotoku, J.; Arimoto, M.; Kawai, N.; Ishikawa, Y.; Kawabata, N. *Nucl. Instr. and Meth.* 2005, A 541, 398–404.

Kirn, Th.; Musienko, Y.; Flugel, Th.; Renker, D. *Nucl. Instr. and Meth.* 1997, A 387, 199–201.

Kishimoto, S.; Adachi, H.; Ito, M. *Nucl. Instr. and Meth.* 2001, A 467-468, 1171–1174.

Kishimoto, S.; Yoda, Y.; Seto, M.; Kobayashi, Y.; Kitao, S.; Haruki, R.; Kawauchi, T.; Fukutani, K.; Okano, T. *Phys. Rev. Lett.* 2000, 85, 1831–1834.

Kishimoto, S.; Yoda, Y.; Seto M.; Kitao S.; Kobayashi, Y.; Haruki, R.; and Harami, T. *Nucl. Instr. and Meth.* 2003, A 513, 193–196.

Kotoku, J.; Kataoka, J.; Kuramoto, Y.; Tsubuku, Y.; Yatsu, Y.; Sato, R.; Ikagawa, T.; Saito, T.; Kawai, N.; Konoue, K.; Miyashita, N.; Imai, M.; Omagari, K.; Kashiwa, M.; Yabe, H.; Imai, K.; Miyamoto; Fujikawa, K.; Masumoto, S.; Usuda, T.; Iljic, T.; Konda, A.; Sugita, S.; Ymanaka, T.; Matsuura, D.; Sagami, T.; Kajiwara, S.; Funaki, Y.; Matsunaga, S.; Shima, T.; Kishimoto, S. *Nucl. Instr. and Meth.* 2006, A 565, 677–685.

Laird, J. S.; Hirao, T.; Onoda, S.; Yamakawa, T.; Wakasa, T.; Abe, H.; Ohyama, H.; and Kamiya, T. *Nucl. Instr. and Meth.* 2005, A 541, 228–235.

Lecomte, R.; Pepin, C.; Rouleau, D.; Dautet, H.; McIntyre, R.J.; McSween, D.; Webb, P. *Nucl. Instr. and Meth.* 1999, A 423, 92–102.

McIntyre, R.J. *IEEE Trans. Electron Devices* 1966, 13, 164–168.

McIntyre, R.J. *IEEE Trans. Electron Devices* 1972, 19, 703–712.

McKay, K. G. *Phys. Rev.* 1954, 94, 877–884.

Moszyński, M.; Czarnacki, W.; Szawlowski, M.; Zhou, B.L.; Kapusta, M.; Wolski, D.; Schotanus, P. *IEEE trans. Nucl. Sci.* 2002, 49, 971–976.

Ochi, A.; Nishi, Y.; Tanimori, T. *Nucl. Instr. and Meth. A* 1996, A 378, 267–274.

Ogasawara, K.; Asamura, K.; Takashima, T.; Saito, Y.; Mukai, T. *Earth, Planets Space* 2006, 58, 1155–1164.

Ogasawara, K.; Hirahara, M.; Miyake, W.; Kasahara, S.; Takashima, T.; Asamura, K.; Saito, Y.; Mukai, T. *Nucl. Instr. and Meth.* 2008, A 594, 50–55.

Pansart, J. P. *Nucl. Instr. and Meth.* 1997, A 387, 186–193.

Paschmann, G.; Shelley, E.G.; Chappell, C.R.; Sharp, R.D.; Smith, L.F. *Rev. Sci. Instr.* 1970, 41, 1706–1711.

Refaat, T.F.; Halama, G.E.; DeYoung, R.J. *NASA/TP* 2000, 210096.

Renker, D. *Nucl. Instr. and Meth.* 2006, A 567, 48–56.

Reucroft, S.; Rusack, R.; Ruuska, D.; Swain, J. *Nucl. Instr. and Meth.* 1997, A 394, 199–210.

Su, Y.K.; Chang, C.Y.; Wu, T.S. *Opt. Quant. Electrn.* 1978, 11, 109–117.

Surette, R. A. *Nucl. Instr. and Meth.* 1994, A 337 588–593.

Suyama, M.; Fukasawa, A.; Haba, J.; Iijima, T.; Iwata, S.; Sakuda, M.; Sumiyoshi, T.; Takasaki, F.; Tanaka, M.; Tsuboyama, T.; Yamada, Y. *IEEE Trans. Nucl. Sci.* 2004, 51, 1056–1059.

Tabata, T.; Ito, R.; Okabe, S. *Nucl. Instr. and Meth.* 1971, 94, 509–513.

Tapan, I.; Duell, A.R.; Gilmore, R.S.; Llewellyn, T.J.; Nash, S.; Tapper, R.J. *Nucl. Instr. and Meth.* 1997, A 388, 79–90.

Webb, P.P.; McIntyre, R.J.; Conradi, J. *RCA Review* 1974, 35, 234–277.

Webb, P.P.; McIntyre, R.J. *IEEE Trans. Electr. Dev.* 1984, 31, 1206–1212.

Wilken, B.; Daly, P.W.; Mall, U.; Aarsnes, K.; Baker, D.N.; Belian, R.D.; Blake, J.B.; Borg, H.; Buchner, J.; Carter, M.; Fennell, J.F.; Friedel, R.; Fritz, T.A.; Gliem, F.; Grande, M.; Kecskemety, K.; Kettmann, G.; Korth, A.; Livi, S.; McKenna-Lawlor, S.; Mursula, K.; Nikutowski, B.; Perry, C.H.; Pu, Z.Y.; Roeder, J.; Reeves, G.D.; Sarris, E.T.; Sandahl, I.; Soraas, F.; Woch, J.; Zong, Q.G. *Ann. Geophys.* 2001, 19, 1355–1366.

Yang, L.; Dzhosyuk, S.N.; Gabrielse, J.M.; Huffman, P.R.; Mattoni, C.E.H.; Maxwell, S.E.; McKinsey, D.N.; Doyle, J.M. *Nucl. Instr. and Meth.* 2003, A 508, 388–393.

Yatsu, Y.; Kuramoto, Y.; Kataoka, J.; Kotoku, J.; Saito, T.; Ikagawa, T.; Sato, R.; Kawai, N.; Kishimoto, S.; Mori, K.; Tamae, T.; Ishikawa, Y.; Kawabata, N. *Nucl. Instr. and Meth.* 2006, A 564, 134–143.

Zullingar, H. R. *J. Appl. Phys.* 1971, 42, 5570–5577.

**Books**

Knoll, G. F., *Radiation Detection and Measurement 3rd ed.*; John Wiley & sons, Inc., 2000.

Saleh, Bahaa E.A.; Teich, M.C.; *Fundamentals of Photonics*, John Wiley & Sons, Inc., 1991.

Sze, S. M. *Physics of Semiconductor Devices 2nd ed.*; John Wiley & sons, Inc., 1981.

**Electronic Media**

Berger, M.J.; Coursey, J.S.; Zucker, M.A.; Chang, J. (1998). NIST ESTAR, http://physics.nist.gov/PhysRefData/Star/Text/contents.html

# INDEX

6

6-OHDA, 379

A

AAA, 334
abnormalities, 374, 375, 380
absorption, xi, 129, 130, 173, 175, 176, 177, 179, 228, 236, 252, 254, 257, 294, 295, 324, 325, 326, 335, 336, 337, 339, 340, 342, 408, 409, 415
absorption coefficient, 325, 326
absorption spectra, 325, 337
abstinence, 252
access, 30, 33, 34, 70, 152, 230, 340, 341
accidental, 100
accuracy, ix, 63, 64, 95, 96, 105, 106, 107, 109, 247, 251, 260, 261, 262, 266, 296, 397
acetate, 248, 267
acetone, 123, 385
acetonitrile, 122, 187
acid, 249, 250, 253, 257, 261, 262, 263, 264, 265, 267, 268, 270, 271, 275, 280, 281, 282, 283, 288, 290, 325, 337, 339, 340, 370, 371, 373
ACS, 156
action potential (AP), viii, 70, 71, 72, 74, 87, 89, 90, 343, 344, 352, 357, 358, 359, 360, 361, 363
activation, xii, 49, 58, 63, 343, 344, 345, 349, 356, 357, 364, 369, 372, 376, 379
activation energy, 49, 58
actuation, 21
actuators, 92
acute, 93, 116, 270, 363, 364, 378, 382
Adams, 92, 158
adaptation, 133
ADC, 88, 400, 401
additives, 256, 259
adhesion, 118, 202, 204
administration, 251, 253, 281, 282
administrative, 251, 294
ADT, 197
adulteration, 268, 269, 270, 272, 289
adverse event, 377
AFM, 169, 216, 217
age, 110, 274, 337, 374, 380
ageing, 271, 272
agent, 266
agents, 260, 274, 349, 377
aggregates, x, 116, 154
aggregation, 131
aging, 274
agonist, 376
aid, 252
AIP, 157
air, 117, 119, 152, 176, 191, 192, 193, 194, 275, 290, 339, 348
albumin, 252, 326
alcohol, 122
algorithm, ix, 95, 96, 98, 103, 105, 106, 107, 108, 109, 110, 239, 248, 274, 279, 302, 303, 304, 319
alkali, xii, 383, 384
alkaline, 392
alkaloids, 266, 273, 289
alkenes, 277
allergic reaction, 257
allergy, 270
alluvial, 276
alpha, 101, 370, 375
ALS, 247
alternative, 40, 151, 247, 269, 327
alternatives, 347, 385
aluminum, viii, 70, 85, 219, 224, 385
amide, 275
amine, 123, 372
amines, 127
amino, 121, 122, 124, 129, 141, 142, 144
amino groups, 122, 124, 141, 142
amorphous, 120, 149, 153, 172, 185, 186, 384
amplitude, 73, 120, 135, 140, 141, 142, 143, 144, 304, 307, 310, 312, 313, 323, 343, 344, 356
anabolic, 257
analgesic, 251, 272
analog, viii, 69, 71, 72, 73, 74, 75, 81, 85, 87, 88, 116, 331, 332, 348
analysts, 223, 255

analytical techniques, 324
analytical tools, 116, 117, 154
angiotensin II, 247, 279
angiotensin II receptor antagonist, 247
animal studies, xii, 369
animal tissues, 257, 260, 285
animals, 246, 258, 259, 260, 261, 283, 285, 352, 372
Anisotropy, 119
annealing, 122
annihilation, ix, 115, 135, 136, 139, 141, 350
anode, 130, 132, 133, 211, 215, 216, 218, 329
antagonist, 247
antagonistic, 103
antagonists, 279
anthocyanin, 263
Anthocyanins, 250, 263, 267, 286
anthracene, 246, 276, 290
antibacterial, 256, 261
antibacterial agents, 261
antibiotic, 256, 262
antibiotics, 232, 245, 246, 248, 253, 257, 259, 260, 261, 262, 276, 279, 285, 286, 291
anticancer, 256, 263
anticancer activity, 256
anticholinergic, 377, 382
anticonvulsant, 248
antidepressant, 249, 266
antidepressants, 246, 249, 250, 279, 280
anti-HIV, 256
antioxidant, 263, 264, 286
antipsychotic, 252, 281
anxiety, 248
anxiolytic, 273
aorta, 350
application, vii, ix, 5, 20, 37, 71, 76, 81, 92, 93, 96, 125, 135, 153, 154, 220, 246, 254, 255, 266, 267, 280, 289, 298, 299, 304, 314, 326, 328, 332, 338, 359
aripiprazole, 252, 281
Aristotle, 227
aromatic compounds, 147, 277
aromatic hydrocarbons, 277
aromatic rings, 153
aromatics, 276, 291
arrhythmia, 343, 350, 355, 356, 360, 364
arrhythmias, 353, 359, 365
arrhythmogenesis, 350, 352, 354, 355, 357, 359, 360
artery, 379
ascorbic, 263
ascorbic acid, 263
Asian, 283, 382
ASIC, 71
aspect ratio, 79, 309
assessment, 51, 232, 248, 265, 269, 272, 282, 287, 359, 378, 380
assumptions, 139, 294
ASTM, 49, 50
asymmetry, 130
asynchronous, 88
atmosphere, 176, 313, 319, 338
atmospheric pressure, 250, 254
atomic force, 216, 389
atomic force microscope, 389
atoms, vii, 3, 4, 176, 326, 406
atrial fibrillation, 361, 363
atrium, 360
atrophy, 374, 380
attacks, 248
atypical, 252
*Aurora*, 403
authentication, 269
authenticity, 268, 269, 270, 271, 288
autofluorescence, 339
automation, 241, 295
availability, xi, 238, 248, 277, 294, 339
averaging, 141
awareness, viii, 45

**B**

Bacillus, 256
Bacillus subtilis, 256
background noise, 239, 417
bacteria, 248, 260, 262
bacterial, 260
bacterial infection, 260
band gap, 173, 176, 179, 214
bandgap, 42
bandwidth, 20, 24, 25, 27, 28, 29, 31, 32, 33, 36, 40, 43, 80, 119, 124, 299
barrier, x, 117, 127, 144, 147, 175, 177, 193, 209, 210, 214, 218, 220, 229, 377, 388
barriers, 152, 177, 220, 388
basal ganglia, xii, 369, 370, 371, 372, 373, 377, 380
batteries, 164, 220
BBB, 377
beating, 344
beef, 259
behavior, 67, 79, 127, 136, 140, 219, 220, 223, 251, 349, 376, 384, 385, 388, 389
Beijing, 69
Belgium, 95, 156
benchmark, 277
bending, 117, 118, 142, 154
benefits, 241, 264, 278, 377
benign, 356, 374
benzene, 119, 123, 153, 200
benzodiazepine, 273
benzodiazepines, 246, 248, 249, 279
beverages, 268
bias, xiii, 50, 74, 81, 127, 129, 130, 132, 146, 147, 163, 169, 181, 193, 195, 196, 299, 330, 331, 385, 390, 400, 405, 406, 407, 409, 411, 414, 415
bible, 120
binding, 165, 166, 173, 252, 343
binding energy, 165, 166, 173
bioactive compounds, 256, 265

bioavailability, x, 227, 228, 251, 253, 264
biocompatibility, viii, 70, 85, 86
biocompatible, viii, 70, 85, 86
bioengineering, 91
biological systems, 150
biomarkers, 268
biophysics, 125
Biosensor, 73, 93
biosynthesis, 273
biotechnological, 247, 279
biotransformation, 250
bipolar, 359, 388, 389
bladder, xii, 369, 370, 371, 372, 373, 374, 375, 376, 377, 378, 379, 380, 381, 382
blocks, 72, 73, 85, 297, 309
blood, 248, 249, 272, 273, 280, 289, 295, 325, 343
blood plasma, 249, 280
blood-brain barrier, 377
body fluid, xi, 293, 295, 324, 325, 329, 332, 335, 339
boiling, 186, 198
bonding, 119, 152
bonds, 119, 122, 168, 250
Boron, 327
Boston, 92, 156, 378
bovine, 258, 260, 261, 262, 281, 283, 285, 286
bowel, 377, 378
bradykinesia, 375
brain, 70, 93, 100, 370, 371, 372, 374, 375
brain structure, 370
brainstem, 370, 371, 372
breakdown, 407
broadband, 18, 36, 41, 43, 44, 309
Brooklyn, 343
bubble, 214
bubbles, 214, 328
buffer, 72, 73, 74, 79, 81, 84, 88, 90, 393
building blocks, 40, 84, 390
buildings, 98, 107
bulk crystal, 120, 145

C

$Ca^{2+}$, 363, 364
cables, 356
cache, 87
caffeine, 246, 249, 279, 280
caffeoylquinic acids, 262, 286
calcium, 214, 215, 343, 347, 351, 353, 354, 355, 356, 357, 359, 361, 362, 363, 364, 365
calibration, 247, 257, 259, 279, 296, 300, 301, 302, 319, 320, 337, 400
Canada, 275, 341
cancer, 250, 270, 339, 340, 342
cancer cells, 342
candidates, xii, 126, 241, 252, 283, 383
capacitance, 7, 8, 16, 17, 18, 19, 20, 28, 29, 38, 74, 76, 82, 83, 89, 170, 191, 204, 205, 296, 331, 386, 410, 411
capacity, xi, 127, 136, 140, 141, 263, 294, 339, 376, 410
capillary, 228, 252, 267, 279, 281
capsule, 251, 265, 270, 340, 342
carbon, 212, 215
carbonyl groups, 213
carboxyl, 119
carboxyl groups, 119
carboxylates, 384
carboxylic, 260
carcinogenic, 270
cardiac arrhythmia, 343, 350, 365
cardiac function, 364
cardiac muscle, 358, 359, 360
cardiac myocytes, 343, 344, 351
cardiovascular disease, 273
carotenoids, 269, 288
carrier, xii, 30, 116, 117, 169, 170, 172, 173, 174, 212, 223, 327, 383, 385, 390, 391, 407, 408, 409, 412
case study, 272
catechins, 270
catecholamine, 359
catheter, 344
cathode, 130, 210, 211, 214, 215, 216, 217, 218, 224, 384
Catholic, 95, 110
cation, 129, 131, 132, 133, 134, 141, 151, 272, 273, 289
cats, 378, 379, 380
cattle, 259, 284
CCC, 138
cell, viii, ix, x, xi, 6, 8, 10, 12, 17, 18, 19, 23, 26, 27, 28, 29, 37, 38, 70, 71, 72, 73, 74, 85, 86, 89, 90, 105, 115, 129, 130, 131, 132, 195, 198, 199, 227, 228, 229, 249, 277, 278, 344, 348, 350, 351, 357, 359, 361, 371, 372, 376
cell culture, viii, xi, 70, 86, 344, 357, 359
cell membranes, 73
cellular neural network, 113
cement, 32, 33, 36
central nervous system, 89, 379, 382
cephalosporin, 253
ceramic, 84
cerebellum, 370, 371
cerebral cortex, 377
cerebrospinal fluid, 295
cerebrovascular, 375
channels, 24, 72, 73, 74, 81, 85, 87, 99, 100, 101, 103, 104, 106, 107, 108, 109, 113, 121, 145, 170, 312, 313, 321, 322, 323, 351, 352, 400, 401
chaos, 362
charge density, 170, 406
charge trapping, 116, 125
chemical composition, 265
chemical degradation, 191

chemical reactions, 177, 325
chemical reactivity, 168
chemical sensing, 118
chemical stability, 264
chemicals, 276, 295
chemisorption, 118
chemometrics, 246, 247, 254, 289
chicken, 260, 261, 262, 285
children, 256
China, 69, 256, 267
Chinese medicine, 266
chiral, 280
chlamydia, 260
chloride, 325, 382
chlorobenzene, 187, 198, 199, 200, 201
chloroform, 187, 198, 199, 200, 201
chlorogenic acid, 268
cholecalciferol, 248
cholinergic, 370, 371
Christmas, 376, 381
chromatograms, 235, 236, 254, 263, 266, 273, 274, 277, 285
chromatographic technique, 289
chromatography, 240, 247, 252, 254, 255, 258, 260, 266, 273, 275, 278, 279, 281, 282, 283, 285, 288, 289, 290
ciprofloxacin, 253, 258, 260, 261, 283
circulation, 90, 370
citalopram, 249, 250
classes, 264, 267, 270, 274, 275
classical, ix, 95, 247
classification, 294
cleaning, 143, 336, 385
clinical diagnosis, 248
closed-loop, 73, 74, 76, 82, 83
clusters, 176
CMOS, viii, xi, xii, 69, 70, 71, 74, 76, 82, 84, 85, 88, 90, 91, 92, 93, 293, 294, 295, 324, 326, 327, 328, 329, 331, 334, 335, 336, 339, 340, 342, 344, 347, 348, 358, 383
CNN, 96, 100, 111, 113
cocaine, 250, 280
codes, 100, 101
coding, 100
cofactors, 131
cognitive, 377, 380, 382
cognitive function, 382
coherence, 309
collaboration, 402, 403
collateral, xii, 369, 372, 373
colors, 100, 103, 104, 107, 108, 355
communication, xiii, 87, 88, 384
compensation, 76, 78, 80, 82, 83, 235, 332
competition, 46, 268
compiler, 92
complexity, viii, xii, 45, 47, 48, 71, 84, 120, 338, 339, 357, 383
compliance, 260, 268, 324
complications, 382
components, vii, viii, x, 3, 20, 32, 36, 37, 38, 40, 43, 44, 46, 47, 48, 55, 87, 90, 97, 125, 135, 144, 227, 228, 235, 236, 239, 255, 263, 265, 266, 270, 271, 272, 274, 277, 286, 309, 339, 346, 347, 349, 370, 371, 402
composition, vii, 3, 4, 263, 264, 265, 267, 270, 272, 274, 277, 287, 291
compounds, xi, 119, 235, 241, 242, 246, 247, 251, 254, 256, 257, 259, 260, 262, 263, 264, 265, 266, 267, 268, 269, 270, 271, 272, 275, 276, 286, 287, 288, 290, 293, 392
computation, 219, 220, 235
concentration, xi, 126, 136, 144, 169, 170, 181, 198, 199, 205, 213, 235, 236, 238, 239, 241, 251, 256, 258, 265, 268, 271, 277, 293, 324, 325, 326, 327, 332, 333, 335, 337, 338, 339, 364, 398
conditioning, 71, 73, 296, 298, 299
conductance, 126, 131, 386, 390
conduction, xii, 92, 120, 161, 173, 179, 180, 182, 200, 344, 352, 356, 357, 358, 359, 360, 362, 383, 384, 388, 389, 391, 406
conduction block, 352, 356
conductive, ix, 115, 117, 121, 122, 127, 128, 144, 145, 148, 149, 150, 151, 152, 153, 163, 165, 166, 167, 168, 170
conductivity, ix, 17, 115, 117, 122, 128, 145, 147, 151, 153, 181, 274
confidence, 66, 251, 273, 324
confidence interval, 66
configuration, 76, 82, 124, 126, 134, 139, 141, 153, 176, 177, 294, 303, 309, 310, 311, 344, 384, 389, 399
conformity, 257
confusion, 406
connectivity, 133, 153, 169, 170
consensus, 175, 210
conservation, 130
constipation, 370, 377
constraints, 71, 82, 326
construction, 96, 344, 357
consumer protection, 268
consumers, 260, 262
consumption, 74, 81, 82, 258, 260, 261, 335, 339, 405
contaminants, 256, 270
contamination, 50, 235, 269, 270, 336
continuity, 18
contraceptives, 249
control, viii, 25, 32, 33, 69, 71, 72, 73, 85, 87, 90, 118, 119, 133, 143, 144, 149, 154, 186, 214, 215, 218, 231, 251, 254, 255, 260, 264, 265, 270, 274, 277, 282, 288, 332, 339, 352, 372, 374, 378, 379
control group, 374
controlled studies, 357
conversion, 70, 87, 88, 269, 331, 339
cooling, 163
copper, 30, 117, 153
coronary arteries, 350, 351
coronary heart disease, 263

correlation, 120, 145, 175, 179, 180, 181, 182, 210, 219, 223, 224, 255, 275, 283, 301, 302, 307, 313, 333, 337, 355, 374, 375
correlation analysis, 307
correlation coefficient, 333, 337
correlations, 180, 221, 223, 224
corridors, 108
corrosion, viii, 60, 70, 85, 118, 274
cosine, 243, 244, 306, 307
cosmic rays, xiii, 398, 400, 401, 402
cost-effective, 348
costs, xi, 46, 294, 295, 339
cotton, 302, 304, 320
coumarins, 266
coupling, 16, 18, 33, 35, 72, 73, 74, 83, 84, 89, 116, 125, 342, 362, 396
covalent, 119
covalent bond, 119
covalent bonding, 119
coverage, 216, 384
covering, 20, 26
cows, 261
CPU, 88, 230
CRC, 278
critical value, xiii, 405, 407
crops, 263
cross-sectional, 325
crosstalk, 72, 87
crude oil, 276
crystalline, 116, 126, 165, 168, 198, 200
crystalline solids, 168
crystallinity, x, 177, 185, 187, 197, 198, 200, 205
crystallization, 200, 210
crystals, 120, 126, 145, 149, 175, 177, 197
CSR, 39
culture, 86, 90, 365
curcumin, 263, 265
curing, 188
customers, 46, 52
cyanobacteria, 250, 280
cycling, 51, 359
cytochrome, 272
cytoskeleton, 349
cytosolic, 250, 364

D

DAD, 236, 246, 247, 248, 249, 251, 252, 253, 254, 255, 256, 257, 258, 259, 260, 261, 262, 263, 264, 265, 266, 267, 268, 269, 270, 271, 272, 273, 274, 275, 276, 277, 278, 280, 281, 284, 286, 288, 289
data analysis, 51, 67
data processing, 240, 340
data set, 56
database, ix, 95, 96, 103, 104, 107, 108
dating, 274
DCA, 276
*de novo*, 376
death, 364
deaths, 270
decay, 125, 131, 132, 141, 142, 144
decomposition, ix, 95, 96, 97, 109, 213, 214, 254, 274, 277
deconvolution, 169, 170, 171
deduction, 323
deep brain stimulation, 380
defects, 51, 116, 117, 120, 153, 176, 220, 223, 413
defibrillation, 344, 359, 360
definition, 242, 269, 356
degenerate, 181
degradation, x, 191, 192, 194, 195, 209, 210, 212, 213, 216, 219, 220, 223, 236, 250, 256, 258, 264, 275, 276, 280, 287, 412
degradation mechanism, x, 209, 210, 213, 216
degradation process, 191, 192, 210
degree of crystallinity, 199, 200
degrees of freedom, 32, 40
delivery, ix, 115, 133, 149
demand, 51, 106
dementia, 375, 377, 381
density, 49, 50, 58, 63, 117, 118, 120, 124, 131, 141, 145, 148, 175, 213, 217, 220, 296, 319, 415, 416
depolarization, 142, 343, 356
deposition, 119, 122, 124, 162, 163, 177, 185, 210, 384, 385
depressed, 356
depression, 249
deprivation, 350
derivatives, 117, 119, 252, 256, 263, 264, 265, 266, 267, 268, 271, 283
desorption, 123, 149
destruction, 380
detection, x, xi, xiii, 227, 228, 235, 239, 241, 246, 247, 248, 249, 250, 251, 252, 253, 254, 255, 257, 258, 259, 260, 261, 262, 263, 266, 267, 268, 269, 270, 271, 272, 273, 275, 277, 280, 281, 282, 283, 284, 285, 286, 287, 288, 289, 290, 291, 293, 294, 295, 308, 324, 325, 326, 329, 334, 335, 336, 338, 339, 342, 364, 405, 406, 407, 412, 416, 417
detection techniques, 228
deviation, 140, 175, 235, 239, 322, 337
dexamethasone, 260, 261, 285
diaphragm, 297
dielectric constant, 19, 29, 30, 33, 34, 39, 127, 172
dielectric function, 170
dielectric permittivity, vii
dielectrics, 4, 9, 30
diet, 263, 264
dietary, 264, 265
differential diagnosis, 375
differential equations, 4, 137
differentiation, 268, 271
diffraction, 188, 189, 229, 302
diffusion, 133, 147, 148, 176, 193, 210, 327, 377
diffusion time, 133
digestion, 265, 287
digitization, 347, 348

DiI, 334
dimensionality, 118
diode laser, 309
diodes, x, xiii, 20, 118, 128, 154, 227, 229, 230, 231, 393, 405, 407
dipole, 177
direct measure, 134, 405
direct observation, 118, 154
disability, 374
discharges, 140, 331
*Discovery*, 362
discrete data, 242
discrimination, 152, 274
disease model, 381
diseases, 250, 253, 257, 260, 295, 357, 381
disorder, xi, 116, 120, 149, 350, 369, 370, 374, 375
dispersion, 7, 8, 9, 10, 12, 13, 14, 18, 19, 23, 32, 36, 37, 40, 43, 277, 351, 352, 353, 354, 357, 363, 364
displacement, 134
distortions, 103
distribution, 47, 52, 54, 55, 56, 57, 60, 61, 63, 64, 65, 138, 152, 170, 172, 175, 181, 215, 298, 307, 314, 315, 317, 321, 352, 359, 363, 382, 412, 413
diuretic, 256
diuron, 276, 290
diversity, 96, 270
division, viii, 69, 70, 73, 74
donor, 406
dopamine, xii, 369, 372, 373, 376, 379, 380
dopamine agonist, 376
dopaminergic, 370, 372, 374, 376, 379, 381, 382
dopaminergic neurons, 370
dopant, 398
dopants, 181
doped, 123, 135, 162, 172, 229, 385
doping, ix, 115, 126, 127, 145, 147, 151, 201, 326, 327, 392
dosage, 269
dosing, 251
double bonds, 168
downsized, 295
drinking, 257, 260, 275, 276
drinking water, 257, 260, 275
drug abuse, 251
drug interaction, 270
drug safety, 267
drugs, xi, 228, 247, 248, 249, 251, 252, 253, 254, 257, 261, 270, 272, 273, 279, 280, 281, 289, 376, 377, 381, 382
Dry mouth, 377
drying, 300
durability, 215
duration, 89, 124, 136, 141, 211, 213, 343, 351, 352, 353, 357, 363, 364
duties, 261
dyes, xi, 266, 274, 287, 344, 360, 361
dysphagia, 370

## E

E. coli, 247
Eastern Europe, 341
economic problem, 268
economics, 370
efavirenz, 252
effluents, 275
egg, 261, 262, 285
elderly, 377, 380, 382
election, 324
electric charge, 231
electric circuit, 137, 138, 139
electric current, 132, 136, 137, 146
electric field, xiii, 4, 6, 16, 20, 128, 136, 143, 145, 146, 147, 148, 161, 162, 163, 168, 169, 173, 181, 213, 359, 405, 406, 407, 408, 409, 415, 417
electrical properties, 187, 197, 198, 200, 201, 205
electrical pulses, 70
electricity, 153
electrocardiogram, 351
electrochemical detection, 290
electrochemical reaction, 210
electrochemistry, 135
electrodes, xii, 70, 72, 85, 90, 91, 117, 122, 134, 135, 144, 145, 152, 153, 154, 162, 163, 164, 165, 168, 169, 175, 176, 177, 181, 186, 187, 202, 205, 344, 357, 359, 383, 384, 385, 387, 388, 389, 390, 392, 393
electroluminescence, 223
electrolyte, viii, 70, 89
electromagnetic, vii, xi, 3, 4, 5, 6, 9, 42, 293, 324, 326, 348
electromagnetic wave, 348
electromagnetic waves, 348
electromigration, 58, 59, 60, 63, 67
electromotive force, 129
electromyogram, 374
electron, xii, 116, 117, 119, 125, 126, 131, 133, 143, 147, 153, 154, 161, 163, 164, 165, 167, 168, 170, 171, 173, 174, 175, 177, 179, 180, 181, 203, 212, 225, 229, 302, 303, 320, 383, 384, 385, 386, 388, 389, 390, 392, 393, 406, 407, 409, 413, 415, 416, 417
electron beam, 164, 167
electron microscopy, 212, 214
electronic structure, 166
electron-phonon, 116, 412
electron-phonon coupling, 116
electrons, xiii, 117, 124, 129, 130, 141, 153, 161, 163, 164, 167, 169, 170, 173, 176, 179, 181, 229, 344, 384, 385, 388, 389, 405, 406, 407, 408, 409, 410, 412, 413, 414, 415, 416, 417
electrophoresis, 228, 252, 281
electrophysiological properties, 379
electrophysiology, 344, 357, 362
electroporation, 359, 360
ELS, 161

email, 155
emission, xii, 119, 165, 327, 339, 340, 345, 346, 347, 349, 361, 383, 397
encapsulated, 86, 219, 220
encephalopathy, 378
endocrine, 290
endurance, 186
energy, x, xiii, 4, 117, 124, 130, 132, 133, 134, 141, 143, 151, 152, 161, 162, 163, 164, 165, 166, 167, 169, 170, 172, 173, 174, 175, 176, 177, 178, 179, 180, 181, 182, 185, 214, 220, 335, 344, 388, 390, 405, 406, 407, 409, 412, 413, 414, 415, 416, 417
energy consumption, 335
energy transfer, 130
entropy, 350
environment, viii, xiii, 70, 86, 117, 143, 191, 241, 256, 275, 295, 385, 405
environmental factors, 314
enzymatic, 247
epicardium, 359
epilepsy, 273
epitaxial growth, 119
epitaxy, 119
epoxy, 86, 220
equilibrium, 132
equipment, 98, 103, 132, 133, 247, 275, 295, 310, 339, 348
erectile dysfunction, 273, 370
ergosterol, 273
Erk, 155
ESI, 263, 267
ester, 250, 269
esters, 269
estimating, 98
estriol, 275
estrogens, 275, 276
etching, 20, 203, 328
ethanol, 122
ethyl acetate, 267
Europe, 265
European Commission, 261
European Union, 257, 258, 259, 260, 261, 284, 285, 286
evaporation, 176, 200, 217
evolution, 166, 288, 363
exaggeration, 372
excitability, 363
excitation, 16, 92, 141, 162, 172, 176, 179, 181, 343, 345, 346, 347, 351, 360, 361, 362, 380, 416
excitatory mechanisms, 379
exciton, 168, 173, 175, 176, 177
execution, ix, 95, 108, 247
Exponential Distribution, 55
exposure, 176, 191, 192, 193, 194, 258, 298
extraction, 97, 102, 175, 187, 247, 255, 259, 265, 271, 273, 279, 280, 281, 284, 285, 289, 290, 291
extrapolation, 59, 60, 63
eyes, 104, 180

**F**

fabricate, 116, 202, 203
fabrication, xii, xiii, 35, 49, 70, 85, 116, 117, 118, 119, 120, 121, 122, 123, 144, 176, 185, 186, 195, 197, 205, 336, 339, 383, 384
factor analysis, 247, 254, 273, 277, 291
failure, 47, 49, 51, 52, 53, 54, 55, 56, 57, 58, 59, 60, 61, 62, 63, 64, 65, 66, 67, 191, 210, 217, 220, 270, 356, 360, 377
faith, 52
false negative, 103, 104
false positive, 103
family, 256, 260, 263
fat, 246, 261, 262
fat soluble, 246
fatty acid, 265, 269, 274
fatty acids, 269, 274
fax, 69
FCC, 25
FDA, 247, 252
February, 41, 42
feed additives, 259
feedback, viii, 69, 72, 73, 74, 82, 83, 84, 409
feeding, 259, 284
fenarimol, 273, 289
fermentation, 254
Fermi, 151, 152, 165, 175
Fermi level, 151, 152, 165, 175
FIB, 61, 62
fiber, xiii, 277, 344, 359, 395, 397, 398, 399, 400, 402
fibers, xiii, 359, 370, 371, 372, 376, 395, 396, 397, 398, 399, 400, 401, 402
fibrillation, 349, 350, 360, 362, 363, 364
film, x, 117, 119, 123, 128, 129, 130, 131, 132, 133, 135, 136, 137, 139, 141, 142, 143, 144, 147, 149, 150, 153, 165, 166, 168, 169, 170, 172, 176, 180, 187, 188, 189, 190, 192, 198, 200, 209, 210, 214, 216, 385, 388
film thickness, 388
films, 116, 122, 124, 131, 132, 133, 142, 143, 144, 149, 150, 163, 166, 167, 170, 172, 175, 176, 177, 180, 181, 188, 190, 198, 199, 200, 218, 336
filters, viii, 3, 18, 20, 23, 24, 25, 26, 27, 31, 41, 42, 43, 87, 100, 101, 141, 294, 321, 336, 346, 347, 348, 351
filtration, 289, 347
fingerprinting, 263, 265
fitness, 108
flatness, 33
flavone, 266
flavonoid, 263, 266, 267, 268, 288
flavonoids, 262, 263, 264, 267, 268, 286, 287, 288
flavor, 262
flexibility, 38, 188, 384
flight, 145, 416
floating, 21, 83

flow, ix, x, 4, 95, 96, 97, 98, 99, 103, 104, 113, 122, 124, 164, 168, 210, 212, 224, 227, 228, 229, 249, 277, 344, 355, 358
fluctuations, 220, 223, 348, 409
fluid, xi, 293, 295, 324, 325, 332, 336, 339
fluorescence, 143, 273, 284, 339, 340, 345, 346, 347, 349, 365
fluorinated, 119
fluoroquinolones, 246, 260, 284, 285
fluoxetine, 249, 250
fluvoxamine, 249, 250
focusing, 406
food, x, 227, 228, 235, 246, 256, 259, 261, 263, 264, 268, 269, 285, 286, 288, 339
*food commodities*, 268
food production, 259
food products, 235
foodstuffs, 257, 283
forensic, 246, 248, 272, 274, 289, 339
forestry, 275, 290
formaldehyde, 255, 282
Fourier, xi, 293, 294, 297, 298, 309, 314, 340, 350
Fourier analysis, xi, 293, 294
fragmentation, 267, 269
France, 44, 275, 341
free energy, 132, 133, 143
free rotation, 168
freedom, 32, 40, 120
freshwater, 276, 280
frontal cortex, 370, 371
fruit juice, 258, 269, 284
fruit juices, 258, 269, 284
fruits, 263, 264, 268, 286
fullerene, 392
functionalization, 118
fungicide, 258, 259, 273, 284
fungicides, 258, 262, 275, 284
fusion, 210
FWHM, 164, 407

G

GaAs, 407
GABA, xii, 369, 370, 371, 372, 373, 379
GABAergic, xii, 369, 372, 373
gait, 380
gamma-aminobutyric acid, 373
ganglia, xii, 369, 370, 371, 372, 373, 377, 380
ganglion, 100, 102
gas, 190, 192, 194, 214, 258, 275, 278, 280
gas chromatograph, 258, 275, 280
gasoline, 277, 291
gastric, 265, 273, 287, 378
gastrointestinal, 339, 340
gastrointestinal tract, 340
Gaussian, 315, 316, 317
generation, viii, 69, 83, 87, 97, 119, 145, 172, 173, 174, 176, 235, 253, 280, 384
genotype, 265
Ger, 156, 157, 392
Germany, 43, 44
gland, 377
glass, 74, 85, 106, 121, 123, 124, 131, 132, 141, 187, 188, 203, 213, 214, 220, 392
global competition, 46
globalization, viii, 45, 46
globus, xii, 369, 372, 373
glucoside, 268
glutamate, 370, 373, 379
glutamatergic, 372, 379
glycine, 370
glycosides, 267, 268, 270
goals, 134
goat milk, 258
gold, viii, 70, 85, 175, 176, 177, 181
gold nanoparticles, 176, 177
grain, 116, 117, 191, 192
grain boundaries, 116, 117
grains, 169, 203
Gram-negative, 260
Gram-positive, 260
grapes, 258, 262, 284, 286
graph, 25, 64, 193, 237
graphite, 153
grazing, 189
Greece, 227, 276
greenhouse, 266, 275, 290
ground water, 275, 290
groups, 117, 118, 119, 121, 122, 123, 124, 141, 142, 144, 197, 213, 248, 270, 276, 350, 357, 384, 385
growth, x, 119, 121, 123, 133, 163, 169, 177, 190, 200, 205, 209, 210, 213, 216, 217, 218, 219, 222, 223, 224, 246, 257, 259, 260, 261, 385
growth rate, 163, 190, 210, 217, 218, 219, 223, 224, 385
GSM, 38
guidance, 91, 103
guidelines, 247, 252, 253, 264, 271
gut, 265

H

half-life, 256
halogen, xii, 229, 329, 337, 347, 383
handling, 289, 295, 351
hands, 410
hanging, 88
hardness, 412
harm, 295
harmonics, 36
harvesting, 130, 132, 133, 147, 148, 149, 150, 152, 265
healing, 266
health, 257, 263, 264, 265, 286, 294, 370
health care, 294
health effects, 263

heart, xi, 263, 272, 343, 344, 346, 347, 349, 350, 351, 352, 353, 354, 355, 357, 358, 359, 360, 361, 362, 363, 364, 365
heart disease, 263, 364
heart failure, 362
heartbeat, 343
heat, 123, 149
heating, 49, 213, 265
heavy metal, 270
heavy metals, 270
height, 102, 103, 235, 310, 316, 317, 320, 326, 388, 412, 413, 414, 415
hemoglobin, 289
herbal, 251, 256, 262, 265, 267, 269, 270, 271, 280, 287, 288
herbal medicine, 262, 267, 269, 270
herbicide, 258, 275, 276, 290
herbicides, 275, 276
herbs, 271
heterogeneity, 143, 269
heterogeneous, 141, 142, 353, 362
heterostructures, 117, 119, 145, 154
hexane, 187
high resolution, 406, 417
high temperature, xiii, 58, 220, 262, 405
high-frequency, 350
high-level, 84
high-performance liquid chromatography, 254, 255, 258, 273, 275, 281, 282, 283, 286, 287, 290
high-speed, 74
hippocampal, 91
hips, 141, 144
HIV, 252
HIV-1, 253
HOMO, 118, 151, 154, 166, 388
homogeneity, 6, 7, 8, 228, 236, 273, 278
honey, 259, 284
hormones, 248, 290
horses, 253
hospitals, 335
host, 10, 14, 32, 39, 116
HPLC, x, xi, 227, 228, 231, 235, 238, 239, 241, 246, 247, 248, 249, 250, 252, 253, 254, 255, 256, 257, 258, 259, 261, 263, 264, 265, 266, 267, 268, 269, 270, 272, 273, 275, 276, 277, 278, 279, 280, 281, 285, 286, 287, 288, 289
HPLC-MS/MS, 265
human, 246, 248, 249, 250, 251, 252, 253, 256, 257, 258, 260, 261, 263, 265, 279, 280, 281, 282, 326, 337, 338, 339, 343, 344, 363
humans, 249, 259, 260, 272, 351
humidity, 192, 211, 313, 314
Hungarian, 95, 96, 105
Hungary, 95, 110
hybrid, 26, 27, 32, 33, 34, 35, 43, 93, 118, 121, 128, 130, 154, 415
hybrid cell, 26, 27
hybrid cells, 26
hybridization, 153
hybrids, 35
hydro, 186, 187, 252, 277
hydrocarbon, 290
hydrophilic, 186, 187, 252
hydrophobic, 186, 187
hydroxyl, 270, 276, 385
hydroxyl groups, 270, 385
hyperactivity, 375, 376, 379, 381
hyperfine interaction, 154
hyperplasia, 374
hypersensitivity, 376
hypnotic, 248
hypothalamic, 376
hypothalamus, 370, 371
hypothesis, 149, 177, 363
hysteresis, 152

I

IBM, 206
ICD, 363
identification, vii, x, xi, 227, 228, 232, 234, 235, 240, 241, 245, 246, 247, 248, 250, 252, 254, 255, 256, 257, 258, 259, 260, 262, 264, 266, 267, 268, 269, 270, 272, 273, 274, 276, 277, 278, 280, 287, 289, 290
identity, 228, 241, 256, 258, 259, 266, 271
idiopathic, 374, 377
IDS, 191, 204, 385, 386, 389, 390
Illinois, 115, 395
illumination, 100, 131, 132, 134, 135, 136, 143, 146, 148, 149, 152, 174, 309, 316, 317, 318, 335, 336, 337, 340, 342, 347
images, 101, 104, 111, 130, 188, 195, 196, 198, 199, 203, 216, 217, 220, 314, 320
imaging, xii, 307, 360, 361, 365, 369, 372, 378, 379, 417
implementation, 10, 14, 20, 26, 27, 32, 33, 37, 38, 91, 272
impurities, x, 120, 141, 176, 200, 201, 227, 229, 235, 236, 237, 238, 239, 251, 253, 254, 255, 256, 265, 277, 282
in situ, xii, 161, 369, 372
in vitro, viii, 69, 70, 73, 90, 91, 250, 252, 265, 287
in vivo, 70, 252, 359, 380
inactivation, 352
incidence, 189, 374
inclusion, 84
incubation, 250
indexing, 241
indication, 236, 241, 265, 268
indicators, ix, 95, 96, 97, 107, 108, 109, 344
indices, 265
indigenous, 256
indium, 124, 125, 135, 141, 210, 215
inductor, 26
industry, vii, x, 46, 49, 53, 55, 209, 218, 227, 251, 253, 314

inert, 85
infarction, 364, 379
infections, 260, 261
inflammatory, 267
inflammatory disease, 267
Information Technology, 95
infrared, x, 161, 162, 164, 173, 236
infrared light, 164, 173
inherited, 364
inhibition, xii, 218, 256, 263, 369, 372, 373, 379
inhibitor, 252, 253, 273, 281
inhibitors, 249
inhibitory, xii, 369, 372, 373, 376, 377
initial state, 194, 195
initiation, 125, 148, 355
injection, xii, 74, 83, 117, 127, 144, 145, 152, 154, 169, 172, 175, 177, 249, 253, 267, 273, 375, 376, 383, 384, 385, 388, 391, 392, 393
injections, 223, 389
injuries, 264
inorganic, 116, 118, 151, 154, 172, 176
InP, 176
insecticide, 276
insecticides, 258, 275
insertion, xii, 22, 24, 25, 30, 357, 383, 384, 385, 388, 389, 390, 391
insight, 116, 152, 154, 181, 350
inspection, 20, 38, 295
instability, 50, 96, 103, 107, 213, 353
institutionalization, 370
instruments, 230, 231, 238, 251, 256, 274
insulation, 399
insulator-semiconductor, 205
integrated circuits, vii, viii, 45, 51, 91, 92, 392
integration, 251, 254, 295, 339
integrity, 50, 122
intensity, ix, xi, 95, 99, 100, 101, 106, 110, 111, 166, 167, 169, 175, 176, 178, 179, 180, 187, 190, 199, 212, 213, 229, 230, 293, 295, 296, 298, 314, 315, 316, 317, 324, 325, 326, 331, 332, 334, 336, 337, 339, 340, 344, 347, 349
interaction, xi, 118, 150, 293, 324, 406, 412
interactions, 113, 270, 407, 412
interface, viii, xii, 50, 69, 71, 72, 85, 87, 88, 89, 92, 93, 117, 118, 120, 128, 134, 144, 146, 147, 151, 153, 154, 169, 170, 172, 173, 175, 176, 177, 181, 182, 191, 201, 205, 210, 213, 214, 216, 220, 223, 224, 230, 255, 273, 328, 383, 384, 385, 388, 391, 393
interfacial properties, 384
interference, 247, 275, 309, 311
intermolecular, 118, 119, 126, 152, 153, 161, 198
internalization, 348
internet, 46
interpretation, 18, 144, 240, 257, 283, 357
interval, 32, 50, 51, 66, 162, 220, 303, 304, 313, 323, 324
intoxication, 273, 289
intramuscular, 253
intramuscular injection, 253
intravenous, 253, 281
intrinsic, vii, ix, 115, 120, 121, 140, 145, 153, 176, 177, 181, 327, 406, 408, 413
inventors, 360
inversion, 358, 390, 391
ionic, 275, 351, 377
ionization, 262, 263, 267, 284, 406, 409, 412
ionization energy, 406
ionizing radiation, 405
ions, 405
IR spectra, 123
irradiation, 167, 175, 181
irradiations, 412
irrigation, 265
ischemia, 350, 353, 354, 355, 358, 359, 361, 362, 363, 364, 374
ischemic, 362, 364
ischemic heart disease, 364
island, 188
isoflavones, 263
isolation, 24, 33, 35, 256, 300, 348
isomers, 269, 283
isorhamnetin, 270
isotropic, 5, 9
Israel, 157
ITO, 128, 135, 136, 141, 142, 143, 203, 210, 211, 213, 214, 215, 216, 217, 218, 219, 223
I-V curves, 127, 222

## J

JAMA, 381
January, 40, 41, 42, 43, 341
Japan, 182, 278, 369, 381
Japanese, 159, 225, 381, 417
Joule heating, 49
Juices, 268, 288
Jun, 403
Jung, 156, 270, 288, 362, 396, 398, 400, 402

## K

kernel, 111
kidney, 260, 261, 262, 273, 285, 286
kidneys, 260, 284
kinetic energy, 161, 164, 169, 406, 407
kinetic studies, 116, 152
kinetics, ix, 115, 117, 132, 134, 140, 144, 145, 152, 154, 271, 352, 355, 359, 363
kinks, 178, 179
Kirchhoff, 137, 139
Korea, 185

L

labeling, 238, 269, 270
lamellae, 187
lamellar, 189
Langmuir, 157
Langmuir-Blodgett, 133
language, 87, 92
Laplace transforms, 137
large-scale, viii, 70
laser, 124, 133, 135, 136, 141, 146, 164, 166, 167, 225, 294, 296, 297, 298, 309, 310, 311, 312, 314, 315, 316, 317, 318, 320, 322, 338, 347, 358
lasers, 308, 310
lattice, 120, 406, 413
law, 325, 337
LC solutions, 232
lead, viii, xii, 27, 38, 45, 51, 56, 59, 73, 81, 103, 109, 116, 119, 154, 197, 210, 217, 220, 249, 268, 269, 270, 295, 340, 347, 355, 369, 372, 377
leakage, 163, 201, 406, 410, 411, 412
learning, 110
LED, ix, 95, 96, 97, 100, 101, 107, 108, 109, 296, 397, 398, 399, 400, 402
left ventricle, 364
left ventricular, 359, 364
left-handed, 40, 44
legislation, 256, 259, 261
legume, 264
lens, 297, 309, 314
lenses, 297, 309, 310
lesions, 360, 370, 372, 375
lettuce, 264, 286
leukoaraiosis, 380
levodopa, 370, 375, 376, 378, 381
Lewy bodies, 375, 377, 381
librarians, 266
Lidocaine, 254
life cycle, 52, 55
lifetime, x, 48, 49, 50, 52, 59, 74, 136, 209, 210, 216, 217, 218, 219, 220, 222, 223, 224
light beam, 135, 336
light emitting diode, 186
light scattering, 300
light-emitting diodes, 393
Light-induced, 142
limitation, 153
limitations, 143, 269, 310
linear, 111, 137, 139, 169, 179, 201, 202, 204, 221, 222, 239, 294, 296, 302, 304, 305, 314, 315, 317, 318, 320, 321, 337, 344, 360, 395
Linear Collider, 402
linkage, 355
liquid chromatography, 228, 246, 247, 253, 254, 255, 258, 260, 263, 267, 270, 273, 275, 277, 278, 279, 280, 281, 282, 283, 284, 286, 287, 288, 289, 290, 291
liquid crystal displays, 392
liquid nitrogen, 352
lithography, 188, 336
liver, 249, 260, 261, 262, 273, 285, 286
livestock, 260
localization, 356, 365
location, x, 80, 81, 88, 105, 106, 108, 109, 161, 172, 181, 295, 349
locus, 370, 371
locus coeruleus, 370, 371
logistics, 295
Lognormal Distribution, 64
London, 92, 113, 157, 158, 364
long-term, 71, 257, 264, 376
losses, 22, 24, 25, 30, 31, 417
low power, 71, 74, 82, 405
low temperatures, 153, 384
lowest unoccupied molecular orbitals, 154
low-level, 97
low-power, 93, 117
low-temperature, 185
lubrication, 118
lumbar, 371
lumen, 265
luminescence, 209, 213
LUMO, 118, 151, 152, 154, 175, 388
lutein, 269
lycopene, 269
lying, 64

M

macrolide antibiotics, 261
Madison, 115
magnesium, 325
magnetic, vii, 3, 4, 6, 16, 44, 236, 249, 282, 364, 395, 396, 406, 416
magnetic field, 4, 16, 395, 396, 406, 416
magnetic resonance, 282
mainstream, 144
maintenance, 350, 379
malignant, 340, 353
Mammalian, 113
management, xii, 369, 377, 381, 382
manifold, 152
manipulation, 238, 243
manufacturer, 230
manufacturing, viii, 45, 46, 228, 265
mapping, vii, xi, 9, 111, 343, 344, 345, 346, 347, 348, 350, 351, 352, 356, 357, 358, 359, 360, 361, 365
maprotiline, 250
marine environment, 290
market, viii, 45, 46, 261, 262, 263
mask, 84, 186, 202, 303, 314, 385
mass spectrometry, 250, 253, 254, 255, 262, 263, 267, 270, 273, 275, 278, 280, 282, 284, 287, 288, 290
Massachusetts, 91, 92, 93

matrix, x, 49, 61, 62, 102, 103, 111, 123, 137, 139, 145, 148, 150, 227, 228, 240, 257, 259, 264, 275, 276, 277, 348, 349
Maximum Likelihood, 66
measurement, xi, 35, 74, 83, 86, 87, 90, 91, 93, 121, 125, 128, 131, 134, 136, 138, 148, 149, 161, 162, 163, 164, 165, 166, 167, 168, 169, 172, 173, 181, 182, 219, 220, 223, 229, 243, 293, 294, 295, 296, 298, 299, 300, 301, 309, 319, 321, 323, 324, 325, 332, 333, 335, 336, 337, 338, 339, 350, 360, 397, 399, 406, 411
measures, 135, 140, 209, 230, 231, 283, 306, 370
meat, 260, 272, 289
MED, 56, 57, 61
media, vii, 3, 4, 5, 6, 9, 16, 120, 362
median, 55, 304
mediators, 172
medication, 375, 376
medicinal plants, 270, 288
medicine, 246, 250, 258, 262, 265, 266, 267, 270, 374, 416
memory, 88, 230, 231
MEMS, 20, 69, 85, 93
men, 249, 374, 375, 379
menadione, 248
metabolic, 251, 253, 280
metabolism, x, 227, 228, 246, 249, 250, 280, 281
metabolite, 246, 248, 249, 250, 252, 257, 258, 272, 273, 275, 279, 280, 282, 283, 290
metabolites, 247, 248, 249, 250, 251, 252, 253, 258, 272, 275, 276, 279, 280, 281, 284, 287, 289, 290, 375
metabolomics, 247
metal nanoparticles, 177, 182
metal oxide, xii, 383, 392
metal-oxide-semiconductor, 70
metals, 4, 26, 85, 122, 175, 176, 177, 187, 215, 388
methanol, 270
methyl group, 276
metric, 350
Mexican, 267, 288
Mexico, 91, 267
microalgae, 280
microbial, 250, 270
microdialysis, 372, 380
microelectrode, viii, 69, 70, 71, 72, 73, 74, 81, 85, 90, 91, 92, 93
microelectrodes, 73, 92, 343, 358
microelectronic technologies, 20
microelectronics, viii, 3
microflora, 258, 280
micrometer, 135, 316
microprocessors, 88, 241
microscope, 198, 203, 211, 216, 220, 302, 303, 320
microscopy, 212, 217
microstructure, 187, 188
*microsystem*, 295, 324, 328, 329, 332, 334, 335, 336, 339, 340, 342
microwave, vii, 3, 4, 5, 6, 20, 32, 36, 40, 41, 42, 43, 44
microwave radiation, vii, 3
midbrain, 370, 371
migration, 50, 132, 133, 210, 213, 215, 218, 223, 225, 229, 240
milk, 246, 258, 259, 260, 261, 262, 283, 284, 285
milnacipran, 249
mimicking, 118
miniaturization, 6
Ministry of Education, 182
Minnesota, 155
minority, 135, 141
mirror, 81, 130, 229
misconception, 51
misconceptions, vii, viii, 45, 67
misleading, 272
misunderstanding, 55
mixing, 337
mixture analysis, 254
MLE, 119
mobile phone, ix, 95, 96, 97, 98, 102
mobility, ix, xii, 115, 116, 117, 119, 120, 125, 126, 127, 128, 145, 146, 148, 149, 150, 151, 152, 153, 167, 169, 173, 179, 180, 181, 185, 186, 187, 188, 190, 191, 193, 194, 197, 200, 201, 202, 204, 205, 258, 383, 386, 388, 390, 392
model system, 133
modeling, 71, 72, 89, 92, 412
models, 6, 7, 8, 41, 67, 101, 151, 247, 277, 364
modulation, 76, 79, 81, 162, 194, 263
modules, viii, 69
moieties, 260
mold, 188
molecular orbitals, 152
molecular structure, 117, 197, 253, 267
molecular weight, 265, 267
molecules, 117, 118, 119, 126, 127, 128, 129, 130, 131, 132, 133, 135, 141, 142, 143, 144, 147, 148, 149, 150, 152, 162, 163, 168, 169, 177, 192, 193, 200, 260, 325, 326, 346, 347
monkeys, 379
monochromatic light, 129
monochromator, 124, 329, 333
monolayer, xi, 72, 118, 123, 128, 133, 144, 151, 169, 170, 198, 202, 344, 345, 357
monolayers, vii, ix, 115, 123, 124, 133, 346, 350, 365
monomeric, 270
Monte Carlo, 365
Moon, 205, 224
Morocco, 342
morphine, 250
morphology, x, 119, 185, 192, 197, 198, 200, 205, 225, 343, 351, 353, 392
MOS, 74, 76, 79, 84
motion, 98, 100, 109, 110, 120, 152, 173, 349, 361
motivation, 117
mouse, 249, 252, 281, 362

movement, 215, 218, 247, 349, 361, 370
MPTP, 372
MRI, 378
mRNA, 372
MRS, xiii, 395, 396, 397, 398, 399, 400, 401, 402, 403
multiple factors, 375
multiplexing, viii, 69, 70, 72, 73, 74, 81, 347, 349
multiplication, xiii, 130, 396, 405, 407, 408, 409, 410, 411, 412, 416, 417
multiplier, 103
multivariate, 274
muscle, 248, 259, 260, 261, 262, 283, 284, 285, 286, 358, 359, 360, 361
muscle relaxant, 248
muscle tissue, 260, 262, 286
mutants, 254
myocardial infarction, 360
myocardial ischemia, 364
myocardium, 343, 360, 361
myocyte, 359, 365
myocytes, xi, 343, 365
myoglobin, 272
myricetin, 253, 281

N

NaCl, 88
NAD, 131
nanodevices, ix, 116
nanoparticles, 133, 176, 177, 181, 182
Nanyang Technological University, 45, 56, 57, 61
naphthalene, 117, 119, 126, 256
narcotic, 272
NASA, 419
Nash, 363, 419
*national*, 271
natural, vii, 3, 4, 100, 105, 106, 126, 128, 130, 240, 263, 264, 266, 269, 271, 287
neck, 375
neglect, 76, 137, 138, 139
nematic, 195, 196
neonatal, 365
nephrotoxic, 270
nerve, 70, 71, 72, 89, 90, 92, 370, 371
nerve cells, 70, 71
nervous system, 70, 100, 369, 370, 382
network, 27, 28, 72, 133, 142
neural network, 113
neural systems, 350
neurogenic, 375, 380, 381
neurogenic bladder, 381
neuroimaging, xii, 369, 370, 372
neurological disability, 374
neuronal loss, 375
neurons, viii, 70, 71, 74, 88, 89, 90, 91, 101, 370, 372, 373, 378, 379
neuropharmacology, 382
neurophysiology, 89
neuropsychiatric disorders, 370
neuroscientists, 70
neurotransmission, 382
neutralization, 132
neutrons, 412
New Jersey, 278
New York, 40, 43, 91, 92, 113, 157, 158, 207, 278, 340, 342, 343, 360
Newton, 359, 364
Nielsen, 206, 207, 379, 381
nigrostriatal, 372, 375, 379
NIST, 420
nitrate, 328
nitride, 123, 327
nitrogen, 150, 188, 352, 385
NMDA, 379
nocturia, 374, 376, 381
nodes, 83
noise, x, 71, 73, 74, 76, 79, 80, 82, 86, 87, 88, 91, 161, 164, 210, 219, 220, 221, 223, 224, 225, 227, 229, 231, 238, 239, 240, 277, 296, 348, 401, 406, 407, 409, 410, 411, 417
non invasive, 70, 71, 296, 306, 338
nonlinear, 41
non-magnetic, vii, 3, 4
nonsmokers, 249
norepinephrine, 375
norfloxacin, 253, 258, 260, 261
normal, xii, xiii, 49, 50, 55, 56, 57, 58, 59, 63, 96, 105, 149, 164, 187, 190, 198, 212, 217, 251, 337, 343, 345, 351, 353, 354, 355, 369, 370, 372, 376, 379, 405, 407, 417
normal conditions, 149
normal distribution, 55, 56, 57
normalization, 238, 242
Northeast, 92
novelty, 294
n-type, 117, 119, 121, 122, 123, 127, 128, 144, 151, 161, 229, 384, 385, 386, 388, 390, 393, 406
nuclear, 92, 236, 249, 282, 364, 416
nuclear magnetic resonance, 187, 236, 249, 254, 255, 364
nuclei, xii, 369, 372, 373
nucleus, xii, 270, 276, 369, 370, 371, 372, 373, 378, 380
nutritional supplements, 257

O

object recognition, 96, 109
observations, 108, 210, 213, 217, 303, 356, 417
obstruction, 374, 375
occlusion, 379
ofloxacin, 253, 260, 261
Ohmic, 182
oil, 265, 276, 277, 377
oils, 265, 287

oligomer, 117, 197
oligomers, 197, 236
olive, 265, 287
olive oil, 265, 287
olives, 265
on-line, 156, 157, 263, 272, 280, 289, 290, 295, 306, 338
opacity, 302
operator, 239
opiates, 273
opioids, 252, 273, 280, 289
opium, 273, 289
opposition, 100, 101, 103, 104, 108
optical, vii, xi, xiii, 4, 5, 113, 124, 125, 143, 152, 164, 172, 174, 176, 188, 195, 198, 199, 203, 217, 220, 230, 293, 294, 295, 296, 297, 298, 300, 301, 308, 309, 310, 311, 313, 314, 316, 318, 320, 324, 325, 326, 327, 329, 332, 334, 335, 336, 339, 340, 342, 344, 346, 347, 348, 349, 350, 351, 352, 353, 355, 356, 357, 358, 359, 360, 361, 365, 395, 396, 397, 398, 399, 402, 412, 416
optical imaging, 309, 359
optical properties, 143, 327
optical systems, xi, 344
optical transmission, 327
optics, 277, 295, 327, 340, 342
optimization, 152, 205, 247, 252
optoelectronic, xii, 154, 223, 383
optoelectronic devices, 223
oral, 249, 251, 252, 253, 280, 281, 282, 376
oral contraceptives, 249
organ, 378
organic, vii, ix, x, xii, 115, 116, 117, 118, 119, 120, 121, 123, 125, 128, 133, 135, 136, 137, 139, 144, 145, 147, 148, 149, 152, 153, 154, 161, 162, 165, 168, 172, 173, 175, 176, 177, 178, 181, 182, 185, 186, 187, 188, 190, 191, 197, 198, 200, 202, 203, 205, 209, 210, 211, 217, 218, 219, 220, 253, 254, 383, 384, 388, 389, 392, 393
organic compounds, 153
organic polymers, 118
organic solvent, x, 178, 185, 186, 187, 197
organic solvents, 178, 187, 197
organization, 46, 362
orientation, xi, 168, 187, 190, 198, 293, 294, 307, 322, 344, 359, 360, 362
oscillation, 320
oscillations, 332, 354, 355, 356, 359, 413
oscillator, 81
outsourcing, viii, 45, 46
overload, 72
oxidation, 131, 133, 246, 276, 290
oxidation products, 246
oxidative, 265, 287
oxide, xi, 50, 123, 125, 135, 141, 142, 162, 163, 187, 210, 294, 327, 328, 329, 330, 331
oxides, 122
oxygen, 117, 150, 192, 193, 210, 276, 350

P

pacing, 353
packaging, viii, 49, 50, 70, 71, 86, 90, 339
paclitaxel, 252, 281
PAHs, 276
pain, 252
pancreatic, 265, 287
paper, ix, 43, 44, 64, 93, 95, 96, 98, 109, 113, 145, 223, 272, 392
parallelism, 4
parameter, 32, 109, 132, 148, 257, 314, 316, 346, 347, 385
parasympathetic, 370, 371, 375
paraventricular, 371
paraventricular nucleus, 371
Paris, 44, 341, 358
Parkinson, xi, xii, 369, 370, 377, 378, 379, 380, 381, 382
parkinsonism, xii, 369, 372, 375, 380, 381
paroxetine, 249, 250
particle detectors, 406
particles, vii, xiii, 3, 4, 16, 17, 181, 212, 405, 406, 408, 412, 417
partition, 377
passivation, 193
passive, 81, 89, 181
pathogenic, 257
pathology, 378
pathophysiological, 364
pathophysiology, 375, 377, 382
pathways, 100, 101, 380
patients, xi, xii, 228, 251, 252, 364, 369, 370, 372, 373, 374, 375, 376, 377, 378, 379, 380, 381, 382
pattern recognition, 108
patterning, 186, 187
PCA, 254, 255
PDAs, 231, 277, 344, 347, 348, 349, 350, 351, 357
PDMS, 86, 188
pedestrians, 98
pelvic, 370, 371, 378
penicillin, 245, 248, 276, 279
perception, 46
percolation, 150
performance, vii, ix, x, xiii, 3, 6, 24, 26, 29, 30, 31, 33, 34, 40, 46, 74, 76, 90, 115, 116, 117, 119, 120, 149, 152, 153, 154, 161, 185, 187, 197, 205, 223, 225, 228, 246, 247, 251, 254, 257, 259, 261, 263, 264, 267, 277, 278, 279, 281, 282, 283, 284, 286, 288, 289, 290, 295, 333, 339, 384, 385, 391, 393, 395, 396
perfusion, 350, 354
periodic, 4, 20, 26, 29, 30, 36, 362
periodicity, 6, 29
Peripheral, 376
permeability, vii, 3, 4, 6, 10, 14, 16, 40, 41
permit, 309
permittivity, vii, 3, 4, 6, 10, 14, 16, 40, 127

perylene, 117, 147
pesticide, 247, 256, 257, 258, 275, 283
pesticides, 248, 257, 258, 270, 275, 276, 279, 283, 284, 289, 290
PET, 379, 416
PET scan, 416
petroleum, 277, 291
PGN, 375
pharmaceutical, x, 227, 246, 248, 251, 253, 281, 283
pharmaceutical companies, 251
pharmaceutical industry, x, 227, 251, 253
pharmaceuticals, 235, 248, 269, 270, 279
pharmacokinetic, 248, 251, 252, 253, 256, 281
pharmacokinetic parameters, 252
pharmacokinetics, x, 227, 228, 253, 280, 281, 282
pharmacological, 256, 267
phase transitions, 152
phenol, 267
phenolic, 246, 262, 263, 264, 265, 267, 268, 269, 271, 280, 286, 287, 288
phenolic acid, 246, 262, 268, 286
phenolic acids, 246, 262, 268, 286
phenolic compounds, 262, 263, 267, 268, 269, 271, 286, 288
phenytoin, 249, 252
Philadelphia, 41, 69, 340, 342
phone, ix, 69, 95, 96, 97, 98, 102, 109
phonon, 120, 169, 170
phonons, 412
photobleaching, 347, 348
photocells, 230
photochemical, 167, 213
photoconductivity, 172, 177
photodegradation, 210
photodetectors, 396
photoelectron spectroscopy, 161
photoemission, 117, 154
photoexcitation, 176, 179
photolithography, 186, 202, 203
Photoluminescence, 212, 213, 224
photon, 166, 167, 175, 176, 177, 178, 179, 180, 347, 416
photonic, 344
photons, 124, 162, 164, 167, 168, 173, 179, 180, 326, 347, 406, 417
photooxidation, 130, 131, 151
photopolymerization, 167, 168
photoresponse, 132
photosynthesis, 130
photosynthetic, 133, 135, 143
photovoltaic, ix, 115, 118, 119, 121, 129, 130, 135, 141, 144, 146, 148, 149, 153, 167
photovoltaic cells, 118, 121, 130, 144
phylum, 89
physical mechanisms, 191
physical properties, 177
physical world, 101
physicians, 340
physicists, 153
physicochemical, 118
physicochemical properties, 118
physics, 59, 120, 144, 155, 224, 395, 416, 420
physiological, 340, 346, 347, 364
phytochemicals, 263, 271
phytotherapy, 264
pig, 250, 259, 260, 284, 350, 351, 352, 358, 360, 361, 362, 364
pigments, 263, 265
pigs, 259, 363
pitch, 195
planar, vii, viii, 3, 6, 9, 10, 27, 33, 40, 41, 69, 70, 73, 74, 85, 90, 93, 153
plane waves, 4
plants, 253, 262, 263, 266, 270, 286, 288
plasma, 187, 248, 249, 250, 251, 252, 253, 280, 281, 282
plasmons, 169
plastic, 408
platelet, 263
platelet aggregation, 263
play, 10, 109, 172, 175, 220, 262, 327, 357
PMMA, xii, 383, 384, 385, 391
Pointing vector, 5
poisoning, viii, 70, 85
poisonous, 266
Poisson, 407
polarity, 130, 134, 141, 147, 274
polarization, 6, 120, 141, 142, 146, 310
polling, 88
pollutants, 276, 290
poly(dimethylsiloxane), 188
polycarbonate, 188, 190
polycrystalline, 175, 177, 180, 181
Polydimethylsiloxane, 86
polymer, x, xii, 167, 168, 186, 188, 189, 197, 200, 209, 210, 213, 214, 215, 216, 217, 218, 223, 224, 225, 383, 392
polymer chains, 189
polymer film, 200
polymer films, 200
polymer materials, x, 209, 210
polymer systems, 200
polymerization, 167, 168, 181
polymers, 118, 186, 187, 189, 210
polymethylmethacrylate, xii, 383
polyphenols, 264, 265, 270, 272, 286, 287, 288
pons, 379
poor, 46, 64, 177, 185, 220, 229, 235, 243, 326, 374, 388
population, 66, 91, 256
pores, 198
pork, 272
portability, 309, 332, 335
ports, 23, 24, 27, 32, 33, 35
Portugal, 293
positive feedback, 409
postmortem, 272, 273, 289
postural hypotension, 370

poultry, 259
powder, 263
power, viii, 3, 20, 33, 36, 38, 39, 44, 71, 74, 81, 82, 88, 129, 132, 164, 220, 230, 296, 297, 309, 310, 322, 333, 339, 348, 405, 411, 417
powers, 310, 312
pre-clinical, 252, 378
prediction, 219, 223
prefrontal cortex, 370, 371
prepolymer, 188
pressure, 250, 254, 262, 270, 294, 343, 375, 385
presynaptic, 382
principal component analysis, 254, 282
printing, 185, 186, 188, 190, 195, 198, 203
prior knowledge, 237
pristine, 167, 391
private, 107
probability, 45, 47, 60, 63, 64, 65, 96, 103, 107, 116, 169, 224, 260, 294, 322, 389, 412, 416
probability density function, 63
probe, 71, 92, 118, 125, 128, 134, 135, 136, 137, 138, 139, 140, 141, 142, 144, 154, 358
procyanidins, 270
producers, 271
production, 45, 46, 55, 254, 258, 260, 406, 412
progesterone, 247, 275
program, 87
proliferation, 219
promote, 260, 262
propagation, 4, 71, 90, 307, 358
property, 4, 134, 140, 187, 198, 247, 373, 408
proportionality, 142, 299, 320, 339
prostate, 374, 380
prostheses, 96
protection, 152, 263, 268, 327
protein, 252, 325, 326, 337, 339
proteins, 272
protocol, 119, 128, 290, 337
protocols, 251
protons, 412
prototype, viii, 3, 25, 28, 29, 33, 69
protozoan parasites, 260
PSD, 220, 221, 222, 223
pseudo, 99
PTA, 248
p-type, 122, 128, 144, 151, 169, 229, 384, 385, 386, 388, 406
public, 107, 262
public health, 262
pulse, 89, 90, 124, 136, 146, 231, 331, 398, 405, 412, 413, 415
pulses, 132, 135, 141, 332, 334, 398, 406, 408, 410, 413, 416
pumps, 343
purification, 187, 223, 259, 385
PVA, xii, 383
PVC, 121, 128
PVN, 371
PVP, 198, 199, 203, 205
pyrimidine, 273

Q

QRS complex, 351
quality assurance, 228, 240
quality control, x, 134, 227, 228, 235, 248, 266, 267
quality of life, xi, 369, 370, 377
quantum, xi, 129, 131, 294, 295, 326, 327, 329, 330, 396, 405, 407, 416
quartz, 163, 187, 229, 329
quasi-periodic, 4, 109
quercetin, 264, 267, 268, 270
*Quercus*, 271
questionnaire, 374, 376
questionnaires, 374
quinolone antibiotic, 253, 260

R

RAC, 67
race, 250
radiation, vii, xi, 3, 4, 16, 230, 277, 293, 309, 324, 326, 332, 406, 412, 416, 420
radiation detectors, 406
radical, 134
radio, 46
radiofrequency, vii, 3, 6, 360
radiofrequency ablation, 360
radiological, 412
radius, 19, 24, 26, 39, 103, 315, 316, 359
rail, 90
Raman, 167, 262
Raman spectra, 167
random, 132, 148, 190, 307, 313, 328, 407, 409
random walk, 132, 148
range, viii, x, 3, 5, 6, 14, 20, 70, 78, 87, 90, 103, 118, 123, 127, 130, 137, 138, 141, 143, 144, 147, 150, 178, 179, 195, 200, 220, 227, 229, 230, 239, 246, 250, 252, 259, 262, 263, 267, 268, 269, 274, 277, 296, 299, 307, 313, 315, 323, 325, 326, 329, 330, 337, 348, 384, 388, 407, 413, 415, 416, 417
rat, 251, 252, 253, 281, 282, 360, 361, 364, 365, 378, 379, 381
rats, 251, 253, 280, 281, 379, 380
reaction center, 135
reactive ion, 123
reactivity, 168, 181
reading, 324
reagent, 295, 325, 332, 337
reagents, 270, 295, 325, 335, 337
real time, 231
reality, 59
recall, 46
recalling, 231
reception, 24
receptive field, 101, 102, 103

receptor agonist, 379
receptors, 370, 375, 376, 377, 379, 380, 382
recognition, x, 96, 108, 109, 227, 228, 255
recombination, 116, 131, 133, 134, 140, 142, 143, 144, 146, 406
recombination processes, 146
reconstruction, 358
recovery, 141, 142, 265
red light, 173, 327
red wine, 248, 267, 271, 288, 289
redistribution, 136, 141
redox, ix, x, 116, 125, 130, 131, 133, 134, 142, 147, 148, 149, 150, 152, 153
reduced bladder capacity, 374
reduction, 38, 132, 213, 242, 295, 301, 309, 316, 318, 320, 326, 349, 361
reference frame, 98, 99
reflection, 155, 311, 325, 327
refractive index, 4, 40, 277, 291, 300
regional, 359, 363
regular, 275, 335, 336, 356
regulation, 258, 284, 285
rejection, 26, 299
relationship, 77, 79, 80, 152, 173, 181, 188, 200, 219, 242, 244, 321, 338, 350, 353, 355, 373, 374
relationships, 70, 116, 350
relaxation, 135, 137, 343, 370, 374
relaxation time, 135, 137
reliability, vii, viii, 45, 46, 47, 48, 49, 50, 51, 52, 53, 54, 55, 56, 57, 59, 60, 61, 63, 65, 66, 67, 105, 106, 185, 223, 224, 225, 240, 272, 302, 335, 339
remodelling, 362
renal, 270
reperfusion, 355, 358, 359, 364
repolarization, 343, 344, 351, 352, 353, 357, 359, 361, 363, 364
reproduction, 88
research, viii, 5, 70, 71, 72, 90, 116, 118, 120, 126, 144, 145, 154, 182, 210, 215, 218, 219, 223, 224, 228, 248, 251, 256, 357, 384
researchers, 5, 82, 247, 412
residuals, 254, 255, 374, 375, 376, 377
residues, 246, 247, 256, 257, 258, 259, 260, 261, 262, 283, 284, 285, 286
resin, 86
resins, 274
resistance, 85, 135, 136, 140, 141, 142, 149, 181, 202, 204, 257, 296, 410
resistive, 72, 74, 82, 396
resistivity, 30, 153, 389, 407
resolution, 96, 97, 103, 107, 108, 132, 143, 149, 169, 230, 235, 236, 238, 247, 251, 253, 254, 257, 277, 282, 299, 314, 329, 338, 344, 347, 348, 350, 361, 405, 406, 407, 416, 417
resonator, 14, 28, 41, 42
resources, 59
respiratory, 253
response time, 195, 295, 347
restitution, 359, 361, 363
retardation, 374
retention, x, 227, 228, 231, 233, 236, 239, 240, 241, 250, 253, 255, 256, 257, 259, 262, 263, 264, 265, 266, 268, 269, 271, 272, 275, 276, 378
retina, ix, 95, 96, 97, 100, 101, 102, 105, 106, 109, 113
retinoids, 249
retinol, 248
returns, 192, 194
rhamnetin, 270
rheological properties, 268
Rhode Island, 91
rhythm, 345, 355
rhythms, 345, 364
right ventricle, 361
rings, 4, 16, 20, 21, 26, 31, 39, 41, 42, 119, 200
ripeness, 265
RISC, viii, 70, 87
risk, 46, 261, 263, 363, 364
risks, 270
RNA, 379
robotics, 96
robustness, 74, 154
ROI, ix, 95, 96, 105, 108, 109
room temperature, 119, 120, 130, 147, 153, 176, 385, 407
room-temperature, 119
roughness, 214, 216, 217, 328
Rouleau, 419
routing, 84
Royal Society, 340
RP-HPLC, 268, 270, 286, 290
rubber, 188, 190, 194, 195

S

safety, 258, 269, 295, 382
saliva, 251, 280, 295
salts, 274
sample, x, xi, 49, 50, 52, 53, 55, 64, 65, 66, 122, 136, 140, 141, 144, 145, 146, 149, 162, 163, 164, 167, 168, 177, 178, 179, 180, 181, 190, 221, 222, 227, 228, 230, 231, 233, 236, 238, 240, 241, 242, 246, 247, 254, 255, 257, 259, 260, 266, 270, 275, 276, 277, 289, 293, 295, 298, 304, 308, 309, 311, 319, 320, 321, 324, 325, 332, 337, 339
sampling, 88, 141, 275
saponin, 263
saponins, 267, 287
sapphire, 141, 164
satisfaction, 46
saturated fat, 269
saturated fatty acids, 269
saturated hydrocarbons, 277
saturation, 76, 78, 79, 90, 124, 127, 169, 192, 193, 201, 202, 294, 299, 315, 338, 348, 386, 390
scalar, 101, 111
scaling, 99, 100, 111, 112, 239

Scanning electron, 203
scanning electron microscopy, 214
scatter, 221, 222
scattering, 169, 188, 300, 303
schema, 91, 397, 398
schizophrenic patients, 252
Schmid, 207, 392
scientists, 145
scintillators, 342, 398, 406, 408
scores, 254, 255
search, 116, 235, 241, 254, 256, 274, 275
searches, 231, 232
searching, 235, 242, 255, 257, 273
Seattle, 40
seawater, 90, 276, 290
sedative, 248
sediment, 276
seed, 263
selecting, x, xi, 185, 205, 294
selectivity, 23, 252, 260, 261, 262, 267, 273, 274
self-assembling, 118, 120, 133
self-assembly, ix, 115, 119, 122, 128, 153, 154
self-ordering, 118
SEM, 59, 62, 203, 214, 329
semiconductor, x, xi, xii, xiii, 116, 117, 119, 125, 129, 133, 135, 136, 141, 143, 151, 152, 153, 163, 176, 177, 181, 185, 186, 187, 198, 200, 201, 202, 203, 205, 227, 229, 230, 294, 326, 327, 336, 347, 358, 383, 384, 385, 388, 405, 406, 409, 417
semiconductors, 116, 117, 118, 119, 120, 125, 162, 168, 172, 177, 182, 186, 197, 205, 229, 342, 384, 393
sensation, 376
sensing, 71, 73, 74, 81, 85, 89, 118
sensitivity, 86, 144, 149, 152, 165, 235, 239, 240, 252, 267, 273, 277, 278, 296, 314, 318, 334, 338, 347, 396
sensors, viii, x, 69, 70, 72, 73, 74, 85, 92, 153, 168, 227, 229, 308, 339, 342, 344
sensory symptoms, 370
separation, 19, 26, 31, 39, 63, 72, 125, 130, 136, 142, 143, 228, 231, 232, 239, 241, 246, 247, 248, 253, 254, 255, 266, 272, 276, 278, 297
sequencing, 81
series, 6, 10, 11, 14, 15, 17, 18, 20, 23, 26, 27, 29, 32, 36, 37, 38, 44, 47, 110, 202, 247, 278, 343, 410
serotonin, 249
sertraline, 249, 250
serum, 248, 249, 250, 252, 281
services, 294
severity, 374
sewage, 275
sex, 290
sex hormones, 290
shade, 99, 354
shape, xi, 4, 55, 103, 212, 236, 241, 293, 294, 315, 325, 339, 346, 396, 400
shaping, 410, 411
shear, 99, 111, 112
sheep, 362
shocks, 344, 359
shoot, 287
shortage, 117
Short-term, 378
shoulder, 166, 167, 169, 216, 235
Si3N4, 122
side effects, 248, 269, 270, 377
sign, 4, 5, 13, 99, 102, 103, 104, 105, 109, 151
signal transduction, 93
signals, viii, xiii, 24, 25, 69, 70, 72, 73, 74, 87, 88, 90, 91, 92, 133, 141, 231, 247, 300, 304, 308, 311, 312, 313, 316, 320, 322, 323, 338, 344, 348, 349, 350, 351, 355, 401, 405, 408, 409, 412, 413, 414, 415, 416
signal-to-noise ratio, viii, 70, 239, 344, 347, 348
signs, ix, 27, 95, 96, 97, 102, 103, 104, 105, 108
sildenafil, 289
silicon, xi, 30, 116, 119, 120, 122, 123, 128, 129, 130, 131, 133, 134, 135, 136, 141, 142, 143, 144, 145, 149, 151, 153, 185, 229, 294, 326, 327, 328, 331, 342, 384, 385, 396, 406, 407, 409, 412, 413, 415, 416
siloxane, 123, 133, 143
silver, 122, 128, 129, 130, 132, 214
similarity, 100, 173, 235, 237, 238, 239, 240, 241, 242, 243, 244, 245, 262, 271, 306, 338, 350
simulation, 31, 35, 91
simulations, 22, 327, 328, 350, 361, 365
sine, 244, 307, 308
Singapore, 40, 209, 225
single crystals, 172, 225
singular, 277, 294, 296, 313
SiO2, 121, 122, 123, 124, 127, 142, 144, 162, 169, 187, 188, 189, 193, 327, 336, 384, 385, 386, 389
SiO2 surface, 169
sites, 73, 74, 81, 345, 348, 349, 354
skin, 154, 258, 284
sleep, 248, 370
sleep disorders, 370
SMA, 254
smokers, 249
smoothing, 223
smoothness, 216
SNc, xii, 369, 372, 373
SNR, 73
sodium, 253, 352
software, 220, 231, 233, 238, 239, 241, 242, 243, 245, 255, 258, 275, 278, 296, 299, 304, 327
soil, 290
solid phase, 279, 280, 285, 290, 291
solid-state, 92, 133, 152, 396, 406, 411
solubility, 187, 197, 274
solutions, 108, 198, 232, 249, 259, 260, 264, 276
solvent, x, 122, 185, 186, 187, 197, 198, 199, 200, 201, 205, 238, 284, 385
solvent molecules, 200
solvents, 197, 198, 199, 200, 201, 274

soybean, 263
space environment, 417
space-time, 350
Spain, 3, 341, 342
spatial, xi, 81, 99, 111, 130, 132, 133, 293, 294, 297, 298, 309, 314, 315, 344, 347, 348, 350, 351, 352, 353, 354, 363, 364, 365
spatial frequency, 298
spatiotemporal, xi, 344, 348, 350, 360, 361, 362
species, 167, 168, 212, 213, 214, 250, 263, 271, 272
specificity, 255, 266
SPECT, 379
spectral analysis, 223, 275
spectral component, 336
spectrophotometric, 251, 295, 324, 325, 329
spectrophotometry, xi, 293, 324, 335
spectroscopic methods, 274
spectroscopy, x, 118, 123, 133, 143, 144, 154, 155, 161, 162, 181, 182, 236, 255, 263, 415
spectrum, 4, 5, 6, 90, 123, 129, 131, 169, 170, 172, 173, 175, 176, 177, 179, 181, 187, 228, 229, 231, 232, 233, 235, 236, 237, 238, 239, 241, 242, 244, 245, 246, 248, 249, 252, 255, 257, 259, 261, 266, 268, 271, 273, 274, 276, 277, 295, 325, 327, 335, 339, 346, 347, 349
speed, 74, 81, 88, 93, 132, 133, 146, 147, 148, 152, 186, 188, 230, 274, 304, 332, 339, 348, 365
sphincter, 374, 375, 380
spin, 122, 154, 186, 188, 189, 190, 198, 200
spinal cord, 70, 370, 371, 376
sputtering, 212
stability, viii, 70, 74, 76, 80, 81, 86, 117, 118, 152, 191, 251, 258, 260, 261, 262, 264, 265, 267, 270, 287, 407
stabilization, ix, 95, 96, 97, 98, 99, 103, 104, 109, 176
stabilize, 210
stages, 265
standard deviation, 66, 239, 303, 304, 337
standardization, 269, 270, 378
standards, 49, 50, 209, 241, 253, 254, 259, 262, 264, 265, 266, 268, 269, 277, 326, 339
state control, 74
statistics, viii, 45, 407, 409
statutory, 260
steady state, 89
steroid, 276, 290
steroid hormone, 276
steroid hormones, 276
stimulus, 90, 352
STM, 167
storage, xii, 51, 235, 238, 267, 272, 274, 288, 295, 331, 348, 349, 369, 370, 371, 372, 374, 375, 376, 378, 380
strategic, 294
strategies, 116, 282
stratification, 364
streams, 295
strength, 152, 239, 409
stress, 49, 51, 57, 58, 59, 60, 63, 67, 210, 211, 213, 214, 215, 221, 222, 223, 374
stress level, 49
stroke, 372
strong interaction, 120
structural characteristics, 361
structural defect, 120
structural defects, 120
subcutaneous injection, 375
substances, 4, 40, 248, 250, 256, 257, 260, 266, 268, 270, 276, 283, 295, 324, 325, 327, 329, 335, 337, 339
substantia nigra, xii, 369, 370, 371, 372, 373, 379, 380
substantia nigra pars compacta, 371, 372
substitution, 268, 270
substrates, 20, 40, 122, 123, 144, 162, 167, 168, 186, 187, 188, 190, 195, 384, 385, 392
subtraction, 238
suffering, 167
sugar, 269
sulfonylurea, 276
Sun, 43, 89, 91, 92, 207, 282, 286
sunlight, 265
superconductors, 220
supplements, 263
suppliers, 53, 274
supply, 265, 333, 390, 391
suppression, 20, 31, 42
surface area, 377
surface chemistry, 120, 145
surface energy, 186
surface modification, 118, 187
surface properties, 118
surface treatment, 177, 186, 187
surface water, 246, 275, 276, 290
surfactants, 275
surgery, 381
surprise, 166
surveillance, 260
suspensions, 143
Sweden, 341
switching, xii, 74, 81, 144, 145, 151, 185, 383
symmetry, 119, 120
sympathetic, 370, 371
symptom, 374, 380
symptoms, 295, 370, 373, 374, 375, 376, 377, 379, 380
synchronization, 331
synchronous, 88
synchrotron, 188, 189
syncytium, 358
syndrome, 350, 351, 358, 363, 364, 374, 379
synthesis, 5, 6, 16, 20, 118, 214, 223, 247, 254, 279, 282, 372, 379
systems, vii, ix, xi, 5, 73, 74, 90, 92, 93, 115, 116, 120, 128, 145, 147, 150, 153, 154, 254, 255, 265, 274, 294, 295, 308, 321, 325, 335, 340, 344, 345, 346, 347, 348, 357, 382

T

tachycardia, 351, 353, 358, 361
Taiwan, 383
tandem mass spectrometry, 250, 253, 280, 282, 284, 290
tantalum, 163
taxa, 250
Taylor series, 110
TCR, 43, 50
TdP, 358
technology, vii, viii, xii, 3, 6, 10, 16, 21, 30, 33, 40, 42, 43, 46, 51, 70, 116, 119, 133, 210, 214, 228, 235, 246, 257, 271, 277, 278, 295, 327, 339, 347, 348, 357, 383
Teflon, x, 209, 210, 218
TEM, 5, 9
temperature, xiii, 50, 51, 57, 58, 67, 81, 120, 147, 163, 186, 205, 211, 220, 231, 261, 262, 314, 332, 384, 385, 405, 411, 412, 414, 415
temperature dependence, 411
temporal, 343, 344, 347, 348
terminals, 231
test data, viii, ix, 45, 51, 55, 60, 63, 67, 95, 103, 104, 107, 108
tetracycline, 254, 260, 261, 262, 282, 283, 285, 286
tetracycline antibiotics, 285, 286
tetracyclines, 246, 258, 260, 261, 262
tetrahydrofuran, 187, 200, 385
Texas, 334
textile, vii, 314
textile industry, vii, 314
Thailand, 256
theory, 40, 92, 136, 175, 176, 213, 220, 330, 350
therapeutic benefits, 377
therapy, 248, 344, 370
thermal evaporation, 211, 214, 220, 385
thermal stability, 258
Thessaloniki, 227
thin film, vii, x, xii, 116, 161, 168, 172, 173, 175, 192, 194, 195, 383, 388, 393
thin films, 116
thoracic, 371
three-dimensional, 255, 344, 357
three-dimensional space, 255
threshold, 103, 108, 110, 173, 176, 177, 191, 193, 195, 201, 202, 204, 235, 238, 239, 240, 241, 268, 386, 390, 406, 417
threshold level, 241
thyroid, 248
thyroid gland, 248
time, viii, x, 16, 45, 47, 49, 51, 52, 54, 55, 56, 57, 60, 63, 65, 66, 69, 70, 72, 73, 74, 81, 88, 99, 109, 110, 111, 118, 119, 125, 132, 133, 135, 136, 137, 138, 141, 142, 143, 145, 149, 154, 167, 191, 192, 193, 194, 200, 212, 214, 219, 220, 221, 222, 227, 230, 231, 233, 235, 236, 238, 239, 241, 253, 255, 256, 259, 261, 262, 263, 264, 265, 266, 267, 269, 270, 272, 274, 275, 277, 295, 298, 328, 332, 334, 335, 347, 350, 353, 378, 398, 405, 410, 415, 416, 417
time resolution, 143, 416, 417
timing, 416
tin, 125, 210
tin oxide, 125
$TiO_2$, 134, 336
TIPS, x, 185, 197, 198, 199, 200, 201, 203, 204, 205
tissue, xi, 85, 91, 248, 260, 339, 343, 344, 345, 346, 351, 356, 357, 365
Titan, 124
title, 145
titration, 124
Tokyo, 161, 182, 340
toluene, 187, 198, 199, 200, 201
tomato, 258, 284
topology, 20, 33, 38, 82, 84
toxic, 260, 262, 270, 271
toxicity, 248, 269, 270, 290
toxicological, 241, 248, 249, 272, 275
toxicology, 272, 289
tracking, 231, 237, 247, 255, 283, 343
traction, 318
trade-off, 76, 81, 83
traditional medicines, 263
traffic, ix, 95, 96, 97, 102, 103, 104, 105, 108, 348
trajectory, 413, 414
*trans*, 132, 252, 419
transactions, 225
transfer, ix, xii, 116, 118, 119, 120, 125, 128, 130, 131, 133, 134, 136, 140, 143, 144, 147, 150, 154, 179, 182, 188, 190, 192, 193, 194, 200, 201, 204, 383, 385, 386, 388, 390
transformation, 28, 98, 99, 109, 111, 112, 240
transformations, 17, 340
transistor, xii, 74, 79, 83, 120, 168, 187, 188, 190, 194, 195, 201, 203, 344, 383, 385, 386, 387
transistors, vii, ix, x, xii, 76, 83, 115, 116, 117, 119, 120, 175, 185, 186, 190, 192, 194, 200, 202, 205, 383, 384, 386, 387, 388, 389, 390, 391, 392, 393
transition, 14, 18, 29, 37, 116, 173, 174, 176, 180, 181, 236, 343, 416
transitions, 309
translation, 99, 112
translational, 120
transmembrane, 343, 350, 351, 358, 359, 360, 361
transmission, 6, 7, 8, 9, 10, 11, 12, 13, 14, 18, 19, 20, 23, 24, 25, 26, 27, 29, 30, 31, 32, 33, 36, 37, 38, 40, 41, 43, 44, 70, 195, 310, 311, 328
transparency, 336
transparent, 4, 125, 133, 134, 135, 229
transport, vii, ix, xii, 107, 115, 116, 117, 118, 119, 120, 121, 128, 130, 144, 145, 146, 147, 148, 149, 150, 151, 152, 153, 154, 163, 190, 192, 210, 275, 383, 384, 385, 389, 390, 391
transport phenomena, 147
traps, x, 161, 172, 180, 205, 220, 384, 385, 391
travel, 132, 133, 153, 168
travel time, 132

trial, 335
tricyclic antidepressant, 246, 249, 279
tricyclic antidepressants, 246, 249, 279
triggers, 101, 363, 398
tritium, 406
tungsten, 229, 329, 347
tunneling, 123, 128, 148, 152, 153, 214, 220, 388, 389
two-dimensional (2D), 101, 187, 188, 189, 242, 255, 289, 346, 348, 350, 357

## U

ubiquitous, 131, 348, 355
ultra-thin, xii, 383, 384
Ultraviolet, x, 117, 123, 154, 161, 167, 168, 228, 229, 230, 232, 236, 241, 245, 246, 247, 248, 249, 250, 251, 252, 253, 256, 257, 258, 259, 262, 263, 264, 265, 266, 267, 268, 269, 270, 271, 272, 273, 276, 277, 278, 280, 281, 282, 284, 288, 289, 291, 336, 397, 398, 399, 400, 402
uncertainty, 132, 286, 306, 319, 350
uniform, 103, 136, 170, 172, 178, 198, 210, 217, 223, 302, 315
updating, 99
urea, 257, 276, 283
urethra, 370, 371
uric acid, 337, 339, 340
urinary, xi, xii, 280, 369, 370, 371, 372, 374, 377, 378, 379, 380, 381
urinary bladder, 381
urinary dysfunction, xii, 369, 372
urinary retention, 378
urinary tract, 370, 371, 378, 379, 380, 381
urine, 247, 248, 249, 250, 251, 253, 257, 258, 270, 273, 279, 280, 283, 289, 295, 326, 337, 338, 370, 376, 380
urology, 374, 378
Utah, 115
UV absorption, 236, 268
UV absorption spectra, 268
UV light, 167
UV radiation, 277
UV spectrum, 123, 229, 232, 236, 241, 246, 249, 257, 266, 268, 273, 276

## V

vacuum, 117, 119, 162, 163, 166, 169, 185, 187, 191, 192, 193, 194, 195, 385, 416
valence, 129, 131, 133, 151, 165, 166, 173, 179, 180, 181, 406
validation, 247, 252, 257, 258, 260, 279, 281, 283, 285, 286
validity, 267
values, ix, xii, 4, 27, 28, 29, 36, 40, 49, 50, 55, 60, 63, 83, 95, 99, 100, 103, 106, 107, 108, 109, 110, 111, 115, 138, 167, 170, 178, 182, 195, 220, 240, 241, 244, 260, 261, 262, 294, 301, 303, 304, 311, 312, 313, 337, 338, 347, 348, 374, 383, 386, 390, 400
van der Waals, 119
van der Waals forces, 119
vapor, 193
variability, 244, 265
variable, 20, 123, 151, 152, 248, 316
variables, 10, 247, 279
variance, 407
variation, 12, 13, 33, 66, 110, 205, 231, 294, 296, 299, 300, 302, 313, 314, 316, 317, 318, 319, 322, 323, 337, 339, 407
vector, 4, 5, 6, 99, 111, 113, 239, 242
vegetables, 263, 264
vehicles, 107
vein, 272
velocity, xiii, 5, 14, 32, 76, 110, 111, 148, 358, 362, 405
venlafaxine, 249, 250
ventricle, 363, 364
ventricles, 351, 360, 361, 363, 364, 365
ventricular arrhythmia, 363
ventricular arrhythmias, 363
ventricular fibrillation, 349, 358, 359, 361, 362, 363, 364
ventricular tachycardia, 351, 353, 358, 361
verapamil, 273
versatility, 344, 348
veterinary medicine, 257, 264, 272
Victoria, 227, 228, 230, 232, 234, 236, 238, 240, 242, 244, 246, 248, 250, 252, 254, 256, 258, 260, 262, 264, 266, 268, 270, 272, 274, 276, 278, 280, 282, 284, 286, 288, 290
vinegar, 246, 262, 286
vinification, 258, 271, 272
visible, 85, 135, 229, 295, 325, 326, 327, 328, 335, 339
vision, 96, 105
visual attention, 113
visual environment, 106
visualization, 298
vitamin A, 249, 279
vitamin C, 264
vitamins, 246, 248, 279
voiding, 370, 371, 374, 375, 376, 378, 380, 381
voids, 67
volatility, 258
voltammetric, 129
vulnerability, 354, 363, 364

## W

walking, 98, 101, 109
wastewater, 276, 290, 291

water, 86, 123, 193, 246, 257, 258, 260, 264, 265, 275, 276, 289, 290, 298, 300, 303, 304, 305, 306, 338, 339, 377
water vapor, 193
wave propagation, 4, 6, 9, 10
waveguide, 10, 41
wavelengths, 230, 236, 249, 258, 277, 296, 310, 327, 330, 349, 361, 408
wavelet, 363
wavelets, 350, 361
weakness, 51
wear, 55, 57
Weibull, 52, 54, 55, 56, 57, 60, 61, 64, 65
Weibull distribution, 52, 54, 55, 56, 57, 60, 64, 65
weight loss, 288, 370
wells, 186, 275
wettability, 198
wetting, 198, 298
windows, 310
wine, 246, 248, 258, 259, 262, 267, 271, 279, 286
wireless, 91
wires, 86
withdrawal, 261
WLAN, 42
women, 249, 374, 375
wood, 271, 272
workstation, 230
writing, 274

## X

xanthophyll, 269
xenon, 229
X-ray diffraction, 155, 188, 189, 198, 199, 200
X-ray photoelectron spectroscopy (XPS), 118, 123, 154, 155
X-rays, 406, 415
xylene, 187, 198, 199, 200, 201

## Y

yarn, xi, 293, 294, 296, 297, 298, 299, 300, 302, 303, 304, 305, 306, 307, 308, 309, 310, 311, 313, 314, 315, 316, 318, 319, 320, 321, 322, 323, 324, 338, 339
yield, ix, xiii, 46, 96, 336, 339, 395, 396, 397, 399, 400, 401
yield loss, 46
yolk, 261, 262, 285

## Z

Zone 1, 318